Miniaturization of Soft Robotic Control Systems and Actuators for Biomedical Applications

by

Run Ze Gao

A thesis
presented to the University of Waterloo
in fulfillment of the
thesis requirement for the degree of
Doctor of Philosophy
in
Mechanical and Mechatronics Engineering

Waterloo, Ontario, Canada, 2023

© Run Ze Gao 2023

Examining Committee Membership

The following served on the Examining Committee for this thesis. The decision of the Examining Committee is by majority vote.

External Examiner:	Daniel J. Preston Assistant Professor Department of Mechanical Engineering Rice University
Supervisors:	Carolyn L. Ren Professor Department of Mechanical and Mechatronics Engineering
	Clark. R. Dickerson Professor Department of Kinesiology and Health Sciences
Internal Members:	Jean-Pierre Hickey Associate Professor Department of Mechanical and Mechatronics Engineering
	James Y. Tung Associate Professor Department of Mechanical and Mechatronics Engineering
Internal-External Member:	Hamed Shahsavan Assistant Professor Department of Chemical Engineering

Author's Declaration

I hereby declare that I am the sole author of this thesis. This is a true copy of the thesis, including any required final revisions, as accepted by my examiners.

I understand that my thesis may be made electronically available to the public.

Abstract

Soft wearable robotics, a specialized branch of soft robotics, stands on the cusp of transforming the field of biomedical devices, particularly in the realm of assistive technology. This innovative approach offers a marked advantage over traditional rigid systems, owing to its inherent compliance and safety features that adapt seamlessly to the user's body. Despite these benefits, soft wearable robotics has faced significant challenges, particularly the often bulky control systems and actuators that have hindered its successful adoption beyond laboratory settings. This thesis seeks to tackle these obstacles head-on, striving to pioneer advancements in miniaturizing control systems and actuators without compromising performance.

By employing a synergy of fluidic dynamics, biomechanics, and user-centered design principles, the research explores two primary categories of advancements: technological and knowledge-focused. The technological advancements target the development of compact and efficient control systems and actuators, essential for real-world adoption. These breakthroughs encompass air microfluidics for sequential gradient control, monolithic sheets for smooth compression, closed-loop regenerative systems for gait-controlled systems, dynamic fluidic cushions, and low-profile actuators and layered toroidal-shaped soft fluidic sensors for prosthetic applications. Meanwhile, the knowledge-focused contributions offer insights into merging microfluidics with soft robotics, designing body-driven electronics-free wearables, and understanding user-centered design approaches. Furthermore, examples of refining and miniaturizing the geometry of soft fluidic actuators to align with established medical device form factors paves the way for more intelligent and seamless integration into existing healthcare technologies are provided. Together, these innovations paint a vivid picture of a future where soft wearable robots become integral to medical devices, enhancing both functionality and user experience.

The first section (Chapters 2, 3, 4, 5) of this thesis examines the promising synergy between microfluidics and soft robotics. It underscores the importance of miniaturization and exact control in areas such as wearable assistive technologies. Two innovative proof-of-concept designs are showcased: a microfluidics-enabled soft robotic sleeve for lymphedema treatment and a dynamically adaptable transtibial prosthetic socket liner. These inventions mark significant advancements in portability, affordability, and efficiency.

In the second section (Chapters 5, 6, 7), the focus shifts to the miniaturization of soft fluidic actuators and sensors, pioneering a breakthrough approach to lymphedema swelling management. By employing a layered arrangement of soft fluidic actuators, this work revolutionizes traditional lymphedema care. It further investigates a soft robotics-inspired dynamic fluidic cushion to alleviate high contact pressures in prosthetic limbs, illustrating its potential integration into prosthetist routines. Moreover, a specialized soft fluidic sensing system for transtibial prosthetic sockets is introduced to detect "pistoning" and vertical displacement of residual limb due to its volume fluctuation, especially useful for those with peripheral neuropathy. A unique feature of this section is the integration of the dynamic fluidic cushion and the soft fluidic sensing system into existing prosthetist workflows.

The third section (Chapter 8) introduces an innovative electronics-free soft robotic knee brace, tailored to alleviate symptoms of unicompartmental tibiofemoral osteoarthritis. Utilizing a closed-loop fluidic regenerative system (CLFR), the brace selectively applies pressure, harnessing body weight to control forces at the knee during different gait phases. Comprising a commercial knee brace, spring-loaded shoe insert, and soft-fluidic actuator, the system underwent rigorous testing in a 60-90 kg body weight range. The tests affirmed the CLFR's synchronization with natural gait and validated its suitability for prolonged skin contact, displaying response times between 250 ms and 400 ms with minimal pressure loss.

The fourth and final section (Chapter 9) outlines a comprehensive laboratory exercise for biomedical engineering students. It details the creation and assessment of a hybrid soft-rigid active finger prosthetic, equipped with a miniaturized, low-profile bellows-style soft fluidic actuator. Skillfully blending mechanical, electrical, and sensor technologies, the lab offers a versatile learning experience that aligns with various educational trajectories. Utilizing cost-effective open-source components, the course engaged 40 undergraduates and was lauded for its immersive methodology. Connecting theory with practice, the lab encourages future expansions into clinical and technical fields, thus enhancing educational enrichment.

In summary, this thesis represents a comprehensive exploration of soft wearable robotics, microfluidics, and biomedical engineering intersections. It contributes vital technological innovations in miniaturization and insights that have the potential to forge new paths for more accessible and effective biomedical solutions.

Acknowledgements

First and foremost, I extend my profound gratitude to my supervisor, Professor Carolyn Ren, whose belief in my abilities made this project possible. She provided me the invaluable opportunity to work under her expert guidance, demonstrating unwavering support and taking a risk on this work. Her faith in my capacity to execute, coupled with her rich knowledge and experience, has been instrumental in every phase of my academic journey towards the completion of my degree.

I must also extend my heartfelt appreciation to my co-supervisor, Professor Clark Dickerson, whose insights and encouragement have been nothing short of inspiring. He recognized the potential in this research, continuously fueling it with innovative ideas and encouraging a perspective that transcended conventional boundaries.

I wish to express my heartfelt thanks to both of my supervisors for their combined wisdom, advice, and guidance. Their patience and relentless pursuit of excellence have been the guiding lights throughout this period, and I am immeasurably grateful for their contribution to my growth and success as a researcher and a leader.

I also wish to thank Professor James Tung, who graciously welcomed me into his research environment, providing a stimulating platform and space to venture into unexplored territories of thought and innovation. He also entrusted me with teaching a fourth-year engineering course, an opportunity that has been a transformative milestone in my academic journey and professional development.

I would also like to thank Professor Monica Maly, who expertly guided me into the clinical aspects of biomedical devices. Her insight and encouragement have not only deepened my understanding but have also provided steadfast support when it was needed most.

I extend my sincere gratitude to the distinguished members of both my comprehensive exam committee and my Ph.D. defense committee: Professor Daniel Preston, Professor Jean-Pierre Hickey, and Professor Hamed Shahsavan. Their valuable time and insights are greatly appreciated.

My academic journey would not have been as enriching and fulfilling without the collective support of the members from the Waterloo Microfluidics Lab, Neural and

Rehabilitation Engineering (NRE) Lab, Digital Industrial Ergonomics and Shoulder Evaluation Laboratory (DIESEL), and Mobilize Clinical Biomechanics Lab. I would like to express my deep gratitude to my fellow colleagues and collaborators: Peter Lee, Vivian Mai, Jordan Savage, Jacqueline Kormylo, Alyson Colpitts, Christian Mele, Aravind Ravi, and Dr. Kendal Marriott. A special note of thanks must be extended to Peter Lee, whose belief in me and willingness to stand beside me during the most trying times has been a beacon of support.

I would like to thank Dr. Matthew Courtney, Wasim Kapadia, and Professor Marie Hébert, who accompanied me on the intricate and often arduous journey of graduate studies. Their camaraderie, understanding, and emotional support have been pillars of strength that made the path more navigable and rewarding.

I extend my thanks to several key contributors who attended group meetings and enriched my work with valuable input: Dr. Weijia Cui, Dr. Pei Zhao, Dr. Ning Qin, Dr. Anna Nguyen, Jeff Farnese, Anson Lau, Noura Ezzo and Yiqi Zhang.

The success of this work owes a great deal to the dedication of the undergraduate co-op students. Serving as the backbone of the lab, their commitment and enthusiasm have not only been instrumental in the research but have also inspired me to reach greater heights. It was truly a privilege to work alongside such an extraordinary group of individuals, each of whom has left an indelible mark on this work. In the order that I had the honor to collaborate with them, I extend my heartfelt gratitude to: Lucas Pilozo-Hibbit, Peter Lee, Vivian Mai, Nick Levinski, Drew Werbowski, Reagan Elizabeth Anderson, Chelsea Huang, Paul Chang, Maya Rukavina-Nolsoe, Marley O'Connell, Jacob Dupui, Amanda Johnson, Adam Yu, Kelly Lu, Rhys Cornelious, Sarah Dykstra, Cameron Sjaarda, and Joanne Jo.

I thank the National Sciences and Engineering Research Council, Government of Ontario, Waterloo Institute for Nanotechnology, University of Waterloo Faculty of Engineering and the Department of Mechanical and Mechatronics Engineering, Praxis Spinal Cord Institute, Centre for Bioengineering and Biotechnology, FACIT, Abbotsford Community Foundation for the financial support in the form of grants and scholarships. I would also like to thank Professor Carolyn Ren for her financial support.

Finally, I am deeply grateful for all the love and support from my family and friends. In particular, I would like to thank my parents, Bo and Lin.

Dedication

to

my parents

Table of Contents

List of Figures xvi

List of Tables xliii

Chapter 1 Introduction 1

1.1 Background and Motivation 1

1.2 Thesis Outline 7

Chapter 2 Literature Review and Perspective 11

2.1 Introduction 11

2.1.1 Independent Functioning Soft Robots 11

2.1.2 Soft Wearable Robots 13

2.1.3 Soft Actuators 14

2.2 Motivation to Bring in Microfluidics 17

2.2.1 Miniaturization 17

2.2.2 Case Study of the Soft Robotic Glove 18

2.2.3 Low-Profile, High Resolution and Digitization 19

2.3 Concerning Actuation and Sensing 21

2.3.1 Power Source for Actuation 21

2.3.2 Flow Control for Actuation 23

2.3.3 Flow Regimes and Significance for Soft Robots 26

2.3.4 Microfluidics and Interfacing with Soft Robots 32

2.4 Concerning Applications 40

2.4.1 Daily Quality of Life 40

2.4.2 Prosthetic Applications 42

2.4.3 Sports and Safety Apparels 43

2.4.4 Haptics 44
2.4.5 Pediatrics 45
2.4.6 Medical Instrumentation (Minimum Invasive Surgery) 45
2.4.7 Educational Tools 47
2.4.8 Pressure Mapping 47
2.4.9 Sensory Testing 47
2.4.10 Human-Machine Interaction 48
2.5 Concerning Aesthetics and Ease of Use 49
2.5.1 Factors for User Adoption 50
2.5.2 Social Acceptance and User Perception 51
2.5.3 Wearability 53
2.5.4 A Few Last Comments of User Adoption 53
2.6 Concluding Remarks 55
Chapter 3 Investigating Miniaturization of Soft Robotic Control Systems Using Passive Air Microfluidics with Applications for Sequential Gradient Compression 56
3.1 Introduction 56
3.2 Air Microfluidic Chip Concept 60
3.3 Simulations 62
3.4 Fabrication 65
3.4.1 Air Microfluidic Chip 65
3.4.2 Air Bladders and Pneumatic Active Compression Sleeve (Lymphedema Sleeve) 65
3.5 Methods 66
3.5.1 Internal and External Pressure Measurements 70
3.5.2 Channel Selection Tests 70

3.6 Results and Discussion 71
3.6.1 Channel Selection Tests 71
3.6.2 Gradient Pressure, Sequential Inflation, Uniform Deflation Tests 73
3.6.3 Limitations and Future Considerations 76
3.7 Concluding Remarks 77
Chapter 4 Investigating Air Microfluidics for Dynamically Fitting Prosthetic Sockets 78
4.1 Introduction 78
4.2 Design Rationale and Fabrication 82
4.2.1 Liner and Soft Actuator Array 82
4.2.2 Air Microfluidic Chip 86
4.2.3 Control Logic and Detailed Explanation of Valve Closure by Utilization of Closing Delta Pressure 90
4.2.4 Residual Limb/Socket Fabrication and Setup 91
4.3 Methodology and Test Setup 92
4.4 Results and Discussion 94
4.4.1 Chip Pressure Response 94
4.4.2 Contact Pressure Test Results 96
4.4.3 Limitations 99
4.5 Concluding Remarks 99
Chapter 5 Investigating Active Air Microfluidics with Overlapping Soft Fluidic Actuators for Smooth Sequential Gradient Compression 100
5.1 Introduction 100
5.2 Design Rationale and Fabrication 104
5.2.1 Air Microfluidic Chips 104
5.2.2 Controlling Active Air Microfluidic Chips 108

5.2.3 Overlapping Soft Fluidic Actuators and Strain-Limiting Layer 114
5.2.4 Testing Setup 120
5.3 Results 123
5.3.1 Performance of Monolithic Sheet of Overlapping Soft Fluidic Actuators 123
5.3.2 Performance of In-Line Air Microfluidic Chips 126
5.3.3 Performance of Combined Air Microfluidic Chips 130
5.4 Discussion 132
5.4.1 Monolithic Sheet of Overlapping Soft Fluidic Actuators 133
5.4.2 Active Air Microfluidic Chips 136
5.4.3 Limitations 142
5.5 Concluding Remarks 142
Chapter 6 Investigating Miniaturization of Soft Robotic Actuators for Prosthetic Socket Fitting 144
6.1 Introduction 144
6.2 Methods and Materials 149
6.2.1 Biofidelic Residual Limb 149
6.2.2 Soft Robotics-Inspired Low-Profile Dynamic Fluidic Cushion 149
6.2.3 Control Box 154
6.2.4 Testing Setup 155
6.3 Results 158
6.3.1 Weighted Tests 158
6.3.2 Static Standing Tests 158
6.3.3 Dynamic Gait Tests 158
6.4 Discussion 159

6.4.1 Limitations of the Study 162
6.5 Conclusion and Future Work 163
Chapter 7 Investigating Miniaturization of Soft Robotic Sensor for Prosthetic Socket Fitting 164
7.1 Introduction 164
7.2 Methods and Materials 168
7.2.1 Fabrication of Multi-Layered Torus-Shaped Balloon 168
7.2.2 Testing Setup 169
7.3 Results and Discussion 171
7.3.1 Water Versus Air 171
7.3.2 Optimal Layer Count for Layered-Donut Balloons 173
7.3.3 Cyclic Loading and Precision 174
7.3.4 Step-Loading, Hysteresis, and Long-Term Stability 177
7.3.5 Limitations 177
7.4 Conclusion and Future Work 179
Chapter 8 Investigating Miniaturization of Control System for Dynamic Knee Brace Using Gait 180
8.1 Introduction 180
8.2 Disadvantage of Active Controlled Systems 182
8.3 Design Rationale 188
8.4 Methodology 191
8.4.1 Fabrications 191
8.4.2 Mechanical Testing Setup 193
8.4.3 On-body Testing Setup 196
8.5 Results 199

8.5.1 Peak Contact Pressure 199
8.5.2 Total Contact Force 202
8.5.3 Response Time 202
8.5.4 Energy Loss 203
8.5.5 Durability 205
8.5.6 Preliminary On-Body Trials 205
8.6 Discussion 207
8.6.1 Benchtop Testing 207
8.6.2 Preliminary On-Body Trials 211
8.6.3 Limitations 212
8.7 Concluding Remarks 213
Chapter 9 Miniaturization of Hybrid Soft-Rigid Active Prosthetics for Hand-on Biomedical Engineering Education 214
9.1 Introduction 214
9.2 Lab Content 217
9.2.1 Problem Background 217
9.2.2 Prosthetic Finger Design (Mechanical System) 218
9.2.3 Fabrications and Mechanical Assembly 221
9.2.4 Sensors and Wiring (Electrical System) 223
9.2.5 Software 226
9.2.6 Bill of Materials 226
9.2.7 Testing and Deliverables 229
9.3 Student Feedback 232
9.3.1 Lab Specific Survey 232

9.3.2 University Student Course Perception 233
9.4 Discussion 233
9.4.1 How the Lab Fits in BME 233
9.4.2 Takeaways from the Pilot 236
9.4.3 Limitations 238
9.4.4 Future Improvements 239
9.5 Concluding Remarks 239
Chapter 10 Conclusion and Recommendations 241
10.1 Contribution of this Thesis 241
10.2 Future Work 245
References 247
Appendix A 278
Appendix B 286
Appendix C 291
Appendix D 302
Appendix D-1 314
Appendix E 315
Appendix F 322
Appendix F-1 322
Appendix F-2 341
Appendix F-3 349
Appendix F-4 357
Appendix F-5 357

List of Figures

Figure 1.1: Fluid Circuit performs the operation of dividing by 10 in an all-fluid digital computer: for every 10 input pulses circuit delivers one output pulse. Input pulses enter from above the plane of circuit through circular, bump like hole attached to straight channel running from top to bottom just to right of center. The 10 identical logic elements, or modules, are arranged in a series of five pairs, three at left and two at right. Each pair contains two steady input 80 streams (small sausage shapes), two outputs (small circular shapes attached to short straight channels), eight control jets (small tear· drop shapes) and eight open vents (large circular shapes). Shallow channels were chemically etched in Dycril plastic by a special process, called Optiform, developed by Bowles Engineering Corporation. For this photograph the channels were filled with white paint to increase the contrast. Normally the working fluid is air. [15] 2

Figure 1.2: Tightened by Artificial Muscle (McKibben Type) leading down arm and finger of a paralyzed girl grasp and hold a pen. [15]..... 3

Figure 1.3: Tree diagram categorizing different types of wearable assistive devices. 5

Figure 2.1: Soft robotic grippers reproduced with permission from Angew. Chemie - Int. Ed. 50, 8 (2011). Copyright 2011, John Wiley & Sons. [12] (b) Bellows-type gripper collecting soft coral; K. C. Galloway et al., Soft Robotic Grippers for Biological Sampling on Deep Reefs, Soft Robot., 3, DOI: 10.1089/soro.2015.0019, 2016; licensed under a Creative Commons Attribution (CC BY) license. [50] (c) A soft robot lengthens through various challenging constrained environments without active control. Instead, the robot passively deforms to navigate the obstacles; reproduced with permission from Sci. Robot. 2, 8 (2017). Copyright 2017, The American Association for the Advancement of Science. [53] (d) Stiffness controllable flexible & learnable manipulator for surgical operations performing bending and elongation; reproduced with permission from IEEE Trans. Robot. 32, 1 (2016).

Copyright 2016, IEEE. [54] (e) Details of a soft-bodied robotic fish; A. D. Marchese et al., Autonomous Soft Robotic Fish Capable of Escape Maneuvers Using Fluidic Elastomer Actuators, Soft Robot., 1, DOI: 10.1089/soro.2013.0009, 2014; licensed under a Creative Commons Attribution (CC BY) license. [51] (f) Image showing the resilience of the untethered soft robot to snow conditions; reproduced with permission from Soft Robot. 1, 3. (2014). Copyright 2014, Mary Ann Liebert, Inc. [52] 12

Figure 2.2: Examples of soft wearable robots: (a) soft wearable glove for post-stroke rehabilitation reproduced with permission from Rob. Auton. Syst. 73 (2015). Copyright 2015, Elsevier. [55] (b) Soft exosuit for post-stroke rehabilitation reproduced with permission from Sci. Transl. Med. 9, 400 (2017). Copyright 2017, The American Association for the Advancement of Science. [24] (c) Soft wearable robot for the shoulder reproduced with permission from Proc. - IEEE Int. Conf. Rehabil. Robot. 02129 (2017). Copyright 2017, IEEE. [34] (d) Soft wearable device for mechanotherapy reproduced with permission from Proc. - 2018 IEEE International Conference on Robotics and Automation (2018). Copyright 2018, IEEE. [57] (e) Soft modular knee sleeve for assisting walking reproduced with permission from Proc. - IEEE Int. Conf. Robot. Autom. (2018). Copyright 2014, IEEE. [59] 14

Figure 2.3: (a) 3D modeling representation of the molds for casting a soft robotic gripper; reproduced with permission from IEEE Int. Conf. Intell. Robot. Syst. (2015). Copyright 2015, IEEE. [70] (b) The heat press lamination fabrication approach to making a soft robotic glove; reproduced with permission from Extrem. Mech. Lett. 27 (2019). Copyright 2019, Elsevier. [35] 16

Figure 2.4: (a) Soft robotic glove based on a pneumatic network SFA; reproduced with permission from IEEE Int. Conf. Intell. Robot. Syst. (2013). Copyright 2013, IEEE. [77] (b) Soft robotic glove based on fibre-reinforced and sleeved SFA; Cappello et al., J. Neuroeng. Rehabil., 15, 59, 2018; licensed under a Creative Commons Attribution (CC BY) license. [23] (c) Soft robotic glove based on

sew-free anisotropic textile composites; reproduced with permission from Extrem. Mech. Lett. 27 (2019). Copyright 2019, Elsevier. [35] 18

Figure 2.5: Concept image showing the difference in profile between a single large bladder constrained by a high stretch strain-limiting fabric (top left), a single large bladder constrained by a low stretch strain-limiting fabric (bottom left), miniaturized bladders constrained by a low stretch strain-limiting fabric (top right), and miniaturized bladders constrained by a low stretch strain-limiting fabric on a curved substrate (bottom right). 19

Figure 2.6: Schematic representation of the frontend and backend of a generic soft wearable robot. Please note that the images of the components are not to scale and only serve as a generic visual representation of each component. 22

Figure 2.7: A 3D scale diagram of the pneumatic in-line microvalve developed by Unger et al., often referred to as Quake's valve; reproduced with permission from Science 288, 5463 (2000). Copyright 2000, The American Association for the Advancement of Science. [86] 25

Figure 2.8: (a) Centerline pressure distribution normalized with outlet pressure Pout. Solutions are compared for the slip and no-slip conditions for five different pressure ratios ($Pr = Pin/Pout$). (b) Centerline velocity distribution normalized with the speed of sound at the inlet Cin. Solutions are compared for the slip and the no-slip conditions the five different pressure ratios ($Pr = Pin/Pout$). Both (a) and (b) are reproduced from [Roy et. Al., "Modeling gas flow through microchannels and nanopores," *J. Appl. Phys.*, vol. 93, no. 8, pp. 4870–4879, 2003], with the permission of AIP Publishing. [93] 29

Figure 2.9: a) Helium mass flow for 1.33 μm channel (95% confidence intervals indicated). The solid curve is the solution to Equation 5, assuming full tangential momentum accommodation, and the dashed curve is the solution to Equation 5 setting Knudsen number to zero (no-slip solution); reproduced with permission from J. Microelectromechanical Syst. 6, 2 (1997). Copyright 1997,

IEEE. [94] b) The comparison of pressure drop with experimental results and 2-D analytical solutions (Equation 5); reproduced with permission from Int. J. Heat Mass Transf. 47 (2004). Copyright 2004, Elsevier. [95]..... 30

Figure 2.10: (a) Viscous flow in the tubes interconnecting the constituent actuators to design soft robots capable of achieving a variety of responses when inflated with a single pressure input; reproduced with permission from Soft Robot. 7, 1 (2020). Copyright 2020, Mary Ann Liebert, Inc. [98] (b) A soft ring oscillator composed of three inverters connected in a loop, resulting in a systematic instability (because no stable state exists); reproduced with permission from Sci. Robot. 4, 31 (2019). Copyright 2019, The American Association for the Advancement of Science. [99] (c) By tuning the nonlinear properties of the actuators with intermediate flow restrictions, a single fluidic supply tube can be used without the need for internal valves to actuate a soft robot; reproduced with permission from Adv. Mater. 31, 3 (2018). Copyright 2018, John Wiley & Sons. [100] (d) Schematic picture of a serial chain of elastic chambers with a single inlet; reproduced with permission from Soft Robot. 7, 2 (2020). Copyright 2020, Mary Ann Liebert, Inc. [101]..... 31

Figure 2.11: (a) Simulation demonstrating the concept of the path of least resistance with parallel microchannels. (b) the exit velocities of the microchannels shown in (a). 33

Figure 2.12: (a) Multimaterial multinozzle 3D printheads reproduced with permission from Nature 575, 7782 (2020). Copyright 2020, Springer Nature. [106] (b) Fabrication of milliscale soft grippers via ultraviolet ozone bonding of PDMS and Mylar sheets; reproduced with permission from Adv. Mater. 30, 7 (2018). Copyright 2018, John Wiley & Sons. [108]..... 34

Figure 2.13: (a) Off-the-shelf piston-diaphragm pump integrated with a control box/backend. (b) Custom low-profile control box/backend by using smaller coreless DC motors with integrated piston-diaphragms in parallel or series..... 36

Figure 2.14: (a) Fully soft strain sensor reproduced with permission from IEEE Sens. J. 12, 8 (2012). Copyright 2012, IEEE. [114] (b) Soft strain sensors placed at each lower limb joint to capture motion in the sagittal plane; reproduced with permission from Int. J. Rob. Res. 33, 14 (2014). Copyright 2014, SAGE Publications. [115] (c) Photos of the sensor illustrating stretching at approximately 0 and 100% strain; reproduced with permission from Adv. Mater. Technol., 2, 9 (2017). Copyright 2017, John Wiley & Sons. [116] 38

Figure 2.15: Concept images showing digitized soft fluid actuator/microfluidics enabled soft robotic sensors arranged in a tight array (a) for sensing compression and normal forces and (b) torque. (c) Concept image showing of incorporating soft organic sensors or small piezoresistive sensors within a digitized soft fluidic actuator/soft microfluidic sensor. 39

Figure 2.16: (a) Pneumatic inflatable inserts used in limb prosthetics, including the Air Contact System, PNEU-FIT, Pump It Up!, and Pneumatic Volume Control System; reproduced with permission from J. Rehabil. Res. Dev. 38, 4 (2001). Copyright 2001, Department of Veterans Affairs. [126] (b) Pneumatic actuator inserts for interface pressure mapping and fit improvement in lower extremity prosthetics; reproduced with permission from Proc. IEEE RAS EMBS Int. Conf. Biomed. Robot. Biomechatronics (2016). Copyright 2016, IEEE. [127] (c) Rendering of smart variable geometry socket (SVGS) technology applied to a transfemoral suction socket; reproduced with permission from J. Prosthetics Orthot. 15, 3 (2003). Copyright 2003, Wolters Kluwer Health, Inc. [128] (d) Socket insert having a bladder system (U.S. Patent 7.655,049 B2) [129]. 43

Figure 2.17: (a) HaptX microfluidic skin; Copyright 2020, HaptX Inc. [64] (b) The feedback control loop of the soft haptic system. The SPA-skin provides a highly conformal interface. A strain sensor of stretchable metallization can be used as the input to a feedback loop used to control the actuator inflation and exerted force. High-speed data acquisition allows strain sensing and actuation

over a range of actuation frequencies from 0 to 100 Hz; reproduced with permission from Soft Robot. 7, 1 (2020). Copyright 2020, Mary Ann Liebert, Inc. [130] 44

Figure 2.18: 3D structure through the injection-induced self-folding; reproduced with permission from Adv. Mater. 30, 38 (2018). Copyright 2018, John Wiley & Sons. [133] 46

Figure 2.19: Relative importance of aesthetics and ease of use for soft wearable robotics to achieve user acceptance and adoption..... 50

Figure 2.20: The technology acceptance model extended to account for psychological attachment; reproduced with permission from Proceedings of the 32nd Annual Hawaii International Conference on Systems Sciences (1999). Copyright 1999, IEEE. [144] 52

Figure 2.21: Guidelines for wearability reproduced with permission from Int. Symp. Wearable Comput. Dig. Pap. (1998). Copyright 1998, IEEE. [47] 53

Figure 3.1: Proof-of-concept rendering of the air microfluidics-enabled soft robotic sleeve toward lymphedema treatment. The construction of the system is shown by an isometric view of the entire system, a top cross-sectional view of the sleeve, a schematic view showing the routing of the tubing, and a close-up view of the air microfluidic chip. The miniature air pump and the two miniature 3/2-way solenoid valves control the airflow in and out of the air microfluidic chip, providing sequential inflation and uniform deflation for the soft air bladders. The soft air bladders apply intermittent gradient compression with the outer strain- limiting layer's help, directing the forces inward onto the forearm. The air bladder actuator closest to the wrist inflates first, followed in sequence by the air bladder above it, with the air bladder closest to the elbow inflating last. Once all the air bladders are inflated, the miniature air pump actively deflates the air bladders evenly. 59

Figure 3.2: An eight-channel air microfluidic chip design concept schematic. The sequential inflation manifold portion (red color) enables sequential inflation and gradient pressure of eight air bladders. The uniform deflation manifold portion (cyan color) enables uniform deflation of the eight air bladders. The arrows show the direction of the flow, and the size of the arrows represents the relative flow rate of each channel. Please note that the arrows are not to scale. 61

Figure 3.3: (a) Simulated steady state fluid flow path through the channels. (b) Plot of the exit velocities of each channel. 64

Figure 3.4: System schematics showing the inflation and deflation cycles. (a) Inflation cycle with red lines marking the airflow pathway and arrows showing the direction of flow. Both 3/2-way solenoid valves are off/de-energized during the inflation cycle, allowing the miniature air pump to transport air from the ambient atmosphere through the inflation chip to the air bladders within the lymphedema sleeve. (b) Deflation cycle with cyan lines marking the airflow pathway and arrows showing the direction of flow. Both 3/2-way solenoid valves are on/energized during the deflation cycle, allowing the miniature air pump to transport air from the air bladders within the lymphedema sleeve through the deflation chip to the ambient atmosphere. The pressure sensor in the system schematics provides feedback to control inflation and deflation cycles by measuring the pressure at the outlet of the miniature air pump. 67

Figure 3.5: (a) Step-by-step fabrications method for creating the air microfluidic chips. Step 1 involves SLA 3D printing of the chip mold. Step 2 involves inserting the stainless-steel tubing to create horizontal connection points for the tubing connecting to the lymphedema sleeve. Step 3 involves pouring PDMS (Sylgard™ 184) mixed at 10:1 ratio into the mold and fully cure. Step 4 involves taking out the cured PDMS and plasma bond with another PDMS slab to create the air microfluidic chip. The PDMS slabs are placed inside an air plasma chamber for 1 minute and 30 seconds (time varies depending on plasma chamber type and power) and quickly taken out and bonded by firmly pressing

the two PDMS slabs together for 30 seconds. Step 5 involves cutting off the excess PDMS from the air microfluidic chip, thus making it smaller. Step 6 involves inserting the connection tubing, which is used to connect to the lymphedema sleeve. (b) Step-by-step fabrications method for creating the lymphedema sleeve. Step 1a and step 1b involve heat pressing the elastic TPU sheets to skin contact fabric and strain-limiting fabric layers. Step 2 involves heat pressing both elastic TPU/fabric sheets and an aluminum template to create the lymphedema sleeve structure with internal soft air bladders. The aluminum template conducts heat sealing the two elastic TPU sheets together, creating the seams of the soft air bladders, and the cutouts within the aluminum template become the internal chambers of the soft air bladders. Step 3 involves inserting and gluing the tubing that connects the lymphedema sleeve with the air microfluidic chip—one tubing per soft air bladder. Step 4 involves rolling the flat sleeve into a tapered cylinder, and heat pressing the elastic TPU seam closed, creating the elastic pull-on lymphedema sleeve for the forearm. 68

Figure 3.6: (a) Component layout schematic of the test setup. A custom PCB with 16 pressure sensors (Adafruit MPRLS) was used to measure each air bladder's internal pressure within the lymphedema sleeve. A Tekscan sensor (9811E) was used to map the actual pressure applied to the forearm model, which was 3D printed. (b) Photo of the prototype control box electronics including an air pressure sensor (Adafruit MPRLS) connected at the outlet of the miniature air pump (Adafruit Product ID: 4699) for control feedback, two motor drivers (Sparkfun TB6612FNG) used to switch the miniature air pump and 3/2-way solenoid valves (uxcell from Amazon.ca) on/off, and an Arduino Nano Every microcontroller to manage all the electronic components. (c) Photo of the miniature air pump, two 3/2-way solenoid valves. (d) Photos of the air microfluidic chips and their mold model. (e) The deflated lymphedema sleeve was wrapped over the forearm model with tubing from each air bladder connected to the air microfluidic chips. (f) Photo of the inflated lymphedema sleeve. (g) The top view of the lymphedema sleeve wrapped over the forearm model shows the Tekscan sensor's placement sandwiched between the

lymphedema sleeve and the forearm model. (h) close-up view of the inflated air bladders within the sleeve. 69

Figure 3.7: Channel selection test air microfluidic chip with 16 parallel channels ranging from 1000 μm down to 50 μm. 71

Figure 3.8: Testing to determine the range of channels to use for sequential and gradient inflation Plot of time versus microchannel characteristic length to reach (a) 100 mbar, (b) 200 mbar, (c) 300 mbar, internal air bladder pressure. Square microchannels of 15 mm length with characteristic length ranging from 1000 μm down to 50 μm were used. The air bladders are of the same size at 120 ml. All microchannels are arranged in parallel fashion on the same air microfluidic chip. The inlet pressure is set to a constant 400 mbar. 5 data points per channel per plot are collected with error bars shown. 72

Figure 3.9: Gradient pressure, sequential inflation, and uniform deflation test were all conducted with the wearable control box shown in Figure 5. (a) Plot showing the gradient pressure of all eight air bladder's internal pressure with corresponding air microfluidic chip channel width after 7 seconds of inflation. (25 data points per air bladder) (b) Plot showing the sequential inflation and uniform deflation of 8 air bladders within a lymphedema sleeve over a 14 second period. (7 seconds inflation and 7 seconds of deflation. (c) Plot showing five iterations of inflation/deflation cycles, which demonstrates the robustness of the air microfluidic chip. (d) The flow chart showing the control schematic of the air microfluidics-enabled lymphedema sleeve system. A single air pressure sensor is connected at the outlet of the miniature air pump, providing pressure reading feedback. If the pressure sensor reading is equal to or above 100 mbar signals that all the air bladders have reached their prescribed pressure and the sequential inflation cycle ends, both 3/2-way solenoid valves open to start the deflation cycle. If the pressure sensor reading is equal to or below 0 mbar, the air bladders have been completely deflated to ambient pressure, and

the uniform deflation cycle ends. The whole process repeats until the end of the lymphedema treatment. 75

Figure 3.10: (a) Measured pressure data showing sequential inflation, uniform deflation, and gradient pressure of the actual compression applied to the arm as captured by the Tekscan sensor with 0.02 s temporal resolution and 1 mbar pressure resolution; and (b) snapshots of Tekscan pressure mapping at every second interval with corresponding images of the actual lymphedema sleeve being sequentially inflated and uniformly deflated. 76

Figure 4.1: Proof-of-concept rendering (left) and picture of the prototype (right) of the air microfluidics-enabled soft robotic transtibial prosthesis for automated residual limb volume fluctuation management. The isometric view shows the entire system, including the prosthesis, the air microfluidic chip, the soft fluidic actuator array and liner, and the wearable control box. 1) air microfluidic chip integrated with 10 pneumatic on-chip valves to control air pressure within each soft fluidic actuator. Different shades of cyan color represent different pressures; 2) 10 soft fluidic actuators situated in between the prosthetic socket and residual limb to apply appropriate compression towards different anatomical locations of the residual limb regardless of residual limb volume fluctuation, minimize the risks of ulcerations and improves comfort. Different shades of cyan color represent different pressures suitable for different anatomical locations; 3) wearable control box including a miniature air pump, two 2/2-way solenoid valves to provide air flow to the microfluidic chip; 4) prosthetic socket holding and supporting the residual limb; 5) fabric liners between the soft fluidic actuators and skin for comfort; and 6) tubing for air transport. 81

Figure 4.2: Overall schematic of the fabrication process. 1) Liquid PDMS is first brushed onto a TPU sheet and hang vertically to drip to become a thin layer (~100 μm) and left on a flat surface to cure. 2) Using a computer-controller cutter, shapes of the PDMS-TPU insert, TPU sheets, and skin-contact fabric are generated.

The insert of each section is cut out as individual pieces and manually placed on top of the base elastomer layer sheet. 3) Skin contact fabric and the base elastomer (TPU) layer are first heat pressed together. Then PDMS-TPU inserts and the top TPU layers are placed over the base elastomer layer and heat pressed altogether. A removeable tab is also placed on top of the PDMS side of the insert to reserve an opening for the tubing. 4) Upon insertion of silicone tubing, removal of the tab, and sealing of the tubing with glue, 5) the flat liner with the actuator array is revolved to form a shape of a tapered cylinder. 84

Figure 4.3: Design of the position and target contact pressures of the soft fluidic actuator array based on general anatomical locations of the transtibial residual limb. 85

Figure 4.4: (a) Schematic of pneumatic control hardware for controlling the on-chip valves in air microfluidic chip and (b) Samples of pneumatic hardware components used to make this system wearable. A Canadian quarter is presented here as a reference of size comparison (diameter of 23.88 mm). 86

Figure 4.5: Each layer of the air microfluidic chip is fabricated separately and assembled via plasma bonding. The fluid channel layer and the valve control layer are made by replica molding of PDMS with a 3D-printed mold using Formlabs Form 3. The membrane layer is made by spin coating Sylgard™ 184 at 10:1 ratio on the surface of a Mylar film, in which the PDMS membrane can then be delaminated after cured. Specifically, 100 um membranes are obtained by spin coating at 1000 RPM for 30 seconds [205]. The three layers are then bonded using air plasma. 88

Figure 4.6: (a) Schematic diagram of the air microfluidic chip designed in this research. The fluid channel layer has a common inlet with a total of 10 outlets, each connected to a soft fluidic actuator. The control layer has common inlet to pressurize and deflect the membrane at the valve locations. (b) Labeling of the on-chip valve numbers and the corresponding actuator number that each on-chip valve is connected to. (c) Cross-section view along on-chip valve 1 and valve 6, with both valves at normally-opened state. The pressure difference

between the control layer and the fluid channel layer is insufficient to close both valves. (d) Upon further increasing the pressure in the control layer, the pressure difference is larger than the pre-designed ΔP_{close} of valve 1 and hence the membrane is fully deflected into fluid channel layer, obstructing the flow at valve 1 location and isolating actuator 1. The same pressure difference is, however, lower than the pre-designed ΔP_{close} of valve 6 and hence the flow path is unobstructed to actuator 6. 89

Figure 4.7: Control Logic with sequences of events illustrating valve closure by utilization of closing delta pressures. 90

Figure 4.8: (a) Residual limb model mold. (b) Residual limb model. (c) Clearance between residual limb model and prosthetic socket. 92

Figure 4.9: Diagram showing differential sequential pressure control enabled by one air microfluidics chip. The fluidic pressure (pressure from the control box to actuators) and control pressure (used to close valves) are represented by shades of red and cyan, respectively. Darker shade represents higher pressure, and lighter shade represents lower pressure. The table shows the fluidic pressure, control pressure of each step, and which valve is closed at which step. For instance, to close valve 1 only, the required pressure must be higher than the sum of valve 1 delta closing pressure and step 1 fluidic pressure and be lower than that for closing valve 2. The arrows represent the fully automated sequence of the pressure control, in which the pressures are changed in step increments via utilization of solenoid valves. 93

Figure 4.10: The overall test setup used for acquiring both the contact pressure mapping and the pressure response curve of the air microfluidic chip. With the 2 2/2 NC solenoids and a microfluidic chip, only one channel of the 4-channel custom-made pressure pump is used to operate the system. 94

Figure 4.11: Optimized design of the air microfluidic chip with volume of 10 cm^3, diameter of 35 mm, thickness of 10 mm, and mass at just 10 g (lighter than an AAA

Alkaline battery). A dark-colored background was to reveal the on-chip valve features as well as the channels inside the chip. A Canadian quarter is in place for size comparison. 95

Figure 4.12: Pressure response curve of the air microfluidic chip. The outlet of each of the 10 on-chip valves was connected to a pneumatic pressure sensor for pressure measurement. A total of 7 pressure levels with 10 on-chip valves were achieved by having the valves 2,3, and 4 to close as a single group, and same for valves 6 and 7. 96

Figure 4.13: (a) Contact pressure mapping obtained as the idealized case. This figure shows the visual illustration of the target contact pressures of each actuator relative to one another. (b) Contact pressure mapping obtained using the proposed system; air microfluidics chip, single pneumatic source, and two solenoid valves. (c) Contact pressure label associated with the color contour of the test results. Both figures share the same color-pressure label. 97

Figure 4.14: Summary of the contact pressure test repeated over 5 times. The contact pressure of the 10 actuators in each test are represented as mean and standard errors (in orange), each placed next to the target contact pressure (blue) for comparison. 98

Figure 5.1: Soft robotics-enabled active compression sleeve utilizing active air microfluidics and overlapping soft fluidic actuators. (a) Tekscan pressure mapping sensors (9811E, Tekscan) capture smooth sequential gradient compression with pressure holding capabilities and fast uniform deflation, presented in a 3D pressure map contour format with a legend indicating compression levels in millibar. (b) The wearable control box with the cover removed, revealing internal components. (c) Image of the soft robotic active compression sleeve worn on a human arm, comprising three key subcomponents: the wearable control box, monolithic sheet of overlapping soft fluidic actuators, and Combined Air Microfluidic Chip. (d) Miniaturized combined air microfluidic chip designed for sequential gradient pressurization,

pressure holding, and fast uniform deflation of soft fluidic actuators. (e) The inflated monolithic sheet of overlapping soft fluidic actuators showing its ability to flex and minimize gaps between each consecutive soft fluidic actuator when bent by hands. 105

Figure 5.2: Schematic rendering of In-Line Air Microfluidic Chips integrated on top of the soft air bladders (without overlapping) in the pneumatic air compression sleeve (Lymphedema sleeve, same as Chapter 3). The chips enable sequential gradient inflation of the air bladders, resulting in a sequential gradient compression on the arm. 107

Figure 5.3: (a) Exploded-assembly diagram illustrating the construction of the pneumatic in-line valve in its normally open state. The valve consists of three main components: the control side PDMS part (illustrated with a cyan-colored air pathway), the fluidic side PDMS part (with a pink-colored air pathway), and an elastic PDMS membrane placed between them. (b) Exploded-assembly diagram representing the pneumatic in-line valve in its closed state. Application of air pressure to the control air pathway (shown in cyan) causes the PDMS membrane to deflect downward, effectively closing the pneumatic in-line valve and halting the airflow through the fluidic pathway (colored pink). (c) Side cross-sectional view of the pneumatic in-line valve, demonstrating the airflow when there is no or insufficient pressure within the control air pathway (in cyan). Under these conditions, air can move freely past the pneumatic in-line valve, as indicated by the arrows indicating the flow direction. (d) Another side cross-sectional view of the valve, showing the PDMS membrane deflecting downward due to air pressure from the control air pathway, resulting in the closing of the pneumatic in-line valve. This deflection obstructs the airflow through the fluidic air pathway (colored pink). (e) Images depicting the integration of passive serpentine resistance channels (left) and pneumatic in-line valves (middle) to form the Combined Air Microfluidic Chip (right). A pencil with approximately 7 mm width was used as a size reference. (f) In-Line Air Microfluidic Chips, with two viewed from the side showing

different sizes and one viewed from the top. The cyan color represents the control side, and the pink color represents the fluid side, as shown in the schematics above. A Canadian quarter coin with a diameter of approximately 24 mm provided scale. (g) Further miniaturized Combined Air Microfluidic Chip, which had the same function as the one shown in (e) but smaller and more compact, demonstrating the potential of the design to be extremely compact and low-profile. 109

Figure 5.4: (a) Fabrication process for the In-Line Air Microfluidic Chips. Step 1: Begin with 3D printing molds using Formlabs Form 3 and Formlabs Clear Resin to shape the fluidic side and control side PDMS parts. Step 2: Pour liquid PDMS (Sylgard 184) into the 3D printed molds and allow it to cure. Step 3: De-mold the cured PDMS parts and create tubing connections by punching holes, while removing any excess PDMS to achieve the smallest microfluidic valve size possible. Step 4: Create a membrane by spin-coating liquid PDMS onto a Mylar substrate and curing it. Step 5: Plasma bond the fluidic side PDMS part with the cured PDMS membrane. The rigid Mylar substrate ensures a flat bonding surface, preventing creases or warping of the PDMS membrane. The PDMS part, being somewhat flexible, allows it to be peeled off along with the PDMS membrane from the Mylar substrate. Step 6: Complete the final modular microfluidic valve by plasma bonding the fluidic side PDMS, now bonded with the PDMS membrane, to the control side PDMS part (b) Fabrication process for the Combined Air Microfluidic Chip, which shares the same steps as the In-Line Air Microfluidic Chips but presented a different diagrammatical presentation. 111

Figure 5.5: (a) Control box with approximate weight of 150 grams and dimensions as shown. (b) Internal components of the control box include a miniature air pump (1528-4700-ND, DigiKey), pressure sensor (3965, Adafruit), 3.7V, 2600mAh lithium polymer battery (B091YF4VH8, Amazon), custom printed circuit board assembly (PCBA) featuring a Seeeduino XIAO Microcontroller (Seeed Studio), two motor drivers (ROB-14451, Sparkfun), and a buck-boost

power converter (2190, Adafruit). The control box also contains 2/2-way valve (LHDB0552115H, The Lee Company), 3/2-way valve (LHDA053115H, The Lee Company), and a 3D printed pneumatic manifold. The arrows indicate the direction of air flow: blue represents air entering the miniature air pump from ambient atmosphere; purple shows air exiting the control box towards the fluid line; cyan illustrates air exiting the control box towards the control line; deep blue indicates air exiting the control box to ambient atmosphere. (c) Fluidic control diagram for Combined Air Microfluidic Chip. The Arabic numeral (1 to 9) indicates the fluidic resistance channels. (d) Fluidic control diagram for In-Line Air Microfluidic Chip. The Arabic numeral (1 to 9) indicates the opening sequence of the in-line valves. The legend is used for both (c) and (d). The lowercase Roman numeral (i to ix) represents the fluidic pathway leading to SFAs. The letter 'e' indicates the exhaust port pathways where air exits to ambient atmosphere from the air microfluidic chips. "PH" stands for pressure holding in-line valves, and "E" stands for exhaust in-line valves. Each air microfluidic chip can control 9 SFAs. The purple color represents the fluidic line, the cyan color indicates the control line, and the dark blue color indicates the exhaust line for both (c) and (d). 113

Figure 5.6: Flow chart depicting the control schemes for (a) Combined Air Microfluidic Chip and (b) In-Line Air Microfluidic Chips..... 114

Figure 5.7: (a) Self-treatment of arm swelling due to lymphedema [252]. (b) Free-floating overlapping pneumatic chambers in the Lympha Press compression device [251]. (c) Numerous commercially available active compression devices exhibit gaps between pneumatic bladder/compression actuators. Top left image shows a cross-sectional view of a commercial pneumatic compression device (Flexitouch, Tactile Medical) with pressure mapping data illustrating the gaps between air bladders [227]. Top middle image displays a pneumatic active compression device when deflated and inflated, clearly demonstrating the gaps between each air bladder [147]. Bottom left image shows a non-pneumatic compression device using shape memory alloy actuators

(Dayspring, Koya Medical), also exhibiting some gaps between actuators as measured by pressure mapping sensor [227]. The right image presents yet another pneumatic compression device, showing the skin immediately following compression therapy, with uneven therapy resulting in bumps and divots (small depressions) on the skin where lymphatic fluid is trapped inside locations with no compression applied (i.e., the bumps) (Aria Free, Aria Health) [228]. 116

Figure 5.8: Fabrication steps for strain-limiting layer. 118

Figure 5.9: (a) Image of the outer strain-limiting layer with clearly visible Velcro straps securing the garment in place for active compression. (b) Image showcasing four monolithic sheets, each consisting of three overlapping SFAs with different overlap percentages: 0%, 10%, 20%, and 40%. (c) Cross-sectional schematic illustrating a monolithic sheet of overlapping SFA with a relatively high strain-limited height. The purple-colored arrows indicate the direction of the force applied by the strain-limiting fabric. (d) Cross-sectional schematic depicting a monolithic sheet of overlapping SFA with a relatively low strain-limited height, reducing the gaps between neighboring SFAs..... 119

Figure 5.10: Testing setup included a pneumatic control box that communicated fluidly with either the In-Line Air Microfluidic Chips or the Combined Air Microfluidic Chip, allowing for sequential and gradient pressurization of the monolithic sheet of overlapping SFAs. A printed circuit board assembly (PCBA) equipped with an array of air pressure sensors (3965, Adafruit) measured and recorded the air pressure within each SFA. Additionally, a Tekscan Pressure Mapping Sensor (9811E, Tekscan) was positioned between the 3D printed forearm model and the overlapping SFA to accurately measure the applied pressure exerted by the overlapping SFA onto the forearm model. To direct forces toward the forearm model, an outer strain-limiting layer covered the overlapping SFA. The solid pink arrows in the figure represent the fluid pathways during experimentation with the Combined Air Microfluidic

Chip, while the dashed blue arrows represent the fluid pathways during experimentation with the In-Line Air Microfluidic Chips. 122

Figure 5.11: Overlapping SFA results measured using three different methods: visual inspection, contact pressure mapping, and average pressure (y-axis, in millibar) vs. length (# of sensels, a measurement of individual pressure sensing points on a pressure map) plot for varying overlapping percentages (0%, 10%, 20%, and 40%). (a) Legend showing applied contact pressure corresponding to color-coded regions as recorded by the Tekscan pressure mapping sensor (9811E, Tekscan) in millibar. (b) Results for low-pressure gradient overlapping SFAs. (c) Results for medium-pressure gradient overlapping SFAs. (d) Results for high-pressure gradient overlapping SFAs. 125

Figure 5.12: (a) 3D line chart showing the Gap Contact Pressure Difference ($\boldsymbol{\Delta PGap}$) for all tested overlapping SFA conditions. The high, medium, and low (z-axis) represent the pressure gradient settings. (b) Images showing the effect of the thickness of the outer strain-limiting layer on the bulkiness of the sleeve. The tested conditions include 2 layers of TPU (Bemis 3913) at 300 µm thick, 4 layers of TPU at 600 µm thick, and 6 layers of TPU at 900 µm thick, all with 40% overlapping SFAs. A Tekscan pressure map at the bottom left corner of each tested condition shows that the contact pressure was similar for all tested conditions. The purple-colored line shows the bump created by the inflated SFA, and the straighter the line, the less bulky and noticeable the sleeve when viewed visually. 126

Figure 5.13: Results of systematic testing for in-line valves, including initial opening and fully open pressures. (a) Plot displaying the $\Delta P_{(open)}$ for each valve, as detailed in Table 5.4, with varying membrane thicknesses. Five tests were conducted per data point. (b) Plot illustrating the average increase in $\Delta P_{(open)}$ for valve VI with a 110-120 µm membrane due to thermal aging. Five tests were conducted per data point, using different in-line valves. The spread is represented by the range bars, and the median is plotted. 128

Figure 5.14: Results for analog sequential gradient inflation with uniform fast passive deflation of SFAs using In-Line Air Microfluidic Chips. (a) Plot illustrating the analog sequential inflation sequence of the chosen valves 1 to 10 for In-Line Air Microfluidic Chips. (b) Low-pressure analog sequential inflation sequence with uniform passive deflation for SFAs 1 to 9. The same legend is used for (c) and (d). (c) High-pressure analog sequential inflation sequence with uniform passive deflation for SFAs 1 to 9. (d) High-pressure analog sequential inflation sequence where the pressure source continued pressurizing the SFAs without deflation, eventually reaching uniform pressure for SFAs 1 to 9..... 129

Figure 5.15: Results for the sequential gradient inflation with pressure holding and uniform fast passive deflation of SFAs using the Combined Air Microfluidic Chip. (a) Sequential gradient inflation with a high-pressure setting. (b) Sequential gradient inflation with a medium-pressure setting. (c) Sequential gradient inflation with a low-pressure setting. (d) Sequential gradient inflation and uniform fast passive deflation without pressure holding. (e) Sequential gradient inflation with pressure holding and uniform fast passive deflation. (f) Sequence of pressurization of the control line of the exhaust and pressure holding in-line valves..... 131

Figure 5.16: Tekscan pressure mapping results of the gradient smooth compression with a monolithic sheet of 9 SFAs with 40% overlap. (a) Smooth gradient compression from wrist to elbow with an image showing the monolithic sheet of overlapping SFAs. (b) Showing smooth gradient compression with uniform smooth compression using the same monolithic sheet of overlapping SFAs. The Tekscan pressure map is overlaid with a plot of the contact pressure, obtained by averaging circumferential pressure readings around the forearm. 132

Figure 5.17: Images showing the staircase pattern on the inline valves from 3D printing. (a) Actual PDMS air microfluidic chip. (b) 3D printed mold..... 138

Figure 6.1: Novel soft robotics-inspired low-profile dynamic fluidic cushion (dynamic cushion) concept providing dynamic cushioning during gait. The dynamic cushion fully pressurizes in <250 ms at heel strike and holds pressure through stance phase to unload pressure at the fibular head (red). The dynamic cushion fully depressurizes under 100 ms at toe-off and remains depressurized throughout swing phase. The section view of the fibular head and dynamic cushion shows when the dynamic cushion pressurizes, a gap wide enough to allow the fibular head to no longer contact the inside walls of the prosthetic socket is created, entirely unloading contact pressure at the fibular head. The dynamic cushions avoid contacting the fibular head and peroneal nerves above and below the fibular head and distribute the contact pressure that would otherwise be on the fibular head onto surrounding soft tissues. A wearable control box (~100 grams) attached to the pylon controls the pressurization and depressurization of the dynamic cushions. Note that the current proof of concept study focuses on developing and testing actuator design. Sensor and controller design to trigger (de)pressurization is beyond the scope of this chapter. The top left image shows a pressure ulcer at the fibular head due to shear and friction from badly fitting prosthesis [269]..... 148

Figure 6.2: Components and fabrications overview. (a) Biofidelic residual limb model with fibular head rigid cover. (b) Soft robotics-inspired low-profile dynamic fluidic cushion design. (c) Fabrication steps for dynamic cushions. (d) Image of equipment used for dynamic cushion fabrication demonstrates the low cost and ease of fabrication. 151

Figure 6.3: (a) Images of thin, medium, and thick fibular head rigid curved plates. The thin plate was made out of Formlabs grey resin, the medium and thick plates were made out of Formlabs clear resin. All fibular head rigid curved plates had the same materials properties. (b) Image showing the pressurized and depressurized dynamic cushions, fibular head rigid curved plate, residual limb model and Tekscan sensor. 152

Figure 6.4: Dynamic cushion designs illustrated with critical dimensions for both TPU and Teflon insert. All dimensions are in inches. 153

Figure 6.5: Control box design. (a) CAD Model of the wearable control box. (b) Diagram of the control scheme for pressurization and depressurization of the dynamic cushions. 155

Figure 6.6: Testing setups. (a) Image showing placements of rigid fibular head cover and surrounding dynamic cushions. (b) Image showing placement of the Tekscan sensor between the prosthetic socket and residual limb model. (c) Image showing weights stacked on the platform connected to the aluminum rod mimicking the tibia. (d) Image showing connections of miniature air pump, solenoid valve, and air pressure sensor to the dynamic cushions. 157

Figure 6.7: Testing results. (a) Plot displaying consolidated Tekscan data comparing no weight to weighted (80 kg) contact pressure at fibular head when the dynamic cushion was manually pressurized using a syringe filled with air. The Tekscan was placed horizontally through the middle of the fibular head. The syringe was filled until approximately 200 mmHg contact pressure (maximum suggested pressure over bony prominences over two hours [282]) at the fibular head was reached or the contact pressure at the fibular no longer decreased with human manual syringe pumping. The purpose of this test was to show that under the full weight of a person, the dynamic cushions are still capable of reducing fibular head contact pressure down to an acceptable level (at least ~200 mmHg) while maintaining pressure on the surrounding soft tissues at an acceptable level as well (at most ~200 mmHg). (b) Static pressure holding test with medium fibular head rigid cover (average of three tests per data point) with preferred rectangular dynamic cushion. (c) Static pressure holding test with thick fibular head cover with preferred rectangular dynamic cushion at an internal pressure of 300 mmHg. (d) Static pressure holding test with thick fibular head cover with preferred rectangular dynamic cushion depressurized (left) and pressurized at 300 mmHg (right). Dynamic gait test displaying

internal pressure of dynamic cushion (solid cyan line) and contact pressure at the fibular head (dotted orange line) over ten continuous cycles of 250 ms pressurization followed by 100 ms depressurization. Two different balloon designs with the medium fibular head rigid cap are shown: (e) Curved and (f) Rectangle. 160

Figure 7.1: Overview of the soft robotics-inspired multi-layered torus-shaped displacement compression sensing system for detecting downward movement in prosthetic sockets. 168

Figure 7.2: (a) The six LDBs manufactured for testing. 3 were small-sized; one from 150-micron thick TPU, one from 300-micron thick TPU, and one from 450-micron thick TPU. Big LDBs were manufactured with larger outside diameter. (b) Top-down view of the manufactured LDBs. (c) Schematic of the LDB fabrication process. The inflatable chamber was fabricated by cutting the desired shape out of 150-micron thick thermoplastic polyurethane (TPU) sheets (3916 Sewfree Thermoplastic Polyurethane, Bemis, Shirley, United States) thermally bonded with an insert of Teflon membrane (8569K36, McMaster-Carr Supply Company, Elmhurst, United States). Space occupied by the Teflon membrane inserts will expand when fluid (air or water) is displaced into the LDB. A small removable paper insert was placed where the tubing would insert into the LDB; this junction was sealed with a handheld heat iron and adhesive (Loctite 495, Henkel, Düsseldorf, Germany) once the elastomer had annealed. (d) Components of the system. (e) Testing setup. 172

Figure 7.3: Results from vertical displacement range testing to characterize the effect of layers on LDB: (a) linearity plot. (b) Applied pressure vs. vertical displacement plot. (c) Pressure difference between internal and applied pressure vs. vertical displacement plot. 175

Figure 7.4: Cyclic loading testing results: (a) Plot for the small-thin LDB. (b) Plot for the big-thin LDB. (c) Box and whisker plot showing precision of peak pressure from cyclic-loading tests for all big 3-layer LDBs. 176

Figure 7.5: (a) Step-loading of the small-thin LDB. (b) Step-loading of the big-thin LDB. (c) Hysteresis results for all 3-layer LDBs derived from step-loading tests. (d) Long-term stability for small-medium LDB over 24 hours at room temperature showing internal air pressure of LDB and change in ambient pressure. (e) Change in ambient pressure versus internal air pressure of LDB during long-term stability testing. 178

Figure 8.1: (a) Pneumatic and signal pathways between components. (b) Preliminary rendering of the control box. (c) Approximate locations and sizes of the components associated with the control box. (d) Design of the knee brace. (e) Schematic of the three-point leverage mechanism. (f) Conceptual schematic of the mini-balloon actuator array. 185

Figure 8.2: (a) A prototype of the knee brace described herein. (b) Showing the air microfluidic chip acting as a manifold and mini-balloon actuators deflated. (c) Mini-balloon actuators inflated before elastic deformation. (d) Showing force transmission straps and ratchet dial for tightening the straps. (e) Control box prototype. (f) Initial testing result of the internal air pressure of the balloon as measured by air pressure sensor. 187

Figure 8.3: Electronics-free soft robotic knee brace enabled by CLFR system. The top left image shows the low-profile CLFR system enabling dynamic three-point bending aimed to counteract the external knee adduction moment (KAM). The top right schematic shows the two critical moments in CLFR pressurization and depressurization control using the user's own body weight and gait: heel strike and toe off. The bottom schematic shows the behavior of the foot bellow and the knee bladder and the direction of airflow between the two during the stance phase, thus providing unloading pressure only during weight-bearing (i.e., stance phase). 188

Figure 8.4: Components of the closed-loop fluidic regenerative system. a) Three bellow sizes used during experimentation varied by spring properties. The gray outer model represents the height of each foot bellow in the relaxed state, and the

cyan inner model represents the height of each foot bellow in the compressed state. Each elastomer shell and spring's diameter were kept constant at 92.7 mm and 50.8 mm, respectively. b) Dimensions of each knee bladder used in each evaluation prototype system. The bladders on the left were used for the hydraulic prototypes, and the bladders on the right were used for the pneumatic prototypes. The yellow bladder was paired with the small foot bellow (9.53 mm relaxed height), blue with the medium foot bellow (12.7 mm relaxed height), and gray with the large foot bellow (22.1 mm relaxed height). c) Connective tubing between foot bellow and knee bladder. 1.587 mm ID used for pneumatic systems and 3.175 mm ID used for hydraulic systems. 190

Figure 8.5: Fabrication process for closed-loop fluidic regenerative system. The schematic outlines the creation of the foot bellow (top left), knee bladder (top right), and the hermetic integration of the two actuators (bottom). 192

Figure 8.6: Overview of test apparatus and components. a) Pneumatic system schematic for control of test apparatus showing control for raising the aluminum plate (left) and lowering the aluminum plate (right). b) Test apparatus comprised of an aluminum plate (b1), a pneumatic cylinder (b2), a Tekscan sensor (b3), and an aluminum support frame (b4). c) Cross-section view of foot bellow actuator used for testing. d) Placement of foot bellow on Tekscan sensor under the aluminum plate. e) Placement of knee bladder on Tekscan Sensor in the Medi M2 Active OA Light Knee Brace. 194

Figure 8.7: (a) Image showing an on-body testing trial. (b) Optotrak camera. (c) IRED markers (singles and rigid body). 199

Figure 8.8: Pressure testing results. (a) Contact pressure at the knee in response to progressive loading of medium pneumatic foot bellow (m-P) from 0 to 90 kg for three different knee bladder dimensions: 30.5 mm (smaller), 39.4 mm (medium), and 43.18 mm (larger). (b) Contact pressure at the knee in response to progressive loading of medium hydraulic foot bellow (m-H) from 0 to 90 kg for three different knee bladder dimensions: 50.8 mm (smaller), 58.4 mm x

50.8 mm oval (medium), and 73.7 mm x 63.5 mm oval (larger) for system m-H. (c) Comparison of internal foot bellow pressure shown as a light blue dotted line and contact pressure at the knee shown as a dark blue solid line as the foot bellow is progressively loaded from 0 to 90 kg. Pressure maps of the contact pressure at the knee recorded by Tekscan sensor are shown at three different weights applied to the foot bellow. 201

Figure 8.9: Comparison of total contact force versus peak contact pressure for pneumatic knee bladders and hydraulic knee bladders when medium foot bellow size was compressed by 90 kg weight. Three tests were conducted per data point with error bars shown. 202

Figure 8.10: Response testing results. (a) Response time of pneumatic system (m-P) and hydraulic system (m-H) overlaid with typical stance phase frontal plane knee moment. (b) Response testing results showing contact pressure at the knee in dark blue (dashed line) and applied weight on the foot bellow in light blue (solid line) for medium pneumatic system (m-P) with a 39.4 mm diameter knee bladder. (c) Response testing results showing contact pressure at the knee in dark blue (dashed line) and applied weight on the foot bellow in light blue (solid line) for medium hydraulic system (m-H) with a 58.4 mm x 50.8 mm oval knee bladder. 204

Figure 8.11: Cyclic loading testing results. (a) Contact pressure at the knee for the complete 2500 steps during cyclic loading testing from medium pneumatic system (m-P) with 39.4 mm diameter knee bladder. (b) Box and whisker plots for medium pneumatic system (m-P) with 39.4 mm diameter knee bladder (blue, left), small pneumatic system (s-P) with 30.5 mm diameter knee bladder (orange, center-left), large pneumatic system (l-P) with 40.6 mm diameter knee bladder (gray, centered), medium hydraulic system (m-H) with 58.4 mm x 50.8 mm (oval) knee bladder (yellow, right-centered) and small hydraulic system (s-H) with 50.8 mm diameter knee bladder (light blue, right) during cyclic loading testing. (c) Contact pressure at the knee for steps 1, 10, 50, 100, 500, 1000,

1500, 2000, and 2500, selected from cyclic loading testing for medium pneumatic system (m-P) with 39.4 mm diameter knee bladder. 206

Figure 8.12: This graph illustrates the average KAM over eight trials for each testing condition. "Brace Loose Deflated" refers to the condition where the brace was worn with loosened unloading straps, and without the use of the CLFR system. "Brace Tight Deflated" represents the scenario where the brace was worn with tightened unloading straps, but without the activation of the CLFR system. Finally, "Brace Tight Inflated" indicates the condition where the brace was donned with tightened unloading straps and the CLFR system was activated. 207

Figure 9.1: Rendered models of the soft-rigid hybrid robotic prosthetic finger when (a) pressurized/flexed, and (b) depressurized/extended. (c) Image of the soft-rigid hybrid robotic prosthetic finger pressurized/flexed. (d) Image of the soft-rigid hybrid robotic prosthetic finger depressurized/extended. (e) Top view of the soft-rigid robotic prosthetic finger pressurized/flexed. (f) Image of the depressurized/deflated bellows-style 5-layer soft fluidic actuator. (g) Image of the pressurized/inflated bellows-style 5-layer soft fluidic actuator. 220

Figure 9.2: Bellows-style soft fluidic actuator manufacturing schematics: a) side view showing the stack or the sheet layers' alignment during the heat pressing process. b) Top view of each layer or sheet. 222

Figure 9.3: a) Exploded view of all the mechanical assembly of the soft-rigid hybrid robotic prosthetic finger. b) Pneumatics schematic of the soft-rigid hybrid robotic prosthetic finger. The letter “P” within a circle represents the air pressure sensor. 223

Figure 9.4: Electrical schematic of the prosthetic finger lab. 225

Figure 9.5: Potential lab deliverable plots: a) internal air pressure within the SFA measured by the air pressure sensor and the bending angle of the prosthetic finger measured by IMU. b) Raw versus scaled versus rectified EMG. c) Rectified & filtered EMG compared to the bend angle of the prosthetic finger. 231

Figure 9.6: Photos of the student working on the soft-rigid robotic prosthetic finger lab. The images have been intentionally stylized and blurred to maintain student privacy. 235

Figure 9.7: a) Image of the plastic boxes containing all the components of the prosthetic finger lab; each box contains one kit. b) Broken parts during the pilot run, including two SFAs, two motor drivers, and an IMU. 237

List of Tables

Table 2.1: Fuel system-level summary reproduced with permission from Soft Robot. 1, 4 (2014). Copyright 2014, Mary Ann Liebert, Inc. [39] 23

Table 3.1: Square channel sizes used for the simulation. 63

Table 3.2: Channel sizes determined based on Channel Selection Tests 73

Table 4.1: Abbreviations for the anatomical locations of the transtibial residual limb. 85

Table 4.2: Legend for Figure 4.7. 91

Table 4.3: Valve features and dimensions for the optimized air microfluidic chip. 95

Table 4.4: Comparison of the contact pressure: original target versus test results. 98

Table 5.1: Dimensions of channels in Combined Air Microfluidic Chip and calculated equivalent hydraulic resistance. The table presents the dimensions of square channels in the Combined Air Microfluidic Chip, with channel numbers corresponding to Figure 5.5c. The calculated equivalent hydraulic resistance values are based on a dynamic viscosity of 1.81×10^{-5} kg/m*s for air at 20 °C and atmospheric pressure (1 atm). 110

Table 5.2: In-line valve dimensions, thermal aging time, and experimentally determined $\Delta P_{(close/open)}$ for In-Line and Combined Air Microfluidic Chips. The table presents the dimensions of the valves, thermal aging time at 90°C in an oven, and the experimentally determined $\Delta P_{(close/open)}$ values for both In-Line and Combined Air Microfluidic Chips. The valve numbers/identifiers in capitalized Roman numerals correspond to Figure 5.5c, d. 112

Table 5.3: Volume and dimensions of soft fluidic actuators. The cross sections were approximated as rectangular due to the compression of the outer strain-limiting layer. The fully pressurized volume was calculated based on a low-profile fit, with no gap between the monolithic sheet of overlapping SFAs and the outer

strain-limiting layer, and an average strain-limited inflation height of 0.5 cm as visually inspected. The soft fluidic actuator (SFA) numbered 1 is located at the wrist, and SFA numbered 9 is located at the elbow, with the rest positioned sequentially in between according to their respective numbers. 118

Table 5.4: Tested in-line valve dimensions. 121

Table 5.5: Tabulated results showing the number of pressure peaks and valleys and the gap pressure difference ($\Delta PGap$) for all the tested conditions. The Gap Contact Pressure Difference shows the mean as well as the ranges based on 3 data points per tested condition. 124

Table 6.1: Dynamic cushion designs and their pressurizing chamber surface area when completely depressurized. The volume when pressurized depends on internal air pressure, which determines the height; thus, using the total surface area multiplied by height yields rough total in-socket pressurized volume. Please note the volume estimation of the pressurized dynamic cushion is only valid when it is squeezed by the limb and the socket. 150

Table 8.1: Naming scheme for different chosen foot bellow – knee bladder pairs. 200

Table 8.2: Energy losses in pneumatic and hydraulic systems. 205

Table 9.1: Bill of materials for the prosthetic finger lab kit. 228

Chapter 1

Introduction

1.1 Background and Motivation

The Tesla valve, a leaky diode or a valvular conduit, was conceived by its eponymous inventor, Nikola Tesla, who secured its patent in 1920 [1]. This innovation was perhaps one of the most renowned and pioneering fluidic logic elements, which employs fluid, typically pneumatics or hydraulics rooted in the theoretical principles of fluid dynamics, to execute either analog or digital operations. Such operations are broadly referred to as fluidics or fluidic logic (**Figure 1.1**). From the early to mid-20th century, fluidics captivated the attention of many researchers, with a primary focus on internal fluidic flow within devices engineered to carry out amplification, logic operations, and diode effects [2]. The ultimate aim was to develop programmable fluidic computers capable of performing tasks akin to those executed by their electronic counterparts [3]–[6]. At that time, these fluidic devices were deemed safer than the contemporary electronic options. However, the swift advancement of microelectronics led to a dwindling interest in fluidics research. The tide turned again in the 1990s and 2010s with the advent of microfluidics [7]–[9] and soft robotics [10]–[12], respectively. These developments ushered in a renewed interest in fluidics as a potential approach to miniaturizing control systems and actuators, particularly for use in soft wearable robotics [13], [14].

Microfluidics, facilitated by the intricate system of microchannels and valves, enables the passive and active sequencing of fluidic actuation without reliance on bulky, electrically driven macro valves, thus paving the way for miniaturized control boxes. These microchannels and minichannels, along with on-chip valves, are embodied in microfluidic chips that are integrated seamlessly with the rest of the soft robot's control hardware.

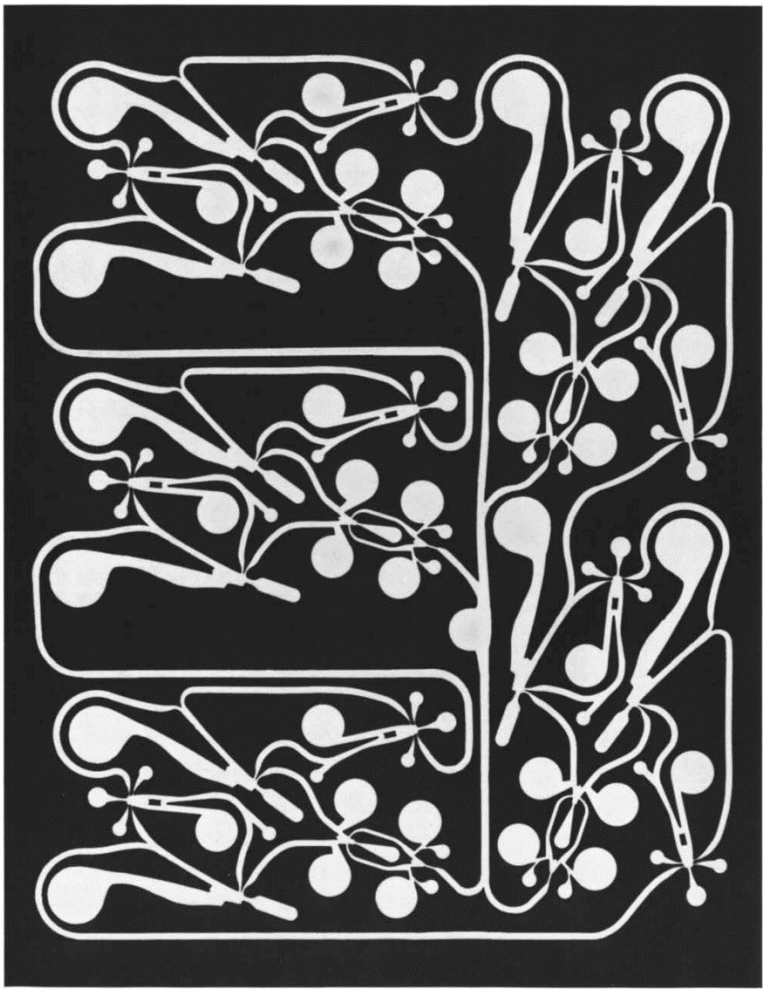


Figure 1.1: Fluid Circuit performs the operation of dividing by 10 in an all-fluid digital computer: for every 10 input pulses circuit delivers one output pulse. Input pulses enter from above the plane of circuit through circular, bump like hole attached to straight channel running from top to bottom just to right of center. The 10 identical logic elements, or modules, are arranged in a series of five pairs, three at left and two at right. Each pair contains two steady input 80 streams (small sausage shapes), two outputs (small circular shapes attached to short straight channels), eight control jets (small tear· drop shapes) and eight open vents (large circular shapes). Shallow channels were chemically etched in Dycril plastic by a special process, called Optiform, developed by Bowles Engineering Corporation. For this photograph the channels were filled with white paint to increase the contrast. Normally the working fluid is air. [15]

Joseph L. McKibben made significant strides in the field of fluid actuators in the 1950s by developing one of the first "soft" fluid actuators. His innovation, referred to as the Pneumatic Artificial Muscle (PAM), is sometimes known as the McKibben Artificial Muscle [15]. McKibben's motivation was personal – he designed the system to aid his daughter, who

suffered from polio and was paralyzed from the neck down. Using the PAM, he created a mechanical orthosis that enabled his daughter to use her fingers.

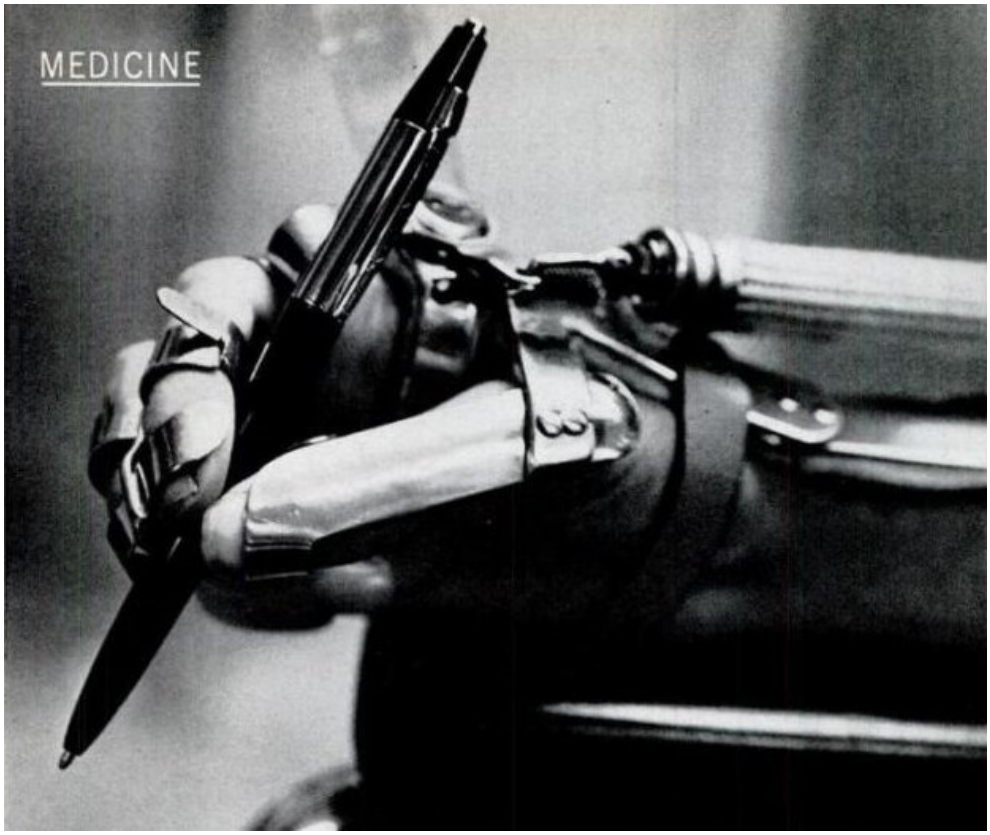


Figure 1.2: Tightened by Artificial Muscle (McKibben Type) leading down arm and finger of a paralyzed girl grasp and hold a pen. [15]

Drawing from orthotics and prosthetics, soft fluid actuators continued to evolve throughout the late 20th century and early 2000's, a progression exemplified by innovations like the "Fluidhand" developed by Vincent Systems GmbH [16], [17]. As technological advancements unfolded over time, they precipitated a surge in research and development concerning a variety of robotic and mechatronic systems that utilize soft actuators. This, in turn, gave rise to a distinct field of study known as Soft Robotics.

Soft robotics [10]–[12] is an interdisciplinary field that is redefining the landscape of body-worn assistive technology for both at-home and mobile use. This technology can be used to facilitate active body compression, akin to manual massages, while offering active movement assistance and providing a safeguard against potential injuries [18]. It is particularly beneficial for individuals grappling with musculoskeletal conditions such as osteoarthritis

[19]–[22] and peripheral vascular disease such as lymphedema [22], as well as those recovering from spinal cord injuries [23], strokes [24], amputations [25], and knee surgeries [26]. The unique advantage of soft robotics over traditional exoskeletons [27] and rigid braces [28], which primarily comprise hard components, is its soft yet highly functional structure [29]. This allows for bespoke body conformity while providing movement assistance and rehabilitation through fluidic pressurization of soft actuators, including mini pneumatic chambers [30], [31], and cable-pulley actuation [32]. Soft robots are not only functional but also economical, given their ability to be manufactured through 3D printing [11], [33] and their integration with fabrics, thereby enabling the production of low-cost, customized devices [34], [35].

Soft wearable robotics and soft robotics in general employ three primary actuation methods. The first one is direct electrical actuation using electroactive polymers [36]. However, the integration of this method into soft wearable robots has proven challenging due to safety concerns related to the requirement for large electric fields, among other technical limitations. As a result, it is seldom used in soft wearable robots. The second method is cable actuation [37], [38], which has undeniably shown its utility, particularly in applications involving gait [24]. Despite its proven effectiveness, it is the third method, fluidic actuation [39], implemented via hydraulics or pneumatics that has become the most prevalent and driving force in soft wearable robotics. Professor George M. Whitesides aptly stated, "It [fluidic pressurization] has proven so simple to implement in prototypes that no better method has yet emerged [10]." Despite its evident merits, fluidic pressurization also presents the most significant hurdle that needs to be overcome for soft wearable robotics to become genuinely beneficial in everyday life. **Figure 1.3** illustrates a tree diagram that categorizes different types of wearable assistive devices, offering a visual overview of the landscape of this emerging field.

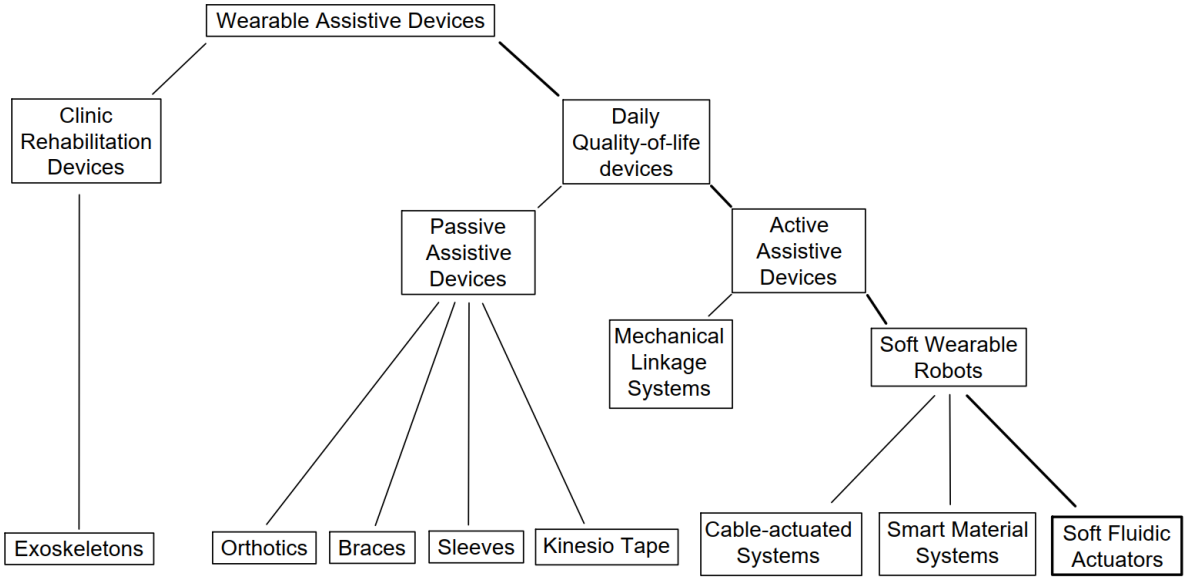


Figure 1.3: Tree diagram categorizing different types of wearable assistive devices.

Much of fluidic-based soft robotics technologies face certain limitations, primarily their need to be connected to an external power source or large and heavy control box when worn on the body [23], [30], [39]–[42]. Additionally, their efficiency is somewhat hampered by the large internal volume of soft fluidic actuators [34], [43], [44], which necessitates pumping substantial amounts of fluid into the soft actuators to achieve the desired compression, forces, or torques. To overcome these obstacles, an urgent need for new technologies and methods arises. This work herein addressed these challenges by harnessing the potential of microfluidics and minifluidics [45], [46] and the concept and philosophy of miniaturization [46] to miniaturize the control and actuation systems of soft wearable robotics-enabled assistive devices while improving their overall function.

The foundational technical core of all proposed projects in this research is the miniaturization of control systems and soft fluidic actuators. Leveraging microfluidic and minifluidic approaches, we, as in individuals and I who collaborated on the work presented here, aimed to augment efficiency, enhance functionality, and shrink the dimensions of each system's control box. The first project focused on developing an active compression sleeve for the treatment of lymphedema and peripheral vascular disease. It is essential to comprehend the users' needs, including ease of use and wearability, an understanding that was bolstered through collaboration with lymphedema specialist, Jacqueline Mary Kormylo. The second initiative aimed to enhance prosthetic socket fit and comfort for individuals with amputation by creating

a dynamic sock. This endeavor was in partnership with local healthcare providers: Prosthetic Ability and Dr. Doug Dittmer's team from Grand River Hospital-Freeport Campus. The third project entailed the development of a gait-controlled soft robotic knee brace designed to aid individuals with unicompartmental osteoarthritis. The intention was to alleviate pain and improve mobility, a goal we aimed to achieve through collaborations with physiotherapists and researchers from the Department of Kinesiology at the University of Waterloo. To pique the interest of more STEM students in the burgeoning field of soft robotics research, we collaborated with the Department of Biomedical Engineering at the University of Waterloo on a final project. This endeavor focused on designing a hands-on lab for an engineering course, streamlining the control system and minimizing finger prosthesis with the aid of hybrid soft-rigid actuators. After piloting in a senior-level undergraduate engineering elective course, it received overwhelmingly positive feedback, demonstrating its efficacy in engaging students with this innovative field.

The work presented herein holds profound significance as it offers immediate and direct benefits to Canadians and global populations alike. The assistive devices we are developing are meticulously designed with users' specific needs in mind, encompassing key factors such as affordability, comfort, and ease of use. Understanding that these devices are not just functional aids but also integral parts of users' everyday lives, we have placed a great emphasis on their aesthetics. With valuable feedback from our collaborators, we are ensuring that these devices not only perform their designated tasks effectively but also align with users' personal styles and preferences. The ultimate goal is to create assistive apparels that can be seamlessly incorporated into daily routines and worn comfortably throughout the day [47], [48]. In essence, this research is not merely about creating assistive devices; it is about improving quality of life, enhancing personal confidence, and promoting greater independence for those who use them. By incorporating these diverse considerations into our design process, we are working towards creating solutions that are truly people-centered and fully attuned to the real-world needs and expectations of users.

The guiding principle of this thesis can be encapsulated in the following statement:

"To miniaturize soft robotic systems, enabling their comfortable integration with the human body, with the goal of assisting those with physical impairments in their activities of

daily living. This endeavor aims to enhance the quality of life for all by facilitating improved rehabilitation strategies and minimizing the risk of injuries."

1.2 Thesis Outline

Chapter 2 provides an in-depth overview and perspective of the potential synergy between microfluidics and soft robotics as a research topic. It also suggests future directions that could utilize the benefits of both fields. Soft robotics has seen tremendous progress and a wide range of applications such as surgical assistance, delicate food handling, and wearable assistive systems, due to its more user-friendly nature compared to traditional hard robotics. The rapid expansion of soft robotics has introduced a myriad of challenges, varying by application. Key challenges include the need for versatile soft materials and precise, swift control for actuation. In wearable systems, miniaturization poses an additional hurdle to creating truly impactful, user-accepted systems. Microfluidics, a field with over two decades of intense research, has yielded fundamental theories and practical tools with potential applications to soft robotics, particularly in miniaturization.

Chapter 3 presents a proof-of-concept for a novel, air microfluidics-enabled soft robotic sleeve designed for lymphedema management. Current solutions, such as compression sleeves and stationary pumps, fall short in terms of portability during daily activities. This dilemma between efficiency and wearability is addressed by our pioneering microfluidic device. Our approach employs compact, lightweight, and affordable air microfluidic chips (measuring 35 mm x 20 mm x 5 mm), offering three key advantages over conventional designs. Firstly, the chip is equipped with 16 fluidic channels of varying cross-sectional areas (0.04 to 1 mm^2), facilitating sequential inflation and uniform deflation of 8 air bladders. This creates a purposeful gradient compression on the arm, enhancing lymph fluid circulation - a design inspired by the principles of microfluidics, particularly hydraulic resistance and paths of least resistance. Secondly, the air microfluidic chip enables significant miniaturization of the control system, reducing the requirement from eight sizeable, energy-demanding valves to two compact solenoid valves, thereby enhancing the device's wearability. Lastly, the absence of moving parts within the air microfluidic chip minimizes both noise and energy consumption. The chapter also elaborates on the cost-effectiveness, simplicity, and scalability of the device's production process. The sequential inflation, uniform deflation, and pressure gradient of the

device are demonstrated and evaluated based on the compression generated and the internal air bladder pressure. This innovative, air microfluidics-enabled sleeve holds enormous potential for enhancing self-care management of lymphedema in the future.

Chapter 4 introduces a novel proof-of-concept for a transtibial prosthetic socket liner designed to dynamically adjust its fit to accommodate residual limb volume fluctuations, a significant issue causing skin ulcerations, diminished prosthetic function, pain, and a reduced quality of life for transtibial amputees. This self-management challenge is further complicated by peripheral neuropathy, which dulls the limb's pressure and pain perception. At the heart of this innovation lies a compact air microfluidic chip (10 cm^3 and 10 grams) equipped with 10 on-chip valves. These valves enable the sequential pressurization of 10 custom-sized actuators to accommodate the unique anatomical pressures of the residual limb. The integration of the microfluidic chip significantly reduces the electromechanical solenoid valves needed for sequential control (from 10 to just 2), diminishing the power, size, weight, and cost of the control box. This makes for a more affordable, wearable prosthetic socket. The proof-of-concept tests have successfully demonstrated the ability to vary applied pressures in the desired sequence and to redistribute pressure. Ultimately, this dynamic prosthesis socket liner shows considerable promise for integrating seamlessly with existing socket fabrication methods. Its potential to manage residual limb volume fluctuations and contact pressure dynamically offers a more comfortable and functional solution for transtibial amputees.

Chapter 5 presents a systematic engineering proof-of-concept study, pioneering a novel approach to managing lymphedema swelling. By integrating a monolithic sheet of overlapping soft fluidic actuators with active air microfluidic systems, we aim to create a smooth, sequential gradient compression. Secondary lymphedema, prevalent in up to 50% of breast cancer survivors, urgently requires such innovation. Our approach seeks to rectify the shortcomings observed in current commercial systems, which often result in gapping issues and excessive reliance on electromechanical components. This leads to trapped lymphatic fluid and restricts the system's use to static home settings. By contrast, our proposed solution ensures a continuous, smooth compression experience and offers a truly portable device with a smartphone-sized control box. Specifically, by overlapping soft fluidic actuators by 40%, we eliminate pressure gaps, resulting in seamless compression. Furthermore, we showcase two effective methods for achieving sequential gradient pressurization: one utilizing in-line air

microfluidic chips with in-line valves only, and the other combining these valves with resistance microchannels, facilitating gradient pressure holding and rapid uniform deflation, which is a feat unattainable by using only resistance microchannels. With this study, we take a significant stride towards revolutionizing lymphedema management, offering promising prospects for improving the lives of those affected by this and related conditions.

Chapter 6 presents a proof-of-concept study that proposes a novel soft robotics-inspired and miniaturized dynamic fluidic cushion for mitigating high contact pressures at bony prominences such as the fibular head. The dynamic cushions were fabricated using a thermoplastic elastomer, and a lamination method was used to seal the cushion's layers. A 3D printed biofidelic model of a transtibial residual limb was made to validate the dynamic cushion's performance. Results showed that the cushion could effectively redistribute contact pressures away from the fibular head to the surrounding soft tissues. This provides targeted cushioning during gait to protect vulnerable areas from high contact pressures, which may lead to skin breakdown and potential ulceration if not attended to. This technology shows promise and has the potential to be integrated into prosthetist workflows.

Chapter 7 introduces a soft robotics-inspired, lightweight, and inexpensive sensing system designed to detect and measure vertical displacement, often referred to as "pistoning," in transtibial prosthetic (TTP) sockets. Particularly beneficial for diabetic individuals with peripheral neuropathy, this system aims to help users self-manage the adverse effects of pistoning, which can lead to skin breakdowns and ulcers. Comprising a multi-layered torus-shaped balloon, the design seamlessly integrates with pin-lock socket systems, and the vertical displacement detection does not impose significant reaction forces on the distal end. Benchtop compression tests were used to evaluate the sensor's characteristics, and systematic and parametric tests, along with 24-hour stability recordings, were conducted. Results revealed that air, due to its compressible nature, was a superior medium for displacement detection, offering a linear full-scale span (FSS) of 4.5mm and a sensitivity of 0.8 kPa/mm for repeatable 0.5 mm vertical displacements. The sensor exhibited high precision, with a total error band as low as 1% FSS, an average hysteresis of 2.84% of FSS, and a 4% FSS drift over 24 hours. These characteristics, coupled with the sensor's low-cost and customizable fabrication, signal a promising solution for daily use, providing TTP users with valuable alerts for downward movement and pistoning.

Chapter 8 introduces a pioneering, electronics-free soft robotic knee brace powered by a closed-loop fluidic regenerative (CLFR) system, designed specifically to alleviate the symptoms of unicompartmental tibiofemoral osteoarthritis (OA), which is a condition marked by the gradual degradation of intra-articular cartilage and resultant chronic stiffness, swelling, and discomfort. The CLFR system strategically applies pressure during the stance phase of gait, using harvested energy to unload forces at the knee, while refraining from applying any forces during the swing phase. This system incorporates a commercial unloading knee brace, a shoe-inserted, spring-loaded bellow, a soft-fluidic actuator (or bladder), and tubing for fluid transfer. We examined the system's performance in terms of knee bladder contact pressure/force, response time, and durability using pressure measurement testing. Six systems of varying bellow volumes and configured either pneumatically or hydraulically, were tested within a bodyweight range of 60-90 kg, producing safe pressure outputs for human skin. The pneumatic and hydraulic systems achieved pressurization response times of 250 ms and 400 ms respectively. During cyclic loading, the pneumatic and hydraulic systems exhibited less than 1% and around 10% pressure loss respectively. Our tests validated the CLFR system's ability to sync with natural gait, producing safe pressure outputs for extended skin contact.

Chapter 9 delineates an immersive laboratory exercise in biomedical engineering, guiding students through the assembly and testing of a hybrid soft-rigid active finger prosthetic with a miniaturized low-profile bellows-style soft fluidic actuator. The lab intricately interweaves mechanical, electrical, and sensor technologies within a hands-on environment, offering a broad, customizable learning experience adaptable to diverse curricula. All materials are open-source, with the necessary components costing approximately $100 per kit, easily sourced from global vendors. This pedagogical approach, initially launched with 40 undergraduates, received positive feedback, successfully engaging students in the tangible societal impacts of their studies. Potential extensions into clinical and technical discussions further enrich this dynamic learning platform. Overall, the lab offers students a comprehensive journey through the prosthetic design process, from initial conception to final testing.

Chapter 10 offers a comprehensive overview of the significant contributions and novel insights generated by my thesis, while simultaneously illuminating the potential avenues for future exploration and development.

Chapter 2

Literature Review and Perspective

The work included in this Chapter is published: **R. Z. Gao** and C. L. Ren, "Synergizing microfluidics with soft robotics: A perspective on miniaturization and future directions," *Biomicrofluidics*, vol. 15, no. 1, p. 11302, Jan. 2021, doi: 10.1063/5.0036991. [46]

2.1 Introduction

To understand the benefits of soft robots, it is better to discern the limitations of traditional hard robots first. In the words of Professor George M. Whitesides, "the most important limitation is that they, [hard robots], are what is called 'non-collaborative,' [10]". Indeed, hard robots are often best used in very predictable and programmable manners [49] requiring impeccable precision and accuracy, such as industrial settings. When it comes to interacting near humans, collaborations with humans, as well as handling soft and delicate objects, soft robots are advantageous over hard robots due to their inherent compliance. This is not to say that hard robots cannot interact with humans, rather a call for improvements upon the current robotic systems, which perhaps involves a hybrid makeup of both hard and soft robotics systems working together. However, as far as this perspective is concerned, the inherently non-threatening and compliant nature of soft matter allows soft robots to work with and help human synergistically.

2.1.1 Independent Functioning Soft Robots

Soft robots can be roughly categorized into two types: independent functioning soft robots and soft wearable robots. The former is the starting point of the field of soft robotics, which began by studying and mimicking animals lacking internal skeletons, such as squid, worm and starfish. Examples (**Figure 2.1**) of this category include soft robotic grippers [12] for handling

soft agricultural and commercial goods as well as biological sampling on deep reefs [50], autonomous soft robotic fish for documenting marine life as non-disruptively as possible [51], an untethered soft robot [52] for traversing in harsh conditions, a "growing" soft robot [53] for potential applications in search and rescue in unstable rubble, and a modular soft manipulator for minimally invasive surgery [54].

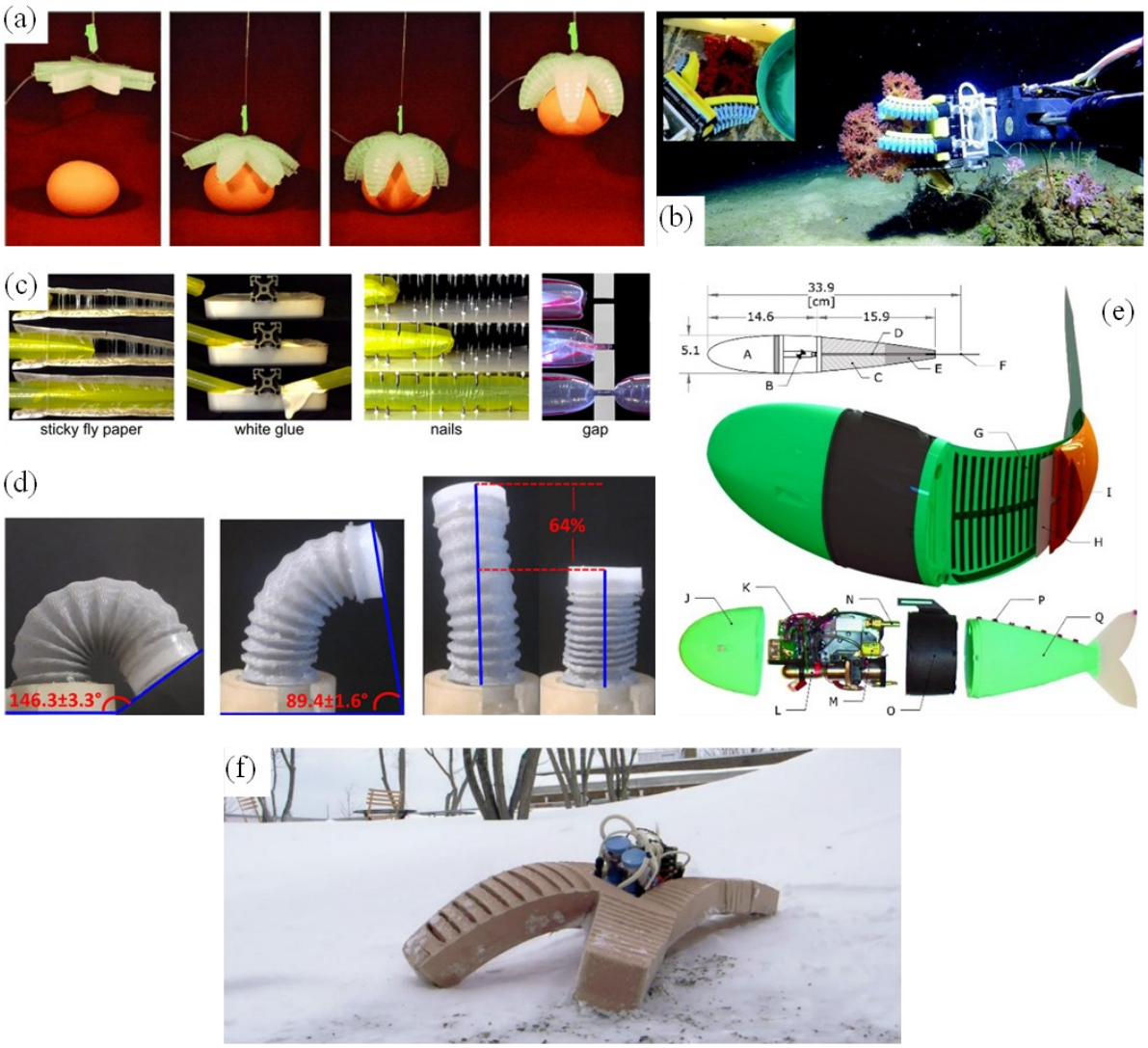


Figure 2.1: Soft robotic grippers reproduced with permission from Angew. Chemie - Int. Ed. 50, 8 (2011). Copyright 2011, John Wiley & Sons. [12] (b) Bellows-type gripper collecting soft coral; K. C. Galloway et al., Soft Robotic Grippers for Biological Sampling on Deep Reefs, Soft Robot., 3, DOI: 10.1089/soro.2015.0019, 2016; licensed under a Creative Commons Attribution (CC BY) license. [50] (c) A soft robot lengthens through various challenging constrained environments without active control. Instead, the robot passively deforms to navigate the obstacles; reproduced with permission from Sci. Robot. 2, 8 (2017). Copyright 2017, The American Association for the Advancement of Science. [53] (d) Stiffness

controllable flexible & learnable manipulator for surgical operations performing bending and elongation; reproduced with permission from IEEE Trans. Robot. 32, 1 (2016). Copyright 2016, IEEE. [54] (e) Details of a soft-bodied robotic fish; A. D. Marchese et al., Autonomous Soft Robotic Fish Capable of Escape Maneuvers Using Fluidic Elastomer Actuators, Soft Robot., 1, DOI: 10.1089/soro.2013.0009, 2014; licensed under a Creative Commons Attribution (CC BY) license. [51] (f) Image showing the resilience of the untethered soft robot to snow conditions; reproduced with permission from Soft Robot. 1, 3. (2014). Copyright 2014, Mary Ann Liebert, Inc. [52]

2.1.2 Soft Wearable Robots

Soft wearable robots are becoming increasingly popular for applications in the biomedical field especially for making assistive technology and rehabilitation. Some examples (**Figure 2.2**) include a soft wearable glove for at-home rehabilitation [55], a soft exosuit for improving walking in post-stroke patients [24], a soft wearable robot for the shoulder [34], a soft wearable biomedical device for lymphedema treatment [56] as well as mechanotherapy [57] and a variety of applications for the lower body, such as for ankle-foot rehabilitation [43] and knee motion [58], [59]. The reason for its popularity lies in its inherent compliance and collaborative characteristics to safely interact with humans [11]. It is the consensus in the field of soft robotics that soft wearable robots do not replace traditional exoskeletons but instead add a new dimension to advance wearable assistive devices, as commented by Connor Walsh in a perspective article: “Soft wearable robots will not replace traditional rigid exoskeletons that are emerging as a valuable clinical tool for patients with severe impairments, but will instead offer complementary capabilities for applications which require soft systems [18].”

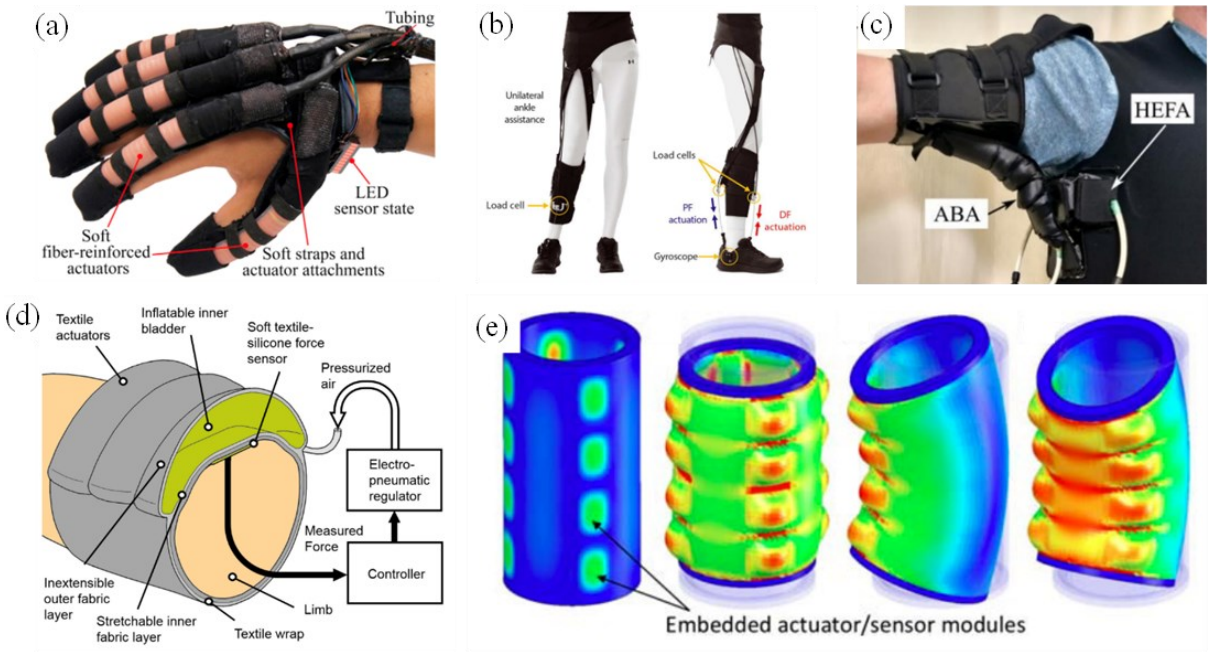


Figure 2.2: Examples of soft wearable robots: (a) soft wearable glove for post-stroke rehabilitation reproduced with permission from Rob. Auton. Syst. 73 (2015). Copyright 2015, Elsevier. [55] (b) Soft exosuit for post-stroke rehabilitation reproduced with permission from Sci. Transl. Med. 9, 400 (2017). Copyright 2017, The American Association for the Advancement of Science. [24] (c) Soft wearable robot for the shoulder reproduced with permission from Proc. - IEEE Int. Conf. Rehabil. Robot. 02129 (2017). Copyright 2017, IEEE. [34] (d) Soft wearable device for mechanotherapy reproduced with permission from Proc. - 2018 IEEE International Conference on Robotics and Automation (2018). Copyright 2018, IEEE. [57] (e) Soft modular knee sleeve for assisting walking reproduced with permission from Proc. - IEEE Int. Conf. Robot. Autom. (2018). Copyright 2014, IEEE. [59]

2.1.3 Soft Actuators

The mainstay of a soft robot is its soft actuators, which have indeed been the research focus even before soft robotics became a real research interest [60]. Many of the soft actuators can trace their origins to robotic artificial muscles driven by the motivation to mimic certain aspects of muscle function. Zhang et al. [44] conducted a systematic review of various types of robotic artificial muscles. No single technology can tackle all the problems, certain soft actuators allow for high dynamic torque applications, for instance, the cable system present in the Exosuit [61] developed by Harvard's Biodesign Lab. Whereas soft fluidic actuators may allow for better conformity to the body, especially across joints and muscles evident by soft robotic gloves [62] and soft grippers [63] for grasping soft and delicate objects, and for applications involving haptics, such as those developed by HaptX [64]. As for smart material actuators such as shape

memory alloy [65], dielectric elastomers/electroactive polymers [66], [67] and electro/magneto-rheological [68], [69], they still require more research and development and technical breakthroughs regarding safety, reliability, response time, force output, efficiency and fabrications before being practical for soft robotic applications as suggested by George M. Whitesides' [10] call for better materials for soft robotics applications. The potential of smart material actuators is immense, as it can directly convert electrical energy into useful mechanical forces and torques. On the other hand, soft fluidic actuators and cable-driven actuators require a medium to convert electrical energy into mechanical energy, which is less efficient than direct energy conversion in theory.

When it comes to practical implementations of soft robots, soft fluidic actuators employing hydraulics (with extension to any liquid) and pneumatics (with extension to any gas) are by far the most common methods [10]. Fluidic pressurization also represents the biggest bottleneck issue that must be solved for soft wearable robots to become genuinely relevant in helping people in everyday lives. Before diving into the challenges facing soft fluidic actuators, its advantages are briefed below. First, the fabrication of soft fluidic actuators is practical and reasonably straightforward. There are two primary types of fabrication methods, molding [41], [52], [70] and heat bonding [35] (**Figure 2.3**). Molding typically uses a two- or three-part 3-D printed or laser-cut mold, where silicone, commonly Elastosil by Wacker or Ecoflex by Smooth-on, is poured into the mold, cured, and bonded by adhesive to at least one other silicone part to create soft fluidic actuators. With the improvements in 3D printing technology, particularly stereolithography (SLA), creating high-quality molds has been streamlined and democratized. Heat bonding uses a heat press to bond two pieces of thermoplastics films, such as polyurethane, polyester, nylon polyamide from 3M or Bemis, to form an elastic balloon. The same thermoplastic films can also be used to create the strain-limiting fabrics [35], which are used in conjunction with the soft fluidic actuators to produce motions, torques, and forces towards the body. Xurographic cutter plotters and laser cutters have automated the process of cutting complex shapes out of thin films allowing the creation of complex strain-limiting fabrics with micrometer precision and accuracy. This opens the door to complex Kirigami skin designs [71] that, when combined with soft fluidic actuators, can create locomotion.

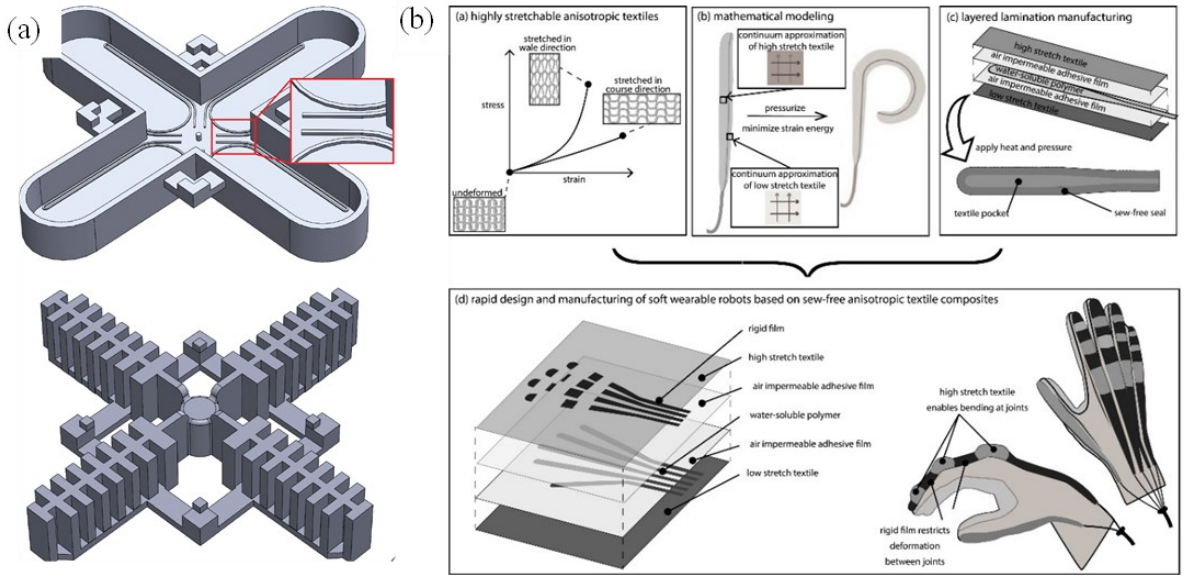


Figure 2.3: (a) 3D modeling representation of the molds for casting a soft robotic gripper; reproduced with permission from IEEE Int. Conf. Intell. Robot. Syst. (2015). Copyright 2015, IEEE. [70] (b) The heat press lamination fabrication approach to making a soft robotic glove; reproduced with permission from Extrem. Mech. Lett. 27 (2019). Copyright 2019, Elsevier. [35]

Second, soft fluidic actuators are highly versatile. They can be designed with or without strain-limiting layers to achieve a variety of motions, torques, and forces and their size can be scaled up or down with accommodating tubing sizes to pair with. The variety of motion is created by inflation of multiple internal chambers, pneumatic bladders, or balloons in a preset sequence which expands low modulus structures while the higher modulus locations resist internal chamber expansion causing a desirable motion. The higher modulus locations can be made by only increasing the thickness of the material or by adding an additional strain-liming layer or material.

Third, soft fluidic actuators are economical. For instance, 1 liter of Ecoflex silicone costs around US$40; 0.84 square meters of Bemis elastomer membrane cost around US$20 from Bemis. If the production of soft fluidic actuators is tuned up to industrial scale, the per-unit cost is further decreased. The major cost of soft fluidic actuators comes from the control systems, which comprises solenoid valves, pumps, pressure sensors, microcontrollers, batteries, etc. The cost of the control system also depends on the application, the number of components, and the size of the soft robot; by rough estimation, the cost of the control system is 70% to 95% of the total cost of making a soft robot.

Lastly, soft fluidic actuators can be miniaturized easily. Albeit, not all soft robots benefit from miniaturization, but it would be particularly useful for some, namely soft wearable robots such as the soft robotic glove for neuromuscular rehabilitation [72]. Nevertheless, even in the realm of soft wearable robots, soft fluidic actuators suit certain applications and fall short for others. The limitations of soft fluidic actuators have been demonstrated by the Soft Exosuit project led by Harvard Biodesign Lab [73], where Bowden cables used in the exosuit replaced McKibben artificial muscles, a type of soft fluidic actuators, used in earlier prototypes.

McKibben artificial muscle [74] is perhaps one of the most well-known soft fluidic actuators that were first introduced in the 1950s. It is a hollow soft braided tubular bladder that shortens when pneumatic or hydraulic energy is applied onto the inner surface of the tube. The advantage of McKibben artificial muscles is that it can generate large forces and has a high power density, hence it has excellent power to weight ratio, and it is simple and inexpensive to manufacture. A feedback PI or PID controller is sufficient to control McKibben artificial muscles [75]. The disadvantage and perhaps the bottleneck of McKibben artificial muscle is that it requires a large compressor or fluidic energy source which limits its applications as untethered mobile systems [39]. Here lies the first challenge: current soft fluidic actuators still lack robustness for applications requiring high dynamic torque, as the pressure requirement would be high, demanding a large pump, which would not be practical to be worn.

2.2 Motivation to Bring in Microfluidics

2.2.1 Miniaturization

Miniaturization of soft fluidic actuators is perhaps a practical means to produce useful and aesthetically pleasing products for users to adopt and embrace; the first step of many to initiate the adoption of soft wearable robots as assistive devices. By all means; aesthetics is a highly subjective topic; depending on the person and the application of the soft wearable robot, the aesthetic tolerance is different. Minimizing the disruption to the human form factor is perhaps a universal aspiration when designing wearable systems, hence, it is a valuable proposition to focus on miniaturizing soft wearable robotic systems into a low-profile form factor that conforms to the human body without impeding motion.

Aesthetics comes with a cost in functionality for certain applications as miniaturization may reduce the amount of pressure, torque and toughness of fluidic actuators. Retaining both functionality and aesthetics calls for fundamental and applied research, which must be application and end-user driven, meaning that the motivation of miniaturizing soft wearable robots should be problem-focused, and only undertaken if it is achievable and satisfies end-user requirements. For instance, if 20 psi pressure or above is required to actuate soft fluidic actuators for a specific application, then miniaturizing the soft fluidic actuators is still desirable to reduce the bulk of the soft robot, but the pump required is too large and that would be the bottleneck, and perhaps an alternative solution exists.

2.2.2 Case Study of the Soft Robotic Glove

The soft robotic glove [76] made by Harvard Biodesign Lab provides insight into the progression of soft wearable robots. It is visually seen that the aesthetics of the glove improves while retaining its functionality from the early pneumatic network bending actuators [77] to the latest sew-free anisotropic textile composites [35] (**Figure 2.4**).

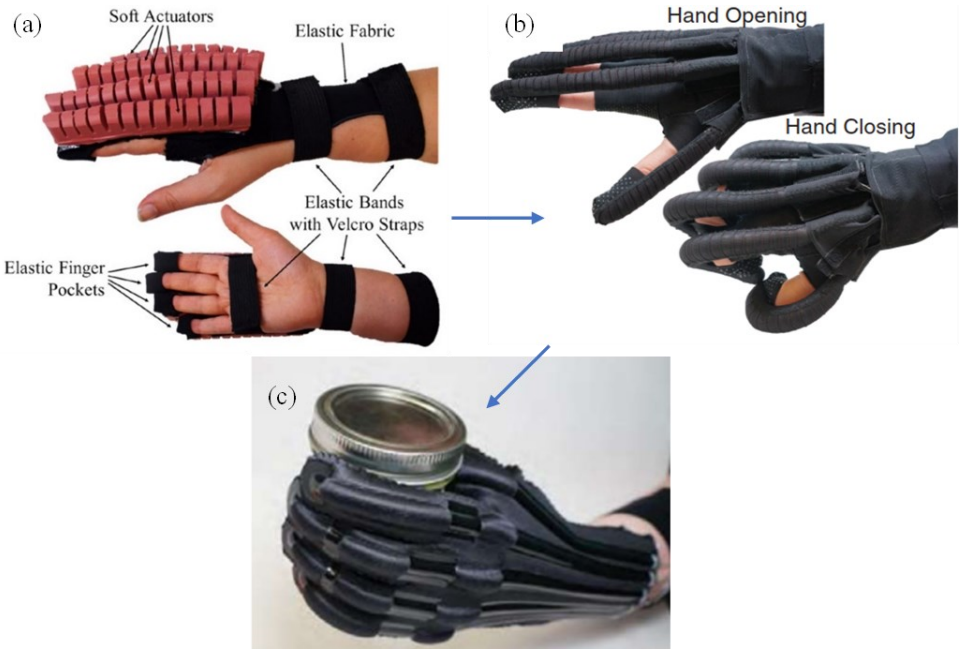


Figure 2.4: (a) Soft robotic glove based on a pneumatic network SFA; reproduced with permission from IEEE Int. Conf. Intell. Robot. Syst. (2013). Copyright 2013, IEEE. [77] (b) Soft robotic glove based on fibre-reinforced and sleeved SFA; Cappello et al., J. Neuroeng. Rehabil., 15, 59, 2018; licensed under a Creative Commons Attribution (CC BY) license. [23] (c) Soft robotic glove based on sew-free anisotropic textile composites; reproduced with permission from Extrem. Mech. Lett. 27 (2019). Copyright 2019, Elsevier. [35]

2.2.3 Low-Profile, High Resolution and Digitization

As previously mentioned, aesthetics is a highly subjective issue, but it can be commonly regarded that low-profile systems are more preferable than bulky systems if the same functionality can be maintained. Hence, the idea is to use multiple smaller low profile soft fluidic actuators to mimic the functionality of a larger soft fluidic actuator, using a simple balloon as an example (**Figure 2.5**).

Miniaturizing soft fluidic actuators is most persuasive in applications where compliance, compression, and conformity are highly valued and it also opens the door for potentially better control systems as each actuator can be considered as a single digital point. In such a strategy, instead of inflating a single large balloon by reading analogue pressure data, a miniaturized balloon can just be considered as an on or off switch, inflated or deflated. When combined in a matrix or an array with strain-limiting layers synergistically, they potentially allow for more efficient motion or means of providing torques and forces, achieving the same functionality as a single soft fluidic actuator, which will be elaborated on in the next section.

It should be noted that not all soft fluidic actuators can be miniaturized, such as those requiring a large bending torque or substantial volume changes and deformation. There would be an argument for using a less stretchy strain-limiting layer with a single not fully inflated soft fluidic actuator to achieve the same low-profile aesthetics, but that is not ideal as the force is concentrated at a single point and difficult to conform to a curved substrate especially for wearable systems. Exaggerated examples are shown in **Figure 2.5** for illustrative purposes.

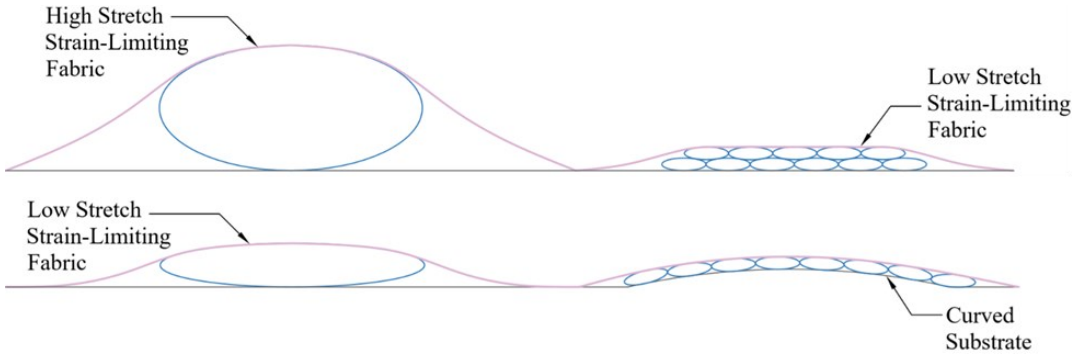


Figure 2.5: Concept image showing the difference in profile between a single large bladder constrained by a high stretch strain-limiting fabric (top left), a single large bladder constrained by a low stretch strain-limiting fabric (bottom left), miniaturized bladders constrained by a low stretch strain-limiting fabric (top right), and miniaturized bladders constrained by a low stretch strain-limiting fabric on a curved substrate (bottom right).

The increase in the number (i.e. arrays or matrices) of mini/micro soft fluidic actuators offers more design possibilities especially in the creation of the next-generation prosthetics, orthotics, haptics and surgical tools, however, it may complicate the fabrication process and increase the amount of tubing required as each mini/micro soft fluidic actuator is independently or semi-independently actuated. This would require extensive automation going forward. A new strategy for control could also be envisioned where instead of controlling soft fluidic actuators by analog sensing of pressure, bending, and forces, soft robots could be controlled by merely counting which actuator is inflated and which ones are not. This philosophy could be considered as the digitization of the analog soft fluidic actuators via miniaturization.

The feasibility to incorporate an array of mini/micro soft fluidic actuators that are individually controlled is best evaluated by examining the possibilities to miniaturize the backend (control box) which involves mainly a DC motor driving a peristaltic pump or piston-diaphragm pump, and a solenoid valve or equivalent to turn the flow on or off. Linearly increasing the number of pumps and valves to match the number of actuators will mitigate the benefits of miniaturizing the actuators as off-the-shelf fluid pumps and valves, regardless of pneumatics or hydraulics, are bulky and inefficient. More recently, solid state stretchy pumps based on the theories of electrohydrodynamics emerge [78]; for this type of pump, miniaturization is not a problem as they are inherently small and flexible. However, safety issues of using high voltages must be addressed for practical implementations. Nevertheless, electrohydrodynamic pumps have the potential to become an essential component for liquid-based soft robots requiring relatively low flow rate and pressure. Alternatively, if the number of pumps and valves can be kept very low by the adoption of microfluidics, the resulted soft robotic system would be truly wearable as the backend (control box) may be pocketed or in a fashion that it does not stick out too much, located more proximally, centrally on the human body, as close to the center of the gravity as possible.

All in all, the motivation of incorporating microfluidics into the creation of soft robotic system are twofold: (1) allowing miniaturization and digitization of soft fluidic actuators; and (2) miniaturizing the size and improving the functionality of the control system for soft robots, with the ultimate goal of creating a soft robot that end-user wants. This section is better ended by directly quoting the statement from Wyss Institute on the development soft robotic glove for neuromuscular rehabilitation: “This holistic approach, [involvement of potential end-users

in every step of the soft robotic glove's testing and development], ensures that technology development goes beyond achieving functionality to incorporate social and psychological design elements that promote translation and seamless adoption by its intended end-users" [72].

2.3 Concerning Actuation and Sensing

The conception of an idea, whether completely novel or a better implementation of an existing solution, should involve both technology developers upstream and stakeholders downstream from the very beginning, perhaps before or after the creation of the first proof of concept. When conceptualizing soft robotics, the first thing that comes to mind for technological developments is undoubtedly actuation, for which, a series of questions need to be answered, which technique to choose, how to control it, at what cost? On top of these, how much miniaturization is appropriate and how to achieve it are valid concerns as well.

As established above, miniaturization is a compromise between functionality and aesthetics if done purely to make the soft fluidic actuators and the control system hardware smaller or an afterthought for further development. However, when miniaturization is considered as part of the strategy for social acceptance of soft wearable robotics, it morphs from the act of miniaturizing existing soft fluidic actuators and its control system into the development of formfitting soft fluidic actuator system for socially acceptable soft wearable robots. We think these two are inherently different and worth a ponder; it changes the perspective on the motive, and we will elaborate further in the following sections. For now, actuation and technical implementation is the topic of discussion.

2.3.1 Power Source for Actuation

Soft wearable robots are applications driven; therefore, the actuation system is unique for different applications, although they do share certain similarities. From a schematic viewpoint, soft wearable robots can be divided into two major components, which can be coined as the frontend and the backend respectively (**Figure 2.6**). The frontend contains soft fluidic actuators and feedback sensors as mentioned in the previous section, and the backend contains a control system, which itself is made up of hardware and software including but not limited to valves, pumps, control sensors, microcontrollers and batteries. The frontend is connected to the

backend and indeed communicates via fluidic and signal pathways. Ideally, miniaturizing the frontend or the backend or both should not compromise the versatility of soft wearable robots, which might seem counterintuitive, but can be done. In the next section, we will introduce some example applications which benefit from the strategies presented here.

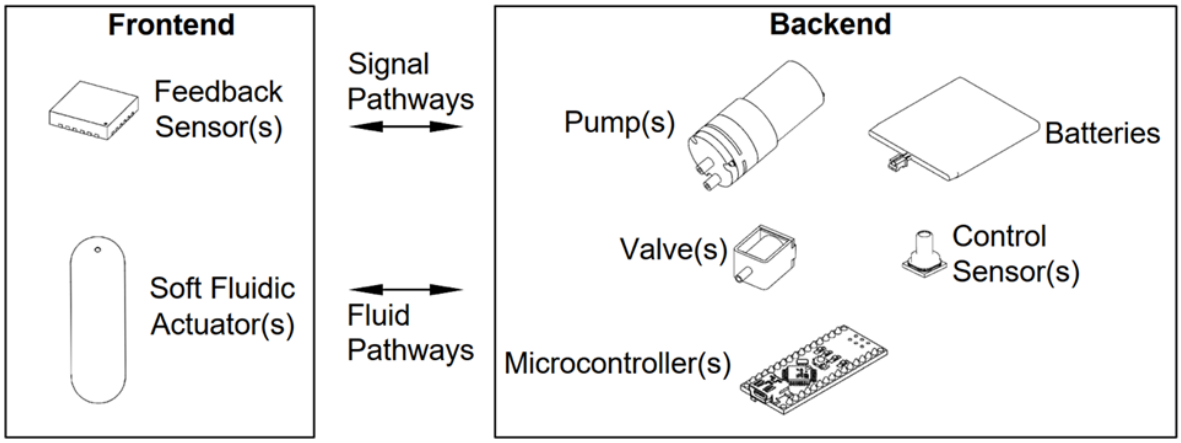


Figure 2.6: Schematic representation of the frontend and backend of a generic soft wearable robot. Please note that the images of the components are not to scale and only serve as a generic visual representation of each component.

As a starting point, the fluidic actuation power source must be optimized for both size and efficiency, and the optimization is application specific as there are various pneumatic/hydraulic energy sources. Wehner et al. [39] explored and quantified the pros and cons of various pneumatic energy sources for soft wearable robots. They also identified key metrics for measuring soft robotic power systems, which are energy density (joules/gram), flow capacity (liters/gram) normalized by the mass of the entire fuel system. Please refer to **Table 2.1** for a fuel system-level summary. Compressed air cylinders can provide high pressures and flow rates but deplete rather quickly resulting in short operating times. Combustion using methane and butane provides too much pressure for most applications, not to mention the safety aspect of using combustible fuel. Onal et al. [79] explored the idea of generating pneumatic pressure via hydrogen peroxide (H_2O_2) decomposition driven by the advantages such as silent operation, bypassing electric energy conversions and the possibility of embedding the chemical pump inside elastomer substrates. However, the limitations of this system such as the temperature increase in the chemical pump, and exhaustive system-level development makes it impractical. In the end, battery-powered microcompressors along with a good fluid recirculation design as well as a reservoir holding pressure to compensate for the

relatively small flow rate produced by the microcompressors might offer an excellent solution for the pneumatic power system used onboard soft wearable robots.

Table 2.1: Fuel system-level summary reproduced with permission from Soft Robot. 1, 4 (2014). Copyright 2014, Mary Ann Liebert, Inc. [39]

	Fuel system mass as evaluated (g)	**Maximum pressure (MPa)**	**Maximum flow rate (SLM)**	**Fuel system energy density (J/g)**	**Efficiency as evaluated (%)**	**Fuel system flow capacity (L/g)**
Microcompressor (small)	130 - 171	0.2 - 0.34	1.7 - 3.5	72.6 - 99.3	36.7 - 39.9	0.78 - 1.38
Microcompressor (large)	422 - 756	0.26 - 0.55	5.7 - 10.7	14.8 - 33.6	31.2 - 40.3	0.17 - 0.37
Liquid CO_2 small	49.9 - 662	5.6	18 - 127	30.4 - 44.1	< 49	0.074 - 0.11
Liquid CO_2 (refillable)	1573	5.6	300	58.1	< 49	0.14
Air cylinder (refillable)	909 - 1975	20 and 30	350 - 650	27.1 - 83.6	< 39	0.05 - 0.14
Butane combustion	62.7	n.a.	n.a.	2.37	0.5	0.094
Hydrogen peroxide decomposition	357	0.0507	n.a.	10 - 28	3.3 - 9, 45	0.04 - 0.05

2.3.2 Flow Control for Actuation

Microvalves have seen a tremendous increase in research and development over the first decade of the 21st century as summarized by a few excellent review articles [80], [81], which is mainly spurred on by the growth of microfluidics and lab-on-chip research. A very recent review article on microvalves [82] indicates that many of the same technical and fundamental challenges still remain. The choice of microvalve for soft robots is the question to be answered. Passive microvalves are merely miniaturized versions of large pneumatic/hydraulic check valves that function like an electrical diode allowing flow in one single direction. Active microvalves can be mechanical or non-mechanical. Most active mechanical microvalves are actuated by a flexible membrane via magnetic, electric, piezoelectric, and thermal actuation,

with the most common and commercially available being miniature solenoid valves [83] and miniature piezoelectric valves [84], [85]. Active non-mechanical microvalves are typically actuated via electrochemical reaction, phase change, and the use of rheological materials, or ferrofluids. Another type of microvalve is called in-line microvalve using external pneumatic pressure actuation [86], [87] , which has robustness and practicality. In-line microvalves are inherently soft and can be directly integrated within soft materials providing outstanding seal and response time. Their downside is that their actuation requires external macroscale mechanical solenoid valves, which must be miniaturized and reduced in number to be used in portable devices such as soft wearable robots.

One of the most widely used in-line microvalve (**Figure 2.7**) is so called Quake's valve [86], [87]. The way it functions is straightforward. A pneumatic control line intersects a fluidic line separated by a monolithic membrane, meaning that all the materials for the entire structure of microvalve are the same. This alleviates the potential of interlayer delamination due to adhesion and thermal failures. The monolithic membrane is typically made out of polydimethylsiloxane (PDMS), which is a soft material with Young's modulus ~750 kPa; hence, allowing large deflection with low pneumatic pressure. When the pneumatic control line is pressurized, the monolithic membrane deflects and closes the fluidic line via pinching with a millisecond response time. The pressure required to close a Quake's valve is simply the minimum pressure needed to close the monolithic membrane plus the back pressure inside the fluidic channel, which could be below 50 mbar [86]. By crossing a single control line over multiple fluidic channels, and varying the width of the monolithic membrane, it is possible for a single control line to independently control each fluidic line based on the level of pneumatic pressure inside the control line, allowing the potential for multiplexing, which reduces the number of external solenoid valves.

The challenge for Quake's valve to be used for soft wearable robots is its need for an external solenoid valve for each in-line valve and the associated bulky control system [88]. However, if one macro-sized solenoid valve or an equivalent can control multiple Quake-style valves, a concept of multiplexing, then it would be a game-changer regarding the number of fluidic elastomer actuators that can be integrated into fabric or reducing the number and size of large fluidic elastomer actuators using a large number of much smaller independently controlled fluidic elastomer actuators. Earlier work on multiplexing via Quake's valves has

been demonstrated by his group [89] where 3574 microvalves were independently actuated by using 22 external control solenoid valves, forming 1000 independent compartments as a microfluidic memory storage device. More work on multiplexing via Quake's valves followed later [90]. Although these systems can help the development of soft wearable robots to achieve better and more efficient control and shrink the size of the control block, the complexity hinders their practicality.

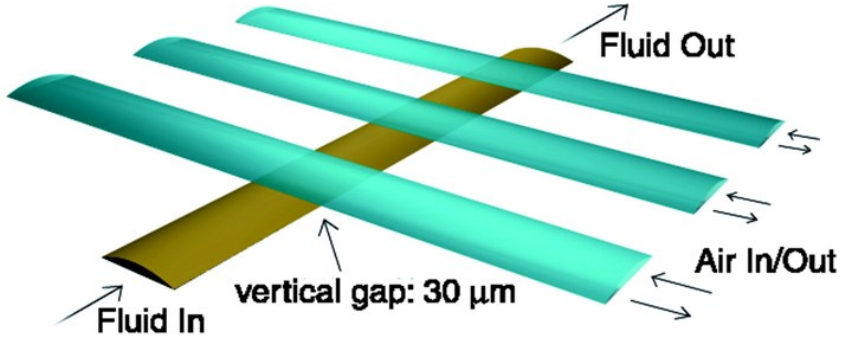


Figure 2.7: A 3D scale diagram of the pneumatic in-line microvalve developed by Unger et al., often referred to as Quake's valve; reproduced with permission from Science 288, 5463 (2000). Copyright 2000, The American Association for the Advancement of Science. [86]

Now, we arrive at the latest development of combinational microfluidic multiplexers. Lee et al. [91] developed a microfluidic multiplexer that can control 19 independent fluidic channels using only 4 control lines, and 8953 channels using only 10 control lines! The previous system can only address 16 independent fluidic channels using 4 control lines. Also, as the number of control lines increases, the capability of microfluidic multiplexer developed by Lee et al. increases exponentially and outpaces any other microfluidic multiplexer. So the multiplexors can decrease the number of external proportional solenoid valves required, but in real applications, demultiplexers and additional proportional solenoid valves are also needed, which halves the efficiency, meaning that to truly control 19 independent fluidic elastomer actuators, a minimum of 8 external proportional solenoid valves are required. Also, all of the previously mentioned fluidic multiplexers are explicitly made with microfluidic applications in mind and fabricated via multilayer soft lithography [86], which might not be appropriate for soft wearable robots. The control channel pressure must also be further reduced from existing microfluidic multiplexers to increase the pneumatic/hydraulic power source efficiency. The elastic monolithic membrane might also need to be upgraded for a higher number of cycles

before failure. Most importantly, an alternative must be found to replace proportional solenoid valves to control the pressure within the control channels to be more efficient and less bulky.

As mentioned before, no single microvalve technology is suitable for all applications. Although the so-called Quake's valve offers much versatility in the form of independent control of a large number of digital on-off soft fluidic actuators, it still requires albeit small but rigid proportional solenoid valves. For certain soft robots requiring mostly dynamic actuation, valves might not be required, which is not to say that no valves exist in the backend, but rather, no valves are required to individually activate each soft fluidic actuator.

2.3.3 Flow Regimes and Significance for Soft Robots

Given that Hagen-Poiseuille's law and Ohm's law are analogous, the equivalent fluidic resistors and capacitors can be identified within a fluidic system. Also, various electric circuit theories can be applied to microfluidic networks that help simplify the design phase of microfluidic chips [8]. In a microfluidic network, the channels with hydraulic resistance become fluidic resistors, the compliant channels or soft chambers become fluidic capacitors, flow rate becomes current, pumps that deliver current and pressure become batteries, and pressure drops due to hydraulic resistances become voltage drops. Kandlikar and Grande [45] defined microchannels as having a characteristic length from 1 μm to 200 μm and minichannels from 200 μm to 3 mm; this definition was based on the rarefaction effect observed in gas as described by the dimensionless Knudsen number, where above 200 μm, rarefaction effect is negligible. However, for simplicity, we will consider any channel below 1 mm and above 999 nm as microchannels.

Usage of hydraulic has certain disadvantages, such as the fact that it requires a reservoir, which increases the bulkiness and weight of the actuation system. Therefore, pneumatics is preferable. It is well known that air is a compressible fluid; in the strictest sense, compressible fluid means that the density of the said fluid changes with changing volume given the same mass of the said fluid. Incompressible fluid in contrast has a constant density under all conditions. However, there is no true incompressible fluid, and even a liquid is slightly compressible under high pressures. Hence, an assumption can be made that any fluid that does not change too much in density during laminar flow can be considered as an incompressible fluid for the purpose of design. The flow and pressure change for air within microchannels,

which will be coined as air microfluidics, precisely satisfies the above criteria to justify the assumption of air as an incompressible fluid at these conditions. The errors associated with the above assumption are tolerable and the equivalent hydraulic resistance is used as a design principle and engineering estimation instead of the fundamental theories. Hence, air microfluidic systems can be modelled using equivalent hydraulic resistance and electrical circuit analogy. The reason that it is named equivalent hydraulic resistance is because it is not a physical property of air, but a design parameter for air microfluidics.

The additive laws of fluidic resistors in series and parallel apply to microfluidic networks; hence passive microfluidic elements can be very powerful in controlling the sequential pressurization of soft fluidic actuators, reducing energy-consuming active valves, and simplifying control of soft wearable robots. It must be noted that the additive laws of fluidic resistors in series and parallel are only valid for the applications where Reynold's number approaches to zero, and for long narrow channels far apart [8]. However, the additive laws can be used as a useful tool for the design of most air microfluidic chips. More accurate pressure drops and flow rates can be determined through semi-analytical solutions, numerical simulations, and experimental measurements.

Henrik Bruus [8] consolidated various hydraulics resistances for straight channels with different cross-sectional area shapes. Equation (2.1) to Equation (2.3) show the hydraulic resistances of three most common channel cross-sectional shapes used in microfluidics, where $a[m]$ is the radius of the circle for Equation (2.1); h[m] and $w[m]$ are respectively the height and width of the rectangle for Equation (2.2); $w[m]$ is the side length of the square for Equation (2.3); $\mu[\frac{kg}{m \cdot s}]$ and $L[m]$ are the fluid dynamic viscosity and length of the fluidic channel for Equations (2.1) to (2.3).

Circle: $$\frac{8}{\pi} \cdot \mu \cdot L \cdot \frac{1}{a^4} \tag{2.1}$$

Rectangle: $$\frac{12 \cdot \mu \cdot L}{1 - 0.63 \cdot (\frac{h}{w})} \cdot \frac{1}{h^3 \cdot w} \tag{2.2}$$

Square: $$28.4 \cdot \mu \cdot L \cdot \frac{1}{w^4} \tag{2.3}$$

If more accurate pressure drop or flow rate is desired, the Hagen Poiseuille's law can be modified for compressible fluids such as air by timing it with an extra correction factor that expresses the average pressure relative to the outlet pressure [92]. Equation (2.4) shows the Hagen-Poiseuille's law for gas flow in round pipe assuming constant viscosity and no-slip boundary condition, where $Q[\frac{m^3}{s}]$ is the volumetric flow rate; $R\ [m]$ and $L[m]$ are the radius and length of the channel respectively; $\mu\left[\frac{kg}{m \cdot s}\right]$ is dynamic viscosity; and $P_i[MPa]$ and $P_o[MPa]$ are inlet pressure and outlet pressure respectively.

$$Q = \frac{\pi \cdot R^4}{16 \cdot \mu \cdot L} \cdot \left(\frac{P_i^2 - P_o^2}{P_o}\right) \tag{2.4}$$

Most of the previous studies on gas flow in microchannels have focused on the slip flow regime studying rarefaction effects and developing models. For instance, Roy et al. [93] developed a two-dimensional (2-D) finite element based model for predicting microscale flow up to the transition regime for reasonably high Knudsen number flow inside microchannels and nanopores. At a Knudsen number of 0.058, a 4%-8% higher-streaming velocity is detected from the slip flow results in the corresponding no-slip solution for the same pressure ratio; the increased velocity is due to lower-shear stress. **Figure 2.8a** shows the channel centerline pressure distribution, and **Figure 2.8b** shows the centerline velocity solution. It can be seen that the pressure distribution between the slip solution condition and the no-slip solution differs very little (~4% maximum difference).

Arkilic et al. [94] studied gas flow in a rigid and straight microchannel and developed a 2-D approximate analytical solution based on a 2-D perturbation of a continuous flow model with first-order slip boundary conditions as shown by Equation (2.5), where $\dot{m}\ [\frac{mg}{s}]$ is the mass flow rate; H, W, and L are height, width and length of the channel respectively all with a unit $[\mu m]$; $\mu[\frac{N \cdot s}{m^2}]$, $R\ [\frac{J}{mg \cdot K}]$, and $T[K]$ are dynamic viscosity, gas constant, and temperature respectively; $P_i[MPa]$ and $P_o[MPa]$ are inlet pressure and outlet pressure respectively; σ is the complete momentum accommodation coefficient which is almost always 1 for engineering calculations; K_o is the outlet Knudsen number. The Knudsen number is 0.155, which means the gas flow is within the transition flow regime. The gas flow occurred in long rigid silicon microchannels with nominal heights of 1.33 μm, nominal width of 52 μm and a length of 7500

μm. The result shows a substantial difference in pressure distribution and mass flow between the slip-flow solution and no-slip solution, and that the slip-flow solution matches experimental data almost perfectly (**Figure 2.9a**).

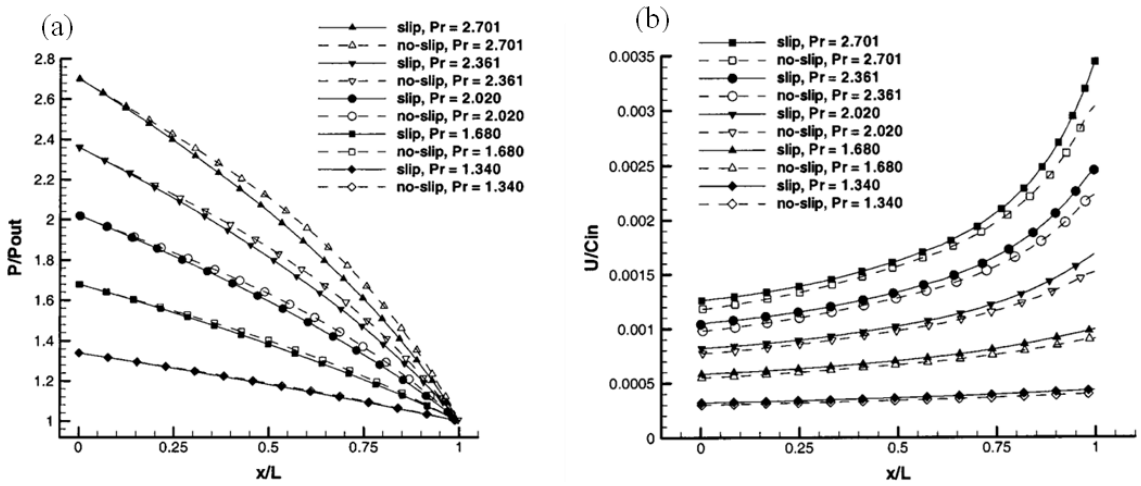


Figure 2.8: (a) Centerline pressure distribution normalized with outlet pressure P_{out}. Solutions are compared for the slip and no-slip conditions for five different pressure ratios ($P_r = P_{in}/P_{out}$). (b) Centerline velocity distribution normalized with the speed of sound at the inlet C_{in}. Solutions are compared for the slip and the no-slip conditions the five different pressure ratios ($P_r = P_{in}/P_{out}$). Both (a) and (b) are reproduced from [Roy et. Al., "Modeling gas flow through microchannels and nanopores," *J. Appl. Phys.*, vol. 93, no. 8, pp. 4870–4879, 2003], with the permission of AIP Publishing. [93]

$$\dot{m} = \frac{H^3 \cdot W \cdot P_o^2}{24 \cdot \mu \cdot L \cdot R \cdot T} \cdot \left[\left(\frac{P_i}{P_o} \right)^2 - 1 + 12 \cdot \sigma \cdot K_o \cdot \left(\frac{P_i}{P_o} - 1 \right) \right] \tag{2.5}$$

Hsieh et al. [95] verified the 2-D analytical solution by Arkilic et al. through looking at the slip regime, where the Knudsen number ranged from 0.001 to 0.02. The channel is 24 mm long with a width of 200 μm and a height of 50 μm. **Figure 2.9b** shows the pressure drop as determined experimentally and by 2-D analytical solutions. Although this 2-D analytical solution (Equation (2.5)) ignores the entrance and exit losses, they are the basis for any gas flow in long microchannels where the entrance and exit losses are small compared to shear stress and gas acceleration; hence inlet and outlet effects could be ignored.

There are other analytical and semi-analytical models reported for simple cross-sections, and most employ the first-order slip boundary condition, which has shown to be relatively accurate up to Knudsen number of 0.1. Hence, it would be sufficient to use Equation (2.5) for accurate calculations of pressure drops and flow rates for air microfluidic systems

[96]. Other models such as Navier-Stokes equations with second-order slip boundary condition, Burnett equations with slip boundary condition, direct simulation Monte Carlo, and lattice Boltzmann are primarily used for much larger Knudsen number in the transition flow and free molecular flow regimes suitable for nanoscale gas flows and hence are outside the scope of this perspective which focuses on discussing microscale systems [7].

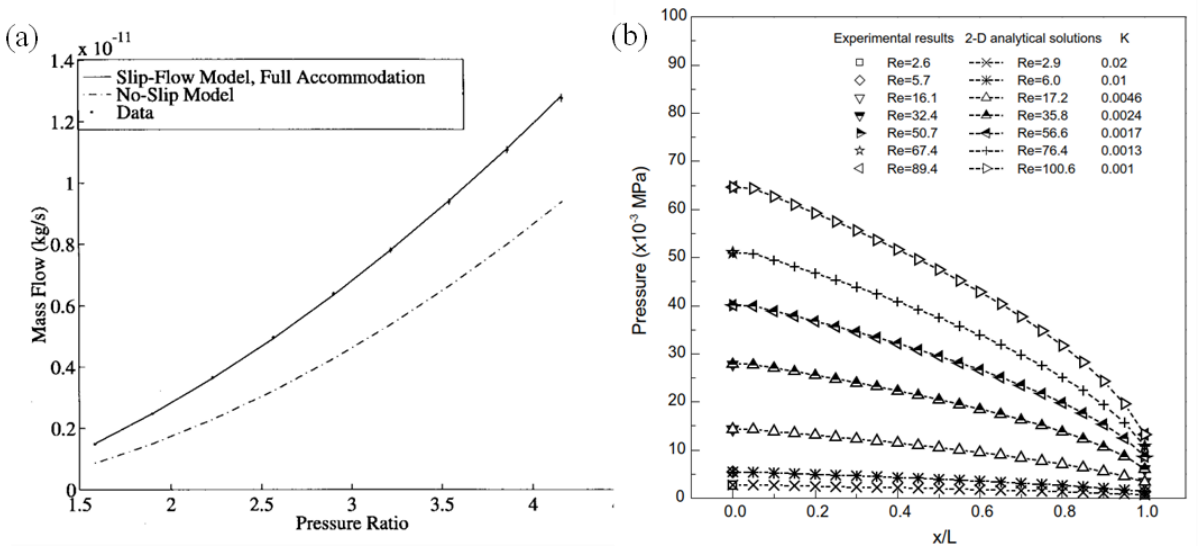


Figure 2.9: a) Helium mass flow for 1.33 μm channel (95% confidence intervals indicated). The solid curve is the solution to Equation 5, assuming full tangential momentum accommodation, and the dashed curve is the solution to Equation 5 setting Knudsen number to zero (no-slip solution); reproduced with permission from J. Microelectromechanical Syst. 6, 2 (1997). Copyright 1997, IEEE. [94] b) The comparison of pressure drop with experimental results and 2-D analytical solutions (Equation 5); reproduced with permission from Int. J. Heat Mass Transf. 47 (2004). Copyright 2004, Elsevier. [95]

Many practical applications of microchannels also incorporate bends, sudden contraction or expansion, T-junctions and Y-junctions. Agrawal [97] reviewed various experimental and numerical investigations. The conclusion of this review suggests that flow separation occurs at the bend and sudden contraction or expansion for laminar gas flow in microchannels resulting in higher pressure drop than straight microchannels. The exact results of these experiments and numerical simulations are not crucial for synergizing microfluidics in soft robotic applications; instead, these minor losses should at least be accounted for within the designs of the air microfluidic systems.

As for applications for soft robots, Vasios et al. [98] used viscous flow to simplify the actuation of fluidic soft robots where narrow tubes are used to achieve sequencing in the

actuation of soft fluidic actuators (**Figure 2.10a**). They also developed modelling and optimization tools to identify optimal tube characteristics for achieving complex target response of soft fluidic actuators. Preston et al. [99] developed a soft ring oscillator, which eliminates the need for hard valves and electronic controls (**Figure 2.10b**). The soft ring oscillator allows periodically oscillating outputs, which can be used in applications including undulating and rolling motions in soft robots, size-based particle separation, pneumatic mechanotherapy, and metering of fluids. Similarly, Gorissen et al. [100] developed hardware sequencing of inflatable nonlinear actuators for autonomous soft robots (**Figure 2.10c**), which uses passive flow restrictions without the need for complex on-board valves or bulky tethers. Ben-Haim et al. [101] exploits bistability of equilibrium states for hyperelastic thin shells, as well as pressure differences induced by viscous effects for reducing the number of fluidic inputs (**Figure 2.10d**). The theme here is using the physics of microfluidics combined with elastic or hyperelastic materials to simplify the control algorithm and control hardware. These are significant first steps and proof of concept that show the potential of synergizing microfluidics with soft robots. Still, much more work needs to be done, especially interdisciplinary collaborations, to apply these fundamental researches to real-world applications.

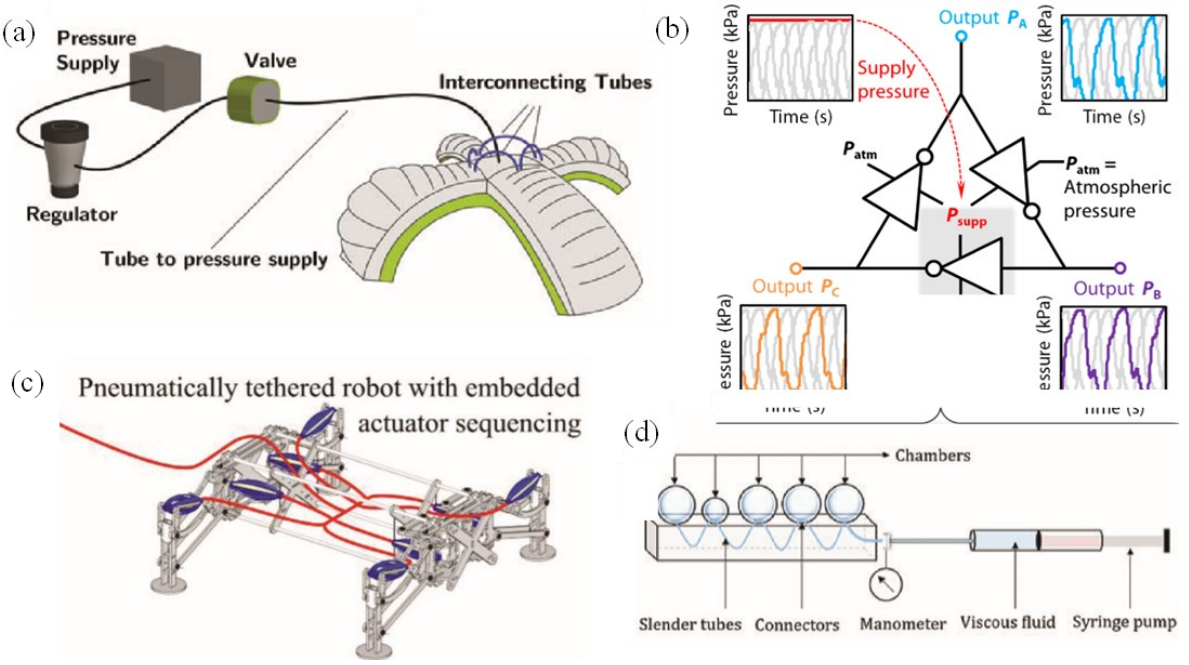


Figure 2.10: (a) Viscous flow in the tubes interconnecting the constituent actuators to design soft robots capable of achieving a variety of responses when inflated with a single pressure

input; reproduced with permission from Soft Robot. 7, 1 (2020). Copyright 2020, Mary Ann Liebert, Inc. [98] (b) A soft ring oscillator composed of three inverters connected in a loop, resulting in a systematic instability (because no stable state exists); reproduced with permission from Sci. Robot. 4, 31 (2019). Copyright 2019, The American Association for the Advancement of Science. [99] (c) By tuning the nonlinear properties of the actuators with intermediate flow restrictions, a single fluidic supply tube can be used without the need for internal valves to actuate a soft robot; reproduced with permission from Adv. Mater. 31, 3 (2018). Copyright 2018, John Wiley & Sons. [100] (d) Schematic picture of a serial chain of elastic chambers with a single inlet; reproduced with permission from Soft Robot. 7, 2 (2020). Copyright 2020, Mary Ann Liebert, Inc. [101]

2.3.4 Microfluidics and Interfacing with Soft Robots

When thinking about microfluidics, perhaps the first thing that comes to mind is microfluidic chip, which for many lab-on-chip applications serves as a platform for passive [102] or active [86], [103] control and manipulation of fluid carrying reagents and biological samples in the microscale and even the nanoscale. Also, microfluidic chip is the physical manifestation of the equivalent hydraulic resistance and capacitance as well as the active control strategies such as Quake's valves. Microfluidic chip that can be used for manipulating fluid to inflate and deflate soft fluidic actuators may be the missing piece for soft robotic applications that require a significantly higher number of soft fluidic actuators (i.e. digitization) and a miniaturized control box to achieve low-profile aesthetics. Although the focus is on using air as the pressurization fluid, liquid may also be substituted for various soft robotic applications.

The compressible characteristic of air and the equivalent hydraulic resistance can be used as tools to design dynamic sequencing for soft fluidic actuators. For example, parallel microchannels below 500 μm may be used as resistors to enable sequential inflation of a series of mini soft fluidic actuators based on the concept of the paths of least resistance (**Figure 2.11**). Elastic inflatable chambers between microchannels may be used as capacitors to store pressure energy. From a fundamental theory perspective, these tools are simple, but practically useful control strategies for a particular soft robot, which requires good microchannel network design that can be proposed and optimized through both simulation and experimental approaches. At the present day, there are no guidelines or simple semi-analytical models to design the microchannel networks to achieve this; albeit, computational fluid mechanics and finite element simulations can provide useful predictions at the expense of cost and time. Very complex pneumatic digital logic can also be built using these tools, as demonstrated by [104].

However, the usefulness of pneumatic digital logic is still unclear for soft robotics. If dynamic sequencing is not desirable, microfluidic chip may be used as a wearable manifold providing a fluidic pathway from the pump to the soft fluidic actuators to minimize the usage of tubing and fittings as seen in the soft robotic knee brace for managing knee osteoarthritis by Gao et al. [105]. Of course, all of this is predicated on having numerous mini/micro soft fluidic actuators.

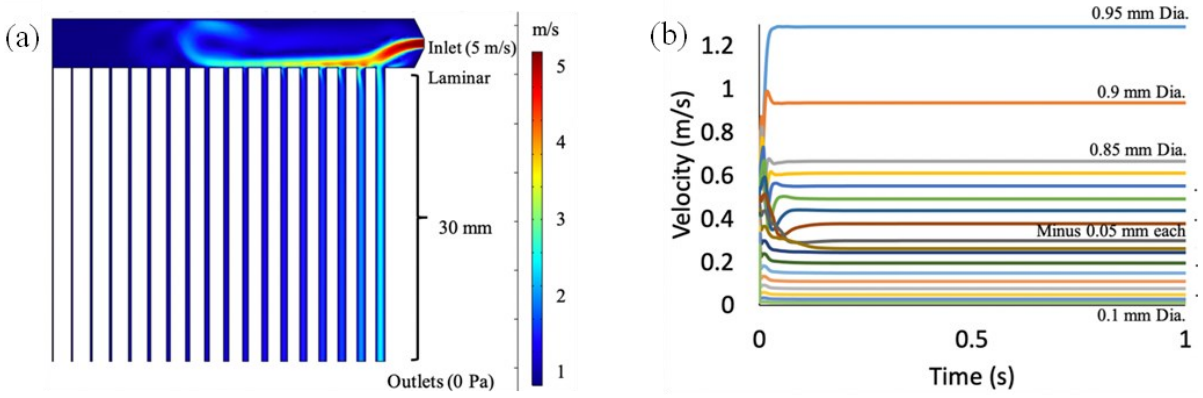


Figure 2.11: (a) Simulation demonstrating the concept of the path of least resistance with parallel microchannels. (b) the exit velocities of the microchannels shown in (a).

To convert this idea into a useful and practical device is complex and currently faces a few challenges. The first of which is how mini/micro soft fluidic actuators and strain-limiting layers can be produced in a reliable, scalable, and efficient manner. As mentioned before, larger-scale soft fluidic actuators are commonly produced via molding, pouring silicone into a 3D printed mold, and then gluing two pieces of silicone together using uncured silicone. This process may have difficulties at a smaller physical scale as the uncured silicone may clog the inlet channels, and the walls may be too thick or unevenly distributed. Skylar-Scott et al. [106] recently introduced a fused deposition modelling (FDM) 3D printing technique whereby polymers with different modulus may be printed at the same time from a specially designed nozzle (**Figure 2.12a**). When higher printing resolution is achieved, this technology has the potential to integrate microfluidic chips within soft robots as one piece. Wirekoh et al. [107] have developed artificial muscles that are flat when uninflated and produce uniaxial tensile stress when inflated as a replacement for bulky McKibben muscles incorporating modulus modifying materials (notably Kevlar strings) into its walls as the strain-limiting mechanism. Another technique is to use soft lithography or one of its variations, such as those introduced

by Taylor et al. [108], where they created milliscale soft robots via ultraviolet ozone bonding of PDMS and Mylar transparencies that can withstand internal pressure exceeding 1000 kPa (**Figure 2.12b**).

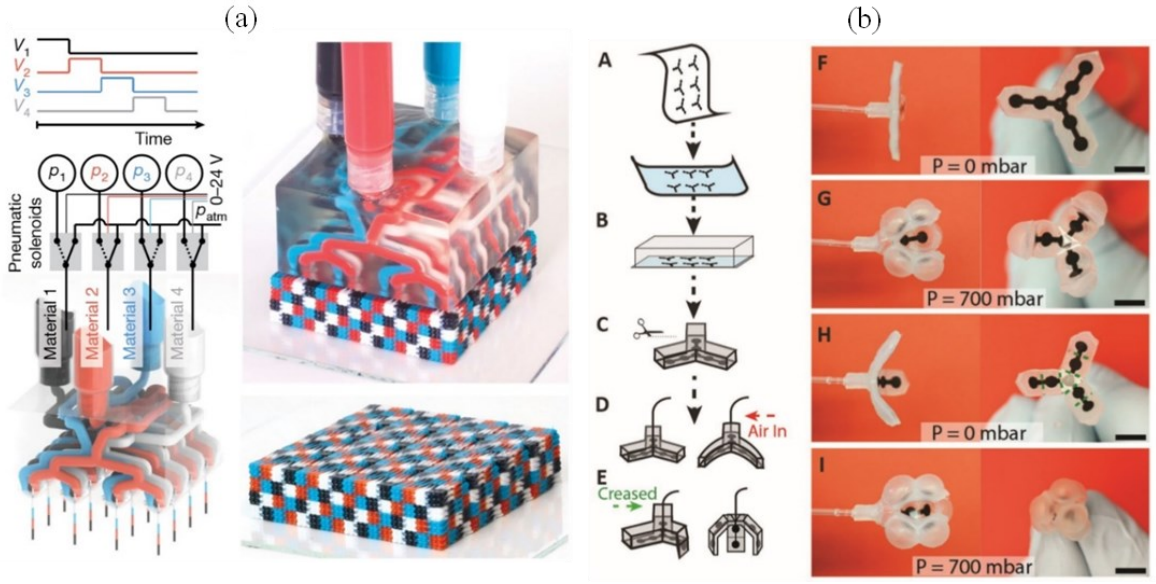


Figure 2.12: (a) Multimaterial multinozzle 3D printheads reproduced with permission from Nature 575, 7782 (2020). Copyright 2020, Springer Nature. [106] (b) Fabrication of milliscale soft grippers via ultraviolet ozone bonding of PDMS and Mylar sheets; reproduced with permission from Adv. Mater. 30, 7 (2018). Copyright 2018, John Wiley & Sons. [108]

Connolly et al. [35] introduced a method to produce soft fluidic actuators, in particular, bending actuators via heat press and taking advantage of the anisotropic property of textiles, which when combined with elastic or rigid plastic film, produces a strain-limiting layer (**Figure 2.3b**). This approach presents a few advantages. First off, the strain-limiting layer can be tailored to produce different desired motions, forces, or torques. Secondly, the elastic and rigid plastic film and the fabric are very thin, enabling low-profile soft wearable robots. On the other hand, the process can be tedious and labour intensive, especially during the washing of the water-soluble polyvinyl alcohol (PVA) film that forms the soft fluidic actuator chamber and gluing the tubing into the inlet of the soft fluidic actuator. This is perhaps acceptable for making larger soft fluidic actuators as presented in [35] and one-off prototypes, but it is not reliable for making a large quantity of mini or micro soft fluidic actuators. The correct fabrication process depends on the application, but the future of producing mini and micro soft fluidic actuators and strain-limiting layers should involve digital manufacturing and lots of automation to ensure quality, scalability, quick design iterations, and low cost.

The second challenge is related to how microfluidic chip should be made. Traditionally, microfluidic chips are fabricated out of glass- or silicon-based materials using photolithography technology or PDMS using soft lithography technology. The latter can be directly translated into making microfluidic chips for soft robotic applications as the softness of PDMS can be tuned readily. With the improvement in 3D printing technology, instead of making the molds via photolithography, molds can be 3D printed to achieve microchannels with a cross-sectional characteristic length of 750 μm or smaller. One lingering issue is concerning how to reliably bond two or more pieces of PDMS extracted from the 3D printed mold because the resulted surfaces are less smooth than those from the molds made via photolithography. Also, methods to integrate microfluidic chips with soft robots are worth investigating. Although they can adhere to the soft robot mechanically or chemically, the ideal way is perhaps to incorporate microfluidic systems directly into the material of soft robots considering the goal of miniaturizing the actuation system as much as possible. This is still a practical challenge as commercial 3D printers are yet to achieve the resolution, material and process required for reliable and cost-effective printing of internal microchannel networks, but increased commercial and research efforts in the 3D printing field make this very promising [109].

Third, tubing for soft wearable robots which potentially involve the use of a large number of mini/micro soft fluidic actuators can become messy and unmanageable very quickly. The tubing should be integrated onto fabric as an extra layer or replaced altogether by fluidic channels as part of the composite fabric. In addition, simple ways of tailoring the modulus of different parts of a piece of fabric are needed, this is perhaps in the form of elastic or plastic membranes that can be heat pressed onto the fabric selectively or built into the fabric manufacturing process.

Fourth, the control box or the backend should be easily pocketable or integrated as part of the clothing. The control box should be as flat and formfitting as possible, well incorporating all the necessary hardware. The control box ideally has a similar size to that of modern-day smartphones, the thinness would be difficult to emulate, but could be achievable where only the pump is slightly thicker while keeping other areas thin (**Figure 2.13a**). The pump needs to be energy efficient. As mentioned prior, battery-powered microcompressors offer the best energy density (J/g) as shown in **Table 2.1**. Among the microcompressors, the piston-

diaphragm pump is currently the most widely available off-the-shelf option, often sold as aquarium pumps or fluid dispensing units for medical devices. These off-the-shelf pumps often have two sections: the motor portion and the piston-diaphragm portion. To make the control box more compact and low-profile, the pump can be integrated with the frame of the control box, where instead of having a separate piston-diaphragm portion (**Figure 2.13a**), it can be integrated directly with the frame or the walls of the control box as compact as possible (**Figure 2.13b).** The frame of the control box also serves to dampen the noise and vibration from the motor. The piston-diaphragm assembly can be custom made via 3D printing and molding. Also, the motor that drives the piston-diaphragm could be reduced in size while retaining an appropriate torque and speed for a particular application by purchasing high-end coreless DC motors such as those offered by Faulhaber Micromo. In addition, multiple pumps can be connected in series and parallel to predominantly increase head pressure or flow rate, respectively, for the reason that a larger pump would increase the thickness of the control box, which is undesirable. Therefore, the focus is to reduce the thickness as much as possible. The empty spaces within the control boxes, as seen in **Figure 2.13**, are reserved for other electronic components such as microcontrollers, pressure sensors, and batteries.

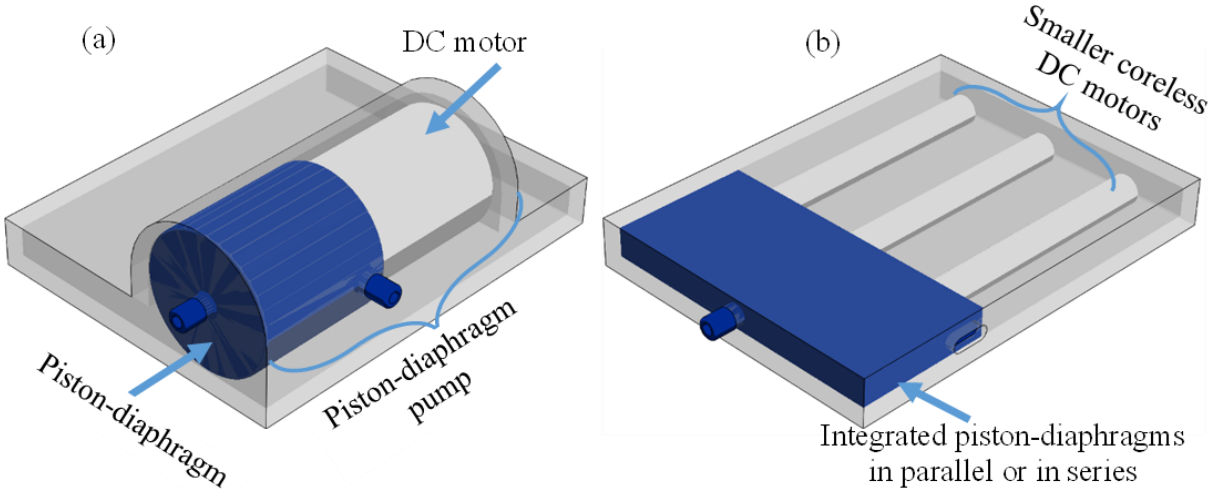


Figure 2.13: (a) Off-the-shelf piston-diaphragm pump integrated with a control box/backend. (b) Custom low-profile control box/backend by using smaller coreless DC motors with integrated piston-diaphragms in parallel or series.

Lastly, the sensors which measure pressure and strain as feedback for controlling actuators need to meet certain criteria based on the applications. In the context of synergizing microfluidics with soft robots, it can be broadly categorized into two sections: soft microfluidic

sensors for soft robots and microfluidics enabled soft robotic sensors. Soft microfluidic sensors are perhaps the first and to date, the most recognized usage for microfluidics with soft robotics. Researchers have been actively investigating microfluidic systems integrated with liquid metal such as gallium and Indium (EGaln) [110]–[112] for sensing purposes. Subsequently, a class of entirely soft sensors that can measure pressure and strain was developed for soft wearable robots. The purpose of these entirely soft strain sensors is to avoid rigid and hard components in soft wearable robots altogether. Park et al. [113] developed a type of hyperelastic pressure transducer by embedding microchannels of conductive liquid eutectic gallium-indium inside silicone rubber. Park et al. [114] subsequently improved the designs of the entirely soft sensor by switching from the soft lithography fabrication technique to a 3D-printing based multi-layer molding technique to create the microchannels that carry the conductive liquid. Also, the capability of the entirely soft sensor is expanded from just sensing pressure to also sensing strain. **Figure 2.14a** shows this entirely soft sensor. Further improvements to this class of entirely soft sensors were made to increase its robustness, eventually reaching results of up to 396% of strain and less than 2% change in electromechanical specifications through 1500 cycles of loading-unloading [115]. All of these improvements enable this type of liquid microfluidic-based strain sensor to monitor hip, knee, and ankle sagittal plane joint angles as a wearable sensor (**Figure 2.14b**). One major disadvantage regarding this type of sensor is the utilization of toxic conductive liquids, which can be hazardous when used as a wearable sensor.

The latest technical improvement of the entirely soft strain sensor resolved the safety issue regarding the potential leakage of the toxic conductive fluid inside microchannels by replacing it with conductive knit fabric as electrode and silicone elastomer as dielectric [116]. The fabrication method has also seen improvements by introducing a batch manufacturing procedure involving laser cutting (**Figure 2.14c**). Entirely soft sensors are preferable for soft wearable robots; however, they are not always necessary as most wearable sensors are miniaturized. For instance, the 9-axis IMU (ICM-20948) by TDK has a package size of only 3 mm x 3 mm x 1 mm, which can be easily encapsulated within soft silicone and integrated as part of the soft wearable robot. Also, EMG sensors have seen a tremendous reduction in size regarding the peripheral equipment required to process the signals, and the EMG electrodes have been developed to be reusable, washable, and integrated with fabric [117], which is spearheaded by Athos, an athletic wearable technology company.

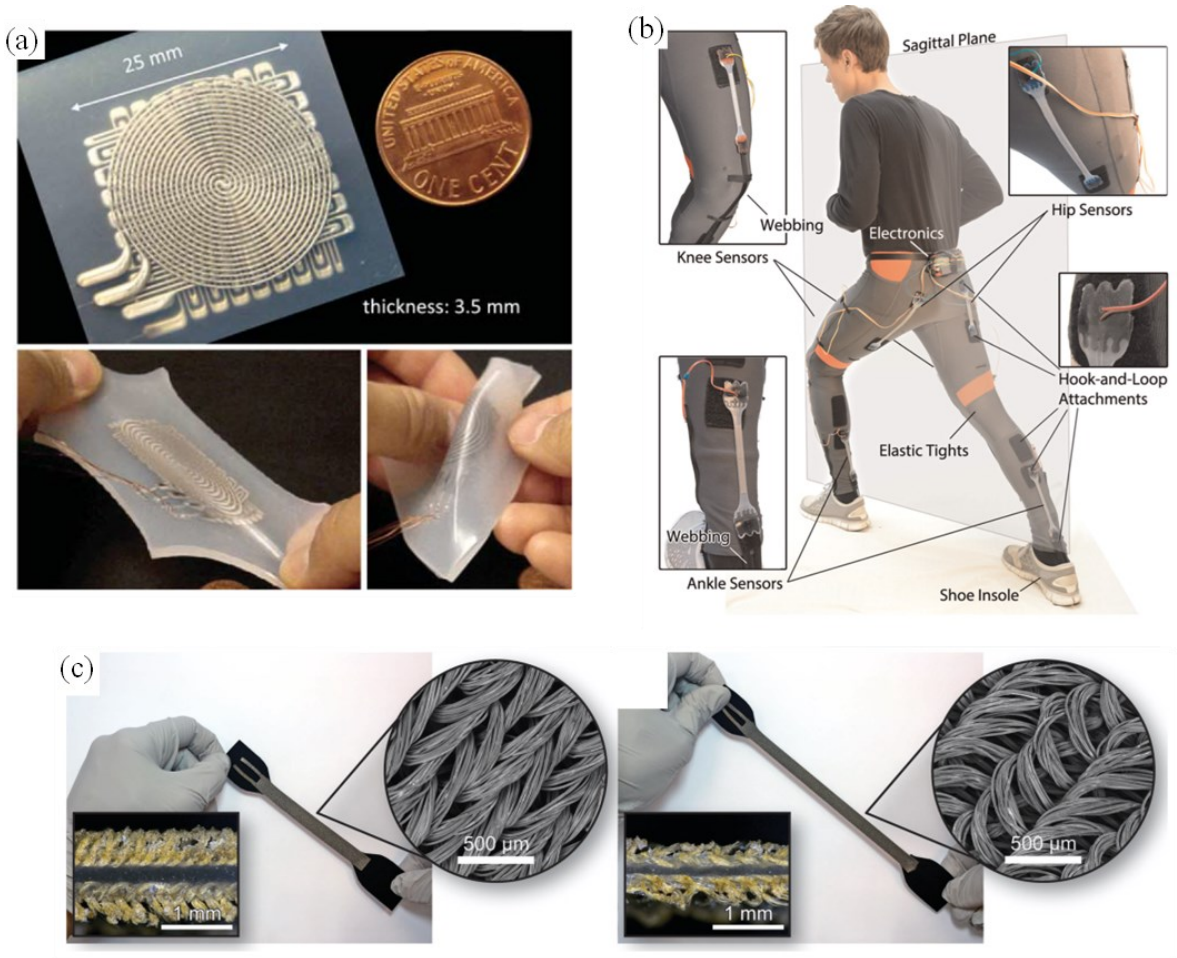


Figure 2.14: (a) Fully soft strain sensor reproduced with permission from IEEE Sens. J. 12, 8 (2012). Copyright 2012, IEEE. [114] (b) Soft strain sensors placed at each lower limb joint to capture motion in the sagittal plane; reproduced with permission from Int. J. Rob. Res. 33, 14 (2014). Copyright 2014, SAGE Publications. [115] (c) Photos of the sensor illustrating stretching at approximately 0 and 100% strain; reproduced with permission from Adv. Mater. Technol., 2, 9 (2017). Copyright 2017, John Wiley & Sons. [116]

As for microfluidics enabled soft robotic sensors, it derives from the idea of digitizing soft fluidic actuators via microfluidics. Basically, soft fluidic actuators that can be arranged in a tight array or stacked measure the force, torque, or compression acted upon them instead of acting as a force, torque or compression provider. The advantage here is that these sensors are compliant and elastic, which could fit over a contour or irregular shapes and create a 3D topographical map of the measured parameters (**Figure 2.15a, b**). Soft organic sensors or small piezoresistive sensors could be placed or float within the digitized soft fluidic actuators or directly integrated with its material to act as pressure or strain sensors (**Figure 2.15c**). The microfluidic channels and tubing connected to these sensors act as a pressurization pathway as

well as a signal pathway. For instance, an ultra-thin electrical wire could be embedded within the microchannels to carry analog electrical signals from the piezoresistive sensor within the digitized soft fluidic actuators. It must be noted, the examples shown in **Figure 2.15** is for illustrative purposes only, and by no means cover any specific application.

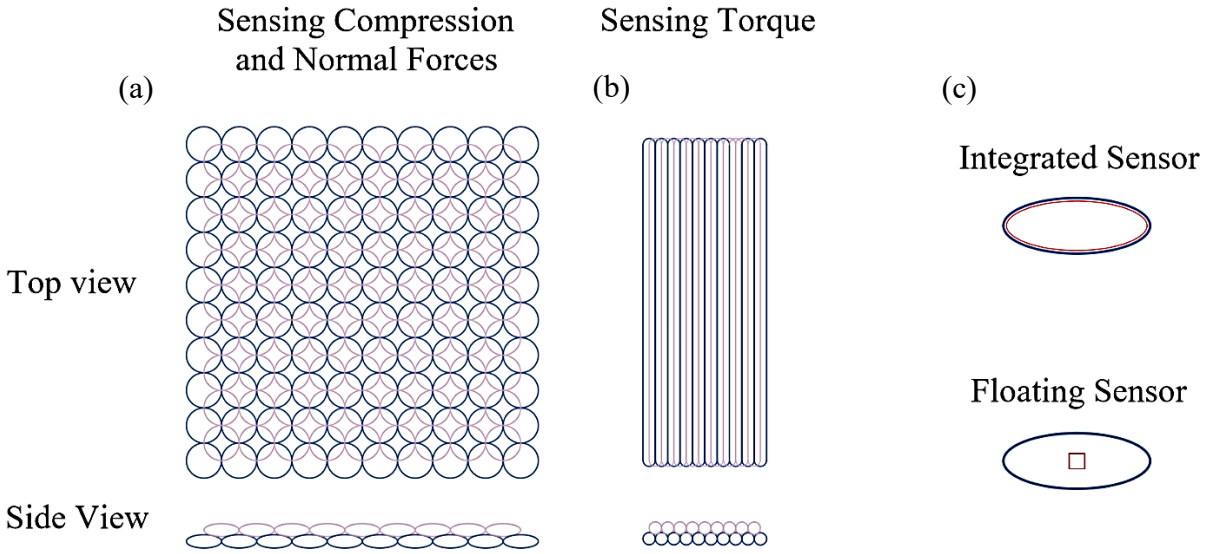


Figure 2.15: Concept images showing digitized soft fluid actuator/microfluidics enabled soft robotic sensors arranged in a tight array (a) for sensing compression and normal forces and (b) torque. (c) Concept image showing of incorporating soft organic sensors or small piezoresistive sensors within a digitized soft fluidic actuator/soft microfluidic sensor.

All in all, this section presents a literature review and perspective on how the actuation of soft robots, especially soft wearable robots, are intertwined with miniaturization. Also, we explored how the same concept used on actuators can be used for sensors, which we coined as microfluidics enabled soft robotic sensors. Microfluidics provides a convenient and direct avenue to allow the inclusion of numerous mini/micro soft fluidic actuators, independent control of said mini/micro soft actuators by different versions of Quake's valve, fast millisecond actuation of numerous mini soft fluidic actuators via microfluidic manifolds and integrated pathways, and sequential inflation patterns via passive microfluidic channel networks via the concept of equivalent hydraulic resistance and capacitance. Although not directly related to microfluidics in a technical sense, reducing the size of the piston-diaphragm pump while retaining an appropriate level of performance is vital for the miniaturization of the control box as the pump is probably the single largest component regarding thickness. The effort spent on research and development of actuation and sensing ultimately allows for the

exploration of entirely new applications and improving existing systems through soft robots. This may lead to a new paradigm regarding wearable assistive technology in terms of making them more dynamic, functionally better, more compliant, and more comfortable. This also opens doors to wearable technologies, which have been mostly limited to sensing, such as haptic wearables that can be used for leisure activities for the elderly via augmented/virtual reality. Below is a compilation of potentially applicable research directions that can have a real impact on the world.

2.4 Concerning Applications

The goal of this section is to provide a glimpse into different types of real-world applications that could benefit from the existing research and development, as mentioned in the previous two sections. The applications described below are intentionally presented in a broad and open-ended fashion as it serves as a guide, a vision, and a springboard for other novel ideas. Experts in each field hold their own opinion on whether microfluidics enabled soft robots are genuinely impactful for a particular application within the said field; nonetheless, the potential is there.

2.4.1 Daily Quality of Life

It is a universally shared aspiration to lead a good life and age gracefully. But life can be unpredictable, a health-related complication, diagnosis of a debilitating disease, slow progression of musculoskeletal disorders, or traumatic injuries often cause a decrease in quality of life. In this fight of self-preservation, there exist many devices that help us heal from acute injuries and manage chronic diseases; we envision this is where soft robots, especially the wearable kind when synergistically combined with microfluidics can provide innovation and new design paradigm to elevate existing solutions or produce completely new categories of useful products. Although microfluidics-enabled soft wearable robots do not ultimately eradicate the root causes of diseases, they can, however, improve an individual's quality of life, and that alone is worth pursuing.

Chronic pain symptoms, impairment and disability [118], [119] are some of the main reasons for a lower quality of life. Chronic musculoskeletal conditions are injuries and pain involving joints, ligaments, muscles, nerves, tendons, and structures that support limbs, neck and back. They are one of the leading contributors to disability worldwide [120] and are often

intertwined with depression [121] in the form of co-morbidity. Therefore, assistive devices that can manage the chronic pain symptoms, and effectively improve the physical function and mobility of their users could improve the users' quality of life tremendously as they also help improve mental health. For chronic conditions, an assistive device should ideally be worn daily, thus ease of use and aesthetics become a focus just as much as functionality. Depending on applications, the primary functionality changes, but the secondary goal should always be to reduce pain symptoms.

The digitized mini/micro soft fluidic actuators along with strain limiting layers can be perhaps used for targeted zonal compression and damping, which can be useful as external biomechanical torques for better range of motion, bracing for stability, enabling dynamic proprioception and massages, and improving various physiological/neuromuscular responses. When the digitized micro/mini soft fluidic actuators are deflated, they are flat and just part of clothing and become functional when inflated. Ideally, tight-fitting apparel should be used as the base for soft wearable robots as they hug the body contour enabling the soft fluidic actuators to become functional with less volume expansion, therefore enhancing the efficiency of the soft fluidic actuators. For more in-depth details on the biomedical applications of soft robotics, readers are directed to comment on the human-in-the-loop development of soft wearable robots [18] by Conor Walsh and an excellent review by Cianchetti et al. [122].

The current commercially available assistive devices for managing musculoskeletal conditions are braces, sleeves, kinesiology tapes and orthotics; these devices can range from $20 off-the-shelf sleeves to customized functional braces in the range of thousands of dollars. Microfluidics enabled soft wearable robots could improve these devices by adding dynamic functionality without introducing any bulk to the limbs as digitized soft fluidic actuators are miniaturized. Only a tolerable amount of bulk in the form of a low-profile control box for fluidic control and transportation that can be pocketed or integrated with fabric is introduced. As mentioned earlier, most of the cost comes down to the control box with the major expenses on the pump, microcontroller and battery as the expenses on the electronic valves and pressure sensors are negligible. It is unlikely to compete on cost alone with a $20 sleeve but instead offers a significant amount of performance boost via dynamic functional improvements that need to be thoroughly and independently verified, which would most likely make it a $200 solution competing with custom functional bracing and orthotic solutions. Although

microfluidics enabled soft wearable robots presents tremendous potential as active assistive devices, they are not meant to replace existing sleeves and braces, but rather complementing the existing lineup of assistive devices for the betterment of patients.

2.4.2 Prosthetic Applications

As mentioned before, one major advantage of using numerous mini/micro soft fluidic actuators is that when they are arranged in a close matrix, they can mimic an evenly distributed area compression force when combined with strain-limiting layers without the need of a large volume that fits over an uneven contour. In other words, by decreasing the size and increasing the number of soft fluidic actuators, the resolution of the treatment area and the ability to control pressure at specific locations dramatically improve. This meant that a 3D entity entirely can be made out of these mini/micro soft fluidic actuators controlled by one single microfluidic chip. These actuators could change in shape, volume, and stiffness that could fit on top of the body contours or fill up spaces within an irregular cavity. For example, prosthetic socket fit and comfort has always been an issue [123], especially for diabetic patients or users experiencing co-morbidities, this is perhaps where the technology presented herein could provide an additional solution or an add-on to existing prosthetic socket fit strategies [124] Instead of replacing current prosthetic socket suspension methods, namely vacuum suction, the two can be combined to provide better socket fit and comfort.

Pneumatic or even hydraulic actuated prosthetic socket (**Figure 2.16**) is not new, as seen in the review by Paterno et al. [125], but the question of its low adoption remains valid. There are many potential answers here, but one interesting answer is perhaps lacking tailored, varying and evenly distributed area compression forces, which make it difficult to fit an uneven contour requiring different compression levels. Regardless, thorough clinical studies would be needed to determine the usefulness of future pneumatic prosthetic sockets and benchmark them against the current best strategies. On a similar vein, cushions, in general, could be modified to produce dynamic fit, comfort and massaging using microfluidics enabled soft fluidic actuators. Whether this technology is appropriate for the application comes down to the cost, reliability, user acceptance, and competitiveness to other emerging solutions.

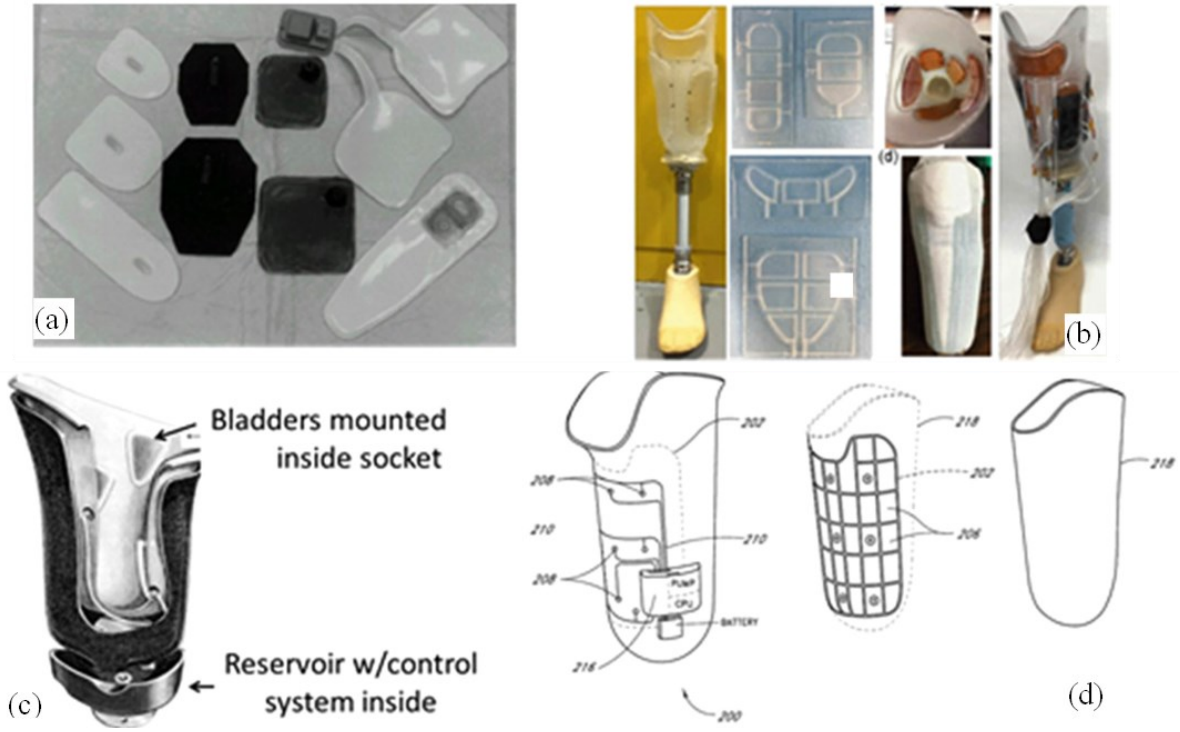


Figure 2.16: (a) Pneumatic inflatable inserts used in limb prosthetics, including the Air Contact System, PNEU-FIT, Pump It Up!, and Pneumatic Volume Control System; reproduced with permission from J. Rehabil. Res. Dev. 38, 4 (2001). Copyright 2001, Department of Veterans Affairs. [126] (b) Pneumatic actuator inserts for interface pressure mapping and fit improvement in lower extremity prosthetics; reproduced with permission from Proc. IEEE RAS EMBS Int. Conf. Biomed. Robot. Biomechatronics (2016). Copyright 2016, IEEE. [127] (c) Rendering of smart variable geometry socket (SVGS) technology applied to a transfemoral suction socket; reproduced with permission from J. Prosthetics Orthot. 15, 3 (2003). Copyright 2003, Wolters Kluwer Health, Inc. [128] (d) Socket insert having a bladder system (U.S. Patent 7.655,049 B2) [129].

2.4.3 Sports and Safety Apparels

Sports and safety apparels (including shoes) present a big commercial market. Miniaturization is perhaps the most important here as the bulk of the control box must be minimized so that it does not interfere with the movement of the person during sports, active leisure activities such as hiking, or working in warehouses or construction sites. This application mostly involves prophylactically minimizing the risks of injuries to muscles and joints, improving protection from helmets and pads, and postural-alignment haptic feedback. Again, the question comes down to whether this technology of using microfluidics enabled mini/micro soft fluidic actuators would be over-engineering existing sports and safety apparels, and whether it is appropriate for specific applications.

2.4.4 Haptics

Haptics is a significant sector where microfluidics enabled mini/micro soft fluidic actuators could become very useful. HaptX [64], a company working on virtual reality exoskeletons, was the first to adopt this technology; they have coined their technology as 'microfluidic skin,' which incorporates numerous silicone-based micro pneumatic bladders on a panel connected to microfluidic channels for fluidic transport (**Figure 2.17a**). In theory, when the micro pneumatic bladders are made sufficiently small and close in an array pattern, users' perception no longer treats them as individual tactile forces but rather a smooth area force. One major challenge with this type of haptic technology is how to create a wearable control box. Since each micro pneumatic bladder requires independent control, a microfluidic valve or equivalent could be used to miniaturize the control box drastically. Alternatively, electromechanical microvalves built into a microfluidic chip could also replace larger solenoid valves. Perhaps the biggest technological challenge here is achieving fast response time of this type of wearable control box for haptic applications requiring simultaneous independent control of multiple soft fluidic actuators.

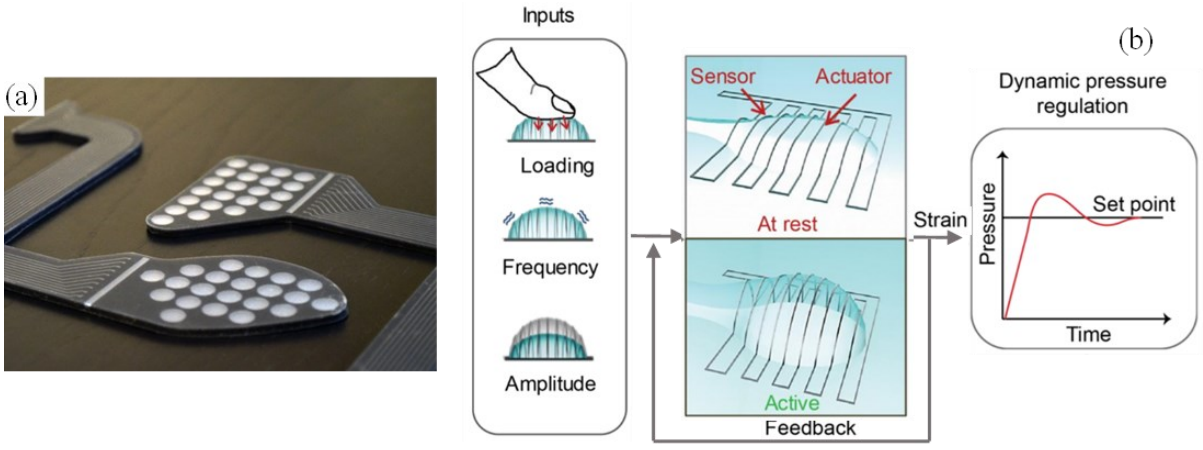


Figure 2.17: (a) HaptX microfluidic skin; Copyright 2020, HaptX Inc. [64] (b) The feedback control loop of the soft haptic system. The SPA-skin provides a highly conformal interface. A strain sensor of stretchable metallization can be used as the input to a feedback loop used to control the actuator inflation and exerted force. High-speed data acquisition allows strain sensing and actuation over a range of actuation frequencies from 0 to 100 Hz; reproduced with permission from Soft Robot. 7, 1 (2020). Copyright 2020, Mary Ann Liebert, Inc. [130]

It must be mentioned that HaptX, as a company, naturally holds patents [131] and patents pending on this technology. Academia's role would be to tackle the fundamental grand challenges regarding better materials, control strategies and miniaturization. For instance,

Sonar et al. [130] presented a soft pneumatic actuator skin (**Figure 2.17b**) incorporating self-sensing that is capable of high-frequency vibrations (~100 Hz). Lastly, perhaps the mini/micro soft fluidic actuators could be further miniaturized and placed together or even overlap with each other to improve the sensation further when touching a smooth surface, perhaps the micro balloon actuators could be so small that they are considered a digital on/off point instead of having to control pressure. Alternatively, magnetorheological or electrorheological fluids could replace the pneumatic system altogether if safety and response time can at least be on par with pneumatic systems.

2.4.5 Pediatrics

Certain versions of microfluidics enabled mini/micro soft fluidic actuators could also be used for pediatric applications and nursing applications for children and toddlers. The functionality of mini/micro soft fluidic actuators is applications dependent, but generally speaking, they are meant for comfort, assurance, a warm embrace and many usages already discussed above.

All of the applications mentioned above share a commonality where the actuation timing is essential, whether using a passive microfluidic chip, a microfluidic wearable manifold, a Quake's valve system, or indeed, any type of microfluidic control system, specific actuation response time must be met. For instance, a system meant to sync with human gait, the actuation must be fast on the millisecond scale. Similarly, a system that is unpredictable, such as a haptic system must minimize the delay between when the signal is received by a valve and the mini/micro soft fluidic actuator, or a massage system requiring predefined sequential inflation and deflation to mimic percussive massage. All in all, activities of daily living such as those described above presents some high impact applications for microfluidics enabled soft robots where miniaturization is perhaps key for user adoption, but for more specialized purposes, what microfluidics bring regarding functionality play a considerable role.

2.4.6 Medical Instrumentation (Minimum Invasive Surgery)

When it comes to medical equipment, one of the first things is surgical instruments, in particular open surgery instruments, due to the conformable nature of soft robotics. Spurred on by recent innovation in automation and robotics, minimum invasive surgery (MIS) is becoming a widespread reality in terms of the number of hospitals capable of delivering MIS but also the

type of surgery possible. One of the initial goals of soft robots in MIS is to improve endoscopes by creating soft and compliant systems that mimic the motion of a worm, snake, or octopus's tentacles. For a more in-depth review of current soft robots in the research phase for MIS and future directions, readers are referred to an excellent review Runciman et al. [132].

Microfluidics allows numerous mini or micro soft fluidic actuators to be fitted onto a soft robot to control locomotion, such as forward propulsion or bending. The idea of digitizing mini or soft fluidic actuators could enable tethered soft robots in the form of an earthworm that could navigate unstructured and arduous paths to perform MIS. In other words, a microfluidics and soft robotics enabled next-generation endoscope that is smaller in size and more functional could be envisioned and created. Ranzani et al. [133] demonstrated the capability of microfluidics with micro-balloon actuators for bending by creating a 12-layer soft peacock spider via multilayer soft lithography (**Figure 2.18**). There is plenty of space in a surgical operation room; therefore, no need to miniaturize the control box. A precision fluid control system such as those from Fluigent, Elveflow, or open-source modular system such as the μPump [134] can be used to control the microfluidics enabled soft robot for MIS applications. The mini/micro soft fluidic actuators could produce locomotion in the form of peristaltic crawling and bend as shown by the peacock spider, at the same time, bringing uninflated bladders/catheter to produce room for surgery and diagnosis via an onboard camera. Similar to existing endoscopes, a channel for surgical tools could be incorporated. Pneumatic actuation would most likely need to be replaced with hydraulic actuation in order to ensure air bubbles do not get trapped inside the human body due to leakage, and hopefully low pressure actuation could be developed to ensure that an accidental burst of a mini/micro soft fluidic actuator do not cause damage to the patient.

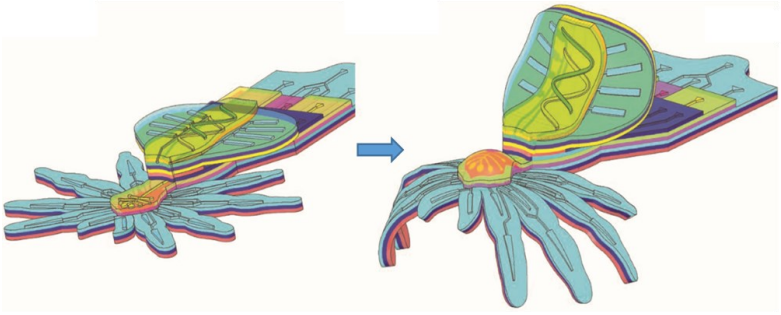


Figure 2.18: 3D structure through the injection-induced self-folding; reproduced with permission from Adv. Mater. 30, 38 (2018). Copyright 2018, John Wiley & Sons. [133]

2.4.7 Educational Tools

Microfluidics enabled soft robots can be used as biomedical education tools as well, where they can be used to mimic both the functionality and aesthetics of organs, tendons, ligaments, and muscles, which when used in conjunction to cadavers, textbooks, and images, could improve the student's learning experience. For instance, multiple soft fluidic actuators, when combined in series, could mimic the motion of tendons and muscles. In addition, the cardiovascular system could be mimicked by microfluidic channels using dyed water as the flow medium to mimic blood or other bodily fluids. This could be particularly useful in the field of biomechanics, kinesiology and physiology.

2.4.8 Pressure Mapping

Also, microfluidics enabled mini/micro soft fluidic actuators could be used as a high resolution (spatially and magnitude-wise) elastic pressure mapping system when assembled in a matrix fashion. The idea here is to embed small piezoresistive sensors or micro-sized soft pressure sensors made from organic materials within the mini/micro soft fluidic actuators, and microchannels as a conduit for signal traces and a pathway to inflate the mini/micro soft fluidic actuators to a predefined initial pressure level and volume. The existing state-of-the-art commercial systems are pressure-sensitive resistors [135], which are thin and flexible at just a few mils, but inelastic due to the dielectric layer used in the laminate. The microfluidics enabled mini/micro soft fluidic actuator arrays are elastic and can be used in a situation requiring said elasticity, such as conforming to a contoured surface and testing the pressure distribution of cushions and apparels.

2.4.9 Sensory Testing

Furthermore, microfluidics enabled mini and micro-sized soft fluidic actuators could be used as a quantitative and objective medical assessment for sensory testing of patients with diabetes or sensory neuropathy in general. For instance, a sock or sleeve embedded with mini and micro-sized soft fluidic actuators along with strain-limiting layers could be worn on the foot and lower leg to test for the extent and severity of loss of protective sensation due to diabetes. The current gold standard is the Semmes-Weinstein monofilament test [136], which can be challenging to implement clinically and introduce inconsistencies in results. For in-

depth discussions on the pros and cons of different types of sensory testing, readers are referred to an excellent review article by Craig et al. [137].

2.4.10 Human-Machine Interaction

The applications above show some improvements or novel new designs in some very practical, albeit specialized applications that are of interest to people of different and perhaps unique expertise. They could be achieved in not too long, given the application is worthwhile, and various engineering challenges are addressed. However, it would be beneficial to end this section on a grander vision, one that perhaps is far from pragmatism, but nonetheless worthwhile. In many science fiction movies, robots live and work among humans not just in the form of specialized robots that are preprogrammed for precision factory or warehouse work, but humanoid robots that can conduct various human labor and activity with better physical attributes, an advantage of mechanical systems instead of biological structures. For these humanoid robots to work safely alongside humans as nursing robots, caretaker robots, chef robots, and many more, there must exist multiple redundant safety and compliance features in the form of software and hardware. As for microfluidics enabled soft robots, they could be used as part of these futurist humanoid robots in the form of an outer skin layer that covers parts of the robot that physically contacts human. This skin layer has two primary functions; one is for sensation, in particular, pressure feedback for the humanoid robot's fine motor control for delicate movements, another is the precise actuation of the fingers, head, and facial expressions. Of course, a futurist humanoid robot will be a combination of different technologies with one of them being microfluidics enabled soft robots.

This section is by no means exhaustive. Therefore, the focus is to provide some insights into what microfluidics can do in addition to life science, and a glimpse into the many hopefully high impact and some wild applications or directions that one can take by synergizing microfluidics and soft robots. In the next section, an often neglected subject during the research and development of novel systems and devices is discussed, that being aesthetics and ease of use.

2.5 Concerning Aesthetics and Ease of Use

Anyone who has worked with soft wearable robotics or wearables, in general, knows the importance of a low-profile sleek form factor, the 21st-century athleisure look; that elusive material or system fueling our imagination; that one day our clothing without changing its form factor can be of physical assistance to us. Regardless of applications, what ultimately frustrates or stall many from implementing the ideal system imaginable is the technology available to them at the time, the fundamental bottlenecks that stand in the way for real-world adoption, the genuine issue of time and resource, and the way of conceptualizing.

Since synergizing microfluidics with soft robots is revolved around and has its utility most magnified in the creation of soft wearable robots. One of the key requirements for wearables is its aesthetics and ease of use which plays the key role in user acceptance and thus justifies the need of a section. As mentioned briefly in the previous sections, aesthetics is a highly subjective topic and can be challenging to quantify. Engineers and designers strive to create goods that appeal to the masses, which is particularly evident in the consumer electronics sector [138]. Therefore, soft wearable robots, a consumer product that is worn on the human body, could be aesthetically scrutinized in the same vein as consumer electronics.

User acceptance and device abandonment have always been issues in assistive technology and wearable technology in general. One-third of wearable assistive devices have been abandoned due to various reasons [139]. Assistive devices come in many different sizes, form factors, and purposes ranging from hardware to software. For instance, aesthetics for a wheelchair is entirely different to wearable insulin pumps or an iPad app for cognitive training or a knee brace for managing osteoarthritis. One can see those above-mentioned devices fall into different categories regarding the inherent form factor and necessity of assistive technology, and therefore cannot be judged according to the same standard. For instance, aesthetics is more forgiven for a device if it only needs to be worn for a short amount of time, is crucial to the user's everyday wellbeing, has historically been bulky and existed for a long time, or has been accustomed by users for its look, users tolerate. **Figure 2.19** is a simplified yet, in our opinion, unequivocal attempt to try to illustrate the importance of aesthetics and ease of use. As I mentioned before, aesthetics is subjective, and **Figure 2.19** is subjective and does not highlight the multifactorial nature of aesthetics and, by extension, the art of design;

still, the message is clear. There are many unknowns regarding the role that soft wearable robots will play, but one thing certain is that soft wearable robots bring a new paradigm regarding functions and designs of wearable devices, therefore, as much as function trumps all, aesthetics and ease of use are perhaps paramount for user acceptance and adoption.

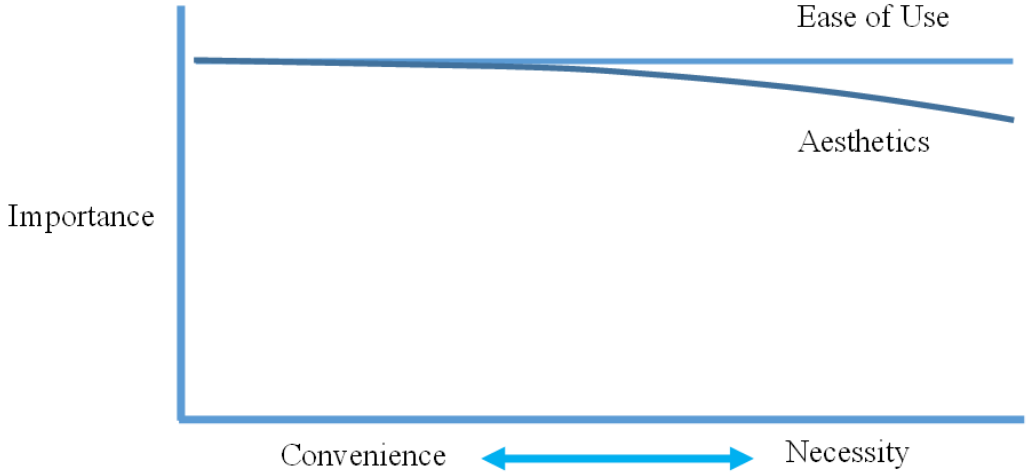


Figure 2.19: Relative importance of aesthetics and ease of use for soft wearable robotics to achieve user acceptance and adoption.

2.5.1 Factors for User Adoption

Soft wearable robots are inherently compliant in the material sense, which is inherently advantageous regarding aesthetics and ease of use as they can conform to the body while potentially donned in ways similar to that of apparel. This is echoed in a review by Veal and Xie in 2016 [140], where they looked at the current and emerging compliant and wearable robotic orthoses and documented advantages and disadvantages of various actuation systems. Their review analysis reveals that compliance, high specific power and force, natural motion characteristics, infinitely variable back-drivability, ease of control, and efficiency are the key performance requirements. At the same time, low mass, slim form, low cost, modularity, environmental compatibility, and quietness are key physical requirements. Lastly, as a must, sanitary cleanliness, safe exposed parts, and limited range of motion, speed, and force are safety requirements.

Not all metrics benefit from miniaturization; therefore, a closer inspection of the metrics is worthwhile. Infinitely variable back-drivability and ease of control perhaps do not benefit much from miniaturization, as they are more related to the design and implementation

of the soft wearable robot. As mentioned earlier, high specific power and force metrics may be negatively affected by miniaturization, although this could be somewhat alleviated by well-designed strain-limiting layers and placement of mini/micro soft fluidic actuators. Compliance and natural motion characteristics should see a considerable boost from miniaturization and especially digitization as multiple mini/micro soft fluidic actuators mimicking that of a large soft fluidic actuator contour to the human body better potentially allowing for less restriction to the movement of the user. Pressurization efficiency should be increased as miniaturization of the soft fluidic actuators reduces the volume of inflation; however, the efficiency of the whole system is applications dependent. Low mass is a direct consequence of miniaturizing the control box, and the slim form factor benefits from miniaturization in two ways; first the volume of the fluidic actuators is decreased; thus they stick out from the body surface less, and second the tubing diameter is reduced and the control box becomes flatter. As mentioned before, most cost of the materials and parts associated with soft robots is from the control system; therefore, the use of less electromechanical valves, smaller pumps and batteries reduces the cost of the device. Smaller pumps do not always translate to quieter performance; however, it does mean that thicker insulation could be used to damp the vibration and lessen the noise produced from the pump. Perhaps an added benefit of miniaturization and digitization of soft fluidic actuators is to improve better ventilation via the gaps between each soft fluidic actuator, thus improving sanitary cleanliness. The above is a general perspective on the pros and cons of miniaturization and digitization. Metrics are often intertwined; a change in one aspect has both positive and negative impacts. As a side note, Veal and Xie also indicated that to wear an orthosis comfortably all day, the weight of an orthosis located on the torso, each foot, or each hand should be less than 15%, 1.25%, or 3.75% of the user's body weight respectively, this correlation based on subjective conclusion from two earlier papers [141], [142]. Also, the thickness of distally located orthosis should ideally have a thickness of 10mm, which is based on various passive orthosis dimensions.

2.5.2 Social Acceptance and User Perception

Diving deeper into the social acceptance side of soft wearable robots. Although no direct studies have been reported on soft wearable robots regarding social perception and adoption, studies on wearable sensors and wearable electronics give a holistic understanding of the social

challenges of soft wearable robotics, albeit indirectly. F.D. Davis proposed [143] that the perceived usefulness and perceived ease of use are the two factors that contribute to the end-user's acceptance of a new information system. Davis proposed a model, which was coined as the technology acceptance model (TAM) with early computer-based information systems in mind, and did not directly consider the proliferation of portable and eventually wearable technologies. Regardless, TAM set the foundation for technology innovators and device makers to recognize the user acceptance side of technological advancements. Malhotra and Galletta [144] later extended the TAM model to include psychological attachment (**Figure 2.20**), which encompasses various social influences that make or break people's commitment to new technologies. In Malhotra and Galletta's own words: "when social influences generate a feeling of compliance, they seem to have a negative influence on the users' attitude toward use of the new information system. However, when social influences generate a feeling of internalization and identification on the part of the user, they have a positive influence on the attitude toward the acceptance and use of the new system." In other words, perhaps the user is more likely to adopt new technology when the said person has personal investments and appreciation for the capabilities and the overall trend of a particular technology, not just the intended use, and that piece of technology has been promoted via means of which the users have a high degree of respect and liking. Similar to Davis, Malhotra and Galletta mainly focused on user acceptance of information technology in a broad business or company setting. However, more specific studies for user acceptance of wearable technology and assistive devices began immerging around the turn of the 21st century.

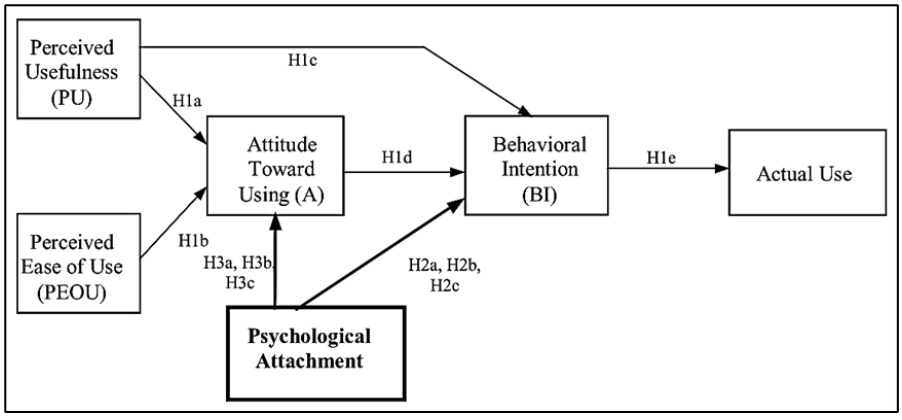


Figure 2.20: The technology acceptance model extended to account for psychological attachment; reproduced with permission from Proceedings of the 32nd Annual Hawaii International Conference on Systems Sciences (1999). Copyright 1999, IEEE. [144]

2.5.3 Wearability

In 1998, Gemperle et al. [47] explored design for wearability. They proposed thirteen guidelines for wearability (**Figure 2.21**) and examined six in detail, which are placement, form language, human movement, proxemics, sizing, and attachment. The researchers found that the most unobtrusive placement for wearable systems on the human body is the collar area, rear of the upper arm, forearm, back, side, and front ribcage, waist and hips, thigh, shin, and top of the foot. Softening the edges of a wearable device and keeping it within the intimate space of the wearer are important design factors to consider. Lastly, due to the variation in the human body, any wearable device must be designed so that it can be worn comfortably for the intended users. Gemperle et al. mentioned accessibility for different activities, weight distribution, thermal concerns, interaction issues, material preferences, and long-term effects on the body are future research directions for design for wearability.

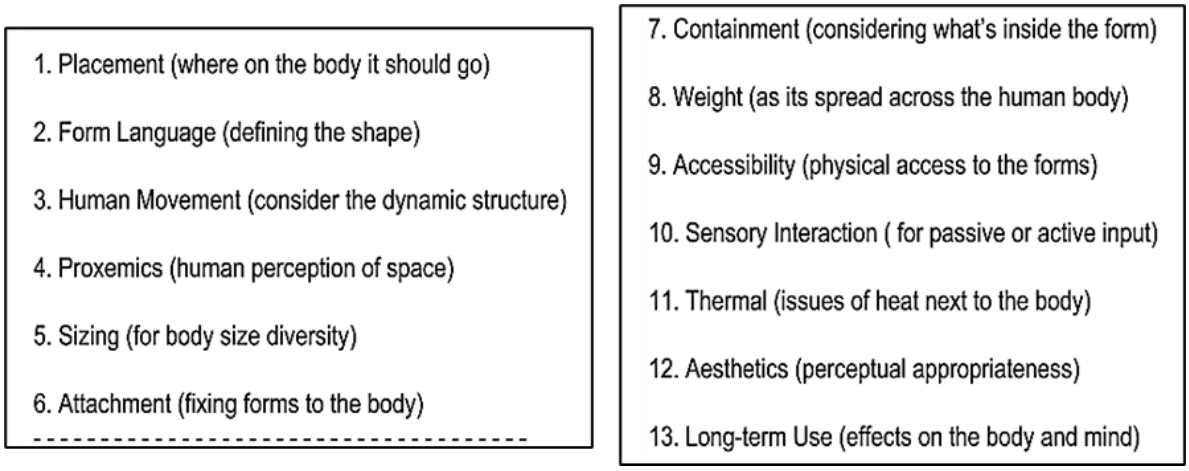


Figure 2.21: Guidelines for wearability reproduced with permission from Int. Symp. Wearable Comput. Dig. Pap. (1998). Copyright 1998, IEEE. [47]

2.5.4 A Few Last Comments of User Adoption

Kintsch and DePaula [145] developed a framework for the successful adoption of assistive technology, which many soft wearable robots are. In the words of Kintsch and DePaula: "Assistive devices are often purchased and tried, but true success fails because users and their caregivers are unable to integrate the device into their daily lives." Indeed, as mentioned earlier, roughly one in three assistive technology device is abandoned [139]. Kintsch and DePaula mentioned that perhaps the high percentage of assistive technology abandonment is due to not involving stakeholders, especially the users in the design and implementation

phases, as well as not fully incorporating the user's goals and preferences in the design. To further elaborate, the adoption process should involve the users, the caretakers, the assistive technology specialists or physical therapists, and the developers of the assistive technology device. Assistive technology has to be not only useful and usable, but also aesthetically pleasing, age-appropriate, fashionable, and culturally and socially acceptable. To this end, the developers of assistive technology should try to design devices in a way that they do not unnecessarily single out the user in his/her social environment; in other words, if a device looks "handicapped," the user will most likely not adopt it. This idea is reinforced by Toney et al. [146], where they mentioned that due to social weight, the user of wearable technology should interact with wearable technology in a streamlined fashioned that masquerade the technology. Of course, for certain assistive technologies, it is difficult, if not impossible, to achieve what is said above. Still, the overall message is undoubtedly helpful in the design of assistive technologies, and soft wearable robotics must follow the same design philosophy as well.

Soft wearable robotics share many design philosophies similar to wearable sensors as both systems have applications in the realm of assistive technology and are worn on the human body. Bergmann and McGregor [48] reviewed wearable sensor design in a biomedical setting from the viewpoint of what patients and clinicians want. The authors pointed out that the key user preferences for wearable sensors are that they are compact, embedded, and simple to operate and maintain, further citing that wearable sensors should blend in with clothing and be comfortable. Regardless of age and health, aesthetics and social stigma are universal concerns with wearable sensors. Also, the authors mentioned that ideally, the users would forget that they are wearing sensors throughout the day. In addition to the user preferences above, users are also concerned with forgetting to wear the sensors and the cost of purchasing wearable sensors. The authors noted that the users prefer to have the wearables sensors embedded into clothing instead of wearing them on top of or underneath clothing. Last but not least, Bergmann and McGregor suggested that "any device developed explores user preferences with the same rigor as they would for engineering related requirements."

It should be to no one's surprise that the clear-cut winner to achieve the most desirable aesthetics, as highlighted by this section, is to use smart materials that transfer electrical energy directly into mechanical energy. That been said, a simultaneous parallel path where mature fabrication techniques, as well as the tools already developed in microfluidics, should be

utilized to the advantage of the designers of soft robots to achieve products that make an immediate impact in people's lives in the near future. Microfluidics could provide some of the technical answers as highlighted in the previous sections, and the philosophy that comes with microfluidics regarding miniaturization, digitization and the intertwined nature of aesthetics and functionality is a welcoming one. Perhaps if designers consider miniaturization or the potential for miniaturization to achieve the desired aesthetics as one of the design criteria, the adoption of soft wearable robots could be profound. In this case, the embodiment of microfluidics, miniaturization and multiplexing, could be illuminating.

2.6 Concluding Remarks

In conclusion, to answer the question posed at the very beginning of this chapter: "microfluidics can be combined with soft robotics, but should it be?" The answer is a yes, whereby, steadfast in its philosophy, but also malleable and creative in its execution. The philosophy is forthright: miniaturizing both the control system and the fluidic actuators while maintaining proper functionality whenever and wherever possible. The execution is much less straightforward; firstly, it must fit the application; secondly, it must be feasible in both fundamentals and practice, and thirdly, it must be advantageous to alternatives. This is challenging, which is the reason driving the need of an interdisciplinary approach, with many fundamental and applied research questions to be answered, in particular, microfluidic control strategies, fabrications, and how to use these tools to benefit our society. We are only scratching the surface of what is possible from synergizing microfluidics with soft robotics; the potential is immense.

Chapter 3

Investigating Miniaturization of Soft Robotic Control Systems Using Passive Air Microfluidics with Applications for Sequential Gradient Compression

The work included in this Chapter is published: **R. Z. Gao**, V. N. T. Mai, N. Levinski, J. M. Kormylo, R. W. Murdock, C. R. Dickerson, and C. L. Ren, "A novel air microfluidics-enabled soft robotic sleeve: Toward realizing innovative lymphedema treatment," *Biomicrofluidics*, vol. 16, no. 3, p. 34101, May 2022, doi: 10.1063/5.0079898 [147]. I contributed to the conceptualization of the idea, fabricated the devices, conducted simulations and experiments, developed the figures, and authored the manuscript.

3.1 Introduction

The lymphatic system, a vital part of the human immune system, is often overlooked by the general population until it has been compromised. It is responsible for the transport of lymph fluid, which is mostly water carrying waste products and toxins for removal and nourishment to tissues throughout the body [148], [149]. Lymphedema, a condition that affects 250 million people worldwide [150], occurs when the transport of lymph fluid is inadequate or disrupted. Secondary lymphedema results from a compromise to the system arising from damage as can occur during mastectomy, radiation therapy, infection, or other injuries to the lymph nodes. It causes subsequent accumulation of excess lymph fluid in tissues [148], [151]. The accompanying symptoms include swelling, pain, discomfort, loss of range of motion, body image issues, and proneness to infection due to the bacteriophilic proteins found in the lymph fluid [148], [152]. It is estimated that at least one in five women who have breast cancer develop lymphedema and on average 75 Canadian women will be diagnosed with breast cancer

every day [152]–[154]. The overall cost of managing this disease for an individual could range from $14,887 to $23,167 beyond primary breast cancer treatment costs [155].

The most widely used modern therapy for lymphedema is Complete Decongestive Physical Therapy (CDPT), which is a collection of methods including manual lymph drainage (MLD), bandaging, exercise, skincare, and a transition to self-care [156]–[158]. MLD involves massaging the patient's affected limb using a squeezing and dragging motion from the distal extremities toward the body to drain fluid from the limb and thus increase lymphatic circulation [159]. It is often followed by bandaging to reduce further swelling. As MLD and bandaging are laborious to perform on oneself, more easily worn compression sleeves have become the mainstay of lymphedema treatment for self-care [160], [161]. With the increasing global pressure of an aging population, self-care systems will be more demanding. Although these traditional compression sleeves have some usefulness, they only provide constant static pressure to the limb, which limits their effectiveness in response to the variations between users and the day-to-day variations in swelling even for the same user. Due to their static compressive nature, these sleeves do not decongest the limb, and instead simply maintain limb volume; they enable management of the disease, but not treatment. An ideal compression sleeve should mimic the MLD treatment by offering controllable gradient compression.

Intermittent pneumatic compression (IPC) devices are considered a feasible additional lymphedema treatment to MLD [162]–[166]. For instance, Turtzo patented a compression sleeve that applies gradient pressure along the limb [167]. Suarez et al. developed a proof of concept for a pneumatic fabric-polymer actuator capable of bending along the curves of the limb by inflating a pre-shaped fabric-based element [56]. Guan et al. developed and modelled a soft actuator-based compression sleeve for the lower limb using large pneumatic bladders [168]. Yoo et al. developed an origami-inspired soft pneumatic actuator capable of delivering both shear and normal force, mimicking the squeezing and dragging motion administered during MLD [169]. There are also commercially available IPC systems [170], [171], which are bulky, heavy and expensive (e.g. >$1000). They are not suitable for people to wear while performing daily activities due to the need for power supplied through wall plugs. On the other hand, portable and affordable pneumatic compression systems (~USD$299) [172] are not very effective due to the limited number of air bladders accommodated. The limitation of these systems stems from the use of electromechanical solenoid valves, the number of which

increases with the number of individually actuated air bladders, ultimately resulting in increases in the electric energy consumption, cost and size/weight of the control box and compromising portability.

Development of a novel solution that enables a portable and affordable pneumatic active compression sleeve offering gradient pressure assisting in lymphedema treatment is critical. This study presents such a novel proof-of-concept solution (**Figure 3.1**). Inspired by earlier work such as microfluidic mazes by Fuerstman et al. [173], an air microfluidic chip forms the core of this solution, containing 16 channels of different cross-sectional sizes, ranging from 0.04 μm^2 to 1 mm^2. This novel chip enables sequential inflation and uniform deflation of 8 soft air bladders providing gradient compression to the forearm (based on existing commercial sleeves). Using the microfluidic chip also reduces the number of valves to 2 mini solenoid valves from otherwise at least 8 bulkier valves of higher energy consumption, allowing the miniaturization of the control box. Another benefit of the air microfluidic chip is that the developed sleeve with a wearable control box can be used more often than its static pneumatic pump counterpart which should better maintain the results from MLD and enable further drainage of the arm, allowing for longer periods between MLD sessions, reducing costs, and contributing to a better quality of life for individuals with lymphedema. While a forearm sleeve with 8 soft air bladders is tested in this study, the same technology can be scaled up to 16 (based on existing commercial full-arm sleeves) or more by increasing the number of channels within the air microfluidic chip without increasing the amount of electromechanical hardware.

For proof-of-concept purposes, this study focused on the development of: i) the microfluidic chip with a channel network for realizing sequential inflation and uniform deflation of eight mini air bladders, ii) robust and inexpensive methods to make the air bladders and integrate them with the sleeve, iii) methods for quantitative evaluation of the effectiveness of the integrated sleeve in providing sequential compression, and iv) a miniaturized control box. The prototype wearable control box (**Figure 3.1**) consisted of a single mini air pump (Adafruit Product ID: 4699) and two miniature 3-position 2-way solenoid valves (uxcell from Amazon.ca). The technology used by this sleeve adopted fundamental microfluidic theory as a design basis as detailed in the following section.

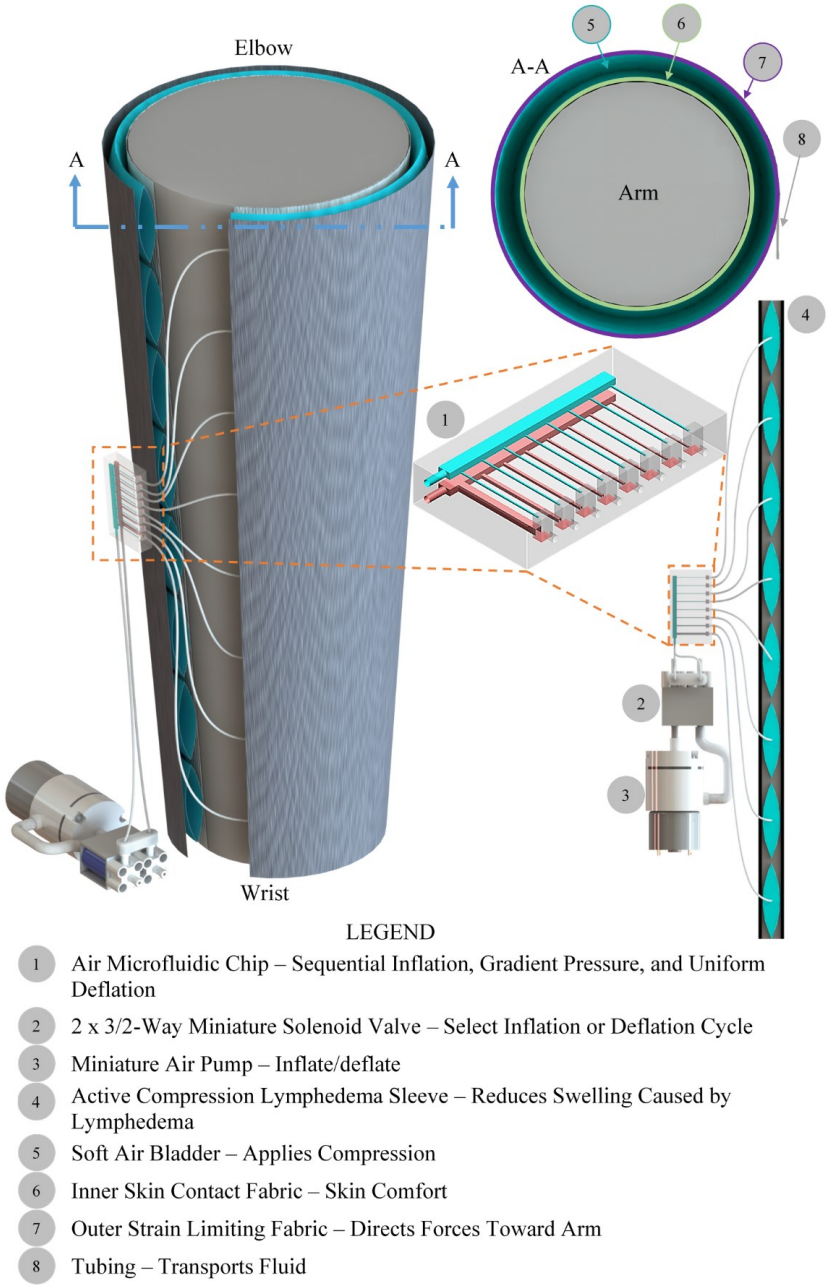


Figure 3.1: Proof-of-concept rendering of the air microfluidics-enabled soft robotic sleeve toward lymphedema treatment. The construction of the system is shown by an isometric view of the entire system, a top cross-sectional view of the sleeve, a schematic view showing the routing of the tubing, and a close-up view of the air microfluidic chip. The miniature air pump and the two miniature 3/2-way solenoid valves control the airflow in and out of the air microfluidic chip, providing sequential inflation and uniform deflation for the soft air bladders. The soft air bladders apply intermittent gradient compression with the outer strain- limiting layer's help, directing the forces inward onto the forearm. The air bladder actuator closest to the wrist inflates first, followed in sequence by the air bladder above it, with the air bladder closest to the elbow inflating last. Once all the air bladders are inflated, the miniature air pump actively deflates the air bladders evenly.

3.2 Air Microfluidic Chip Concept

The soft robotic system presented here is designed to have two manifolds, one for inflation and the other for deflation (**Figure 3.2**). Each manifold contains 8 parallel microchannels, named an "air microfluidic chip". Eight soft pneumatic actuators, which are air bladders, were connected to the air microfluidic chip for sequential actuation during inflation and uniform actuation during deflation. When this soft robotic system was integrated with a wearable sleeve, it produced a massaging motion that mimics MLD. Although typical macroscale fluidic design centers around engineering to compensate for pressure loss along a channel due to hydraulic resistance, the technology described herein advantageously utilized these principles as design guidelines for the air microfluidic chip. and thereby facilitates lymph fluid circulation. The performance of the integrated system was further optimized through experimental investigations and testing with the practical constraints associated with the fabrication of microfluidic chips, air bladders, and sleeves.

The core innovation was the use of a channel network (**Figure 3.2**) to enable gradient compression with a miniaturized control box. The sequential inflation of the air bladders was realized by balancing the flow resistance or pressure loss in each channel within the sequential inflation manifold of the air microfluidic chip, which quantified the internal friction of a fluid flow that results in the viscous dissipation of mechanical energy into thermal energy [46], [174], [175]. The uniform deflation effect is created by ensuring the channels inside the uniform deflation manifold portion of the air microfluidic chip are of equal flow resistance as the smallest inflation channel.

While there are many ways to manipulate the hydraulic resistance (R_{hyd}), varying the dimensions of the channel cross-sections is effective as the resistance is roughly inversely proportional to the square of the area shown in Equations (3.1) to (3.3) [176]. More details of the method for deriving these equations can be found elsewhere [177].

The Hagen-Poiseuille's Law dictates that fluid first flows through the path of least resistance in parallel pathways [176], [177], mimicking an electrical circuit [178]. Therefore, in a manifold, the least resistant fluidic pathway will fill up first, followed by the second least resistant, then the third, and so on. This principle allows for a sequential delay and gradient pressure in the filling of the parallel air chambers connected with the channels of differing resistances. The above-mentioned fluid dynamics are valid for incompressible fluids and thus

cannot be directly applied to a gaseous flow which was implemented in this study, as gas is a compressible fluid. However, the fundamentals of hydraulic resistance are used here for engineering design guidance and subsequently were refined experimentally. The analytical results aim to demonstrate that the hydraulic resistance is directly proportional to a^{-4}, where a represents the characteristic length of the microchannels. This implies that the resistance is highly sensitive to changes in the characteristic length. As such, sequential inflation of a series of bladders using air becomes feasible by varying the characteristic length, provided the microchannels are fabricated with precision and can be sufficiently small.

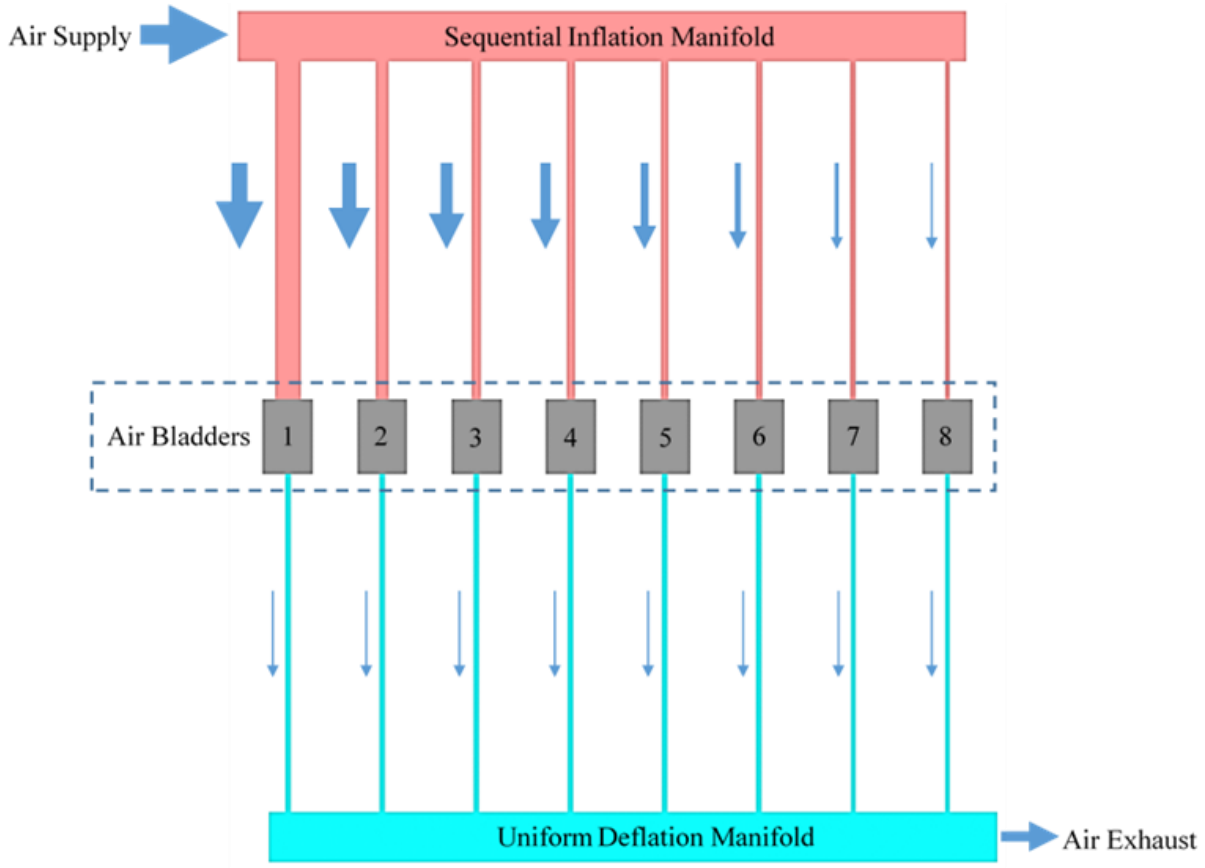


Figure 3.2: An eight-channel air microfluidic chip design concept schematic. The sequential inflation manifold portion (red color) enables sequential inflation and gradient pressure of eight air bladders. The uniform deflation manifold portion (cyan color) enables uniform deflation of the eight air bladders. The arrows show the direction of the flow, and the size of the arrows represents the relative flow rate of each channel. Please note that the arrows are not to scale.

Circle: $$\boldsymbol{R_{hyd} = \frac{8}{\pi}\mu L\frac{1}{a^4}} \quad (3.1)$$

Rectangle: $$\boldsymbol{R_{hyd} = \frac{12\mu L}{1-0.63(h/w)}\frac{1}{h^3 w}} \quad (3.2)$$

Square: $$\boldsymbol{R_{hyd} = \frac{12\mu L}{1-0.917\times 0.63}\frac{1}{h^4}} \quad (3.3)$$

where a[m] is the circle radius, h[m] and w[m] are the height and width of the rectangle and square channels, respectively, L[m] is the length of the fluid channel, and $\mu\left[\frac{\mathrm{kg}}{\mathrm{m}*\mathrm{s}}\right]$ is the dynamic viscosity of the fluid.

3.3 Simulations

Although the term "pressure loss" across an internal fluid channel refers to the same effect as hydraulic resistance, the terms are not directly synonymous, as pressure loss technically only describes an effect of hydraulic resistance. The Hagen-Poiseuille Law ($\Delta p = R_{hyd}Q$,) describes their relationship where Δp[Pa] denotes the pressure drop, $R_{hyd}\left[\frac{\mathrm{Pa}\cdot\mathrm{s}}{\mathrm{m}^3}\right]$ is the hydraulic resistance, and $Q[\frac{\mathrm{m}^3}{\mathrm{s}}]$ is the volumetric flow rate.

The Hagen-Poiseuille's Law, when combined with the Darcy-Weisbach equation that describes the relationship between pressure loss and friction, $\frac{\Delta p}{L} = \frac{2f_F G^2}{\rho D_h}$, allows the equations for hydraulic resistance in channels of different cross-sections to be derived. Here, $\frac{\Delta p}{L}[\frac{\mathrm{Pa}}{\mathrm{m}}]$ is the frictional pressure gradient, f_F is the dimensionless Fanning friction factor, equivalent to one-fourth of the Darcy friction factor more commonly used in fluid mechanics, $G[\frac{\mathrm{kg}}{\mathrm{m}^2\cdot\mathrm{s}}]$ is the mass flux, $\rho[\frac{\mathrm{kg}}{\mathrm{m}^3}]$ is the density of the fluid, and $D_h[m]$ is the equivalent hydraulic diameter.

A simple 2-D approximation simulation (**Figure 3.3**) was performed using the commercial software, COMSOL Multiphysics (version 5.5) to illustrate the fundamentals mentioned above, capturing the flowrates due to microchannel flow resistances. Please be aware that the 2-D simulation results aim to provide approximate ranges for the characteristic length of microchannels needed to induce sequential inflation of air bladders via airflow. They are not intended to specify the exact dimensions of the microchannels, which will be determined experimentally.

The Navier-Stokes equation was solved together with the continuity equation to obtain the flow field. No-slip boundary condition was used as all the channels falling within the continuum flow regime, an average velocity of 5 [m/s] was set as the inlet velocity and atmospheric pressure was applied to the outlets. Channel sizes are detailed in **Table 3.1**. In addition, this model uses COMSOL's default implicit solver, and its mesh is a free triangular element type, with the predefined normal element size. Please note that only a 2D simulation was conducted which does not involve the cross-sectional geometry because the simulation was only used to prove the feasibility of sequential inflation, rather than providing specific design parameters. It is not necessary to perform a 3D simulation of the actual system which is computationally expensive.

Figure 3.3a is the predicted steady state fluid flow path through the channels. It can be seen that the highest velocity is present in the rightmost channel, the largest, followed by a lower velocity in the channel to its left, until the leftmost channel with almost zero velocity. The largest and the smallest channels has a characteristic length of 1 mm and 50 μm, respectively. **Figure 3.3b** plots the exit velocities of each channel, which clearly shows the principle of paths of least resistance in the parallel microchannels. Due to the different exit velocities and thus different flow rates supplied to the air bladders that are inflated sequentially.

Table 3.1: Square channel sizes used for the simulation.

Channel	Width (μm)
1	1000
2	600
3	300
4	250
5	200
6	175
7	150
8	125
9	100
10	90
11	80
12	75
13	70
14	65
15	60
16	55
17	50

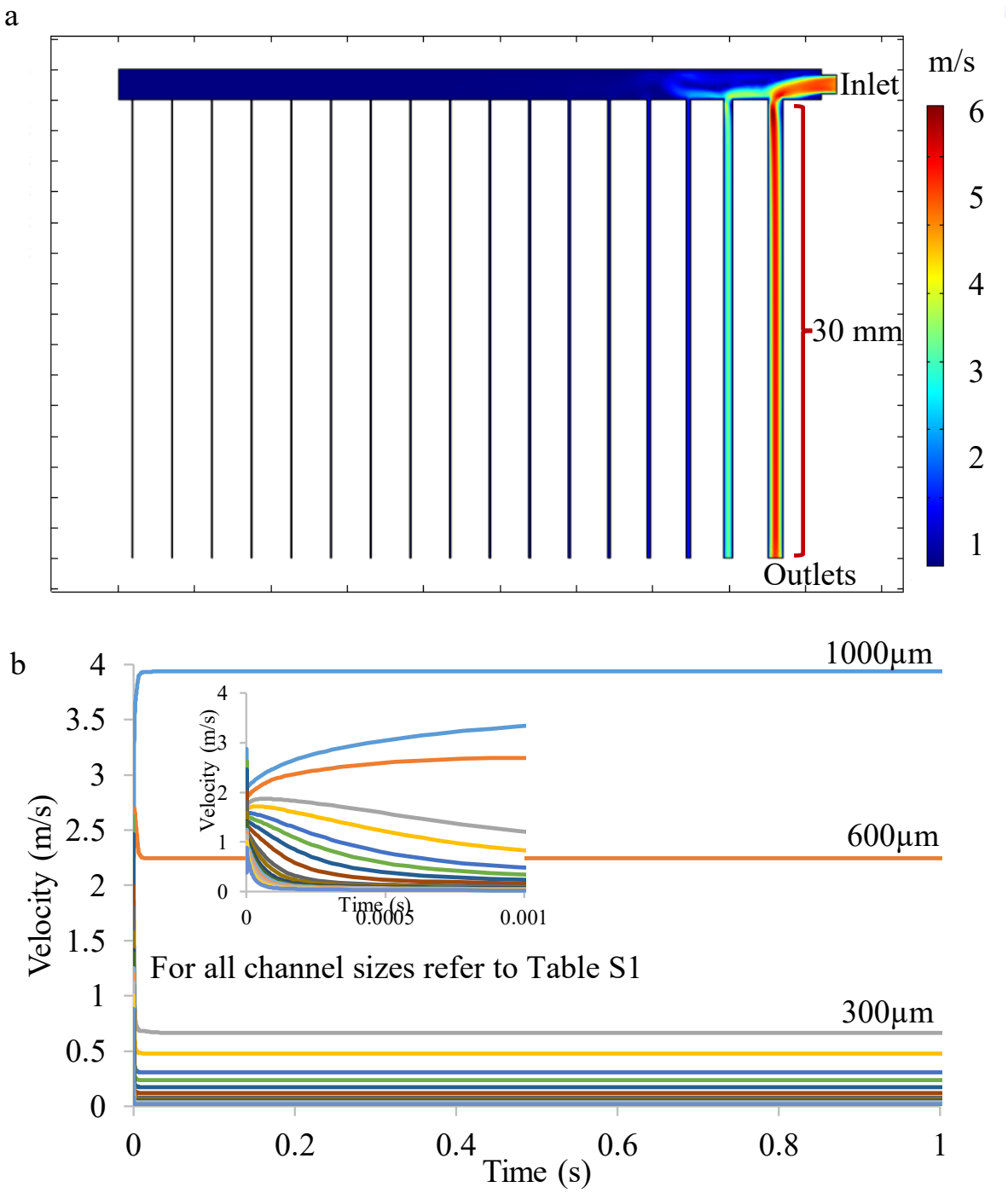


Figure 3.3: (a) Simulated steady state fluid flow path through the channels. (b) Plot of the exit velocities of each channel.

3.4 Fabrication

3.4.1 Air Microfluidic Chip

The air microfluidic chip is the core that connects the air pressure pump and the air bladders within the lymphedema sleeve, as shown in **Figure 3.1**. Two separate air microfluidic chips were fabricated individually to streamline testing, one for sequential inflation and gradient compression and another for uniform deflation. When the system is turned on, air was pumped from the ambient atmosphere into the sequential air microfluidic chip through a single inlet (**Figure 3.4a**), passing through the 8 parallel microchannels to supply air to inflate the 8 air bladders sequentially. During deflation, the air is vacuumed through the uniform deflation air microfluidic chip through a single outlet (**Figure 3.4b**) out to the ambient atmosphere. The two 3/2-way miniature solenoid valves control whether the air pump is activated for inflation or deflation.

The step-by-step fabrication process of the air microfluidic chip is depicted in **Figure 3.5a**. The air microfluidic chip consisted of two slabs of Sylgard™ 184 polydimethylsiloxane (PDMS), one of which contained the channel design created by replica molding a 3D printed mold (Form 3 by Formlabs). These two pieces were then plasma bonded together. At 35 mm x 20 mm x 5 mm, each chip is under 3.5 cm^3, enabling the microfluidic chip to be effective in its purpose yet inconspicuous on the wearer. Due to the difficult nature of fabricating circular microchannels, square channels were used (**Equation 3.3**).

3.4.2 Air Bladders and Pneumatic Active Compression Sleeve (Lymphedema Sleeve)

Well-known fabrication processes in the field of soft robotics for creating textile-based soft fluidic actuators were attempted to make the air bladders with little success. For instance, the method that employs water-soluble polyvinyl alcohol (PVA) as a temporary insert (later washed out using water) to create an inflatable chamber [35] often caused channel blockage because the PVA in the bladder cannot be completely cleaned and as a result the residual particles enter the channels. A robust and inexpensive method was then developed to make soft air bladders from two sheets of elastic thermoplastic polyurethane (TPU). The TPU sheets is Bemis 3218, which is 50 microns thick with a hardness of 84 (Shore A) and a melting range of 100-125 ^oC. The step-by-step fabrication process is depicted in **Figure 3.5b**.

Firstly, two TPU sheet were heat-pressed onto a skin contact fabric layer and a strain-limiting fabric layer, respectively, where the strain-limiting layer may be stiffer than the skin contact fabric layer. Afterwards, the two combined TPU/fabric sheets were heat-pressed together with a custom-made aluminum heat press template, thus creating the soft air bladders. The aluminum heat press template was designed using Solidworks and cut using CNC waterjet. Following this, elastic tubing (1/32" ID x 3/32" OD) were inserted and glued. Lastly, the flat sheet of TPU/Fabric/Tubing was rolled into a cone shape and heat pressed at the seam, allowing it to conform to the forearm of a lymphedema patient. It must be noted that an elastic/stretchy pull-on sleeve design was chosen as it allows easy donning/doffing of the sleeve. The elastic outer fabric layer (spandex) provides enough stretch for donning while directing pressure inward towards the forearm. This method proved to be efficient and repeatable, and may be scaled up in a manufacturing environment outside a research laboratory. Also, the lymphedema arm sleeve size used in this study was meticulously designed based on existing literature [179] and feedback from clinicians to be donned by stage 2 or stage 3 lymphedema patients. Different patients require a different size, but the novelty of the innovation for lymphedema treatment is evidenced.

3.5 Methods

A prototype wearable control box was used for testing and prototyping. A general component layout schematic of the test setup is shown in **Figure 3.6a**. The control box electronics and active fluidic hardware are shown in **Figure 3.6b** and **Figure 3.6c**. The mini air pump is turned on to begin a treatment cycle, drawing air from the ambient atmosphere through the sequential inflation air microfluidic chip (**Figure 3.6d**) to the soft air bladders within the lymphedema sleeve (**Figure 3.6e, f, h**). As soon as a certain preset pressure level is reached at the pressure sensor, the two 3/2-way miniature solenoid valves open to allow the mini air pump to vacuum the air out of the soft air bladders through the uniform deflation air microfluidic chip (**Figure 3.6d**) and exhaust into external atmosphere. The volume of the fully inflated soft air bladder (**Figure 3.6f, h**) was between 95 ml (smallest air bladder at the wrist) to 145 ml (largest air bladder at the elbow), with an approximate increment of 7 ml between each consecutive air bladder.

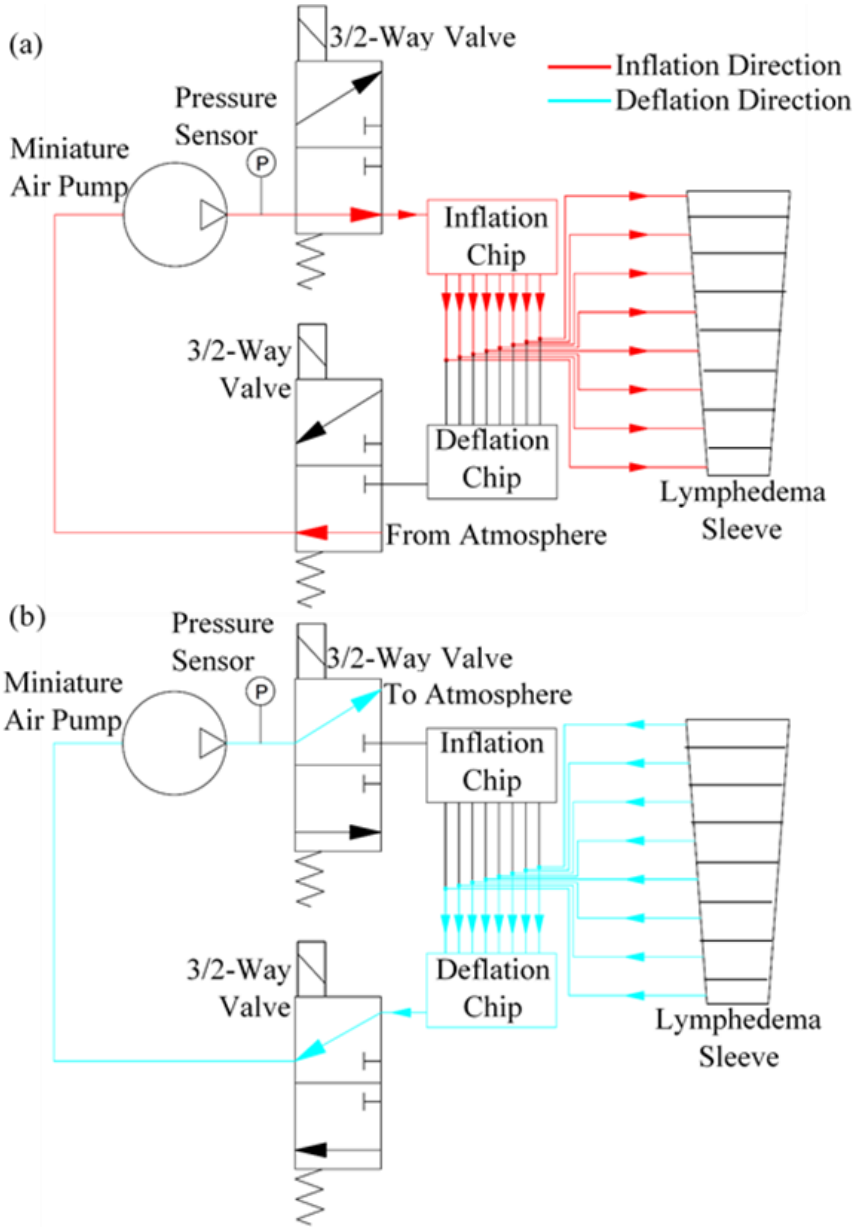


Figure 3.4: System schematics showing the inflation and deflation cycles. (a) Inflation cycle with red lines marking the airflow pathway and arrows showing the direction of flow. Both 3/2-way solenoid valves are off/de-energized during the inflation cycle, allowing the miniature air pump to transport air from the ambient atmosphere through the inflation chip to the air bladders within the lymphedema sleeve. (b) Deflation cycle with cyan lines marking the airflow pathway and arrows showing the direction of flow. Both 3/2-way solenoid valves are on/energized during the deflation cycle, allowing the miniature air pump to transport air from the air bladders within the lymphedema sleeve through the deflation chip to the ambient atmosphere. The pressure sensor in the system schematics provides feedback to control inflation and deflation cycles by measuring the pressure at the outlet of the miniature air pump.

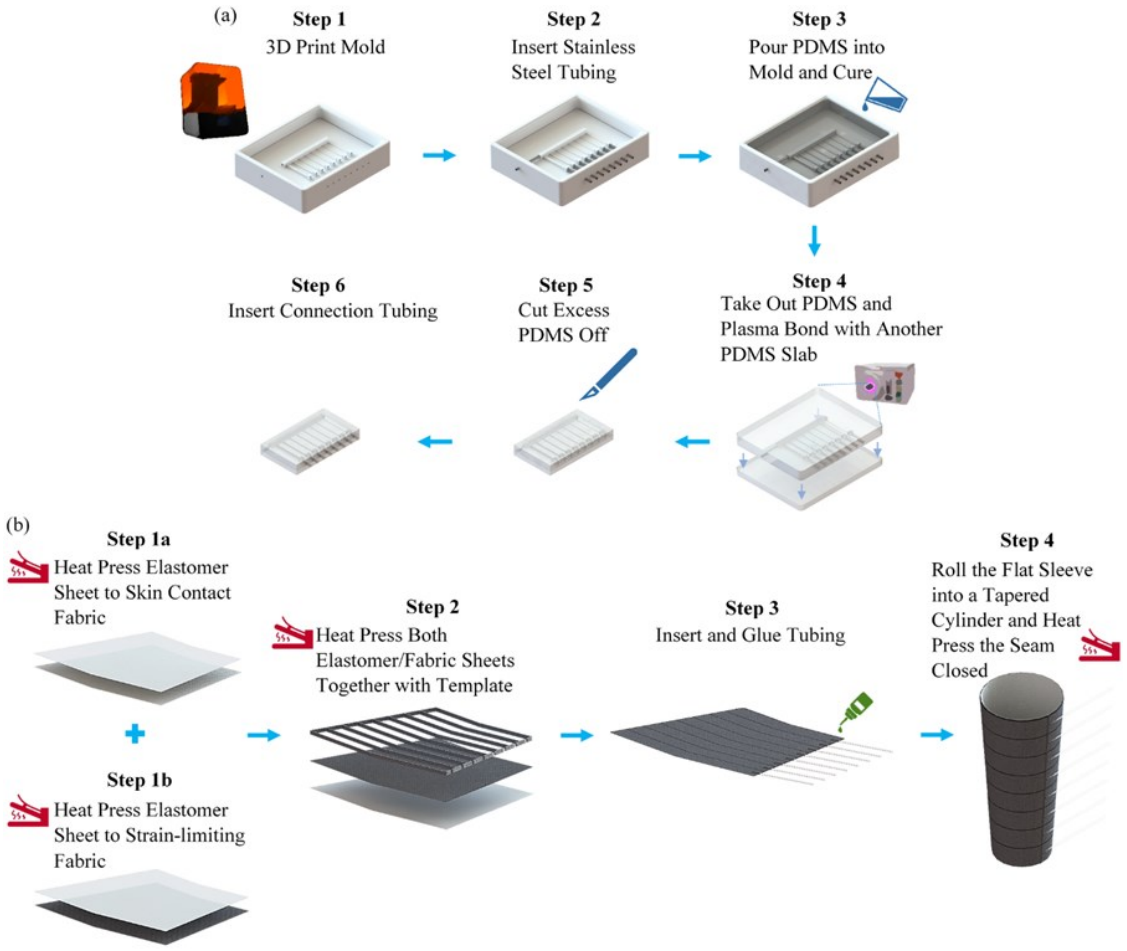


Figure 3.5: (a) Step-by-step fabrications method for creating the air microfluidic chips. Step 1 involves SLA 3D printing of the chip mold. Step 2 involves inserting the stainless-steel tubing to create horizontal connection points for the tubing connecting to the lymphedema sleeve. Step 3 involves pouring PDMS (Sylgard™ 184) mixed at 10:1 ratio into the mold and fully cure. Step 4 involves taking out the cured PDMS and plasma bond with another PDMS slab to create the air microfluidic chip. The PDMS slabs are placed inside an air plasma chamber for 1 minute and 30 seconds (time varies depending on plasma chamber type and power) and quickly taken out and bonded by firmly pressing the two PDMS slabs together for 30 seconds. Step 5 involves cutting off the excess PDMS from the air microfluidic chip, thus making it smaller. Step 6 involves inserting the connection tubing, which is used to connect to the lymphedema sleeve. (b) Step-by-step fabrications method for creating the lymphedema sleeve. Step 1a and step 1b involve heat pressing the elastic TPU sheets to skin contact fabric and strain-limiting fabric layers. Step 2 involves heat pressing both elastic TPU/fabric sheets and an aluminum template to create the lymphedema sleeve structure with internal soft air bladders. The aluminum template conducts heat sealing the two elastic TPU sheets together, creating the seams of the soft air bladders, and the cutouts within the aluminum template become the internal chambers of the soft air bladders. Step 3 involves inserting and gluing the tubing that connects the lymphedema sleeve with the air microfluidic chip—one tubing per soft air bladder. Step 4 involves rolling the flat sleeve into a tapered cylinder, and heat pressing the elastic TPU seam closed, creating the elastic pull-on lymphedema sleeve for the forearm.

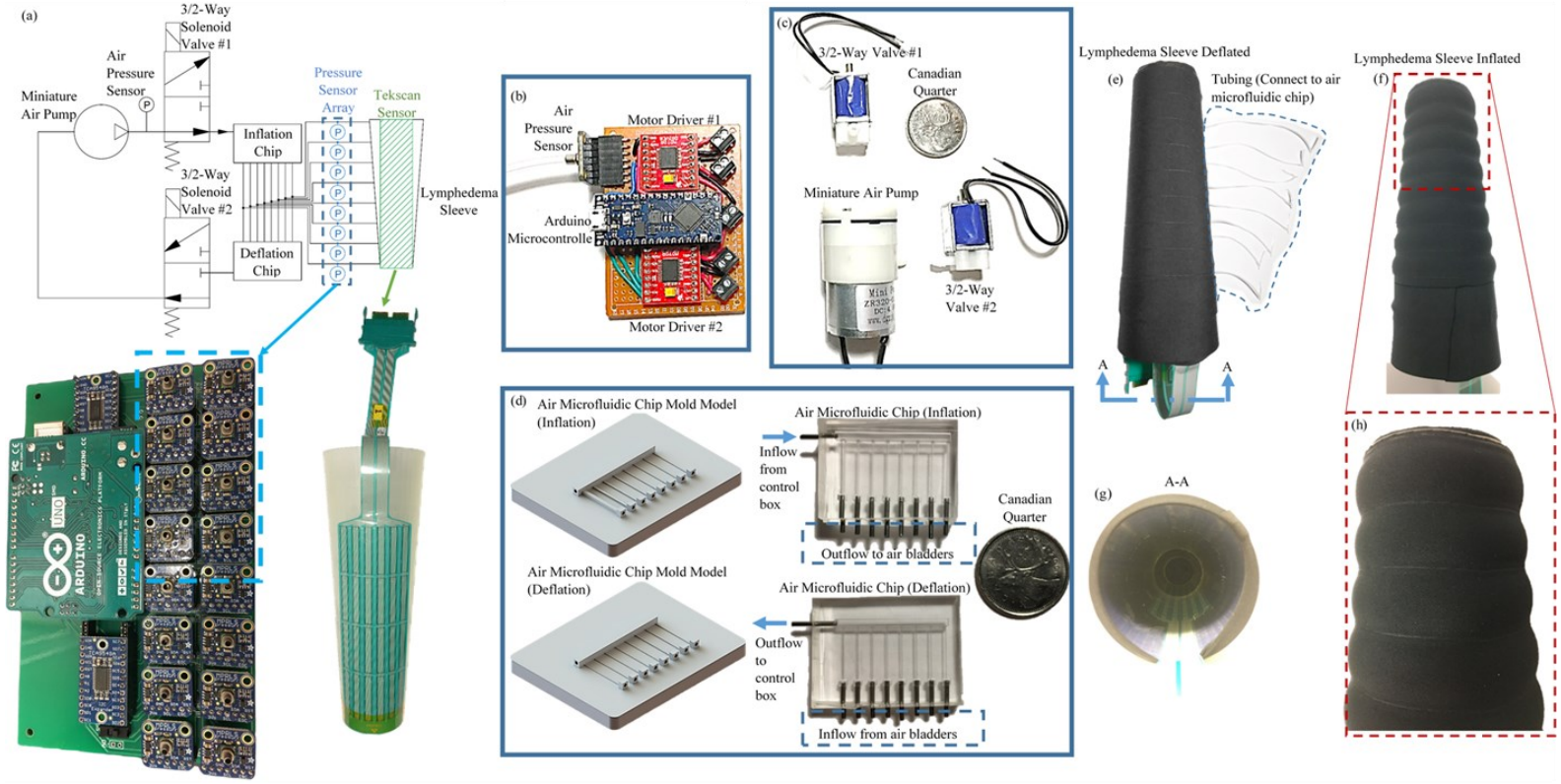


Figure 3.6: (a) Component layout schematic of the test setup. A custom PCB with 16 pressure sensors (Adafruit MPRLS) was used to measure each air bladder's internal pressure within the lymphedema sleeve. A Tekscan sensor (9811E) was used to map the actual pressure applied to the forearm model, which was 3D printed. (b) Photo of the prototype control box electronics including an air pressure sensor (Adafruit MPRLS) connected at the outlet of the miniature air pump (Adafruit Product ID: 4699) for control feedback, two motor drivers (Sparkfun TB6612FNG) used to switch the miniature air pump and 3/2-way solenoid valves (uxcell from Amazon.ca) on/off, and an Arduino Nano Every microcontroller to manage all the electronic components. (c) Photo of the miniature air pump, two 3/2-way solenoid valves. (d) Photos of the air microfluidic chips and their mold model. (e) The deflated lymphedema sleeve was wrapped over the forearm model with tubing from each air bladder connected to the air microfluidic chips. (f) Photo of the inflated lymphedema sleeve. (g) The top view of the lymphedema sleeve wrapped over the forearm model shows the Tekscan sensor's placement sandwiched between the lymphedema sleeve and the forearm model. (h) close-up view of the inflated air bladders within the sleeve.

3.5.1 Internal and External Pressure Measurements

For measuring the internal pressure of each of the 8 soft air bladders within the lymphedema sleeve, a customized pressure sensor array printed circuit board (PCB) was developed (**Figure 3.6a).** It hosts 16 MPRLS ported pressure sensors with two TCA9548A multiplexers and an Arduino Uno Microcontroller. Only 8 pressure sensors were used for the 8 soft air bladders.

To quantitatively verify the compression effects of the sleeve, the Tekscan F-Socket pressure system (**Figure 3.6a**), a paper-thin flexible sheet of force-sensitive resistor (FSR) matrix (9811E), was used to map the compression gradient applied to the limb when the sleeve is worn on the arm. A 3D printed tapered cylinder is used to mimic an actual lymphedema patient's arm (**Figure 3.6g**). The pneumatic active compression sleeve is pulled over the 3D printed tapered cylinder with the FSR sheet sandwiched in between to capture the actual compression applied by the soft air bladders onto the tapered cylinder.

3.5.2 Channel Selection Tests

Although the fluids theories provided a design guideline for realizing the sequential inflation through varying channel cross-sectional areas, the further improvements of the channel and microfluidic chip design occurred through experimental investigations with the practical constraints acknowledged. Soft lithography technology [180] has been commonly used to make microfluidic chips through replica molding. The mold is usually made of photoresist on silicon wafers via photolithography technology, which is expensive and laboursome. 3D printer is then chosen to make the mold in this study.

For simplicity, all the channels have a square cross section with the size range listed in **Table 3.2**. For the deflation microfluidic chip, the channel size was 200 μm while the channel size varied from 200 μm to 1000 μm in the inflation chip (**Figure 3.6d**). This size range was determined based on experimental testing of channels ranging from 50 μm to 1000 μm for their impact on inflation and deflation with the fabrication constraints (**Figure 3.7**). Due to the limitation of the 3D printer, smaller than 50 μm wide channels cannot be printed. An open-source precision benchtop pump with pressure set to a constant 400 mbar was used [181]. Each channel was connected to a soft air bladder of 120 ml, which is the average size of the lymphedema sleeve air bladders (**Figure 3.6e-h**) when fully inflated. Three different test sets with five different tests each were conducted: time to reach an internal pressure of 100 mbar

(**Figure 3.8a**), 200 mbar (**Figure 3.8b**), and 300 mbar (**Figure 3.8c**) within the air bladders. 200 mbar and 300 mbar are well beyond the recommended lymphedema compression treatment levels but were included for comparison purposes.

Channel	Width (µm)
1	1000
2	800
3	700
4	600
5	500
6	400
7	350
8	300
9	250
10	200
11	175
12	150
13	125
14	100
15	75
16	50

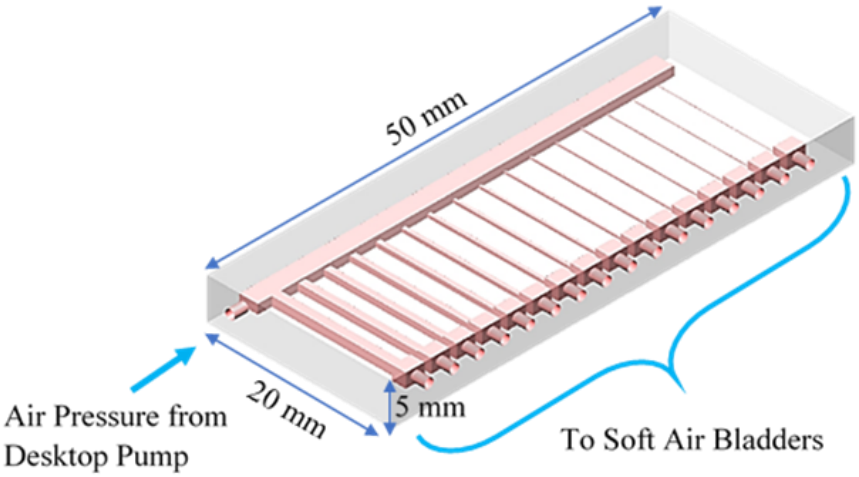


Figure 3.7: Channel selection test air microfluidic chip with 16 parallel channels ranging from 1000 µm down to 50 µm.

3.6 Results and Discussion

3.6.1 Channel Selection Tests

Test results were consistent with an error bar of less than ± 1 second for most test points. It can be seen that channel sizes larger than 500 µm did not provide a significant sequential inflation effect with just a few milliseconds between 1000 µm and 500 µm channels to reach the desired pressure levels. Channels smaller than 200 µm have a drastically larger time difference in reaching the desired pressure. Channel sizes ranging between 500 µm and 200 µm has the most uniform spacing in terms of time when reaching the desired pressure, in addition, they are well within the resolution of the 3D printer; therefore, channel sizes ranging from 500 µm to 200 µm were thus chosen to be used for the final air microfluidic chip.

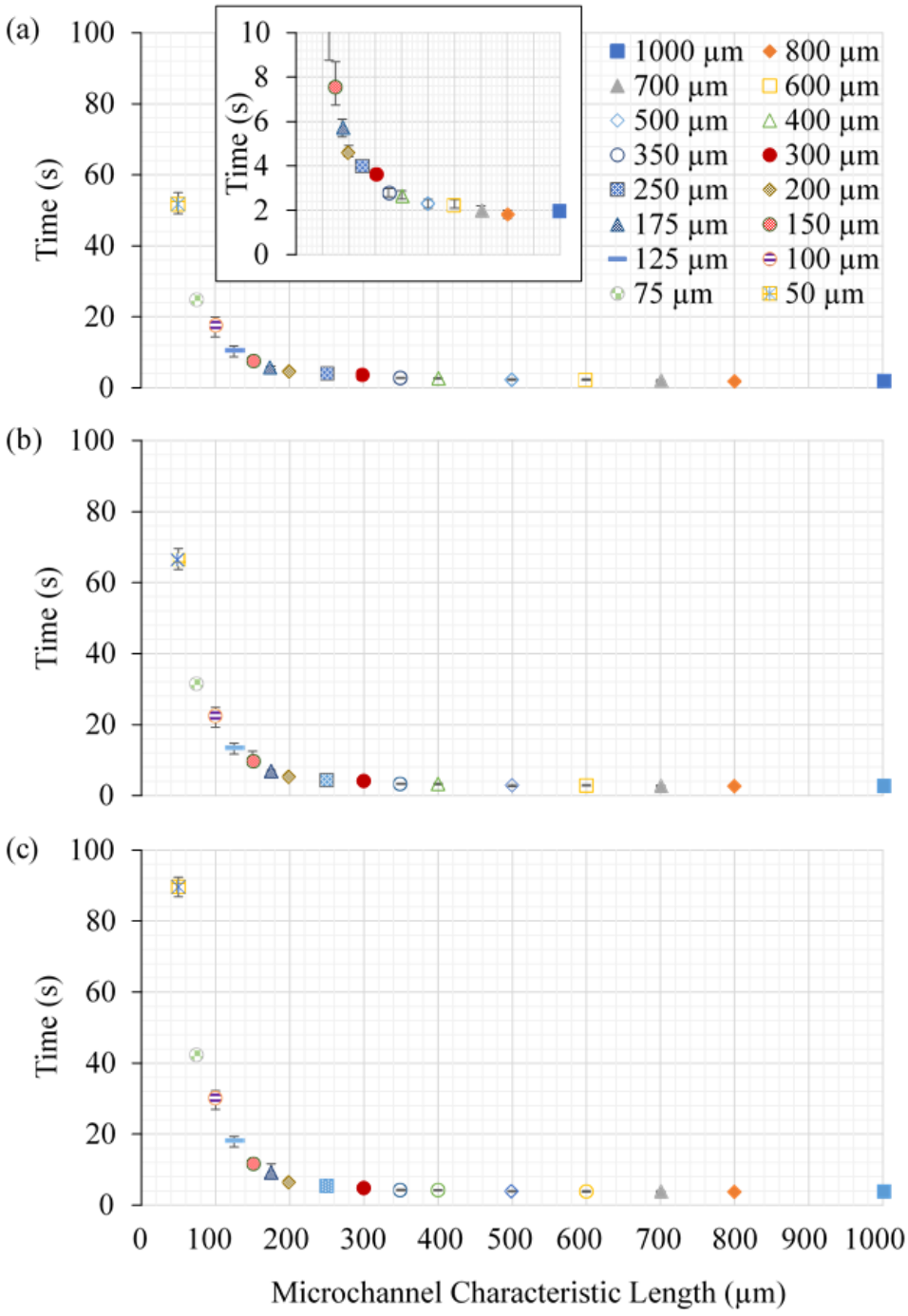


Figure 3.8: Testing to determine the range of channels to use for sequential and gradient inflation Plot of time versus microchannel characteristic length to reach (a) 100 mbar, (b) 200 mbar, (c) 300 mbar, internal air bladder pressure. Square microchannels of 15 mm length with characteristic length ranging from 1000 µm down to 50 µm were used. The air bladders are of the same size at 120 ml. All microchannels are arranged in parallel fashion on the same air microfluidic chip. The inlet pressure is set to a constant 400 mbar. 5 data points per channel per plot are collected with error bars shown.

3.6.2 Gradient Pressure, Sequential Inflation, Uniform Deflation Tests

Table 3.2 shows the channel width of the final air microfluidic chips for use with the 8-bladder lymphedema sleeve. Since channel 1 connects to the first air bladder, which does not require a delay, 1000 µm was chosen. The other 7 inflation channels were selected after further fine-tuning between 500 µm to 200 µm as determined from the channel selection tests. All the deflation channels were determined to be the smallest channel size of 200 µm. Instead of using a desktop pressure system, the miniature air pump with the prototype wearable control box was used for these tests.

Table 3.2: Channel sizes determined based on Channel Selection Tests

Channel	Width (µm)
Inflation 1	1000
Inflation 2	500
Inflation 3	375
Inflation 4	325
Inflation 5	275
Inflation 6	250
Inflation 7	225
Inflation 8	200
All Deflation	200

All compression pressures are based on existing commercially available at-home lymphedema treatment system's compression parameters. **Figure 3.9a** demonstrates that the gradient pressure is achieved inside a series of air bladders within a lymphedema sleeve using an air microfluidic chip. **Figure 3.9b** shows the sequential inflation capabilities to their desired pressure level over a 7 second period and the uniform deflation over a 7 second period. **Figure 3.9c** demonstrates the repeatability and consistency of the air microfluidic chip. During these tests, the control box is programmed with simple on/off feedback (**Figure 3.9d**). It maintained its performance without any degradation; thus, a single pressure sensor can reliably control the inflation and deflation cycles of the lymphedema sleeve.

It is important to measure the actual pressure applied to the arm; therefore, a pressure data of the actual compression applied to the arm was captured by the Tekscan sensor (**Figure**

3.10). **Figure 3.10a** shows a plot of the Tekscan sensor data with 0.02 s temporal resolution and 1 mbar pressure resolution. **Figure 3.10b** shows the snapshots of Tekscan pressure mapping at every second intervals with corresponding images of the actual lymphedema sleeve being sequential inflated and uniformly deflated. The inflation sequence is clearly demonstrated starting from the first mapped bladder actuator at the wrist to the last at the elbow. Due to the imprecision and limitation of the Tekscan sensor at low pressures, these pressure maps provided only qualitative information; nonetheless, they were valuable in displaying the pressure exerted by the sleeve onto the limb in practice. Some of the blank horizontal gaps and concentration points within the Tekscan pressure map resulted from the air bladder not perfectly conforming to the curvature of the arm, thus causing some uneven compression points. Thinner and softer TPU may be used to improve the air bladders to conform better to the curvature of the arm. The blank vertical gaps are due to the physical gaps between each bladder as a result of the fabrication method. The vertical gaps may be eliminated or improved by revising the fabrication method to allow overlapping of soft air bladders. The pressure peak of air bladder 7 appears after the first six air bladders (**Figure 3.10a**) due to internal pressure balancing as all the air bladders are fluidly connected. This may be eliminated by adding microfluidic valves to eliminate any possibility of backflow of fluid from one air bladder to another during the uniform deflation phase. Air bladders 2 and 3 are quite close in pressure applied to the arm so are air bladders 5 and 6, this may be due to the fact that the sleeve is donned via pull-on which may cause certain locations to be looser and others to be tighter causing slight uneven inflation of air bladders. This may be improved by exploring alternate donning methods such as Velcro and/or magnet latching. In addition, the overall system may benefit from exploring alternative inflation methods such as placing certain resistance microchannels within the air microfluidic chip to be in series instead of strictly parallel. Overall, the results prove the robustness and performance of the solid-state air microfluidic chip are adequate for sequential inflation, uniform deflation, and achieving gradient pressure with a pneumatic lymphedema sleeve with potential for numerous improvements to increase robustness.

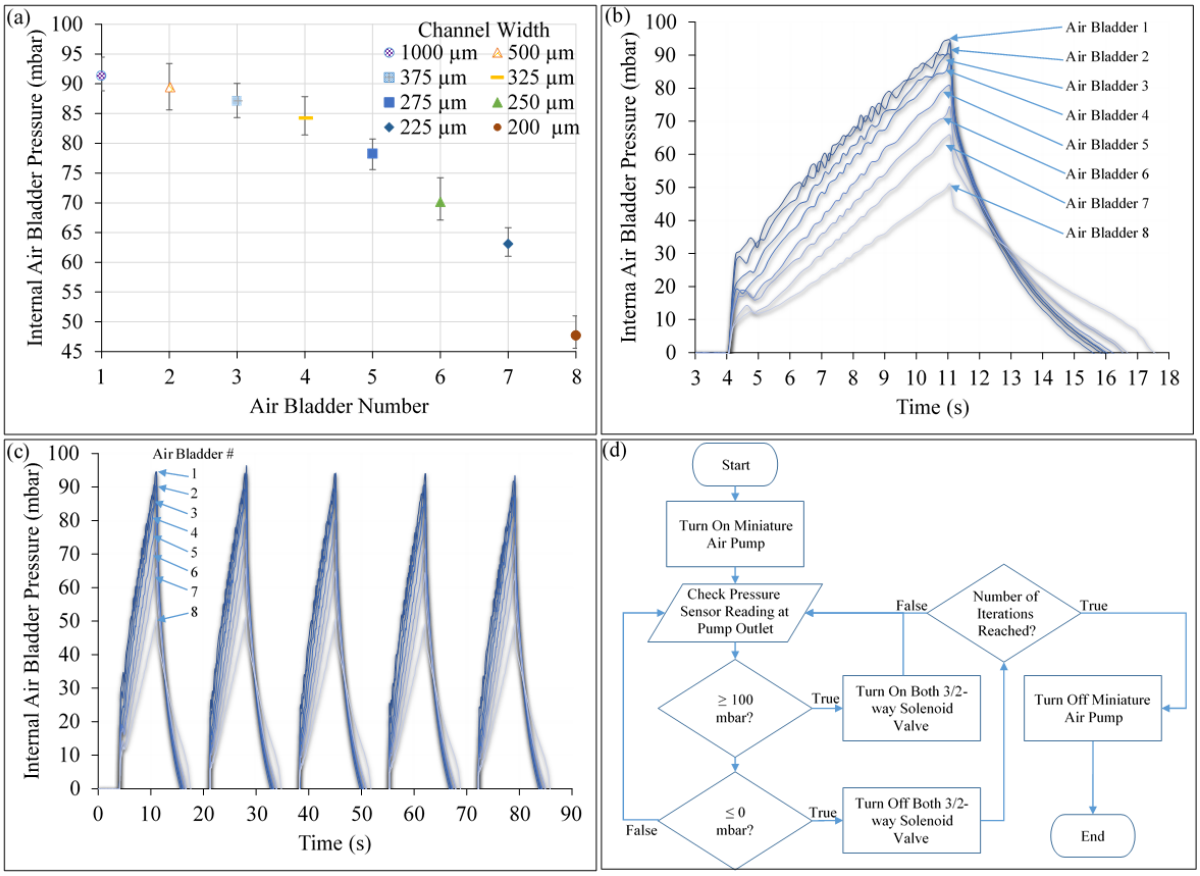


Figure 3.9: Gradient pressure, sequential inflation, and uniform deflation test were all conducted with the wearable control box shown in Figure 5. (a) Plot showing the gradient pressure of all eight air bladder's internal pressure with corresponding air microfluidic chip channel width after 7 seconds of inflation. (25 data points per air bladder) (b) Plot showing the sequential inflation and uniform deflation of 8 air bladders within a lymphedema sleeve over a 14 second period. (7 seconds inflation and 7 seconds of deflation. (c) Plot showing five iterations of inflation/deflation cycles, which demonstrates the robustness of the air microfluidic chip. (d) The flow chart showing the control schematic of the air microfluidics-enabled lymphedema sleeve system. A single air pressure sensor is connected at the outlet of the miniature air pump, providing pressure reading feedback. If the pressure sensor reading is equal to or above 100 mbar signals that all the air bladders have reached their prescribed pressure and the sequential inflation cycle ends, both 3/2-way solenoid valves open to start the deflation cycle. If the pressure sensor reading is equal to or below 0 mbar, the air bladders have been completely deflated to ambient pressure, and the uniform deflation cycle ends. The whole process repeats until the end of the lymphedema treatment.

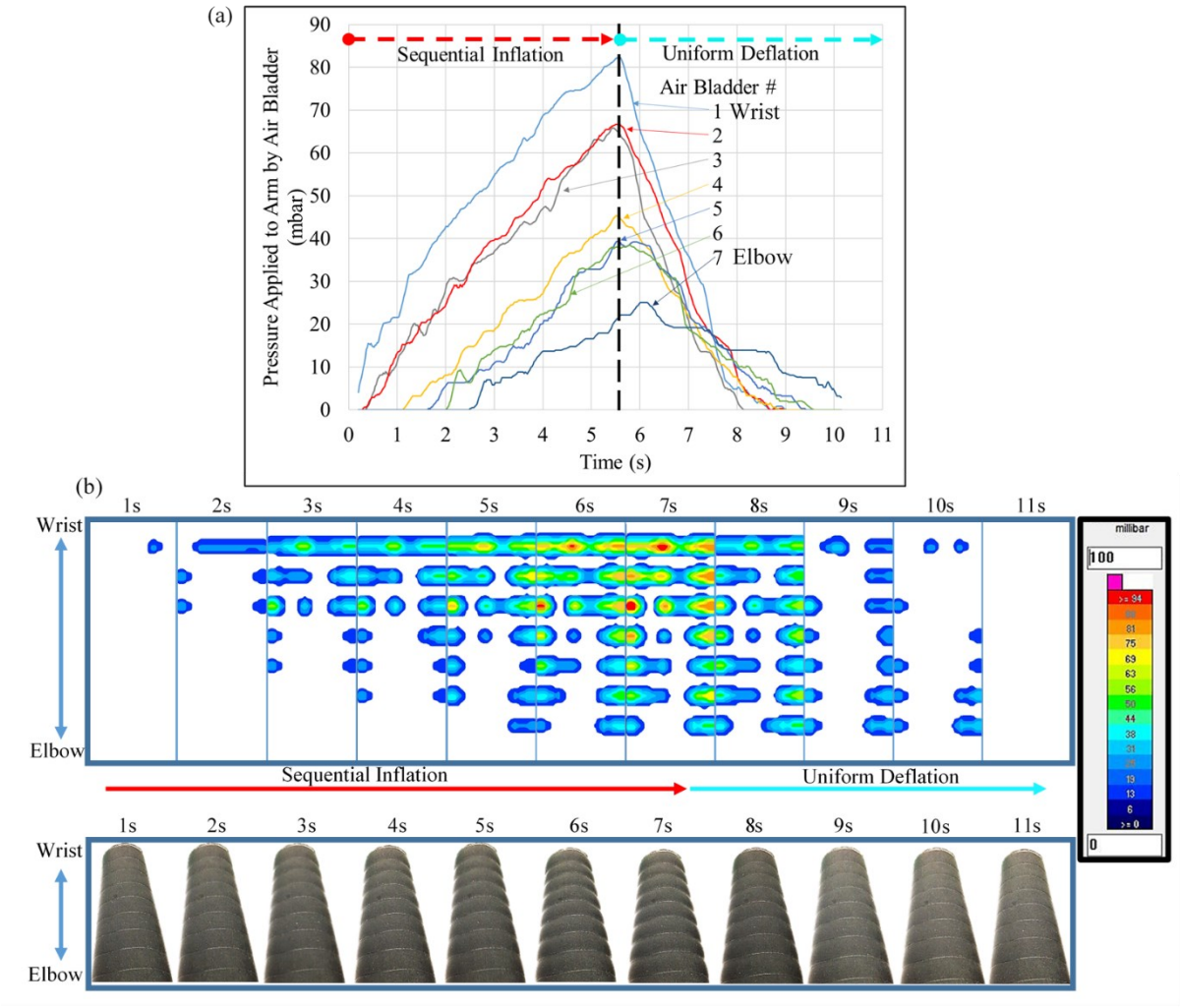


Figure 3.10: (a) Measured pressure data showing sequential inflation, uniform deflation, and gradient pressure of the actual compression applied to the arm as captured by the Tekscan sensor with 0.02 s temporal resolution and 1 mbar pressure resolution; and (b) snapshots of Tekscan pressure mapping at every second interval with corresponding images of the actual lymphedema sleeve being sequentially inflated and uniformly deflated.

3.6.3 Limitations and Future Considerations

3D printer resolution was a limiting factor in fabrication; although channels below 100 µm width were possible, they were inconsistent and thus potentially inaccurate. We tested only square channels in this study. However, future studies can explore channels with different aspect ratios, especially those that are flat yet wide. The spacing between channels was maintained at 2 mm to prevent potential bonding issues that could lead to leakage between channels. To use more channels below 200 µm width, both 3D printer resolution and accuracy must be increased. Alternative manufacturing methods such as high precision CNC milling

may provide a way to produce molds with features below 200 µm. Another limitation during the testing of the air microfluids-enabled lymphedema sleeve was the usage of a rigid and tapered cylinder-shaped forearm; it was sufficient for the proof-of-concept demonstrated, but it does not represent a compressible, geometrically complex actual human arm. For future directions, an air microfluidic chip utilizing channels from 500 µm to 50 µm can be used to increase the number of soft air bladders that can be sequentially inflated to achieve a full arm lymphedema sleeve. The air microfluidic chip's channel sizes can be further fine-tuned based on clinical trials.

3.7 Concluding Remarks

This chapter discussed a proof-of-concept for a sequentially inflating followed by uniform deflating with gradient compression built-in soft robotic sleeve towards lymphedema treatment that remains simple and lightweight for ease of use. Based on the fundamental microfluidic principles and the fabrication methods developed in-house, we developed a valve-less chip that produced delayed and gradient pneumatic actuation that mimicked the massaging motions of MLD.

Moving forward, we hope to develop this system further to produce a fully integrated prototype that uses an integrated wearable control box and a full-size arm sleeve. Following this, we expect to begin clinical trials to evaluate the effectiveness and better understand users want and need in a portable active compression sleeve for lymphedema treatment.

Chapter 4

Investigating Air Microfluidics for Dynamically Fitting Prosthetic Sockets

The work included in this Chapter is published: P. S. Lee[1], **R. Z. Gao[1]**, A. Colpitts, R. W. Murdock, D. Dittmer, A. Schirm, J. Y. Tung, and C. L. Ren, "Air microfluidics-enabled soft robotic transtibial prosthesis socket liner toward dynamic management of residual limb contact pressure and volume fluctuation," *Biomicrofluidics*, vol. 16, no. 3, p. 34107, May 2022, doi: 10.1063/5.0087900 [25]. Together, Peter S. Lee and Run Ze Gao fabricated the device and conducted the experiments. Peter S. Lee wrote the manuscript. Run Ze Gao developed the idea and assisted with the writing of the manuscript.

[1] Contributed equally to this work.

4.1 Introduction

Every 30 seconds, a leg is amputated globally due to diabetes [182]. More than 80% of lower-limb amputations in the world occur due to diabetic foot ulcers [183], and more than 70% of the lower-limb amputation are transtibial (amputation across the tibia) [184]. Diabetic amputees also suffer from peripheral neuropathy, which causes numbness, loss of sensation, swelling, and pain in the lower extremities. Considering its role as the predominant interface between the residual limb and prosthetic, fit and comfort of the prosthetic socket are crucial for diabetic amputees' quality of life and preventing pressure ulcerations [123], [185]. User abandonment rate, a critical indicator of the device quality and associated medical care [186], was reported to be as high as 40% to 60% for lower-limb prostheses [187]. The main reason is the discomfort and/or dissatisfaction associated with the fit of the prosthesis which causes constant recurrence of pain during the use of prosthesis [188], [189]. Such a high abandonment rate justifies the urgent need to develop novel solution(s)

to improve socket fit and comfort for diabetic amputees. This need becomes more urgent than ever due to the rapidly increasing rate of people living with diabetes, projected to increase by 25% by 2030 and 51% by 2045 [190] with just under half a billion in 2019. This study proposes a novel proof-of-concept transtibial prosthetic socket liner to provide dynamic fit between the residual limb and the prosthetic socket by leveraging air microfluidics technology.

Typically, fabric and silicone liners are employed as an interfacing layer between the residual limb and the prosthetic socket to control humidity and maintain fit (Meulenbelt, Geertzen, Jonkman, & Dijkstra, 2009). However, a transtibial amputee's residual limb undergoes frequent volume fluctuations, varying up to -11% to +7% throughout the day [125], [191]. This change in residual limb volume is more volatile during the maturation period immediately post-amputation [192]. Since volume fluctuations can occur at any time, amputees need to manually change the number of liners worn to adjust gaps and maintain a stable fit. If an excess number of liners are worn, the residual limb is susceptible to localized damage to the skin, commonly referred to as pressure ulcerations (or ulcers). In fact, pressure ulcers due to poor fit are the most reported skin injuries in lower limb prosthesis use [193], [194]. Prolonged exposure to elevated pressures is known to relate to increased risk for ulcers, potentially evolving into more serious conditions such as deep tissue injuries [195]. On the other hand, wearing an insufficient number of liners may result in unstable fit and increased risk of soft tissue injuries induced by stress concentrations [196]. Hence, the stability and optimal fit of the prosthesis, as well as the residual limb health are reliant on the cognitive ability of the amputees to perceive and correctly account for the change in residual limb volume. Unfortunately, for diabetic amputees, peripheral neuropathy causes poor tactile sensations in the leg, limiting the user's ability for self-management of socket fit.

Several approaches have been investigated to prevent pressure ulcers during prosthesis use. Some methods utilize the anatomy of the residual limb with varying stiffness to design a multi-material prosthesis [197], [198]. Though the use of multi-materials allows for variable contact pressure which can help in preventing ulcers, it cannot account for the fluctuations in limb volume. Other approaches incorporate inflatable pneumatic actuator inserts as an interfacing layer between the prosthetic socket and the residual limb [126], [199]. While the compressible nature of air is beneficial for providing a conforming fit to irregularly shaped residual limb to compensate for volume fluctuation, these inserts cannot provide pressures adjusted automatically according to the residual limb's anatomy. A more recently investigated idea comprises of pneumatic actuator

inserts as a volume and pressure-compensating interface [127], [129]. While this approach can help achieve an adaptive interface, the additional mass and cost of components added to the prosthesis due to the need for the same number of pressure regulator and pressure sensor for each individual pneumatic actuator challenges these approaches. Therefore, a novel intervention is required where the additional components are largely miniaturized such that the entire system can be integrated into prosthetic devices [125], conforming with the spatial constraints.

This work herein presents a proof of concept of a novel air microfluidics-enabled soft actuator-based wearable system targeted for automated management of socket fit in response to the residual limb volume fluctuation in transtibial prosthesis as shown in **Figure 4.1**. A key advance of the proposed approach is the application of air microfluidics which enables miniaturization of the pneumatic components and thus reduction in the required power, cost and added mass. Rather than creating a new type of prosthetic socket, the typical silicone/fabric limb liner is replaced with a single layer of liner with integrated soft fluidic actuators as an interfacing layer. Formed in an array of 10 actuators of desired sizes, these soft fluidic actuators are designed to be inflated to varying pressures based on the anatomy of the residual limb to reduce pain and prevent pressure ulcerations [200], [201].

In this pressure-driven system, 10 soft fluidic actuators are designed for 10 anatomical locations respectively. They are inflated to passively conform with the surface contour of the limb and to reach the designed pressures in order to redistribute risky pressures associated with limb volume fluctuations. The applied pressure at each anatomical location is maintained at an optimal level regardless of residual limb volume fluctuation by automatically adjusting the volume of the soft fluidic actuators. Ideally, pressure sensors should be integrated for feedback-based automatic control, which is not implemented in this proof-of-concept study. The air microfluidic chip has 10 on-chip pneumatic microfluidic valves designed for sequential manipulation of the fluid flow to the 10 soft fluidic actuators via consecutive valve closure. Use of the air microfluidic chip minimizes the number and size of hardware components required, allowing the system to be run with only one pressure source, and two solenoid valves as seen by the control box in **Figure 4.1**. A detailed discussion about the design approach, rationale, fabrication methods, as well as quantitative verification is presented to show the potential of integrating air microfluidics-enabled soft robotics in transtibial prosthetic sockets.

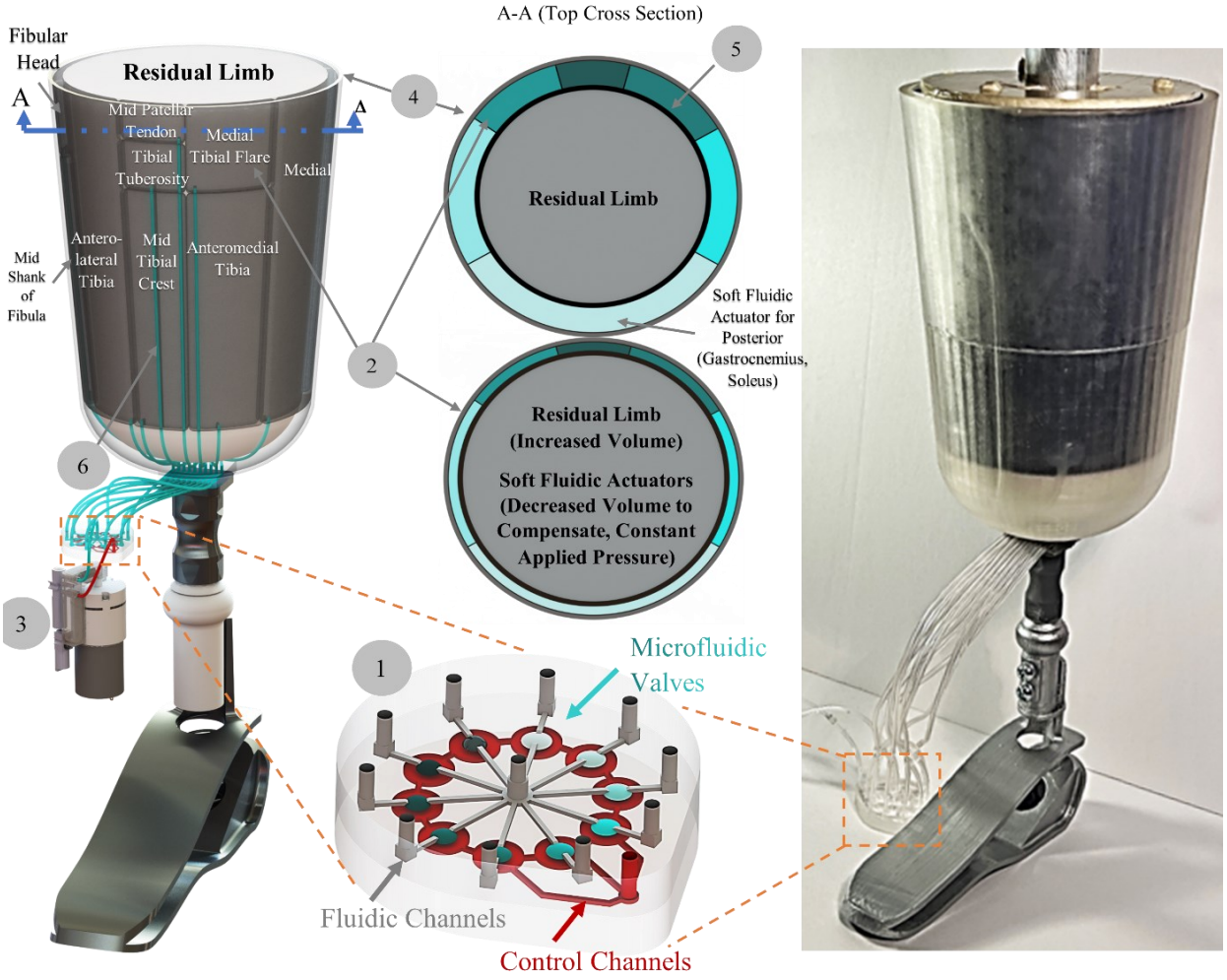


Figure 4.1: Proof-of-concept rendering (left) and picture of the prototype (right) of the air microfluidics-enabled soft robotic transtibial prosthesis for automated residual limb volume fluctuation management. The isometric view shows the entire system, including the prosthesis, the air microfluidic chip, the soft fluidic actuator array and liner, and the wearable control box. 1) air microfluidic chip integrated with 10 pneumatic on-chip valves to control air pressure within each soft fluidic actuator. Different shades of cyan color represent different pressures; 2) 10 soft fluidic actuators situated in between the prosthetic socket and residual limb to apply appropriate compression towards different anatomical locations of the residual limb regardless of residual limb volume fluctuation, minimize the risks of ulcerations and improves comfort. Different shades of cyan color represent different pressures suitable for different anatomical locations; 3) wearable control box including a miniature air pump, two 2/2-way solenoid valves to provide air flow to the microfluidic chip; 4) prosthetic socket holding and supporting the residual limb; 5) fabric liners between the soft fluidic actuators and skin for comfort; and 6) tubing for air transport.

4.2 Design Rationale and Fabrication

4.2.1 Liner and Soft Actuator Array

A crucial feature of the innovation is an array of soft fluidic actuators integrated into the socket liner to directly interface with the prosthetic socket. Each soft fluidic actuator has an inflatable chamber enclosed with highly elastic material [122], [202], with a tubing attached to connect this chamber to a pressure source. When fluids (i.e. air) are displaced into this chamber through the inserted tubing and the chamber is pressurized via the pressure source, hoop stress is induced to elastically deform the enclosure material and expands the actuator's volume. Provided that the hoop stress does not exceed the elastic limit, the actuator can fully restore its elastic deformation and return to its original state upon deflation.

The soft fluidic actuators are fabricated via thermal bonding of two sheets of Bemis 3916 Sewfree® Thermoplastic Polyurethane (TPU) at 110°C, stacked with the tubing and an insert placed in between the two TPU sheets. This insert material is a piece of TPU with one side coated with Sylgard™ 184 Polydimethylsiloxane (PDMS) to assist in forming the inflatable chamber because the cured PDMS does not bond with TPU during the thermal bonding. The insert has slightly smaller dimensions than the two TPU sheets and thus thermal bonding occurs only at the area outside the perimeter of the insert [203]. This also implies that the surface area of the insert material corresponds to the area of the inflatable chamber.

Typically, a water-soluble polymer such as Polyvinyl Alcohol (PVA) is used as the insert material to create inflatable chambers [35]. However, PVA inserts need to be dissolved manually, which involves pumping water in and out of the actuator repetitively because PVA can crumple or partially dissolve in relative humidity conditions, clogging the tubing. In addition, the actuators no longer become treatable with heat (i.e. repaired or modified) upon full dissolution and removal of PVA, because there no longer exists a layer that prevents the thermal bonding of the TPU sheets. In case there exists a defect or a puncture, the entire actuator must be remade because the inflatable chamber will simply close upon reapplication of heat.

We developed a new type of insert material comprised of a piece of TPU sheet with one side coated with a layer of PDMS. This insert is made by brushing an uncured mixture of liquid PDMS and curing agent at 10:1 ratio onto a sheet of TPU, followed by hanging this sheet vertically

to drip out the excess via gravity. Upon curing of the PDMS for a minimum of 72 hours at room temperature, strong adhesion is formed between a thin layer of PDMS (100 to 200 μm thickness) and the TPU sheet. Under the temperature used for thermal bonding of the TPU sheets (110 °C), the cured PDMS is not thermally activable for fusion bonding. Hence, the PDMS side of the insert allows the inflatable chamber to be formed, whereas the TPU side of the insert bonds to the enclosing TPU sheet. This anchors the entire surface area of the insert and prevents the movement or crumpling of the material. This new method allows the actuator to be repaired or modified post-fabrication. In case of a puncture, a small patch of TPU can be placed over the location of defect and repaired by applying heat and pressure.

To achieve a connection between the actuators and the pressure source for inflation and deflation, a silicone tubing is inserted and glued into the chamber. Prior to thermal bonding of the insert material and the two enclosing TPU sheets, a small removeable tab is placed on the edge of PDMS side of the insert to reserve a small slot of opening connected to the inflatable chamber. The tab is then removed upon thermal bonding of the materials, and the silicone tubing is inserted and glued to provide complete seal. The overall schematic of the fabrication process is detailed in **Figure 4.2**.

Knowing the importance of accounting for different pressure tolerances in the residual limb anatomy [200], the soft actuator array is carefully designed based on the pain thresholds and pressure tolerances of typical transtibial amputation residual limbs [201]. For convenience, the soft fluidic actuators are also labeled with numbers 1 through 10, in increasing contact pressure order (i.e., actuator 1= lowest, actuator 10 = highest). The anatomical locations and their abbreviations used herein are summarized in **Table 4.1**.

The layout of the soft fluidic actuator array is as shown in **Figure 4.3**. While each of the actuators is inflated to maintain specific contact pressures as per the array design, its soft and compliant nature also allows for the compensation of irregular changes in the gap between the actuators and the socket. Hence, by monitoring and controlling the contact pressures applied by the soft actuators onto the limb and the socket, the volume fluctuation is also compensated.

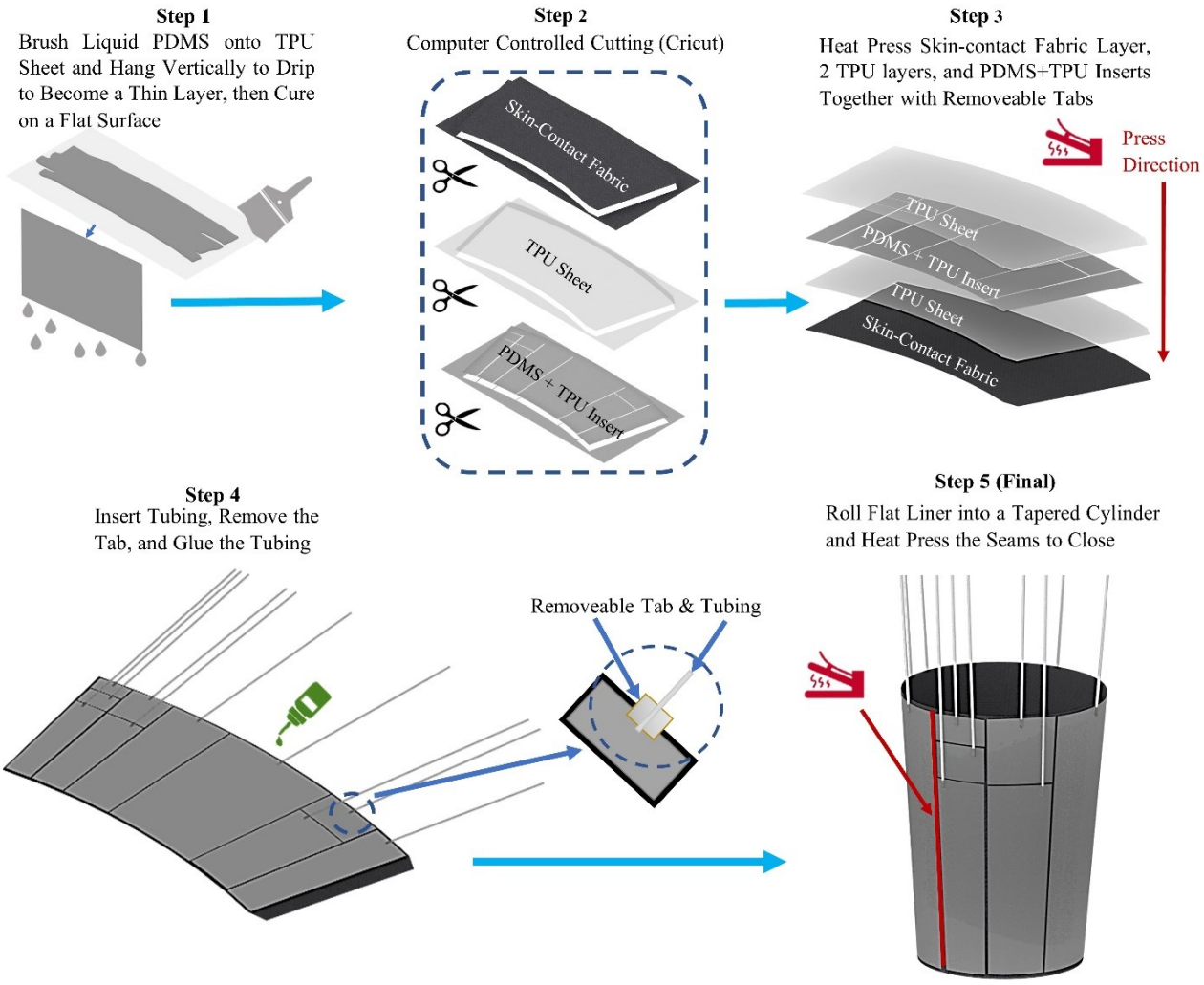


Figure 4.2: Overall schematic of the fabrication process. 1) Liquid PDMS is first brushed onto a TPU sheet and hang vertically to drip to become a thin layer (~100 µm) and left on a flat surface to cure. 2) Using a computer-controller cutter, shapes of the PDMS-TPU insert, TPU sheets, and skin-contact fabric are generated. The insert of each section is cut out as individual pieces and manually placed on top of the base elastomer layer sheet. 3) Skin contact fabric and the base elastomer (TPU) layer are first heat pressed together. Then PDMS-TPU inserts and the top TPU layers are placed over the base elastomer layer and heat pressed altogether. A removeable tab is also placed on top of the PDMS side of the insert to reserve an opening for the tubing. 4) Upon insertion of silicone tubing, removal of the tab, and sealing of the tubing with glue, 5) the flat liner with the actuator array is revolved to form a shape of a tapered cylinder.

Table 4.1: Abbreviations for the anatomical locations of the transtibial residual limb.

Actuator Number	Anatomical Location of the Transtibial Residual Limb	Abbreviation	Target Contact Pressure (mbar)
1	Posterior: Popliteal, Soleus, Gastrocnemius	P	50
2	Anterolateral Tibia	ALT	60
3	Mid Shank of Fibula	MSF	70
4	Medial	M	80
5	Anteromedial Tibia	AMT	95
6	Medial Tibial Flare	MTF	120
7	Mid Tibial Crest	MTC	140
8	Fibular Head	FH	160
9	Tibial Tuberosity	TT	180
10	Mid Patellar Tendon	MPT	190

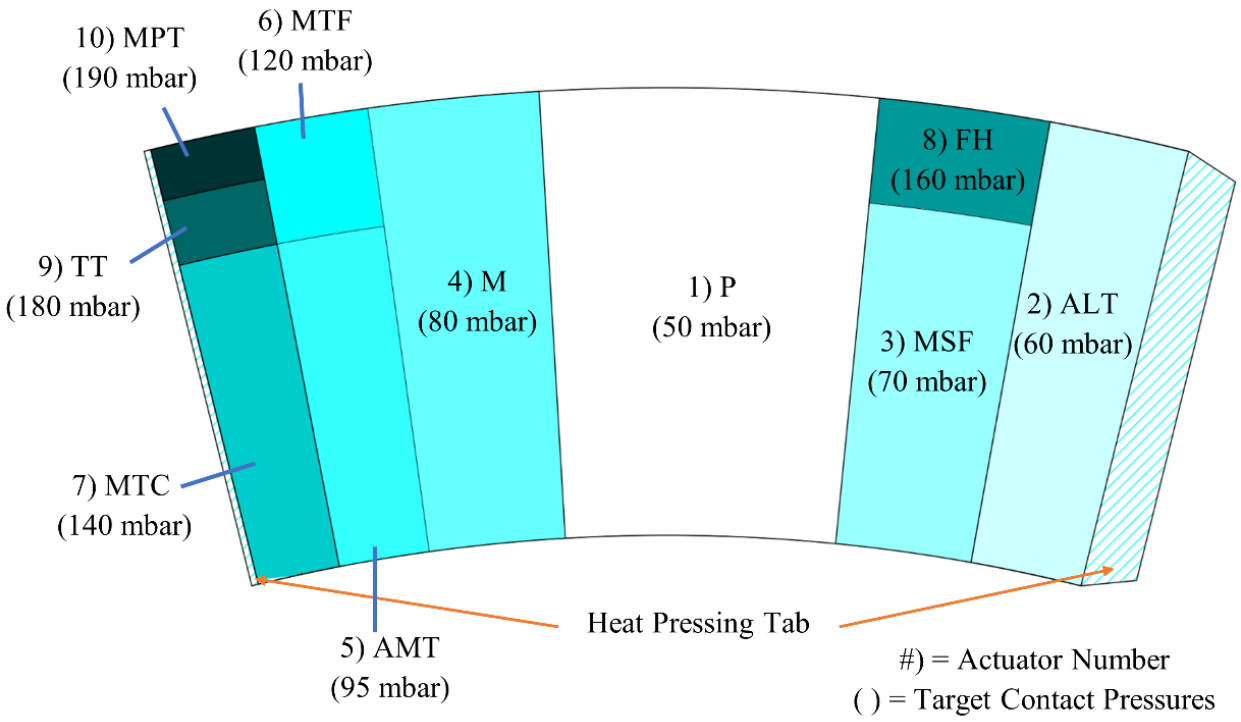


Figure 4.3: Design of the position and target contact pressures of the soft fluidic actuator array based on general anatomical locations of the transtibial residual limb.

4.2.2 Air Microfluidic Chip

At the core of the innovation is the air microfluidic chip designed to govern the actuators' pressures through binary flow control. With this air microfluidic chip, the system can be operated with a single wearable mini air pressure source, 2 additional normally closed solenoid valves, and a single pneumatic pressure sensor for pressure feedback. The pneumatic control hardware schematic is illustrated in **Figure 4.4a**. Two 2/2 Normally Closed (NC) solenoid valves are used to: i) isolate chip layers from the pump to protect from pressure overshoots that occur while changing the reference pressures, and ii) directional control of pressurized fluid for separating the fluid channel layer versus the control layer when displacing fluid, which allows the system to run reliably using one pressure source. Sample components can be used for making this system wearable is shown in **Figure 4.4b**. This device is a breakthrough in pneumatic wearable systems that otherwise require the same number of solenoid valves as actuators for achieving sequential flow control. The power consumption, size, mass and cost of the control box is dominated by the number of solenoid valves accommodated, which influences the level of wearability significantly. Using on-chip valves largely reduces the number of solenoids required, and hence reducing the added mass, size, power consumption and cost of the entire wearable system.

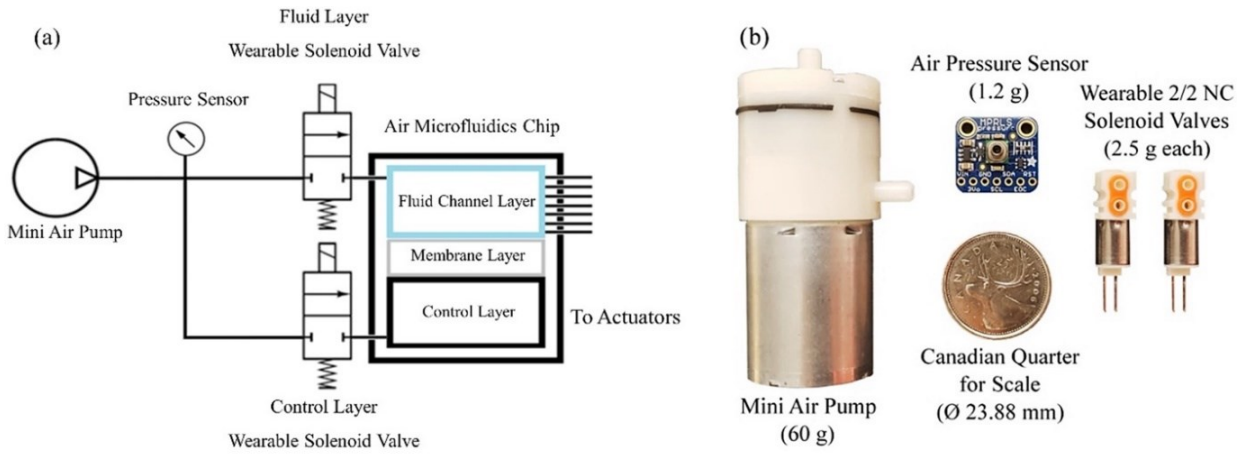


Figure 4.4: (a) Schematic of pneumatic control hardware for controlling the on-chip valves in air microfluidic chip and (b) Samples of pneumatic hardware components used to make this system wearable. A Canadian quarter is presented here as a reference of size comparison (diameter of 23.88 mm).

In this study, 2 solenoid valves were used to sequentially control 10 actuators enabled by the integrated 10 on-chip pneumatic valves. For applications needing more soft fluidic actuators with different pressure levels, the number of on-chip pneumatic valves can be increased whilst

using the same 2 solenoid valves. This is predicated on the level of fabrication precision, resolution, and accuracy, detailed in **Figure 4.5**. The concept of this on-chip valve is similar to that of the Quake's valve [86], comprising of three layers: i) a fluid channel layer, ii) a control layer, and iii) a membrane layer placed between the two layers. Instead of the original Quake-style valve with a semi-cylindrical seat at the control points [86], an improved design similar to the bowl-shaped seat is utilized [204]. The on-chip valve refers to this semi-spherical bowl-shaped feature located in the fluid channel layer, in which the membrane can deflect into. The on-chip valve is normally-opened, meaning that the fluid can flow through the valve unobstructed prior to the closure of the valve. When the control layer is given a reference pressure higher than the pressure in the fluid channel layer, a force imbalance is induced to deflect the membrane into the fluid channel layer. Until this force imbalance is relieved, the fluid flow is physically obstructed by the membrane, hence functioning as a mechanical valve. The structure of the microfluidic chip is as shown in **Figure 4.6a**.

By design, the pressure applied in the control layer must be higher than the pressure in the fluid channel layer in order to close these on-chip valves. The amount of pressure difference required to fully close the on-chip valve (denoted 'ΔP_{close}' from hereon) is governed by the design of the on-chip valve features. Valve design features include surface area, depth of membrane deflection, shape of the valve, and radius of curvature. The physics behind designing valves with different ΔP_{close} revolves around the force required to fully deflect the membrane into the valve feature. The surface area of a valve determines the area in which the membrane can respond to a given pressure. For the same pressure, a smaller force is applied at the valve with a small surface area, compared to a valve with a large surface area. Hence, the pressure required to close the valve (ΔP_{close}) increases as the surface area decreases. The depth of membrane deflection governs the vertical height that the membrane must displace to close the valve. The higher the depth of membrane deflection, the more force required to fully close the valve, and hence higher ΔP_{close} is required. In the similar context, ΔP_{close} increases as the radius of curvature increases. Utilizing these valve design features, the on-chip valves can be designed to have different ΔP_{close}.

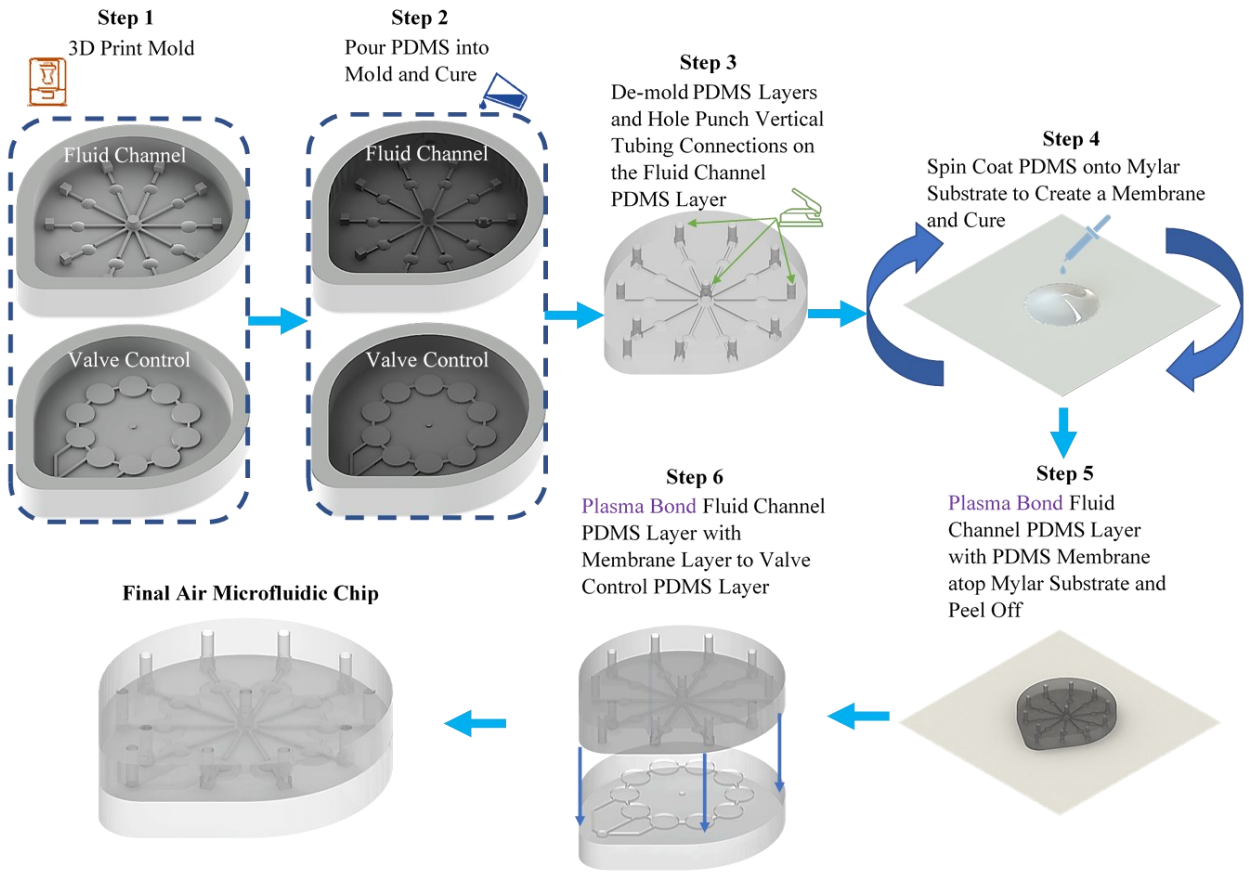


Figure 4.5: Each layer of the air microfluidic chip is fabricated separately and assembled via plasma bonding. The fluid channel layer and the valve control layer are made by replica molding of PDMS with a 3D-printed mold using Formlabs Form 3. The membrane layer is made by spin coating Sylgard™ 184 at 10:1 ratio on the surface of a Mylar film, in which the PDMS membrane can then be delaminated after cured. Specifically, 100 um membranes are obtained by spin coating at 1000 RPM for 30 seconds [205]. The three layers are then bonded using air plasma.

With the air microfluidic chip requiring a total of 10 on-chip valves as per the soft actuator array design, all 10 on-chip valves can be made to have different ΔP_{close} for each on-chip valve. This allows the chip to control the internal pressure of the actuators in a sequential order, obtained by matching the outlet of the on-chip valves with the actuators, in the order of highest to lowest ΔP_{close} and highest to lowest internal pressure required, respectively. Similar to the numbering of the actuators, each on-chip valve is also assigned a number for convenience of reference, with valve 1 having the lowest ΔP_{close} closing first in the sequence and valve 10 having the highest ΔP_{close} closing last in the sequence. As shown in **Figure 4.6b**, each of the on-chip valves is connected to one soft fluidic actuator, and the numbering system is formulated such that the on-chip valve number (i.e. valve 1) matches with the actuator number (i.e. actuator 1 – Posterior:

Popliteal, Soleus, Gastrocnemius). With the valves numbered from lowest to highest ΔP_{close} and actuators numbered from lowest to highest target pressure, the sequential control of on-chip valves corresponds to the sequential control of soft fluidic actuators.

For a given pressure difference between the control layer and fluid channel layer, the on-chip valves with a lower ΔP_{close} than the given pressure difference are closed, while the valves with higher ΔP_{close} are remained connected to the pressure source. An example of this manipulation is demonstrated in **Figure 4.6c, d**. At any given reference pressure, the number of actuators connected or isolated from the pressure source is controlled by simply manipulating the pressure difference of the control layer and fluid channel layer, and the valves are closed sequentially from the lowest to highest ΔP_{close}. Detailed sequence of events and the plot of control signal assigned to the control layer for sequential closure of the on-chip valves are shown in following **Section 4.2.3.**

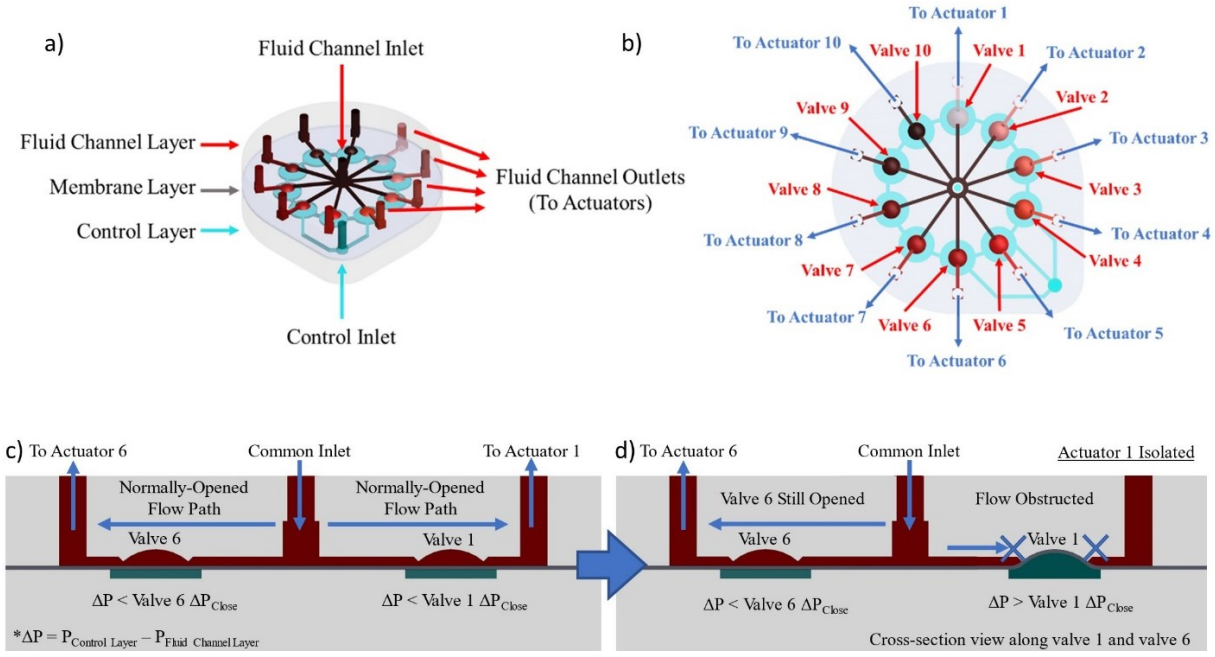


Figure 4.6: (a) Schematic diagram of the air microfluidic chip designed in this research. The fluid channel layer has a common inlet with a total of 10 outlets, each connected to a soft fluidic actuator. The control layer has common inlet to pressurize and deflect the membrane at the valve locations. (b) Labeling of the on-chip valve numbers and the corresponding actuator number that each on-chip valve is connected to. (c) Cross-section view along on-chip valve 1 and valve 6, with both valves at normally-opened state. The pressure difference between the control layer and the fluid channel layer is insufficient to close both valves. (d) Upon further increasing the pressure in the control layer, the pressure difference is larger than the pre-designed ΔP_{close} of valve 1 and hence the membrane is fully deflected into fluid channel layer, obstructing the flow at valve 1 location and isolating actuator 1. The same pressure difference is, however, lower than the pre-designed ΔP_{close} of valve 6 and hence the flow path is unobstructed to actuator 6.

4.2.3 Control Logic and Detailed Explanation of Valve Closure by Utilization of Closing Delta Pressure

Each of the actuators is controlled by one of the on-chip valves accordingly. Each on-chip valve is a sandwiched structure with one control channel perpendicularly arranged with the flow channel in the height direction. The control and flow channels are separated by a thin membrane and the flow channel can be closed or open by adjusting the pressure of the control channel to deflect the membrane. We define the pressure difference required to close a valve as closing delta pressure. For a given pressure difference between the control layer and fluid channel layer, the on-chip valves with a lower closing delta pressure than the given pressure difference are closed, while the valves with higher closing delta pressure are remained connected to the pressure source. Hence, at any given reference pressure, the number of actuators connected or isolated from the pressure source is controlled by simply manipulating the pressure difference of the control layer and fluid channel layer, and the valves are closed sequentially from the lowest to highest closing delta pressure. Detailed sequence of events and the plot of control signal assigned to the control layer for sequential closure of the on-chip valves are shown in **Figure 4.7** and **Table 4.2**.

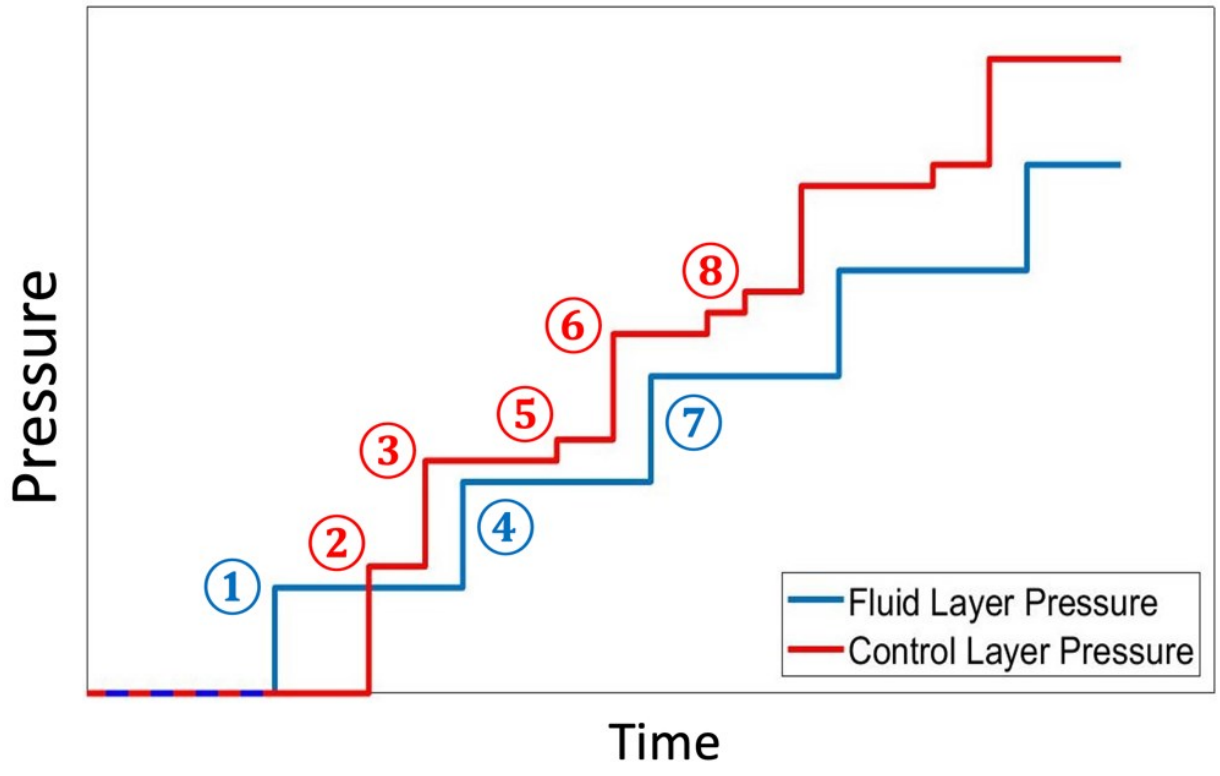


Figure 4.7: Control Logic with sequences of events illustrating valve closure by utilization of closing delta pressures.

Table 4.2: Legend for Figure 4.7.

SEQUENCE OF EVENTS	
①	First Step Reference – Initial Inflation of actuators, all valves are opened and hence all actuators are connected to the pressure source.
②	First Valve Closure – The pressure difference between the control layer and fluid layer exceeds the closing delta pressure of the first valve, which isolates actuator number 1 (lowest pressure) from pressure source.
③	Preparation to Second Step Reference – The control layer pressure is increased to the first valve's closing delta pressure plus the next step reference pressure. This ensures that the first valve remain closed upon the next step increase in fluid layer pressure.
④	Second Step Reference – Fluid layer is provided with the second reference pressure, all actuators except actuator number 1 achieve this reference pressure.
⑤	Second Valve Closure – Pressure in control layer is increased again to close the second valve, which isolates actuator number 2 (second lowest pressure) from pressure source.
⑥	Preparation to Next Step Reference – The control layer pressure is increased again to the second valve's closing delta pressure plus the next reference pressure.
⑦	Next Step Reference – Fluid reference pressure increased to the next step reference. All actuators except actuators number 1 and 2 achieve this pressure.
⑧	Example: Multiple Valve Closure – This is an example of how the number of actuators connected or isolated can be varied simply by manipulating the pressure difference in two layers. In this example, both actuators number 3 and 4 are isolated in the same reference pressure. Conversely, the opening of the valves works in the same logic.
. . .	
PROCESS REPEATS UNTIL THE FINAL VALVE IS CLOSED	

4.2.4 Residual Limb/Socket Fabrication and Setup

As the focus of this work is on the development and evaluation of the air microfluidics technology and its synergy with soft actuators in prosthetic systems, only minimal biofidelity is considered in preparing the limb model and the prosthetic socket setup. The shape of the residual limb is idealized as a tapered cylinder with a hemispherical endcap, made by casting FlexFoam-iT™ V, a flexible Urethane foam, with a 3D printed mold (**Figure 4.8a**).

The stiffness of this foam material is experimentally determined by performing Quasi-static compression tests [206], which are done as per the ASTM standard test method [207]. The foam material's stiffness is determined to be around 140 kPa, which is within the range of the biomechanical model of the residuum soft tissues of 120 – 260 kPa [208], [209]. A hollow 1-¼ inch diameter Aluminum 6061 rod of 0.065-inch wall thickness is also determined to be sufficient

to represent the mechanical properties of the tibia when placed 30 mm from the bottom of the hemispherical end of the limb [210]. The fabricated residual limb is as shown in (Figure 4.8**b**). Two prosthetic sockets are made via 3D printing, per clinicians' advice, 1 mm and 4 mm radial clearance are used to represent a typical setup in clinical prosthesis use (Figure 4.8**c**), and loose prosthesis fit, respectively.

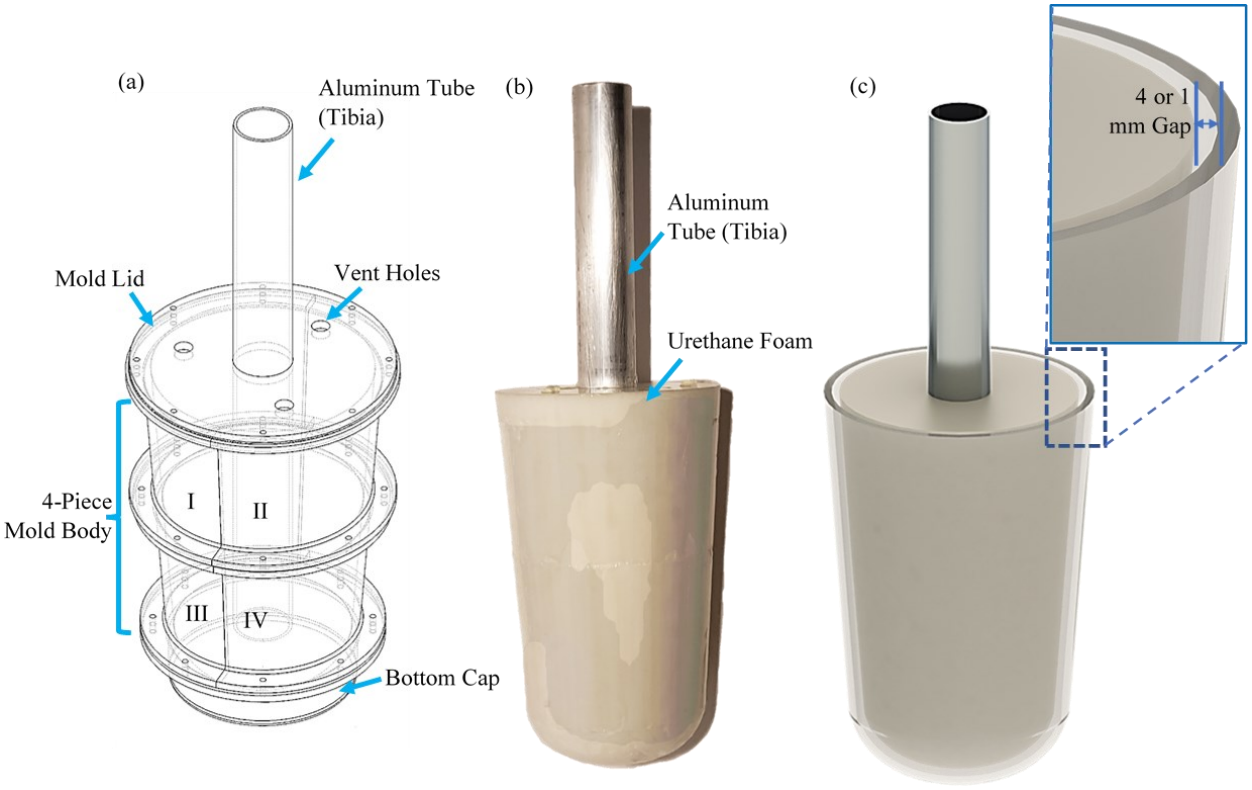
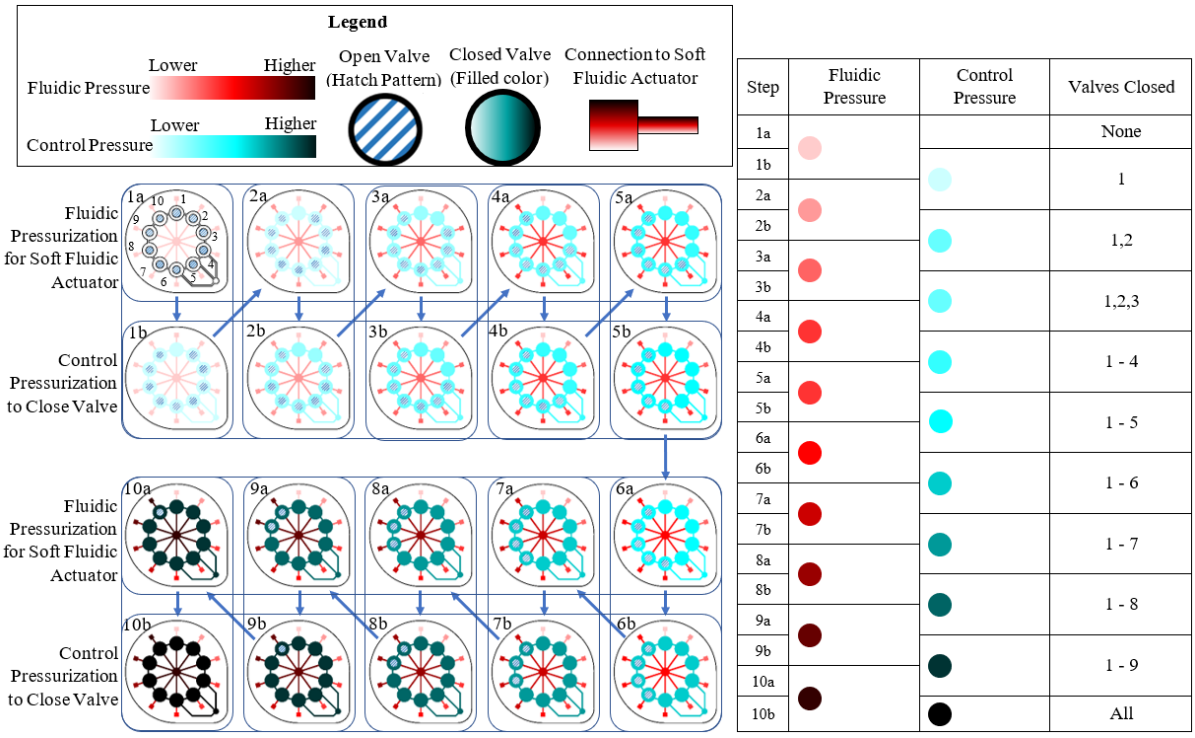


Figure 4.8: (a) Residual limb model mold. (b) Residual limb model. (c) Clearance between residual limb model and prosthetic socket.

4.3 Methodology and Test Setup

The air microfluidic chip is optimized via iterative design method, in which the valve features are varied while keeping PDMS mix ratio, curing temperature, and membrane thickness all the same to obtain the optimal design providing the most consistent response. To verify the microfluidic chip capabilities to provide the sequential flow control, the outlet of each of the 10 on-chip valves was connected to a pressure sensor. Below is an example showing the test setup. The test starts by inflating all 10 soft fluidic actuators to the pressure matching the actuator 1's pressure (lowest pressure), followed by the closure of valve 1. Actuator 1 is then isolated from the pressure source and is prevented from any further inflation. The remaining 9 soft actuators are then inflated to the

pressure matching actuator 2's pressure (second lowest pressure), followed by closure of valve 2 which prevents any further inflation into actuator 2. This process continues until all 10 actuators are inflated to their corresponding pressures. **Figure 4.9** shows the sequence of closing all 10 on-chip valves.



Step	Fluidic Pressure	Control Pressure	Valves Closed
1a			None
1b			1
2a			
2b			1,2
3a			
3b			1,2,3
4a			
4b			1 - 4
5a			
5b			1 - 5
6a			
6b			1 - 6
7a			
7b			1 - 7
8a			
8b			1 - 8
9a			
9b			1 - 9
10a			
10b			All

Figure 4.9: Diagram showing differential sequential pressure control enabled by one air microfluidics chip. The fluidic pressure (pressure from the control box to actuators) and control pressure (used to close valves) are represented by shades of red and cyan, respectively. Darker shade represents higher pressure, and lighter shade represents lower pressure. The table shows the fluidic pressure, control pressure of each step, and which valve is closed at which step. For instance, to close valve 1 only, the required pressure must be higher than the sum of valve 1 delta closing pressure and step 1 fluidic pressure and be lower than that for closing valve 2. The arrows represent the fully automated sequence of the pressure control, in which the pressures are changed in step increments via utilization of solenoid valves.

The liner with integrated soft actuator array is first slid onto the simulated limb, then the assembly is placed into the socket. To monitor the contact pressure applied by the actuators onto the limb, two Tekscan F-Socket™ (Tekscan, Boston, USA) force-sensitive-resistor sensor arrays (Model 9811) are placed between the liner and the limb model. The array of sensors is evenly distanced 0.5 in apart from one another, and the integrated 5x5 interpolation was adopted in the Tekscan F-Socket™ software to map the pressure distribution. In this test setup, each of the soft fluidic actuator is also connected to an air pressure sensor for purpose of recording the internal

pressure responses. It should be noted that both Tekscan sensors and air pressure sensors are used only for verification purposes and are not part of the wearable prosthesis system. In addition, one custom-made pressure pump [134] and two solenoid valves were used as a desktop test pneumatic source to control the actuator pressures via the air microfluidic chip. The overall test setup is as shown in **Figure 4.10**.

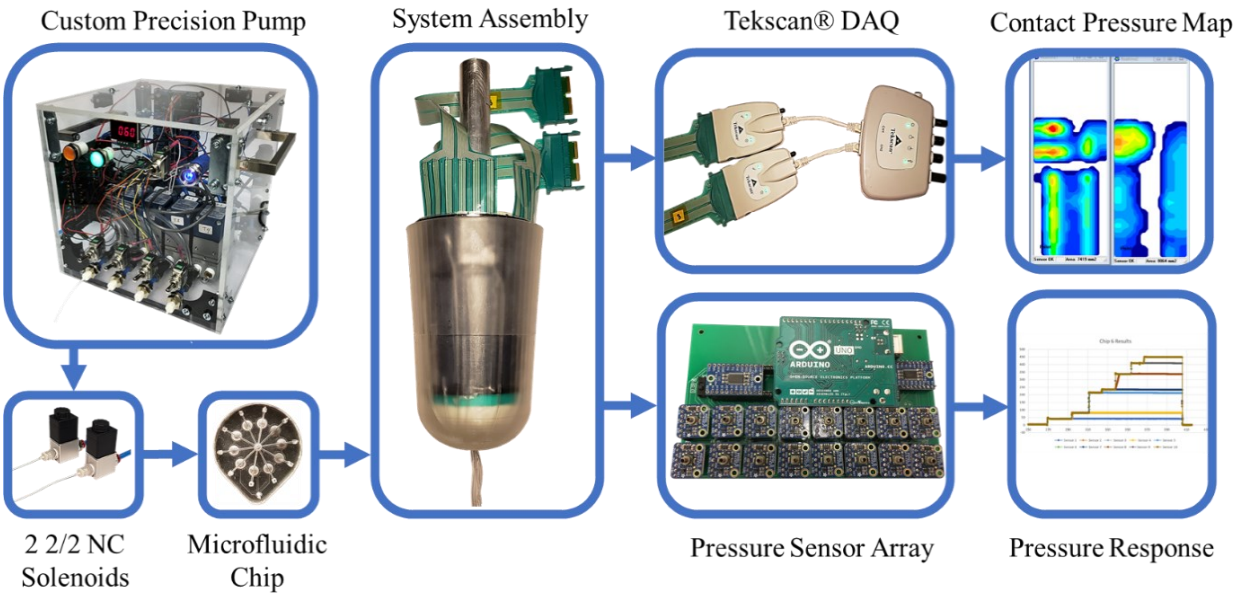


Figure 4.10: The overall test setup used for acquiring both the contact pressure mapping and the pressure response curve of the air microfluidic chip. With the 2 2/2 NC solenoids and a microfluidic chip, only one channel of the 4-channel custom-made pressure pump is used to operate the system.

4.4 Results and Discussion

4.4.1 Chip Pressure Response

An actuator array comprised of 10 actuators and a total of 7 internal pressure levels were designed to achieve the desired contact pressure distributions. Consequently, the air microfluidics chip included a total of 10 on-chip valves designed with 7 different ΔP_{close}, as shown in **Table 4.3**. The final design of the air microfluidics chip with 10 on-chip valves is shown in **Figure 4.11**.

Table 4.3: Valve features and dimensions for the optimized air microfluidic chip.

Valve #	1	2	3	4	5	6	7	8	9	10
Shape	Offsetted Hemisphere									
Radius of Curvature [mm]	2.78	2.28	2.28	2.28	1.99	1.76	1.76	1.63	1.51	1.34
Offset Distance [mm]	2.28	1.78	1.78	1.78	1.44	1.16	1.16	0.98	0.81	0.54
Membrane Deflection Depth [mm]	0.45	0.50	0.50	0.50	0.55	0.60	0.60	0.65	0.70	0.80
Surface Area [mm^2]	7.44	6.90	6.90	6.90	6.62	6.37	6.37	6.36	6.36	6.42



Figure 4.11: Optimized design of the air microfluidic chip with volume of 10 cm^3, diameter of 35 mm, thickness of 10 mm, and mass at just 10 g (lighter than an AAA Alkaline battery). A dark-colored background was to reveal the on-chip valve features as well as the channels inside the chip. A Canadian quarter is in place for size comparison.

As shown in **Figure 4.12**, the pressure response results without the actuators demonstrate the 7 desired pressure levels were achieved as per the original valve design intention. Moreover, this verifies the ability of the air microfluidic chip to sequentially open and close the on-chip valves on demand, even when the reference pressure is changing. Due to the design of the on-chip valves, however, the opening and closing of the on-chip valves are always done in a sequential manner – closing in order of lowest to highest ΔP_{close} and opening in order of highest to lowest ΔP_{close}.

The transient response for the fifth step reference pressure was slightly slower than the others because the gap between the ΔP_{close} of the valve 7 and valve 8 was not large enough. Hence,

when the valve 7 fully closes, valve 8 is also partially closed. Consequently, a slower inflation rate was observed because valve 8 then needs to relieve the pre-introduced force imbalance in the membrane first, before the fluids are transported to the actuator. This lag can be eliminated by designing the on-chip valves to have a bigger difference in ΔP_{close}, which can be attained with a higher resolution fabrication equipment. Overall, the pressure response was consistent. Based on the current system, it takes about two minutes to completely close all 10 valves.

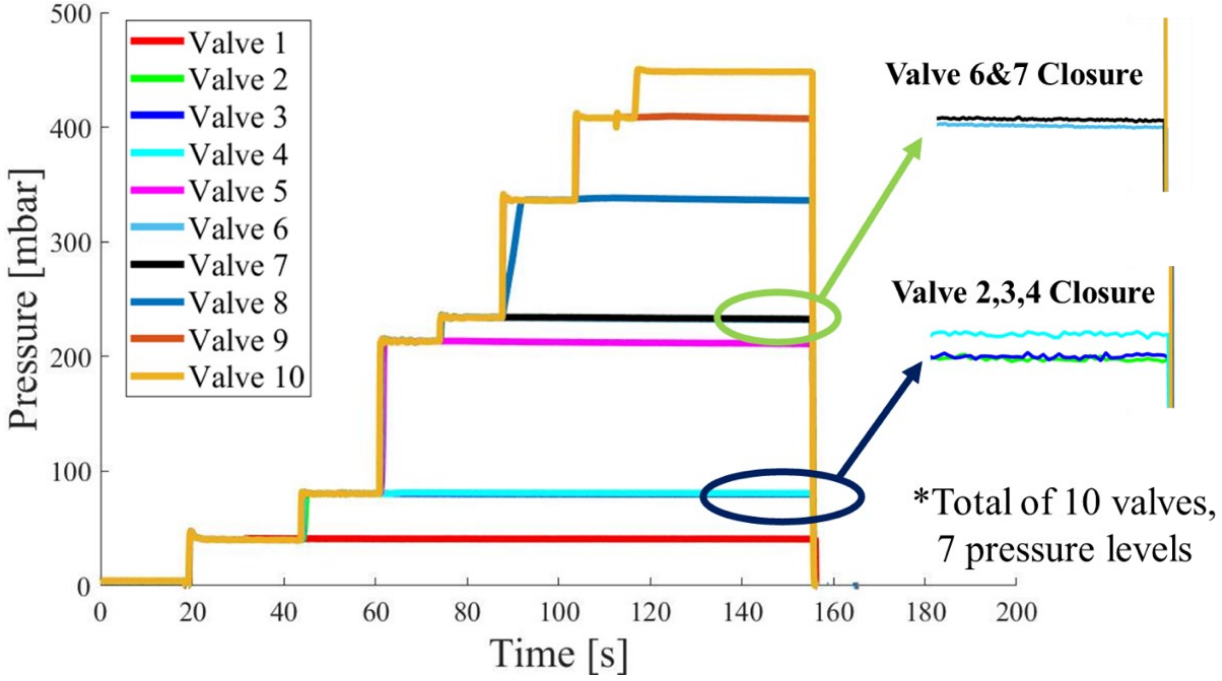


Figure 4.12: Pressure response curve of the air microfluidic chip. The outlet of each of the 10 on-chip valves was connected to a pneumatic pressure sensor for pressure measurement. A total of 7 pressure levels with 10 on-chip valves were achieved by having the valves 2,3, and 4 to close as a single group, and same for valves 6 and 7.

4.4.2 Contact Pressure Test Results

Based on the input from practicing clinicians (senior physiatrist (Doug Dittmer, Senior Physiatrist and Sports Medicine Physician, Department of Physical and Rehabilitation Medicine, Grand River Hospital) and senior prosthetist (Andreas Schirm, Certified Prosthetist)), an idealized contact pressure mapping distribution was attained as a target for this study. This ideal case of contact pressure mapping as shown in **Figure 4.13a**, was obtained by manually inflating the actuators with multiple pressure sources until the desired contact pressure was acquired. The contact pressure between the liner and the limb model recorded using the proposed system was as desired, as shown in **Figure 4.13b**.

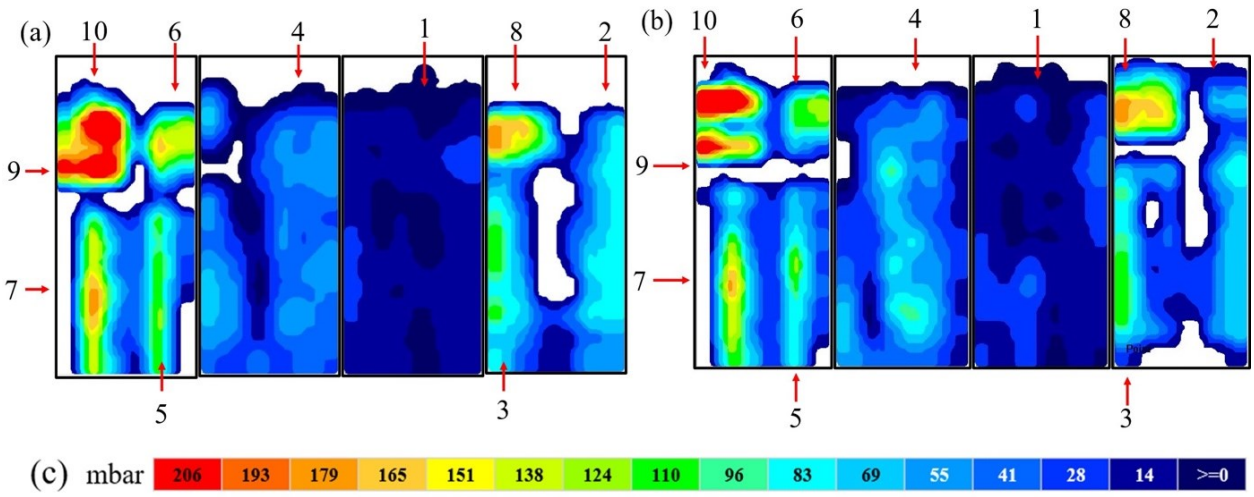


Figure 4.13: (a) Contact pressure mapping obtained as the idealized case. This figure shows the visual illustration of the target contact pressures of each actuator relative to one another. (b) Contact pressure mapping obtained using the proposed system; air microfluidics chip, single pneumatic source, and two solenoid valves. (c) Contact pressure label associated with the color contour of the test results. Both figures share the same color-pressure label.

When the socket model with 1 mm radial clearance was used, slight precompression was induced but there were no issues with the inflation of the actuators. For the socket setup with 4 mm radial clearance, the inflation of the actuators provided enough strain to fill up the gap naturally. The first step reference pressure provided initial volume displacement of the actuators to fill up the gap, and also provided about 35 mbar of contact pressure as a minimum gripping pressure from all actuators onto the limb. The force sensitive parts of the limb were then isolated from the pressure source to maintain the minimum gripping contact pressure, while the other actuators remained connected to the pressure source to proceed to the next pressure levels. The final result is a well-distributed contact pressure mapping with the peak contact pressure being less than 200 mbar. Comparison of the original target contact pressures and the pressure range observed for each anatomical location is summarized in **Table 4.4**. The same test was repeated a total of 5 times to ensure the consistency of the results. The results are as shown in **Figure 4.14**. With the ability of the air microfluidic chip being able to control the connection and isolation of the actuators from the pressure source on demand, all the test results were consistent, and the end results were always the same. For example, if one of the actuators exhibited an abnormally high or low of contact pressure, the air microfluidic chip was able to roll back to that specific actuator, modify the pressure, and re-regulate the pressure levels from that actuator onwards.

Table 4.4: Comparison of the contact pressure: original target versus test results.

Actuator Number	Target Contact Pressure (mbar)	Contact Pressure Range (mbar)
1	50	26~51
2	60	63~76
3	70	51~101
4	80	63~88
5	95	88~101
6	120	113~125
7	140	125~150
8	160	150~163
9	180	175~188
10	190	188~200

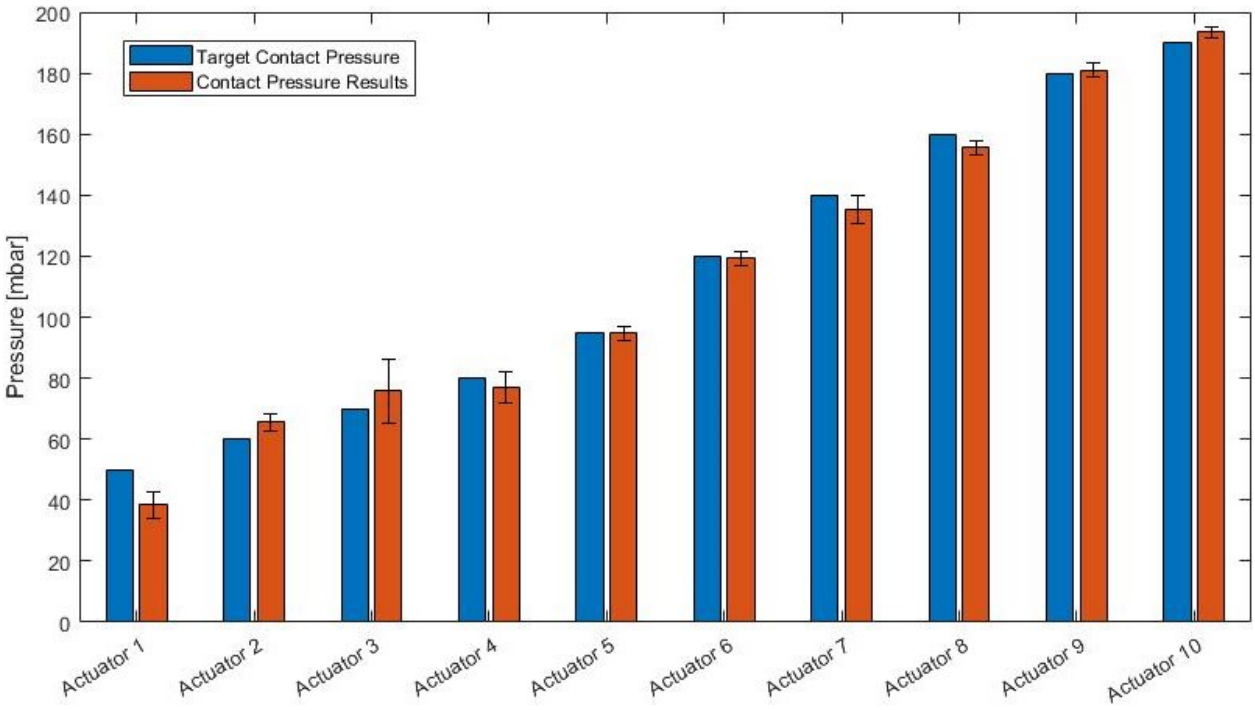


Figure 4.14: Summary of the contact pressure test repeated over 5 times. The contact pressure of the 10 actuators in each test are represented as mean and standard errors (in orange), each placed next to the target contact pressure (blue) for comparison.

It should also be noted that upon achieving the desired contact pressure mapping during the first test run, the internal pressures of all actuators were recorded through the pressure sensor array. By doing so, the pressure sensor array and force-sensitive-resistor sensor are no longer required in the test setup to attain the same contact pressure results for this static non-loading study.

Specifically, in this case, the same results can be obtained using the proposed wearable system, comprised of a single pressure source, two solenoid valves, and a single pressure sensor. This implies that the contact pressures are dependent on the internal pressures of the soft fluidic actuators. To establish the relationship between the internal pressures and the contact pressures, advanced non-linear continuum mechanics models such as Neo-Hookean model or Mooney-Rivlin model may be utilized in the future when designing the liner. Similarly, recent advancements of Finite Element Methods for soft fluidic actuators could assist with predicting the pressure distribution of the liner in the future [211].

4.4.3 Limitations

While the concept has demonstrated potential, the current study is based on a simplified, non-biofidelic physical prosthetic and residual limb model. Future work will include testing the concept on a biofidelic model with body weight and gait that exhibits residual limb volume fluctuation with modifications to the actuator size, placement, and target pressure. While control is largely based on internal air pressure sensors, they measure internal soft actuator pressure which may require calibration and interpolation to acquire actual external contact pressure, which could introduce errors and imprecision. As an alternative for sensing, knitted soft fabric pressure sensors can be directly integrated into the prosthesis liner or socket to directly measure external contact pressure for control feedback.

4.5 Concluding Remarks

This study demonstrates a proof-of-concept study for a novel air microfluidics-enabled soft robotic transtibial prosthetic socket liner for managing residual limb volume fluctuation and pressure management, which are crucial for amputee's quality of life and safety. The air microfluidic chip with 10 on-chip pneumatic valves at just 10 cm^3 and 10 grams, lighter than a AAA battery, drastically reducing the number of electromechanical solenoid valves required to inflate/deflate 10 soft fluidic actuators independently to the desired pressure levels. Future work will focus on improving the design of the entire system with biofidelic models of the prosthesis and residual limb to further verify the proof of concept towards potential clinical trials. Overall, the proposed air microfluidics-enabled soft robotic transtibial prosthetic socket liner opens the door for small, economic wearable dynamic socket liners to compete with existing silicone/fabric socket liners while adding performance for socket fit and comfort.

Chapter 5

Investigating Active Air Microfluidics with Overlapping Soft Fluidic Actuators for Smooth Sequential Gradient Compression

Run Ze Gao conceived the idea. The device fabrication and experimental procedures were collaboratively undertaken by Drew Werbowski, Chelsea Huang, and Run Ze Gao. Run Ze Gao authored the manuscript.

5.1 Introduction

Secondary lymphedema is a prevalent and chronic condition affecting a substantial number of breast cancer survivors worldwide [150], with an incidence ranging from 7% to 47% [212]. Surpassing the collective prevalence of AIDS, Parkinson's disease, multiple sclerosis, muscular dystrophy, and Alzheimer's disease [213], [214], secondary lymphedema poses a significant health burden [155]. The condition arises due to trauma to the lymphatic system, commonly occurring during breast cancer surgeries and treatments, where lymph nodes are removed or damaged, leading to disruption in lymphatic circulation and consequent fluid buildup in the affected arm [148], [151]. Notably, stage 1 lymphedema is marked by visible swelling [215], which, if left untreated, progresses to more severe stages with increased pain and disability due to heightened viscosity of the accumulated lymphatic fluid [148], [152]. This includes reduced arm range of motion, strength, and dexterity, along with challenges in terms of aesthetics and social burden [216]–[218]. Advanced-stage lymphedema may necessitate surgical intervention [219]–[221]. Managing lymphedema require frequent Complete Decongestive Physical Therapy [222], involving manual lymphatic drainage (MLD), compression bandaging/garments, exercises to promote lymphatic drainage, and diligent skin

care [223]. However, MLD [224], a critical treatment, is often challenging for lymphedema patients to perform self-care due to reduced arm mobility and strength [222]. Accessing specialized lymphedema treatment can be costly and difficult in certain regions of the world, further exacerbating the burden on affected individuals [225].

State-of-the-art pneumatic compression pumps offer an effective automated alternative to MLD, significantly improving the quality of life for patients [162]–[166], [226]. However, most of these advanced compression pumps are designed for static at-home use and suffer from bulkiness and noticeable gaps between each actuator [227], [228]. These current pneumatic compression pumps lack two crucial aspects: first, the ability to provide smooth compression in a low-profile form factor; and second, they heavily rely on a large number of electromechanical components, restricting their use to static at-home settings. To address these limitations, the novel system presented in this study combines a monolithic sheet of overlapping soft fluidic actuators, achieving a low-profile smooth gradient compression profile, with an active air microfluidic system incorporating pneumatic in-line valves and microchannels for sequential gradient control. The result is a portable package that overcomes the shortcomings of traditional compression pumps and enhances the mobility and convenience for individuals in managing lymphedema.

Other approaches, such as smart material-based systems utilizing shape memory alloys made with Nickel/Titanium (Ni-Ti) [229], [230] or refrigerant fluids [231], are also being explored. However, these systems often require heating elements for activation, leading to the use of relatively thick insulation layers to prevent warming the skin, which may not be ideal for patient comfort. Additionally, the construction of these smart material-based systems often results in noticeable gaps between each actuator [227], similar to pneumatic compression pumps, which can trap lymphatic fluid over time, causing it to thicken and potentially limiting the efficacy of the treatment. As a result, the combination of monolithic sheet of overlapping soft fluidic actuators and active air microfluidics presented in this study represents a promising advancement in achieving a more effective and user-friendly solution for managing lymphedema.

The work herein systematically explores different percentage of overlapping soft fluidic actuators to determine the most optimal overlapping percentage that would create a

low-profile smooth gradient compression while reducing the number of soft fluidic actuators required to cover the entire length of the treatment area. If traditional methods were to be used, a large number of electromechanical solenoid valves would be used to control the overlapping soft fluidic actuators, which would create a bulky control box, instead, through synergizing with active air microfluidics [46], a miniaturized portable control box is realized.

In our previous work (**Chapter 3**), we focused exclusively on using microchannels for passive control of air bladders-based compression sleeves for lymphedema swelling of the forearm [147]. While this approach proved efficient for controlling eight soft air bladders and proved to be robust and reliable as there were no moving parts, it encountered limitations when attempting to scale up to accommodate more than eight bladders, thereby restricting its use primarily to the forearm without gradient pressure holding. To increase the number of soft air bladders while maintaining gradient sequential inflation, one would need to add increasingly narrow microchannels in parallel. However, this presented challenges as it surpassed the printing resolution of most 3D printers available at the time of this thesis (2023). Moreover, this approach would result in decreased deflation speed with increasingly narrower microchannels, reducing the overall duty cycle, which indicates how many inflation and deflation cycles can be executed within a set time frame. Additionally, the risk of micro particulates becoming lodged inside increasingly narrower microchannels grew, potentially causing partial blockages and inconsistent flow rates. These issues prompted us to explore novel approaches, leading to the development of the In-Line and Combined Air Microfluidic Chips and monolithic sheet of overlapping soft fluidic actuators, as presented in this study, which effectively address these limitations and advancing management of swelling due to lymphedema.

Drawing inspiration from microfluidic in-line pinch valves, we designed and tested active air microfluidic chips with and without microfluidic channels configured in series. The original microfluidic in-line pinch valves, also known as Quake's style valve, were pioneered by Stephen S. Quake in the year 2000 [86]. For this engineering study, we have made specific modifications to the Quake's style valve, which will be thoroughly discussed in the following sections, to make it more compatible with the mentioned control strategies and a pneumatic system. The choice of Quake's style valve was driven by its advantages, including ease of fabrication through soft lithography [180], biocompatibility, as it is most often made from

polydimethylsiloxane (PDMS), and robustness for both digital on-off control and analog sequential gradient control [25], [89], [91]. Analog sequential gradient control involves gradually opening a series of in-line valves in a predetermined sequence by continuously (i.e., analog) reducing their control pressure at a predefined rate. This concept was inspired by our previous work on using on-chip pneumatic valves to control the dynamically adjusting prosthetic liner, as discussed in **Chapter 4** [25]. Despite having different names, in-line valves and on-chip pneumatic valves essentially serve the same purpose. The term "in-line" is derived from the arrangement of on-chip pneumatic valves, where they are either daisy-chained in a line or placed one after another in a serpentine microchannel, reflecting the geometry of their integrated layout and fluid flow pathway. Thus, the term "in-line" is chosen for this chapter to accurately represent this arrangement.

Prior works have explored the use of fluidic demultiplexers [232] and fluidic circuitry [233], [234] to control large arrays of soft actuators, but these approaches were primarily digital in nature and faced challenges when attempting to scale-up the size and achieve fine-tuned precise gradient pressure for air microfluidics-control of soft fluidic actuators, as indicated by **Figure A.2** in **Appendix A**. Additionally, a distinct family of control strategies, identifiable as kink or snapping-type valves rooted in nonlinear mechanical instability, is effective in achieving sequential and oscillating control [13], [99], [235]–[239]. While these designs have proven suitable for independent and autonomous soft robots, they are currently limited, in the authors' opinion, by challenges in further miniaturization and manufacturing. This limitation makes them less suitable for truly wearable devices and may also lead to pulsatile motion, a characteristic that is undesirable for active compression applications. Another proposed solution was a pneumatic random-access memory for controlling soft robots [240]; however, this approach also remained digital in nature and lacked robustness, relying on 2-position, 4-way, 4-port valves (4/2 valves), which cannot be easily miniaturized. Electrically driven soft valves [241], electrorheological fluid valves [242], and liquid metal logic-based systems [243] require high voltage or are bioincompatible to be considered safe for wearable systems. Consequently, these novel technologies may be considered impractical, bulky, unsafe and/or potentially over-engineered for the specific application of active compression sleeves.

The integration of analog sequential gradient control using pneumatic in-line valves directly within garments is a promising concept, which is coined as “In-Line Air Microfluidic Chips”, but its efficacy is hindered by fabrication challenges in a laboratory environment. However, this approach lays the groundwork for combining pneumatic in-line valves with microchannels, resulting in a powerful combination that achieves robust sequential gradient compression with pressure holding capabilities, coined as “Combined Air Microfluidic Chip”. When brought together, these advancements offer an easy-to-design and fabricate solution for achieving effective and efficient compression.

The convergence of active air microfluidic control with overlapping soft fluidic actuators leads to the creation of a soft robotic active compression sleeve capable of providing active, smooth, and sequential gradient compression with pressure holding capabilities and a fast passive uniform deflation (**Figure 5.1**). This innovative technology has the potential to revolutionize pneumatic compression for the treatment of lymphedema and circulatory disorders, bridging the gap between portability and performance that has posed challenges for pneumatic sequential gradient compression. The following section will present the fabrication and results of this study, delving deep into the design rationales and thoroughly discussing every aspect of this systematic investigation.

5.2 Design Rationale and Fabrication

5.2.1 Air Microfluidic Chips

The core functional unit of the active air microfluidic chips explored herein are pneumatic in-line valves. The operation of pneumatic in-line valves are well documented in existing literature [25], [204]. The fundamental idea is that the in-line valves are constructed by a single fluidic channel and control channel, separated by a membrane. Air is pumped into both the fluidic and control channels of the in-line valves. Through a pressure difference between the two channels, the membrane deflects towards the fluidic channel. This physically obstructs the air flow and acts as a normally open mechanical valve. The combination of in-line valves with a range of closing pressures allows for sequential inflation of the air chambers and gradient compression of the arm. Opening the fluidic channel to the atmosphere facilitates a uniform deflation of the air chambers.

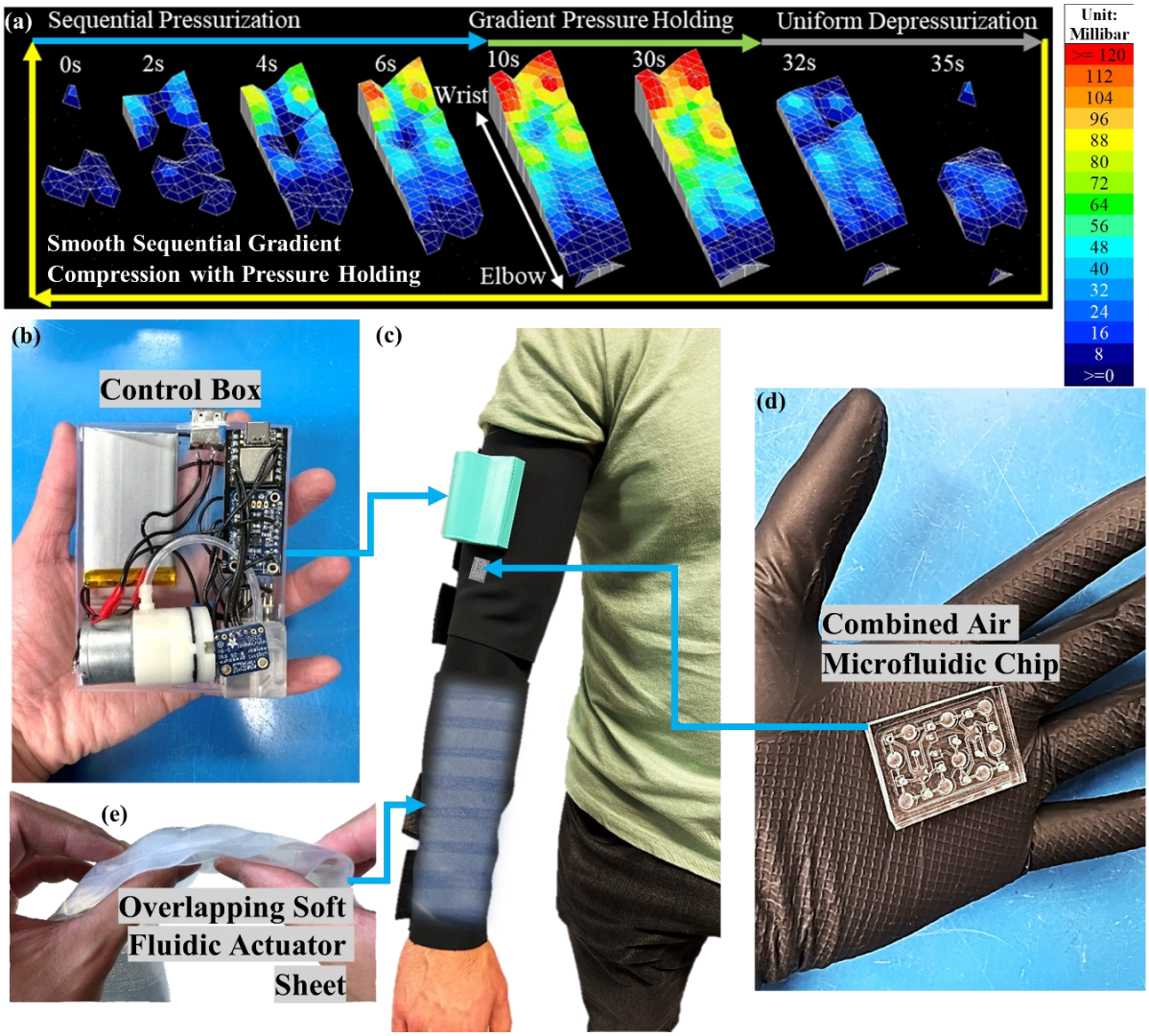
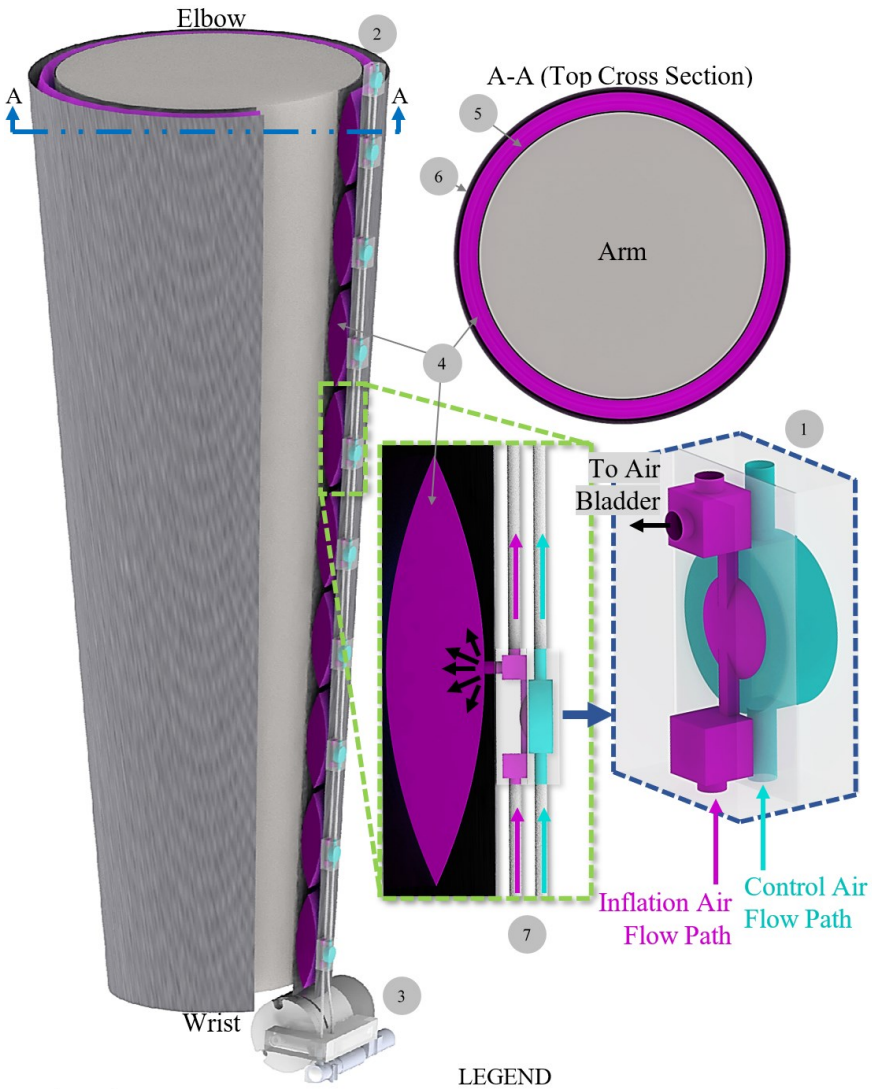


Figure 5.1: Soft robotics-enabled active compression sleeve utilizing active air microfluidics and overlapping soft fluidic actuators. (a) Tekscan pressure mapping sensors (9811E, Tekscan) capture smooth sequential gradient compression with pressure holding capabilities and fast uniform deflation, presented in a 3D pressure map contour format with a legend indicating compression levels in millibar. (b) The wearable control box with the cover removed, revealing internal components. (c) Image of the soft robotic active compression sleeve worn on a human arm, comprising three key subcomponents: the wearable control box, monolithic sheet of overlapping soft fluidic actuators, and Combined Air Microfluidic Chip. (d) Miniaturized combined air microfluidic chip designed for sequential gradient pressurization, pressure holding, and fast uniform deflation of soft fluidic actuators. (e) The inflated monolithic sheet of overlapping soft fluidic actuators showing its ability to flex and minimize gaps between each consecutive soft fluidic actuator when bent by hands.

Two types of air microfluidic chips were designed and produced: the In-line Air Microfluidic Chips and the Combined Air Microfluidic Chip. The In-line Air Microfluidic Chips, each embedded with a unique pneumatic in-line valve, is designed to integrate

seamlessly with garments and tubing, facilitating analog sequential gradient control when daisy chained, as illustrated in **Figure 5.2**. The design does not utilize microchannels and, unlike many lab-on-chip devices, features pneumatic in-line valves not strictly micro-sized **Figure 5.3a-d, f**. Despite this, the ethos of microfluidics, miniaturizing the control system, is upheld, warranting the title 'air microfluidic chip.' A significant aspect of the design is the differential pressure ($\Delta P_{close/open}$) which determines the opening and/or closing pressure of the valve, explored in **Chapter 4**. $\Delta P_{close/open}$ is determined by subtracting pressure within fluidic air pathway from the pressure within control air pathway as shown by **Equation (5.1)**. In other words, $\Delta P_{close/open}$ is the threshold pressure for in-line valve operation, which when above the threshold pressure, the valve closes, below the threshold pressure, the valve opens. Although ΔP_{close} and ΔP_{open} are the same, we will use ΔP_{close} when discussing in-line valves that perform its main function by closing and ΔP_{open} when discussing in-lines valves that perform its main function by opening. Moreover, $\Delta P_{close/open}$ is used when in-line valve in general is discussed. When a series of these valves are connected and open one after another in a sequence, they create a gradient inflation sequence, allowing corresponding SFA to inflate sequentially, akin to an air microfluidic chip with only microchannels. With no microchannels involved, rapid deflation is possible through passive deflation into the external atmosphere, negating the need for power-consuming active vacuum suction. Nonetheless, the fabrication of these in-line chips can prove challenging, particularly in laboratory settings, necessitating the introduction of the second type of chip, one that combines in-line valves with microchannels.

$$\Delta \boldsymbol{P}_{\boldsymbol{close/open}} = \boldsymbol{P}_{\boldsymbol{Control\ Line}} - \boldsymbol{P}_{\boldsymbol{Fluidic\ Line}} \tag{5.1}$$



LEGEND	
1	**In-Line Air Microfluidic Chip** – Applies Sequential Inflation, Uniform Deflation, and Gradient Pressure to the Soft Fluidic Actuators for Lymphedema Treatment. Can be Directly Integrated atop the Soft Fluidic Actuators; Pneumatically Controlled without Electricity or any Metallic Component
2	**Active Compression Lymphedema Sleeve** – Reduces Swelling Caused by Lymphedema
3	**Wearable Control Box** – Includes a 30 Gram Miniature Air Pump, 1 Miniature 2/2-Way Solenoid Valve, and 1 Miniature 3/2-Way Solenoid Valve, and a Single Pressure Sensor.
4	**Soft Air Bladder** – Applies Compression
5	**Inner Skin Contact Fabric** – Skin Comfort
6	**Outer Strain Limiting Fabric** – Directs Forces Toward Arm
7	**Tubing** – Transports Fluid

Figure 5.2: Schematic rendering of In-Line Air Microfluidic Chips integrated on top of the soft air bladders (without overlapping) in the pneumatic air compression sleeve (Lymphedema sleeve, same as **Chapter 3**). The chips enable sequential gradient inflation of the air bladders, resulting in a sequential gradient compression on the arm.

The Combined Air Microfluidic Chip employs microfluidic channels to stimulate sequential and gradient inflation of SFA **Figure 5.3g**. Instead of merely relying on parallel channels to induce sequential gradient inflation, as detailed in **Chapter 4**, this chip design leverages series-connected channels **Figure 5.3e**. The increased channel resistance is attributed to the reduction of cross-sectional area and elongation of the channel. This unique design allows an infinite number of SFAs to sequentially inflate by merely extending a single microchannel's length and establishing connections at different points along its path. However, real-world factors like manufacturing tolerance and the number of SFAs required for the application impose certain limitations on this method.

The second component of the Combined Air Microfluidic Chip, the in-line valves, are used primarily for pressure holding **Figure 5.3e**. Their functioning is digital, i.e., either 'on' or 'off.' Consequently, the differential pressure (ΔP_{close}) of each in-line valve can be the same or very similar as long as all the valves close after a threshold pressure is reached, the system operates efficiently. This design simplifies fabrication since the ΔP_{close} for each in-line valve only needs to be similar, rather than precise. Moreover, these in-line valves also enable rapid deflation sequences. Therefore, the Combined Air Microfluidic Chip embodies the strengths of both the solid-state air microfluidic chip from **Chapter 3** and the active air microfluidic chip with on-chip valves from **Chapter 4**, while remaining relatively straightforward to produce. The fabrication methods for both types of air microfluidic chips employing soft lithography [180] are detailed in **Figure 5.4**.

5.2.2 Controlling Active Air Microfluidic Chips

The control box (**Figure 5.5a, b**) used for both types of chips was identical, with the only difference being the fluidic pathway routing of the 3/2-way and 2/2-way solenoid valves to control the opening and closing of the in-line valves. The fluidic control diagrams for the Combined Air Microfluidic Chip and the In-Line Air Microfluidic Chip are shown in **Figure 5.5c** and **Figure 5.5d**, respectively. Flow charts outlining the control scheme for both In-Line Air Microfluidic Chips and Combined Air Microfluidic Chip can be found in **Figure 5.6**. A comprehensive discussion on the advantages and disadvantages of both types of Air Microfluidic Chips will be provided in **Section 5.4 Discussion**.

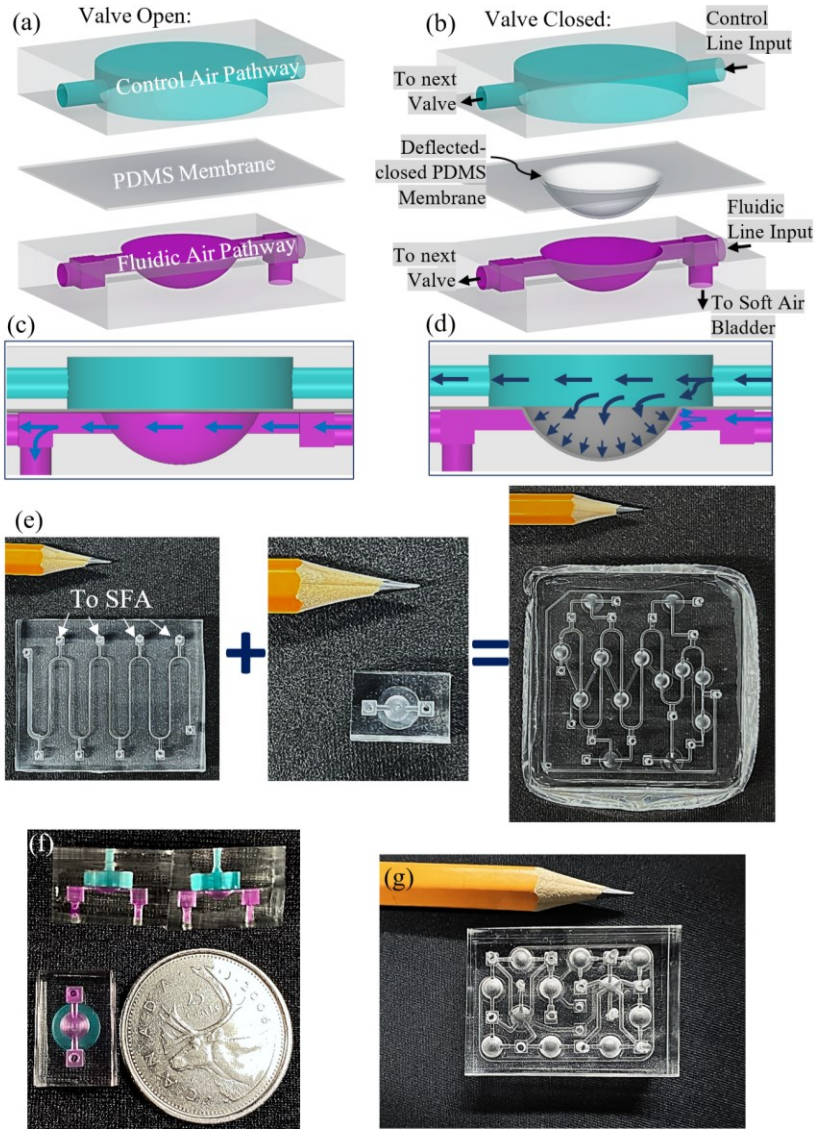


Figure 5.3: (a) Exploded-assembly diagram illustrating the construction of the pneumatic in-line valve in its normally open state. The valve consists of three main components: the control side PDMS part (illustrated with a cyan-colored air pathway), the fluidic side PDMS part (with a pink-colored air pathway), and an elastic PDMS membrane placed between them. (b) Exploded-assembly diagram representing the pneumatic in-line valve in its closed state. Application of air pressure to the control air pathway (shown in cyan) causes the PDMS membrane to deflect downward, effectively closing the pneumatic in-line valve and halting the airflow through the fluidic pathway (colored pink). (c) Side cross-sectional view of the pneumatic in-line valve, demonstrating the airflow when there is no or insufficient pressure within the control air pathway (in cyan). Under these conditions, air can move freely past the pneumatic in-line valve, as indicated by the arrows indicating the flow direction. (d) Another side cross-sectional view of the valve, showing the PDMS membrane deflecting downward due to air pressure from the control air pathway, resulting in the closing of the pneumatic in-line valve. This deflection obstructs the airflow through the fluidic air pathway (colored pink). (e) Images depicting the integration of passive serpentine resistance channels (left) and

pneumatic in-line valves (middle) to form the Combined Air Microfluidic Chip (right). A pencil with approximately 7 mm width was used as a size reference. (f) In-Line Air Microfluidic Chips, with two viewed from the side showing different sizes and one viewed from the top. The cyan color represents the control side, and the pink color represents the fluid side, as shown in the schematics above. A Canadian quarter coin with a diameter of approximately 24 mm provided scale. (g) Further miniaturized Combined Air Microfluidic Chip, which had the same function as the one shown in (e) but smaller and more compact, demonstrating the potential of the design to be extremely compact and low-profile.

Table 5.1 presents the size and dimensions of the air microfluidic channel lengths for the Combined Air Microfluidic Chip. These channel dimensions were experimentally determined to achieve the required sequential and gradient inflation, and the results will be shown in later sections. The in-line valves embedded within the air microfluidic chips vary in height, membrane thickness, and thermal aging time, thereby affecting their $\Delta P_{close/open}$ characteristics. The parameters of the in-line valves chosen for both the In-Line Air Microfluidic Chip and Combined Air Microfluidic Chip are shown in **Table 5.2**.

Table 5.1: Dimensions of channels in Combined Air Microfluidic Chip and calculated equivalent hydraulic resistance. The table presents the dimensions of square channels in the Combined Air Microfluidic Chip, with channel numbers corresponding to **Figure 5.5c**. The calculated equivalent hydraulic resistance values are based on a dynamic viscosity of 1.81 x 10^{-5} kg/m*s for air at 20 °C and atmospheric pressure (1 atm).

		Combined Air Microfluidic Chip Channel Numbers								
		1	2	3	4	5	6	7	8	9
Channel Dimensions	Channel Length (mm)	3.5	20	20	20	20	14	10	7	6
	Channel Width (μm)	1000	515	500	500	450	400	350	250	200
	Channel Cross-Sectional Area (mm^2)	1,000,000	265,225	250,000	250,000	202,500	160,000	122,500	62,500	40,000
Channel Resistance (kg/m^4s)		1.80E+6	1.46E+8	1.65E+8	1.65E+8	2.51E+8	2.81E+8	3.43E+8	9.22E+8	1.93E+9

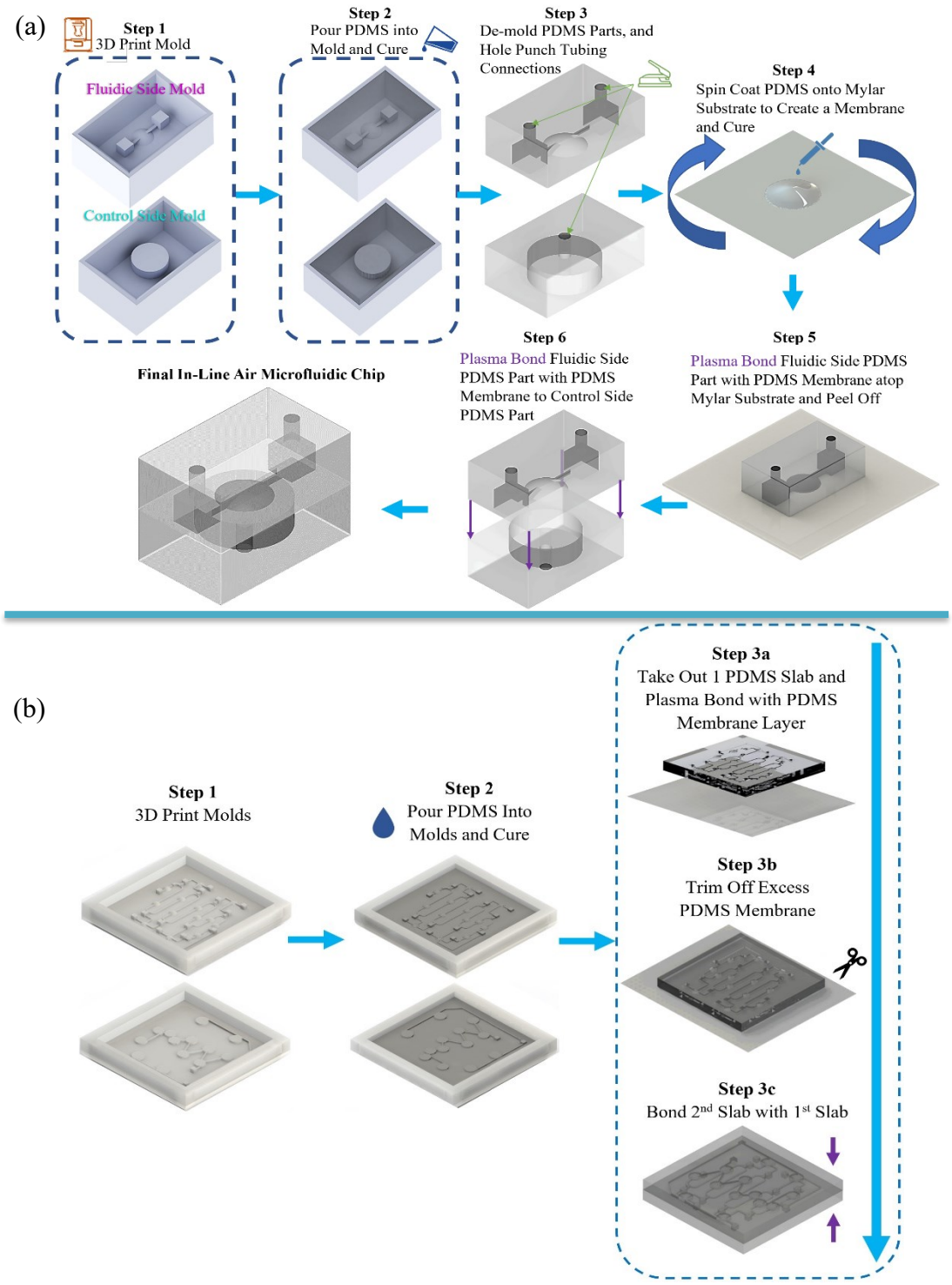


Figure 5.4: (a) Fabrication process for the In-Line Air Microfluidic Chips. Step 1: Begin with 3D printing molds using Formlabs Form 3 and Formlabs Clear Resin to shape the fluidic side and control side PDMS parts. Step 2: Pour liquid PDMS (Sylgard 184) into the 3D printed molds and allow it to cure. Step 3: De-mold the cured PDMS parts and create tubing connections by punching holes, while removing any excess PDMS to achieve the smallest microfluidic valve size possible. Step 4: Create a membrane by spin-coating liquid PDMS onto

a Mylar substrate and curing it. Step 5: Plasma bond the fluidic side PDMS part with the cured PDMS membrane. The rigid Mylar substrate ensures a flat bonding surface, preventing creases or warping of the PDMS membrane. The PDMS part, being somewhat flexible, allows it to be peeled off along with the PDMS membrane from the Mylar substrate. Step 6: Complete the final modular microfluidic valve by plasma bonding the fluidic side PDMS, now bonded with the PDMS membrane, to the control side PDMS part (b) Fabrication process for the Combined Air Microfluidic Chip, which shares the same steps as the In-Line Air Microfluidic Chips but presented a different diagrammatical presentation.

Table 5.2: In-line valve dimensions, thermal aging time, and experimentally determined $\Delta P_{(close/open)}$ for In-Line and Combined Air Microfluidic Chips. The table presents the dimensions of the valves, thermal aging time at 90°C in an oven, and the experimentally determined $\Delta P_{(close/open)}$ values for both In-Line and Combined Air Microfluidic Chips. The valve numbers/identifiers in capitalized Roman numerals correspond to **Figure 5.5c, d**.

		In-Line Air Microfluidic Chip Valve Numbers										**Combined Air Microfluidic Chip**	
		1	2	3	4	5	6	7	8	9	Exhaust (E)	Pressure Holding (PH)	Exhaust (E)
Valve Dimensions	Diameter (mm)	3.6	3.6	3.6	3.6	3.6	3.6	3.6	3.6	3.6	3.6	3.6	3.6
	Height (mm)	1.1	1.1	1.0	1.1	1.0	0.9	0.8	0.9	0.7	0.6	1.1	0.6
	Surface Area (mm^2)	13.4	13.4	13.4	13.4	12.7	12	11.4	12	10.8	10.2	13.4	10.2
	Membrane Thickness (μm)	110-120	110-120	110-120	110-120	110-120	80-90	110-120	80-90	110-120	80-90	80-90	80-90
Thermal Aging (hrs)		12	6	2	0	0	0	0	0	0	0	0	0
$\Delta P_{(close/open)}$ (mbar)		190	170	155	145	125	105	85	55	35	10	100	10
Valve Identification According to Table 5.4		VI	VI	VI	VI	V	IV	III	IV	II	I	VI	I

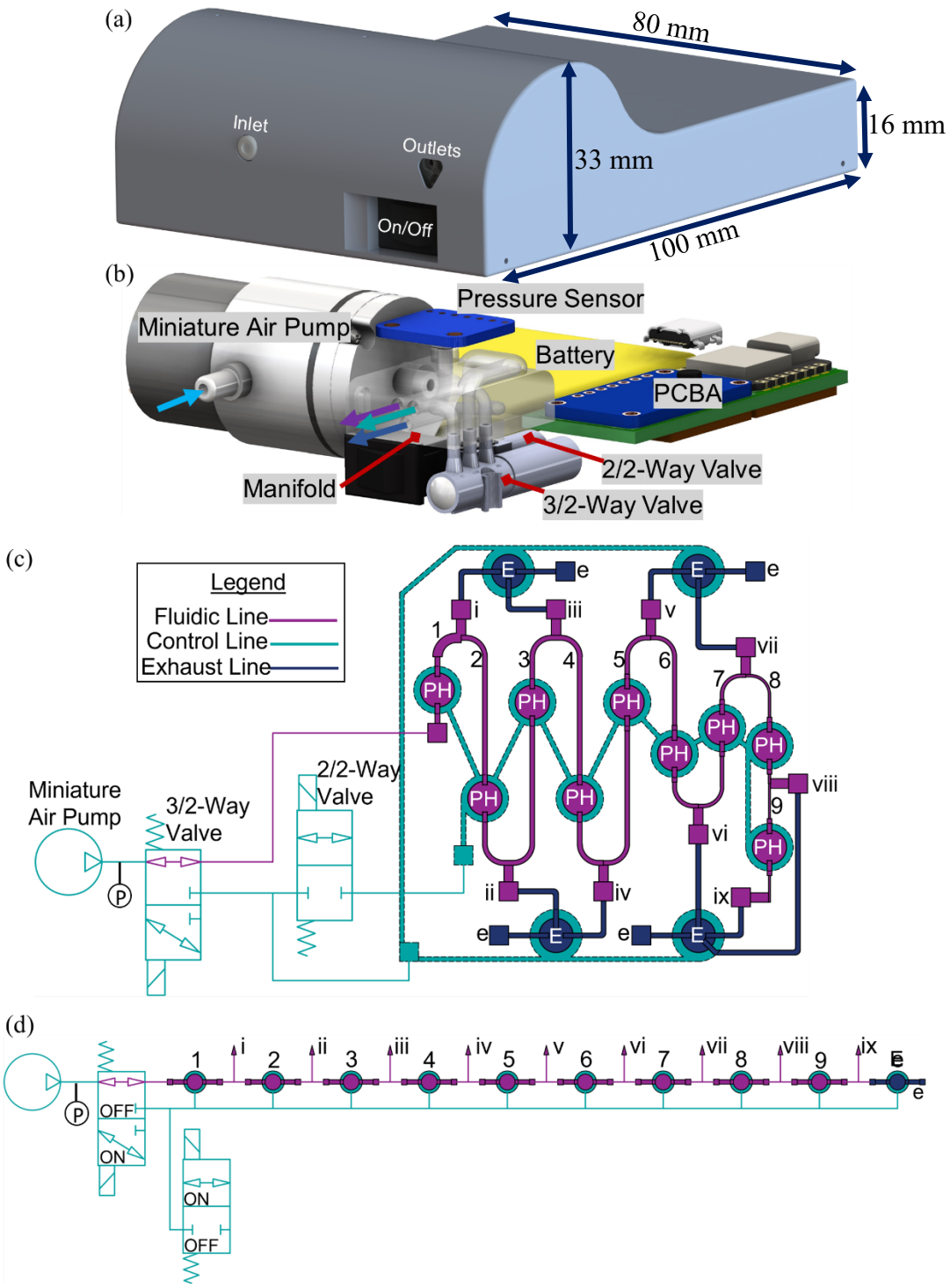


Figure 5.5: (a) Control box with approximate weight of 150 grams and dimensions as shown. (b) Internal components of the control box include a miniature air pump (1528-4700-ND, DigiKey), pressure sensor (3965, Adafruit), 3.7V, 2600mAh lithium polymer battery (B091YF4VH8, Amazon), custom printed circuit board assembly (PCBA) featuring a Seeeduino XIAO Microcontroller (Seeed Studio), two motor drivers (ROB-14451, Sparkfun), and a buck-boost power converter (2190, Adafruit). The control box also contains 2/2-way

valve (LHDB0552115H, The Lee Company), 3/2-way valve (LHDA053115H, The Lee Company), and a 3D printed pneumatic manifold. The arrows indicate the direction of air flow: blue represents air entering the miniature air pump from ambient atmosphere; purple shows air exiting the control box towards the fluid line; cyan illustrates air exiting the control box towards the control line; deep blue indicates air exiting the control box to ambient atmosphere. (c) Fluidic control diagram for Combined Air Microfluidic Chip. The Arabic numeral (1 to 9) indicates the fluidic resistance channels. (d) Fluidic control diagram for In-Line Air Microfluidic Chip. The Arabic numeral (1 to 9) indicates the opening sequence of the in-line valves. The legend is used for both (c) and (d). The lowercase Roman numeral (i to ix) represents the fluidic pathway leading to SFAs. The letter 'e' indicates the exhaust port pathways where air exits to ambient atmosphere from the air microfluidic chips. "PH" stands for pressure holding in-line valves, and "E" stands for exhaust in-line valves. Each air microfluidic chip can control 9 SFAs. The purple color represents the fluidic line, the cyan color indicates the control line, and the dark blue color indicates the exhaust line for both (c) and (d).

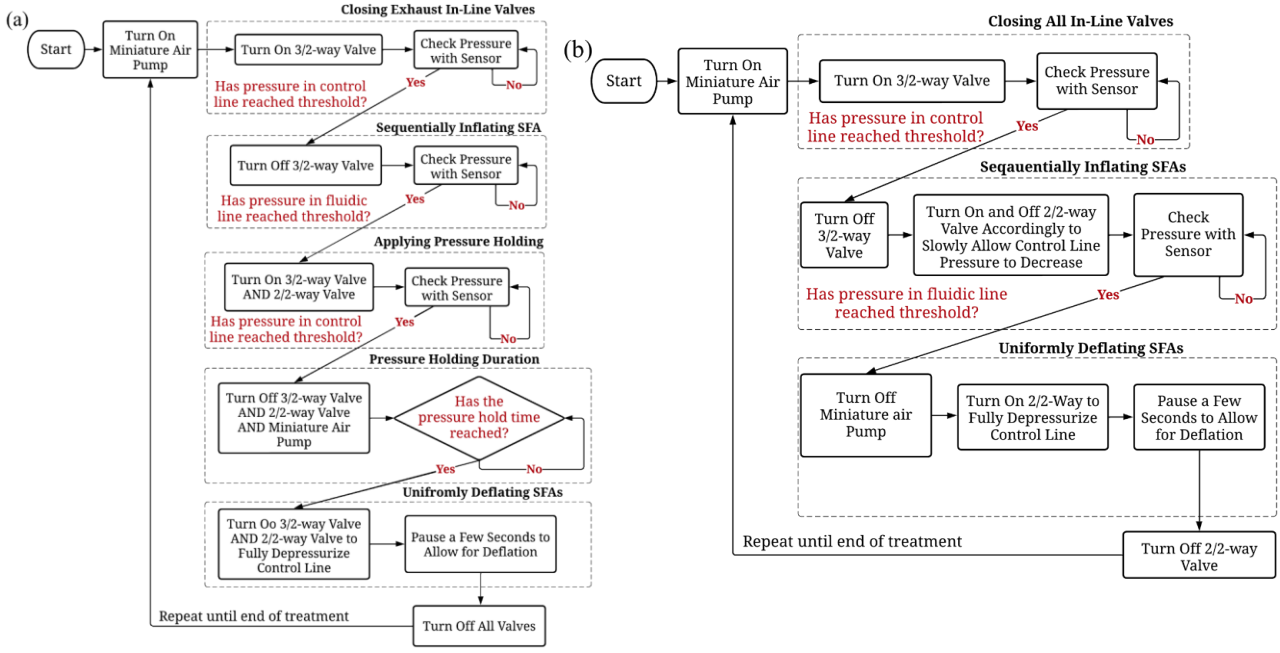


Figure 5.6: Flow chart depicting the control schemes for (a) Combined Air Microfluidic Chip and (b) In-Line Air Microfluidic Chips.

5.2.3 Overlapping Soft Fluidic Actuators and Strain-Limiting Layer

Manual lymphatic drainage (MLD) [244] is considered the gold standard for conservative treatment due to its effectiveness, but replicating the intricate motion of human hands (**Figure 5.7a**) in a robotic system is challenging. However, researchers in the field of soft robotics aim to mimic the function of MLD to achieve similar treatment outcomes [245]–[248]. For secondary lymphedema resulting from breast cancer treatment, swelling in the arm occurs due

to compromised lymph nodes responsible for draining lymphatic fluids. If not cleared promptly, the fluid thickens and becomes trapped, reducing the efficacy of any compression system. The main obstacle in replicating human motion using robotics is the presence of gaps between air bladders, leading to uneven compression and fluid trapping (**Figure 5.7c**). To address this, we explore overlapping soft fluidic actuators, similar to bandaging principles [249], to eliminate gaps and achieve smooth gradient compression. However, merely overlapping actuators is not enough, as the strain limiting layer (**Figure 5.9a**) is essential to evenly distribute forces and reduce bulk, ensuring better patient outcomes and compliance. Commercial active compression sleeves with overlapping actuators are scarce, and while some have 30% overlap (**Figure 5.7b**) [250], independent floating chambers may shift and still cause uneven compression [251]. Despite the importance of overlapping, no studies have validated its efficacy in reducing gapping issues in active compression sleeves or determined the optimal overlapping percentage for smooth compression. Therefore, our study not only addresses potential shifting but systematically tests overlapping percentages for optimized performance.

Various fabrication techniques are available for soft fluidic actuators (SFAs), including replica molding, 3D printing, and thermal lamination. While these methods are feasible, replica molding and 3D printing tend to produce SFAs with relatively thick walls. In this study, we introduce a novel approach to fabricate a monolithic single sheet of overlapping SFAs and its outer strain-limiting layer, as depicted in **Figure 5.8**. This innovative method is presented in detail, offering a more streamlined and efficient process for creating SFAs with reduced wall thickness.

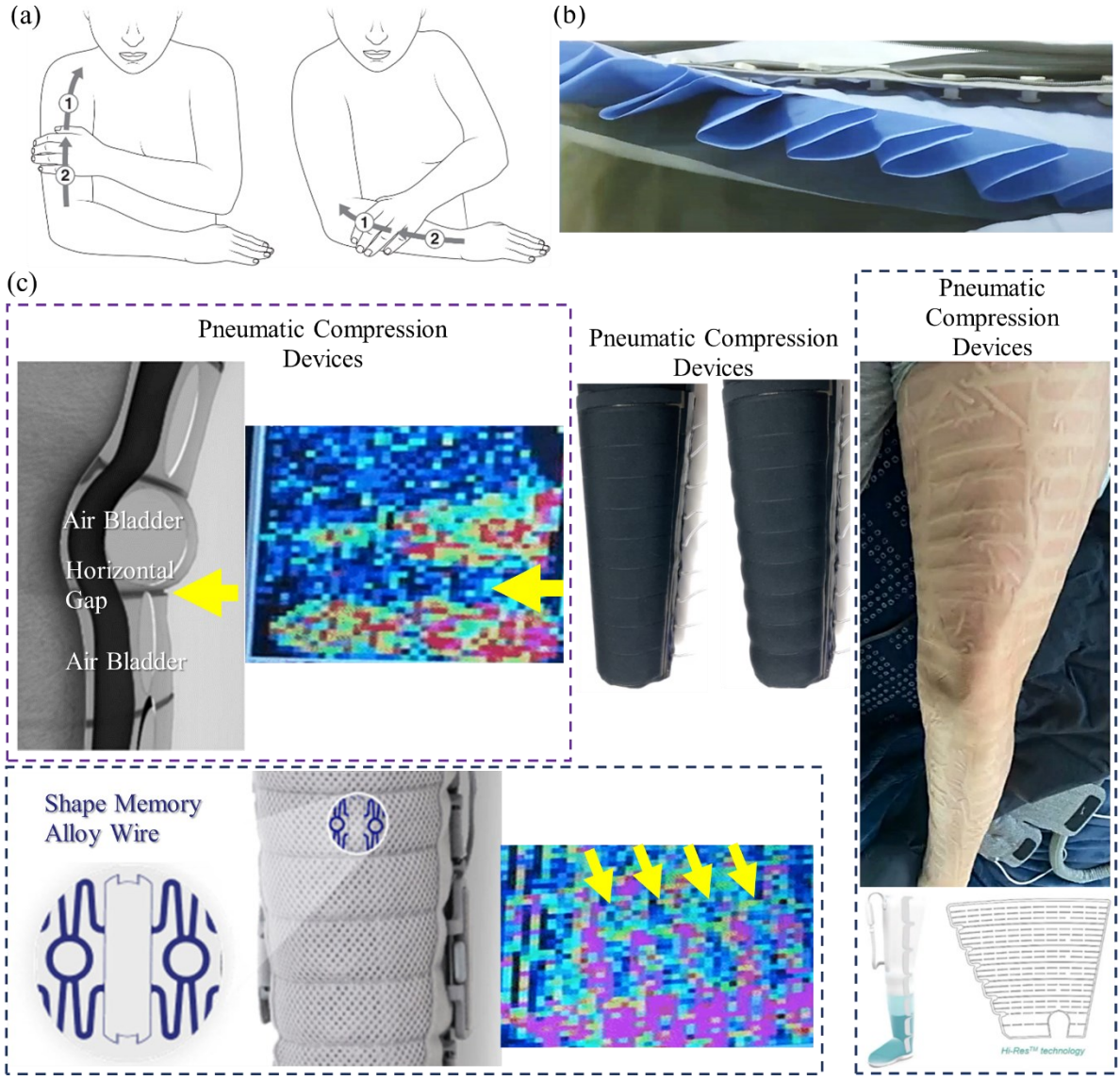


Figure 5.7: (a) Self-treatment of arm swelling due to lymphedema [252]. (b) Free-floating overlapping pneumatic chambers in the Lympha Press compression device [251]. (c) Numerous commercially available active compression devices exhibit gaps between pneumatic bladder/compression actuators. Top left image shows a cross-sectional view of a commercial pneumatic compression device (Flexitouch, Tactile Medical) with pressure mapping data illustrating the gaps between air bladders [227]. Top middle image displays a pneumatic active compression device when deflated and inflated, clearly demonstrating the gaps between each air bladder [147]. Bottom left image shows a non-pneumatic compression device using shape memory alloy actuators (Dayspring, Koya Medical), also exhibiting some gaps between actuators as measured by pressure mapping sensor [227]. The right image presents yet another pneumatic compression device, showing the skin immediately following compression therapy, with uneven therapy resulting in bumps and divots (small depressions) on the skin where lymphatic fluid is trapped inside locations with no compression applied (i.e., the bumps) (Aria Free, Aria Health) [228].

Although the outer strain-limiting layer may be fully integrated with the overlapping soft fluidic actuators, they were kept separate from the overlapping soft fluidic actuators for easier parametric testing. The outer strain-limiting layer was securely fastened onto a cone-shaped structure representing the forearm of a lymphedema patient using a Velcro cinch strap, a gold standard for active compression garments, which remained unchanged throughout the testing (**Figure 5.9a**). Monolithic sheets of overlapping soft fluidic actuators with 0% overlap, approximately 10% overlap, approximately 20% overlap, and approximately 40% overlap were tested (**Figure 5.9b**). The overlapping percentage was determined based on the equation relating overlapping distance to the soft fluidic actuator width, as depicted in **Figure 5.9c, d** and calculated simply with Equation (5.2).

$$\boldsymbol{Overlap}\ \% = \frac{\boldsymbol{Overlapping\ Distance}}{\boldsymbol{Soft\ Fluidic\ Actuator\ Width}} \tag{5.2}$$

Please note that any overlap exceeding 50% would cause the highest point of one soft fluidic actuator to overlap with the neighboring actuator, which would be inefficient and lead to a larger strain-limited height, adding bulk to the active compression sleeve. The strain-limited height is crucial because if it is too high (**Figure 5.9c**), the outer strain-limiting fabric may not provide enough strain-limiting force to keep the overlapping SFAs' pressure chambers in contact with the inner skin contact fabric, resulting in gaps between each neighboring SFA. However, when the strain-limited height is low (**Figure 5.9d**), the gaps between neighboring SFAs are minimized. Therefore, achieving smooth sequential gradient compression is a function of both the SFA overlap percentage and the strain-limited height. That being said, the strain-limited height issue can be easily resolved by incorporating a formfitting outer strain-limiting layer that hugs the skin, which is why Velcro is used, allowing the user to adjust the initial tightness for a personalized fit. **Table 5.3** below presents the volume and dimensions of the soft fluidic actuators used in this study. The individual shapes of each SFA are shown in **Figure A.3** in **Appendix A**.

Table 5.3: Volume and dimensions of soft fluidic actuators. The cross sections were approximated as rectangular due to the compression of the outer strain-limiting layer. The fully pressurized volume was calculated based on a low-profile fit, with no gap between the monolithic sheet of overlapping SFAs and the outer strain-limiting layer, and an average strain-limited inflation height of 0.5 cm as visually inspected. The soft fluidic actuator (SFA) numbered 1 is located at the wrist, and SFA numbered 9 is located at the elbow, with the rest positioned sequentially in between according to their respective numbers.

	Soft Fluidic Actuator Numbers								
	1	2	3	4	5	6	7	8	9
Fully Pressurized Volume (ml)	39.9	42.4	45.0	47.6	50.1	52.7	55.2	57.8	60.3
Surface Area when flat (cm^2)	79.8	84.9	90.0	95.1	100.2	105.3	110.5	115.6	120.7
Length (cm)	19.9	21.2	22.5	23.8	25.1	26.3	27.6	28.9	30.2
Width (cm)	4	4	4	4	4	4	4	4	4
Height (cm)	0.5	0.5	0.5	0.5	0.5	0.5	0.5	0.5	0.5

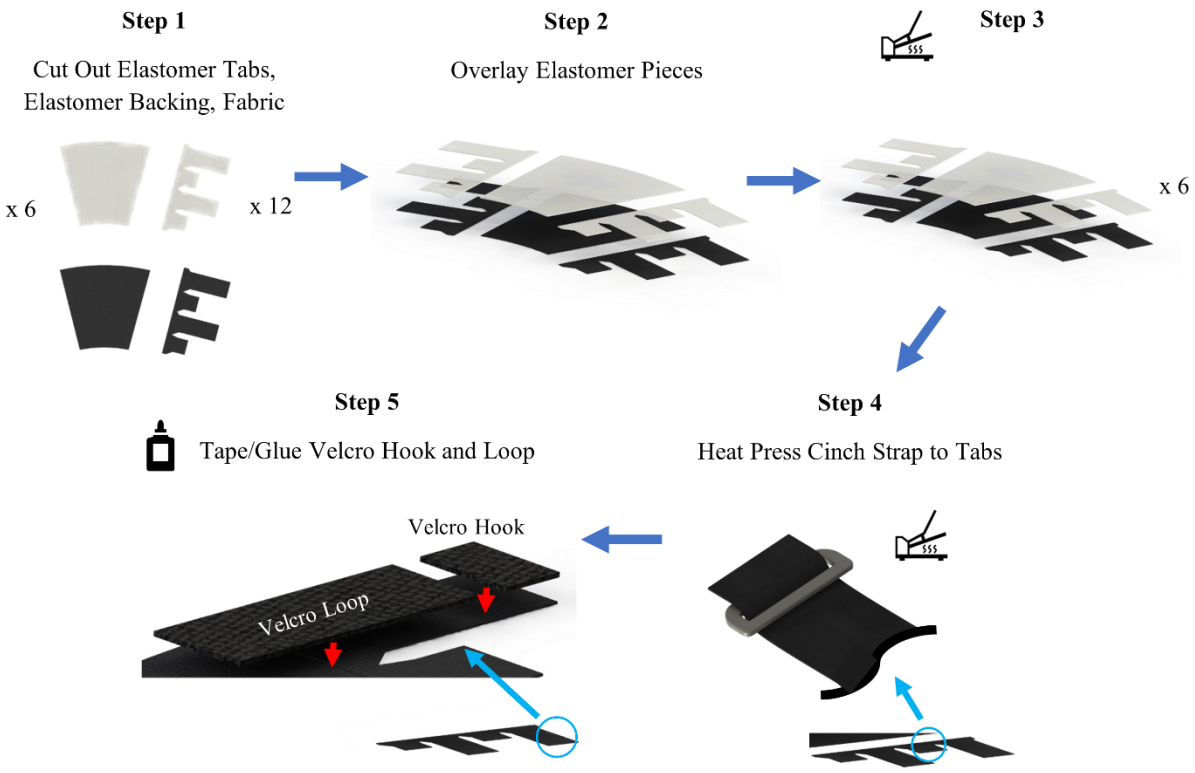


Figure 5.8: Fabrication steps for strain-limiting layer.

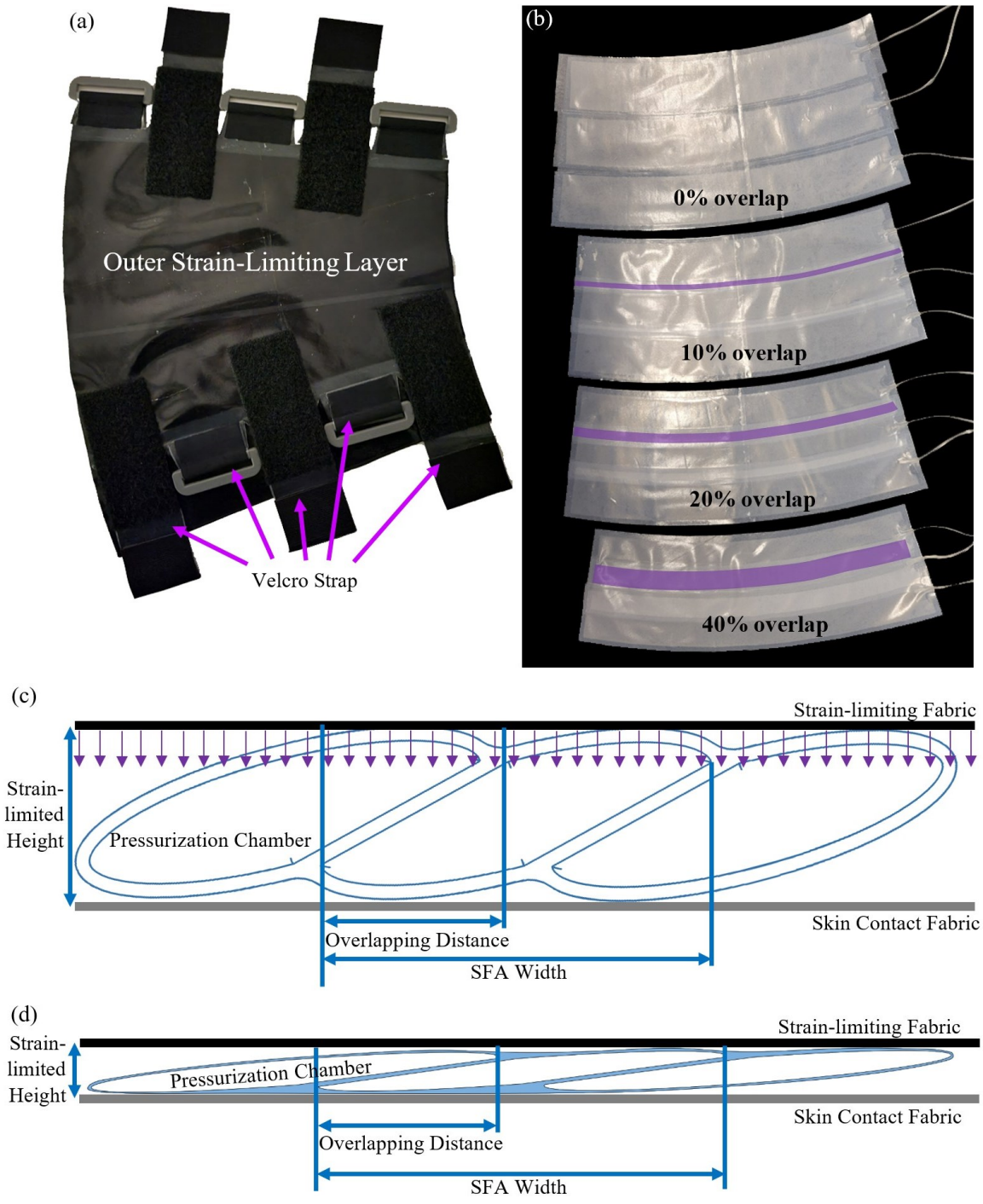


Figure 5.9: (a) Image of the outer strain-limiting layer with clearly visible Velcro straps securing the garment in place for active compression. (b) Image showcasing four monolithic sheets, each consisting of three overlapping SFAs with different overlap percentages: 0%, 10%, 20%, and 40%. (c) Cross-sectional schematic illustrating a monolithic sheet of overlapping SFA with a relatively high strain-limited height. The purple-colored arrows indicate the direction of the force applied by the strain-limiting fabric. (d) Cross-sectional schematic depicting a monolithic sheet of overlapping SFA with a relatively low strain-limited height, reducing the gaps between neighboring SFAs.

5.2.4 Testing Setup

All tests were conducted using the setup depicted in **Figure 5.10**, with slight variations made for different experiments. Each test was repeated a minimum of 3 times to ensure reliability and accuracy of the results.

The first series of tests aimed to determine the optimal percentage of overlapping for the soft fluidic actuators at various pressure points. A monolithic sheet containing three soft fluidic actuators was pressurized to three different levels of pressure gradient, covering the entire range of compression treatment pressures used for reducing lymphedema swelling. Each test was recorded in three formats: visually inspecting the overlapping soft fluidic actuators under pressure, using a Tekscan pressure mapping system, and plotting the average pressure in the horizontal direction based on the Tekscan sensor data. It is important to note that the Tekscan sensor, being a flat sheet with an array of independent force-sensitive resistors, may introduce inconsistencies and errors, especially when placed over contoured surfaces. Additionally, for the pressurization of overlapping SFAs, a customized desktop pneumatic control unit [134] was used instead of the wearable control box shown in **Figure 5.10**.

The second set of tests focused on systematically examining factors affecting the ΔPclose/open of in-line valves, which serve as the central control units of the active air microfluidic chips. The testing involved varying single valve feature parameters at a time, while keeping the PDMS (Sylgard 184, Dow Chemical Company) mixing ratio (10 parts A to 1 part B) and the temperature and length of curing time constant (90 ^{o}C for 4 hours). The dimensions of the valves are listed in **Table 5.4**. Two different membrane thicknesses (110-120 μm from 750 RPM spin coating speed and 80-90 μm from 1000 RPM spin coating speed) were evaluated for each valve size. Additionally, valve VI underwent thermal aging from 0 to 48 hours.

To measure the ΔP_{open} of the in-line valves, a pressure sensor (3965, Adafruit) was connected to the control channel, and another one was connected to the fluidic channel of the valve. The fluidic channel pressure was held constant at 100 mbar, while the control channel was set to a higher pressure. The control channel pressure was slowly decreased until it reached the fluidic channel pressure, facilitating the opening of the valve. Due to imperfections in the membrane and the valve's internal surfaces, air leakage was sometimes observed on the fluidic

side by the pressure sensor. Therefore, two pressure measurements were recorded to assess how well the valve opens. The initial opening pressure measurement was recorded when the fluidic channel read 10 mbar, and the fully open control channel pressure was recorded when the pressure sensor read 100 mbar in the fluidic channel, indicating that the valve was fully open. Larger differences between the initial opening pressure and fully open pressure indicated more significant air leakage in the in-line valve, meaning the valve's seal was weaker when the two pressures differed and stronger when they were identical (**Figure A.1** in **Appendix A**).

The third set of tests involved evaluating the effectiveness of using in-line valves for sequential and gradient inflation of SFAs in an active compression sleeve designed to manage lymphedema and other conditions requiring sequential gradient compression. Based on specific criteria, the valves that best suited the requirements of the In-Line and Combined Air Microfluidic Chips were selected to proceed with the subsequent testing, which included analog sequential gradient compression and smooth sequential gradient compression with pressure holding, both followed by fast passive uniform deflation. The established criteria for the active air microfluidic chips and its system were as follows: (1) The ability to sequentially inflate a series of 9 overlapping SFAs within 60 seconds using a wearable control box, (2) capability of pressure holding without any leakage for at least 10 seconds, and (3) uniform deflation within 10 seconds. Additionally, it was essential to achieve gradient compression without any gaps between the SFAs to ensure optimal performance.

Table 5.4: Tested in-line valve dimensions.

		Tested In-Line Valve Numbers					
		I	II	III	IV	V	VI
Valve Dimensions	Diameter (mm)	3.60	3.60	3.60	3.60	3.60	3.60
	Height (mm)	0.60	0.70	0.80	0.90	1.00	1.10
	Surface Area (mm2)	10.15	10.78	11.38	12.00	12.65	13.36

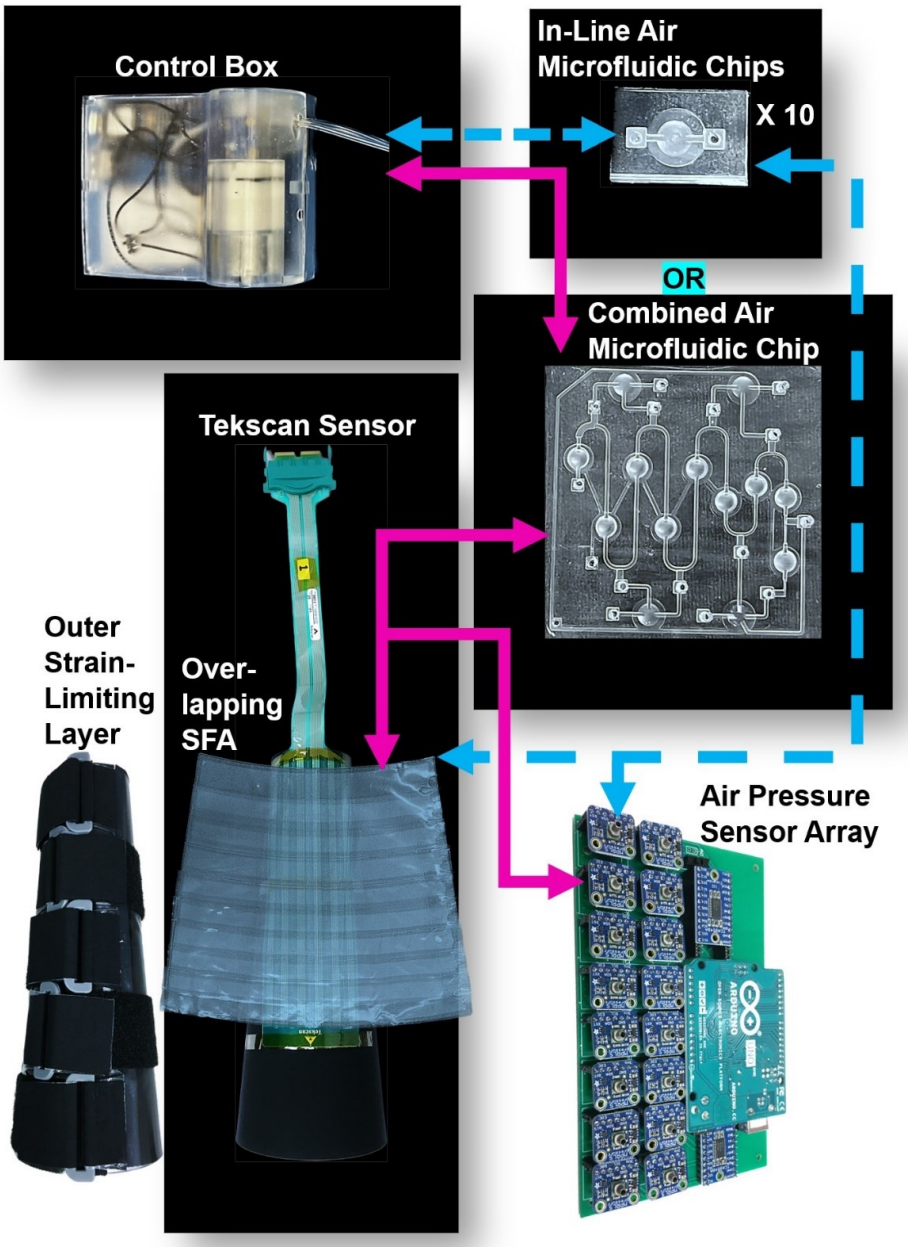


Figure 5.10: Testing setup included a pneumatic control box that communicated fluidly with either the In-Line Air Microfluidic Chips or the Combined Air Microfluidic Chip, allowing for sequential and gradient pressurization of the monolithic sheet of overlapping SFAs. A printed circuit board assembly (PCBA) equipped with an array of air pressure sensors (3965, Adafruit) measured and recorded the air pressure within each SFA. Additionally, a Tekscan Pressure Mapping Sensor (9811E, Tekscan) was positioned between the 3D printed forearm model and the overlapping SFA to accurately measure the applied pressure exerted by the overlapping SFA onto the forearm model. To direct forces toward the forearm model, an outer strain-limiting layer covered the overlapping SFA. The solid pink arrows in the figure represent the fluid pathways during experimentation with the Combined Air Microfluidic Chip, while the dashed blue arrows represent the fluid pathways during experimentation with the In-Line Air Microfluidic Chips.

5.3 Results

5.3.1 Performance of Monolithic Sheet of Overlapping Soft Fluidic Actuators

At low-pressure gradients (**Figure 5.11b**), SFAs with 0% overlap exhibited three local contact pressure peaks and two local contact pressure valleys in between the peaks. The average gap contact pressure difference between the local peaks and valleys was 21% relative to the maximum contact pressure (ΔP_{Gap}), calculated using Equation (5.3), where Pp is the local peak pressure, Pv is the local valley pressure, n is the number of local valleys. This gap contact pressure difference quantifies the variations in pressure distribution. In contrast, SFAs with 10% to 40% overlap showed no local peaks or valleys at low-pressure gradients, resulting in a 0% gap contact pressure difference. The number of local peaks and valleys, along with the gap contact pressure difference, can be used to justify the optimal percentage of overlap for each contact pressure gradient setting (**Table 5.5**).

As the contact pressure gradient increased, more overlap was necessary for the SFAs to minimize the number of local contact pressure peaks and valleys and reduce the gap contact pressure difference. For instance, at 20% overlap, no local pressure peaks or valleys were observed at low and medium contact pressure gradient settings. At 40% overlap, no local pressure peaks or valleys were observed at any contact pressure gradient setting, resulting in a 0% gap contact pressure difference across all contact pressure gradients (**Figure 5.12a**). These results demonstrate that increased overlapping of SFAs led to more uniform pressure distribution and improved compression performance at higher contact pressure gradients.

$$\boldsymbol{\Delta P_{Gap}}\ (\%) = \frac{\sum_{i=1}^{n} \boldsymbol{Pp_i - Pv_i}}{\boldsymbol{n * Pp_1}} \tag{5.3}$$

Figure 5.11 illustrates the increase in bulkiness of the active compression sleeve as the contact pressure gradient setting increases. To address this issue and reduce the sleeve's bulkiness, another set of tests was conducted to investigate the effect of using a thicker and more rigid thermoplastic polyurethane (TPU) layer in the outer strain-limiting fabric. The results of this test are presented in **Figure 5.12b**. By visually inspecting the corner where the edge of the soft fluidic actuators resides, it was evident that the outer strain-limiting layer with 6 layers of TPU sheets (900 µm thick, Bemis 3916) exhibited the least sleeve bulging compared to those with 2 layers (300 µm thick) or 4 layers (600 µm thick) of TPU. This finding suggested

that using a thicker and more rigid TPU layer can effectively reduce the overall bulkiness of the active compression sleeve.

As can be seen in **Figure 5.11**. As the contact pressure gradient setting increased, the bulkiness of the active compression sleeve increased as well when inspected visually. Another set of tests were done to determine the effect of having a thicker and thus more rigid TPU layer on the outer strain-limiting fabric with the aim of reducing bulkiness of the sleeve, and the results are shown in **Figure 5.12b**. It can be visually seen by inspecting the corner of the where the edge of the SFA reside that the outer strain-limiting layer with 6 layers of TPU sheets or 900 μm thick (Bemis 3916) had the least sleeve bulging compared to 2 layers (300 μm thick) or 4 layers (600 μm thick) of TPU.

It is essential to consider that the inelasticity of the Tekscan sensor and its application onto a rigid tapered cylinder may not uniformly capture circumferential compression. As each soft fluidic actuator under internal pressure attempted to straighten, minor pinch points of lower pressure can occur at certain locations, resulting in slight dips in pressure circumferentially. These factors should be considered when interpreting the pressure data obtained from the Tekscan sensor.

Table 5.5: Tabulated results showing the number of pressure peaks and valleys and the gap pressure difference ($\boldsymbol{\Delta P_{Gap}}$) for all the tested conditions. The Gap Contact Pressure Difference shows the mean as well as the ranges based on 3 data points per tested condition.

Pressure Gradient	Percentage Overlap (%)	# of Local Pressure Peak	# of Local Pressure Valley	Gap Contact Pressure Difference (%)
Low	0	3	2	21 ± 2
	10	0	0	-
	20	0	0	-
	40	0	0	-
Medium	0	3	2	46 ± 4
	10	3	2	21 ± 3
	20	0	0	-
	40	0	0	-
High	0	3	2	55 ± 5
	10	3	2	40 ± 3
	20	2	1	14 ± 3
	40	0	0	-

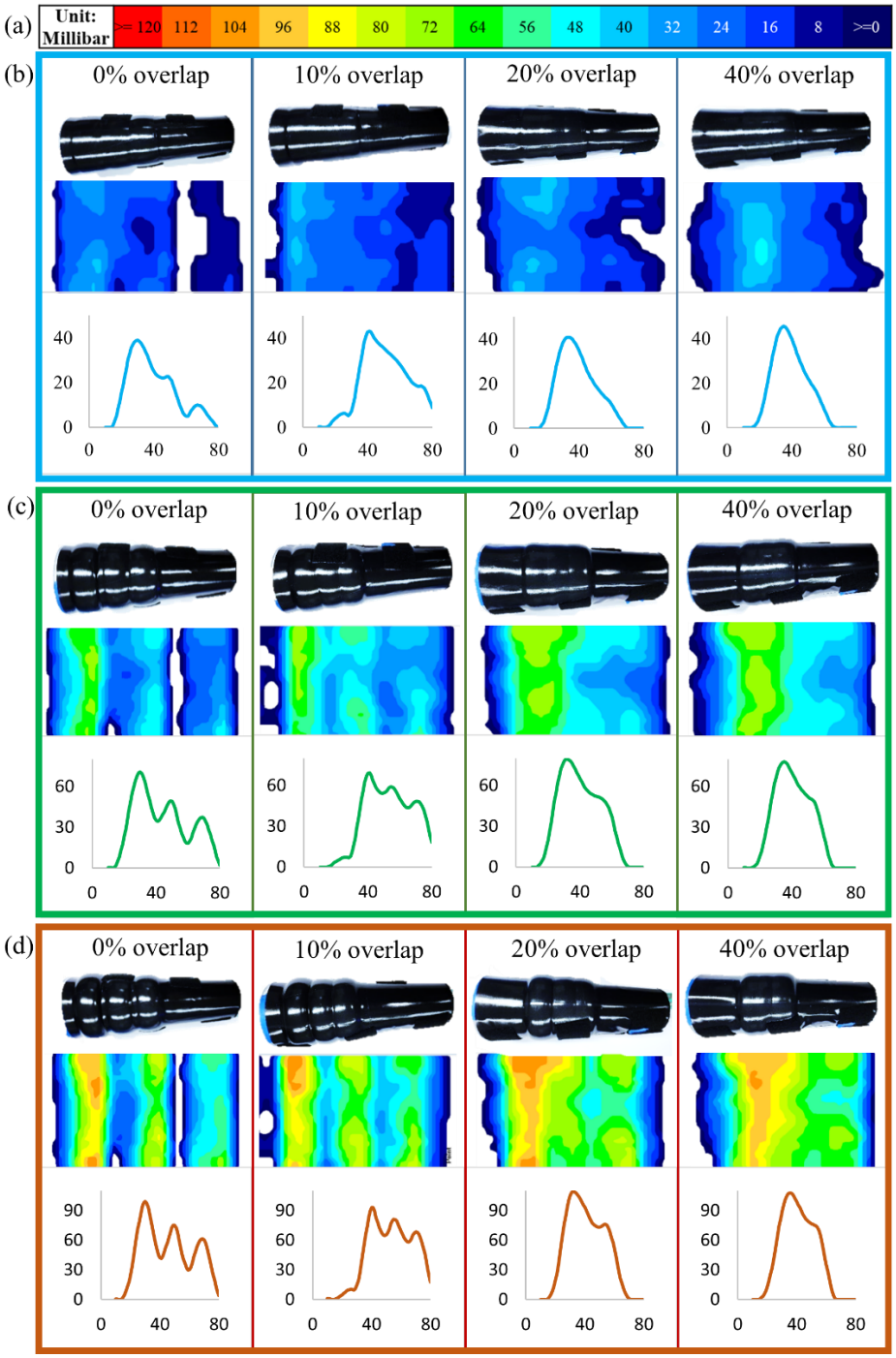


Figure 5.11: Overlapping SFA results measured using three different methods: visual inspection, contact pressure mapping, and average pressure (y-axis, in millibar) vs. length (# of sensels, a measurement of individual pressure sensing points on a pressure map) plot for varying overlapping percentages (0%, 10%, 20%, and 40%). (a) Legend showing applied contact pressure corresponding to color-coded regions as recorded by the Tekscan pressure mapping sensor (9811E, Tekscan) in millibar. (b) Results for low-pressure gradient overlapping SFAs. (c) Results for medium-pressure gradient overlapping SFAs. (d) Results for high-pressure gradient overlapping SFAs.

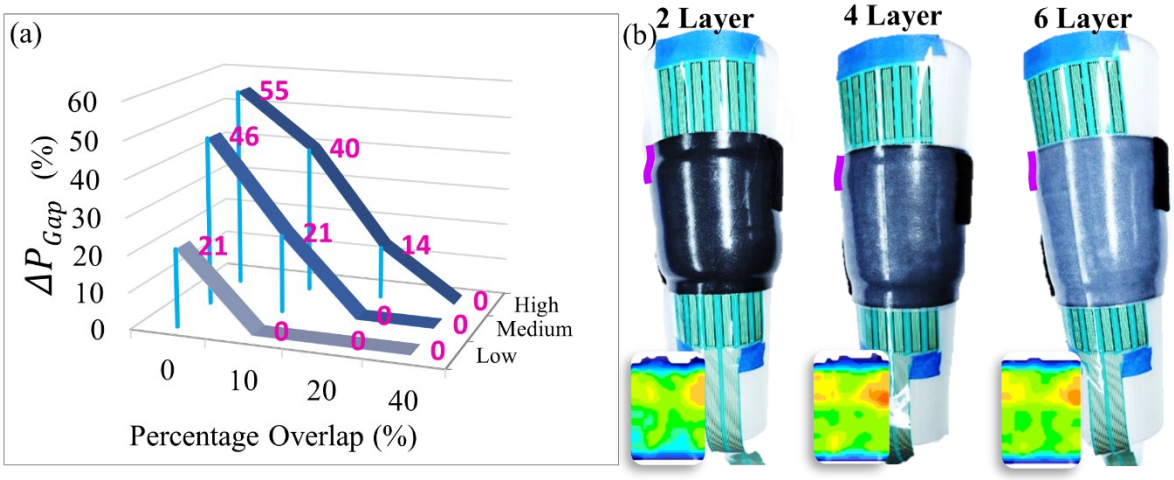


Figure 5.12: (a) 3D line chart showing the Gap Contact Pressure Difference ($\boldsymbol{\Delta P_{Gap}}$) for all tested overlapping SFA conditions. The high, medium, and low (z-axis) represent the pressure gradient settings. (b) Images showing the effect of the thickness of the outer strain-limiting layer on the bulkiness of the sleeve. The tested conditions include 2 layers of TPU (Bemis 3913) at 300 µm thick, 4 layers of TPU at 600 µm thick, and 6 layers of TPU at 900 µm thick, all with 40% overlapping SFAs. A Tekscan pressure map at the bottom left corner of each tested condition shows that the contact pressure was similar for all tested conditions. The purple-colored line shows the bump created by the inflated SFA, and the straighter the line, the less bulky and noticeable the sleeve when viewed visually.

5.3.2 Performance of In-Line Air Microfluidic Chips

Figure 5.13 presents the testing results of the in-line valves. In **Figure 5.13a**, the effects of varying the size and membrane thickness of the in-line valves are shown. The box-and-whisker plot version of **Figure 5.13a** can be found in **Figure A.4** in **Appendix A**. The valve sizes are detailed in **Table 5.4**. It can be observed that with increasing valve size, the $\Delta P_{(open)}$ (pressure difference when the valve opens) also increased. For sizes I and II, the two different membrane thicknesses did not display significant differences. However, from sizes III to VI, the thicker membrane (110 – 120 µm) resulted in a notably larger $\Delta P_{(open)}$. The range bars in the chart illustrate that $\Delta P_{(open)}$ can exhibit substantial variation for each tested condition, represented by the wide range of values (not to be confused with error bars or standard deviation bars).

Similarly, as depicted in **Figure 5.13b**, the $\Delta P_{(open)}$ increased with increasing thermal aging time for the tested valve size VI. Partial thermal aging test results for valve size II, III, and V can be found in **Figure A.5** in **Appendix A**. The spread of $\Delta P_{(open)}$ was considerable for each tested condition, often overlapping with other thermal aging times. Specifically, $\Delta P_{(open)}$ values were captured at every hour from 0 to 12 hours of aging, every 4 hours from 12 to 24

hours, and a single measurement was taken at the 48-hour mark. Thermal aging data for each of the tested samples of valve VI is presented in **Figure A.6** in **Appendix A**.

After selecting suitable in-line valves for conducting analog sequential control of SFAs, we transformed each in-line valve into an In-Line Air Microfluidic Chips which was an action of fluidly interconnecting their fluidic lines and control lines as illustrated in **Figure 5.2**. The characteristics of these valves are listed in **Table 5.2**. To evaluate the suitability of the valves for analog sequential control of SFAs, we assessed their sequential opening behavior by continuously decreasing the pressure in their fluidly interconnected control lines (hence the term "analog sequential control") at a rate of 2.6 mbar per second, while maintaining a constant 100 mbar fluidic line pressure. Ideally, the time intervals between the opening of consecutive valves should be equal, and the differences between the initial opening pressure and fully open pressure of the valves should be minimal. This ideal behavior is graphically represented in **Figure 5.14a**, where each valve's response is shown as a vertical or near-vertical line. However, it was observed that not all time intervals between the opening of consecutive valves were equal, and all the valves exhibited some difference between their initial opening and fully open pressure.

Figure 5.14b and **Figure 5.14c** demonstrate the versatility of the same set of In-Line Air Microfluidic Chips, effectively functioning for both low-pressure and high-pressure analog sequential inflation, as well as for uniform fast passive deflation. The total time required for sequential inflation was approximately 35 seconds and 40 seconds for low- and high-pressure settings, respectively. For passive uniform deflation, all nine SFAs deflated to less than 10 millibar internal air pressure within approximately 10 seconds, irrespective of the pressure setting (high or low). In **Figure 5.14d**, it is evident that when the exhaust in-line valve did not open during deflation, the pressure eventually equalized due to the fluidic line interconnection among all the In-Line Air Microfluidic Chips and their connected SFAs.

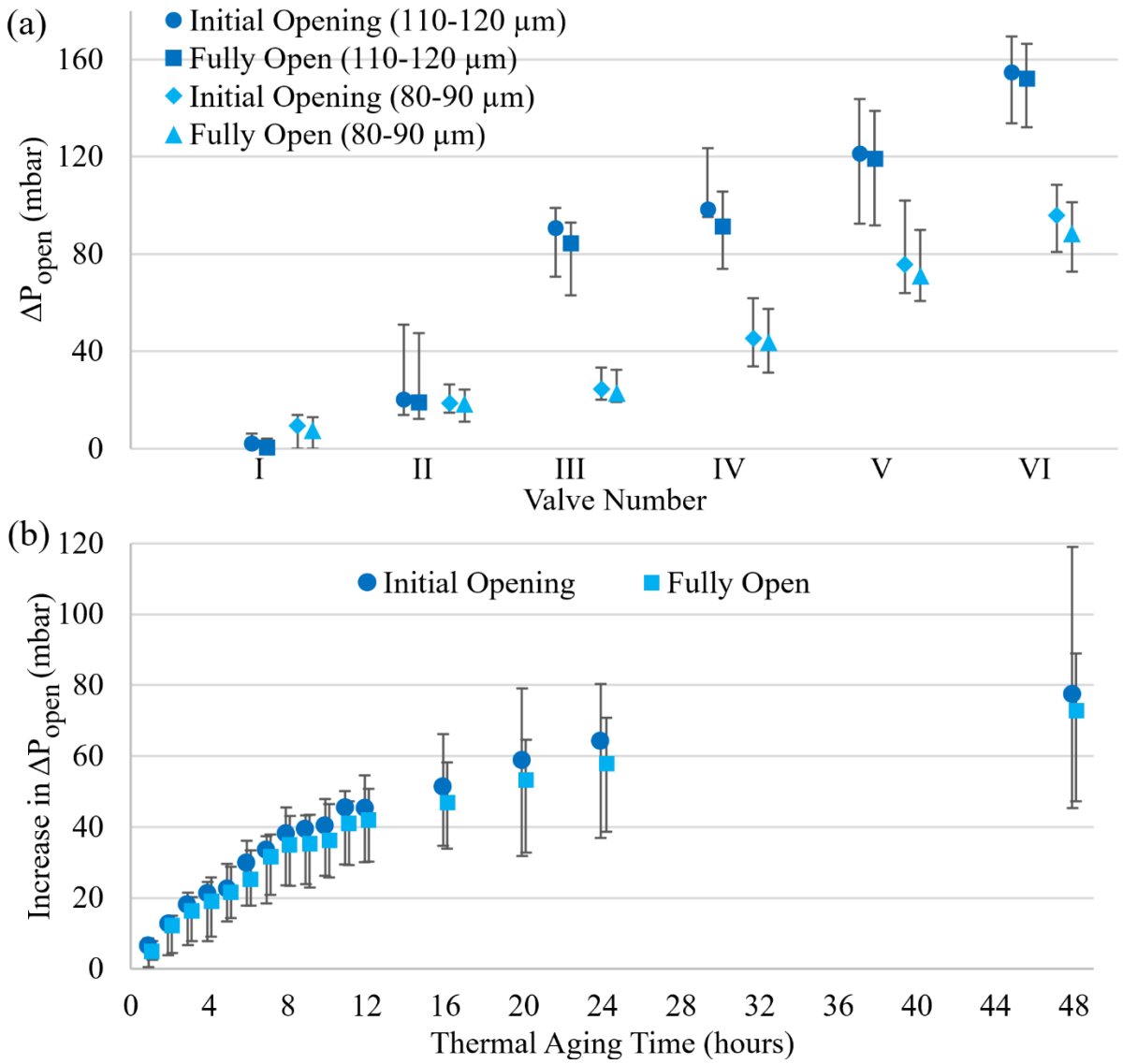


Figure 5.13: Results of systematic testing for in-line valves, including initial opening and fully open pressures. (a) Plot displaying the $\Delta P_{(open)}$ for each valve, as detailed in **Table 5.4**, with varying membrane thicknesses. Five tests were conducted per data point. (b) Plot illustrating the average increase in $\Delta P_{(open)}$ for valve VI with a 110-120 µm membrane due to thermal aging. Five tests were conducted per data point, using different in-line valves. The spread is represented by the range bars, and the median is plotted.

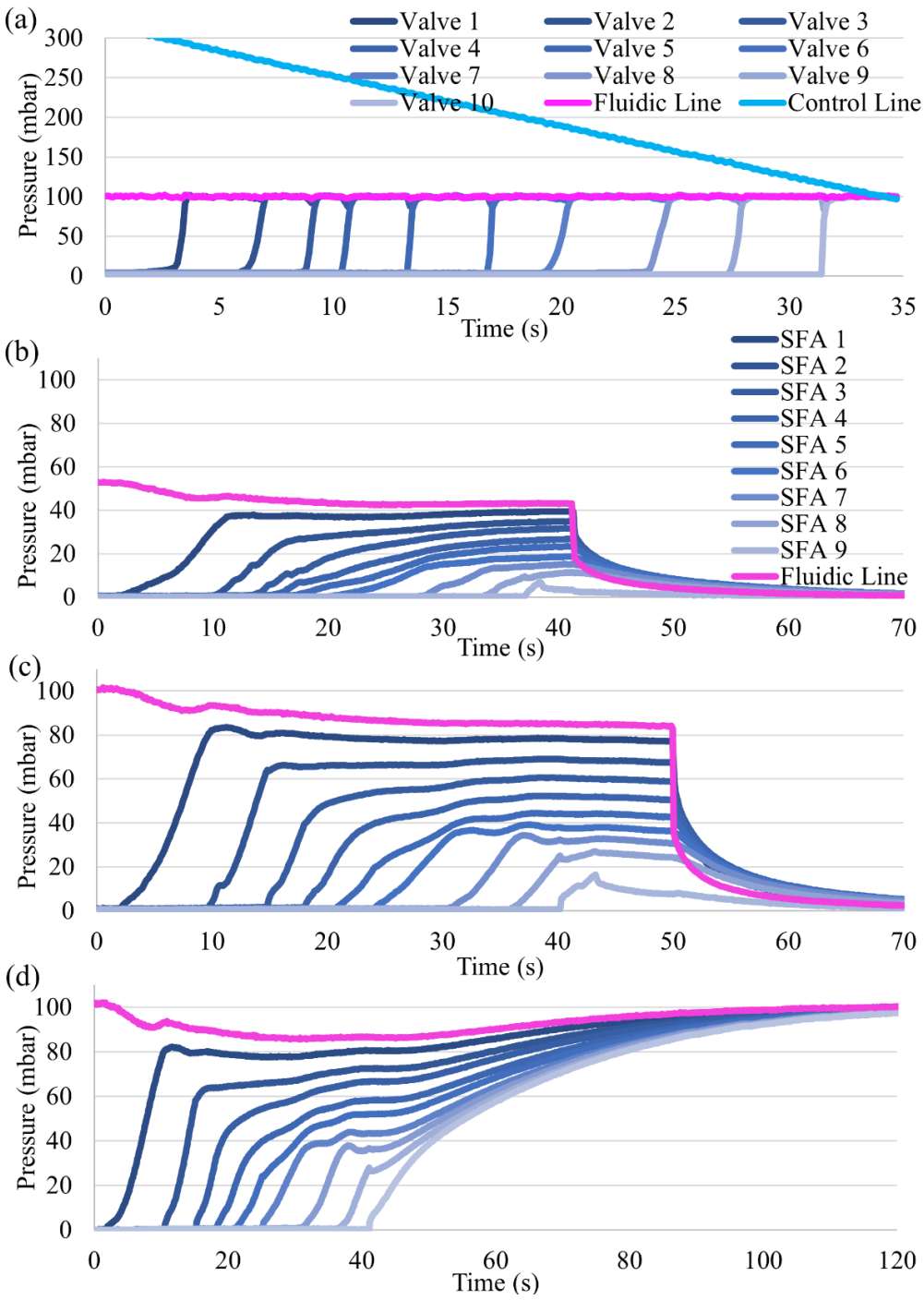


Figure 5.14: Results for analog sequential gradient inflation with uniform fast passive deflation of SFAs using In-Line Air Microfluidic Chips. (a) Plot illustrating the analog sequential inflation sequence of the chosen valves 1 to 10 for In-Line Air Microfluidic Chips. (b) Low-pressure analog sequential inflation sequence with uniform passive deflation for SFAs 1 to 9. The same legend is used for (c) and (d). (c) High-pressure analog sequential inflation sequence with uniform passive deflation for SFAs 1 to 9. (d) High-pressure analog sequential inflation sequence where the pressure source continued pressurizing the SFAs without deflation, eventually reaching uniform pressure for SFAs 1 to 9.

5.3.3 Performance of Combined Air Microfluidic Chips

Figure 5.15a, **Figure 5.15b**, and **Figure 5.15c** demonstrate the sequential inflation of 9 SFAs using the Combined Air Microfluidic Chip under high pressure, medium pressure, and low pressure settings, respectively. This confirms that the Combined Air Microfluidic Chip is capable of maintaining sequential inflation at different pressure levels. It is worth noting that, unlike the In-Line Air Microfluidic Chips, which allow SFAs to begin inflation one at a time (**Figure 5.14**) due to the use of in-line valves, the Combined Air Microfluidic Chip starts the inflation of all 9 SFAs simultaneously. However, the SFAs experience drastically different inflation rates due to the presence of microfluidic resistance channels.

In **Figure 5.15d**, the sequential inflation of SFAs occurred from 0 to 10 seconds, followed by uniform fast deflation from 14 to 20 seconds. Between 10 and 14 seconds, the pressures within the fluidly interconnected SFAs started to equalize, and given enough time, they would eventually become equal. **Figure 5.15e** illustrates the sequential gradient inflation from 0 to 10 seconds, followed by pressure holding from 10 to 32 seconds, and finally, uniform passive deflation from 32 to 35 seconds. To enable sequential gradient inflation, the exhaust valves must first be closed, which was activated at pressures above 150 mbar (ΔP_{close}). Meanwhile, the control lines of the pressure holding valves were kept below their ΔP_{close} threshold, keeping them open during the sequential gradient inflation phase. Once the sequential gradient inflation sequence was completed, the pressure holding valves closed by increasing their control line pressure above their ΔP_{close}. The control line pressure of the exhaust valves was also increased to the same pressure as the control lines of the pressure holding valves to ensure no air leaks out, although this step may not have been necessary. After the pressure holding phase ended, the exhaust valves opened to allow the SFAs to uniformly deflate while keeping the pressure holding valves closed to prevent any potential backflow. Once all the pressures within the SFAs reached a minimum pressure, the pressure holding valves opened, and the cycle can be repeated.

Integration of the Combined Air Microfluidic Chip with the monolithic sheet of 9 overlapping SFAs (40% overlap) resulted in the creation of smooth sequential gradient compression, as depicted in **Figure 5.17a**. Part of the monolithic sheet can also be used for

smooth uniform compression if necessary, as shown in **Figure 1.17b**. The effectiveness of the smooth sequential gradient compression was demonstrated on a real human forearm.

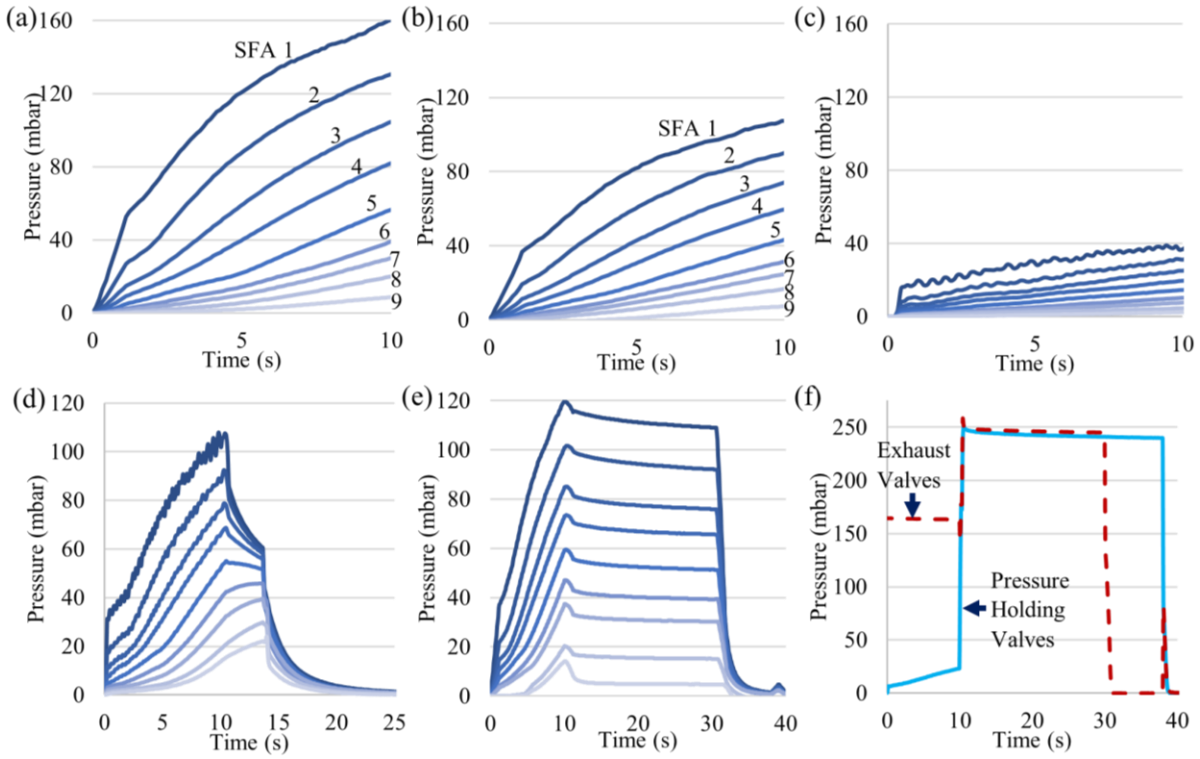


Figure 5.15: Results for the sequential gradient inflation with pressure holding and uniform fast passive deflation of SFAs using the Combined Air Microfluidic Chip. (a) Sequential gradient inflation with a high-pressure setting. (b) Sequential gradient inflation with a medium-pressure setting. (c) Sequential gradient inflation with a low-pressure setting. (d) Sequential gradient inflation and uniform fast passive deflation without pressure holding. (e) Sequential gradient inflation with pressure holding and uniform fast passive deflation. (f) Sequence of pressurization of the control line of the exhaust and pressure holding in-line valves.

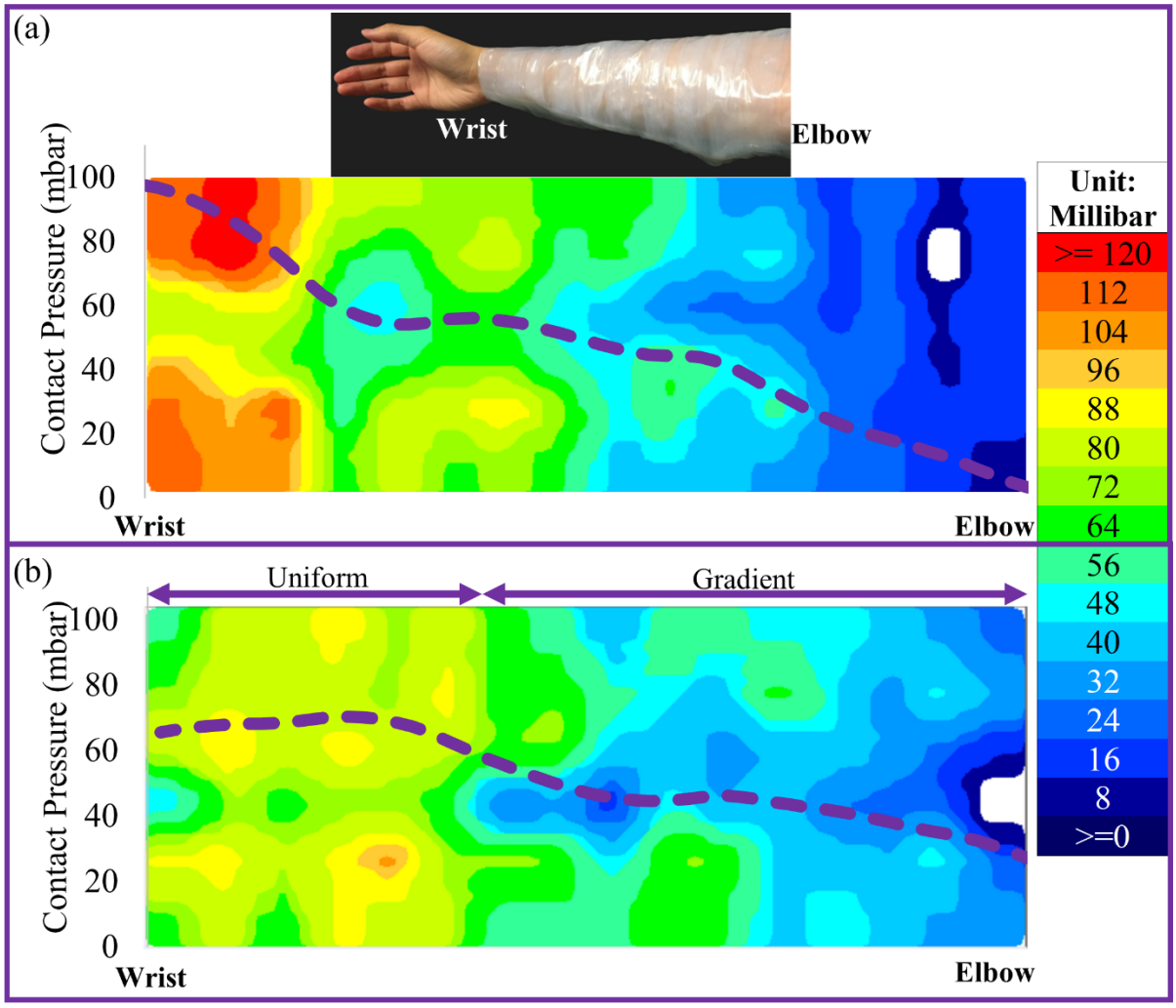


Figure 5.16: Tekscan pressure mapping results of the gradient smooth compression with a monolithic sheet of 9 SFAs with 40% overlap. (a) Smooth gradient compression from wrist to elbow with an image showing the monolithic sheet of overlapping SFAs. (b) Showing smooth gradient compression with uniform smooth compression using the same monolithic sheet of overlapping SFAs. The Tekscan pressure map is overlaid with a plot of the contact pressure, obtained by averaging circumferential pressure readings around the forearm.

5.4 Discussion

Miniaturizing active assistive devices, such as active compression sleeves designed for managing lymphedema and peripheral vascular diseases, necessitates a comprehensive and holistic strategy. The approach presented this this chapter entails the concurrent downsizing of both the frontend (actuators) and backend (control box) components while ensuring that their functionalities are preserved or even enhanced [46]. In this discussion section, we delve into the potential benefits, limitations and implications of utilizing monolithic overlapping soft

fluidic actuators as well as both types of active air microfluidic chips in the miniaturization process. By examining these technologies, we aim to shed light on novel approaches that could positively impact the field of assistive medical devices, offering more efficient and effective solutions for patients with lymphedema and other peripheral vascular conditions.

5.4.1 Monolithic Sheet of Overlapping Soft Fluidic Actuators

Manual lymphatic drainage (MLD) continues to be the gold standard for conservatively managing lymphedema swelling. This preferred approach by lymphedema specialists has gained widespread acceptance among medical practitioners and individuals living with lymphedema. In response to the demand for more accessible and cost-effective solutions, commercial medical devices such as pneumatic active compression sleeves and non-pneumatic sleeves are being developed to emulate the effects of MLD. Although pneumatic compression devices have demonstrated effectiveness comparable to MLD [223], their adoption and user compliance remain challenging due to their inherent bulkiness, which hinders portability and aesthetics, limiting them for mostly home use. To address these concerns and improve the performance of pneumatic compression devices, we presented a novel approach: the monolithic sheet of monolithic overlapping soft fluidic actuators (SFAs). Our study pioneers the systematic testing of this innovative concept, which, to the best of our knowledge, has not been explored in existing literature. By reducing bulkiness while maintaining or enhancing device performance, our research contributes to enhancing the usability and effectiveness of pneumatic compression devices for lymphedema management.

The question arises as to why a monolithic sheet of overlapping SFAs is preferred over using individual pneumatic chambers and gluing them together. The answer lies in the challenges posed by the latter approach. When individual free-floating pneumatic chambers are employed, they tend to shift around inside the sleeve, creating undesirable gaps if they are too far apart or cause excessive pressure if they overlap extensively. Moreover, the use of glue alters the properties of the pneumatic chamber walls, leading to rigidity or increased thickness, making it difficult for the device to contour effectively around the limb. Alternative methods involving casting silicone to create soft fluidic actuators would make the fabrication process complex and result in a bulky system [40]. To overcome these issues, we opted for a monolithic sheet of overlapping SFAs crafted from Bemis 3913, which offers thermal lamination [35] at

a mere 300 μm thickness at the overlapping portions when depressurized. This choice was deemed optimal as it effectively addresses the challenges related to shifting, pressure distribution, and limb contouring, while maintaining a streamlined and efficient fabrication process.

The chosen pressure levels for the study are derived from established figures found in literature and clinical practices, which also matches well with existing commercial systems [170], [250]. The low-pressure setting aligns with the commonly used pressure during MLD, typically below 30 mmHg / 40 mbar [253]. The medium-pressure level is comparable to the highest pressure that some physiotherapists apply during MLD, usually below 60 mmHg / 80 mbar, in order to avoid any microvascular damages [254]. As for the high-pressure level, it approaches but remains lower than the acceptable compression level for users that is considered comfortable, as well as the pressure level at which traumatic injuries to the lymphatic walls and skin may develop, which is around 110 to 120 mmHg / 147 to 160 mbar [253], [255]. By adhering to these well-established pressure ranges, our study ensures the safe and effective application of compression therapy for managing lymphedema and related conditions, promoting optimal therapeutic outcomes and patient safety.

The test results revealed three key findings. Firstly, a 40% overlap demonstrated no pressure gaps (**Figure 5.11**) between SFAs across all pressure settings, establishing it as the optimal overlapping percentage. Lower percentages exhibited visible gaps, particularly at high pressure levels. Conversely, any higher percentage of overlap proved unnecessary and led to excessive overlap, resulting in an increased number of SFAs required to cover the same surface area as a sleeve with less overlap. Due to its proximity to 20% overlap, 30% overlap was not tested as no significant difference was observed between them. For 20% overlap, no gap was observed at low and medium pressure settings, while only a small gap emerged at the high-pressure setting. Consequently, we increased the overlap until no gap was evident at high pressure, reaching the determined optimum of 40% overlap (**Figure 5.12a**). Accordingly, 20% overlap suffices when solely low or medium pressure is required, and if only low pressure is needed, 10% overlap is adequate. Beyond a 50% overlap, the SFAs began to resemble linear actuators akin to bellows-style actuators [256], leading to increased bulging and negating the purpose of reducing gaps between pneumatic chambers for smooth active compression. Hence, maintaining the overlap within the optimal range of 20% to 40% depending on pressure

settings used ensures efficient compression functionality while avoiding excessive overlapping, ultimately offering an effective and streamlined solution for managing lymphedema and peripheral vascular conditions.

Secondly, as anticipated, a thicker outer strain-limiting layer effectively restricts the expansion of SFAs, thereby reducing bulkiness, as evident in **Figure 5.12b**. When considering the forearm and upper arm regions, employing a more rigid outer strain-limiting layer, like the 6-layer of Bemis TPU showcased in this chapter, proves to be a suitable choice. However, it is essential to note that the elbow region necessitates articulation, making the use of a rigid layer impractical. Instead, a less rigid and more flexible outer strain-limiting layer, such as the 2 or 4-layer of Bemis TPU featured in this chapter, would be better suited for this specific area.

Furthermore, exploring alternative solutions, like employing linked articulating plates or chainmail akin to medieval armor, could be a viable option to accommodate articulation at the elbow [257]. However, this topic lies outside the scope of the present study and warrants further investigation in future research. By judiciously selecting the appropriate outer strain-limiting layer for different regions, our study contributes to the development of a more versatile and efficient active compression sleeve, catering to the unique requirements of various body segments while maintaining optimal compression performance.

Lastly, our study demonstrates the successful creation and testing of a low-profile, portable, and active compression sleeve with smooth compression by utilizing a monolithic sheet of 9 overlapping SFAs at 40% overlap, combined with a suitably strong strain-limiting layer. The resulting sleeve exhibits remarkable performance, with each SFA starting from ~100 mbar and gradually decreasing by approximately 10 mbar for each subsequent SFA, effectively establishing a smooth gradient compression pattern (**Figure 5.16a**). This smooth and uniform pressure application is advantageous for specific scenarios, where certain parts of the affected limb require uniform compression. In addition to gradient compression, we also evaluated the combined effect of partial uniform compression using three SFAs at 70 mbar, followed by gradient compression using six SFAs, each decreasing contact pressure by approximately 10 mbar (**Figure 5.16b**). This test further corroborates the versatility of the monolithic sheet of 40% overlapping SFAs, as it successfully achieves both smooth gradient compression and

smooth uniform compression, catering to varying compression needs. The number of SFAs required for the sleeve depends on the length of the affected limb and the width of the SFAs.

Overall, the monolithic sheets of SFAs represent a substantial advancement in the design and fabrication of pneumatic compression devices for effectively managing lymphedema swelling and other conditions requiring smooth compression. The comprehensive and systematic testing conducted in this study yields valuable quantitative and qualitative data, offering essential insights for researchers and designers to consider and implement in their future work. As the adoption of soft robotics-enabled devices with overlapping actuators, regardless of whether they are based on fluidic systems, continues to expand, similar levels of systematic testing become imperative to validate their usefulness and desirability for specific applications. By providing a solid foundation of empirical evidence, our research contributes to the wider acceptance and implementation of innovative technologies in the field of assistive medical devices, ultimately enhancing the quality of life for individuals facing lymphedema and peripheral vascular challenges.

5.4.2 Active Air Microfluidic Chips

The miniaturization of the backend (i.e., the control box) is accomplished through the incorporation of active air microfluidic chips. In contrast to previous approaches that utilized passive air microfluidic chips with parallel fluidic resistance channels (as discussed in **Chapter 3**), limited by slow deflation phases due to the sole reliance on fluidic resistance channels for sequential inflation and uniform deflation, the active air microfluidic chips utilize pneumatic-controlled in-line valves inspired by the Quake's Valve used in lab-on-chip devices [86]. This innovative solution effectively addresses the limitations of passive chips by actively controlling sequential inflation and depressurization, allowing for dynamic gradient compression. While employing active microfluidic chips introduces concerns regarding moving parts and their suitability for controlling sequential gradient compression, this study explores and tests two distinct types of active air microfluidic chips. The first is the In-Line Air Microfluidic Chip, and the second is the Combined Air Microfluidic Chip. Although they differ physically in terms of setup and design, both types serve the same overall function, namely enabling sequential gradient inflation and rapid passive deflation. Below, we discuss the advantages and drawbacks of employing these two types of active air microfluidic chips in

the context of miniaturized compression devices for managing lymphedema and peripheral vascular diseases.

5.4.2.1 In-Line Air Microfluidic Chips

As depicted in **Figure 5.14**, when the in-line valves are operational, they exhibit exceptional performance, delivering highly repeatable, precise, and accurate analog sequential gradient inflation and uniform fast passive deflation of SFAs. However, the process of selecting suitable chips necessitated the use of a "cherry-picking" strategy, where only fabricated in-line valves that matched the pre-determined sequential inflation pattern were utilized. Consequently, the in-line valves chosen for analog sequential testing were not in perfect order, as indicated in **Table 5.2**. Despite having the same geometric dimensions, membrane thickness, and thermal aging, the fabricated in-line valves may display significant variations in $\Delta P_{(open)}$. This variability is evident in **Figure 5.13**, where the large range bars signify inconsistencies in $\Delta P_{(open)}$ among the fabricated in-line valves.

The inconsistency in the size of in-line valves (**Figure 5.13a**) may be attributed to two primary factors. Firstly, variations in membrane thickness were seen even with the same spin coating speed, where membranes were formed with thickness ranging from 80 to 90 μm at 750 RPM and 110 to 120 μm at 1000 RPM. This difference could lead to variations in $\Delta P_{(open)}$. Secondly, the 3D printing process (Form 3, Formlabs) used to create the molds for soft lithography [180] inevitably introduced stair-case patterns, as depicted in **Figure 5.17**, with a vertical z-axis resolution of 25 μm. Even when PDMS was created from the exact same mold, tiny variations caused by dust particles, mold degradation over repeated use, or slight warping of the resin-based mold during PDMS curing at 90°C, may result in different initial opening pressure and fully open pressure, further contributing to discrepancies in $\Delta P_{(open)}$. Additionally, the large quantity of in-line valves tested led to the fabrication of many valves with the same design and shape but from different molds, thereby creating additional differences in $\Delta P_{(open)}$. Lastly, human errors and inherent variations in handcrafted and assembled devices within an academic laboratory setting also played a role in compounding the differences in $\Delta P_{(open)}$ for the same in-line valve design.

Regarding thermal aging of in-line valves (**Figure 5.13b**), inconsistencies can be attributed to several factors. As mentioned in the previous paragraph, differences in $\Delta P_{(open)}$

were already present due to variations in size during fabrication. Additionally, the slight variation in thermal aging temperature further compounded the differences in $\Delta P_{(open)}$ among the valves [258]. Despite these challenges, the median data points in **Figure 5.13** reveal the promising potential of in-line valves if a perfect micromachined metallic mold could be utilized with uniform thickness membranes. In such an ideal scenario, the need for "cherry picking" valves to fit the sequential inflation criteria could be eliminated and replaced with an automated and scaled-up process for commercial use, where each valve type would possess the same $\Delta P_{(open)}$ within acceptable tolerances.

In this envisioned scenario, In-Line Air Microfluidic Chips could achieve true robustness, allowing the combination of over 20 or more In-Line Air Microfluidic Chips for analog sequential control of SFAs. However, it is important to acknowledge that currently, these chips remain primarily research devices due to fabrication challenges.

Overall, achieving analog sequential control poses significant challenges due to the need for numerous in-line valves with varying $\Delta P_{(open)}$ to establish the sequential control pattern. The differences in $\Delta P_{(open)}$ between each consecutive in-line valve can be as small as 10 or even 20 millibars, demanding exceptionally high manufacturing tolerance. Recognizing this complexity, the Combined Air Microfluidic Chip was conceived and developed as a solution to address this problem.

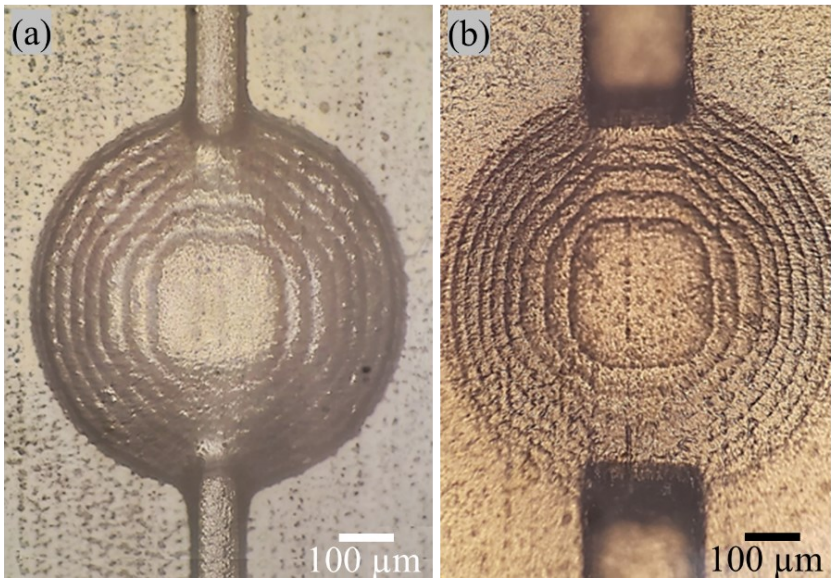


Figure 5.17: Images showing the staircase pattern on the inline valves from 3D printing. (a) Actual PDMS air microfluidic chip. (b) 3D printed mold.

5.4.2.2 Combined Air Microfluidic Chips

By integrating fluidic resistance microchannels and in-line valves into a single chip, aptly named the Combined Air Microfluidic Chip, this innovative approach streamlines the sequential control process and simplifies the system, offering a more practical and efficient solution for managing pneumatic active compression compared to In-Line Air Microfluidic Chips. Moreover, the Combined Air Microfluidic Chip eliminates the need for numerous individual In-Line Air Microfluidic Chips that would otherwise require daisy-chaining their fluid and control lines. Instead, the Combined Air Microfluidic Chip is a single chip with all the components integrated on-chip, albeit requiring longer tubing to connect to each individual SFA.

The Combined Air Microfluidic Chip utilizes fluidic resistance microchannels, which, unlike parallel resistance channels discussed in **Chapter 3**, are arranged in series to form a compact serpentine fluidic pathway (**Figure 5.5c**). Compared to parallel resistance channels, which require an entirely new channel for each consecutive SFA, series resistance channels offer an advantage by sharing channel resistance among multiple SFAs. This design approach reduces the length and space required for microchannels on-chip, making it more efficient. For clarity in testing, the chip configuration in **Figure 5.3e** was used, presenting microchannels and in-line valves in a neat and easily understandable layout. However, further reduction of the chip's size is possible by shortening the characteristic length of resistance channels and maximizing space utilization, as shown in **Figure 5.3g**. In this case, the serpentine channels are replaced by non-uniform and random channels to achieve space-saving benefits. It is noteworthy that a single in-line valve used for exhaust can simultaneously control 3 or 4 SFA/channel pairs, meaning it can cut off flow through multiple channels (**Figure 5.3e**, **g**). The capacity of a single in-line valve to control multiple SFA/channel pairs depends on the size (i.e., diameter and height) of the in-line valve and the cross-sectional area of the intersecting channel. However, the specific details of this aspect are beyond the scope of the current work.

The Combined Air Microfluidic Chip employs two distinct sizes of in-line valves, specifically, two different valve designs with varying ΔP_{close} values, where one size is for exhaust and another for gradient pressure holding (**Table 5.2**). While the raw number of valves

may increase, there will always be just two different types. For instance, the ratio of SFAs to the number of in-line valves required for gradient pressure holding is 1:1, with an additional in-line valve needed for exhaust. In simpler terms, for every two SFAs, three in-line valves are necessary—two for pressure holding (of one size) and one for exhaust (of another size). Similarly, if there are 20 SFAs, a minimum of 21 in-line valves is required: 20 for pressure holding (of one size) and 1 for exhaust (of another size), assuming all 20 SFAs can share a single exhaust in-line valve.

The advantage of using only two different-sized valves was that their ΔP_{close} can be relatively large, around 90 millibars or more, compared to In-Line Air Microfluidic Chips where ΔP_{open}, as mentioned above, was as small as 10 to 20 millibars. With a 90-mbar difference in ΔP_{close}, the manufacturing tolerance was greatly improved. As long as the ΔP_{close} for all the pressure holding valves was higher than that of the exhaust valves, the system will function effectively. The main functions of pressure holding valves and exhaust are to control flow by opening or closing, with sequential inflation managed by the resistance channels. One crucial consideration is that the control lines for all the pressure holding valves and exhaust valves may be fluidly interconnected to reduce the number of active electromechanical solenoid valves required. This approach is similar to the multiplexing work done by Lee et al. using pneumatic-controlled in-line microvalves [91]. On the other hand, if the control lines are for the exhaust and pressure holding valves are not interconnected, all the valves can be of the same size, albeit necessitating an additional 2/2-way solenoid valve. While this configuration increases the size of the control box and adds some cost, it presents a viable alternative for specific applications.

The robust performance of the Combined Air Microfluidic Chip was demonstrated in **Figure 5.15**, affirming its versatility in accommodating different pressure settings, with or without pressure holding. It is important to note that during gradient pressure holding, the pressure measurement exhibited a slight decrease (**Figure 5.15e**). This phenomenon can be attributed to the minor stretching of the elastomer material comprising the walls of the SFA and the outer strain-limiting layer. Despite this observation, the chip's performance remained consistent and reliable. A noteworthy advantage of the Combined Air Microfluidic Chip was its uniform passive deflation time of less than 5 seconds, compared to approximately 10

seconds for In-Line Air Microfluidic Chips. This improvement is attributed to the presence of four exhaust valves in the Combined Air Microfluidic Chip (**Figure 5.5c**), whereas In-Line Air Microfluidic Chips utilized only a single exhaust valve (**Figure 5.5d**). The increased number of exhaust valves increased flow rate which expedited the deflation process, enhancing the chip's efficiency.

In **Figure 5.15f**, it can be observed that the control line pressure for the pressure holding valve experienced a slight increase of about 25 millibars. This effect is due to the fluidic line side compressing the air on the control line side, as the membrane can deflect in both directions (**Figure 5.3c**, **d**). Whether the control lines for both pressure holding and exhaust valves were fluidly interconnected or separated, the system performed as expected. In one configuration, the **Figure 5.15f** would display a single red dotted line, while in the other configuration, it would show two distinct lines.

All in all, the Combined Air Microfluidic Chip exhibited robust and reliable performance, accommodating various pressure settings and pressure holding conditions. The chip's improved deflation time and efficient design make it a promising solution for pneumatic active compression devices, offering enhanced functionality and potential for practical application in medical settings. Regardless of the specific configuration chosen for the control lines, the chip consistently met performance expectations, validating its efficacy and suitability for pneumatic compression.

In the broader context of soft robotics, the integration of microfluidic resistance channels and fluidic in-line valves presents an attractive option for systems with predefined operational sequences, as it offers the potential to minimize the size of control systems and reduce the cost of control hardware, such as electromechanical solenoid valves and the size of batteries. As the fabrication processes improve and produce in-line valves with more consistent $\Delta P_{close/open}$ values, there is the exciting prospect of leveraging in-line valve not only for sequential pressurization but also for individual selective pressurization via multiplexers and demultiplexers. This advancement would further enhance the versatility and capabilities of soft robotics, enabling sophisticated and precise control over various components and functions within the system.

5.4.3 Limitations

The study conducted herein does have some limitations that warrant acknowledgment. Firstly, durability testing for both the monolithic sheet of overlapping SFAs and active air microfluidics was not conducted. The testing focused on exploring the feasibility of overlapping SFAs to reduce compression gaps and incorporating in-line valves and resistance microfluidic channels for smooth sequential gradient pneumatic compression, rather than assessing the mechanical strength and long-term endurance of individual components. For future advancements and potential commercial applications, it would be essential to conduct more comprehensive durability testing, potentially using tougher materials and adopting a more industrial and robust manufacturing methodology. Such testing could provide a clearer understanding of the system's long-term viability and reliability.

Another limitation of the study is that the pressure mapping studies were performed using a rigid forearm model instead of utilizing a real human forearm. While the results demonstrate the efficacy of overlapping SFAs in creating smooth compression in a controlled setting, it is essential to recognize the need for future clinical studies. These studies would involve testing the overlapping SFAs on an actual human limb, which is soft and dynamic, to determine whether the observed benefits translate to real-world scenarios. Only through such clinical studies can we validate the practicality and effectiveness of the overlapping SFAs in a clinical context.

5.5 Concluding Remarks

This study introduces a novel concept of achieving smooth sequential gradient compression with uniform fast passive deflation through the integration of a monolithic sheet of overlapping soft fluidic actuators and an active air microfluidic chip. This combination enables miniaturization of both the front end and back end, resulting in a portable active pneumatic compression sleeve with a wearable control box. The implementation of this technology has the potential to significantly enhance the quality of life for individuals who require sequential compression for managing lymphedema swelling and other peripheral vascular diseases. The performance of the overlapping soft fluidic actuators was thoroughly tested, and the optimal overlapping percentage was identified, ensuring the seamless functioning of the compression

system. Additionally, two types of active air microfluidic chips were fabricated, and their respective advantages and limitations were discussed in detail.

Overall, the integration of active air microfluidics and overlapping soft fluidic actuators represents a substantial advancement in miniaturizing active compression devices while simultaneously improving their functionality. The combination of these innovative components provides a portable and efficient solution for smooth sequential compression with rapid deflation, thereby addressing the challenges associated with conventional compression methods. The outcomes of this study hold promising implications for the development of more accessible and user-friendly compression devices, potentially transforming the way lymphedema swelling and other peripheral vascular diseases are managed. However, it is important to note that further research and clinical studies will be essential to validate and optimize this technology for practical and widespread use in real-world scenarios. The potential impact of this work extends beyond the realm of medical devices, as the concept of combining soft fluidic actuators and active microfluidics may inspire advancements in other areas of soft robotics and wearable technology.

Chapter 6

Investigating Miniaturization of Soft Robotic Actuators for Prosthetic Socket Fitting

Run Ze Gao conceived the idea. The device fabrication and experimental procedures were collaboratively undertaken by Marley O'Connell and Run Ze Gao. Run Ze Gao authored the manuscript.

6.1 Introduction

Approximately three-quarters of individuals with lower-limb amputation who use prostheses reported experiencing skin problems [193] due to pressure ulcers that remain a challenge for prosthetists and individuals with amputation care. Maintaining skin integrity is further challenged by the rapidly growing population of diabetic individuals with amputation [190], accounting for 80% of lower-limb amputations worldwide [259]. Diabetic individuals with amputation suffer from peripheral neuropathy, which causes a loss of sensation in the toes and feet, sharp pain, and an increased risk of foot ulcers [260], leading to poor management of prosthetic socket fit. Socket management is also exacerbated by residual limb volume fluctuations of +/- 10% a day [261], often resulting in excessive pressures inside the socket, particularly at bony prominences like the fibular head. High pressures at the fibular head for prolonged periods risk skin breakdown and painful pressure ulcerations. Pressure ulcers develop due to elevated interface pressures, including sustained exposure to force or shear [262], which is worsened by poor fit of prosthetic socket. Reduced circulation and healing in the lower extremities by diabetes make the prosthesis difficult to wear (or worn minimally) while recovering. Furthermore, solutions that are economical, functional, and easy to be

incorporated into prosthetics workflow are scarce. The significantly decreased quality of life of individuals with amputation [263] urgently calls for novel solutions.

With over 70% of lower-limb amputations across the tibia [184], this proof-of-concept study focuses on transtibial prosthetics. Most custom prosthetic sockets are fabricated using traditional plaster mold and thermoforming processes along with modular socket systems/direct systems [264]. Multiple training/preparatory sockets and custom-fabricated liners to account for high residual limb atrophy during the early post-amputation phase are tedious, iterative, time-consuming, and costly [192], [265]. Similarly, permanent/definitive sockets for "mature" residual limbs with relatively stable residual limb shape and volume can also require multiple rectifications to address poor socket fit due to continued muscle atrophy, volume fluctuation, and/or edema. Despite improvements in novel fabrication techniques such as additive manufacturing [266], most current sockets are static systems that do not address/resolve such dynamic changes.

Typically, liners, socks, pads or inserts made of fabric, silicone, urethane, or other gel-like materials are used to adjust socket fit manually [267], which is challenging to accommodate residual limb volume fluctuation throughout the day [191]. Wearing too many layers of prosthetic socks results in sustained high pressures over bony prominences. Not wearing enough layers of prosthetic socks causes unstable fit, increasing the risk of skin breakdown and soft tissue injuries [268], [269]. Some socket systems consider variable volume in the design [270]. Others use limb anatomy to create multiple-material prostheses with variable rigidity [197], allowing for adjustable contact pressures at different parts of the residual limb. 3D printing has also been used to create replaceable inserts [271]. However, these are static systems, which do not account for dynamic fluctuations in limb volume and still rely heavily on manual adjustments for socket fit. Manual adjustments depend heavily on individuals with amputation to detect pressure discrepancies which are compromised by peripheral neuropathy. In other words, individuals living with amputation who suffer peripheral neuropathy may not detect skin breakdown leading to pressure ulceration. It must be noted that diabetic individuals who undergo amputation have already developed peripheral neuropathy; therefore, the disease is carried over post-amputation.

Passive vacuum suspension methods involve expelling air from the prosthetic socket through a one-way valve to create negative pressure between the liner and the socket, especially during gait. While this method has been proven to reduce pistoning during gait [272], the degree of volume change (e.g., 3.7% on average with up to 8.5% increase in volume in a 30-minute walk [191]) is not ideal. Furthermore, the total surface weight-bearing socket that closely matches the shape of the individual with amputation's residual limb without specific weight-bearing structures and/or dedicated relief areas is required for vacuum suspensions to operate; therefore, fillers are still required if volume loss occurs due to muscular atrophy. The lack of relief areas may still be problematic for bony prominences prone to skin breakdown.

Inspired by patellar-tendon-bearing socket designs [273], shaping the socket to exactly replicate the residual limb is not desirable. Instead, cavities for bony prominences are necessary to accommodate pressure-intolerant regions of the residual limb, such as the distal tibia, the fibular head, and the tibial tubercle, by offloading to pressure-tolerant regions (i.e., soft tissues). Misalignment between the bony prominences and designed cavities often occurs due to gait, shifting weight, pistoning (i.e. vertical displacement) and bell clapping effects, volume fluctuation, and muscular atrophy, increasing risks of pinching at pressure-sensitive regions. In particular, pistoning effects during gait typically occur dynamically between the swing and stance phases and even during the stance phase itself [274].

Active methods typically aim to create a 'smart' socket by integrating a dynamic control system with at least one electromechanical or fluidic actuator to produce a better fit. Elevated vacuum suspension utilizes an integrated pump to create a vacuum of approximately -70 kPa between the liner and the socket [275], but this may cause undesirable residuum volume increase [276] that can worsen edema for diabetic individuals with amputation in a poorly fitted socket due to atrophy or volume fluctuation.

Other methods integrate inflatable bladders with fluids, including pneumatic/air [126], [199], water [128], or magnetorheological fluid [277], into the socket. Most of these methods have a response time that is too slow to respond dynamically to gait [278]. The difference between existing inflatable bladder systems lies in miniaturizing the control box [46], [127], allowing for different pressures. While these methods can deliver a harmonious fit to the

specific shape of the residual limb, some normal forces still occur on top of bony prominences as the actuators contact the bony prominences [25]. These methods can be helpful at negating volume fluctuation for healthy residual limbs but are not ideal for healing tissues over bony prominences that have already been compromised, where ideally, no pressure or very low pressure is exerted on compromised tissues. Additionally, existing systems have not generally considered ease of fabrication, which is essential for integrating into the prosthetist's fabrication processes. Typical issues such as overinflating and durability/leakage also hinder the adoption of inflatable bladder methods [25].

The proof-of-concept study aims to address the above problems by proposing a novel soft robotics-inspired low-profile dynamic fluidic cushion or simply dynamic cushion, specially designed to redistribute and alleviate localized pressures away from pressure intolerant bony prominences to the surrounding regions while syncing with gait through dynamic feedback control (**Figure 6.1**), especially during the weight-bearing stance phase of gait, which are beneficial to individuals with amputation with difficult limb geometry and high chances of skin breakdown. The traditional air bladders were re-designed to be very thin (<0.5mm) when depressurized for easy fabrication and integration with the socket by prosthetists using low-cost materials and tools. Furthermore, a dynamic system capable of rapidly adjusting pressures while syncing with gait to mitigate elevated pressures due to pistoning was examined.

The proposed dynamic cushion can be considered a temporary add-on that works with any suspension methods, including pin-lock, suction, and elevated vacuum. The dynamic cushions can relieve pressure at bony prominences within 250 milliseconds to pressurize fully before mid-stance of gait where peak pressure occurs as the residual limb supports the full body weight. The dynamic cushion can also depressurize quickly enough (< 100 milliseconds) to avoid exerting unnecessary forces onto the surrounding tissues and nerves during the swing phase, where the residual limb is not under any stress. In addition, due to the low-profile nature of the system, it does not cause the prosthetic socket to tilt or misalign even when the cushions are fully inflated/pressurized.

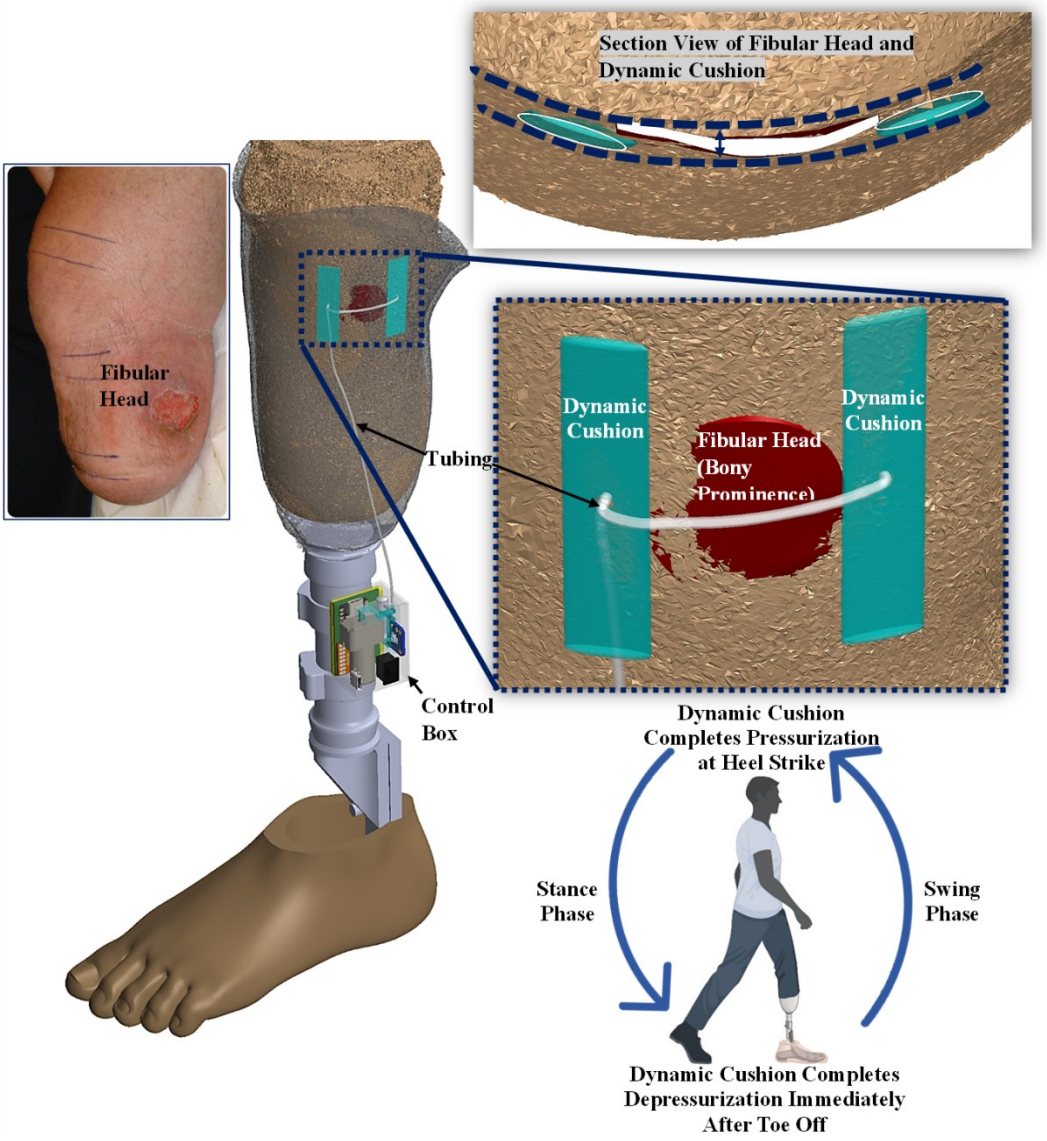


Figure 6.1: Novel soft robotics-inspired low-profile dynamic fluidic cushion (dynamic cushion) concept providing dynamic cushioning during gait. The dynamic cushion fully pressurizes in <250 ms at heel strike and holds pressure through stance phase to unload pressure at the fibular head (red). The dynamic cushion fully depressurizes under 100 ms at toe-off and remains depressurized throughout swing phase. The section view of the fibular head and dynamic cushion shows when the dynamic cushion pressurizes, a gap wide enough to allow the fibular head to no longer contact the inside walls of the prosthetic socket is created, entirely unloading contact pressure at the fibular head. The dynamic cushions avoid contacting the fibular head and peroneal nerves above and below the fibular head and distribute the contact pressure that would otherwise be on the fibular head onto surrounding soft tissues. A wearable control box (~100 grams) attached to the pylon controls the pressurization and depressurization of the dynamic cushions. Note that the current proof of concept study focuses on developing and testing actuator design. Sensor and controller design to trigger (de)pressurization is beyond the scope of this chapter. The top left image shows a pressure ulcer at the fibular head due to shear and friction from badly fitting prosthesis [269].

6.2 Methods and Materials

6.2.1 Biofidelic Residual Limb

The proof-of-concept study comprised benchtop mechanical testing. A biofidelic residual limb model was used (**Figure 6.2a**). The biofidelic residual limb model consisted of a foam core and a polyurethane outer shell with a similar stiffness to the soft tissue of the residual limb and the epidermis. An aluminum rod was embedded in the limb model to simulate the residual bone. A detailed design, rationale and validation of the biofidelic residual limb model can be found in the thesis by Robin Murdock [279]. A curved rigid plate was 3D-printed to mimic a bony prominence: the fibular head. Three rigid fibular head plates of different nominal thicknesses were created to test the effectiveness of the dynamic cushion at unloading contact pressures (**Figure 6.3a**). The fibular head was chosen since it is pressure intolerant/deformation sensitive [201]; therefore, any vertical or lateral movement may cause discomfort and skin breakdown. In addition to the distal end, the fibular head is commonly reported as an area of discomfort and potential skin breakdown by both literature [280], [281] and prosthetists (Andreas Schirm, Prosthetic Ability, Canada). However, the same dynamic cushioning strategy may be applied to other bony prominences, such as the tibial crest and distal fibula.

6.2.2 Soft Robotics-Inspired Low-Profile Dynamic Fluidic Cushion

The dynamic cushion was a collaborative effort with Dr. Doug Dittmer (Amputation physiatrist) and Andreas Schirm (Prosthetist). The fabrication method was inspired by work in creating soft robotic actuators via thermal lamination strategies [35]. Essential guidelines for the design of the dynamic cushion are to i) avoid covering bony prominences to prevent direct compression, ii) avoid peroneal nerves innervating movement and sensation of the limb by avoiding areas above and below the fibular head to minimize possible discomfort, iii) an architecture that has the potential to be fabricated and customized by prosthetists, iv) keep the system simple but still be effective, and v) minimize the duration of compression on soft tissues surrounding the bony prominences by millisecond pressurization and depressurization responses. Four dynamic cushion designs were proposed for testing, as shown in **Figure 6.2b**. **Table 6.1** shows the total surface area of the four designs when fully depressurized. When

squeezed by the limb and the socket, the full height of a pressurized dynamic cushion may vary between 2 to 10 mm, confirming its low-profile form factor (**Figure 6.4**).

Table 6.1: Dynamic cushion designs and their pressurizing chamber surface area when completely depressurized. The volume when pressurized depends on internal air pressure, which determines the height; thus, using the total surface area multiplied by height yields rough total in-socket pressurized volume. Please note the volume estimation of the pressurized dynamic cushion is only valid when it is squeezed by the limb and the socket.

Soft Robotics-Enabled Low-Profile Dynamic Fluidic Cushion (Dynamic Cushion) Design	Dynamic Cushion Depressurized Total Surface Area – Zero Volume (cm^2)
Horseshoe	14
Double Curved	9.35
Rectangle	17.35
Four-Ellipse	37.72

The steps and equipment/tools for making the dynamic cushions are shown in **Figure 6.2c** and **Figure 6.2d**, respectively. The one-time equipment/tool cost was around CAD 700 at the time of publishing the article. The horseshoe design maximizes the unloading contact area surrounding the fibular head; it was a single piece requiring a single tubing, therefore, easy to fabricate. The double-curved design avoided the tissue above and below the fibular head while optimizing the contact area around the fibular head to unload pressure. The rectangle design avoided the tissue below and above the fibular head and was the most straightforward shape to fabricate and customize. Lastly, the four-ellipse design contained the largest surface area while avoiding the most tissue and nerves above and below the fibular head; however, it required most tubing.

Each dynamic cushion was created using Bemis 3916 Sewfree® Thermoplastic Polyurethane (TPU) sheets by thermal bonding at 110°C. The inflatable cavity was created using Teflon® polytetrafluoroethylene (PTFE) supplied by McMaster Carr, which does not adhere to TPU during thermal bonding, thus creating an inner inflatable chamber. The desired elastomer and insert shapes were first designed using computer-aided design software (AutoCAD). The TPU and Teflon were cut into the designed shapes using Computer Controlled Cutting (Cricut). The Teflon was sandwiched between two TPU layers which were heat-pressed together. Silicone tubing was inserted into the actuator and glued to seal the opening. The dynamic cushion may be integrated within the prosthetic liner, located between

the skin and the liner or between the liner and the socket, facilitating appropriate cushion location surrounding the fibular head.

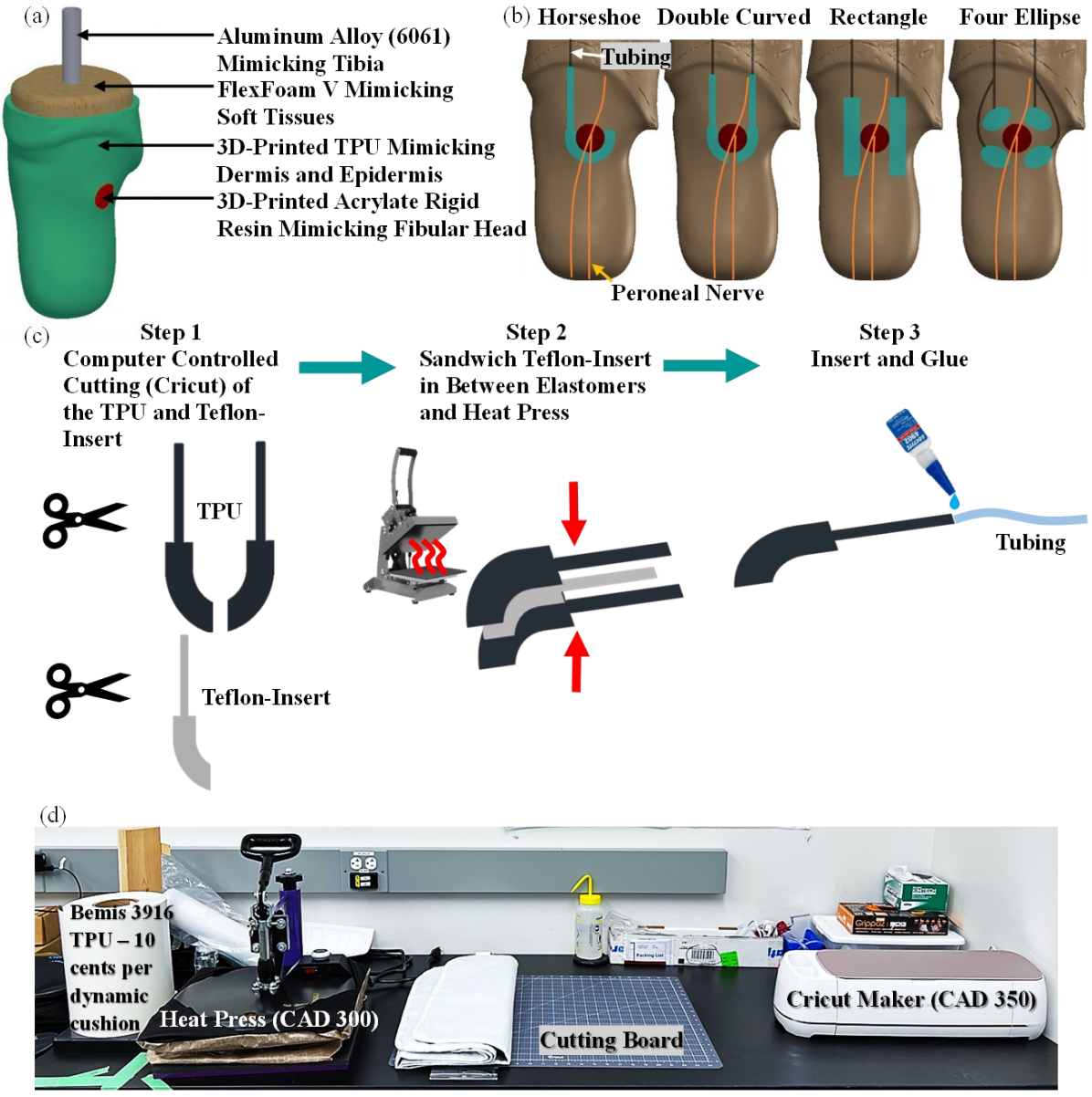


Figure 6.2: Components and fabrications overview. (a) Biofidelic residual limb model with fibular head rigid cover. (b) Soft robotics-inspired low-profile dynamic fluidic cushion design. (c) Fabrication steps for dynamic cushions. (d) Image of equipment used for dynamic cushion fabrication demonstrates the low cost and ease of fabrication.

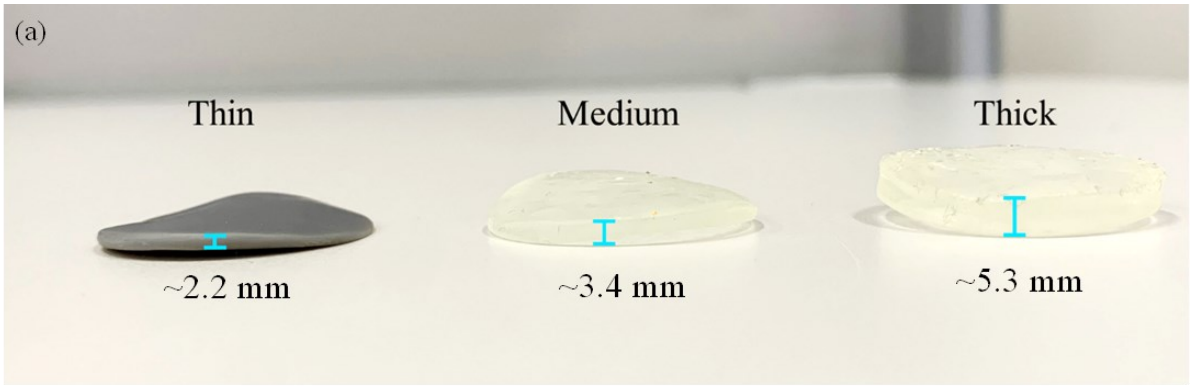




Figure 6.3: (a) Images of thin, medium, and thick fibular head rigid curved plates. The thin plate was made out of Formlabs grey resin, the medium and thick plates were made out of Formlabs clear resin. All fibular head rigid curved plates had the same materials properties. (b) Image showing the pressurized and depressurized dynamic cushions, fibular head rigid curved plate, residual limb model and Tekscan sensor.

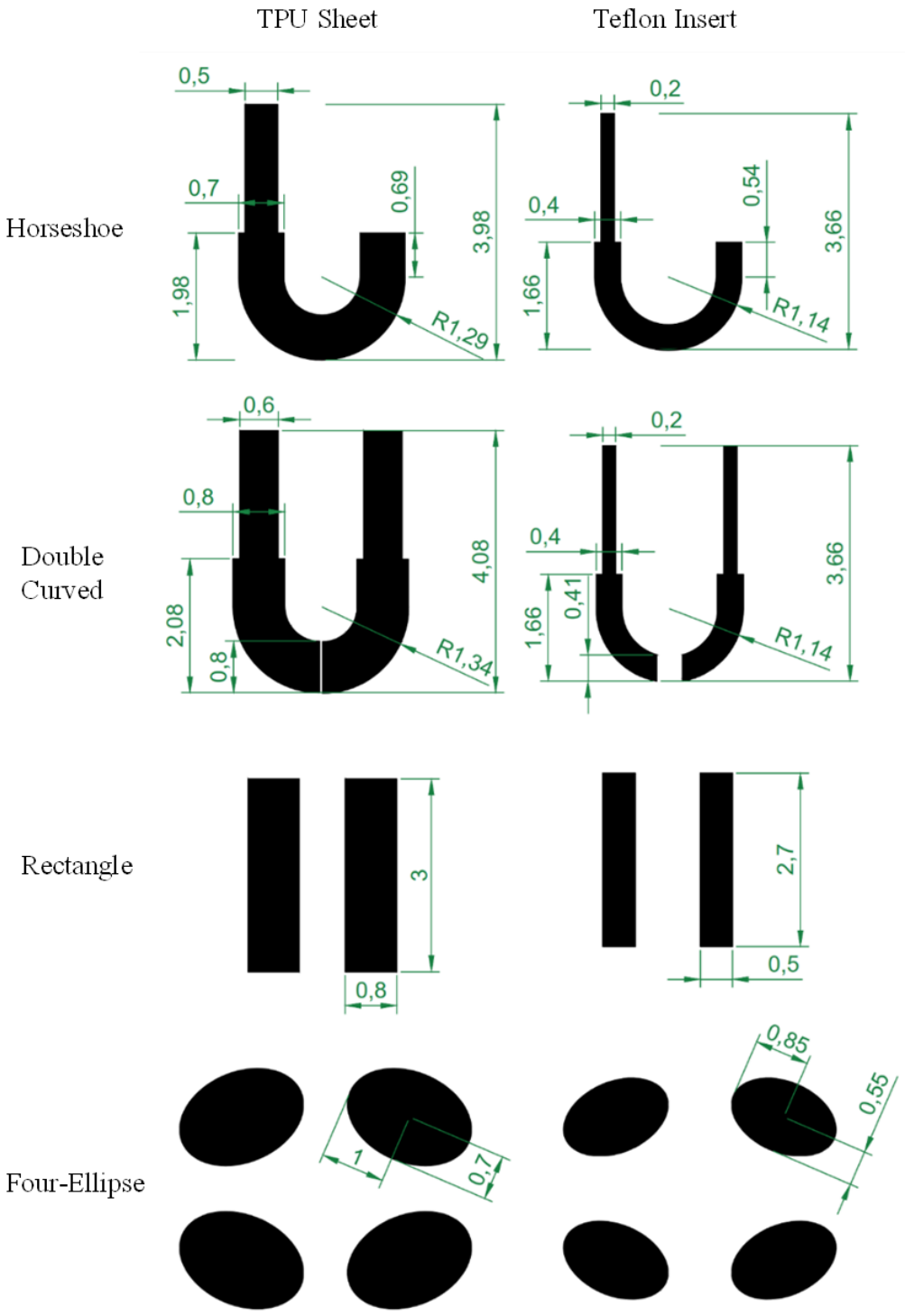


Figure 6.4: Dynamic cushion designs illustrated with critical dimensions for both TPU and Teflon insert. All dimensions are in inches.

The TPU and Teflon sheet were 150 microns and 75 microns thick, respectively. The tubing had an outer diameter of 2.38 mm, which may be routed to the control box (attached to a different part of the prosthesis) through cut-outs on the surface of the prosthetic socket. The

tubing through the cut-outs was a tight squeeze fit and could be sealed off from the external atmosphere by glue or epoxy. Therefore, suction suspension forces should not be compromised. The overall fully depressurized thickness of the dynamic cushion was ~375 microns. The tubing was perpendicular to the flat surface of the dynamic cushion and was therefore not located between the socket wall and the residual limb; therefore, prosthetists, in theory, do not need to change their socket design to integrate this system. The material cost of a dynamic cushion was almost negligible at less than a U.S. dollar.

Although the dynamic cushion was only on one side of the prosthetic socket, the anterolateral directed force by the medial tibial flare would counteract the medially directed force by the dynamic cushion surrounding the fibular head. Therefore, no lateral movements should be created due to the inflation/pressurization of the dynamic cushions.

6.2.3 Control Box

A wearable control box design was optimized by minimizing its size and weight (~100 grams). It consisted of a 3.7 V, 1800 mAh battery (~USD 15) from Amazon, a motor controller (~USD 7) from Sparkfun, a Seeeduino XIAO microcontroller (~USD 4), a miniature air pump to provide pressurization (~USD 7) from Amazon, a miniature 2/2-way normally closed electromechanical solenoid valve (~USD 7) from Amazon to provide passive depressurization to the atmosphere, and an air pressure sensor (~USD 15) for pressure feedback from Adafruit (**Figure 6.5a**). The total cost of the control box was around USD 55 when individual components were purchased off the shelf.

Although there were no specific guidelines for acceptable prosthetic weights, orthoses guidelines for comfortable all-day wear existed and can be borrowed to evaluate whether 100 grams was reasonable. The guideline suggested the total unsupported or unpowered mass positioned on foot should be less than 1.25% of the user's body weight for comfortable all-day wear [140]. Therefore, without accounting for the actual weight of the prosthesis, a person weighing at least 8 kg should be able to wear the 100-gram control box on their foot comfortably all day. To further reduce the burden of the control box, the control box can be positioned on the pylon just below the socket to remain even closer to the center of the user's body mass to further minimize changes to the moment of inertia. These discreet locations were chosen to avoid adding bulk to the socket and reduce disruption to everyday activities. **Figure**

6.5b shows the proposed control scheme. The control scheme used a simple digital control strategy where the miniature air pump enables pressurization of the dynamic cushions. A single 2-port-2-way solenoid valve exhausts air from the dynamic cushions for depressurization based on signal feedback from an air pressure sensor.

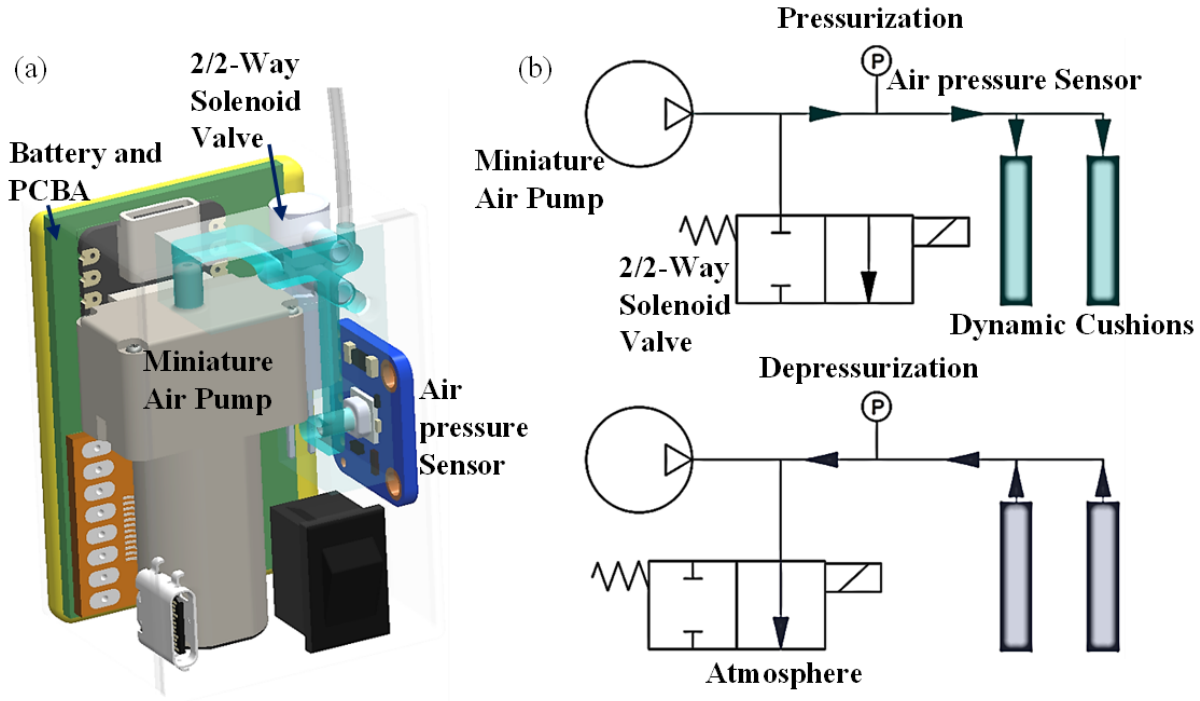


Figure 6.5: Control box design. (a) CAD Model of the wearable control box. (b) Diagram of the control scheme for pressurization and depressurization of the dynamic cushions.

6.2.4 Testing Setup

Figure 4 shows the setups for the parametric and systematic tests below. The rigid fibular head cover was taped to the surface of the residual limb model with Kinesiotape simulating the bony prominence. The depressurized dynamic cushions were taped onto the residual limb, surrounding the fibular head cover (**Figure 6.6a**). The assembly was then placed into the socket (**Figure 6.6b**). To monitor and record the contact pressure between the residual limb and socket, a Tekscan F-Socket™ force-sensitive-resistor sensor was secured between the residual limb and the socket. Note the Tekscan sensor was used solely for verification purposes and was not a part of the wearable system.

Human body weight, which could vary from less than 20 kg to over 80 kg is an important parameter to consider when designing and testing prosthetic sockets and their

cushioning systems. Therefore, a range of 0 to 80 kg weight was tested to ensure the dynamic cushions effectively achieve suitable contact pressure at and around bony prominences, particularly the fibular head. For the weighted test, the biofidelic residual limb with the attached dynamic cushions was placed inside the prosthetic socket, which was attached to the foot and pylon to simulate natural upright stance. Varying weights (0 kg, 20 kg, 40 kg, 60 kg, and 80 kg) were placed on a platform attached to the residual limb "tibia" to simulate human body weight applied through the bone (**Figure 6.6c**). An air syringe was used to manually inflate the dynamic cushions to the desired pressure as observed on the Tekscan software (**Figure 6.3b**).

The biofidelic residual limb and dynamic cushions were placed inside the prosthetic socket for the dynamic gait and static standing tests. The dynamic cushions were connected to a miniature air pump as a pneumatic source and a solenoid valve to control the dynamic cushions as necessary automatically (**Figure 6.6d**). Additionally, the system was connected to an air pressure sensor to measure the internal pressure response. Parametric and systematic testing on the following parameters were conducted using the methodologies and testing setup described herein: body weight, soft fluidic actuator shape, fibular head thickness, and dynamic response time.

Each dynamic cushion design and fibular head rigid cap thickness were tested at varying static pressure-holding intervals relating to circumstances where a constant pressure needs to be maintained in the socket, such as standing. Specifically, tests were conducted with internal dynamic cushion pressures of 75 mmHg, 150 mmHg, 225 mmHg, 300 mmHg, and 375 mmHg and the corresponding changes in contact pressure at the fibular head were recorded.

Each dynamic cushion design and fibular head rigid cap thickness (**Figure 6.3a**) were tested at varying unloading/loading intervals corresponding to gait cycle lengths. This test aimed to mimic pistoning conditions and the bony prominence misaligned from its pressure relief cavity. Pressurization and depressurization response times and repeatability were recorded. Due to the limitation of the static benchtop test, actual pistoning could not be simulated. Thus, to mimic the high contact pressure during the stance phase intervals, high

contact pressure was also seen in the swing-phase intervals, which is normally not observed in reality as the residual limb does not support the body weight.

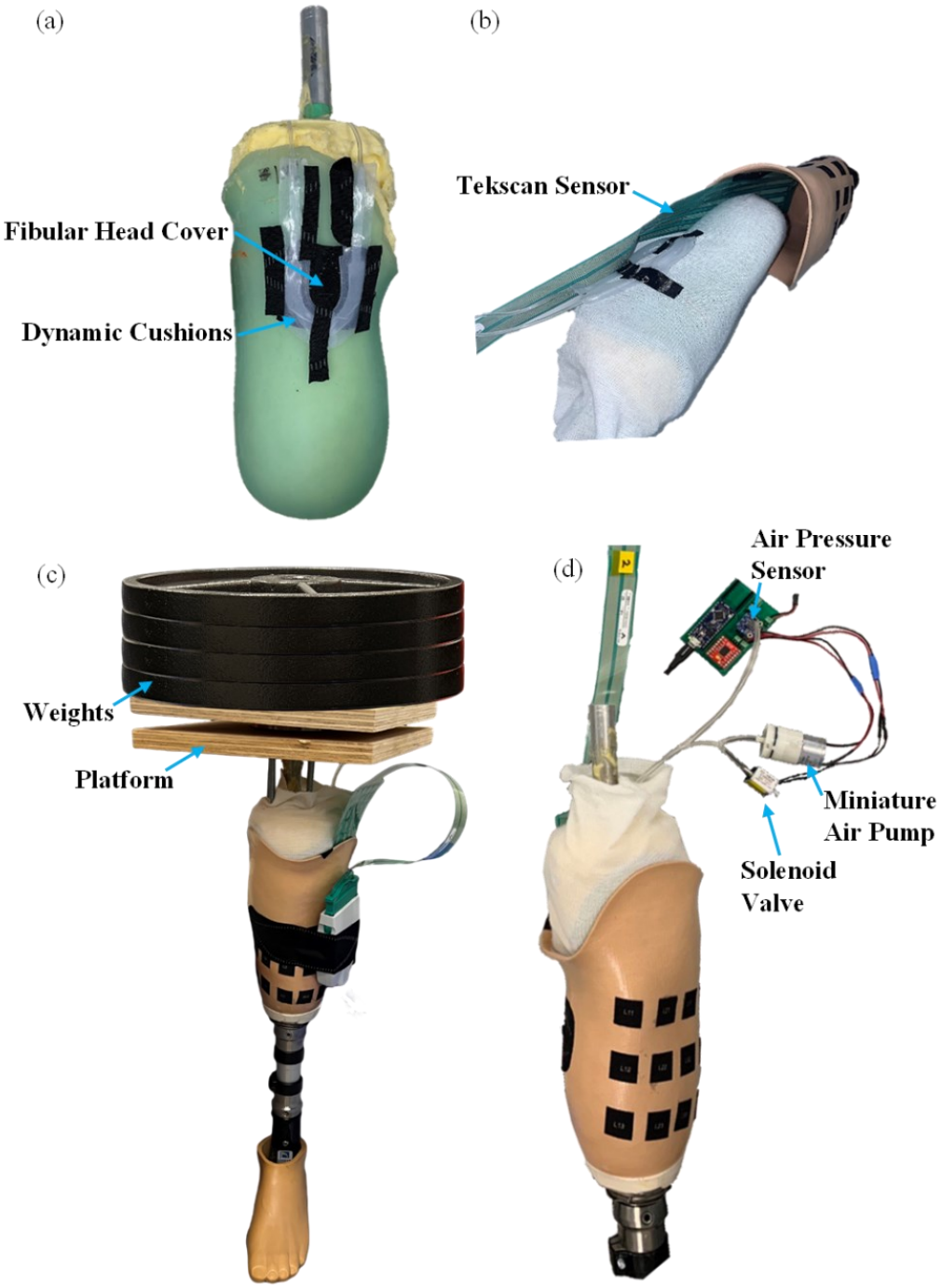


Figure 6.6: Testing setups. (a) Image showing placements of rigid fibular head cover and surrounding dynamic cushions. (b) Image showing placement of the Tekscan sensor between the prosthetic socket and residual limb model. (c) Image showing weights stacked on the platform connected to the aluminum rod mimicking the tibia. (d) Image showing connections of miniature air pump, solenoid valve, and air pressure sensor to the dynamic cushions.

6.3 Results

6.3.1 Weighted Tests

As shown in **Figure 6.7a** (see **Figure B.7** of **Appendix B**, which shows more weight tests), the dynamic cushion effectively mitigates and distributes the contact pressure from the fibular head to the surrounding soft tissues. Peak pressure reduction at the fibular head of 60% at 80 kg, 61% at 60 kg, 50% at 40 kg, and 43% at 20 kg were observed. When fully pressurized, the dynamic cushions' applied pressure onto fibular head surrounding tissues reached a maximum of approximately 250 mmHg, which is less than 50% of peak contact pressure on top of the fibular head.

6.3.2 Static Standing Tests

As the internal pressure of the dynamic cushions increased, the contact pressure at the fibular head decreased (**Figure 6.7b**). After a specific internal pressure threshold was reached, the fibular head contact pressure reached zero, as the dynamic cushions successfully eliminated pressure from the fibular head so that it was no longer in contact with the socket. The pressure was redistributed from the fibular head to surrounding soft tissues (**Figure 6.7c**, **Figure B.8**, **Figure B.9** and **Figure B.10** of **Appendix B**). When the dynamic cushions were depressurized, there was a high contact pressure at the bony prominence (fibular head). When the dynamic cushions were pressurized, the pressure was distributed to either side of the fibular head where the dynamic cushions were located, causing the pressure at the fibular head to reach more acceptable levels (**Figure 6.7d**).

6.3.3 Dynamic Gait Tests

In every trial, the dynamic cushions effectively decreased the fibular head contact pressure (**Table B.1** in **Appendix B** provides a complete set of plots). The designs with double curved (**Figure 6.7e**) and rectangles (**Figure 6.7f**) are included in the main text. As the dynamic cushions pressurized and their internal pressure increased, the contact pressure at the fibular head decreased simultaneously. Conversely, as the dynamic cushions depressurized and their internal pressure decreased, the contact pressure at the fibular head concurrently returned to the initial state of high contact pressure. The average internal pressure for the double-curved and rectangle designs reached 470 mmHg and 287 mmHg, respectively, with a standard

deviation of 8 mmHg and 11 mmHg over 10 simulated gait cycles. In both cases, the contact pressure at the fibular head decreased consistently from well over 200 mmHg to approximately 10 mmHg in less than 250 milliseconds. The dynamic cushions took less than 100 milliseconds to exhaust air from fully pressurized to depressurized.

6.4 Discussion

The advantage of benchtop mechanical testing is that poor socket fit can be tested without causing harm to humans. Therefore, the biofidelic residual limb model and its corresponding socket were purposefully oriented to simulate a poorly fitted socket. This is not to say that the socket must be poorly fitted for the dynamic cushion to provide any benefit, but instead simulating a training/preparatory socket where the residual limb no longer fits well over time due to atrophy during the early post-amputation phase. In addition, body weight may also change over time. Therefore, a permanent/definitive socket that fits well with the user's current body weight may have a poor fit in the future.

A higher contact pressure at the fibular head was observed in the zero weight case than that of 80 kg case, which was likely attributable to the larger weight forcing the residual limb to sink into the socket, making the fibular head align with the proper pressure relief location inside the socket. This finding also shows that a static socket with pressure relief cavities alone may not adapt to a dynamic residual limb for daily use, as a fixed pressure relief location may misalign with the bony prominences. Unlike traditional cushion designs, dynamic cushions do not put any pressure on the bony prominences. With further clinical testing, they may prove to allow for healing of skin breakdowns while allowing individuals with amputation to continue using prosthetic sockets. It must be said that in a perfectly fitting socket, the dynamic cushions are obviously unnecessary, and they may create unnecessary pressure.

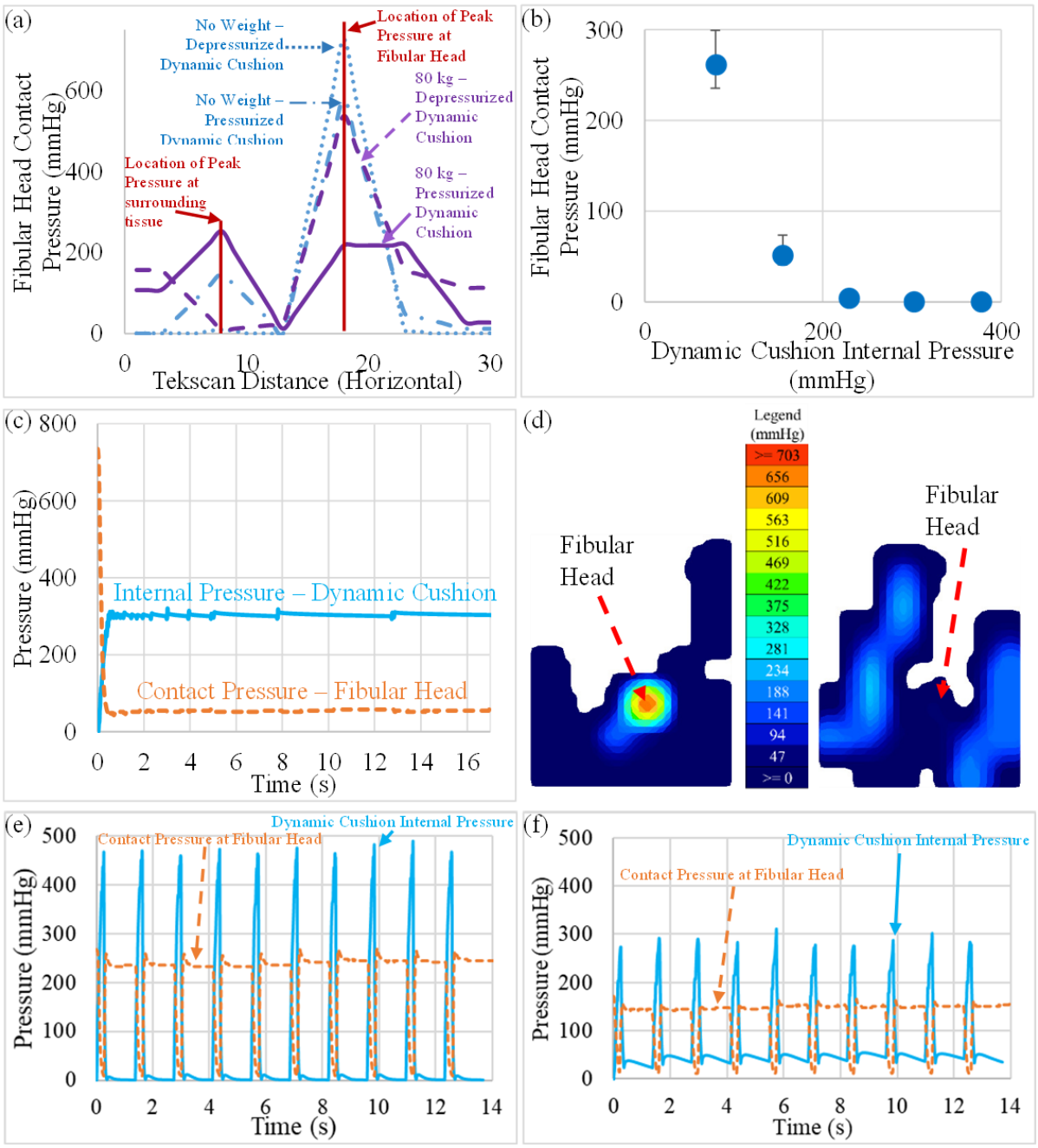


Figure 6.7: Testing results. (a) Plot displaying consolidated Tekscan data comparing no weight to weighted (80 kg) contact pressure at fibular head when the dynamic cushion was manually pressurized using a syringe filled with air. The Tekscan was placed horizontally through the middle of the fibular head. The syringe was filled until approximately 200 mmHg contact pressure (maximum suggested pressure over bony prominences over two hours [282]) at the fibular head was reached or the contact pressure at the fibular no longer decreased with human manual syringe pumping. The purpose of this test was to show that under the full weight of a person, the dynamic cushions are still capable of reducing fibular head contact pressure down to an acceptable level (at least ~200 mmHg) while maintaining pressure on the surrounding

soft tissues at an acceptable level as well (at most ~200 mmHg). (b) Static pressure holding test with medium fibular head rigid cover (average of three tests per data point) with preferred rectangular dynamic cushion. (c) Static pressure holding test with thick fibular head cover with preferred rectangular dynamic cushion at an internal pressure of 300 mmHg. (d) Static pressure holding test with thick fibular head cover with preferred rectangular dynamic cushion depressurized (left) and pressurized at 300 mmHg (right). Dynamic gait test displaying internal pressure of dynamic cushion (solid cyan line) and contact pressure at the fibular head (dotted orange line) over ten continuous cycles of 250 ms pressurization followed by 100 ms depressurization. Two different balloon designs with the medium fibular head rigid cap are shown: (e) Curved and (f) Rectangle.

The miniature air pump can pressurize the dynamic cushions from 0 mmHg to 300 mmHg, which completely unloads contact pressures on the fibular head from peak pressure of 734 mmHg down to 50 mmHg, which was a 90% reduction, in under 250 milliseconds, which should be sufficient to protect the fibular head during the entirety of the stance phase. The average stance phase is around 0.59 to 0.67 seconds [283], and peak pressure experienced by the residual limb typically occurs after midstance about halfway through the stance phase when the residual limb supports the entire body weight. Therefore, a 250 ms response time should be sufficient to pressurize the dynamic cushion fully before reaching midstance. The pressure on surrounding tissues remained, on average, below 200 mmHg, which is considered the maximum suggested pressure over bony prominences over two hours [282]. The dynamic cushions have minimal volume when depressurized (**Table 6.1**); therefore, a miniature air pump has enough flow rate to achieve the required pressure, given the fast response time of 250 milliseconds. The static standing test also demonstrated that when standing, a 40-gram miniature air pump was sufficient to keep the dynamic cushions at enough internal air pressures (i.e. 300 mmHg) to unload the contact pressure at bony prominences.

A 40-gram miniature pump was sufficient to dynamically pressurize and depressurize the dynamic cushions to synchronize with the gait cycle. The dynamic cushions fully pressurized at heel-strike and maintained internal pressure throughout the stance phase to unload the high contact pressure at the bony prominence. At toe-off, the dynamic cushions fully depressurized and maintained the depressurized state throughout the swing phase to alleviate unnecessary pressure on surrounding soft tissues, such that minimal contact pressure was maintained inside the socket during gait. Overinflation should not be an issue for the dynamic cushion as a pressure-control feedback loop was used. The dynamic cushions'

connection to tubing was secured by flexible superglue (Loctite 4906), which prevented leakage.

Although all four designs were effective at unloading the high pressure at the fibular head, the simplest design with two rectangles is likely most desirable for the prosthetist because it is easy to fabricate, requires less tubing and connection joints, and thus is easy to customize for different users and different bony prominences. The rectangle design also alleviated forces on the peroneal nerves above and below the fibular head, which is essential for the users' well-being. The horseshoe design is not as desirable as it exerted excess pressure on the peroneal nerves below the fibular head, which may be undesirable for the users from a clinical perspective, as mentioned by prosthetist (Andrea Schirm, Prosthetic Ability, Kitchener, Canada). Lastly, the two curved balloon design did not exert pressure on surrounding nerves; however, it may be more complex to fabricate and customize for the prosthetist than the rectangle design. Nevertheless, different designs were explored to showcase the possibilities with this simple fabrication method and potential usages with other bony prominences, difficult-to-manage areas, and areas that may require healing from skin breakdown.

One could debate the merit of the dynamic cushions if the socket itself can be iteratively and continuously rectified to always provide a perfect fit. It comes down to cost and the preference of the prosthetists and individuals with amputations. The authors believe that dynamic cushions could be a useful temporary add-on for quickly modifying and customizing local socket fit for training/preparatory sockets during the maturation phase when the individual with amputation is experiencing discomfort or skin problems at a particular bony prominence. For permanent/definitive sockets, dynamic cushions may still be useful. However, a more comprehensive strategy that manages the entire residual limbs fit not just a bony prominence such as proposed by Sanders et al. [284] or Lee et al. [25] may provide greater volume management.

6.4.1 Limitations of the Study

In this proof-of-concept study, a biofidelic model of a residual limb was used for benchtop engineering testing, which was static and did not fluctuate in volume. Hence, it could not fully capture the residual limb's pistoning and bell-clapping effects within a socket. Also, the biofidelic residual limb model did not wholly capture the material characteristics of a real

human residual limb. The dynamic gait test used a benchtop setup and did not capture ground reaction forces, kinematics, and dynamics of an actual individual with amputation's gait. The weighted tests went up to 80 kg due to safety concerns and thus did not entirely capture or represent the population. Although the dynamic cushions and actuation were explored, sensing when unacceptable movements within the socket and volume fluctuation occur was still lacking.

6.5 Conclusion and Future Work

This study described a proof-of-concept for a novel soft robotics-inspired low-profile dynamic fluidic cushion for pressure and volume fluctuation management in individuals with transtibial amputation, specifically targeted dynamic pressure relief for bony prominences prone to ulceration. The developed fabrication methods for the dynamic cushions were cost-effective, simple with minimal tubing and connection needs, and thus have the potential to integrate with prosthetists' workflow. The study showed dynamic cushions could reduce the high contact pressure at the bony fibular head and redistribute loads to the surrounding soft tissues. Future work will incorporate distal-end soft robotics-inspired sensors for sensing pistoning to enable precise actuation of dynamic cushions. All in all, the proposed soft robotics-inspired low-profile dynamic fluidic cushion was a stepping stone for residual limb volume and tissue management for socket comfort.

Chapter 7

Investigating Miniaturization of Soft Robotic Sensor for Prosthetic Socket Fitting

The work included in this Chapter is published: A. J. Yu[1], **R. Z. Gao[1]**, P. S. Lee, C. Mele, D. Dittmer, A. Schirm, C. L. Ren, and J. Y. Tung, "Soft Robotics-Inspired Sensing System for Detecting Downward Movement and Pistoning in Prosthetic Sockets: Proof of Concept Study," *Prosthetics and Orthotics International.* Run Ze Gao conceived the idea. The device fabrication and experimental procedures were collaboratively undertaken by Adam Yu and Run Ze Gao. Run Ze Gao authored the manuscript.

[1] Contributed equally to this work.

7.1 Introduction

Diabetic foot complications are the leading cause of lower extremity amputations, placing an enormous social, economic, and medical burden on healthcare systems worldwide [190], [285]. Over 85% of lower-limb amputations are preceded by an active foot ulcer [285]. Diabetic individuals living with amputation may also have peripheral neuropathy, causing a loss of sensation to pain and developing numbness in peripheral extremities [286]. These factors make it challenging for transtibial prosthetic (TTP) users to monitor residual limb health, especially when the residual limb is not visible within the socket.

Residual limb tissue is not accustomed to weight bearing, with intense loading causing tissue injury and ulceration when not properly managed or treated [195], [287], [288]. Therefore, optimizing socket fit is crucial to prevent skin breakdown, facilitate mobility, and improve quality of life for individuals living with amputation [287], [289]. Changes in residual limb volume are a central cause of poor prosthetic fit and may cause discomfort and loosening, putting the user at an increased risk of falling [290]. "Pistoning" refers to the vertical

displacement of the residual limb within the socket and is considered one of the best indicators of whether proper suspension and fit are occurring [291]. “Downward movement” may occur when the residual limb drops deeper into the prosthetic socket over a prolonged period [292], frequently arising from limb volume loss. Like pistoning, downward movement can be a major source of discomfort and is associated with skin ulceration. A critical indicator of the device quality and associated medical care, 40-60 percent of individuals living with amputation reported dissatisfaction, and >50 percent of patients reported pain during prosthetic use [187].

Various factors are related to poor prosthetic fit (and associated pistoning and downward movement). One main factor is the volume change of the residual limb, which can fluctuate between -11 to +7 percent every day [191] and is typically self-managed by manually donning or doffing liners and socks to maintain fit. This is particularly important during the maturation of the residual limb as volume fluctuations are most volatile during this early period, lasting up to 18 months [125] Donning too many socks may lead to a build-up of pressure and shear, which can cause dangerous skin conditions, including skin lesions and pressure ulcers [193], [194]. Not enough socks will increase undesired loading on the residual limb (e.g., downward movement, pistoning) and can lead to deep tissue injury and impaired lymphatic drainage [195]. The condition of the residual limb is highly dependent on the ability of the user (and prosthetist, to a lesser degree) to self-manage the fit and comfort of the prosthesis.

Since the mid-20th century, healthcare professionals have studied how to build more comfortable and better-fitting prosthetics [293]. Today, the need for better fitting prosthetic sockets for diabetic individuals living with transtibial amputation is motivated by the increasing prevalence of diabetes at unprecedented rates. Currently, half a billion individuals worldwide are living with diabetes, and this number is expected to increase by 25 percent by the year 2030 [294]. Self-management can be quite challenging as many diabetic individuals living with amputation suffer from peripheral neuropathy, which limits their ability to sense pain, discomfort, or pressure at the distal end. Although advancements in automatic dynamic socket adjustment are being explored[25], [284], cost and complexity may inhibit automatic adjusting socket adoption. Additionally, sensors are still required to provide feedback control.

Many sensors have been developed to monitor pressure and shear at the residual limb and socket interface. Commercially available force-sensitive resistor (FSR) -based sensors such as the F-Socket (Tekscan, Norwood, United States) are flexible enough to fit in the socket unobtrusively. However, FSR sensors are primarily research and clinical tools unsuitable for long-term use due to drift and durability issues [295]. The Motio Stepwatch (Adapttech, Birmingham, United Kingdom), a real-world activity monitor specifically designed for lower limb prosthetic users, is undergoing beta testing [296]. It is on the verge of becoming commercially available as a wearable medical device.

Recent advances in wearable technology have led to the development of sensors that can be integrated into liners [297], [298]. Kwak et al. developed thin strain-based sensors that directly adhere to the residual limb under sock layers and communicate with modules and consumable electronics (e.g., smartphones) via NFC and Bluetooth [299]. While these sensors do not require socket modifications and can monitor the residual limb's health, compliance in donning the sensor may introduce an additional cognitive burden.

The recent development in textile and microfluidic technologies has led to the development of a range of small flexible sensors that show promise in prosthetic settings but have not yet been tested for this purpose [300]–[303]. Fluid-based pressure sensors, particularly soft fluidic sensors,[304]–[306] are well suited for prosthetics as they are flexible and malleable to be integrated into the inner socket where irregular and unique curvatures exist [307]. While optical sensors are relatively low profile and exhibit modest drift and hysteresis,[308], [309] their reliability may be of concern due to potential damage to the optical fiber or optoelectronic components during daily use and may be susceptible to electromagnetic interference [310]

Prior developments in pursuing a low-profile soft sensor have largely ignored vertical displacement associated with pistoning and downward movement at the distal end. A sensor that can detect whether pistoning or downward movement has occurred but cannot measure the severity or degree of pistoning or downward movement may limit its use in a practical sense. In addition, long-term sensor performance, reusability, and durability remain fundamental issues, as demonstrated by the lack of long-term data (in the hours to days) reported in the literature.

It must be noted that the prosthetic socket is a highly customized system; even small changes to the thickness or shape of the liner may require the prosthetist to modify the shape or profile of the socket. Therefore, it was recommended that a customizable sensor should be easily integrated into the socket fabrication workflow to afford distal-end sensing while minimizing disruption to the shape of the interface between the socket and the residual limb.

We propose a novel proof-of-concept socket sensing system inspired by soft robotics [46] at the distal end to detect and monitor the vertical displacement of the residual limb within the socket (**Figure 7.1**). The sensing system employs a novel, as far as the authors are aware, multi-layered torus-shaped balloon, or simply layered-donut balloon (LDB) to detect the undesired pistoning or downward movement of the residual limb into the prosthetic socket.

This device is intended for use within a socket that utilizes a pin-locking or vacuum suspension system. The pin lock fits through the hole of the LDB sensor. It is intended for prosthetic users who may have difficulty monitoring the health of the distal end of their residual limb due to reduced sensation. A. Schirm, prosthetist (Prosthetic Ability, Kitchener, Canada), was consulted throughout the design process. The LDB sensor was designed so a prosthetist could customize and fabricate them in their clinic without using expensive machinery. Furthermore, the device had to be incorporable into the prosthetist's workflow during socket fabrication.

The LDB sensors in this work are lightweight, inexpensive, easy to fabricate, and devoid of rigid components that interface with the residual limb. We hypothesized that the LBD sensor may detect downward movement or pistoning up to half an inch (or 12.7 mm) as specified by a prosthetist (A. Schirm) while imparting less than 20 kPa of pressure onto the distal end. Additionally, we postulate that the LDB sensor possesses adequate sensitivity to inform the user of the amount of downward movement or pistoning with negligible drift over eight hours. Furthermore, we hypothesize that an LDB with more layers at the same initial pressure can achieve greater vertical displacement while imparting less pressure onto the distal end.

In the subsequent sections, we introduce the methods and materials employed for the fabrication of the LDB and describe the testing setup utilized in our study. Following this, we delve into the results and provide a comprehensive discussion of our findings. Finally, we

summarize our research findings and offer insights into potential future directions and implications.

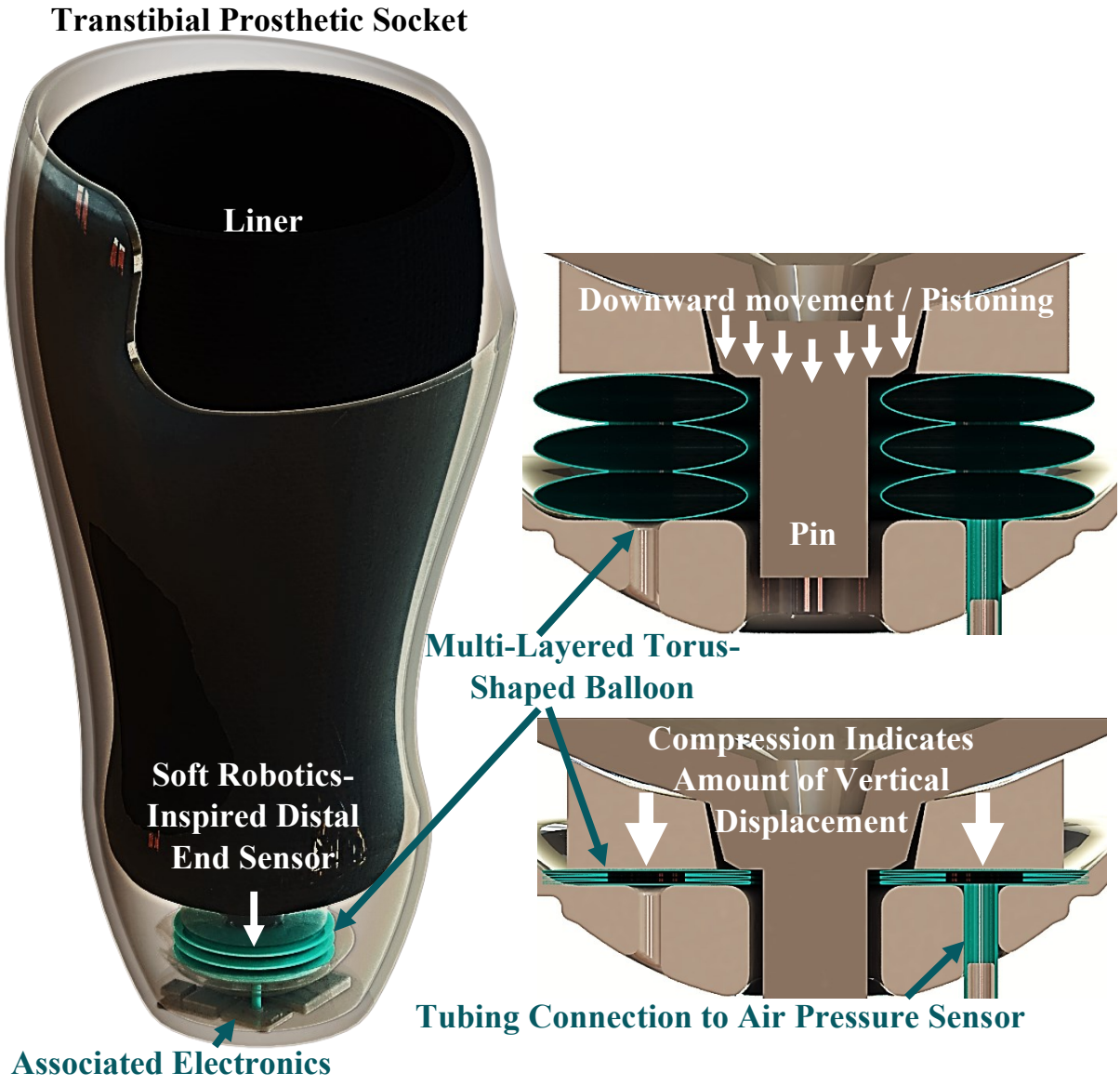


Figure 7.1: Overview of the soft robotics-inspired multi-layered torus-shaped displacement compression sensing system for detecting downward movement in prosthetic sockets.

7.2 Methods and Materials

7.2.1 Fabrication of Multi-Layered Torus-Shaped Balloon

The "frontend" of the sensing system is the LDB used for vertical displacement sensing (**Figure 7.2a, b**). A schematic detailing the fabrication process is shown in **Figure 7.2c** and an

in-depth, step-by-step guide for the fabrication of the LDB can be found in **Appendix D**. The use of Thermoplastic Polyurethane (TPU) as the main component of this device has many advantages. Firstly, elastic materials are expected to exhibit little-to-no hysteresis under low-pressure conditions, as detailed in the testing below. Secondly, the fabrication process is straightforward and does not require sophisticated technology. For example, hobbyist cutting machines (Maker 3, Cricut, South Jordan, United States) and heat presses (DK20S, Geo Knight, Brockton, United States) may be used to drive down fabrication costs and enable in-clinic production. Thirdly, small punctures or damages in LDB may be repaired by applying a small patch of TPU and applying heat and pressure, improving longevity. **Figure C.1** of **Appendix** documents the dimensions of the LDBs used for testing.

The "backend" of the sensing system (**Figure 7.2d**) consists of a fluid pressure sensor (MPRLS Ported Breakout Sensor, Adafruit, New York City, United States) and a microcontroller (Seeeduino XIAO, Seeed Technology, Shenzhen, China). The fluid pressure sensor was connected to the LDB via 1/16" inner diameter Tygon tubing (S3 E-3603, Saint-Gobain, Paris, France). A one-way pressure valve (6079T54, McMaster-Carr Supply Company, Elmhurst, United States) was used to inflate the LDB to its initial pressure for prototyping and testing purposes. A 3D-printed Polylactic Acid (PLA) holder with a thin, flat top piece protects the LDB from accidental puncture by the liner's pin. The bottom piece of the holder had a slightly raised concave lip to prevent excessive compression (**Figure 7.2e**), which may lead to lysis of the LDB.

7.2.2 Testing Setup

Mechanical benchtop testing provides a reliable method for characterizing the proof-of-concept LDB sensor before proceeding to clinical trials. All tests were performed using a UniVert tensile testing machine (CellScale, Waterloo, Canada) in compression mode with controlled displacement (**Figure 7.2e**). The LDB holders were modified to attach directly to the tensile testing machine. The UniVert machine simultaneously measures force and displacement. In total, four tests were conducted: 1) vertical displacement range, 2) precision characteristics via cyclic loading, 3) hysteresis via stair-step pattern, and 4) long-term stability assessed continuously over 24 hours. Water, as a medium, was solely subjected to the vertical displacement range test since it did not satisfy the required criteria for advancing to the

subsequent evaluations, as elaborated in the ensuing section. Conversely, when air served as the medium, all tests were completed.

For testing vertical displacement range, the space between the two surfaces of the tensile testing machine was set to 12.7 mm with an LDB placed in the PLA holder. The LDB was inflated to 12.7 mm height, indicated by a non-zero contact force with the load cell. The LDB was compressed at 0.21 mm/s (or 12.7 mm/min) until the limit of the load cell (50 N) was reached. With the majority of the weight supported by the prosthetic socket (and not solely through the sensor), coupled with the proof-of-concept scope of this study, body weight of a real user was not tested for this proof-of-concept study. Testing focused on characterizing pressure-displacement properties. Compression rate was selected to examine vertical displacement range of LDB without inducing large impulses to simulate standing or static positioning.

Displacement limits were chosen considering prior reports and prosthetist feedback. A user's perception of prosthetic suspension is significantly influenced by the displacement of soft tissue at the distal end (such as the skin) compared to by skeletal movement, like that of the tibia [311], [312]. Since the liner is in contact with the LDB, the vertical displacement of the distal end of the liner relative to the socket is used as the basis for evaluation. Eshraghi et al.'s review reported vertical movements between the distal end of the liner and the socket ranging from 0 mm to 5 mm, some extreme cases experiencing up to 16 mm of displacement [313]. Prosthetist (A. Schirm) has observed vertical movements of up to half an inch (12.7 mm). Newton et al. suggested that a vertical displacement of 10 mm or less is generally considered desirable, while displacements greater than 20 mm are often associated with symptoms and prosthetic malfunction [314]. However, there is no universally agreed-upon limit for the acceptable amount of displacement [313]. Considering all the information, the LDB sensor has been designed to detect up to 12.7 mm (half an inch) of vertical displacement. Krouskop [282] indicates that 20 kPa of continuous pressure for 2 hours is acceptable and may not lead to skin breakdown. Thus, the pressure exerted by the LDB on the distal end should remain below this threshold to ensure comfort and functionality.

For characterizing precision, 3 trials of 30 cycles of loading with a vertical displacement rate of 1.5 mm/s and displacement height of 3 mm were performed on each LDB

using the same tensile testing machine. The testing velocity was selected to accurately assess the system's performance under rapid cyclical loading, emulating users' gait patterns[315] within the limitations of the testing setup. A displacement height of 3 mm was selected, as it falls within the documented vertical displacement range of 0 to 5 mm between the liner and the socket [313]. The internal pressures were selected to investigate the impact of varying the baseline pressure, which is the minimum level required to fully inflate the LDB without exerting excessive pressure on the distal end of the residual limb.

To characterize hysteresis, the LDB was loaded in a stair-step pattern of 5 steps (i.e., 6 data points including initial baseline pressure) and unloaded in reverse order. In order to provide sufficient resolution to identify hysteresis in the system effectively, each step displacement was selected to be 0.5 mm; the load was applied for 300 seconds (or 5 minutes) before moving to the next step. Before testing, each LDB was inflated to a baseline pressure of 1.5, 2, or 2.5 kPa in the tensile testing machine (i.e., initial internal pressures were 1.5, 2, and 2.5 kPa). For long-term stability testing, each LDB was inflated to an internal pressure of 2 kPa and sat undisturbed at room temperature for 24 hours while continuously recording LDB's internal pressure, temperature (thermocouple SEN-00251, Sparkfun), and atmospheric pressure.

7.3 Results and Discussion

7.3.1 Water Versus Air

A key choice in the design of LDB is its internal fluid medium, considering both compressible and incompressible fluids. This section describes a comparison of different fluids (i.e. water vs. air) as the medium for the LDB. Initial testing revealed two important characteristics for an LDB filled with water; first, negligible hysteresis was observed by the water LDB due to the low initial internal pressure and incompressible nature of water (**Figure C.3** of **Appendix C**). These results also show that a displacement of 1 to 2 mm (i.e. approximately 1.5 mm linear full-scale span) will cause the pressure to increase beyond the acceptable range for the distal end soft tissues to bear. For example, a displacement of less than 2 mm causes the water pressure to increase above 20 kPa (**Figure C.3** of **Appendix C**), exceeding acceptable limits for risk of ulceration [282]. Due to this, the remaining testing used air as the medium for LDB.

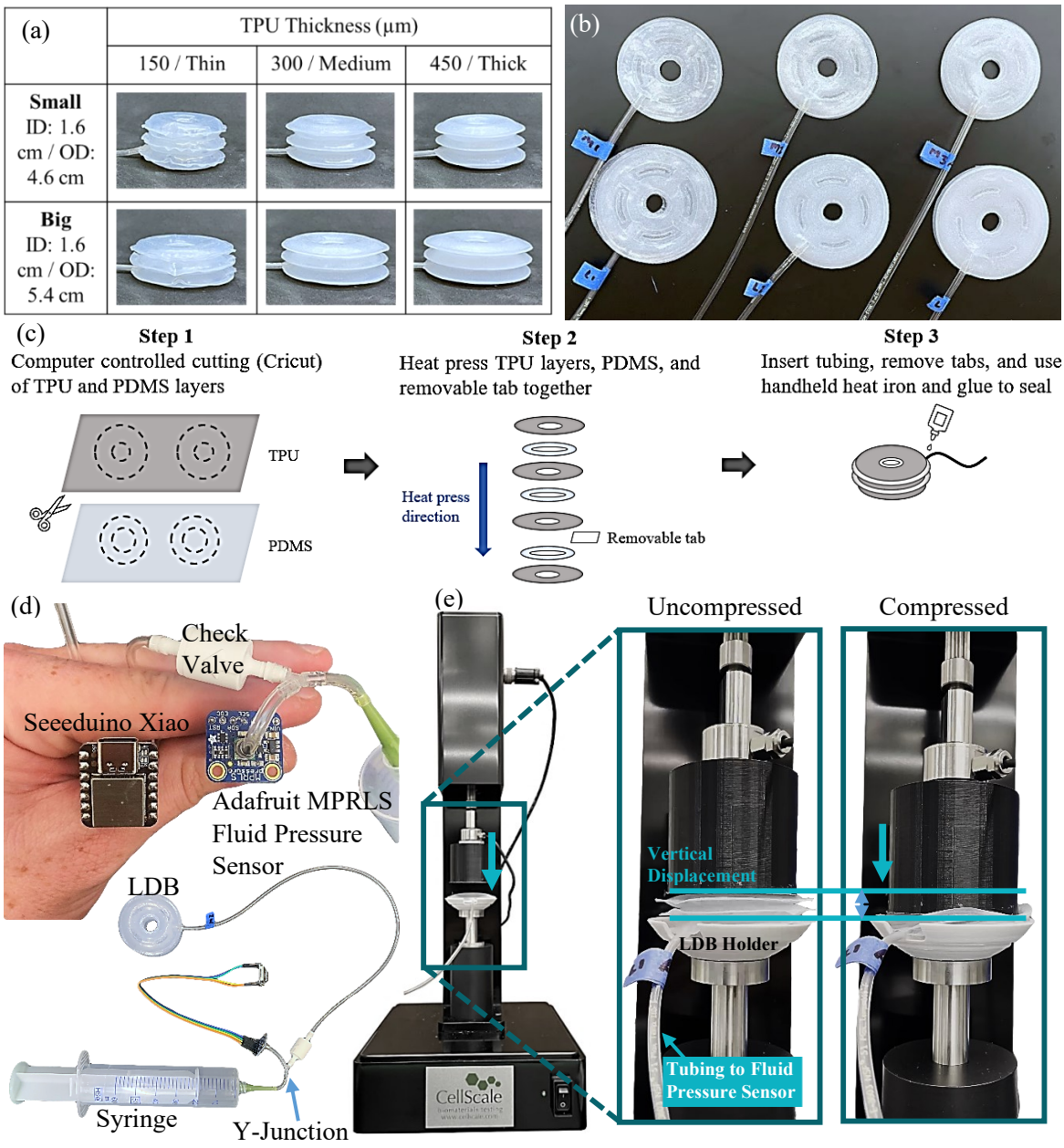


Figure 7.2: (a) The six LDBs manufactured for testing. 3 were small-sized; one from 150-micron thick TPU, one from 300-micron thick TPU, and one from 450-micron thick TPU. Big LDBs were manufactured with larger outside diameter. (b) Top-down view of the manufactured LDBs. (c) Schematic of the LDB fabrication process. The inflatable chamber was fabricated by cutting the desired shape out of 150-micron thick thermoplastic polyurethane (TPU) sheets (3916 Sewfree Thermoplastic Polyurethane, Bemis, Shirley, United States) thermally bonded with an insert of Teflon membrane (8569K36, McMaster-Carr Supply Company, Elmhurst, United States). Space occupied by the Teflon membrane inserts will expand when fluid (air or water) is displaced into the LDB. A small removable paper insert was placed where the tubing would insert into the LDB; this junction was sealed with a handheld heat iron and adhesive (Loctite 495, Henkel, Düsseldorf, Germany) once the elastomer had annealed. (d) Components of the system. (e) Testing setup.

Although preliminary tests using water in a completely sealed fluidic system indicated that the internal pressure within the LDB increases too rapidly, surpassing the safety threshold for both skin tissue and the LDB material, water may still be a viable medium in an open fluidic system. In an open system, there would be no back pressure on the LDB when compressed; therefore, the LDB would not be under any significant stress. By incorporating a device that measures hydrostatic pressure, such as a gauge, on the exterior of the prosthetic socket while fluidly connected to an LDB, users can easily monitor the pressure visually, ensuring safe operation. In an open system, it is essential to calibrate for potential water evaporation to maintain long-term pressure stability equivalent to that observed in a fully sealed fluidic system, as illustrated in **Figure C.2** of **Appendix C**.

7.3.2 Optimal Layer Count for Layered-Donut Balloons

Vertical displacement range testing was conducted to determine the optimal number of layers for LDB (**Figure 7.3**). Specifications from prosthetist (A. Schirm) indicated that a displacement of up to half an inch (or 12.7 mm) might occur in cases of severe downward movement. Therefore, a 1-layer configuration was not considered as it could not inflate to 12.7 mm height.

2-layer, 3-layer, and 5-layer LDBs were characterized and results are presented herein. A linear relationship was determined between internal LDB fluidic pressure and external distal end applied pressure (**Figure 7.3a**). The two and three-layer LDB had above 0.99 R^2 (coefficient of determination), whereas the five-layer had above 0.98 R^2. The LDB demonstrated decreasing stiffness with increasing layer count, as shown in **Figure 7.3b**. The 2-layer, 3-layer, and 5-layer LDB reached an external applied pressure of 20 kPa at 7 mm, 7.1 mm, and 7.4 mm vertical displacement, respectively. In all three cases, the applied pressure exponentially increases after 25 kPa with increasing vertical displacement after 7.5 mm.

Figure 7.3c compares difference between externally applied pressure and internal LDB fluidic pressure versus vertical displacement for the tested LDBs. The 5-layer LDB shows inconsistencies where the internal LDB fluidic pressure drops below externally applied pressure between 2.5 and 3.5 mm vertical displacement and a drastic increase in pressure difference after 5 mm vertical displacement. The 2-layer LDB consistently had a higher pressure difference than the 3-layer LDB, which shows that the 2-layer LDB was less efficient

than the 3-layer LDB (i.e., more pressure transfer loss between externally applied pressure and internal LDB pressure). Overall, considering the 3-layer LDB had a R^2 above 0.99, and was more efficient than the 2-layer LDB, with a useful vertical displacement range of approximately 7 mm, which can be considered the full-scale span (FSS) as the applied pressure at 7 mm is less than 20 kPa (the acceptable limit for risk of ulceration [282]), it was chosen for all the following testing.

While the tested LDB could not attain a 12.7 mm vertical displacement, it demonstrates potential as a proof of concept. In real-world applications, a 12.7 mm displacement may not be necessary since the sensor would likely prompt the user to wear additional socks well before reaching this threshold. Nevertheless, an FSS of 12.7 mm remains a valuable feature.

The highly non-linear relationship observed between pressure difference and vertical displacement in the 5-layer LDB (**Figure 7.3c**) could be due to the presence of the Teflon insert used to construct the internal pressure chamber of each LDB layer. The insert may inadvertently impede fluidic pathways between layers and cause uneven pressure distribution. One possible enhancement involves using a dissolvable insert, such as a polyvinyl alcohol (PVA) membrane or dissolvable paper. Should this prove feasible, it would enable the creation of LDBs with additional layers, potentially extending the useful FSS to the desired 12.7 mm (half an inch) while maintaining an applied pressure below 20 kPa (the acceptable limit for risk of ulceration).

7.3.3 Cyclic Loading and Precision

Cyclic loading testing aimed to determine the precision and performance of LDB during fast dynamic loading similar to gait. The average standard deviation of the peak pressure (the maximum pressure at each cycle) for small and big LDBs was .136 kPa/1.10% of FSS (**Figure C.6** of **Appendix C**) and .043 kPa/ 0.84% of FSS (**Figure 7.4c**), respectively. Since the fluidic pressure sensor samples at 5 Hz, it is likely able to detect pistoning during gait as the mean ambulatory velocity for individuals living with transtibial amputation is 0.85 ± 0.2 m/s and 0.99 ± 0.2 m/s for vascular and traumatic amputation, respectively [316]. The LDB (i.e. frontend) is a fluidic system that responds instantaneously; therefore, the backend's sampling rate determines the sensing system's response time. As seen in **Figure 7.4a, b**, and **Figure C.4** of **Appendix C**, the LDB showed remarkably consistent peak pressure within each trial. Box-

whisker plots of the peak pressure for each trial (**Figure 7.4c**) show that the LDB was precise and did not fail under cyclic loading, which may be experienced within a prosthetic environment due to pistoning during gait.

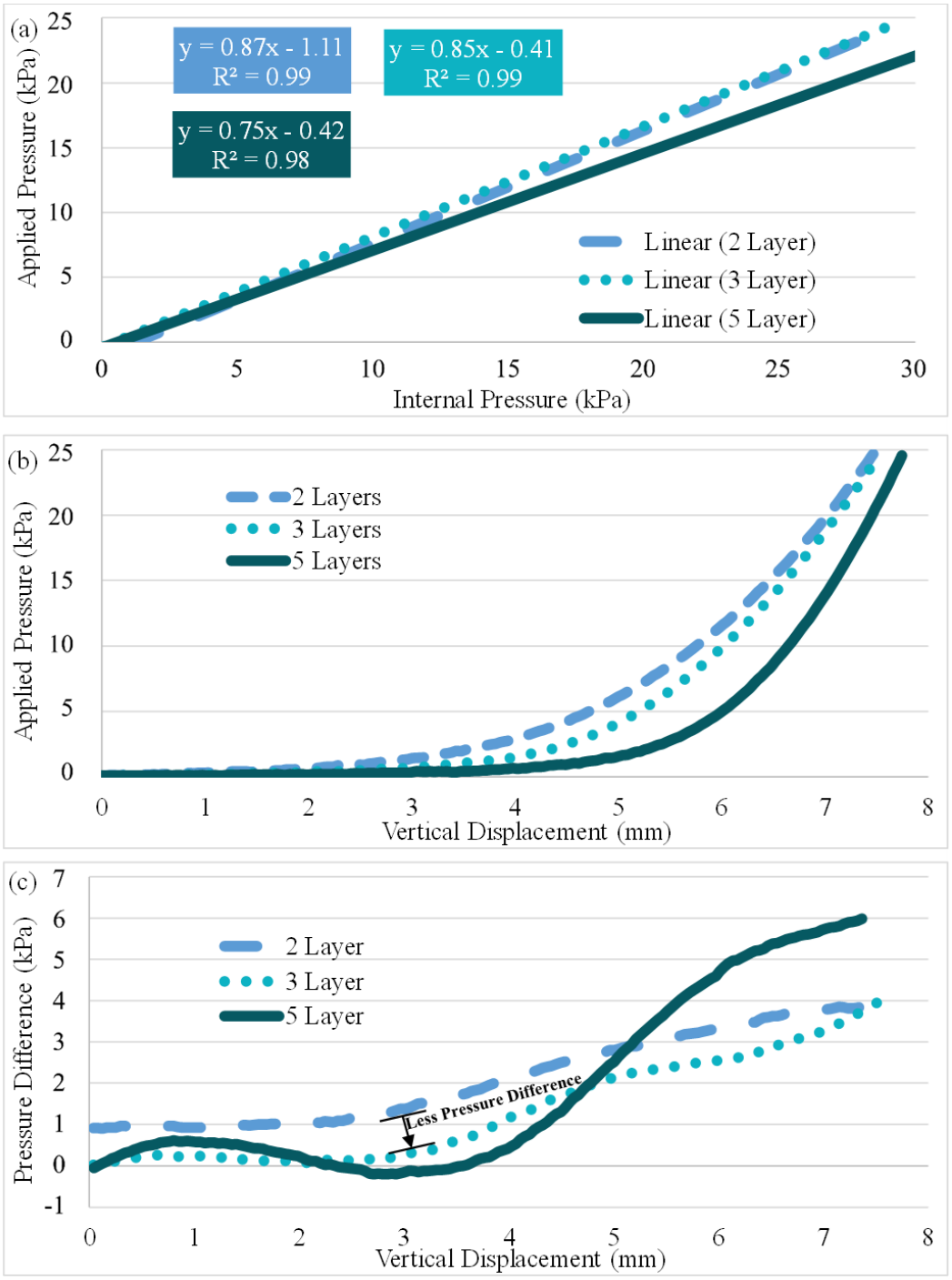


Figure 7.3: Results from vertical displacement range testing to characterize the effect of layers on LDB: (a) linearity plot. (b) Applied pressure vs. vertical displacement plot. (c) Pressure difference between internal and applied pressure vs. vertical displacement plot.

The smaller the size of the LDB (**Figure 7.4a, b**), the thicker the wall of the LDB (**Figure 7.4c**), and the higher the LDB's initial internal air pressure (**Figure 7.4c**), the more the pressure will increase when the displacement range and displacement rate were kept constant. An ideal sensor that measures the amount of pistoning and downward movement would minimize imparted pressure/applied reaction force to the distal end to avoid discomfort and tissue breakdown. Therefore, it was evident the best LDB with the most precision while imparting the least amount of applied reaction force was the big-thin LDB initialized to 1.5 kPa internal pressure.

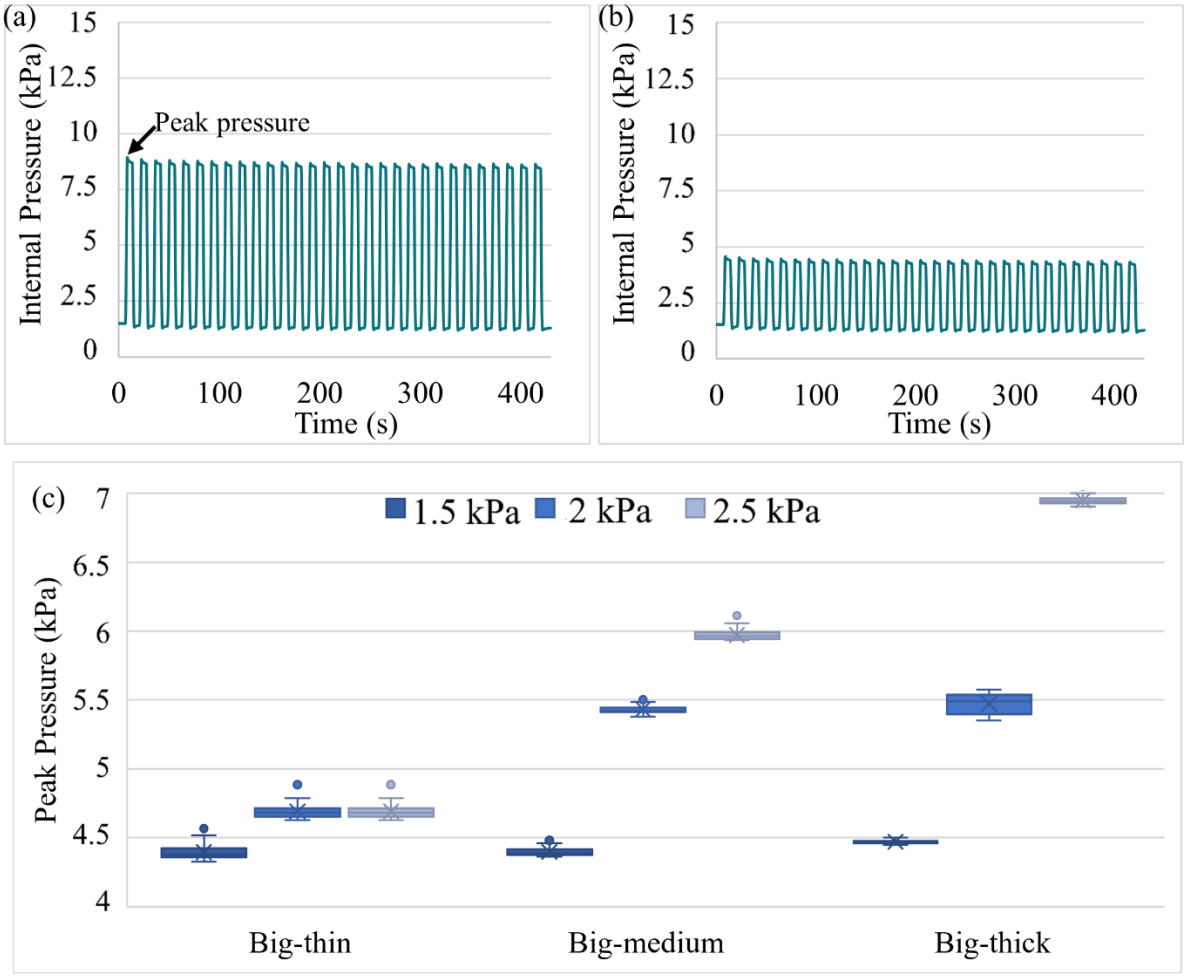


Figure 7.4: Cyclic loading testing results: (a) Plot for the small-thin LDB. (b) Plot for the big-thin LDB. (c) Box and whisker plot showing precision of peak pressure from cyclic-loading tests for all big 3-layer LDBs.

7.3.4 Step-Loading, Hysteresis, and Long-Term Stability

The step-loading testing (**Figure 7.5a, b**, and **Figure C.5** of **Appendix C**) and its corresponding hysteresis testing (**Figure 7.5c** and **Figure C.6** of **Appendix C**) were used to simulate the performance of LDB when the downward movement is gradual throughout the day. Neither small nor big LDBs experienced significant hysteresis. Less than 0.1 kPa difference was detected over 5 minutes at each step hold (0.5 mm), confirming a repeatable resolution of at least 0.5 mm. In addition, a sensitivity of 0.8 kPa/mm (i.e. 0.8 kPa internal air pressure change per 1 mm of measured vertical displacement) was characterized. Hysteresis for all LDBs was minimal at an average of 2.84% of FSS with a standard deviation of 1.48% of FSS. LDBs that were bigger and with thicker walls exhibited slightly more hysteresis than smaller LDBs with thinner walls, which may be explained by the thicker material and increased total area under tension, which causes more energy loss due to internal friction and hoop stress.

Long-term stability testing at a low initial internal pressure of 2 kPa showed that LDB fluctuated at most 0.15 kPa/4% of FSS throughout 24 hours. Ambient pressure influenced the LDB stability, as shown in **Figure 7.5d**, with a linear fitting R^2 value of 0.83 (**Figure 7.5e**). **Figure C.7** of **Appendix C** shows the remaining long-term stability testing and ambient temperature during testing. The fluctuation due to ambient pressure was considered negligible as the increase in pressure due to vertical displacements that exceed 2 mm was much higher than 0.15 kPa. The effect of environmental temperature changes and more considerable atmospheric pressure changes due to elevation were outside the study's scope.

7.3.5 Limitations

Several limitations should be considered, given the proof-of-concept study only focused on LDB characteristics. While effective for initial validation, the testing apparatus cannot fully simulate human gait. Firstly, it cannot create the residual limb's bell-clapping motion (horizontal movement). The residual limb and the liner are soft and compliant; however, the testing apparatus's surfaces contacting the LDB were rigid. Compliance of the interface was missing during this study and may heavily influence measurement noise and confidence. Lastly, the LDB itself cannot reach half an inch (12.7 mm) vertical displacement without imparting pressure/applied reaction force too high to be considered safe onto the distal end of the residual limb. One solution may be adding a pneumatic capacitor to the system, reducing

its stiffness. Further bench testing, case studies, and clinical trials will need to be conducted to determine the efficacy of the LDB sensor during real-world use.

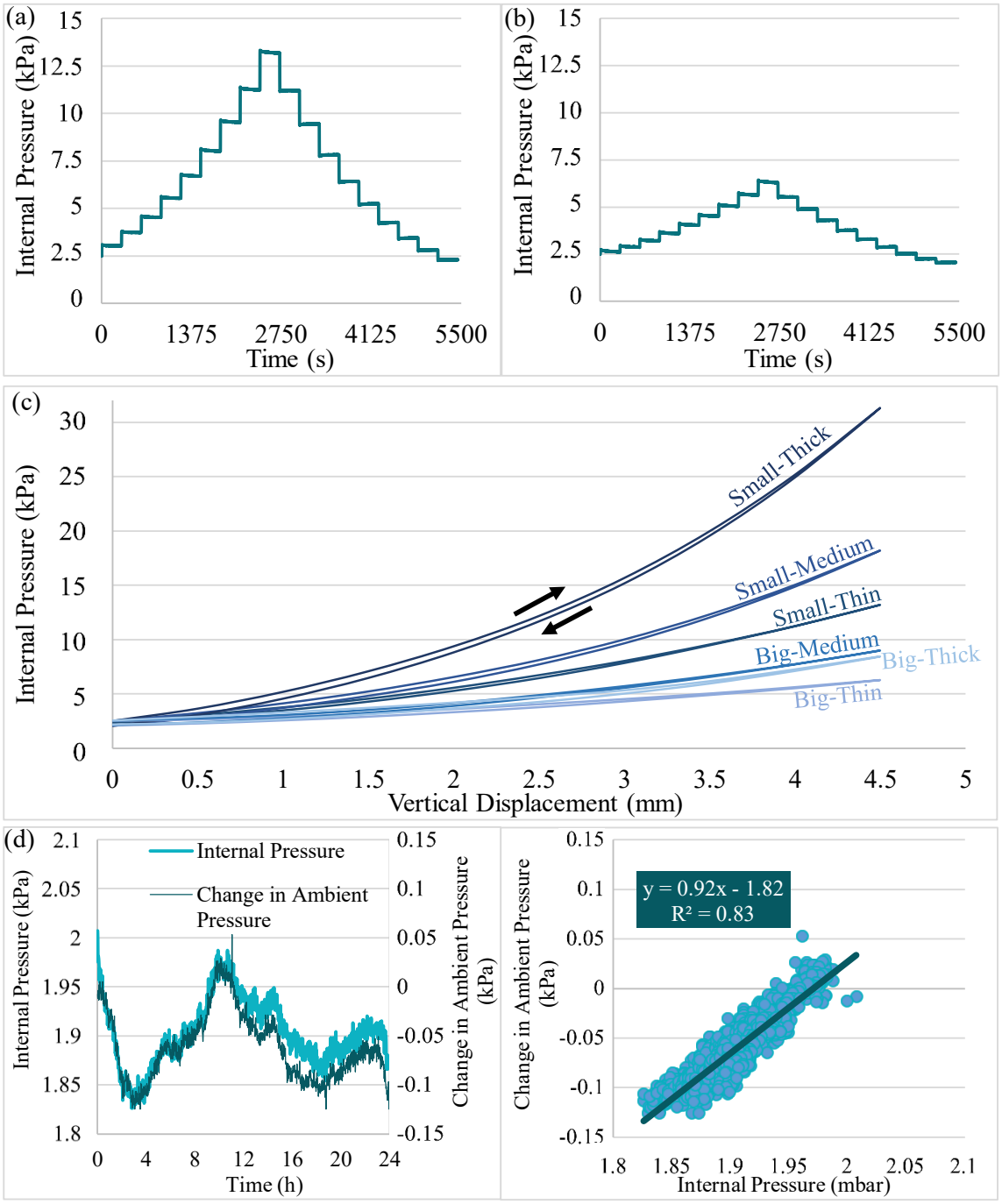


Figure 7.5: (a) Step-loading of the small-thin LDB. (b) Step-loading of the big-thin LDB. (c) Hysteresis results for all 3-layer LDBs derived from step-loading tests. (d) Long-term stability for small-medium LDB over 24 hours at room temperature showing internal air pressure of LDB and change in ambient pressure. (e) Change in ambient pressure versus internal air pressure of LDB during long-term stability testing.

7.4 Conclusion and Future Work

In this chapter, a novel soft robotics-inspired multi-layered torus-shaped balloon sensor to measure the downward movement of the residual limb within a socket was designed, fabricated, and characterized. The sensing system exhibited promising initial benchtop testing results and can be fabricated without expensive equipment and materials.

In the near future, the control box will be manufactured and made portable with the implementation of a battery and Bluetooth microcontroller. This will allow for the device to be used in case studies involving TTP users.

In the more distant future, there are many possible ways to augment the design of the sensor. A balloon that exhibits complex 3D geometry that follows the contour of the residual limb would allow for multi-directional sensing.

Chapter 8

Investigating Miniaturization of Control System for Dynamic Knee Brace Using Gait

Part of the work included in this Chapter is submitted to journal: A. Johnson[1], **R. Z. Gao[1]**, K. Marriott, C. R. Dickerson, M. R. Maly, and C. L. Ren, "Electronics-Free Soft Robotic Knee Brace for Dynamic Unloading During Gait for Knee Osteoarthritis," *Journal of Medical Devices*. Run Ze Gao conceived the idea. The device fabrication and experimental procedures were collaboratively undertaken by Amanda Johnson and Run Ze Gao. Amanda Johson and Run Ze Gao collectively authored the manuscript.

[1] Contributed equally to this work.

8.1 Introduction

Osteoarthritis (OA) is a leading cause of pain and disability globally [317], placing a substantial burden on both individuals and society due to its large impact on limiting mobility [318], [319]. OA is a dynamic disease involving a complex interplay between multiple mechanical and biological processes that includes an imbalance between joint repair and damage, leading to changes in multiple joint structures, including but not limited to a progressive loss of articular cartilage [21]. Although no longer considered as only a 'wear and tear' disease, aberrant loads across the joint influence the development and progression of OA, impairing joint-level structure and function, leading to pain, inflammation, muscle weakness, and disability [320]. Several identified important and modifiable risk factors for the development and progression of knee OA include limb malalignment [321], altered gait biomechanics [322], muscle weakness [323], and previous joint trauma [324]. For individuals with varus malalignment of the lower limb ("bow-legged"), deviations in the loading axis (alignment of the hip, knee and

ankle) are associated with an increased external adduction moment (KAM) about the knee and increased loads on the medial tibiofemoral compartment [325], [326]. Evidence suggests a positive relationship between the development and progression of medial tibiofemoral OA with both varus malalignment [321] and a greater KAM [327]–[329]. Although the rate of progression varies by individual, the frequency and severity of symptoms associated with knee OA increase with age, becoming more debilitating over time [330]. Currently, knee OA affects about 240 in 100,000 people worldwide, specifically 13% of women and 10% of men 60 years and older [331]. The prevalence of knee OA is highly associated with age and body weight [320] and thus, is expected to increase alongside rising global life expectancy and obesity rates [332].

Several non-pharmacological and non-surgical treatments aim to modify known risk factors for knee OA. Evidence-based clinical guidelines strongly recommend education, exercise, and weight loss with adjunct biomechanical interventions, such as knee bracing, to address changes in the joint's biomechanical environment [333]–[335]. While these strategies do not currently stop the development or progression of knee OA, they aim to ease the burden of OA and improve OA-related symptoms, which directly affect an individual's well-being and quality of life [336]. As the condition progresses and non-invasive approaches lose effectiveness, more expensive and invasive interventions, such as surgery, injections, and non-steroidal anti-inflammatory drugs (NSAIDs) are considered. Surgical options for knee OA include osteotomy, arthroscopy, and arthroplasty [337]. However, long surgical wait times and, in some cases comorbidities (significant heart and vascular diseases) or risk factors (age and weight) may limit the approval and success of surgery [338]. While effective in pain relief, NSAIDs are often restricted for individuals with age-related comorbidities such as high blood pressure, heart disease, and kidney disease [339]. The chronic nature of knee OA places a tremendous burden on the individual and healthcare system to support elective surgeries, post-surgical care, medication, and rehabilitation [340].

Assistive wearable devices such as knee braces can be effective, non-invasive, and relatively affordable options for the daily management of knee OA [341]. For knee OA, unloader-type knee braces are often recommended [342]. Unloader-type knee braces shift the load of the body away from the affected knee compartment [343]. Unfortunately, while these braces effectively mitigate and improve knee OA symptoms, over 20% of individuals abandon

their usage during the first six months of treatment due to reasons including: inadequate pain relief, issues with donning and doffing, and leg swelling [344]. Typically, unloader-type knee braces are constructed from metal and rigid thermoplastic. While such materials can provide sufficient offloading, these braces are rigid, non-conforming, and minimally adjustable [345]. The bulky design, uncomfortable fit, constant pressure, and lack of aesthetic appeal are all considered to be contributors to low user compliance [344], [346].

Recent advancements in knee braces have seen the use of pneumatic systems, which enable unloading with increased comfort and conformability compared to rigid offloading methods [347]–[349]. These systems can be passive or active. In passive systems, the air bladders are pressurized prior to use and remain at constant pressure through wear [350]. In active systems, the bladders are dynamically pressurized and depressurized by an additional control mechanism [105]. While active systems can better align with an individual's gait and provide improved results over passive systems, the associated control mechanism adds undesirable weight and bulkiness, which may deter compliance [351]. In the subsequent section, we delve into the reasons why active systems fall short in fulfilling the requirements of a dynamic unloading brace designed to combat knee osteoarthritis.

8.2 Disadvantage of Active Controlled Systems

In our initial research, we conceived and developed an advanced, active control knee brace, equipped with air microfluidics to facilitate dynamic knee unloading [105]. The engineering of this active knee brace revolves around the principal feature of dynamic unloading, achieved through a three-point leverage system [105]. As an additional advantage, the brace incorporates dynamic zonal compression, augmenting proprioception and stability [352]. The amplification of proprioception and stability is well-documented to alleviate pain associated with knee osteoarthritis [353].

The active knee brace's hardware is separated into two portions. The first of which is the control box, which contains the air pump, mini solenoid valve, pressure sensor, microcontroller, and batteries. The control box provides a pneumatic pathway and a signal pathway, as schematically depicted in **Figure 8.1a**, to and from the air microfluidic chip and the inertial measurement unit (IMU), respectively. **Figure 8.1b** shows an early design rendering of the control box, the dimension of which is shown as well. The approximate location on the

human lower extremity and the relative size compared to the human lower extremity of the control box, air microfluidic chip, and IMU are shown in **Figure 8.1c**. The control box is made out of a tough elastomer with flow channels built-in connecting to the air pump, the mini solenoid valve, and the pressure via squeeze fit. Both software and hardware safety features are implemented to ensure that all the components function according to their manufacturer's specifications.

The second hardware portion consists of the balloon actuator arrays, the fabrics, the strain limiting layer, and the air microfluidic chip. The active knee brace is designed based on the classical idea of the three-point leverage mechanic as seen in **Figure 8.1e**, where the forces are applied to the lateral side of the knee and the medial side of the shank and thigh to creating an external abduction moment at the knee to offset the external adduction moment which is associated with the progression of the medial tibiofemoral OA.

The active unloader knee brace uses arrays of small and low-profile air-filled balloons positioned on the body in a pattern that provides the highest level of three-point leverage and pain-relief while not impeding normal gait as seen in **Figure 8.1d**. The balloon arrays are more advantageous over the large balloon as they mimic the same amount of compression while distributing the force over a larger area to minimize concentrated pressure and shear on the user's leg. Besides, the small volume allows for fast actuation at the millisecond scale, allowing for dynamic compression during the gait cycle. Each balloon actuator is connected to a mini tubing with an inner diameter of 500 μm and an outer diameter of 1 mm. All balloon actuators connect to a microfluidic chip, which acts as a wearable pneumatic manifold for the distribution of the air pressure into each balloon actuators in under 250 milliseconds while providing a controlled depressurization sequence (i.e., which balloon actuators to deflate first, second, third and so on and at what deflation rate). A single tubing connects the microfluidic chip with the control box.

The strain limiting layer, a concept from soft robotics, made from elastomers direct the compression inward while limiting the expanding volume of the balloon actuators, as seen in **Figure 8.1f**. The strain-limiting layer is shaped in a way that encompasses all the balloon actuators and acts as the medium for force transmission to enable three-point leverage. There

are two layers of fabric, a skin-contact inner layer and a strain-limiting outer layer with the mini-balloon actuator array sandwiched in-between.

The user defines the base pressure, the max pressure, as well as the sequence of the deflation. The rate and the sequence of the deflation are controlled by the geometry of the exhaust microchannels within the air microfluidic chip, which is tailor-made for each user. During the inflation cycle, both the air pump and the solenoid valve work in unison to inflate the balloon actuators from the base pressure to the max pressure. During the deflation cycle, the solenoid valve opens to deflate the balloon actuators. Both the air pump and the solenoid valve are on-off controlled, with feedback from a pressure sensor. The pressure within the air bladders is slightly different from the pressure at the air pump; however, the differences should be minimal. To avoid oscillation at the set pressure due to air pump and solenoid valve constantly turning on and off to reach an exact pressure, an acceptable range of pressure from the set pressure is prescribed and the sampling frequency of the pressure sensor is capped at an appropriate level to accommodate the on-off control scheme.

Preliminary trials of the prototype active knee brace (**Figure 8.2a-e**) have exposed significant challenges associated with an active, battery-powered pneumatic knee brace. The main bottleneck originates from the control box. Despite the relaxation of requirements to allow for a 500 ms inflation phase and a 500 ms deflation phase (not factoring in any sensor delay in identifying different gait phases), as opposed to the 250 ms required for gait synchronization [283], the force exerted onto the knee is minuscule. It proves insufficient to meaningfully unload the knee. As **Figure 8.2f** demonstrates, the inflation phase barely manages to increase pressure beyond 40 mbar / 4 kPa, which is less than substantial. Furthermore, the deflation phase fails to completely release all the pressure, not reaching zero as required.

Though a larger control box featuring a more robust air pump for inflation and a stronger solenoid valve for deflation could meet the desired 250 ms inflation and deflation timeframes and reach pressure levels suitable for knee unloading, around 500 mbar or 50 kPa [26], its size and weight would significantly surpass the predetermined acceptable limit of approximately 250 grams. This is a crucial factor considering the wearability and comparable dimensions of a typical smartphone in 2023, the year of this thesis' publication. It is projected that a control box

capable of inflating to an internal pressure of 500 mbar in under 250 ms would weigh nearly 1 kg, a figure that is simply unviable.

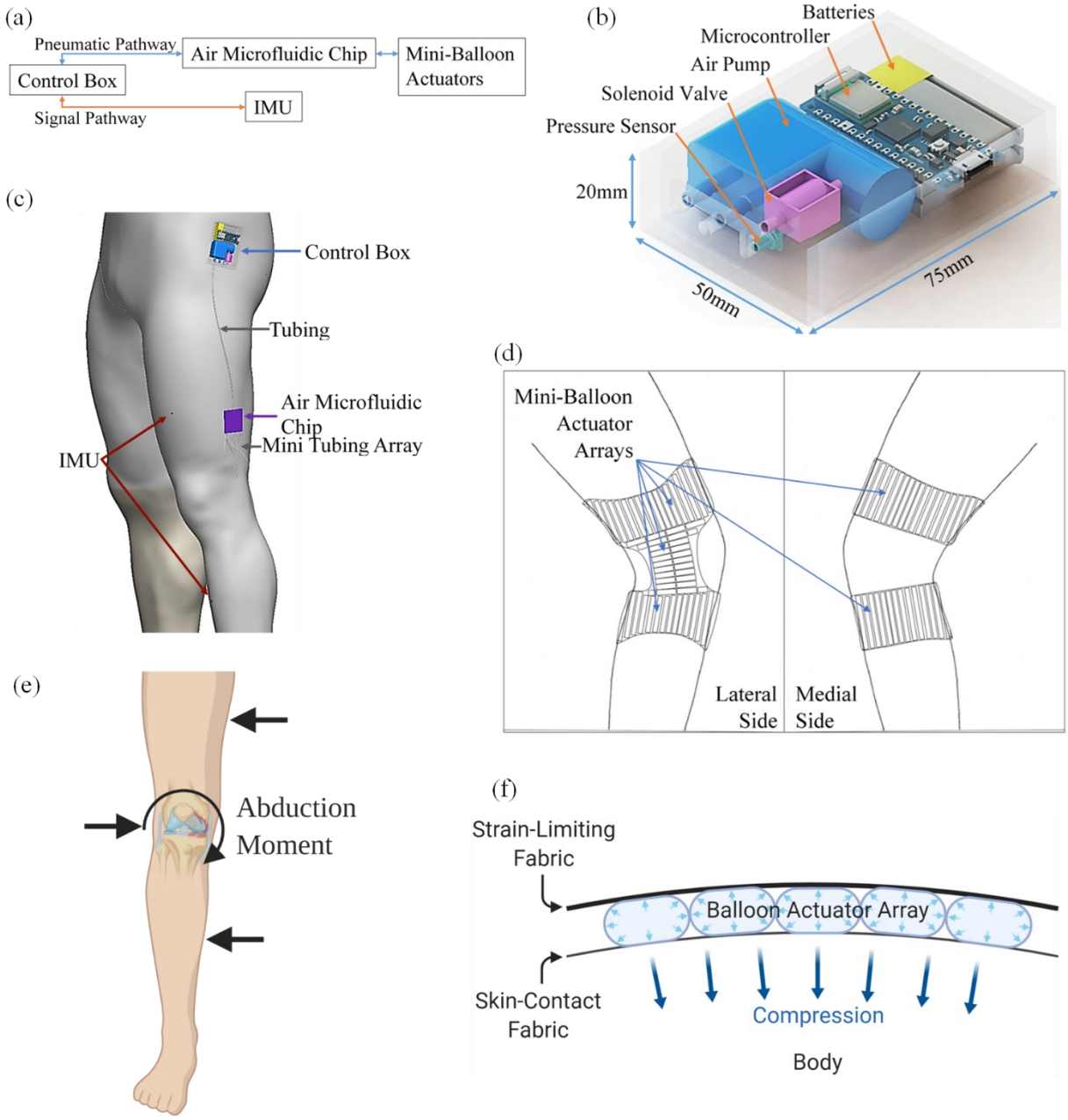


Figure 8.1: (a) Pneumatic and signal pathways between components. (b) Preliminary rendering of the control box. (c) Approximate locations and sizes of the components associated with the control box. (d) Design of the knee brace. (e) Schematic of the three-point leverage mechanism. (f) Conceptual schematic of the mini-balloon actuator array.

If the aforementioned challenges are not substantial enough, another significant bottleneck lies in the necessity for a reliable and consistent sensor to identify the precise

moments of heel strike and toe-off. The detection of these instances is critical to initiate the inflation and deflation sequences, respectively. However, accomplishing this is far from a simple task. One possible approach, as illustrated in **Figure 8.1c**, is to use an Inertial Measurement Unit (IMU) to identify the thigh and shank angles, thereby determining the individual's position within the gait cycle. Regrettably, this method is not entirely dependable, and issues like sensor drift could introduce complications.

An alternative strategy might involve integrating a force sensor within the shoe to detect when the heel makes contact with the ground and when the toe disengages. Nevertheless, this solution comes with its own set of hurdles such as sensor durability and the practical constraint of routing wiring or maintaining a wireless sensor's battery charge within the module. Furthermore, any delay in processing the sensor signal or executing the control algorithm could erode the already limited time available to actuate the balloon actuators. These complexities add to the litany of challenges faced in the design of an effective active knee brace.

The third, and rather unexpected, bottleneck surfaced during the prototyping phase of the active knee brace. Due to the integration of feedback sensors, balloon actuators, and a control box, the need arose for a highly customized or modified knee brace, as depicted in **Figure 8.2a-e**. This requirement not only complicates the fabrication process, but it also inflates the cost due to the inclusion of various electronic components and hardware. This increase in price could potentially place the active knee brace beyond the affordable range for many potential users. Moreover, many individuals already have preferred knee braces, some even owning several varieties for different days or activities. As such, these users would likely prefer to modify their familiar and comfortable existing knee braces to incorporate active features, rather than invest in an entirely new and different model. Thus, the cost and the personalized nature of knee braces present another significant challenge to the wider acceptance of the active knee brace design.

Consequently, the aforementioned challenges prompted us to reassess our design strategy for the dynamic knee brace. The critical necessity to further miniaturize the control box, while still maintaining the rapid response time and power necessary to actuate the unloading mechanism at levels effective for managing osteoarthritis, became evident. Additionally, the system needed to be more robust, cost-effective, and reliable. This led us to

develop a system devoid of electronics, instead controlled by the human movement itself, such as gait. The result is a purely mechanical system that remains active. We detail this innovative design proof of concept and the results of our initial testing in the subsequent sections of this chapter.

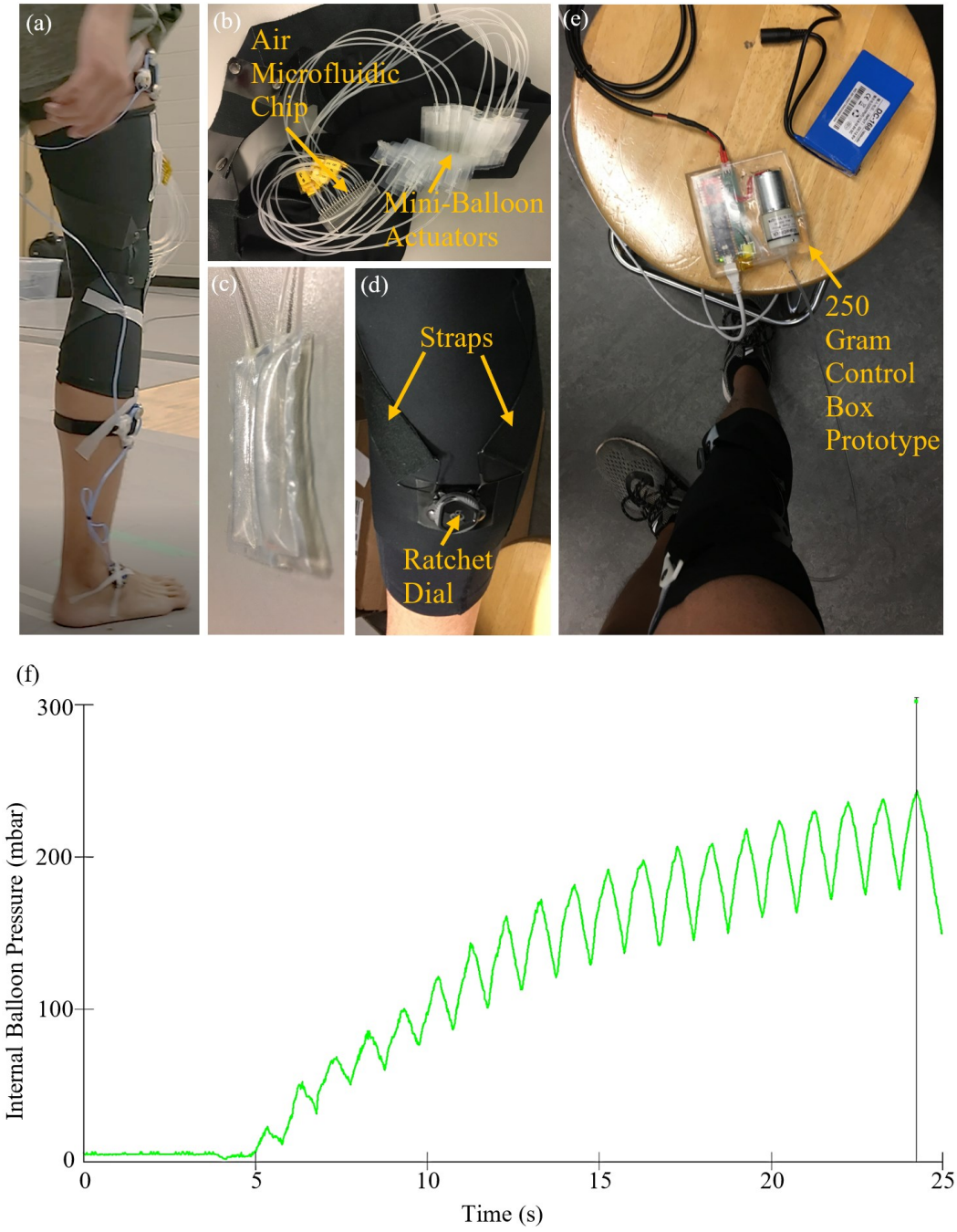


Figure 8.2: (a) A prototype of the knee brace described herein. (b) Showing the air microfluidic chip acting as a manifold and mini-balloon actuators deflated. (c) Mini-balloon actuators inflated before elastic deformation. (d) Showing force transmission straps and ratchet dial for

tightening the straps. (e) Control box prototype. (f) Initial testing result of the internal air pressure of the balloon as measured by air pressure sensor.

8.3 Design Rationale

This proof-of-concept study presents a novel electronics-free active soft robotic knee brace enabled by closed-loop fluidic regenerative (CLFR) system for dynamic unloading in unicompartmental tibiofemoral OA (**Figure 8.3**). The CLFR system is hermetic, self-power harvesting and purely mechanical, naturally synchronizing to the user's gait without the use of sensors or electromechanical components.

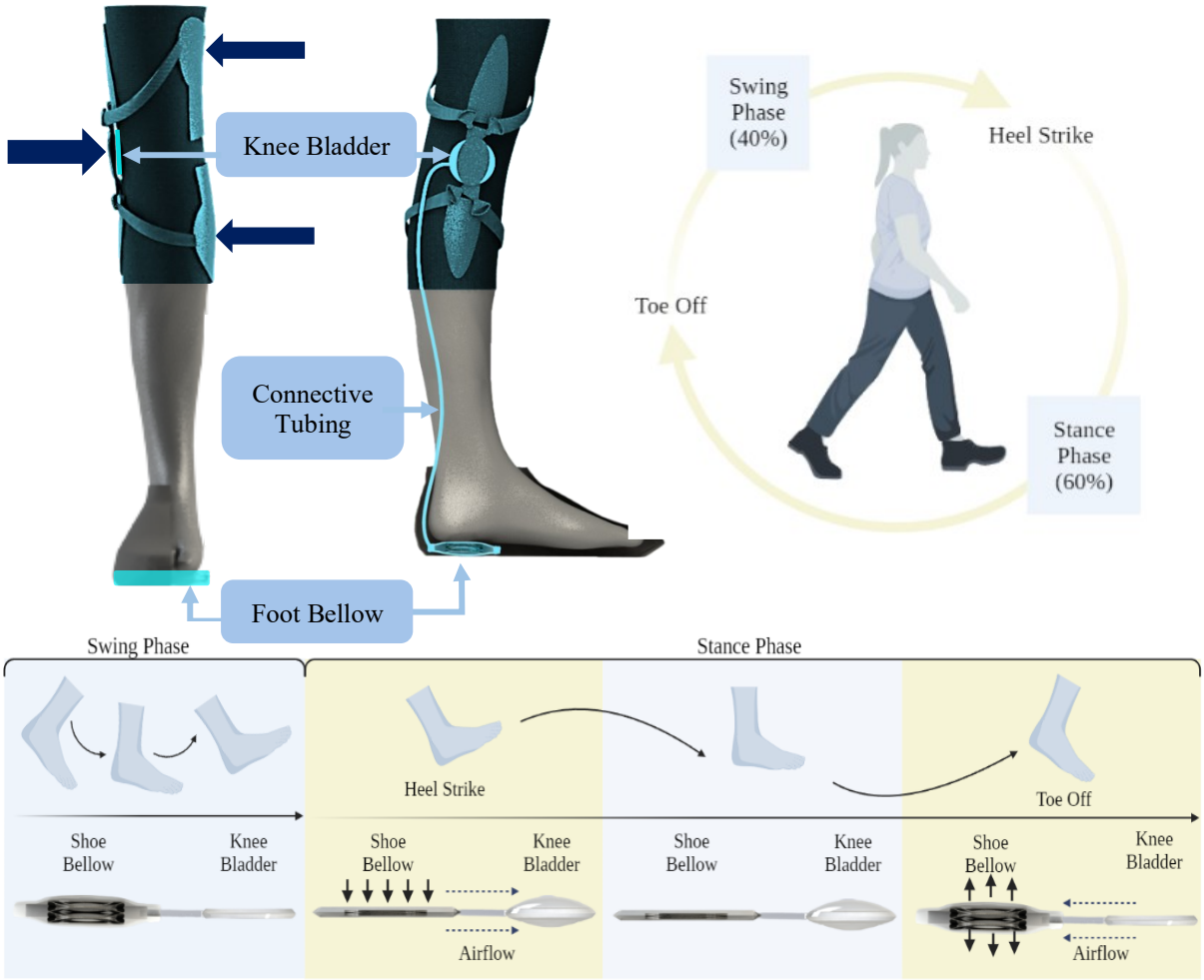


Figure 8.3: Electronics-free soft robotic knee brace enabled by CLFR system. The top left image shows the low-profile CLFR system enabling dynamic three-point bending aimed to counteract the external knee adduction moment (KAM). The top right schematic shows the two critical moments in CLFR pressurization and depressurization control using the user's own body weight and gait: heel strike and toe off. The bottom schematic shows the behavior of the

foot bellow and the knee bladder and the direction of airflow between the two during the stance phase, thus providing unloading pressure only during weight-bearing (i.e., stance phase).

The novel concept of harvesting energy utilizing the user's body mass during the stance phase was inspired by the work of Chin and colleagues, Hirai and colleagues, and Takaiwa and Noritsugu on pneumatic power harvesting for ankle-foot orthoses [354]–[356]. The aforementioned work utilized the pneumatic power harvested during gait to actuate a cam-follower locking mechanism, thus controlling ankle motion to manage foot drop [355]. The CLFR system uses a similar method of power generation via the compression of a bellow; however, there are several key modifications. First, Chin et al. focus on power harvesting during the load-bearing phase of gait with actuation or power usage during the swing phase [355]. In contrast, the CLFR system initiates power harvesting starting with heel strike and utilizes the collected power instantaneously for the duration of the stance phase. Second, Chin et al. present a compact design targeting the ankle and foot with additional fluidic valves for exhausting or drawing fluid from the external atmosphere [355]. In contrast, the CLFR system focuses on an energy harvesting bellow capable of powering an elongated hermetic closed-loop pneumatic or hydraulic system extending from the heel to the mid-line of the knee. The novel hermetic closed-loop system reduces mechanical complexity, thus increasing reliability and preventing unwanted particles such as dirt and dust from entering the pneumatic system. Third, Shveda et al. use a textile-based pneumatic energy harvesting system for soft assistive robotics, where additional components such as valves and energy storage components are used, which is effective in creating motion and torque via soft robotic actuators for upper extremity applications [357] rather than gait and hermetic closed-loop design as presented herein. In summary, according to the authors' best knowledge, for the first time, a wearable electronics-free hydraulic system is achieved via a hermetic closed-loop design.

The CLFR system is composed of four essential components. Firstly, it includes a unicompartmental tibiofemoral unloading brace, with the Medi M2 Active OA Light Knee Brace (Medi GmbH & Co. KG, Bayreuth, Germany) featured in this study. Secondly, a foot bellow positioned beneath the user's heel and arch enables dynamic pressurization at heel strike and depressurization at toe-off for the knee bladder (**Figure 8.4a**). Thirdly, the system features a soft fluidic actuator in the form of a single bladder, situated at the knee joint line on the lateral side. This component effectively unloads the affected medial compartment by applying an

opposing force to the KAM during the stance phase of gait (**Figure 8.4b**). Moreover, the foot bellow also serves to dampen the impact at heel strike, potentially reducing abnormal kinetics during weight-bearing activities. Lastly, small-diameter tubing facilitates the transfer of fluidic energy, in the form of air or water pressure, between the connected foot bellow and knee bladder (**Figure 8.4c**). The CLFR system's modular design allows for integration with any existing knee brace while maintaining a low-profile, cost-effective manufacturing process, and high reliability. The proof-of-concept validation explored herein will investigate the ability of the CLFR system to maintain safe contact pressure values at the knee [282], achieve desired inflation and deflation response time to minimize KAM, and assess the reliability and durability of the system concerning energy loss and cyclic-loading.

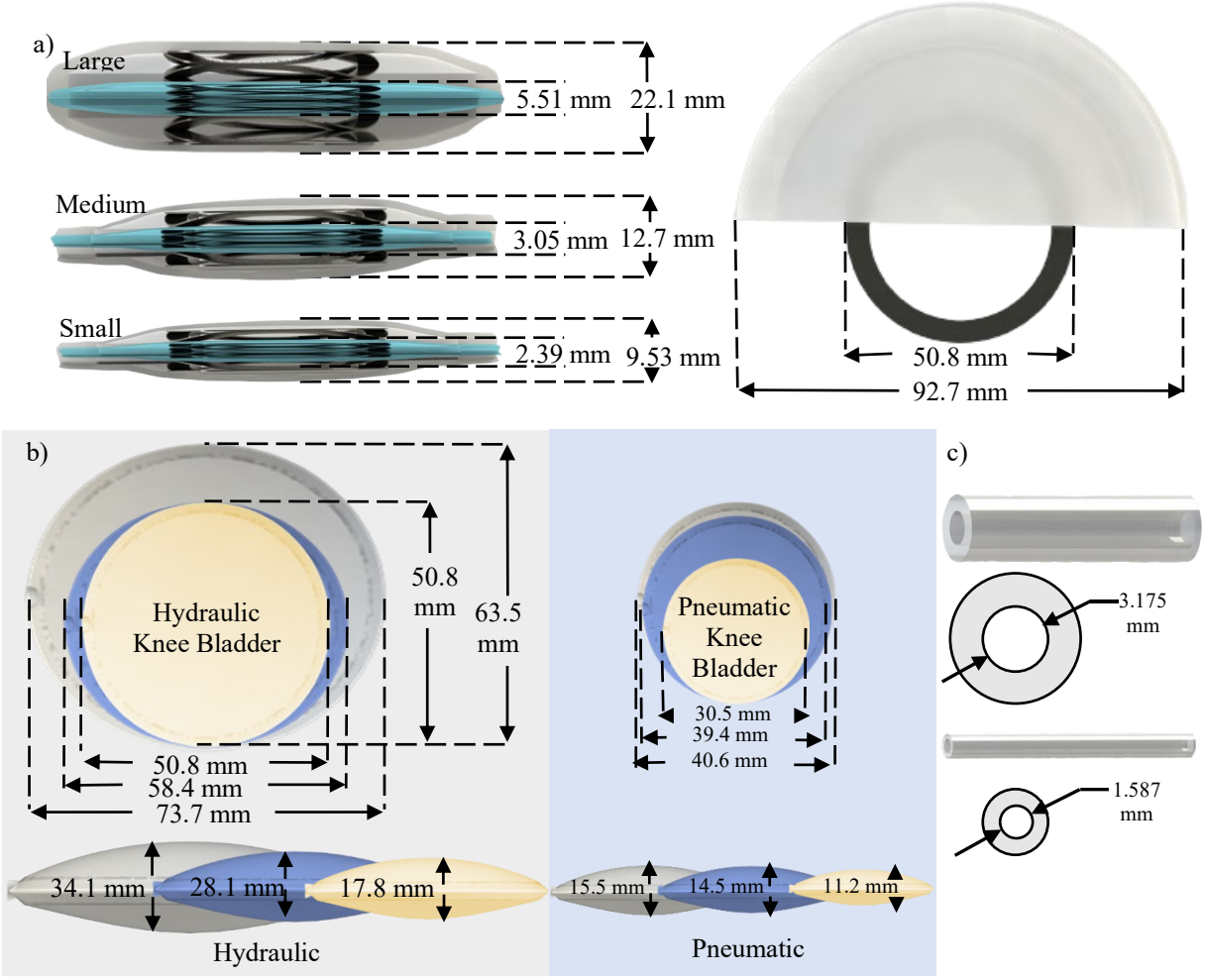


Figure 8.4: Components of the closed-loop fluidic regenerative system. a) Three bellow sizes used during experimentation varied by spring properties. The gray outer model represents the height of each foot bellow in the relaxed state, and the cyan inner model represents the height

of each foot bellow in the compressed state. Each elastomer shell and spring's diameter were kept constant at 92.7 mm and 50.8 mm, respectively. b) Dimensions of each knee bladder used in each evaluation prototype system. The bladders on the left were used for the hydraulic prototypes, and the bladders on the right were used for the pneumatic prototypes. The yellow bladder was paired with the small foot bellow (9.53 mm relaxed height), blue with the medium foot bellow (12.7 mm relaxed height), and gray with the large foot bellow (22.1 mm relaxed height). c) Connective tubing between foot bellow and knee bladder. 1.587 mm ID used for pneumatic systems and 3.175 mm ID used for hydraulic systems.

8.4 Methodology

8.4.1 Fabrications

The CLFR system design emphasizes elegant simplicity and modularity. The foot bellow employed features a circular shape and measures 92.7 mm in diameter, based on the heel size of a US men's size 8 Nike Air Max shoe (Nike, Inc., Beaverton, United States). This particular shoe model was chosen for sizing purposes, as its midsole comprises a rigid air bladder, which could potentially influence future versions and integrations of the CLFR system. The circular shape was selected to maximize heel contact and streamline the fabrication process. Similarly, the knee bladder also adopts a circular shape, with its diameter varying in accordance with the volume of the connected foot bellow.

The foot bellow was fabricated following the process outlined in **Figure 8.5** and **Figure E.6** of **Appendix E** using Bemis 3916 SewFree® (Bemis Associates Inc., Shirley, United States) Thermoplastic Polyurethane (TPU) and corrosion-resistant high-carbon steel stacked wave disc springs (McMaster-Carr Supply Company; Models 3726N359, 3726N357, 3726N356, Elmhurst, United States). The TPU sheets were cut into 20 circles and 30 rings matching the desired dimensions (specified in **Figure 8.4b**). The TPU circles were divided and stacked to form two 10-layer circles, while the 30 rings were stacked to create one 30-layer ring. The three components were then individually heat pressed at 110 ℃, each circle was pressed for 30 seconds, and the ring was pressed for 90 seconds. Following heat pressing, the desired disc spring was placed in the center of one of the two TPU circles. The TPU ring was then centered around the spring, and the second TPU circle was placed on top, encasing the spring. The bellow was then heat pressed at 70 ℃ for 10 minutes.

The knee bladder was fabricated using the same 150-micron thick TPU as the foot bellow and 75-micron thick Teflon® polytetrafluoroethylene (McMaster-Carr Supply

Company; Model 8569K36) as an insert. The TPU and Teflon were cut to the desired dimensions to create four TPU circles/ovals and one Teflon circle/oval. The Teflon insert was then sandwiched between two layers of TPU and together, heat pressed at 110 ℃ for 30 seconds. The Teflon created the pressurization chamber as it does not stick to the TPU sheets during heat press.

Following the fabrication of both the foot bellow and knee bladder, the two were hermetically integrated (Loctite 4902 Instant Adhesive, Henkel, Düsseldorf , Germany) by a single length of 1.587 mm ID (pneumatic systems) or 3.175 mm ID (hydraulic systems) Tygon® tubing (Saint-Gobain, Paris, France) (**Figure 8.4c**). The length of the tubing was held constant at 60 cm, chosen based on the lower leg length of an average person (40 cm), with the additional length for the bellow to sit under the heel without the tubing being taut.

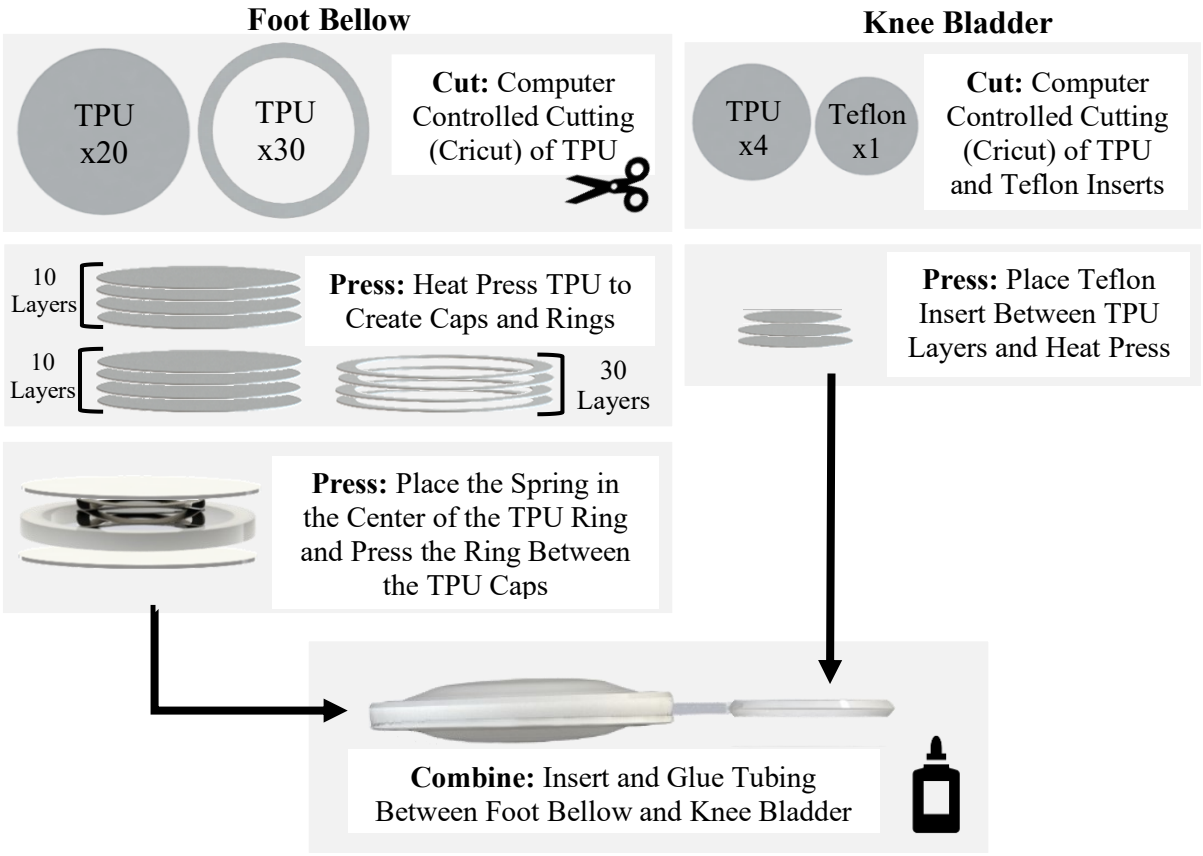


Figure 8.5: Fabrication process for closed-loop fluidic regenerative system. The schematic outlines the creation of the foot bellow (top left), knee bladder (top right), and the hermetic integration of the two actuators (bottom).

Six variations of the CLFR system were designed and fabricated to explore characteristics. The design and fabrication processes for all six systems remained consistent and varied only by the foot bellow's height and the knee bladder's diameter. The height of the foot bellow was determined by the height of the spring chosen during fabrication. Three spring sizes were selected under the constraint that the resting height must be less than 1"/25.4 mm to minimize influence during gait [358]. The spring was selected based on the criteria of maximizing the diameter with respect to the foot bellow diameter (92.7 mm or 3.6") and maximizing the delta height between the compressed and relaxed states (**Figure 8.6c**). As such, and considering the supply available through McMaster-Carr Supply Company, 1.6"/40.64 mm diameter springs with compressed heights of 0.094"/2.387 mm or small, 0.12"/3.048 mm or medium, and 0.217"/5.511 mm or large were chosen.

Two foot bellows of each spring height were constructed: one as a pneumatic system and the other as a hydraulic system (**Figure 8.4a**). Hereon, the systems will be identified by the relative height ('s' for small, 'm' for medium, and 'l' for large) and system ('H' for hydraulic systems or 'P' for pneumatic systems). For example, s-H refers to small hydraulic foot bellow, and l-P refers to large pneumatic foot bellow. Each foot bellow fabricated as a hydraulic system had an additional piece of 1.587 mm ID Tygon® tubing inserted into the bellow opposite to the connective tubing. A nylon plastic check valve (McMaster-Carr Supply Company; Model 6079T54) was then inserted into the open end of the additional length of tubing to prevent backflow when the system was filled. Using the Faro Edge ScanArm HD (Faro, Lake Mary, United States), 3D scans of the foot bellows were collected. These scans were used to determine the resting volumes of 36 ml, 42 ml and 56 ml for small, medium, and large foot bellows, respectively. Water was chosen as the working fluid for the hydraulic systems, as it is widely available and non-toxic.

8.4.2 Mechanical Testing Setup

The design of the CLFR was evaluated using a mechanical testing apparatus intended to mimic heel strike and loading during human gait (**Figure 8.6b**). Mechanical benchtop testing provides a reliable method for characterizing the proof-of-concept before proceeding to clinical trials. An aluminum plate was attached to the distal end of the piston contained in a dual-acting round body air cylinder (McMaster-Carr Supply Company; Model 6498K615) capable of

delivering 200 lbs/90 kg at 40 psi/275 kPa internal pressure. For all tests, the foot bellow was placed directly beneath the aluminum plate, as shown in **Figure 8.6d**. The pneumatic piston was actuated by a 5/3 solenoid valve (McMaster-Carr Supply Company; Model 4666A9) connected to a compressed air source, and two direct current relays to control the state of the valve. As the connected Arduino Uno (Arduino, Somerville, United States) powered the left relay, as seen on the left of **Figure 8.6a**, the valve facilitated airflow to lower the piston, thus dropping the plate onto the foot bellow. When the right relay was powered by the Arduino Uno, as seen on the right of **Figure 8.6a**, the valve allowed airflow into the air cylinder to raise the piston and return the foot bellow to the relaxed state. A Tekscan pressure mapping sensor (Tekscan Medical Sensor 9811E with a total of 96 sensels, Tekscan, Norwood, United States) was placed beneath the foot bellow to measure the pressure (**Figure 8.6d)**. The foot bellow covered 36 sensels. A small-sized Medi M2 Active OA Light Knee Brace was fitted onto a 3D printed rigid model of a small-sized knee per the specifications provided on the Medi sizing chart. The knee brace was tuned until the desired snug fit was achieved. A Tekscan force sensor (Medical Sensor 9811E) was placed between the lateral unloading mechanism and the body of the knee brace. The knee bladder was placed between the lateral unloading mechanism of the knee brace and the Tekscan sensor at the location of the lateral meniscus, as shown in **Figure 8.6e**. The knee bladder contacted 15 sensels.

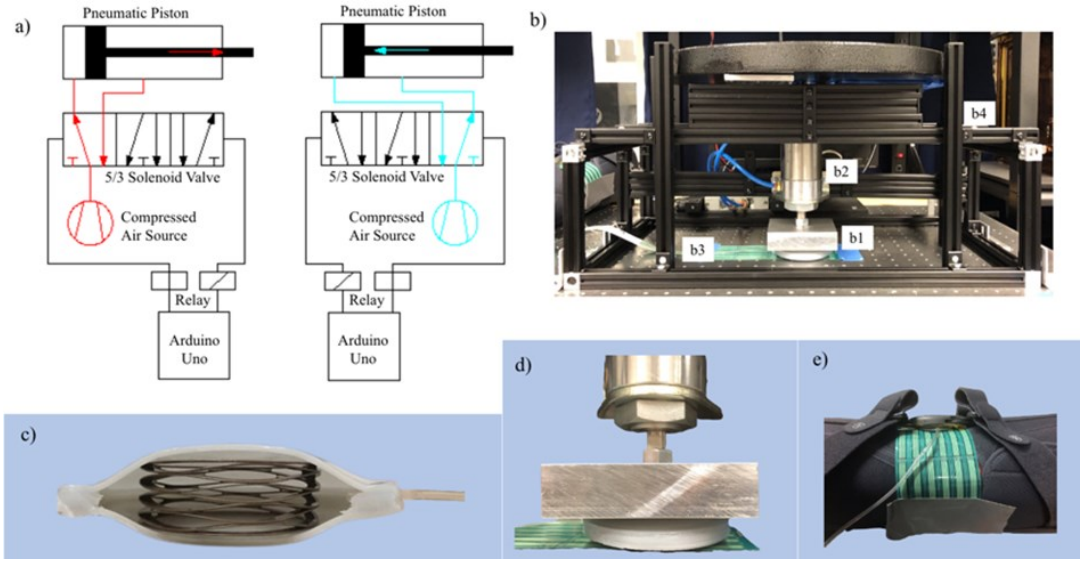


Figure 8.6: Overview of test apparatus and components. a) Pneumatic system schematic for control of test apparatus showing control for raising the aluminum plate (left) and lowering the aluminum plate (right). b) Test apparatus comprised of an aluminum plate (b1), a pneumatic

cylinder (b2), a Tekscan sensor (b3), and an aluminum support frame (b4). c) Cross-section view of foot bellow actuator used for testing. d) Placement of foot bellow on Tekscan sensor under the aluminum plate. e) Placement of knee bladder on Tekscan Sensor in the Medi M2 Active OA Light Knee Brace.

As the CLFR system is intended for regular wear with direct contact on the user's skin, the system must demonstrate the ability to maintain safe pressure ranges at the knee. Krouskop [282] showed pressures between 300 and 500 mmHg are necessary to cause tissue breakdown and thus 500 mmHg/666.6 millibar will serve as the upper threshold for safety. The CLFR system was incrementally loaded from 0 to 200 lbs/90 kg to determine the achievable pressure range. This incremental loading was achieved by utilizing a high resistance (undersized) tubing connection to the inlet responsible for lowering the pneumatic piston. As a result, the pressure delivered from the plate ramped-up to 90 kg. The contact pressure exerted by the knee bladder was recorded using a Tekscan sensor sampled at 100 Hz. A second Tekscan sensor recorded the pressure applied to the foot bellow. The data acquisition of knee bladder pressure and foot bellow pressure was synchronized. Each of the six bellows was evaluated by varying the dimensions of the knee bladder and ensuring the knee contact pressure remained below 500 mmHg/666.6 millibar. Initial testing was conducted comparing the knee contact pressure from each foot bellow when paired with different knee bladder dimensions. The initial testing aimed to determine knee bladder sizing that would result in safe output pressure ranges. Additionally, a knee bladder size that led to a similar knee peak contact pressure below the safe threshold at around 500 mbar was selected for each foot bellow and used for the remaining testing for clarity and ease of comparison.

The CLFR system must achieve pressurization before the peak KAM occurs. Gait analysis on individuals with unicompartmental medial knee OA demonstrated that the two peaks of the KAM occur at around 30% and 75% through the stance phase, with stance phase for individuals with moderate to severe OA lasting around 890 ms [359]–[361]. As such the first peak KAM occurs approximately 267 ms into the stance phase. Thus, considering the variation in gait cycle time, target pressurization and depressurization time for the CLFR system is ideally < 250 ms. The foot bellow was loaded to 90 kg for five steps using the testing apparatus to examine CLFR systems' response time. The loading on the foot bellow and the resulting contact pressure from the knee bladder were recorded using two Tekscan sensors. All

recorded contact pressures at the knee represented peak values, and all recorded contact forces corresponded to the total contact force.

As the CLFR system is intended for daily use, the system's efficiency, reliability, and durability required evaluation. The first method sought to determine energy losses in the CLFR system that may occur at junctions between actuators and connective tubing, highlighting the system's efficiency. The internal pressure of the foot bellow was compared to both the internal pressure and external contact pressure of the knee bladder using two Adafruit MPRLS Ported Pressure Sensor Breakout Boards (Adafruit, New York City, United States) inserted directly into each actuator and the previously used Tekscan sensors. The second method performed cyclic loading of the CLFR system to 90 kg for 2500 cycles. Individuals with knee OA take an average of 5000 gait cycles per day, 2500 with each foot [362]. The loading was delivered in five 500-step cycles, with a maximum of two minutes between cycles. During the rest period, the setup was untouched to minimize inconsistencies between trials. This minimized sensor drift, especially at high loading, and ensured successful data collection. The contact pressure created by the knee bladder was recorded using a Tekscan sensor. A calibration equation was developed to correct the errors in the collected data due to sensor drift [295]. The equation was calculated by loading the sensor with a known weight of 90 kg for 500 steps, aligning with a collection cycle. The supporting figure and resulting equation can be found in **Figure E.5** of **Appendix E**.

The chosen knee bladders (**Table 8.1**) for pneumatic systems s-P, m-P, and l-P had diameters of 30.5 mm, 39.4 mm, and 40.6 mm, respectively. Similarly, the chosen knee bladders for hydraulic systems s-H, m-H, and l-H had diameters of 50.8 mm, 58.4 mm x 50.8 mm (oval), and 73.7 mm x 63.5 mm (oval), respectively.

8.4.3 On-body Testing Setup

8.4.3.1 Motion Capture

The procedure for on-body testing involved utilizing the Optotrak Certus Motion Capture System (NDI, Waterloo, Canada) and force plates embedded within the floor. This set-up captured the participant's movements in three-dimensional space and measured the ground reaction force during gait (**Figure 8.7a**). First Principles software (NDI, Waterloo, Canada)

simultaneously collected data from both motion capture system and force plates. This data was subsequently processed through Visual3D (C-Motion, Boyds, United States) to calculate the kinematics and kinetics via inverse dynamics, ultimately yielding the KAM data.

The Optotrak system is an optoelectronic mechanism encompassing several camera units (**Figure 8.7b**) that detect Infrared Emitting Diodes (IREDs, **Figure 8.7c**). Each camera is fitted with three lenses to pinpoint the IREDs' location within a three-dimensional framework. By strategically placing the IREDs on the body, we can trace the subject's position and motion throughout the experiment. These IREDs, assembled in triads on rigid plastic bodies, were securely attached to the participant's thigh, lower leg, and foot using medical-grade tape and elastic bands. This arrangement enabled the tracking of individual body segments as they moved. Additionally, while the participant stood stationary, we created a virtual body model (or avatar) using a pointer to identify certain anatomical landmarks. These included various points on the upper and lower extremity, such as the anterior and posterior superior iliac spines, greater trochanter, medial and lateral femoral epicondyles, fibular head, tibial tuberosity, medial and lateral malleolus, first, second and fifth metatarsal head, and calcaneus.

Post IREDs and electrode placement, the participant underwent two standardized gait analyses - one wearing athletic shoes and the other wearing a knee brace integrated with the CLFR system. Each gait analysis set required a calibration trial where the participant stood in a static, reference position. This posture helped to establish a baseline "zero" joint angle for the hip, knee, and ankle, from which subsequent joint angles during gait were derived. The participant attempted three distinct positions to compare the variations' impact on the calculated joint angles during gait. Subsequently, the participant conducted two hip swing trials (one for each leg) necessary to ascertain the hip joint center's location. During each trial, the participant flexed and extended the relevant hip slowly while maintaining a straight lower extremity. A chair was provided for support during the one-leg standing segments.

The final stage of the trial required the participant to walk across a ten-meter pathway, a sequence to be repeated a minimum of 8 times. During this phase, the 3D kinematics and ground reaction forces were simultaneously recorded. The pathway featured two embedded force plates that measured the forces applied during each footfall on the plates. The participant

completed this set of walking trials wearing both athletic shoes and the knee brace integrated with the CLFR system, all at a self-selected speed (**Figure 8.7a**).

8.4.3.2 Participant

Given the preliminary nature of this on-body trial, we conducted our tests with a single healthy participant. The participant was a 27-year-old male, standing at a height of 177 cm and weighing 73 kg. He had no existing conditions that might affect his gait. It is important to note that the observations and conclusions drawn from this trial are based solely on the experience of this participant and might not be applicable to a broader demographic. Future studies would benefit from a more diverse pool of participants, including varying ages, body types, and those with conditions like OA, to provide a more comprehensive understanding of the system's efficacy.

8.4.3.3 Knee Brace, shoe, and CLFR System

The participant wore a standard running shoe for the trials, a typical choice for daily activities (**Figure 8.7a**). This shoe type is known for its comfort and flexibility, which makes it suitable for assessing the CLFR system's adaptability to common footwear worn by individuals living with OA [363]. The CLFR system incorporated in the test consisted of a large foot bellow and a large pneumatic knee bladder. The foot bellow, in its relaxed state, had a height of 22.1 mm. Meanwhile, the knee bladder had a diameter of 40.6 mm, ensuring an ample contact area with the knee for dynamic unloading. Connecting the foot bellow and the knee bladder was a flexible tubing of 60 cm in length, with an inner diameter of 1.587 mm. This tube was affixed to the side of the leg using tape, allowing for some slack and ensuring that it did not impede the participant's natural gait.

In future trials, it might be worth considering varying the components of the CLFR system. This could include the use of bellows and bladders of different sizes, as well as tubing with varying lengths and diameters. Such adjustments could allow us to better understand how these factors influence the system's performance, and customize the system to accommodate the needs of different individuals.

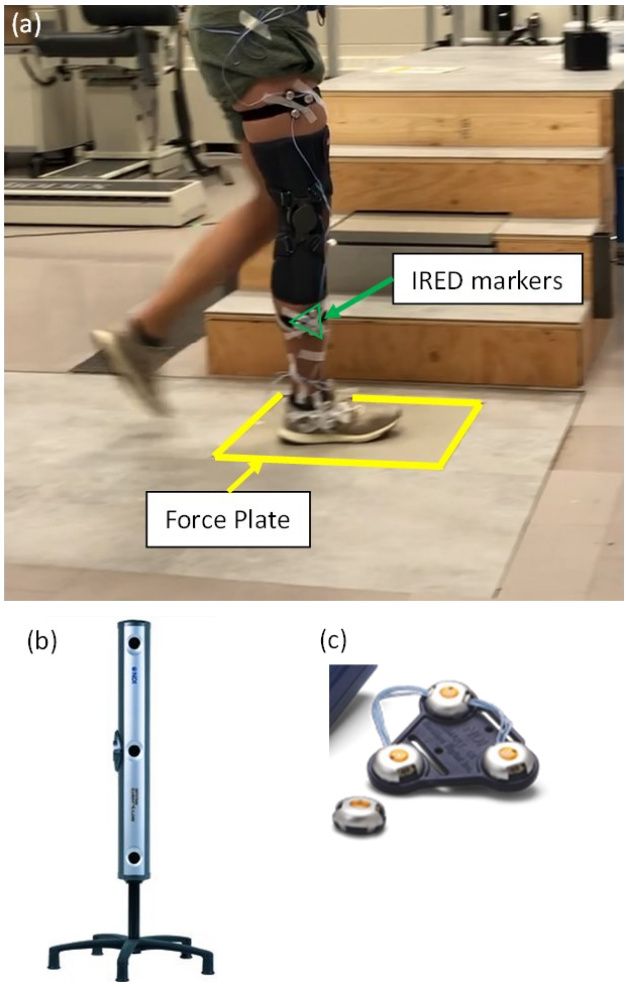


Figure 8.7: (a) Image showing an on-body testing trial. (b) Optotrak camera. (c) IRED markers (singles and rigid body).

8.5 Results

8.5.1 Peak Contact Pressure

Figure 8.8a shows the results of initial testing of different knee bladder sizes on the resulting knee contact pressure for system m-P, where a larger knee bladder (40.6 mm diameter) led to a decreased knee contact pressure (dotted purple line) and a smaller knee bladder (30.5 mm) led to an increased knee contact pressure (dashed red line). Similar trends occurred for system m-H when paired with a smaller knee bladder and a larger knee bladder (**Figure 8.8b**). The results for the initial testing of the remaining systems can be found in **Figure E.1** of **Appendix E**.

The variation of each system's peak contact pressure across the weight range relevant to the population experiencing knee OA, 150 lbs to 200 lbs (68 to 90 kg) was also evaluated

[364], [365]. As seen in **Figure 8.8a**, system m-P with a 39.4 mm diameter knee bladder (solid blue line) reached 480 millibar at 68 kg, with continued pressurization to 530 millibars at 90 kg. System m-H with a 58.4 mm x 50.8 mm (oval) knee bladder reached 506 millibars at 68 kg and continued to pressurize to 514 millibars at 90 kg as seen in **Figure 8.8b** (solid blue line). Similar results occurred for the l-P, l-H, and s-H systems (**Figure E.1a, b, d** of **Appendix E)**. Overall, the CLFR systems, excluding the s-P system (**Figure E.1c** of **Appendix E**), experienced an average increase of 38 millibars from 68 kg to 90 kg.

As the foot bellow is compressed, the volume decreases, and the internal pressure increases until a maximum compression is reached. At this point, internal pressure in the foot bellow/knee bladder (pressure losses between foot bellow and knee bladder in a pneumatic system presented herein is negligible) remains constant regardless of further increases in applied weight. Contact pressure at the knee continued to rise (though more gradually) even after the plateau of internal pressure, and this was hypothesized to be consequent to the material properties of the knee bladder. However, further investigation would be needed into the material characteristics of TPU to determine the exact cause, which is outside the scope of the study presented herein. This can be visualized by **Figure 8.8c**, which demonstrates the rise of contact pressure at the knee (dark blue, solid line) in parallel with the plateau of the foot bellow's internal pressure (light blue, dashed line). The accompanying contact pressure map at the knee demonstrates the increase in pressure and the non-uniform contact pressure where pressure was highest at the center of the knee bladder and gradually diminished towards the edges of the knee bladder.

Table 8.1: Naming scheme for different chosen foot bellow – knee bladder pairs.

Foot bellow sizes	**Knee bladder sizes (diameter)**					
	Pneumatics			**Hydraulics**		
	40.6 mm	**39.4 mm**	**30.5 mm**	**73.7mm x 63.5 mm oval**	**58.4 x 50.8 mm oval**	**50.8 mm**
22.1 mm (large)	l-P (chosen)	-	-	l-H (chosen)	-	-
12.7 mm (medium)	-	m-P (chosen)	-	-	m-H (chosen)	-
9.53 mm (small)	-	-	s-P (chosen)	-	-	s-H (chosen)

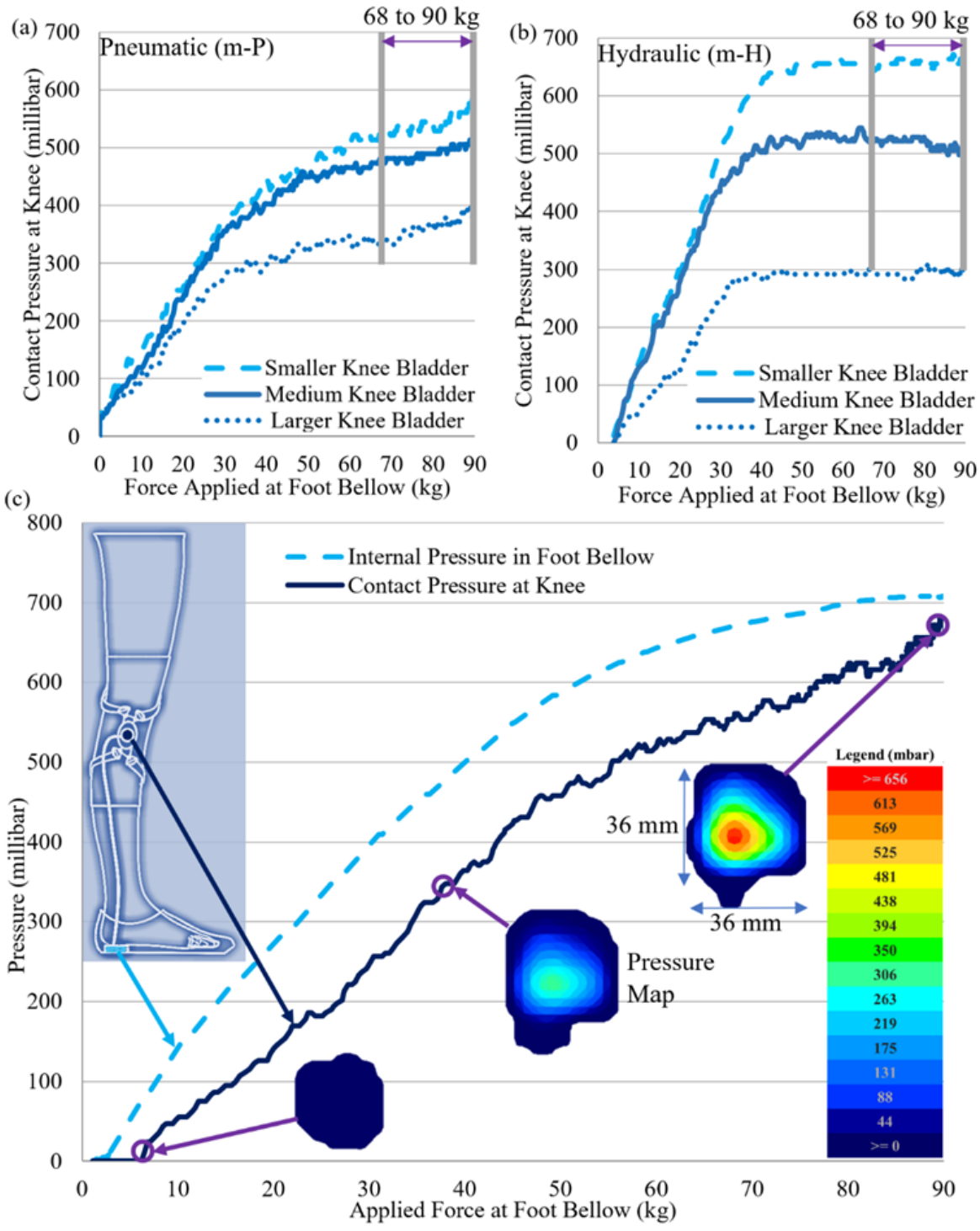


Figure 8.8: Pressure testing results. (a) Contact pressure at the knee in response to progressive loading of medium pneumatic foot bellow (m-P) from 0 to 90 kg for three different knee bladder dimensions: 30.5 mm (smaller), 39.4 mm (medium), and 43.18 mm (larger). (b) Contact pressure at the knee in response to progressive loading of medium hydraulic foot bellow (m-H) from 0 to 90 kg for three different knee bladder dimensions: 50.8 mm (smaller), 58.4 mm x 50.8 mm oval (medium), and 73.7 mm x 63.5 mm oval (larger) for system m-H. (c) Comparison

of internal foot bellow pressure shown as a light blue dotted line and contact pressure at the knee shown as a dark blue solid line as the foot bellow is progressively loaded from 0 to 90 kg. Pressure maps of the contact pressure at the knee recorded by Tekscan sensor are shown at three different weights applied to the foot bellow.

8.5.2 Total Contact Force

Using the same foot bellow (medium) and testing setup (90 kg weight), a larger knee bladder with a higher surface area generated increased contact force (**Figure 8.9**), in contrast to the peak knee bladder contact pressure. The hydraulic knee bladders exhibited higher total contact forces, as they were larger than the pneumatic knee bladders given that force is the product of pressure and area.

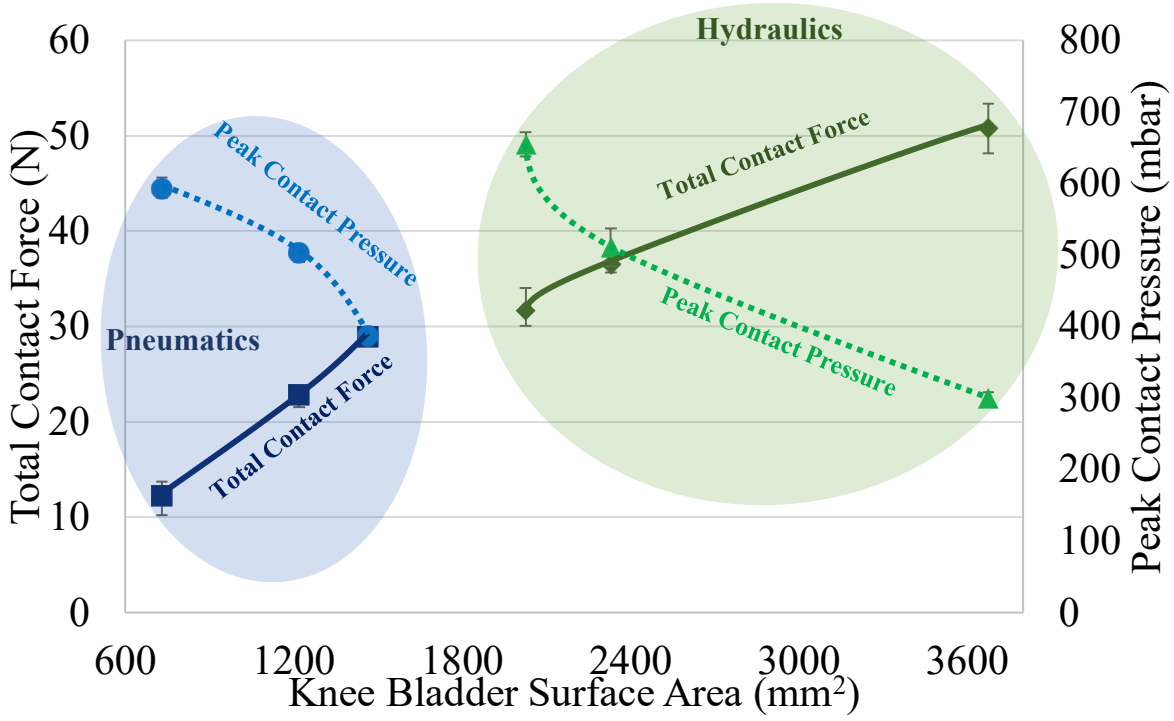


Figure 8.9: Comparison of total contact force versus peak contact pressure for pneumatic knee bladders and hydraulic knee bladders when medium foot bellow size was compressed by 90 kg weight. Three tests were conducted per data point with error bars shown.

8.5.3 Response Time

Response time for pressurization of each CLFR system was calculated by comparing the instance of loading on the foot bellow during the stance phase of gait, simulated heel strike, to the instance where the threshold pressurization, as determined in the aforementioned experiment, was reached. The pneumatic systems yielded target pressurization of < 250ms, with

an average response time of 200 ms and 246 ms for systems m-P and l-P, respectively (**Figure 8.10a**). The hydraulic systems yielded response times of 452 ms and 644 ms for systems s-H and m-H, respectively (**Figure 8.10a**). System l-H failed to fully pressurize under rapid loading, and thus a response time was not generated.

The depressurization rates were calculated using the instance of declining loading on the foot bellows during simulated toe-off, to the instance where contact pressure on the knee reached zero. The pneumatic systems had average depressurization rates of 148 ms and 111 ms for systems m-P and l-P, respectively. Hydraulic systems s-H and m-H demonstrated depressurization rates of 905 ms and 813 ms, respectively. Minimal delay existed in the pneumatic systems (**Figure 8.10b**), while a delay occurred in the hydraulic systems (**Figure 8.10c**), which was approximately 400 ± 50ms between the peak applied pressure on the foot bellow and peak contact pressure at the knee. Response times for the remaining systems can be found in **Figure E.2** of **Appendix E**.

8.5.4 Energy Loss

Energy loss in each CLFR system was separated into internal energy losses, occurring between the bellow and knee bladder, and transfer energy losses, arising between the internal knee bladder and resulting external contact pressure (**Table 8.2**). The pneumatic systems experienced an average of 0.11 ± 0.035% internal energy loss (internal air pressure difference between foot bellow and knee bladder). In comparison, the hydraulic system experienced an average of 10.1 ± 5% internal energy loss. The transfer energy loss (pressure difference between internal air pressure of the knee bladder and the applied peak contact pressure by the knee bladder onto the knee) in the pneumatic systems averaged 46.1 ±10%. In contrast, the hydraulic systems demonstrated 48.8 ±7% transfer energy loss.

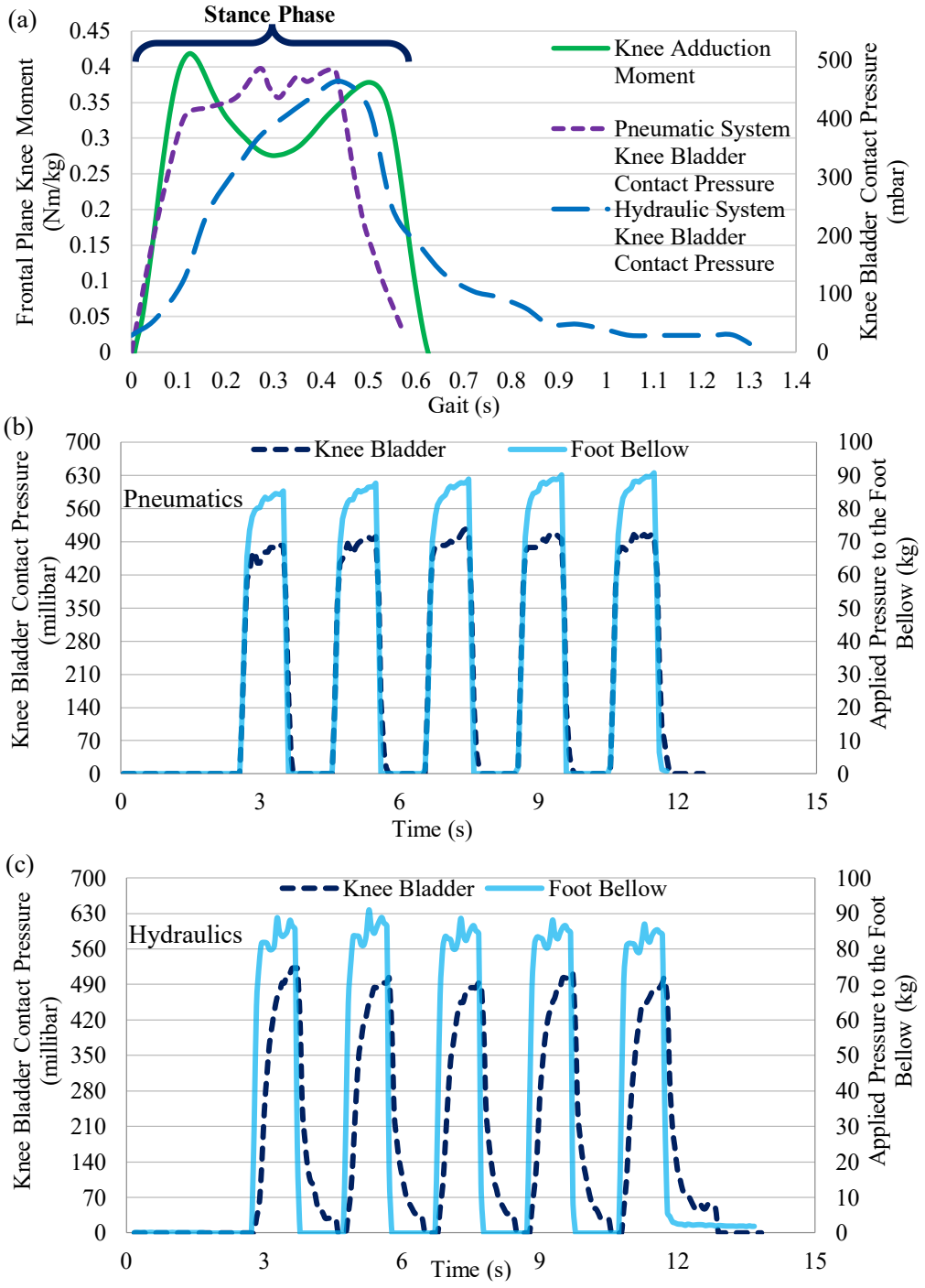


Figure 8.10: Response testing results. (a) Response time of pneumatic system (m-P) and hydraulic system (m-H) overlaid with typical stance phase frontal plane knee moment. (b) Response testing results showing contact pressure at the knee in dark blue (dashed line) and applied weight on the foot bellow in light blue (solid line) for medium pneumatic system (m-P) with a 39.4 mm diameter knee bladder. (c) Response testing results showing contact pressure at the knee in dark blue (dashed line) and applied weight on the foot bellow in light blue (solid line) for medium hydraulic system (m-H) with a 58.4 mm x 50.8 mm oval knee bladder.

Table 8.2: Energy losses in pneumatic and hydraulic systems.

Energy Loss	System Type					
	Pneumatic			Hydraulic		
	s-P	m-P	l-P	s-H	m-H	l-H
Internal Foot Bellow Pressure to Internal Knee Bladder Pressure (%)	0.15	0.11	0.08	10.7	5.19	14.4
Internal Knee Bladder Pressure to External Contact Pressure at the Knee (%)	56.7	39.3	42.0	41.3	49.8	55.3

8.5.5 Durability

Durability was also evaluated using the results from cyclic loading testing. For visualization, **Figure 8.11a** shows the entire 2500 steps for system m-P, while **Figure 8.11c** shows steps 1, 10, 50, 100, 500, 1000, 1500, 2000 and 2500 in more detail for system m-P. Cyclic loading results for the remaining systems can be found in **Figure E.3** and **Figure E.4** of **Appendix E**. The standard deviation was calculated using the peak value from each step. The pneumatic systems had standard deviations of 36.2 millibars, 43.5 millibars, and 24.5 millibars for systems s-P, m-P and l-P, respectively. The hydraulic systems had standard deviations of 15.2 millibars and 32.7 millibars for systems s-H and m-H, respectively. **Figure 8.11b** shows box and whisker plots for all systems. As mentioned above, system l-H could not pressurize under rapid loading, which could not provide usable data during this test.

8.5.6 Preliminary On-Body Trials

Initial on-body trials conducted on a healthy participant without osteoarthritis revealed interesting insights (**Figure 8.12**). When the participant wore only the brace, with the unloading straps pulled tight and without using the CLFR system (termed "Brace Tight Deflated"), there was an average reduction in peak knee adduction moment (KAM) of approximately 8% during the stance phase, compared to when the brace was worn with loose unloading straps ("Brace Loose Deflated"). Conversely, when the participant wore the brace with the unloading straps tightened and the CLFR system activated ("Brace Tight Inflated"), the average peak KAM reduction decreased to approximately 3.7%, compared to the "Brace Loose Deflated" condition. Interestingly, it was observed that when only the brace was worn, with tight unloading straps

and without the CLFR system ("Brace Tight Deflated"), the KAM during about 40% to 60% of the stance phase was higher than in the "Brace Loose Deflated" condition. This increase was not observed when the participant wore the brace with tight unloading straps and the activated CLFR system ("Brace Tight Inflated").

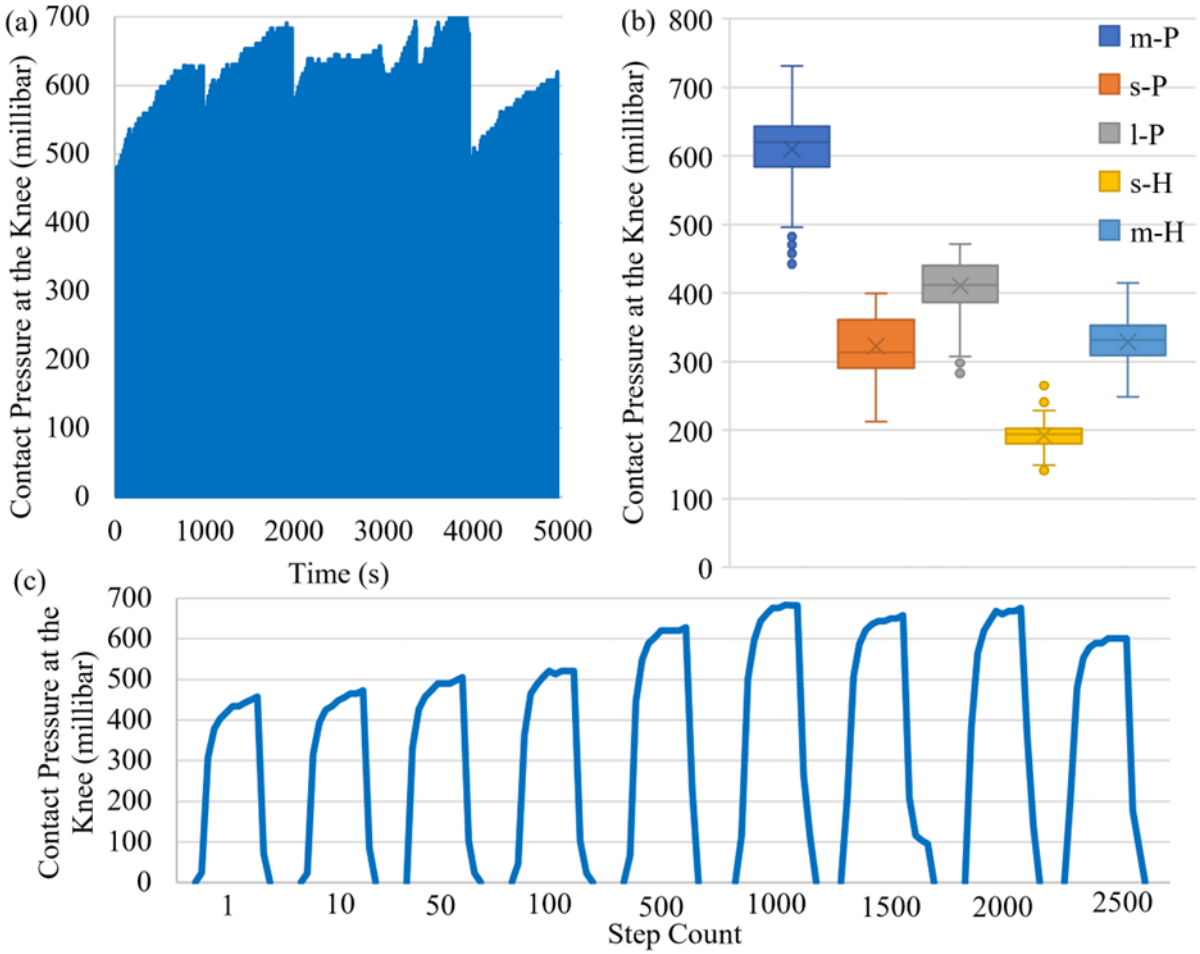


Figure 8.11: Cyclic loading testing results. (a) Contact pressure at the knee for the complete 2500 steps during cyclic loading testing from medium pneumatic system (m-P) with 39.4 mm diameter knee bladder. (b) Box and whisker plots for medium pneumatic system (m-P) with 39.4 mm diameter knee bladder (blue, left), small pneumatic system (s-P) with 30.5 mm diameter knee bladder (orange, center-left), large pneumatic system (l-P) with 40.6 mm diameter knee bladder (gray, centered), medium hydraulic system (m-H) with 58.4 mm x 50.8 mm (oval) knee bladder (yellow, right-centered) and small hydraulic system (s-H) with 50.8 mm diameter knee bladder (light blue, right) during cyclic loading testing. (c) Contact pressure at the knee for steps 1, 10, 50, 100, 500, 1000, 1500, 2000, and 2500, selected from cyclic loading testing for medium pneumatic system (m-P) with 39.4 mm diameter knee bladder.

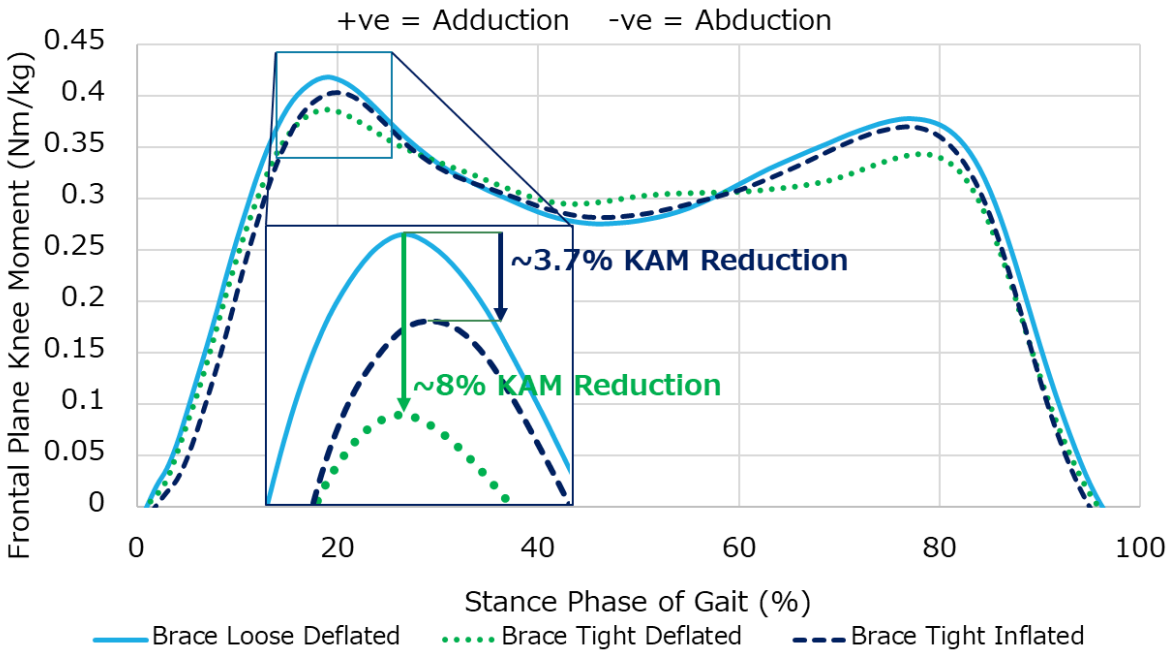


Figure 8.12: This graph illustrates the average KAM over eight trials for each testing condition. "Brace Loose Deflated" refers to the condition where the brace was worn with loosened unloading straps, and without the use of the CLFR system. "Brace Tight Deflated" represents the scenario where the brace was worn with tightened unloading straps, but without the activation of the CLFR system. Finally, "Brace Tight Inflated" indicates the condition where the brace was donned with tightened unloading straps and the CLFR system was activated.

8.6 Discussion

8.6.1 Benchtop Testing

The pressure performance testing of the CLFR systems achieved promising results for dynamic unloading in unicompartmental tibiofemoral osteoarthritis during gait across several metrics. This proof-of-concept study aimed not to determine which system works best for knee unloading, but to demonstrate characteristics and performance of various designs, and ultimately allow customized or tailored systems for individuals. In order to reduce the risk of tissue damage to users of the CLFR system, a threshold of less than 670 millibars was set, as justified to be below the range of thresholds associated with skin tissue breakdown [282]. All of the pneumatic systems remained below the threshold with maximum observed pressures of 610 millibars, 592 millibars, and 317 millibars for the l-P, m-P, and s-P systems, respectively. The hydraulic systems, when paired with the smaller knee bladder and in the case of l-H, the medium knee bladder, caused the pressure to exceed the threshold value reaching over 700

millibars. While this falls within the established range for tissue damage, the CLFR system may not cause expected skin breakdown as pressure is intermittent and not continuous. Overall, when modifying knee bladder sizes, the CLFR system achieved varying 'plateau' pressures within a range unlikely to cause tissue damage across the target weight range of 150 to 200 lbs or 68 to 90 kg. [26], [365]. However, further clinical investigations are required to confirm this outcome.

The systems generated a plateauing knee contact pressure, starting around 45 kg bodyweight (**Figure 8.8a, b**). As expected, an increase in knee bladder volume decreased the peak contact pressure and vice versa (**Figure 8.8a, b**). Conversely, an increase in knee bladder surface area led to an increase in total contact force, and a decrease in knee bladder surface area led to a decrease in total contact force (**Figure 8.9**). This demonstrated the customizability of the CLFR system through the ability to change and adapt contact pressure to individual need. Individuals with knee OA vary in weight, gait duration, and severity of symptoms including peak KAM and joint misalignment and thus may require different output pressures for the CLFR system to be effective [366]. Additionally, these results pose the question: is the peak contact pressure more important or the total contact force? The answer depends on the type of unloading knee brace and its mechanism. For a knee brace with a rigid unloading mechanism, most, if not all, of the force produced by the knee bladder is used for actuating the unloading mechanism with little to no deformity [367]. Therefore, the total contact force would be more important. However, peak contact pressure may be more important for softer knee braces with compliant (i.e., flexible or elastic) unloading mechanisms. For instance, while a larger knee bladder with a smaller peak contact pressure may produce higher total contact force, that does not necessarily translate to a higher amount of unloading through a compliant 3-point bending mechanism as force is distributed to areas surrounding the lateral mid-line of the knee instead of concentrated at a single point right on the mid-line of the knee, which is inefficient at activating a compliant 3-point bending mechanism for unloading [349]. In comparison, a smaller knee bladder with a smaller total contact force but a higher peak pressure has more concentrated force at a point on the mid-line of the knee, activating the 3-point bending mechanism more. Therefore, peak contact pressure may be a more relevant indicator of the amount of unloading for knee braces with a compliant unloading mechanism. Regardless, the authors believe both peak contact pressure and total contact force applied by the knee bladder

should be considered when designing CLFR systems. Further, more advanced fluidic actuators such as pneumatic artificial muscles [368] or soft fluidic actuators [46] may be used instead of a circular bladder for CLFR-enabled dynamic knee braces for managing OA.

The initial validation testing also confirmed the ability of the CLFR system to pressurize and depressurize in less than 250 ms, the required response time to apply maximum unloading prior to peak KAM during the stance phase in medial unicompartmental OA. Simply put, the CLFR system is fast enough to counter the external KAM during only the stance phase of gait [369]. The pneumatic systems, s-P, m-P, and l-P, successfully pressurized at an average of 219.3 ms and depressurized at an average of 108 ms (**Figure 8.10a**, **Figure 8.10b**, **Figure E.2a, c** of **Appendix E**). The hydraulic systems, s-H and m-H showed substantial delay (**Figure 8.10a**, **Figure 8.10c**, **Figure E.2b** of **Appendix E**); thus, they could not achieve pressurization and depressurization rates useful in the real world. The hydraulic systems required an average of 548 ms to pressurize and 859 ms to depressurize, which is too slow to align with gait. Additionally, l-H was unable to pressurize under rapid loading conditions (**Figure E.2d** of **Appendix E**), and thus a response time could not be collected. Water is an incompressible fluid with a drastically higher viscosity than air. As such, the hydraulic systems experienced much higher pressure losses due to hydraulic resistance compared to the pneumatic systems contributing to the notable delays [370]. One way to reduce hydraulic resistance is to increase the internal diameter of the tubing connecting the foot bellow and the knee bladder. However, any tubing with a diameter larger than 3.175 mm would be subjectively bulky, which may deter people from compliant use of such a product. Another potential method is to divide an oversized tubing into a plurality of smaller tubing with equivalent cross-sectional area for liquid transportation. Furthermore, the surface of the tubing may be modified to reduce hydraulic resistance or use a lower-density liquid [371].

Both pneumatic and hydraulic systems demonstrated advantages and disadvantages in achieving the design objective. The pneumatic systems were light, required smaller tubing, and demonstrated minimal delay. However, a larger volume of air was needed to achieve the necessary pressure, given the compressible nature of the gas. As such, knee bladder size was restricted, limiting the unloading force (**Figure 8.9**). On the other hand, hydraulic systems were heavier, required larger tubing, and demonstrated notable delays during testing. The advantage of the hydraulic system, given liquid is incompressible, was a smaller volume was required to

achieve the necessary pressures. This allowed for a larger knee bladder surface area and, thus, higher unloading forces. Further investigation will determine the optimal design for a clinical setting considering exerted unloading forces and user comfort [141], [282]. The authors believe that the incompressible nature of hydraulic CLFR systems can be a preferred choice as it can achieve high total contact force with a smaller foot bellow, which is desirable if the delay can be minimized during pressurization and depressurization. The foot bellow should be miniaturized as much as possible in order to minimize disruption to the users' natural gait and be designed in a way such as a lateral wedge insole to further reduce KAM [372].

Tests assessing the durability of the system also provided promising results. The CLFR system was able to perform 2500 steps, the equivalent of one day of walking for most individuals with knee OA [362]. During cyclic loading, the pneumatic systems performed complete inflation and deflation cycles from 0 millibars to the determined peak, followed by deflation to 0 millibars (**Figure 8.11a, c**). The system's fast response and dynamic nature allow the user to experience no unloading during the swing phase and experience unloading only during the stance phase. Nonetheless, a clinical trial is necessary to determine whether this soft robotic knee brace could provide more comfort than typical knee OA unloader braces that provide constant unloading pressure at the knee, which could improve user compliance and knee brace adoption. The hydraulic systems could not complete the deflation in the duration provided (1 second) and thus remained partially inflated (**Figure E.3c, d, Figure E.4c, d** of **Appendix E**).

Energy loss was evaluated as a measure of efficiency, highlighting the ability of the system to consistently deliver required pressure. Internal energy loss between the foot bellow and knee bladder during response time testing (transient effect) in the pneumatic systems was negligible at 0.11 ± 0.035% (**Table 8.2**). The 10.1 ± 5% internal energy loss during response time testing (transient effect) observed in the hydraulic system was due to the nature of incompressible viscous fluid flow, where there was insufficient flow going from the foot bellow to the knee bladder to fully pressurize the knee bladder during the first half of stance phase. Eventually, the internal pressure within the foot bellow and knee bladder equalized. Further, a comparable and notable reduction occurred in the pneumatic and hydraulic systems between internal knee bladder pressure and external knee bladder applied peak contact pressure of 46.1 ±10% and 48.8 ±7% (**Table 8.2**), respectively; this was expected as the knee experienced

approximately half of the internal pressure in the perpendicular plane from the knee bladder, proportional to the section of the bladder in contact with the knee. Internally driven forces in other planes (not oriented towards the knee) would not have contributed to the contact pressure at the knee. Additionally, the cross-sectional hoop stress also contributed to the observed losses [373]. The combination of relatively stable fluctuations under cyclic loading tests and minimal energy losses, especially by the pneumatic systems indicated a robust design and fabrication method to experience regular and repeated wear without dramatically reducing functionality.

8.6.2 Preliminary On-Body Trials

The objective of these preliminary on-body trials was not to confirm or refute the effectiveness of the CLFR system in reducing KAM for individuals living with OA. Instead, the aim was to discern potential improvements for the CLFR system and refine the design of the foot bellow and the knee bladder. Given that the CLFR system was only tested on a single healthy individual without knee OA, it would be inappropriate to draw definitive conclusions regarding its effectiveness in reducing KAM. Nonetheless, these initial trials have offered invaluable insights into the operation and functionality of the CLFR system when worn on the body.

As observed in **Figure 8.12**, the wearing of the brace with tightened straps yields a predictable reduction in KAM. This observation aligns with numerous studies in the literature, reaffirming that unloader-type braces are effective in reducing KAM [26], [342]. Surprisingly, however, the incorporation of the CLFR system appears to diminish the extent of KAM reduction. Multiple potential reasons could explain this observation, but it remains speculative until proper clinical trials are conducted with the CLFR system involving multiple individuals living with OA. In this context, we can only hypothesize some potential explanations for the lesser reduction of KAM when the CLFR system is utilized. Given that all trials were conducted on the same individual—who is healthy and without OA—the impact of the presence or absence of the CLFR system in the brace should be comparable. In other words, any reduction in KAM, regardless of its magnitude compared to an individual living with OA, should be valid. However, we must consider the potential influence of unknown factors on the test results, such as overstimulation leading to muscle activation that resists the three-point unloading force exerted by the brace. For instance, if the brace equipped with the CLFR system becomes tighter than the brace without it, this might unexpectedly result in a smaller KAM reduction. If this

holds true—at least for healthy subjects—then the reduction in KAM achieved by knee braces is linked to the amount of force applied (i.e., the tightness of the strap), and an inflection point exists beyond which increased force no longer results in reduced KAM.

Another potential explanation relates to the physical shape and possibly the location of the CLFR system. It is unlikely that the knee bladder and the tubing significantly influence the KAM reduction, compared to using the brace without the CLFR system. This is because the knee bladder shares a similar surface area, shape, and location to that of a standard 3-point unloading knee brace cushion. The tubing, which merely transfers fluid between the foot bellow and the knee bladder, does not exert any force onto the body or hinder motion. This brings us to the foot bellow. Indeed, the alignment of the foot impacts the direction of the ground reaction force [374], [375]. The foot bellow, located centrally underneath the heel, might cause the foot to deviate from its normal position, leading to an unnatural gait and subsequently a smaller KAM reduction. Therefore, the placement and design of the foot bellow require systematic testing in a clinical trial. This will enable us to determine an optimal design, which might vary from individual to individual.

8.6.3 Limitations

Given the proof-of-concept nature of this study, several limitations should be considered. While effective for initial validation, the testing apparatus cannot address some attributes of human gait. Firstly, the knee air bladder and brace are positioned on a 3D-printed rigid model of a knee and surrounding leg. While the shape of the model is accurate to the dimensions of a small knee provided by the Medi sizing chart, the material will provide no ‘give’ or reaction when the pressure is applied, in contrast to a human limb. Additionally, the foot bellow made full direct contact in the vertical direction, aligning with gravity, during compression. However, in human gait, the foot bellow may be tilted when making contact with the ground . Thus, not all ground reaction forces would effectively compress the foot bellow. The future direction of the CLFR system development will focus on integrating the foot bellow with a shoe. Possible designs could include CLFR integration directly into the shoe in the midsole or as an additional component, such as an insole or insert. The initial validation compressed the foot bellow via an aluminum plate, moving linearly. A human foot will provide different contact forces (given the material and geometric differences), and body weight may not be linearly applied. Thus, a

clinical investigation during human gait must verify the transferability of the preliminary results presented.

8.7 Concluding Remarks

The proof-of-concept study presents a self-powered energy-harvesting soft robotic knee brace capable of generating a safe range of contact pressures considering tissue damage within the required time frame of <250ms, providing promising potential to counteract external KAM experienced by individuals with knee OA. These results indicate that the system has the potential to successfully unload the knee during the stance phase of gait and may, with further clinical testing, prove to be a beneficial wearable treatment to slow/prevent progression and/or improve symptoms in those with knee OA. The proof-of-concept data also indicates that the soft robotic knee brace will be robust enough to endure regular and repeated use. Further research and investigation are required to determine the system's viability when tested in clinical settings, specifically an extension of the presented results when the system experiences human gait. Overall, this novel electronics-free soft robotic knee brace enabled by closed-loop fluidic regenerative system paves the way for a new paradigm regarding dynamic robotic knee brace design.

Chapter 9

Miniaturization of Hybrid Soft-Rigid Active Prosthetics for Hand-on Biomedical Engineering Education

The work included in this Chapter is submitted to journal: **R. Z. Gao**, P. S. Lee, A. Ravi, C. L. Ren, C. R. Dickerson, and J. Y. Tung, "Hybrid Soft-Rigid Active Prosthetics Laboratory Exercise for Hands-On Biomechanical and Biomedical Engineering Education," *Journal of Biomechanical Engineering.* Run Ze Gao and Peter Lee conceived the idea together. The device fabrication and experimental procedures were collaboratively undertaken by Run Ze Gao and Peter Lee. Run Ze Gao authored the manuscript.

9.1 Introduction

Biomechanical and biomedical engineering (BME) is undergoing a revolutionary transformation fueled by continuous technological advancements. With the integration of state-of-the-art robotic technologies, traditional biomedical systems are evolving at an unprecedented pace, leading to previously unthinkable innovations. Additionally, this rapidly changing landscape is becoming increasingly interdisciplinary. BME education now demands a multifaceted pedagogical approach and active learning that blends elements from various disciplines, including medicine, computer science, electrical engineering, mechanical engineering, materials science, and even psychology [376], [377]. This convergence of diverse fields is not just an option, but a necessity, as it opens new frontiers in developing medical solutions that are more efficient, personalized, and adaptable to a range of healthcare scenarios.

Given the swift technological advancements and increased complexity in the real-world BME landscape, curriculum for BME is challenged to mirror these developments [378]. Theoretical knowledge alone is no longer sufficient; students must gain hands-on exposure to the latest technologies that are shaping the field. BME students need to gain a comprehensive understanding of this advanced technology. Soft robotics, a relatively new branch emphasizing flexibility and compliance, is gaining significant traction within the field of BME [122]. Recently, a recognized open-access resources for teaching soft robotics hands-on is the Soft Robotics Toolkit [379]. A collaborative effort by Harvard University and Trinity College Dublin with additional contributors, this platform has emerged as an invaluable learning tool. Having undergone rigorous pilot studies and user tests, the Soft Robotics Toolkit has received widespread positive feedback for its comprehensive subject matter coverage [380].

The Soft Robotics Toolkit provides detailed content on a variety of topics, from actuator designs and sensor technology to controls, and includes extensive documentation on modeling and manufacturing processes. Furthermore, it features an array of case studies and projects that expose learners to complex real-world scenarios. However, despite its usefulness, the Soft Robotics Toolkit may not be entirely fit for purpose in every context. The case studies and projects it offers can be vast and open-ended, potentially posing challenges for integration into a well-defined, structured, and graded lab with clear deliverables. Large-scale adoption of these resources may also prove challenging, particularly in larger class settings, due to the sheer quantity of materials required.

Additionally, the Soft Robotics Toolkit lacks depth and variety of sensing, actuation, and control elements commonly seen in electromechanical devices. Notably, it lacks coverage of certain sensing modalities, such as those used in electromyography (EMG), and does not include key control methods (e.g., proportional integral derivative (PID) control). While the Soft Robotics Toolkit has been successfully integrated into classrooms at the secondary (K-12) level to promote STEM, its focus remains primarily on a manually actuated soft robotic gripper, which lacks authentic BME application [381]–[383]. Further enhancements are needed to expand the activity across varying class sizes and curricula in a post-secondary BME classroom.

It is critical to understand that soft robotic systems may not independently fulfill many real-world functions due to their inherent limitations, including a lack of structural rigidity [384]. As such, the emergence of soft-rigid hybrid systems has been a promising development, marrying the advantages of soft robotics with the structural robustness of traditional rigid mechanisms [385]. Moreover, the functionality of these hybrid systems can be further augmented when integrated with sophisticated sensors and robust control software. This combination of soft-rigid elements, sensors, and software allows for the creation of more versatile and adaptive biomedical devices that can better address real-world needs [386].

In order for BME students to develop a comprehensive understanding of advanced electromechanical device design, we propose a hands-on lab activity introducing the design, fabrication, and testing of an active hybrid soft-rigid prosthetic finger. The proposed activity offers students the opportunity to explore the technical requirements of each component and potential synergies offered when harmoniously combined [387]. This integrated learning approach will equip students with the skills needed to navigate and contribute to the cutting-edge landscape of BME, ultimately translating their knowledge into creation of useful real-world products, and/or services beneficiary to the society [388].

In this chapter, we introduce an engaging three to five-hour hands-on laboratory exercise focused on the creation of a hybrid soft-rigid robotic prosthetic finger, referred to henceforth in this chapter as the 'prosthetic finger.' This innovative finger prosthesis is actuated by pneumatic hardware, controlled via a PID controller, and is equipped with an EMG sensor. The laboratory session offers a comprehensive exploration of the prosthetic finger, encompassing all stages of its development - from design and fabrication to assembly and testing. This self-contained lab effectively teaches students the foundational principles of soft-rigid hybrid robotics using the tangible example of prosthetic finger design. Notably, the exercise provides an integrative learning experience, covering mechanical, electrical, and software elements, which are the key facets of BME pedagogy [387].

The hands-on lab was successfully piloted in a senior/4th-year elective engineering course titled 'Neuro and Rehabilitation Engineering' (BME 588) with 40 students during the Winter 2023 Semester (January to April 2023) at the University of Waterloo (Canada). Both students and instructors provided highly favorable feedback.

The ensuing sections of this chapter detail the design, contents, and student deliverables for the lab. A comprehensive Discussion section explores feedback from the students, assesses the lab's strengths, identifies what aspects were particularly effective, and suggests areas for potential improvement.

In the spirit of open access and knowledge sharing, we provide all laboratory materials, from bill of materials and CAD design to software, in the **Appendix F-4** section of this thesis. These resources can be accessed freely under the Creative Commons license (CC BY 4.0), enabling a wide application of this teaching approach.

9.2 Lab Content

9.2.1 Problem Background

While the primary purpose of the prosthetic finger lab is to teach BME students about the integration of mechanical, electrical, and software systems within soft-rigid wearable robotic assistive devices, it is important to inform the real-world applicability of this lab. Skills and knowledge acquired through working with this prosthetic finger could be directly applied to developing commercially viable products. This direct connection to real-world applicability can serve as a powerful motivator for students, as it makes evident the concepts and techniques learned in class can translate directly into career skills and potential innovations in BME.

To comprehensively understand the current landscape, we present a comparison with commercially available finger prostheses. Partial hand amputations represent the most common type of upper extremity amputation, affecting an estimated 1 in 18,000 individuals or approximately 2 million people in the United States alone [389]. Commercial solutions seek to restore form and functionality, aiming to alleviate the burdens experienced by individuals and communities impacted by these amputations. Commercially available finger prostheses, designed to restore both form and function, can be categorized into three primary classes: passive functional, body-powered, and externally powered devices. For more detailed information regarding partial-hand prosthesis, we refer the reader to read an excellent review article by Graham et al. [390].

Passive functional prostheses most commonly use a passive ratcheting mechanical mechanism to lock the prosthetic into various degrees of flexion, thereby enhancing

functionality and overall movement. When an extension of the prosthesis is required, the amputee can engage a button or a spring-loaded release mechanism to revert the prosthetic to its neutral resting position. While adjusting the degree of flexion is straightforward, the inability of these prostheses to autonomously flex and extend with the movement of the residual limb may pose a limitation for some users. Form can be restored by using a silicone cover that closely imitates skin texture and appearance.

Body-powered finger prostheses, which appear mechanical, harness the user's remaining joints and anatomical structures to restore range of motion. They function independently of external batteries and electricity, which offers advantages such as improved sensory and positional feedback, a decreased rate of user fatigue, and synchronized movement with the natural actions of the hand. However, the mechanical design of these devices may be perceived as cosmetically unappealing. Additionally, the design, which encloses the digit, increases the width around the remaining anatomical joints, which could pose discomfort or usability issues for some users.

To our knowledge, there are no commercially available externally powered finger prostheses at the time of writing this thesis. In this lab, we demonstrate a cutting-edge device that could potentially fill this gap in the commercial market for finger prostheses, which is expected to both illuminate and motivate students. This same design could be expanded to create partial hand prostheses or prostheses for amputations above the wrist.

9.2.2 Prosthetic Finger Design (Mechanical System)

Acting as the core mechanical component, the prosthetic finger (**Figure 9.1**), operates as a single-joint prosthetic device. Its design is intended to replicate the interphalangeal joint. All the CAD files can found in **Appendix F-4**.

In specific learning environments where topics of interest include more advanced control techniques such as multivariable control, the lab kit can be expanded to include a multi-joint finger prosthesis or even a fully operational 21 degrees-of-freedom hand prosthesis [256]. These more complex devices can also be engineered using the soft fluidic actuator system. While the use of this type of bellows-structured soft fluidic actuators [391], [392] is prevalent within the soft robotics community, the authors extend recognition to Vincent Systems GmbH. Their innovative 'Fluidhand' [16], [17] significantly influenced the design of the prosthetic

finger we present in this chapter, specifically tailored for educational applications. This acknowledgment underscores the value of shared innovation and connects our educational tool to the broader context of existing advancements in soft robotics.

Importantly, multi-joint finger prostheses require increased resource requirements. Greater numbers of soft fluidic actuators (SFAs) necessitate a corresponding increase in the number of air valves, motor drivers, and inertial measurement units (IMUs) components for effective control of the system.

As an educational model, the prosthetic finger is not designed to be a scale replica of a human finger (**Figure 9.1**). Its structure incorporates a sturdy base, designed to contain a shifting center of mass within the support to prevent tipping. This enables the system to stand upright on a table and maintain stability during hands-on interactions. The IMU is intentionally exposed to facilitate exercising hands-on wiring. The tubing connecting the SFA is also routed to facilitate repeatable connections. The prosthetic finger is designed to bend 90 degrees, incorporating 3D-printed distal and intermediate phalanges, and a 3D-printed flexible hinge. The IMU is attached to the distal phalange by a M3 bolt and nut. The 5-layer bellow-style SFA enables the prosthetic finger to bend. Instead of a shaft-style hinge, a flexible hinge is selected for its easier assembly and better tolerancing. Note the rendered image of the prosthetic finger (**Figure 9.1a, and 1b**) is intended to clearly show the motion and features of the prosthetic finger and may not indicate the exact shape or color of the pressurized SFA. **Figure 9.1c, 1d, and 1e** display actual images of the prosthetic finger, with the pressurized/flexed and depressurized/extended states viewed from the side, as well as the pressurized/flexed state viewed from the top. **Figure 9.1f, and 1g** depict the low-profile 5-layer bellows-style SFA in both deflated and inflated states, respectively. If a greater bending angle with a lower internal air pressure is desired, additional layers may be employed.

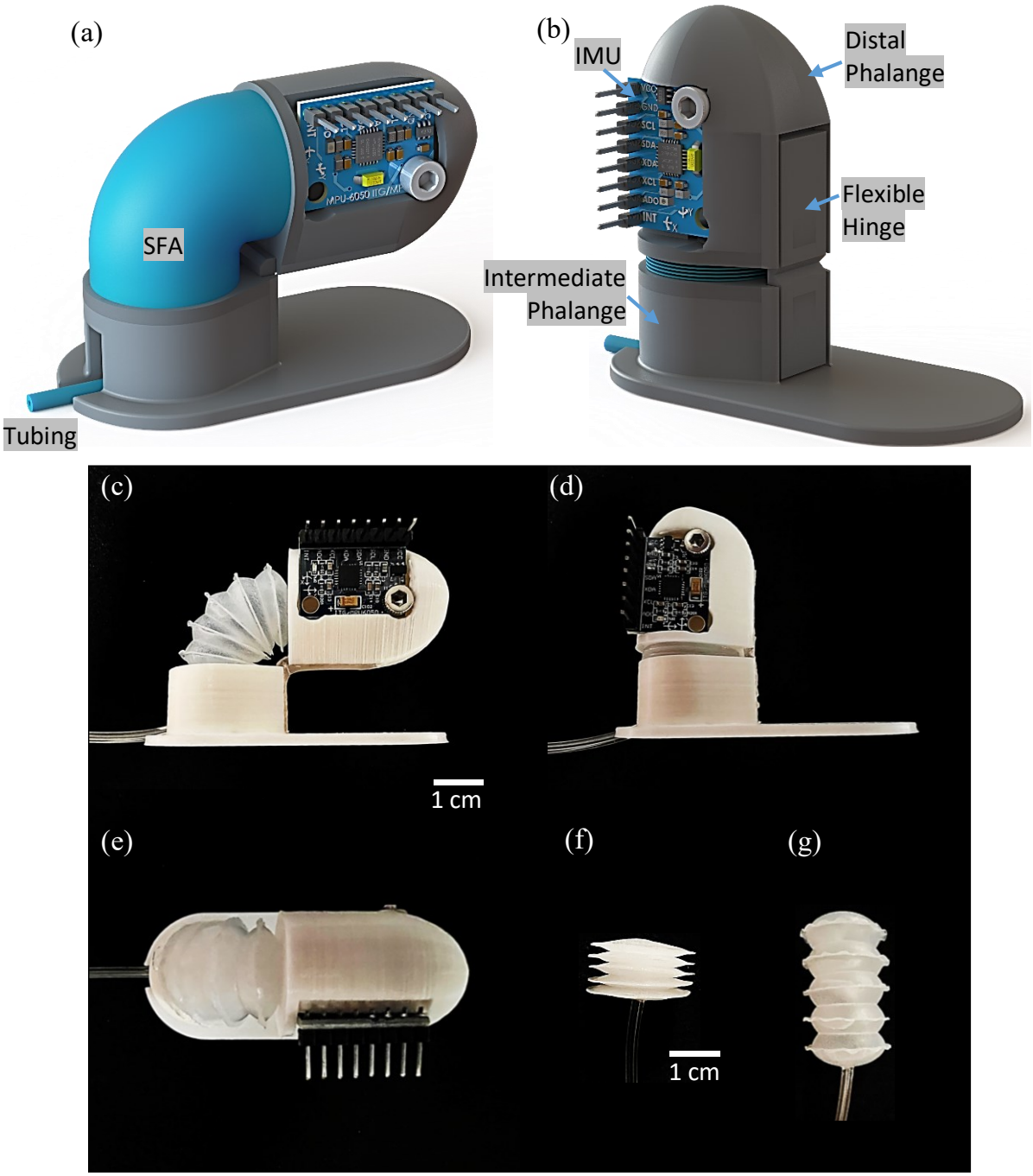


Figure 9.1: Rendered models of the soft-rigid hybrid robotic prosthetic finger when (a) pressurized/flexed, and (b) depressurized/extended. (c) Image of the soft-rigid hybrid robotic prosthetic finger pressurized/flexed. (d) Image of the soft-rigid hybrid robotic prosthetic finger depressurized/extended. (e) Top view of the soft-rigid robotic prosthetic finger pressurized/flexed. (f) Image of the depressurized/deflated bellows-style 5-layer soft fluidic actuator. (g) Image of the pressurized/inflated bellows-style 5-layer soft fluidic actuator.

9.2.3 Fabrications and Mechanical Assembly

9.2.3.1 Soft Fluidic Actuators

The instructor has the flexibility to decide whether the students will craft the soft fluidic actuators themselves or if they will work with prefabricated units. Creating a soft fluidic actuator involves a thermal bonding process that uses a heat press. The Step-by-Step Guide for Fabricating Low-Profile Bellows-Style Soft Fluidic Actuators (**Appendix F-3**) provides a detailed, step-by-step guide for this process. **Figure 9.2**, meanwhile, presents a simplified schematic of the process. **Figure 9.2a** depicts a side-view schematic of the sheet layers' alignment during the heat pressing process, which results in a Soft Fluidic Actuator (SFA). **Figure 9.2b** provides a top-down view of the shape of the sheets.

Though **Figure 9.2a** only shows the top and bottom layers, additional middle layers can be incorporated depending on the complexity of the SFA design. For example, an SFA with five layers would have three middle layers, each composed of two TPU Middle sheets enclosing a Teflon Insert sheet. Each layer is separated by a sheet of Separating Paper for easier fabrication. Each layer can be heat pressed individually before all layers are bonded via heat press, forming the low-profile bellows-style SFA.

To create an entry point for the 0.79 mm (1/32”) ID x 2.38 mm (3/32”) OD tubing, a 2 mm diameter hole punch is utilized. This method ensures a round hole, which is crucial for creating a hermetic seal when bonding the tubing to the SFA, something a Cricut cutter may have difficulty achieving at this hole size.

The design of each sheet, as shown in **Figure 9.2b**, is realized using AutoCAD. Once the shape of each sheet is drawn, they are exported in Bitmap (.bmp) file format and imported into the Cricut Design Space software for cutting. Further details about configuring the Cricut cutter can be found in **Appendix F-3**. The design CAD files of the SFA can be found in **Appendix F-4**.

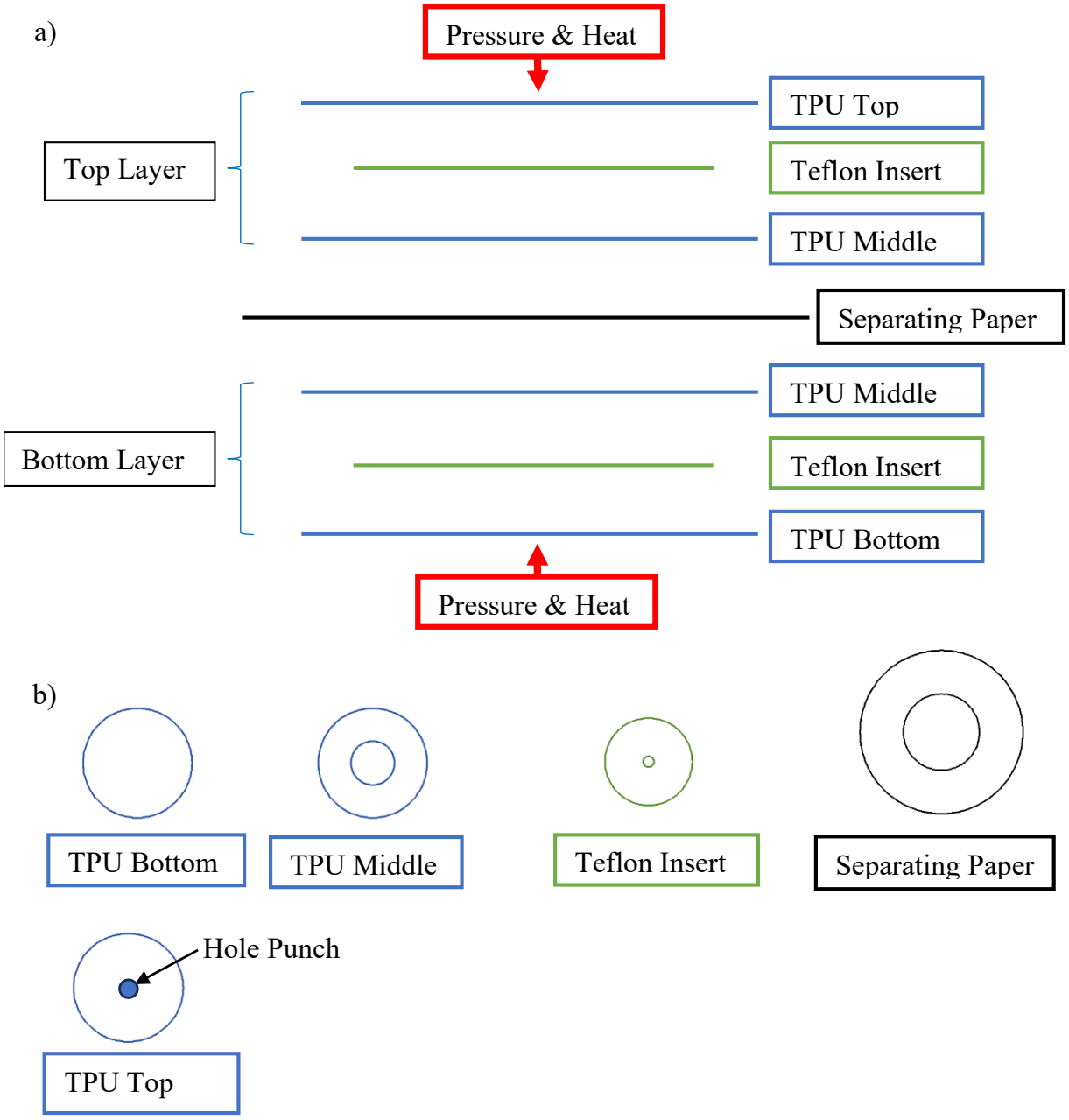


Figure 9.2: Bellows-style soft fluidic actuator manufacturing schematics: a) side view showing the stack or the sheet layers' alignment during the heat pressing process. b) Top view of each layer or sheet.

9.2.3.2 Assembly

The distal and intermediate phalanges are fused deposition modeling (FDM) 3D printed using any rigid filament or stereolithography (SLA) 3D printed using any rigid resin. The flexible hinge is FDM 3D printed using flexible filament or SLA 3D printed using flexible resin. Any

commercially available 3D printer should work. The CAD files of the distal phalange, intermediate phalange, and the flexible hinge are provided in **Appendix F-4**.

The assembly of parts, detailed in the **Appendix F-1**, uses adhesive. The nut and bolt can be manually tightened, thereby attaching the IMU to the prosthetic finger. **Figure 9.3a** provides an exploded view of the prosthetic finger assembly, while **Figure 9.3b** presents the lab's pneumatics schematic. When active pressurization is required, the miniature air pump is activated, pushing air through the de-energized 3-port / 2-way miniature solenoid valve into the SFA. Conversely, passive depressurization of the SFA is facilitated by switching off the miniature air pump and activating the solenoid valve. This allows air within the SFA to be passively released into the atmosphere. For more detailed images of the pneumatic connections, please refer to the corresponding section in **Appendix F-1**.

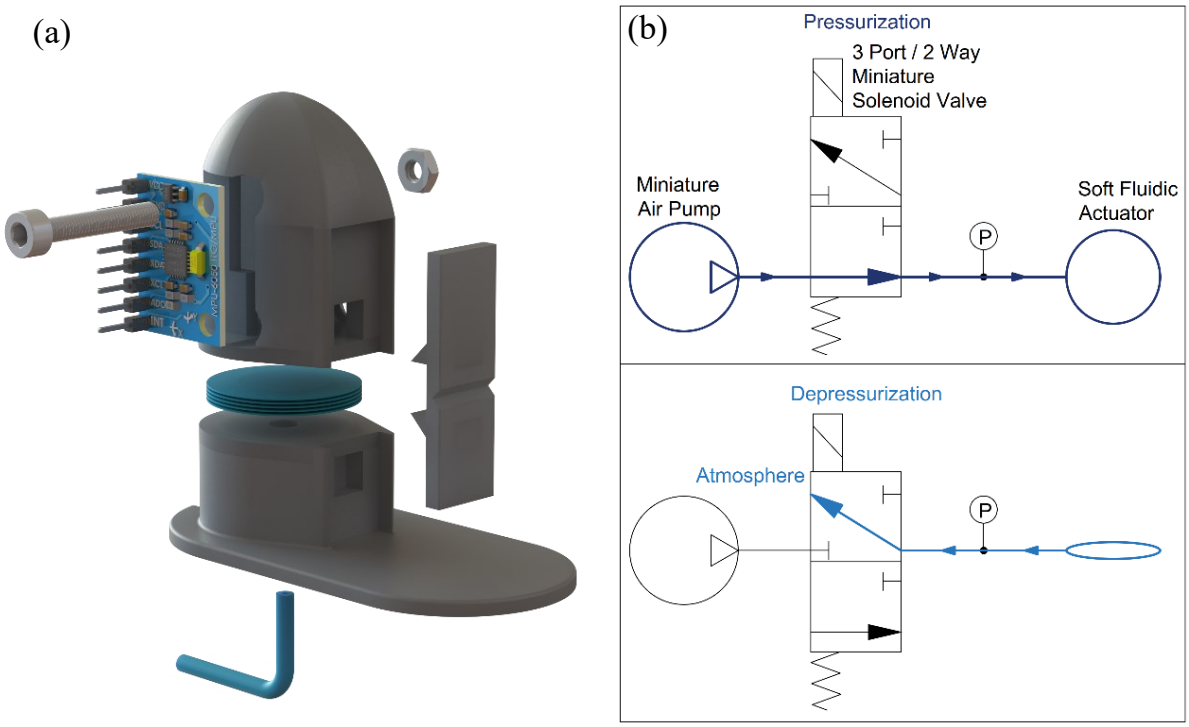


Figure 9.3: a) Exploded view of all the mechanical assembly of the soft-rigid hybrid robotic prosthetic finger. b) Pneumatics schematic of the soft-rigid hybrid robotic prosthetic finger. The letter "P" within a circle represents the air pressure sensor.

9.2.4 Sensors and Wiring (Electrical System)

Sensors and wiring are integral to systems and devices used in BME, including but not limited to assistive devices, diagnostic systems, and instrumentation. Therefore, it is crucial that

students gain hands-on experience wiring these systems and understanding their complexities instead of a pre-assembled "black box" control system. For this reason, the prosthetic finger lab employs breadboards and jumper wires. We favor this approach over using printed circuit boards (PCBs) due to the flexibility and ease of wiring it offers. Additionally, breadboards provide a blank canvas for students to work with, unlike the semi-finished nature of PCBs. The system is also safe, with most components operating at less than 5 volts and within milliamp current ranges. This setup also allows instructors to emphasize the importance of not touching live wires when the power is on.

As for the design software, an open-source hobbyist CAD software for circuit prototyping, Fritzing (Berlin, Germany), was selected over professional PCB design and schematic software such as Autodesk Eagle (San Rafael, California, United States) or Altium (La Jolla, California, United States). Fritzing's suitability for breadboard-based wiring and its intuitive and easy-to-understand graphical user interface makes it a suitable choice for this lab. Considering students may not have ample time to fully familiarize themselves with all the electronic components and their wiring schematics, Fritzing provides a user-friendly way to streamline the prototyping process. Its features include to-scale and graphically accurate component size and shape representation. **Figure 9.4** presents the wiring schematic created using Fritzing. The Fritzing file is included in **Appendix F-4**.

We opted for a metal electrode EMG sensor due to its reusability, contrasting with disposable gel-electrode EMGs that are replaced after each use. A potential drawback of using the metal electrode approach is the requirement for thorough skin preparation to minimize impedance at the skin-electrode junction. If not properly addressed, this could introduce an unacceptable noise into the signal. The cleaning process involves cleaning the skin surface with alcohol and hair removal prior to attaching the electrodes. Despite these preparations, utilizing metal electrodes will prove more economical over repeated use, particularly when accommodating larger class sizes. Students can explore and experiment with the placement of the electrodes. For an in-depth description and actual images of the electrical system, please consult the detailed guidance provided in the **Appendix F-1** and **Appendix F-2**.

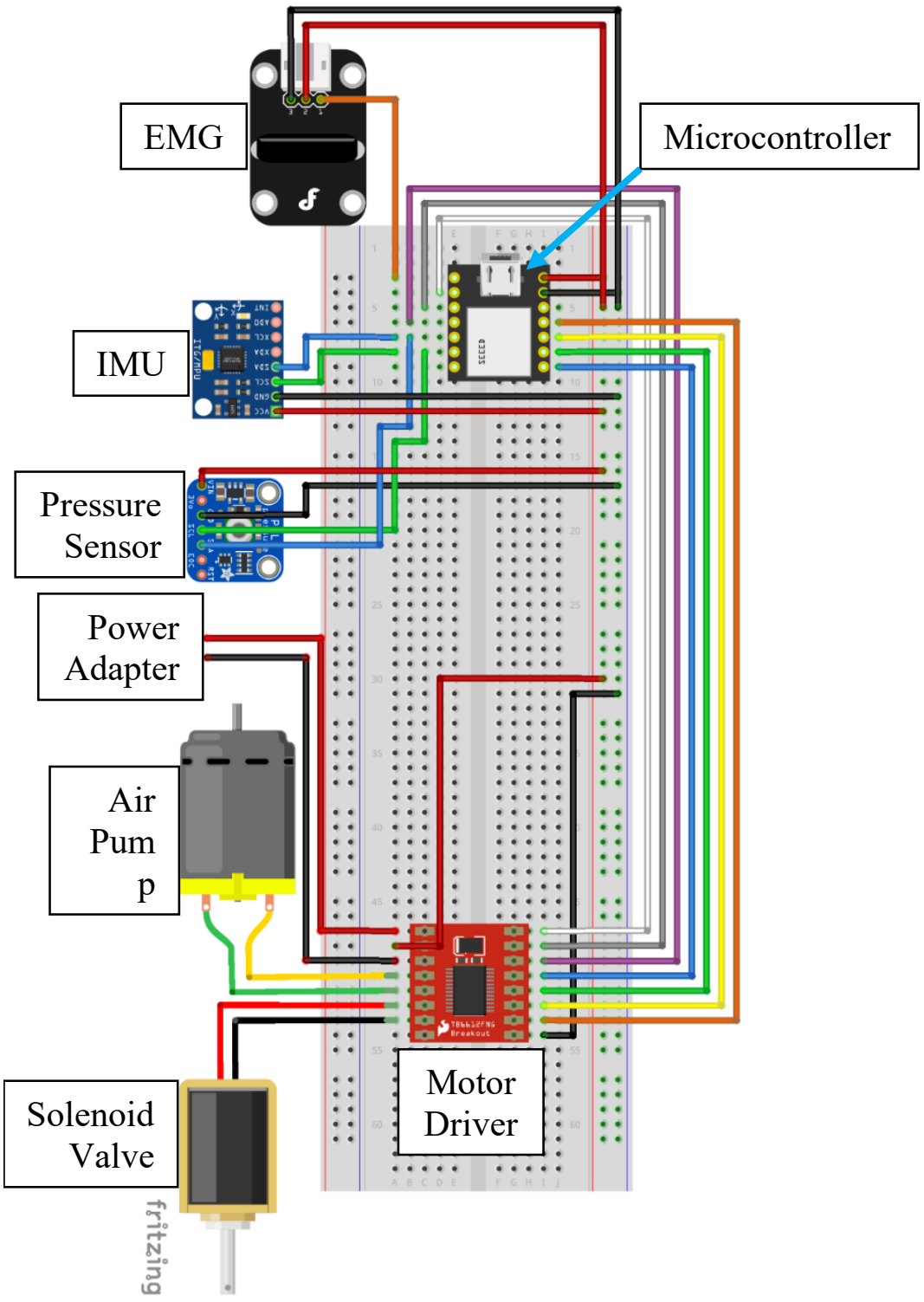


Figure 9.4: Electrical schematic of the prosthetic finger lab.

9.2.5 Software

The software for this project, written in Arduino, provides the opportunity for a highly tailored teaching approach. Please see **Appendix F-4** for the software files. Instructors can use a preprogrammed system or have students code from scratch or write specific sections of code. The prosthetic finger lab software allows PID control of the air pump and solenoid valve, enabling the system to reach a desired preset pressure based on feedback from the pressure sensor.

Additionally, an IMU is used to capture the bending angle of the prosthetic finger, with results displayed in the serial monitor. The EMG sensor is employed as a digital on/off switch control mechanism for the prosthetic finger, registering muscle exertion. Practically, a preset threshold determines if the SFA inflates or deflates. If muscle exertion indicated by the EMG signal surpasses this threshold, the SFA inflates; below the threshold, the SFA deflates.

Students are encouraged to explore different aspects of the system, including tuning the PID controller, adjusting the pressure setpoint, and modifying the digital filter coefficient for the EMG signal. They will have access to the raw, scaled, rectified, and filtered EMG output via the serial monitor for plotting. While not currently included in the lab, the software also has the potential for generating power spectral density plots through Fast Fourier Transforms (FFT). This could be especially useful informative for analyzing features of EMG signals and exploring phenomena such as fatigue and its impact on EMG signals, potentially leading to changes in the actuation of the prosthetic finger.

9.2.6 Bill of Materials

Our preference for thermal bonding stems from several reasons: 1) the casting/molding process can be messy in a classroom environment due to potential leaks, mixing, and spillage of liquid silicone; 2) it can be challenging to accurately estimate the amount of silicone needed per group because of potential leakages from the mold; 3) given its chemical nature, liquid silicone represents a potential safety hazard; 4) the demolding process can be tricky and might inadvertently damage the soft fluidic actuator; 5) casted or molded soft fluidic actuators tend to be bulkier than those produced through thermal bonding, which will likely affect their functionality or usability. Instructors can mitigate these potential issues by choosing thermally bonded TPU sheets while still providing a rich, hands-on learning experience for students.

Table 9.1 below details the bill of materials (BoM) required for each kit used in the lab. The BoM in Excel spreadsheet format (Bill of Materials.xlsx) can also be found in **Appendix F-4**. The method of deployment can be flexible, depending on available time and instructor preference. For instance, if time is constrained or a more focused learning objective is desired, the prosthetic fingers can be prefabricated and provided to students. All kit components would be reusable in this scenario, promoting resource efficiency for subsequent student cohorts.

Alternatively, the instructor may allow students to fabricate the prosthetic fingers themselves. This approach would render the prosthetic finger a consumable item, while providing a more immersive and comprehensive learning experience. In such a case, instructors may allow students to retain their creations as a tangible reminder of the activity. This decision, while potentially increasing costs, could contribute to a more engaging and memorable learning experience.

The costs indicated in BoM were determined at the time of publication. It is important to note the total costs specified do not factor in additional charges such as shipping, taxes, and import duties. Should specific components prove challenging to procure or exceed budget limitations, suitable alternatives may be sourced from other suppliers.

Two essential tools for the fabrication process are the Cricut EasyPress Mini Heat Press (South Jordan, Utah, United States) and the Cricut Maker Machine (a computer-controlled desktop cutting machine). These tools may be shared among participants, thereby managing costs. The instructor has the flexibility to determine the number of heat presses and cutting machines required based on class size and available resources.

Please note that the specific brand of heat press is not a strict requirement. Any heat press that can reliably achieve a temperature of 110 °C should be sufficient for the purposes of this lab. This flexibility allows for adaptations based on local availability and institutional budget constraints, ensuring the broader applicability of this lab exercise.

Most of the required components for this lab can be conveniently purchased online from popular suppliers (e.g., DigiKey Electronics, McMaster-Carr Supply Company, Amazon). However, one exception is Bemis 3916 Thermoplastic Polyurethane (TPU), which is produced by Bemis (Shirley, Massachusetts, United States) and distributed by Can-Do National Tape (Nashville, Tennessee, United States). Procuring this TPU necessitates a quote

request. Additional hand tools, such as scissors, mallets, cutting boards, wire strippers, multimeters, tweezers, and screwdrivers, may also be needed and are not included in the BoM.

In our experience, Bemis 3916 TPU has demonstrated exceptional robustness as a material for the soft fluidic actuator, and can be thermally bonded at relatively low temperatures. An alternative material option could be Cricut SportFlex Iron-On or any elastic thermoplastic sheet that can be thermally bonded. Note that the temperature required for secured thermal bonding is dependent on the material choice. The temperature setting of 110 °C is based on the glue line temperature of Bemis 3916 [393]

We found the process of thermally bonding TPU sheets to create soft fluidic actuators to be more suitable for a classroom setting than casting or molding soft fluidic actuators using materials such as ECOFLEX by Smooth-On (Macungie, Pennsylvania, United States) [394]. Our preference for thermal bonding stems from several reasons: 1) the casting/molding process can be messy in a classroom environment due to potential leaks, mixing, and spillage of liquid silicone; 2) it can be challenging to accurately estimate the amount of silicone needed per group because of potential leakages from the mold; 3) given its chemical nature, liquid silicone represents a potential safety hazard; 4) the demolding process can be tricky and might inadvertently damage the soft fluidic actuator; 5) casted or molded soft fluidic actuators tend to be bulkier than those produced through thermal bonding, which will likely affect their functionality or usability. Instructors can mitigate these potential issues by choosing thermally bonded TPU sheets while still providing a rich, hands-on learning experience for students.

Table 9.1: Bill of materials for the prosthetic finger lab kit.

Name	Quantity	Description	Supplier	Supplier Part Number	Unit Cost (USD)	Subtotal (USD)
Air Valve	1	3/2-Valve at 5V	Digikey/Adafruit	1528-4663-ND	2.95	2.95
Air Pump	1	Air Pump at 5V	Digikey/Adafruit	1528-4699-ND	7.95	7.95
Adafruit MPRLS Ported Pressure Sensor	1	Pressure Sensor	Digikey/Adafruit	1528-2713-ND	14.95	14.95
Seeeduino Xiao Microcontroller (Arduino)	1	Microcontroller with Digital I/O at 3.3v	Digikey/Seeed Technology	1597-102010328-ND	5.4	5.4
TB6612FNG Motor Driver Board	1	Drives Valves and Pump	Digikey/Sparkfun	1568-1755-ND	12.09	12.09
AC to DC 12V 1A Adapter	1	Power Pump and Valve	Amazon	B085WK2W6W	5.98	5.98

Breadboard and Jumper Wire Set	1	Breadboard (USD 10.99 for 3)	Amazon	B07H7V1X7Y	3.66	3.66
TPU	1	Soft Fluidic Actuator for Prosthetic Finger	Bemis	Bemis 3916	-	-
Separating Paper	1	Soft Fluidic Actuator for Prosthetic Finger (USD 40.33 for 12" x 500 ft.)	McMaster-Carr	3637N126	-	-
Teflon Insert	1	Soft Fluidic Actuator for Prosthetic Finger (USD 61.20 for 12" x 20 ft.)	McMaster-Carr	8569K15	-	-
Tubing	1	Soft Fluidic Actuator for Prosthetic Finger (USD 18 for 50 ft.)	McMaster-Carr	5233K91	-	-
3D Printed Hinge (Flexible Resin or Filament)	1	Prosthetic Finger	Formlabs/ (FDM Flexible Filament)	RS-F2-FL80-01	-	-
3D Printed Joints (Rigid Resin or Filament)	2	Prosthetic Finger	Formlabs/ (FDM Rigid Filament)	RS-F2-GPCL-04	-	-
Glue	1	Prosthetic Finger Integration (USD 5.44 for 4)	Amazon	B002U3CMZ6	1.36	1.36
M3 Hex Nut	1	Prosthetic Finger Integration (USD 5.71 for 100)	McMaster-Carr	90370A203	0.06	0.06
M3 Hex Bolt	1	Prosthetic Finger Integration (USD 14.33 for 100)	McMaster-Carr	91290A121	0.14	0.14
Gravity Analog EMG Sensor by OYM	1	EMG Sensor	Digikey/DFRobot	1738-1367-ND	49.5	49.5
IMU	1	For measuring bending angle (USD 9.99 for 3)	Amazon	B00LP25V1A	3.33	3.33
					Total Cost:	**107.37**

Additional Fabrication Components (Shared by Students)

Cricut EasyPress Mini Heat Press	1	For soft fluidic actuator fabrication	Cricut	2007468	49.99	
Cricut Maker Machine	1	For soft fluidic actuator fabrication	Cricut	2004193	249.99	
Hole Punch	1	For soft fluidic actuator fabrication	McMaster-Carr	3424A59	11.47	

9.2.7 Testing and Deliverables

The lab provides a series of thought-provoking questions to stimulate student engagement and facilitate a deeper understanding of the key concepts. Instructors can tailor the required deliverables to suit the students' skill level and previous experience. For instance, the instructor may request students to present plots of their EMG signals in various formats, display the output from the IMU, and/or provide a video demonstrating the proper functionality of their device, all in a lab report. Alternatively, instructors could set more demanding tasks, such as formal reports, in which students emphasize key results and provide an analysis of the overall prosthetic system, contextualized within the broader scholarly discourse on myoelectric prosthetics. By adjusting the deliverables, instructors can tailor the activity to remain challenging yet achievable, supporting each student's learning journey.

Figure 9.5 presents potential deliverables for the students. **Figure 9.5a** depicts a plot comparing the internal air pressure within the SFA and the bending angle of the prosthetic finger, as measured by the IMU. The observed spikes in both pressure and angular measurements can be ascribed to the control system. While the PID controller modulates the air pump to adjust pressure levels, the inability of the on/off solenoid valve to accommodate proportional control results in these pronounced spikes. **Figure 9.5b** exhibits a plot of the raw, scaled, and rectified EMG signal. **Figure 9.5c** juxtaposes the rectified and filtered EMG signal with the bending angle of the prosthetic finger. It is evident that as long as the EMG signal surpasses the set threshold, the prosthetic finger bends. Conversely, the prosthetic finger straightens once the EMG signal drops below this threshold.

During the straightening phase, the finger does not fully return to its baseline state. This is attributable to the system's passive deflation nature, in which air inside the SFA is gradually released to the atmosphere via pressure differential rather than active negative pressure. Instructors can allow students to modify the setup, switch to an active exhaust system, and analyze the resultant differences. This adjustment would necessitate the inclusion of an additional 3 port 2-way solenoid valve, similar to the arrangement outlined by Gao et al. [147]. Moreover, the instructors may encourage students to experiment with varying threshold levels and potentially explore the concept of proportional control.

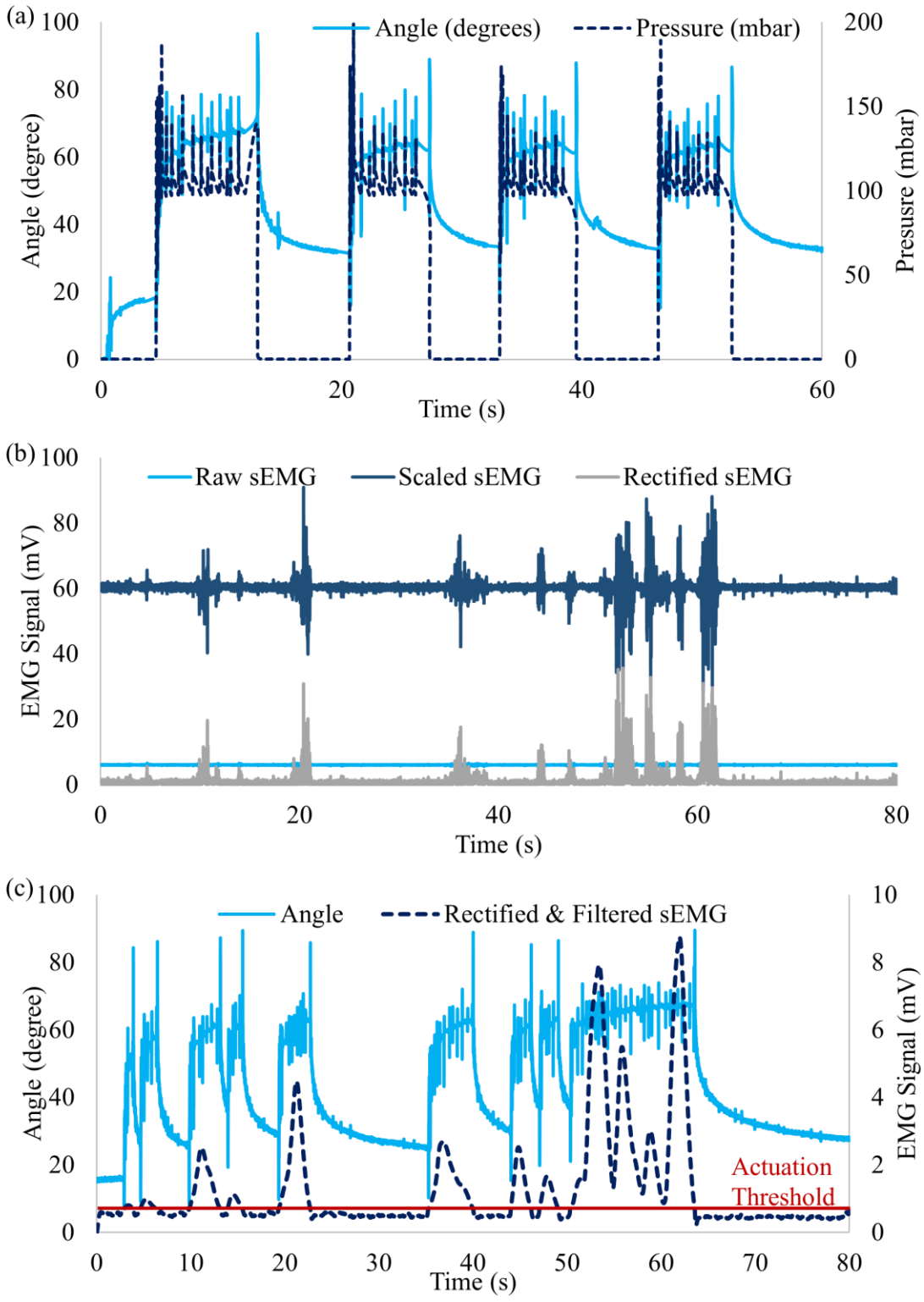


Figure 9.5: Potential lab deliverable plots: a) internal air pressure within the SFA measured by the air pressure sensor and the bending angle of the prosthetic finger measured by IMU. b) Raw versus scaled versus rectified EMG. c) Rectified & filtered EMG compared to the bend angle of the prosthetic finger.

9.3 Student Feedback

The students' response to the lab was very positive, indicated by their feedback. The following are excerpts from two anonymous surveys: one specifically designed for the lab, and a formal survey conducted through the University of Waterloo's official Student Course Perception course feedback system. Responses from the lab-specific survey are designated by 'LS' followed by a number, while feedback from the Student Course Perception is indicated by 'SCP' and a number. The complete student responses from the Lab Specific Survey can be found in **Appendix F-4**. The comprehensive University Student Course Perception report is available upon request by contacting the corresponding author.

9.3.1 Lab Specific Survey

LS1 – "I really enjoyed the labs and they made me very excited about the rest of the course. This is the type of content that I also really wish I had more exposure to earlier in my degree as it would have provided useful context for the technical content I was learning about in other courses (ex. signal processing, controls, mechanical design, electronics, etc.)."

LS2 – "Great lab, very helpful instructing team, overall great experience."

LS3 – "Great hands on lab with real learning! I like that we had to figure some things out, without everything spelled out exactly."

LS4 – "Would love to have more labs like this across all courses!"

LS5 – "Amazing and definitely useful for hands-on learning."

LS6 – "I love everything about this lab. I don't come from an engineering background, so the wiring component and using the Arduino were both especially useful for me!"

LS7 – "The labs were very enjoyable and a nice break from lecture content to expose us to how the content is used in real life. "

LS8 – "I think not having a report definitely helps with me actually learning and caring what goes on in the lab. This is probably one of the only labs I will remember after I graduate."

9.3.2 University Student Course Perception

SCP1 – “I really enjoyed the hands on lab activities that gave me exposure to the applications of course content.”

SCP2 – “I liked the course’s format. With more spread out assignments, and participation labs - the course encouraged learning for enjoyment rather than learning just for marks.”

SCP3 – “Add additional hands-on laboratory sessions.”

SCP4 – “Perhaps more hands on components, or an assignment that is technical instead of just writing (making our own prosthetic for example).”

SCP5 – “I would like to have more workshops to develop hands on learning of what we are being taught or more labs that were more us (the students) doing the work.”

SCP6 – “Lab instructions could be more clear and concise.”

SCP7 – “More hands on Labs. The labs were really great, wish there were more.”

SCP8 – “Cool labs.”

SCP9 – “The professors genuine interest in their respective fields and the labs being hands-on, able to focus on the actual activity instead of questions for a lab report.”

9.4 Discussion

9.4.1 How the Lab Fits in BME

Many academic programs offer in-depth teaching of topics within the realm of biomedical/biomechanical engineering (BME), with each course typically focused on a singular aspect, such as mechanical systems, electrical systems, software systems, or fundamental sciences. This level of specialized instruction is undeniably valuable, allowing students to develop expertise in specific areas of this broad field. However, the integration of focused knowledge from core courses into a biomedical device remains a challenge in many curricula. Creating and optimizing biomedical devices, such as prosthetics, implants, or diagnostic tools, often involves integration of multiple systems working in concert while considering the clinical needs, user perceptions, and regulatory and economic policies. Despite

this reality, the current academic landscape tends to compartmentalize these topics, potentially leaving students underprepared to integrate their knowledge across different subsystems [395].

In order to bridge this gap, educators strive to integrate cutting-edge technologies grounded in real-world applications into the learning process, enabling students training in current techniques and tools. However, this process must be carefully managed to ensure affordability and practicality in a post-secondary educational setting. The expense of procuring and maintaining sophisticated technology could become a barrier for many institutions, possibly limiting access to quality education [396]. Therefore, educational strategies may focus on cost-effective means to introduce these advancements into the classroom. The presented lab activity aims to serve as a practical, implementable learning strategy to expose and immerse students in emerging and established technologies.

The presented hands-on lab activity focused on hybrid soft-rigid robotic prosthetics has been successfully piloted in a class of 40 senior engineering students from biomedical (11), mechanical (20), mechatronics (5), nanoengineering (2), system design (1), and management (1) engineering programs. This lab not only bolsters their technical proficiency but also fosters teamwork, interdisciplinary collaboration, and communication skills. Further, it motivates students to explore beyond the curriculum. Interdisciplinary collaboration is especially beneficial as it simulates a team-based work environment, where individuals from different disciplines come together to work towards a common objective [397]. In addition, the lab kit is affordable at ~$100 USD per kit, with most components being reusable. **Figure 9.6** presents a collage of photos of the students actively engaged in the lab activities.



Figure 9.6: Photos of the student working on the soft-rigid robotic prosthetic finger lab. The images have been intentionally stylized and blurred to maintain student privacy.

While the prosthetic finger lab was originally designed for a senior elective course in biomedical engineering focusing on neuro and rehabilitation engineering, its applicability extends beyond that context. The activity may be integrated into courses focusing on wearable technology, biomechanical instrumentation, biophysical signal processing, assistive technology, and/or human biomechanics. The lab could even serve as a foundation for capstone design projects for upper-year students. However, educators must ensure that the prosthetic finger lab aligns with and supports specific course's learning objectives. In essence, the lab should offer clear, tangible benefits that enhance the students' understanding of specific course material [396]. Therefore, it is crucial to carefully evaluate the lab's suitability for a course, making revisions as necessary to optimize its relevance and effectiveness.

Given that all lab materials are open-access, instructors may revise the lab according to their specific needs, ensuring alignment with their respective courses' themes and learning outcomes. They can augment, modify, or omit parts of the lab to suit their pedagogical requirements best, making it a flexible and adaptable educational tool.

9.4.2 Takeaways from the Pilot

The duration of the lab depends on the extent of the preparatory work done. If the SFAs and 3D printed parts are prefabricated, and the software code is already provided, 3 hours divided into two 1.5-hour or three 1-hour sessions should suffice. However, if the students are tasked with fabricating the SFAs and programming the software, each activity would likely require an additional hour, effectively extending the total lab time to 5 hours. All activities need not occur in a structured classroom setting; instructors may allow students to work on certain aspects of the lab outside the designated hours. The necessary components conveniently fit into clear plastic boxes, as shown in **Figure 9.7a**, facilitating easy transport and organization. Should additional time be available, instructors could elevate the complexity of the lab by encouraging students to design and test a multi-jointed prosthetic finger or even multiple digits featuring abduction and adduction movements, as described in Ref. [256]. Additional challenges would deepen students' comprehension of (multi-joint) prosthetics and introduce advanced (multivariate) control schemes. Introducing multiple EMG sensors could also facilitate independent control of multiple digits, offering a richer, more engaging exploration of prosthetic functionality [398].

For safety during SFA fabrication and prosthetic finger assembly, gloves should be provided, particularly during glue application. The lab can accommodate both individual and group work. Student feedback suggests that group sizes should not exceed four individuals for optimal collaboration and learning. In our experience, a ratio of three well-versed instructors or teaching assistants (TA) for every ten groups of four students (or less), affords a conducive learning environment where each group member contributes to the objectives, and minimizes social loafing [399]. With more students or groups per instructor or TA, the instructional team may experience challenges such as addressing multiple queries from groups simultaneously, thus decreasing attention and the quality of teaching.

Given the intricate nature of this lab, involving individual electronic components, wiring, moving mechanical parts, and coding, all outside of a pre-assembled "black box," mistakes are inevitable. During our pilot lab, for instance, two SFAs were over-pressurized and plastically deformed due to wiring errors (**Figure 9.7b**). Additionally, two motor drivers and one IMU were damaged due to incorrect wiring. Despite these mishaps, students

recognized these instances as valuable learning opportunities. This constructive perspective provided essential lessons for future careers, as evidenced by student feedback (LS3). Consequently, students are encouraged to learn from errors rather than providing a flawless, step-by-step guide. However, this necessitates additional spare components on hand to accommodate such incidents.

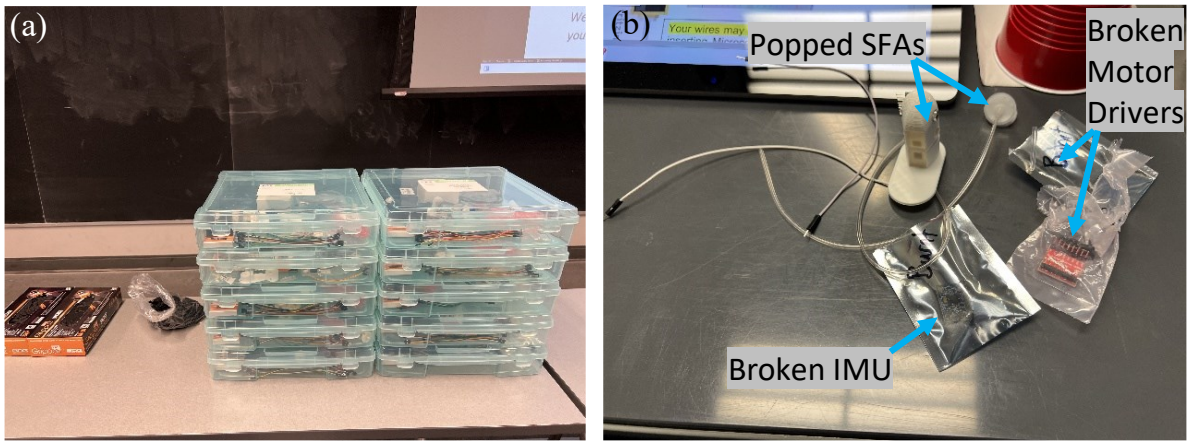


Figure 9.7: a) Image of the plastic boxes containing all the components of the prosthetic finger lab; each box contains one kit. b) Broken parts during the pilot run, including two SFAs, two motor drivers, and an IMU.

The prosthetic finger lab not only immerses students in a practical application but also establishes a platform for learning, which may not always be feasible due to the 'black box' nature of many lab settings (e.g., LEGO Mindstorms robot [400]), often used for introductory engineering courses. As suggested by student feedback SCP 5, students appreciate labs that place them in the driving seat, enabling them to execute the majority of the work. While not explicitly mentioned in the students' feedback, many found the moment of successfully controlling the prosthetic finger's movements and measuring the corresponding internal SFA air pressure using their arm muscles and EMG, to be a pivotal 'Eureka' moment. This moment was a significant motivator, reinforcing active learning achieved by integrating EMG, IMU, electrical systems, pneumatic systems, and soft-rigid robotic prosthetic components. We believe such comprehensive understanding and application are difficult to attain with only one or two of these elements exercised in isolation.

The choice of a pneumatic system is strategically made to offer students a hands-on opportunity to assemble the tubing, test for leakage, and ensure the synergistic functioning of

all components in a safe environment. In cases where the connections are suboptimal, the worst-case scenario is plastic deformation, leakage, or popping of the SFA, which does not pose any danger. Students can easily overpower the SFA's force and quickly disconnect the tubing to release pressure in emergencies. Further, instructors can install a pressure relief valve to ensure the system does not exceed a predefined pressure threshold. Switching to a motorized system could potentially introduce safety concerns that are more challenging to address, such as overheating, excessive vibration, and issues with torque regulation. A motorized system could also increase complexity and cost, given the additional need for components like gears and cables [401]. Thus, the pneumatic system provides a more straightforward, safer, and cost-effective approach for this lab setting.

As evidenced by their feedback, students greatly appreciated the hands-on nature of the labs, expressing a desire for more similar experiences (see student feedback LS4, SCP3, SCP4, SCP5, and SCP7). Interestingly, student feedback highlighted that the lab activities were more enjoyable, meaningful, and memorable when the focus was not strictly on lab report completion (see student feedback LS8, SCP2, and SCP9). During the pilot run, the instructors simplified the deliverables by requiring students submit a video demonstration of the functioning system (a compilation of the student team submitted videos can be seen in the **Appendix F-5**), along with a basic lab report comprising of answers to the proposed questions supported by data analyses. While simple, this less formal report format was effective in verifying student comprehension of the system and successful achievement of the learning outcomes without imposing a heavy burden. Eliminating the preoccupation with graded report submissions and pressure of adhering to rubric criteria likely minimized student stress levels, enabling them to focus on the activity and fostering group collaboration. While our implementation seemed to foster deeper learning and engagement, the activity may be revised to include formal assessments.

9.4.3 Limitations

There are three primary limitations associated with the prosthetic finger lab. Firstly, it does not involve quantitative measurement and analysis of human motion, an essential component of biomechanics. Secondly, the current lab does not delve into the process of analog-to-digital conversion, a crucial aspect of digital acquisition systems widely used in research and

development. Thirdly, the control system implemented is relatively basic, utilizing a PID controller rather than more advanced options such as a postural [402] or pattern recognition controller [403]. However, these limitations do not diminish the lab's educational value. Each limitation presents an opportunity for expansion; additional labs and lectures could be introduced to address these areas and further deepen students' understanding of these topics. Thus, while these are current limitations, they highlight potential avenues for future curriculum enhancement.

9.4.4 Future Improvements

Two areas of potential improvement for this lab have been identified. Firstly, the clarity and brevity of the lab instruction could be improved, as suggested by the student feedback SCP6. However, it is important to note that our aim is not to develop an exhaustive step-by-step guide that could potentially overshadow the exploratory nature of the exercise. Instead, we aim to create an instruction manual that enables students to understand the lab's requirements at a glance, promoting independent problem-solving and discovery.

Secondly, the lab could be enriched by integrating technologies such as electroencephalogram (EEG), haptics, and motion capture systems. The inclusion of EEG would enable students to explore brain-computer interfaces. Haptics may allow the prosthetic finger to better interact with squishy objects like berries and rigid objects like glassware. Similarly, introducing a motion capture system would allow students to control the prosthetic finger using their body movements. These enhancements would increase the depth and breadth of the learning experience and keep the lab in line with advancing technologies in the field, but potentially at the cost of additional complexity and cost.

9.5 Concluding Remarks

We have introduced an innovative, hands-on laboratory focused on soft-rigid hybrid robotic prosthetics, providing all materials in an open-access format. The lab, in a pilot with 40 senior engineering students, garnered overwhelmingly positive feedback. Based on student evaluations, the merits and limitations of this hands-on lab are discussed. Overall, the lab offers an affordable, straightforward, and safe setup with real-world implications that effectively exercises a range of biomedical/biomechanical engineering concepts to students, particularly

system integration. We are confident that this lab enhances the teaching of biomedical/biomechanical engineering and can be a valuable addition to related courses at the post-secondary level. We hope educators will leverage the information presented here to integrate these methods into their curricula, thereby enriching their students' learning experiences.

Chapter 10

Conclusion and Recommendations

10.1 Contribution of this Thesis

Much of the contemporary development in soft wearable robots remains tethered within the confines of research labs, primarily focused on the allure of novelty and miniaturization. This pursuit often inadvertently sidelines the quintessential goal of practicality and enhanced aesthetics, which are crucial for broader user acceptance in real-world scenarios. While some argue that the quest for miniaturization inevitably compromises functionality due to the necessary downsizing of components, which is a common issue in traditional motorized and power-electronic systems, this perspective can be revolutionized by soft wearable robots. By grounding designs in the principles of foundational physics and biology, such as fluid dynamics, biomechanics, and physiology, and integrating or even emulating the expert practices of physiotherapists, medical specialists, and caregivers, researchers can create solutions that epitomize both elegance and functionality. This concept resonates with the idea of biomimicry in the domain of autonomous soft robots. This thesis champions the notion that miniaturization and optimal performance are not mutually exclusive. Rather, they can harmoniously coexist, enhancing each other's merits. At its heart, the true potential of soft robots lies in their inherent flexibility and safety for human interaction. Yet, they also possess the latent ability to be streamlined, maintaining their potency in a sleek and low-profile form. This marriage of form and function underscores the transformative power of soft robotics.

The process of miniaturizing soft wearable robots varies based on the system in question. At its core, this miniaturization encompasses both the refinement of actuators (often referred to as the frontend) and the streamlining of control systems (or the backend). It's noteworthy that the soft wearable robots depicted in this thesis diverge significantly from

traditional robotic imagery. A primary insight from this thesis is the realization that some of these robots don't rely on batteries or standard electronic control systems at all. This underscores the importance of tailoring control systems, actuators, and sensors to align seamlessly with the intended purpose and specific applications. Such customization ensures that while these robots may not fit the conventional mold, they are meticulously designed to excel in their designated roles.

This work introduces systems that employ soft fluidic actuators, harnessing their capabilities to perform tasks through compression, force, torque, and sensing. While these systems represent just a fraction of the vast soft robotics landscape, they signify a foundational step, paving the way for commercialization or acting as precursors for more intricate systems with advanced materials and controls. Soft wearable robots, as assistive devices, are on an evolutionary trajectory, anticipated to benefit from improved materials, refined control systems, integration with rigid components, and potentially even non-fluidic actuation strategies. Technological advancements, as history suggests, take time. Yet, for the present, soft fluidic actuators stand out as the most developed and viable platform for tangible applications, particularly those necessitating miniaturization. It's paramount that researchers and designers embed the ethos of miniaturization early in the design phase of assistive soft wearable robots. This proactive approach preempts the pitfalls of retrospective design changes, which often stumble upon insurmountable challenges. For designs seemingly resistant to miniaturization, it may be time to reimagine the foundational design approach altogether.

This thesis establishes the groundwork, encompassing both technological innovations and underlying principles, for miniaturizing control systems and actuators in soft robotic systems intended for biomedical applications. In the realm of applied research, the ultimate aspiration for these soft wearable robots is to transition from conceptual to tangible, providing real-world benefits to society. Every technological innovation carries its constraints, and fluid-based soft robots are no exception. The projects highlighted in this thesis, though representative of critical challenges such as upper limb treatment of peripheral vascular conditions through an active compression sleeve and lower extremity aids like knee braces and prosthetics, are not exhaustive. However, the foundational technologies and guiding principles introduced can be adapted, enhanced, and applied to a wide array of other systems.

In terms of control systems, for applications that involve slow, predictable sequences of pressurization and depressurization, one can employ microfluidic systems. These incorporate passive features like microchannels and active elements such as in-line pinch valves. For scenarios that require synchronization or activation in response to body movements or gait, body-driven systems prove beneficial. When it comes to actuators and sensors, the lens of application-centric design is pivotal. By tailoring design based on user needs rather than mere novelty, miniaturization seamlessly integrates into the design process. This avoids the afterthought of needing to condense already developed systems. A preference should be given to designs that are both elegant and straightforward over those cluttered with sensors and costly components. This isn't to discredit complex systems; rather, it underscores that each system type has its distinct purpose and utility. Furthermore, this thesis posits that the aesthetics achieved through miniaturization can influence a device's societal acceptance, making it just as crucial as functional and system performance criteria.

Chapters 3 through 5 showcase the effectiveness, elegance, and simplicity of employing passive air microfluidic components, such as microchannels, and active components like in-line pinch valves within an ultra-compact framework, embodied as air microfluidic chips. These components facilitate a pre-programmed sequential pressurization of a series of soft fluidic actuators. Their application spans from the management of lymphedema and peripheral vascular conditions, to addressing the volume fluctuations of residual limbs in lower extremity prosthetic sockets. These projects present dual contributions. Technologically, the air microfluidic components have the potential to revolutionize the miniaturization of control systems for similar soft fluidic actuator-enabled assistive devices that need predetermined sequences of pressurization and depressurization at moderate rates. Intellectually, these chapters enrich the current repository of knowledge on the research and design of active compression sleeves, managing conditions like lymphedema and deep vein thrombosis, as well as self-adjusting prosthetic liners. They provide researchers with design theories and principles that can inspire further innovations in assistive devices, enhancing the quality of life for end users.

In the realm of soft fluidic actuator and sensor design for miniaturizing soft wearable robots, chapters 5, 6, 7, and 9 delve into distinct designs: active compression mechanisms, dynamic fluidic cushion inserts for prosthetic sockets, sensors to detect downward movement

in prosthetic sockets, and a finger prosthesis for educational use. While these designs vary, they share a common thread: each is tailored to specific user needs and boasts a sleek, low-profile design without compromising and often enhancing functionality compared to existing commercial systems. These designs offer two central insights. Firstly, they underscore the potential for actuators to double as sensors, and vice versa, albeit application dependent. Secondly, they emphasize the pivotal role of an actuator's geometry in miniaturization. The designs underscore the need for careful consideration in the placement and design of soft fluidic actuators to ensure optimal functionality, miniaturization, and alignment with existing device paradigms. Miniaturization should adapt to available spaces and adhere to established, real-world-tested device designs rather than trying to redefine or repurpose these spaces. While this is not a call to avoid innovation in medical device form factors, it stresses the significance of societal norms, user adoption, and existing perceptions. Recognizing these factors is crucial, as they can either facilitate or hinder the integration of novel technologies. Ultimately, the technological advancements presented in these chapters contributes to the progression of their respective application domains.

Chapter 8 presents a unique perspective on miniaturization, highlighting that it is not merely reliant on technological advancements but also fundamental human biomechanics. This is exemplified in our development of a soft robotic unloader knee brace for osteoarthritis management. Initially, we envisaged an electronically controlled, air-pumped system. However, we soon realized that such a setup would either be too slow or too cumbersome. Consequently, we turned our focus towards the mechanics of human gait. We discovered that utilizing body weight and natural gait movement was the perfect synchronization mechanism to unload the knee during the weight-bearing stance phase. This revelation was our eureka moment, where we realized the potential of a body-driven, electronics-free soft wearable robot. The knee brace's contribution in this chapter extends beyond its design and function. It also revolutionizes the concept of unloading knee brace design, highlighting the importance of basic principles and technical knowledge in this transformation.

All in all, the principles and insights shared in this thesis directly answer the pressing call for applied research in the field of soft wearable robots, particularly those destined to move beyond laboratory settings into the practical, real-world applications that will ultimately benefit end users. However, this work is not the conclusion of the journey towards

miniaturizing soft wearable robots; it is merely the commencement. There remains a vast expanse of uncharted territory ripe for innovation, fertile ground for technological advancement, and a deep well of knowledge yet to be tapped.

10.2 Future Work

While most of the work carried out in this thesis has focused on engineering benchtop proof-of-concept testing, the extensive process of validating these systems within a clinical setting remains largely unexplored. For example, the design of the gait-controlled soft robotic knee brace could be refined and adapted for various knee conditions as part of comprehensive rehabilitation strategies. Potential modifications could include the incorporation of pneumatic artificial muscles or other types of low-profile fluid actuators in place of traditional air bladders for dynamic knee brace actuation. However, the incorporation of such changes necessitates meticulous consideration of the internal air volume within fluid actuators, as the foot bellows' limited space within a shoe could interfere with the user's natural gait if the volume is excessive. It's also worth noting that soft wearable robots employing body-driven systems have potential applications beyond just unloading knee braces.

As simulation methodologies continue to advance, coupled with the rapid growth in computational power, there emerges a promising potential to simulate a vast majority of soft robotic systems. This technological progression could serve as a game-changer, allowing researchers and developers to bypass time-consuming and resource-intensive trial-and-error experiments in the laboratory. By leveraging high-fidelity simulations, the development cycle could be streamlined, fostering faster innovation and optimization in the field of soft robotics.

With advancements in fabrication techniques such as 3D printing and the utilization of micro-milling machines, the miniaturization of air microfluidic control systems can be enhanced. Higher resolution fabrication can lead to smoother molds, enabling the reduction in size of both microchannels and pneumatic in-line valves. This technological progress could ultimately facilitate the reliable manufacturing of demultiplexers capable of controlling the pressurization and depressurization of individual soft fluidic actuators within useful pressure ranges. Such improvements would substantially augment the capabilities of air microfluidic chips, extending their functionality beyond sequential control.

In the realm of actuator design, much emphasis has been placed on the creation of systems that facilitate compression, torque, or force. However, the role of shear, a crucial aspect in numerous biomedical applications, has often been overlooked, despite its profound implications. Designers must consider the coupling of sensors with a shear actuator, and also thoughtfully account for miniaturization and real-world applications. The pursuit of novelty should not result in large, bulky systems that hold little practical value in real-world scenarios. Instead, the design process should focus on creating compact, functionally robust systems that effectively incorporate the dimension of shear.

The dynamic prosthetic cushion and the distal end actuator ought to be harmoniously integrated to engineer a system that autonomously adjusts the fit of a user's prosthetic via a feedback mechanism. This holistic solution can maintain a sleek, miniaturized form while also accommodating the volume fluctuations of the residual limb and providing relief to bony prominences within the socket. Thus, through thoughtful design, comfort and functionality can be achieved without sacrificing the aesthetics and convenience of a low-profile device.

The hybrid soft-rigid finger prosthetic lab offers tremendous scope for enhancement. The incorporation of haptic technology, motion capture systems, and brain-computer interface capabilities can ensure that the lab remains a beacon of innovation in this evolving field. These advancements are not just additions but are crucial to equipping students with hands-on experience and knowledge of the latest advancements in soft robotics and related technologies. By incorporating these sophisticated tools, the lab can provide an immersive and state-of-the-art environment that can prepare students for the rapidly developing landscape of soft robotics.

Viewed from a broader perspective, the relentless pursuit of miniaturization in soft wearable robots should persist, irrespective of the actuation method employed – be it fluidic control, cable systems, smart materials, or other innovative mechanisms. Perhaps in the not-too-distant future, we will witness the ubiquity of soft robots equipped with miniaturized control systems and sleek, low-profile actuators and sensors. These will be interwoven seamlessly into every facet of our lives, assisting us with day-to-day activities, contributing to disease treatment and injury recovery, providing entertainment, enriching educational experiences in classrooms, enhancing our living conditions, and even aiding us in the exploration of new and thrilling environments.

References

[1] N. Tesla, “Valvular Conduit,” US1329559A, Feb. 03, 1920

[2] H. H. Glaettli, “Digital Fluid logic Elements,” 1964, pp. 169–243. doi: 10.1016/S0065-2458(08)60221-1.

[3] A. K. Gehring, M. Jacoby, and T. D. Reader, “Pure Fluid Computer,” US3190554A

[4] J. W. Joyce, “Fluidics: Basic Components and Applications,” Adelphi, 1983.

[5] J. A. Meyer and J. W. Joyce, “The Fluid Amplifier and its Application in Medical Devices,” *Anesth Analg*, vol. 47, no. 6, Nov. 1968, doi: 10.1213/00000539-196811000-00015.

[6] R. Gottron, V. Kumar, and A. Corrado, “Fluidic Applications in North America,” *IFAC Proceedings Volumes*, vol. 8, no. 1, pp. 531–538, Aug. 1975, doi: 10.1016/S1474-6670(17)67511-6.

[7] S. G. Kandlikar, S. Garimella, D. Li, S. Colin, and M. King, *Heat Transfer and Fluid Flow in Minichannels and Microchannels*. 2013. doi: 10.1016/C2011-0-07521-X.

[8] Henrik. Bruus, *Theoretical Microfluidics*. 2008.

[9] G. M. Whitesides, “The origins and the future of microfluidics,” *Nature*, vol. 442, no. 7101, pp. 368–373, 2006, doi: 10.1038/nature05058.

[10] G. M. Whitesides, “Soft Robotics,” *Angewandte Chemie - International Edition*, vol. 57, no. 16, pp. 4258–4273, 2018, doi: 10.1002/anie.201800907.

[11] C. Majidi, “Soft Robotics: A Perspective—Current Trends and Prospects for the Future,” *Soft Robot*, vol. 1, no. 1, pp. 5–11, 2013, doi: 10.1089/soro.2013.0001.

[12] F. Ilievski, A. D. Mazzeo, R. F. Shepherd, X. Chen, and G. M. Whitesides, “Soft robotics for chemists,” *Angewandte Chemie - International Edition*, vol. 50, no. 8, pp. 1890–1895, 2011, doi: 10.1002/anie.201006464.

[13] D. J. Preston *et al.*, “Digital logic for soft devices,” *Proc Natl Acad Sci U S A*, vol. 116, no. 16, pp. 7750–7759, 2019, doi: 10.1073/pnas.1820672116.

[14] A. Rajappan *et al.*, “Logic-enabled textiles,” *Proceedings of the National Academy of Sciences*, vol. 119, no. 35, Aug. 2022, doi: 10.1073/pnas.2202118119.

[15] S. W. Angrist, “Fluid Control Devices,” *Sci Am*, vol. 211, no. 6, pp. 80–89, 1964, [Online]. Available: http://www.jstor.org/stable/24931729

[16] I. N. Gaiser, C. Pylatiuk, S. Schulz, A. Kargov, R. Oberle, and T. Werner, “The FLUIDHAND III: A Multifunctional Prosthetic Hand,” *JPO: Journal of Prosthetics*

and Orthotics, vol. 21, no. 2, 2009, [Online]. Available: https://journals.lww.com/jpojournal/Fulltext/2009/04000/The_FLUIDHAND_III__A_Multifunctional_Prosthetic.5.aspx

[17] S. Schulz, C. Pylatiuk, and G. Bretthauer, "A New Class of Flexible Fluidic Actuators and their Applications in Medical Engineering," *at - Automatisierungstechnik*, vol. 47, no. 8, Jan. 1999, doi: 10.1524/auto.1999.47.8.390.

[18] C. Walsh, "Human-in-the-loop development of soft wearable robots," *Nat Rev Mater*, vol. 3, no. 6, pp. 78–80, 2018, doi: 10.1038/s41578-018-0011-1.

[19] A. D. Woolf and B. Pfleger, "Burden of major musculoskeletal conditions," *Bull World Health Organ*, vol. 81, no. 9, pp. 646–656, 2003, doi: S0042-96862003000900007 [pii].

[20] A. Hammond, "Rehabilitation in musculoskeletal diseases," *Best Pract Res Clin Rheumatol*, vol. 22, no. 3, pp. 435–449, 2008, doi: 10.1016/j.berh.2008.02.003.

[21] D. J. Hunter and S. Bierma-Zeinstra, "Osteoarthritis.," *Lancet*, vol. 393, no. 10182, pp. 1745–1759, Apr. 2019, doi: 10.1016/S0140-6736(19)30417-9.

[22] L. M. G. Bianchi *et al.*, "Diagnosis and Treatment of Post-Prostatectomy Lymphedema: What's New?," *Current Oncology*, vol. 30, no. 5, pp. 4512–4526, Apr. 2023, doi: 10.3390/curroncol30050341.

[23] L. Cappello *et al.*, "Assisting hand function after spinal cord injury with a fabric-based soft robotic glove," *J Neuroeng Rehabil*, vol. 15, no. 1, pp. 1–10, 2018, doi: 10.1186/s12984-018-0391-x.

[24] L. N. Awad *et al.*, "A soft robotic exosuit improves walking in patients after stroke," *Sci Transl Med*, vol. 9, no. 400, p. eaai9084, 2017, doi: 10.1126/scitranslmed.aai9084.

[25] P. S. Lee *et al.*, "Air microfluidics-enabled soft robotic transtibial prosthesis socket liner toward dynamic management of residual limb contact pressure and volume fluctuation," *Biomicrofluidics*, vol. 16, no. 3, p. 34107, May 2022, doi: 10.1063/5.0087900.

[26] U. Della Croce *et al.*, "A preliminary assessment of a novel pneumatic unloading knee brace on the gait mechanics of patients with knee osteoarthritis.," *PM R*, vol. 5, no. 10, pp. 816–824, Oct. 2013, doi: 10.1016/j.pmrj.2013.06.008.

[27] US Bionics Inc., "PHEONIX Medical Exoskeleton," 2018. https://www.suitx.com/phoenix-medical-exoskeleton (accessed Dec. 01, 2018).

[28] D. S. Reinsdorf, C. A. Richburg, J. M. Czerniecki, and P. M. Aubin, "Development of a robotic unloader brace for investigation of conservative treatment of medial knee osteoarthritis," *IEEE International Conference on Rehabilitation Robotics*, vol. 2019-June, pp. 931–937, 2019, doi: 10.1109/ICORR.2019.8779367.

[29] S. Kim, C. Laschi, and B. Trimmer, "Soft robotics: A bioinspired evolution in robotics," *Trends Biotechnol*, vol. 31, no. 5, pp. 287–294, 2013, doi: 10.1016/j.tibtech.2013.03.002.

[30] P. Polygerinos, K. C. Galloway, E. Savage, M. Herman, K. O'Donnell, and C. J. Walsh, "Soft robotic glove for hand rehabilitation and task specific training," *Proc IEEE Int*

Conf Robot Autom, vol. 2015-June, no. June, pp. 2913–2919, 2015, doi: 10.1109/ICRA.2015.7139597.

[31] C. Grosjean, G. B. Lee, W. Hong, Y. C. Tai, and C. M. Ho, "Micro Balloon Actuators for Aerodynamic Control," in *Proceedings of the IEEE International Conference on Micro Electro Mechanical Systems (MEMS)*, 1998, pp. 166–171. doi: 10.1109/MEMSYS.1998.659748.

[32] A. T. Asbeck, S. M. M. De Rossi, I. Galiana, Y. Ding, and C. J. Walsh, "Stronger, smarter, softer: Next-generation wearable robots," *IEEE Robot Autom Mag*, vol. 21, no. 4, pp. 22–33, 2014, doi: 10.1109/MRA.2014.2360283.

[33] A. Fischer, S. Rommel, and A. Verl, "3D Printed Objects and Components Enabling Next Generation of True Soft Robotics," in *Soft Robotics: Transferring Theory to Application*, A. Verl, A. Albu-Schäffer, O. Brock, and A. Raatz, Eds., Berlin: Springer-Verlag Berlin Heidelberg, 2015, pp. 198–208. doi: 10.1007/978-3-662-44506-8.

[34] C. T. O'Neill, N. S. Phipps, L. Cappello, S. Paganoni, and C. J. Walsh, "A soft wearable robot for the shoulder: Design, characterization, and preliminary testing," *IEEE International Conference on Rehabilitation Robotics*, vol. 02129, pp. 1672–1678, 2017, doi: 10.1109/ICORR.2017.8009488.

[35] F. Connolly, D. A. Wagner, C. J. Walsh, and K. Bertoldi, "Sew-free anisotropic textile composites for rapid design and manufacturing of soft wearable robots," *Extreme Mech Lett*, vol. 27, pp. 52–58, 2019, doi: 10.1016/j.eml.2019.01.007.

[36] Y. Bar-Cohen, *Electroactive polymer (EAP) actuators as artificial muscles*. SPIE.

[37] C. Laschi and M. Cianchetti, "Soft Robotics: New Perspectives for Robot Bodyware and Control," *Front Bioeng Biotechnol*, vol. 2, no. January, pp. 1–5, 2014, doi: 10.3389/fbioe.2014.00003.

[38] R. Kruidhof, H. van der Kooij, J. F. Veneman, F. C. T. van der Helm, and R. Ekkelenkamp, "A Series Elastic- and Bowden-Cable-Based Actuation System for Use as Torque Actuator in Exoskeleton-Type Robots," *Int J Rob Res*, vol. 25, no. 3, pp. 261–281, 2006, doi: 10.1177/0278364906063829.

[39] M. Wehner *et al.*, "Pneumatic Energy Sources for Autonomous and Wearable Soft Robotics," *Soft Robot*, vol. 1, no. 4, pp. 263–274, 2014, doi: 10.1089/soro.2014.0018.

[40] D. Rus and M. T. Tolley, "Design, fabrication and control of soft robots," *Nature*, vol. 521, no. 7553, pp. 467–475, 2015, doi: 10.1038/nature14543.

[41] B. Mosadegh *et al.*, "Pneumatic networks for soft robotics that actuate rapidly," *Adv Funct Mater*, vol. 24, no. 15, pp. 2163–2170, 2014, doi: 10.1002/adfm.201303288.

[42] D. P. Holland, S. Berndt, M. Herman, and C. J. Walsh, "Growing the Soft Robotics Community Through Knowledge-Sharing Initiatives," *Soft Robot*, vol. 5, no. 2, pp. 119–121, 2018, doi: 10.1089/soro.2018.29013.dph.

[43] Y. L. Park *et al.*, "Design and control of a bio-inspired soft wearable robotic device for ankle-foot rehabilitation," *Bioinspir Biomim*, vol. 9, no. 1, pp. 1–17, 2014, doi: 10.1088/1748-3182/9/1/016007.

[44] J. Zhang *et al.*, “Robotic Artificial Muscles : Current Progress and Future Perspectives,” *IEEE TRANSACTIONS ON ROBOTICS*, vol. 35, no. 3, pp. 761–781, 2019.

[45] S. G. Kandlikar and W. J. Grande, “Evolution of microchannel flow passages-thermohydraulic performance and fabrication technology,” *Heat Transfer Engineering*, vol. 24, no. 1, pp. 3–17, 2003, doi: 10.1080/01457630304040.

[46] R. Z. Gao and C. L. Ren, “Synergizing microfluidics with soft robotics: A perspective on miniaturization and future directions,” *Biomicrofluidics*, vol. 15, no. 1, p. 11302, Jan. 2021, doi: 10.1063/5.0036991.

[47] F. Gemperle, C. Kasabach, J. Stivoric, M. Bauer, and R. Martin, “Design for wearability,” *International Symposium on Wearable Computers, Digest of Papers*, vol. 1998-Octob, pp. 116–122, 1998, doi: 10.1109/ISWC.1998.729537.

[48] J. H. M. Bergmann and A. H. McGregor, “Body-worn sensor design: What do patients and clinicians want?,” *Ann Biomed Eng*, vol. 39, no. 9, pp. 2299–2312, 2011, doi: 10.1007/s10439-011-0339-9.

[49] B. Matthias, S. Oberer-treitz, H. Staab, E. Schuller, and S. Peldschus, “Injury Risk Quantification for Industrial Robots in Collaborative Operation with Humans,” in *ISR/ROBOTIK*, 2010, pp. 171–176.

[50] K. C. Galloway *et al.*, “Soft Robotic Grippers for Biological Sampling on Deep Reefs,” *Soft Robot*, vol. 3, no. 1, pp. 23–33, 2016, doi: 10.1089/soro.2015.0019.

[51] A. D. Marchese, C. D. Onal, and D. Rus, “Autonomous Soft Robotic Fish Capable of Escape Maneuvers Using Fluidic Elastomer Actuators,” *Soft Robot*, vol. 1, no. 1, pp. 75–87, 2014, doi: 10.1089/soro.2013.0009.

[52] M. Karpelson *et al.*, “A Resilient, Untethered Soft Robot,” *Soft Robot*, vol. 1, no. 3, pp. 213–223, 2014, doi: 10.1089/soro.2014.0008.

[53] E. W. Hawkes, L. H. Blumenschein, J. D. Greer, and A. M. Okamura, “A soft robot that navigates its environment through growth,” *Sci Robot*, vol. 2, no. 8, pp. 1–8, 2017, doi: 10.1126/scirobotics.aan3028.

[54] T. Ranzani, M. Cianchetti, G. Gerboni, I. De Falco, and A. Menciassi, “A Soft Modular Manipulator for Minimally Invasive Surgery: Design and Characterization of a Single Module,” *IEEE Transactions on Robotics*, vol. 32, no. 1, pp. 187–200, 2016, doi: 10.1109/TRO.2015.2507160.

[55] P. Polygerinos, Z. Wang, K. C. Galloway, R. J. Wood, and C. J. Walsh, “Soft robotic glove for combined assistance and at-home rehabilitation,” *Rob Auton Syst*, vol. 73, pp. 135–143, 2015, doi: 10.1016/j.robot.2014.08.014.

[56] E. Suarez, J. J. Huaroto, A. A. Reymundo, D. Holland, C. Walsh, and E. Vela, “A Soft Pneumatic Fabric-Polymer Actuator for Wearable Biomedical Devices: Proof of Concept for Lymphedema Treatment,” pp. 5452–5458, 2018, doi: 10.1523/JNEUROSCI.2534-08.2008.

[57] C. J. Payne *et al.*, “Force Control of Textile-Based Soft Wearable Robots for Mechanotherapy,” in *2018 IEEE International Conference on Robotics and Automation*, Brisbane, 2018, pp. 5459–5465. doi: 10.1109/ICRA.2018.8461059.

[58] Y. L. Park, J. Santos, K. G. Galloway, E. C. Goldfield, and R. J. Wood, “A soft wearable robotic device for active knee motions using flat pneumatic artificial muscles,” *Proc IEEE Int Conf Robot Autom*, pp. 4805–4810, 2014, doi: 10.1109/ICRA.2014.6907562.

[59] Y. L. Park, B. R. Chen, C. Majidi, R. J. Wood, R. Nagpal, and E. Goldfield, “Active modular elastomer sleeve for soft wearable assistance robots,” *IEEE International Conference on Intelligent Robots and Systems*, pp. 1595–1602, 2012, doi: 10.1109/IROS.2012.6386158.

[60] J. Shintake, V. Cacucciolo, D. Floreano, and H. Shea, “Soft Robotic Grippers,” *Advanced Materials*, vol. 30, no. 29. pp. 1–33, 2018. doi: 10.1002/adma.201707035.

[61] J. Kim *et al.*, “Reducing the metabolic rate of walking and running with a versatile, portable exosuit,” *Science (1979)*, vol. 365, no. 6454, pp. 668–672, 2019, doi: 10.1126/science.aav7536.

[62] Y. M. Zhou *et al.*, “Soft robotic glove with integrated sensing for intuitive grasping assistance post spinal cord injury,” *Proc IEEE Int Conf Robot Autom*, vol. 2019-May, pp. 9059–9065, 2019, doi: 10.1109/ICRA.2019.8794367.

[63] Soft Robotics Inc., “Soft Robotics,” 2020. https://www.softroboticsinc.com/ (accessed Feb. 19, 2020).

[64] HaptX, “Industrial-grade haptic technology,” 2020. https://haptx.com/technology/ (accessed Feb. 19, 2020).

[65] J. Mohd Jani, M. Leary, A. Subic, and M. A. Gibson, “A review of shape memory alloy research, applications and opportunities,” *Mater Des*, vol. 56, pp. 1078–1113, 2014, doi: 10.1016/j.matdes.2013.11.084.

[66] A. O’Halloran, F. O’Malley, and P. McHugh, “A review on dielectric elastomer actuators, technology, applications, and challenges,” *J Appl Phys*, vol. 104, no. 7, 2008, doi: 10.1063/1.2981642.

[67] Y. Bar-cohen and I. A. Anderson, “Electroactive polymer (EAP) actuators — background review,” *Mech Soft Mater*, vol. 1, no. 5, pp. 1–14, 2019.

[68] J. W. Sohn, G. W. Kim, and S. B. Choi, “A state-of-the-art review on robots and medical devices using smart fluids and shape memory alloys,” *Applied Sciences (Switzerland)*, vol. 8, no. 10, 2018, doi: 10.3390/app8101928.

[69] J. S. Kumar, P. S. Paul, G. Raghunathan, and D. G. Alex, “A review of challenges and solutions in the preparation and use of magnetorheological fluids,” *International Journal of Mechanical and Materials Engineering*, vol. 14, no. 1, 2019, doi: 10.1186/s40712-019-0109-2.

[70] R. A. Bilodeau, E. L. White, and R. K. Kramer, “Monolithic fabrication of sensors and actuators in a soft robotic gripper,” *IEEE International Conference on Intelligent Robots and Systems*, vol. 2015-Decem, pp. 2324–2329, 2015, doi: 10.1109/IROS.2015.7353690.

[71] A. Rafsanjani, Y. Zhang, B. Liu, S. M. Rubinstein, and K. Bertoldi, “Kirigami skins make a simple soft actuator crawl,” *Sci Robot*, vol. 3, no. 15, pp. 1–8, 2018, doi: 10.1126/scirobotics.aar7555.

[72] Wyss Institute, “Soft Robotic Glove for Neuromuscular Rehabilitation,” 2020. https://wyss.harvard.edu/technology/soft-robotic-glove/ (accessed Feb. 19, 2020).

[73] Harvard’s Wyss Institute, “Soft Exosuits,” 2018. https://biodesign.seas.harvard.edu/soft-exosuits (accessed Dec. 01, 2018).

[74] Ching-Ping Chou and B. Hannaford, “Static and dynamic characteristics of McKibben pneumatic artificial muscles,” no. 3, pp. 281–286, 2002, doi: 10.1109/robot.1994.350977.

[75] A. D. Marchese, K. Komorowski, C. D. Onal, and D. Rus, “Design and control of a soft and continuously deformable 2D robotic manipulation system,” *Proc IEEE Int Conf Robot Autom*, pp. 2189–2196, 2014, doi: 10.1109/ICRA.2014.6907161.

[76] Wyss Institute at Harvard University, “Soft Robotic Glove,” 2018. https://wyss.harvard.edu/technology/soft-robotic-glove/ (accessed Dec. 01, 2018).

[77] P. Polygerinos *et al.*, “Towards a soft pneumatic glove for hand rehabilitation,” *IEEE International Conference on Intelligent Robots and Systems*, pp. 1512–1517, 2013, doi: 10.1109/IROS.2013.6696549.

[78] V. Cacucciolo, J. Shintake, Y. Kuwajima, S. Maeda, D. Floreano, and H. Shea, “Stretchable pumps for soft machines,” *Nature*, vol. 572, no. 7770, pp. 516–519, 2019, doi: 10.1038/s41586-019-1479-6.

[79] C. D. Onal, X. Chen, G. M. Whitesides, and D. Rus, “Soft Mobile Robots with On-Board Chemical Pressure Generation,” in *Robotics Research : The 15th International Symposium ISRR*, H. I. Christensen and O. Khatib, Eds., Cham: Springer International Publishing, 2017, pp. 525–540. doi: 10.1007/978-3-319-29363-9_30.

[80] K. W. Oh and C. H. Ahn, “A review of microvalves,” *Journal of Micromechanics and Microengineering*, vol. 16, no. 5, 2006, doi: 10.1088/0960-1317/16/5/R01.

[81] A. K. Au, H. Lai, B. R. Utela, and A. Folch, “Microvalves and micropumps for BioMEMS,” *Micromachines (Basel)*, vol. 2, no. 2, pp. 179–220, 2011, doi: 10.3390/mi2020179.

[82] J. Qian, C. Hou, X. Li, and Z. Jin, “Actuation Mechanism of Microvalves : A Review,” *Micromachines (Basel)*, vol. 11, no. 172, pp. 1–39, 2020, doi: 10.3390/mi11020172.

[83] The Lee Company, “Solenoid Valves,” 2020. https://www.theleeco.com/products/electro-fluidic-systems/solenoid-valves/ (accessed Feb. 20, 2020).

[84] S. Hirai and K. Kato, “Micro pneumatic valves for wearable robotic systems,” *Proceedings - IEEE International Workshop on Robot and Human Interactive Communication*, vol. 2015-Novem, pp. 652–657, 2015, doi: 10.1109/ROMAN.2015.7333584.

[85] Viking AT, “Piezo MicroValve / Miniature Valve,” 2020. http://www.vikingat.com/piezo-products/piezo-microvalve-miniature-valve (accessed Feb. 20, 2020).

[86] M. A. Unger, H.-P. Chou, T. Thorsen, A. Scherer, and S. R. Quake, “Monolithic Microfabricated Valves and Pumps by Multilayer Soft Lithography,” *Science (1979)*, vol. 288, no. 5463, pp. 113–116, Apr. 2000, doi: 10.1126/science.288.5463.113.

[87] K. Hosokawa and R. Maeda, “Pneumatically-actuated three-way microvalve fabricated with polydimethylsiloxane using the membrane transfer technique,” *Journal of Micromechanics and Microengineering*, vol. 10, no. 3, pp. 415–420, 2000, doi: 10.1088/0960-1317/10/3/317.

[88] K. Brower *et al.*, “An open-source, programmable pneumatic setup for operation and automated control of single- and multi-layer microfluidic devices,” *HardwareX*, vol. 3, no. September 2017, pp. 117–134, 2018, doi: 10.1016/j.ohx.2017.10.001.

[89] T. Thorsen, S. J. Maerkl, and S. R. Quake, “Microfluidic large-scale integration,” *Science (1979)*, vol. 298, no. 5593, pp. 580–584, 2002, doi: 10.1126/science.1076996.

[90] P. N. Duncan, T. V. Nguyen, and E. E. Hui, “Pneumatic oscillator circuits for timing and control of integrated microfluidics,” *Proceedings of the National Academy of Sciences*, vol. 110, no. 45, pp. 18104–18109, 2013, doi: 10.1073/pnas.1310254110.

[91] D. W. Lee, I. Doh, Y. Kim, and Y.-H. Cho, “Advanced combinational microfluidic multiplexer using multiple levels of control pressures,” *Lab Chip*, vol. 13, no. 18, p. 3658, 2013, doi: 10.1039/c3lc50513h.

[92] G. P. Brown, A. Dinardo, G. K. Cheng, and T. K. Sherwood, “The flow of gases in pipes at low pressures,” *J Appl Phys*, vol. 17, no. 10, pp. 802–813, 1946, doi: 10.1063/1.1707647.

[93] S. Roy, R. Raju, H. F. Chuang, B. A. Cruden, and M. Meyyappan, “Modeling gas flow through microchannels and nanopores,” *J Appl Phys*, vol. 93, no. 8, pp. 4870–4879, 2003, doi: 10.1063/1.1559936.

[94] E. B. Arkilic, M. A. Schmidt, and K. S. Breuer, “Gaseous slip flow in long microchannels,” *Journal of Microelectromechanical Systems*, vol. 6, no. 2, pp. 167–178, 1997, doi: 10.1109/84.585795.

[95] S. S. Hsieh, H. H. Tsai, C. Y. Lin, C. F. Huang, and C. M. Chien, “Gas flow in a long microchannel,” *Int J Heat Mass Transf*, vol. 47, no. 17–18, pp. 3877–3887, 2004, doi: 10.1016/j.ijheatmasstransfer.2004.03.027.

[96] R. W. Barber and D. R. Emerson, “Challenges in modeling gas-phase flow in microchannels: From slip to transition,” *Heat Transfer Engineering*, vol. 27, no. 4, pp. 3–12, 2006, doi: 10.1080/01457630500522271.

[97] A. Agrawal, “A Comprehensive Review on Gas Flow in Microchannels,” *Micro-Nano Scale Transport*, vol. 2, no. 1, pp. 1–40, 2011.

[98] N. Vasios, A. J. Gross, S. Soifer, J. T. B. Overvelde, and K. Bertoldi, “Harnessing Viscous Flow to Simplify the Actuation of Fluidic Soft Robots,” *Soft Robot*, vol. 7, no. 1, pp. 1–9, 2020, doi: 10.1089/soro.2018.0149.

[99] D. J. Preston *et al.*, “A soft ring oscillator,” *Sci Robot*, vol. 4, no. 31, pp. 1–9, 2019, doi: 10.1126/scirobotics.aaw5496.

[100] B. Gorissen *et al.*, "Hardware Sequencing of Inflatable Nonlinear Actuators for Autonomous Soft Robots," *Advanced Materials*, vol. 31, no. 3, pp. 1–7, 2019, doi: 10.1002/adma.201804598.

[101] E. Ben-Haim, L. Salem, Y. Or, and A. D. Gat, "Single-Input Control of Multiple Fluid-Driven Elastic Actuators via Interaction between Bistability and Viscosity," *Soft Robot*, vol. 7, no. 2, pp. 259–265, 2020, doi: 10.1089/soro.2019.0060.

[102] M. Courtney, X. Chen, S. Chan, T. Mohamed, P. P. N. Rao, and C. L. Ren, "Droplet Microfluidic System with On-Demand Trapping and Releasing of Droplet for Drug Screening Applications," *Anal Chem*, vol. 89, pp. 910–915, 2017, doi: 10.1021/acs.analchem.6b04039.

[103] M. Hébert, M. Courtney, and C. L. Ren, "Semi-automated on-demand control of individual droplets with a sample application to a drug screening assay," *Lab Chip*, vol. 19, no. 8, pp. 1490–1501, 2019, doi: 10.1039/c9lc00128j.

[104] W. H. Grover, R. H. C. Ivester, E. C. Jensen, and R. A. Mathies, "Development and multiplexed control of latching pneumatic valves using microfluidic logical structures," *Lab Chip*, vol. 6, no. 5, p. 623, May 2006, doi: 10.1039/b518362f.

[105] R. Z. Gao, K. Marriott, C. R. Dickerson, M. R. Maly, and C. L. Ren, "Design and Preliminary Implementation of an Air Microfluidics Enabled Soft Robotic Knee Brace Towards the Management of Osteoarthritis," in *2020 42nd Annual International Conference of the IEEE Engineering in Medicine & Biology Society (EMBC)*, 2020, pp. 4502–4505. doi: 10.1109/EMBC44109.2020.9175677.

[106] M. A. Skylar-Scott, J. Mueller, C. W. Visser, and J. A. Lewis, "Voxelated soft matter via multimaterial multinozzle 3D printing," *Nature*, vol. 575, no. 7782, pp. 330–335, 2019, doi: 10.1038/s41586-019-1736-8.

[107] J. Wirekoh and Y. L. Park, "Design of flat pneumatic artificial muscles," *Smart Mater Struct*, vol. 26, no. 3, 2017, doi: 10.1088/1361-665X/aa5496.

[108] J. M. Taylor, K. Perez-Toralla, R. Aispuro, and S. A. Morin, "Covalent Bonding of Thermoplastics to Rubbers for Printable, Reel-to-Reel Processing in Soft Robotics and Microfluidics," *Advanced Materials*, vol. 30, no. 7, pp. 1–8, 2018, doi: 10.1002/adma.201705333.

[109] R. D. Sochol *et al.*, "3D printed microfluidics and microelectronics," *Microelectron Eng*, vol. 189, pp. 52–68, 2018, doi: 10.1016/j.mee.2017.12.010.

[110] H. J. Kim, C. Son, and B. Ziaie, "A multiaxial stretchable interconnect using liquid-alloy-filled elastomeric microchannels," *Appl Phys Lett*, vol. 92, no. 1, pp. 1–4, 2008, doi: 10.1063/1.2829595.

[111] K. Khoshmanesh *et al.*, "Liquid metal enabled microfluidics," *Lab Chip*, vol. 17, no. 6, pp. 974–993, 2017, doi: 10.1039/c7lc00046d.

[112] M. D. Dickey, R. C. Chiechi, R. J. Larsen, E. A. Weiss, D. A. Weitz, and G. M. Whitesides, "Eutectic gallium-indium (EGaIn): A liquid metal alloy for the formation of stable structures in microchannels at room temperature," *Adv Funct Mater*, vol. 18, no. 7, pp. 1097–1104, 2008, doi: 10.1002/adfm.200701216.

[113] Y. L. Park, C. Majidi, R. Kramer, P. Brard, and R. J. Wood, "Hyperelastic pressure sensing with a liquid-embedded elastomer," *Journal of Micromechanics and Microengineering*, vol. 20, no. 12, 2010, doi: 10.1088/0960-1317/20/12/125029.

[114] Y. L. Park, B. R. Chen, and R. J. Wood, "Design and fabrication of soft artificial skin using embedded microchannels and liquid conductors," *IEEE Sens J*, vol. 12, no. 8, pp. 2711–2718, 2012, doi: 10.1109/JSEN.2012.2200790.

[115] Y. Mengüç *et al.*, "Wearable soft sensing suit for human gait measurement," *International Journal of Robotics Research*, vol. 33, no. 14, pp. 1748–1764, 2014, doi: 10.1177/0278364914543793.

[116] A. Atalay *et al.*, "Batch Fabrication of Customizable Silicone-Textile Composite Capacitive Strain Sensors for Human Motion Tracking," *Adv Mater Technol*, vol. 2, no. 9, pp. 1–8, 2017, doi: 10.1002/admt.201700136.

[117] J. Berg, H. Butt, D. Jayalth, and C. Wiebe, "System and method for monitoring biometric signals," US 2015/0148619 A1, 2017

[118] R. H. Dworkin and M. J. Gitlin, "Clinical aspects of depression in chronic pain patients," *Clinical Journal of Pain*, vol. 7, no. 2. pp. 79–94, 1991. doi: 10.1097/00002508-199106000-00004.

[119] S. M. Banks and R. D. Kerns, "Explaining high rates of depression in chronic pain: A diathesis-stress framework," *Psychol Bull*, vol. 119, no. 1, pp. 95–110, 1996, doi: 10.1037/0033-2909.119.1.95.

[120] World Health Organization, "Musculoskeletal conditions," 2018. https://www.who.int/news-room/fact-sheets/detail/musculoskeletal-conditions (accessed Jun. 26, 2019).

[121] World Health Organization, "Depression," 2020. https://www.who.int/news-room/fact-sheets/detail/depression (accessed Feb. 21, 2020).

[122] M. Cianchetti, C. Laschi, A. Menciassi, and P. Dario, "Biomedical applications of soft robotics," *Nat Rev Mater*, vol. 3, pp. 143–153, 2018, doi: 10.1038/s41578-018-0022-y.

[123] J. B. Webster, K. N. Hakimi, R. M. Williams, A. P. Turner, D. C. Norvell, and J. M. Czerniecki, "Prosthetic fitting, use, and satisfaction following lower-limb amputation: A prospective study," *J Rehabil Res Dev*, vol. 49, no. 10, pp. 1493–1504, 2012, doi: 10.1682/JRRD.2012.01.0001.

[124] J. T. Kahle, "Conventional and Hydrostatic Transtibial Interface Comparison," *Journal of Prosthetics*, vol. 11, no. 4, pp. 85–91, 1999.

[125] L. Paterno, M. Ibrahimi, E. Gruppioni, A. Menciassi, and L. Ricotti, "Sockets for Limb Prostheses: A Review of Existing Technologies and Open Challenges," *IEEE Trans Biomed Eng*, vol. 65, no. 9, pp. 1996–2010, Sep. 2018, doi: 10.1109/TBME.2017.2775100.

[126] J. E. Sanders and D. V. Cassisi, "Mechanical performance of inflatable inserts used in limb prosthetics," *J Rehabil Res Dev*, vol. 38, no. 4, pp. 365–374, 2001.

[127] W. Carrigan, C. Nothnagle, P. Savant, F. Gao, and M. B. J. Wijesundara, "Pneumatic actuator inserts for interface pressure mapping and fit improvement in lower extremity prosthetics," *Proceedings of the IEEE RAS and EMBS International Conference on Biomedical Robotics and Biomechatronics*, vol. 2016-July, pp. 574–579, 2016, doi: 10.1109/BIOROB.2016.7523687.

[128] R. M. Greenwald, R. C. Dean, and J. Wayne, "Volume Management: Smart Variable Geometry Socket (SVGS) Technology for Lower-Limb Prostheses," *Journal of Prosthetics and Orthotics*, vol. 15, no. 3, pp. 107–112, 2003, doi: 10.1097/00008526-200307000-00011.

[129] V. L. Phillips, "Scoket Insert Having a Bladder System," US 7.655,049 B2, 2001

[130] H. A. Sonar, A. P. Gerratt, S. P. Lacour, and J. Paik, "Closed-loop haptic feedback control using a self-sensing soft pneumatic actuator skin," *Soft Robot*, vol. 7, no. 1, 2020.

[131] J. Rubin and R. Crockett, "Whole-body human-computer enterface," 9,652,037 B2, 2015

[132] M. Runciman, A. Darzi, and G. P. Mylonas, "Soft Robotics in Minimally Invasive Surgery," *Soft Robot*, vol. 6, no. 4, pp. 423–443, 2019, doi: 10.1089/soro.2018.0136.

[133] T. Ranzani, S. Russo, N. W. Bartlett, M. Wehner, and R. J. Wood, "Increasing the Dimensionality of Soft Microstructures through Injection-Induced Self-Folding," *Advanced Materials*, vol. 30, no. 38, pp. 1–6, 2018, doi: 10.1002/adma.201802739.

[134] R. Z. Gao, M. Hébert, J. Huissoon, and C. L. Ren, "μPump: An Open-Source Pressure Pump for Precision Fluid Handling in Microfluidics," *HardwareX*, vol. 7, pp. 1–23, 2020, doi: 10.1016/j.ohx.2020.e00096.

[135] Tekscan, "Pressure Mapping, Force Measurement & Tactile Sensors," 2020. https://www.tekscan.com/ (accessed Feb. 21, 2020).

[136] Y. Feng, F. J. Schlösser, and B. E. Sumpio, "The Semmes Weinstein monofilament examination as a screening tool for diabetic peripheral neuropathy," *J Vasc Surg*, vol. 50, no. 3, pp. 675-682.e1, 2009, doi: 10.1016/j.jvs.2009.05.017.

[137] A. B. Craig, M. B. Strauss, A. Daniller, and S. S. Miller, "Foot Sensation Testing in the Patient With Diabetes: Introduction of the Quick & Easy Assessment Tool," *Wounds*, vol. 26, no. 8, pp. 221–231, 2014.

[138] Consumer Technology Association, "CES," 2020. https://www.ces.tech/ (accessed Feb. 21, 2020).

[139] B. Phillips and H. Zhao, "Predictors of Assistive Technology Abandonment," *Assistive Technology*, vol. 5, no. 1, pp. 36–45, 1993, doi: 10.1080/10400435.1993.10132205.

[140] A. J. Veale and S. Q. Xie, "Towards compliant and wearable robotic orthoses: A review of current and emerging actuator technologies," *Med Eng Phys*, vol. 38, no. 4, pp. 317–325, 2016, doi: 10.1016/j.medengphy.2016.01.010.

[141] R. G. Soule and R. F. Goldman, "Energy cost of loads carried on the head, hands, or feet.," *J Appl Physiol*, vol. 27, no. 5, pp. 687–90, 1969, doi: 10.1152/jappl.1969.27.5.687.

[142] G. J. Bastien, P. A. Willems, B. Schepens, and N. C. Heglund, "Effect of load and speed on the energetic cost of human walking," *Eur J Appl Physiol*, vol. 94, no. 1–2, pp. 76–83, 2005, doi: 10.1007/s00421-004-1286-z.

[143] F. D. Davis, "A technology acceptance model for empirically testing new end-user information systems: theory and results," M.I.T., 1985. doi: oclc/56932490.

[144] Y. Malhotra and D. F. Galletta, "Extending the technology acceptance model to account for social influence: theoretical bases and empirical validation," in *Proceedings of the 32nd Annual Hawaii International Conference on Systems Sciences*, Maui, 1999, p. 14. doi: 10.1109/hicss.1999.772658.

[145] A. Kintsch and R. DePaula, "A Framework for the Adoption of Assistive Technology," *Proceedings of SWAAAC 2002: Supporting Learning Through Assistive Technology*, pp. 1–11, 2002.

[146] A. Toney, B. Mulley, B. H. Thomas, and W. Piekarski, "Social weight: Designing to minimise the social consequences arising from technology use by the mobile professional," *Pers Ubiquitous Comput*, vol. 7, no. 5, pp. 309–320, 2003, doi: 10.1007/s00779-003-0245-8.

[147] R. Z. Gao *et al.*, "A novel air microfluidics-enabled soft robotic sleeve: Toward realizing innovative lymphedema treatment," *Biomicrofluidics*, vol. 16, no. 3, p. 34101, May 2022, doi: 10.1063/5.0079898.

[148] "Lymphedema," *Canadian Cancer Society*. https://www.cancer.ca/en/cancer-information/diagnosis-and-treatment/managing-side-effects/lymphedema/?region=on (accessed May 29, 2020).

[149] M. A. Swartz, "The physiology of the lymphatic system," *Advanced Drug Delivery Reviews*. 2001. doi: 10.1016/S0169-409X(01)00150-8.

[150] A. K. Greene, "Epidemiology and morbidity of lymphedema," in *Lymphedema: Presentation, Diagnosis, and Treatment*, 2015. doi: 10.1007/978-3-319-14493-1_4.

[151] M. J. Brennan and L. T. Miller, "Overview of treatment options and review of the current role and use of compression garments, intermittent pumps, and exercise in the management of lymphedema," in *Cancer*, 1998. doi: 10.1002/(sici)1097-0142(19981215)83:12b+<2821::aid-cncr33>3.0.co;2-g.

[152] E. D. Paskett, J. A. Dean, J. M. Oliveri, and J. P. Harrop, "Cancer-related lymphedema risk factors, diagnosis, treatment, and impact: A review," *Journal of Clinical Oncology*. 2012. doi: 10.1200/JCO.2012.41.8574.

[153] B. Smoot *et al.*, "Upper extremity impairments in women with or without lymphedema following breast cancer treatment," *Journal of Cancer Survivorship*, 2010, doi: 10.1007/s11764-010-0118-x.

[154] T. DiSipio, S. Rye, B. Newman, and S. Hayes, "Incidence of unilateral arm lymphoedema after breast cancer: A systematic review and meta-analysis," *Lancet Oncol*, 2013, doi: 10.1016/S1470-2045(13)70076-7.

[155] Y. C. T. Shih *et al.*, "Incidence, treatment costs, and complications of lymphedema after breast cancer among women of working age: A 2-year follow-up study," *Journal of Clinical Oncology*, 2009, doi: 10.1200/JCO.2008.18.3517.

[156] D. S. C. Ko, R. Lerner, G. Klose, and A. B. Cosimi, "Effective treatment of lymphedema of the extremities," *Archives of Surgery*, vol. 133, no. 4, pp. 452–458, 1998, doi: 10.1001/archsurg.133.4.452.

[157] "Lymphedema," *Canadian Cancer Society*. https://www.cancer.ca/en/cancer-information/diagnosis-and-treatment/managing-side-effects/lymphedema/?region=on (accessed May 29, 2020).

[158] J. Ezzo *et al.*, "Manual lymphatic drainage for lymphedema following breast cancer treatment," *Cochrane Database of Systematic Reviews*. 2015. doi: 10.1002/14651858.CD003475.pub2.

[159] R. Koul *et al.*, "Efficacy of complete decongestive therapy and manual lymphatic drainage on treatment-related lymphedema in breast cancer," *Int J Radiat Oncol Biol Phys*, 2007, doi: 10.1016/j.ijrobp.2006.09.024.

[160] C. H. Turtzo, "Compression Sleeve for Treating Lymphedema," US 6,254,554 B1, 2001

[161] R. J. Damstra and H. Partsch, "Compression therapy in breast cancer-related lymphedema: A randomized, controlled comparative study of relation between volume and interface pressure changes," *J Vasc Surg*, vol. 49, no. 5, pp. 1256–1263, 2009, doi: 10.1016/j.jvs.2008.12.018.

[162] M. Zaleska, W. L. Olszewski, and M. Durlik, "The effectiveness of intermittent pneumatic compression in long-term therapy of lymphedema of lower limbs," *Lymphat Res Biol*, vol. 12, no. 2, pp. 103–109, 2014, doi: 10.1089/lrb.2013.0033.

[163] M. Zaleska, W. L. Olszewski, M. Cakala, J. Cwikla, and T. Budlewski, "Intermittent Pneumatic Compression Enhances Formation of Edema Tissue Fluid Channels in Lymphedema of Lower Limbs," *Lymphat Res Biol*, vol. 13, no. 2, pp. 146–153, 2015, doi: 10.1089/lrb.2014.0010.

[164] J. L. Feldman, N. L. Stout, A. Wanchai, B. R. Stewart, J. N. Cormier, and J. M. Armer, "Intermittent pneumatic compression therapy: A systematic review," *Lymphology*, vol. 45, no. 1, pp. 13–25, 2012.

[165] F. Comerota, Anthony J.; Aziz, "The case for intermittent pneumatic compression," *J Lymphoedema*, vol. 4, no. 2, pp. 57–64, 2009.

[166] A. Szuba, R. Achalu, and S. G. Rockson, "Decongestive lymphatic therapy for patients with breast carcinoma-associated lymphedema: A randomized, prospective study of a role for adjunctive intermittent pneumatic compression," *Cancer*, vol. 95, no. 11, pp. 2260–2267, 2002, doi: 10.1002/cncr.10976.

[167] C. H. Turtzo, "Compression Sleeve for Treating Lymphedema," US 6,254,554 B1, 2001

[168] D. Guan, R. Liu, C. Fei, S. Zhao, and L. Jing, "Fluid–Structure Coupling Model and Experimental Validation of Interaction Between Pneumatic Soft Actuator and Lower Limb," *Soft Robot*, 2020, doi: 10.1089/soro.2019.0035.

[169] H. J. Yoo *et al.*, “Wearable lymphedema massaging modules: Proof of concept using origami-inspired soft fabric pneumatic actuators,” in *IEEE International Conference on Rehabilitation Robotics*, 2019. doi: 10.1109/ICORR.2019.8779525.

[170] Tactile Medical, “Tactile Medical.” https://tactilemedical.com/%0A (accessed Sep. 09, 2020).

[171] C. E. Fife, S. Davey, E. A. Maus, R. Guilliod, and H. N. Mayrovitz, “A randomized controlled trial comparing two types of pneumatic compression for breast cancer-related lymphedema treatment in the home,” *Supportive Care in Cancer*, vol. 20, no. 12, pp. 3279–3286, 2012, doi: 10.1007/s00520-012-1455-2.

[172] Spryng, “Spryng.” https://spryngme.com/products/spryng (accessed Nov. 03, 2020).

[173] M. J. Fuerstman *et al.*, “Solving Mazes Using Microfluidic Networks,” *Langmuir*, vol. 19, no. 11, pp. 4714–4722, May 2003, doi: 10.1021/la030054x.

[174] B. E. Rapp, *Microfluidics: Modeling, mechanics and mathematics*, First. Elsevier, 2017. doi: 10.1016/c2012-0-02230-2.

[175] S. Choi, M. G. Lee, and J.-K. Park, “Microfluidic parallel circuit for measurement of hydraulic resistance,” *Biomicrofluidics*, vol. 4, no. 3, Sep. 2010, doi: 10.1063/1.3486609.

[176] H. Bruus, *Theoretical Microfluidics*, First. Oxford University Press, 2008.

[177] B. E. Rapp, *Microfluidics: Modeling, mechanics and mathematics*, First. Elsevier, 2017. doi: 10.1016/c2012-0-02230-2.

[178] K. W. Oh, K. Lee, B. Ahn, and E. P. Furlani, “Design of pressure-driven microfluidic networks using electric circuit analogy,” *Lab on a Chip*. 2012. doi: 10.1039/c2lc20799k.

[179] J. Sitzia, “Volume measurement in lymphoedema treatment: examination of formulae,” *Eur J Cancer Care (Engl)*, vol. 4, no. 1, pp. 11–16, 1995, doi: 10.1111/j.1365-2354.1995.tb00047.x.

[180] Y. Xia and G. M. Whitesides, “SOFT LITHOGRAPHY,” *Annual Review of Materials Science*, vol. 28, no. 1, pp. 153–184, Aug. 1998, doi: 10.1146/annurev.matsci.28.1.153.

[181] R. Z. Gao, M. Hébert, J. Huissoon, and C. L. Ren, “µPump: An open-source pressure pump for precision fluid handling in microfluidics,” *HardwareX*, vol. 7, 2020, doi: 10.1016/j.ohx.2020.e00096.

[182] UN News, “One lower limb lost to diabetes every 30 seconds, UN agency says,” Nov. 14, 2005. https://news.un.org/en/story/2005/11/159922 (accessed Jul. 16, 2023).

[183] A. J. M. Boulton, “The diabetic foot: grand overview, epidemiology and pathogenesis,” *Diabetes Metab Res Rev*, vol. 24, no. S1, pp. S3–S6, May 2008, doi: 10.1002/dmrr.833.

[184] A. Johannesson, G. U. Larsson, N. Ramstrand, A. Turkiewicz, A. B. Wiréhn, and I. Atroshi, “Incidence of lower-limb amputation in the diabetic and nondiabetic general population: A 10-year population-based cohort study of initial unilateral and contralateral amputations and reamputations,” *Diabetes Care*, vol. 32, no. 2, pp. 275–280, 2009, doi: 10.2337/dc08-1639.

[185] S. Brunelli, C. Bonanni, C. Foti, and M. Traballesi, “A LITERATURE REVIEW OF THE QUALITY OF LIFE, HEALTH STATUS AND PROSTHESIS SATISFACTION IN OLDER PATIENTS WITH A TRANS-TIBIAL AMPUTATION,” *CANADIAN PROSTHETICS & ORTHOTICS JOURNAL*, vol. 3, no. 1, May 2020, doi: 10.33137/cpoj.v3i1.33640.

[186] E. Batbaatar, J. Dorjdagva, A. Luvsannyam, and P. Amenta, “Conceptualisation of patient satisfaction: a systematic narrative literature review,” *Perspect Public Health*, vol. 135, no. 5, pp. 243–250, Sep. 2015, doi: 10.1177/1757913915594196.

[187] E. C. Baars, E. Schrier, P. U. Dijkstra, and J. H. B. Geertzen, “Prosthesis satisfaction in lower limb amputees: A systematic review of associated factors and questionnaires.,” *Medicine*, vol. 97, no. 39, p. e12296, Sep. 2018, doi: 10.1097/MD.0000000000012296.

[188] G. M. Berke *et al.*, “Comparison of satisfaction with current prosthetic care in veterans and servicemembers from Vietnam and OIF/OEF conflicts with major traumatic limb loss,” *The Journal of Rehabilitation Research and Development*, vol. 47, no. 4, p. 361, 2010, doi: 10.1682/JRRD.2009.12.0193.

[189] L. E. Pezzin, T. R. Dillingham, E. J. MacKenzie, P. Ephraim, and P. Rossbach, “Use and satisfaction with prosthetic limb devices and related services 11No commercial party having a direct financial interest in the results of the research supporting this article has or will confer a benefit on the author(s) or on any organization with which the author(s) is/are associated.,” *Arch Phys Med Rehabil*, vol. 85, no. 5, pp. 723–729, May 2004, doi: 10.1016/j.apmr.2003.06.002.

[190] P. Saeedi *et al.*, “Global and regional diabetes prevalence estimates for 2019 and projections for 2030 and 2045: Results from the International Diabetes Federation Diabetes Atlas, 9th edition,” *Diabetes Res Clin Pract*, vol. 157, p. 107843, 2019, doi: 10.1016/j.diabres.2019.107843.

[191] W. J. Board, G. M. Street, and C. Caspers, “A comparison of trans-tibial amputee suction and vacuum socket conditions,” *Prosthet Orthot Int*, vol. 25, no. 3, pp. 202–209, 2001, doi: 10.1080/03093640108726603.

[192] A. T. Tantua, J. H. B. Geertzen, J. J. A. M. van den Dungen, J. K. C. Breek, and P. U. Dijkstra, “Reduction of residual limb volume in people with transtibial amputation,” *J Rehabil Res Dev*, vol. 51, no. 7, pp. 1119–1126, 2014, doi: 10.1682/JRRD.2013.11.0243.

[193] H. E. Meulenbelt, J. H. Geertzen, M. F. Jonkman, and P. U. Dijkstra, “Determinants of Skin Problems of the Stump in Lower-Limb Amputees,” *Arch Phys Med Rehabil*, vol. 90, no. 1, pp. 74–81, 2009, doi: 10.1016/j.apmr.2008.07.015.

[194] N. L. Dudek, M. B. Marks, and S. C. Marshall, “Skin problems in an amputee clinic,” *Am J Phys Med Rehabil*, vol. 85, no. 5, pp. 424–429, May 2006, doi: 10.1097/01.phm.0000214272.01147.5a.

[195] M. Graser, S. Day, and A. Buis, “Exploring the role of transtibial prosthetic use in deep tissue injury development: a scoping review,” *BMC Biomed Eng*, vol. 2, p. 2, 2020, doi: 10.1186/s42490-020-0036-6.

[196] J. E. Sanders, D. S. Harrison, K. J. Allyn, and T. R. Myers, “Clinical Utility of In-Socket Residual Limb Volume Change Measurement,” *Prosthet Orthot Int*, vol. 33, no. 4, pp. 378–390, Dec. 2009, doi: 10.3109/03093640903214067.

[197] D. M. Sengeh and H. Herr, “A Variable-Impedance Prosthetic Socket for a Transtibial Amputee Designed from Magnetic Resonance Imaging Data,” *JPO: Journal of Prosthetics and Orthotics*, vol. 25, no. 3, 2013, doi: 10.1097/JPO.0b013e31829be19c.

[198] C. Comotti, D. Regazzoni, C. Rizzi, and A. Vitali, “Multi-material design and 3D printing method of lower limb prosthetic sockets,” in *Proceedings of the 3rd 2015 Workshop on ICTs for improving Patients Rehabilitation Research Techniques*, New York, NY, USA: ACM, Oct. 2015, pp. 42–45. doi: 10.1145/2838944.2838955.

[199] G. Pirouzi, N. A. Abu Osman, A. Oshkour, S. Ali, H. Gholizadeh, and W. Wan Abas, “Development of an Air Pneumatic Suspension System for Transtibial Prostheses,” *Sensors*, vol. 14, no. 9, pp. 16754–16765, Sep. 2014, doi: 10.3390/s140916754.

[200] M. J. Highsmith *et al.*, “Interventions to Manage Residual Limb Ulceration Due To Prosthetic Use in Individuals with Lower Extremity Amputation: *A Systematic Review of the Literature*,” *Technol Innov*, vol. 18, no. 2, pp. 115–123, Sep. 2016, doi: 10.21300/18.2-3.2016.115.

[201] W. C. Lee, M. Zhang, and A. F. Mak, “Regional differences in pain threshold and tolerance of the transtibial residual limb: Including the effects of age and interface material,” *Arch Phys Med Rehabil*, vol. 86, no. 4, pp. 641–649, 2005, doi: 10.1016/j.apmr.2004.08.005.

[202] S. Konishi, F. Kawai, and P. Cusin, “Thin flexible end-effector using pneumatic balloon actuator,” *Sens Actuators A Phys*, vol. 89, no. 1–2, pp. 28–35, Mar. 2001, doi: 10.1016/S0924-4247(00)00533-1.

[203] A. Yousefpour, M. Hojjati, and J.-P. Immarigeon, “Fusion Bonding/Welding of Thermoplastic Composites,” *Journal of Thermoplastic Composite Materials*, vol. 17, no. 4, pp. 303–341, Jul. 2004, doi: 10.1177/0892705704045187.

[204] Y.-S. Lee, N. Bhattacharjee, and A. Folch, “3D-printed Quake-style microvalves and micropumps,” *Lab Chip*, vol. 18, no. 8, pp. 1207–1214, 2018, doi: 10.1039/C8LC00001H.

[205] H. Lee, S. Chang, and E. Yoon, “A Flexible Polymer Tactile Sensor: Fabrication and Modular Expandability for Large Area Deployment,” *Journal of Microelectromechanical Systems*, vol. 15, no. 6, pp. 1681–1686, Dec. 2006, doi: 10.1109/JMEMS.2006.886021.

[206] J. V. Mane *et al.*, “Mechanical Property Evaluation of Polyurethane Foam under Quasi-static and Dynamic Strain Rates- An Experimental Study,” *Procedia Eng*, vol. 173, pp. 726–731, 2017, doi: 10.1016/j.proeng.2016.12.160.

[207] ASTM International, “ASTM International - ASTM D3574-17 Standard Test Methods for Flexible Cellular Materials—Slab, Bonded, and Molded Urethane Foams,” West Conshohocken, Mar. 2017.

[208] M. Zhang, M. Lord, A. R. Turner-Smith, and V. C. Roberts, “Development of a non-linear finite element modelling of the below-knee prosthetic socket interface,” *Med Eng Phys*, vol. 17, no. 8, pp. 559–566, Dec. 1995, doi: 10.1016/1350-4533(95)00002-5.

[209] A. S. Dickinson, J. W. Steer, and P. R. Worsley, “Finite element analysis of the amputated lower limb: A systematic review and recommendations,” *Med Eng Phys*, vol. 43, pp. 1–18, May 2017, doi: 10.1016/j.medengphy.2017.02.008.

[210] W. Tarapoom and T. Puttapitukporn, “Stress Distribution in Human Tibia Bones using Finite Element Analysis,” *Engineering Journal*, vol. 20, no. 3, pp. 155–167, Aug. 2016, doi: 10.4186/ej.2016.20.3.155.

[211] M. S. Xavier, A. J. Fleming, and Y. K. Yong, “Finite Element Modeling of Soft Fluidic Actuators: Overview and Recent Developments,” *Advanced Intelligent Systems*, vol. 3, no. 2, p. 2000187, Feb. 2021, doi: 10.1002/aisy.202000187.

[212] N. L. Stout Gergich, L. A. Pfalzer, C. McGarvey, B. Springer, L. H. Gerber, and P. Soballe, “Preoperative assessment enables the early diagnosis and successful treatment of lymphedema,” *Cancer*, vol. 112, no. 12, pp. 2809–2819, Jun. 2008, doi: https://doi.org/10.1002/cncr.23494.

[213] A. Szuba and S. G. Rockson, “Lymphedema: Anatomy, Physiology and Pathogenesis,” *Vascular Medicine*, vol. 2, no. 4, pp. 321–326, Nov. 1997, doi: 10.1177/1358863X9700200408.

[214] S. G. Rockson, “Lymphedema,” *Am J Med*, vol. 110, no. 4, pp. 288–295, Mar. 2001, doi: 10.1016/S0002-9343(00)00727-0.

[215] B. C. Sleigh and B. Manna, *Lymphedema*. StatPearls Publishing, Treasure Island (FL), 2022. [Online]. Available: http://europepmc.org/abstract/MED/30725924

[216] M. R. Fu, S. H. Ridner, S. H. Hu, B. R. Stewart, J. N. Cormier, and J. M. Armer, “Psychosocial impact of lymphedema: a systematic review of literature from 2004 to 2011,” *Psychooncology*, vol. 22, no. 7, pp. 1466–1484, Jul. 2013, doi: 10.1002/pon.3201.

[217] V. Velanovich and W. Szymanski, “Quality of life of breast cancer patients with lymphedema,” *The American Journal of Surgery*, vol. 177, no. 3, pp. 184–188, Mar. 1999, doi: 10.1016/S0002-9610(99)00008-2.

[218] E. D. Paskett, M. J. Naughton, T. P. McCoy, L. D. Case, and J. M. Abbott, “The Epidemiology of Arm and Hand Swelling in Premenopausal Breast Cancer Survivors,” *Cancer Epidemiology, Biomarkers & Prevention*, vol. 16, no. 4, pp. 775–782, Apr. 2007, doi: 10.1158/1055-9965.EPI-06-0168.

[219] D. W. Chang, “Combined Approach to Surgical Treatment of Lymphedema,” *Lymphat Res Biol*, vol. 19, no. 1, pp. 23–24, Feb. 2021, doi: 10.1089/lrb.2020.0098.

[220] M. V. Schaverien and C. J. Coroneos, “Surgical Treatment of Lymphedema,” *Plast Reconstr Surg*, vol. 144, no. 3, pp. 738–758, Sep. 2019, doi: 10.1097/PRS.0000000000005993.

[221] K. Gallagher, K. Marulanda, and S. Gray, “Surgical Intervention for Lymphedema,” *Surg Oncol Clin N Am*, vol. 27, no. 1, pp. 195–215, Jan. 2018, doi: 10.1016/j.soc.2017.08.001.

[222] B. B. Lasinski *et al.*, “A Systematic Review of the Evidence for Complete Decongestive Therapy in the Treatment of Lymphedema From 2004 to 2011,” *PM&R*, vol. 4, no. 8, pp. 580–601, Aug. 2012, doi: 10.1016/j.pmrj.2012.05.003.

[223] A. L. Moseley, C. J. Carati, and N. B. Piller, “A systematic review of common conservative therapies for arm lymphoedema secondary to breast cancer treatment,” *Annals of Oncology*, vol. 18, no. 4, pp. 639–646, Apr. 2007, doi: 10.1093/annonc/mdl182.

[224] E. Vodder, “Die manuelle Lymphdrainage und ihre medizinischen Anwendungsgebiete,” *Erfahrungsheilkunde*, vol. 16, no. 7, 1966.

[225] A. M. Flores *et al.*, “Lymphedema Signs, Symptoms, and Diagnosis in Women Who Are in Minority and Low-Income Groups and Have Survived Breast Cancer,” *Phys Ther*, vol. 100, no. 3, pp. 487–499, Mar. 2020, doi: 10.1093/ptj/pzaa002.

[226] T. S. Maldonado *et al.*, “Assessment of quality of life changes in patients with lower extremity lymphedema using an advanced pneumatic compression device at home,” *J Vasc Surg Venous Lymphat Disord*, vol. 9, no. 3, pp. 745–752, May 2021, doi: 10.1016/j.jvsv.2020.10.013.

[227] J. Pamplin, J. Baldwin, and J. Rodrick, “Active Wearable Compression with Shape Memory Actuators for Treating Chronic Edema,” *Shape Memory and Superelasticity*, vol. 8, no. 2, pp. 142–149, 2022, doi: 10.1007/s40830-022-00379-w.

[228] EarlyBirds Innovation Ecosystem, “EarlyBirds weekly webinar with Aria Health (a ResMed company),” May 10, 2021. https://youtu.be/Unn5SwMo_84 (accessed Aug. 09, 2023).

[229] S. G. Rockson *et al.*, “A non-randomized, open-label study of the safety and effectiveness of a novel non-pneumatic compression device (NPCD) for lower limb lymphedema,” *Sci Rep*, vol. 12, no. 1, p. 14005, Aug. 2022, doi: 10.1038/s41598-022-17225-9.

[230] S. G. Rockson *et al.*, “Clinical Evaluation of a Novel Wearable Compression Technology in the Treatment of Lymphedema, an Open-Label Controlled Study,” *Lymphat Res Biol*, vol. 20, no. 2, pp. 125–132, Apr. 2022, doi: 10.1089/lrb.2020.0126.

[231] V. Sanchez *et al.*, “Smart Thermally Actuating Textiles,” *Adv Mater Technol*, vol. 2000383, pp. 1–10, 2020, doi: 10.1002/admt.202000383.

[232] N. W. Bartlett, K. P. Becker, and R. J. Wood, “A fluidic demultiplexer for controlling large arrays of soft actuators,” *Soft Matter*, vol. 16, no. 25, pp. 5871–5877, 2020, doi: 10.1039/C9SM02502B.

[233] J. D. Hubbard *et al.*, “Fully 3D-printed soft robots with integrated fluidic circuitry,” *Sci Adv*, vol. 7, no. 29, Jul. 2021, doi: 10.1126/sciadv.abe5257.

[234] S. Jadhav *et al.*, "Scalable Fluidic Matrix Circuits for Controlling Large Arrays of Individually Addressable Actuators," *Advanced Intelligent Systems*, May 2023, doi: 10.1002/aisy.202300011.

[235] L. C. van Laake, J. de Vries, S. Malek Kani, and J. T. B. Overvelde, "A fluidic relaxation oscillator for reprogrammable sequential actuation in soft robots," *Matter*, vol. 5, no. 9, pp. 2898–2917, Sep. 2022, doi: 10.1016/j.matt.2022.06.002.

[236] E. Gallardo Hevia *et al.*, "High-Gain Microfluidic Amplifiers: The Bridge between Microfluidic Controllers and Fluidic Soft Actuators," *Advanced Intelligent Systems*, vol. 4, no. 10, p. 2200122, Oct. 2022, doi: 10.1002/aisy.202200122.

[237] L. Jin, A. E. Forte, and K. Bertoldi, "Mechanical Valves for On-Board Flow Control of Inflatable Robots," *Advanced Science*, vol. 8, no. 21, p. 2101941, Nov. 2021, doi: 10.1002/advs.202101941.

[238] C. J. Decker *et al.*, "Programmable soft valves for digital and analog control," *Proceedings of the National Academy of Sciences*, vol. 119, no. 40, Oct. 2022, doi: 10.1073/pnas.2205922119.

[239] P. Rothemund *et al.*, "A soft, bistable valve for autonomous control of soft actuators," *Sci Robot*, vol. 3, no. 16, Mar. 2018, doi: 10.1126/scirobotics.aar7986.

[240] S. Hoang, K. Karydis, P. Brisk, and W. H. Grover, "A pneumatic random-access memory for controlling soft robots," *PLoS One*, vol. 16, no. 7, p. e0254524, Jul. 2021, doi: 10.1371/journal.pone.0254524.

[241] S. Xu, Y. Chen, N. P. Hyun, K. P. Becker, and R. J. Wood, "A dynamic electrically driven soft valve for control of soft hydraulic actuators," *Proceedings of the National Academy of Sciences*, vol. 118, no. 34, Aug. 2021, doi: 10.1073/pnas.2103198118.

[242] T. Huang *et al.*, "A lightweight flexible semi-cylindrical valve for seamless integration in soft robots based on the giant electrorheological fluid," *Sens Actuators A Phys*, vol. 347, p. 113905, Nov. 2022, doi: 10.1016/j.sna.2022.113905.

[243] M. Garrad, H.-Y. Chen, A. T. Conn, H. Hauser, and J. Rossiter, "Liquid Metal Logic for Soft Robotics," *IEEE Robot Autom Lett*, vol. 6, no. 2, pp. 4095–4102, Apr. 2021, doi: 10.1109/LRA.2021.3068118.

[244] R. Koul *et al.*, "Efficacy of complete decongestive therapy and manual lymphatic drainage on treatment-related lymphedema in breast cancer," *Int J Radiat Oncol Biol Phys*, 2007, doi: 10.1016/j.ijrobp.2006.09.024.

[245] M. Schara, M. Zeng, B. Jumet, and D. J. Preston, "A low-cost wearable device for portable sequential compression therapy," *Front Robot AI*, vol. 9, Nov. 2022, doi: 10.3389/frobt.2022.1012862.

[246] M. Zhu *et al.*, "A Peristaltic Soft, Wearable Robot for Compression Therapy and Massage," *IEEE Robot Autom Lett*, vol. 8, no. 8, pp. 4665–4672, Aug. 2023, doi: 10.1109/LRA.2023.3287773.

[247] J. H. (Heather) Kim, J. Stilling, M. O'Dell, and C. H.-L. Kao, "KnitDema: Robotic Textile as Personalized Edema Mobilization Device," in *Proceedings of the 2023 CHI*

Conference on Human Factors in Computing Systems, New York, NY, USA: ACM, Apr. 2023, pp. 1–19. doi: 10.1145/3544548.3581343.

[248] M. Pawar, H. K. Wazir, and V. Kapila, "A Lymphatic Drainage Robot for Lymphedema Rehabilitation," in *2022 44th Annual International Conference of the IEEE Engineering in Medicine & Biology Society (EMBC)*, IEEE, Jul. 2022, pp. 2598–2601. doi: 10.1109/EMBC48229.2022.9871226.

[249] M. King, A. Deveaux, H. White, and D. Rayson, "Compression garments versus compression bandaging in decongestive lymphatic therapy for breast cancer-related lymphedema: a randomized controlled trial," *Supportive Care in Cancer*, vol. 20, no. 5, pp. 1031–1036, May 2012, doi: 10.1007/s00520-011-1178-9.

[250] Lympha Press, "Lympha Press - Dynamic Compression Therapy." Jul. 2021.

[251] Lympha Press USA, "Evidence-based Use of Pneumatic Compression - Karen Ashforth," Feb. 23, 2021. https://youtu.be/sNire4YML6k (accessed Aug. 09, 2023).

[252] S. Crowhurst, P. Hammond, A. Chafranskaia, L. Durkee, and S. Phan, "How to Do Self Lymphatic Massage on Your Upper Body," 2019.

[253] E. Foldi, "Massage and Damage to Lymphatics," *Lymphology*, vol. 28, no. 1, pp. 1–3, 1995.

[254] O. Eliska and M. Eliskova, "Are Peripheral Lymphatics Damaged by High Pressure Manual Massage?," *Lymphology*, vol. 28, no. 1, pp. 21–30, 1995.

[255] A. Zelikovski, M. Manoach, Sh. Giler, and I. Urca, "Lympha-Press: A new pneumatic device for the treatment of Lymphedema of the limbs," *Lymphology*, vol. 13, no. 2, pp. 68–73, 1980.

[256] P. S. Lee, C. Sjaarda, R. Cornelious, R. Z. Gao, K. Lu, and C. Ren, "Naturally Compliant Dexterous Anthropomorphic Hand via Novel Modular Soft-Rigid Hybrid Robotics Approach: Design Rationale, Assembly Methods, and Evaluation," in *32nd IEEE International Conference on Robot and Human Interactive Communication (RO-MAN)*, Busan: IEEE, 2023.

[257] P. S. Lee, C. Sjaarda, R. Z. Gao, J. Dupuis, M. Rukavina-Nolsoe, and C. L. Ren, "Soft-Rigid Hybrid Revolute and Prismatic Joints using Multilayered Bellow Soft Pneumatic Actuators: Design, Characterization, and its Applications as Soft-Rigid Hybrid Gripper," SORO-2022-0214.R1, 2023.

[258] D. T. Eddington, W. C. Crone, and D. J. Beebe, " Development of Process Protocols to Fine Tune Polydimethysiloxane Material Properties," in *7th lnternational Conference on Miniaturized Chemical and Biochemical Analysis Systems* , Squaw Valley, Oct. 2003, pp. 1089–1092.

[259] A. Hingorani *et al.*, "The management of diabetic foot: A clinical practice guideline by the Society for Vascular Surgery in collaboration with the American Podiatric Medical Association and the Society for Vascular Medicine," *J Vasc Surg*, vol. 63, no. 2, pp. 3S-21S, 2016, doi: 10.1016/j.jvs.2015.10.003.

[260] A. L. Carrington *et al.*, “Peripheral vascular and nerve function associated with lower limb amputation in people with and without diabetes,” *Clin Sci*, vol. 101, no. 3, pp. 261–266, 2001, doi: 10.1042/CS20010018.

[261] J. E. Sanders and S. Fatone, “Residual limb volume change: Systematic review of measurement and management,” *J Rehabil Res Dev*, vol. 48, no. 8, pp. 949–986, 2011, doi: 10.1682/JRRD.2010.09.0189.

[262] S. Bhattacharya and R. Mishra, “Pressure ulcers: Current understanding and newer modalities of treatment,” *Indian Journal of Plastic Surgery*, vol. 48, no. 1, pp. 4–16, 2015, doi: 10.4103/0970-0358.155260.

[263] H. Nakajima, S. Yamamoto, and J. Katsuhira, “Effects of diabetic peripheral neuropathy on gait in vascular trans-tibial amputees,” *Clinical Biomechanics*, vol. 56, no. May, pp. 84–89, 2018, doi: 10.1016/j.clinbiomech.2018.05.005.

[264] E. Normann, A. Olsson, and T. H. Brodtkorb, “Modular socket system versus traditionally laminated socket: A cost analysis,” *Prosthet Orthot Int*, vol. 35, no. 1, pp. 76–80, 2011, doi: 10.1177/0309364610392812.

[265] X. Yang *et al.*, “Material, design, and fabrication of custom prosthetic liners for lower-extremity amputees: A review,” *Med Nov Technol Devices*, vol. 17, p. 100197, 2023, doi: https://doi.org/10.1016/j.medntd.2022.100197.

[266] Y. Wang, Q. Tan, F. Pu, D. Boone, and M. Zhang, “A Review of the Application of Additive Manufacturing in Prosthetic and Orthotic Clinics from a Biomechanical Perspective,” *Engineering*, vol. 6, no. 11, pp. 1258–1266, 2020, doi: 10.1016/j.eng.2020.07.019.

[267] E. C. T. Baars and J. H. B. Geertzen, “Literature review of the possible advantages of silicon liner socket use in trans-tibial prostheses,” *Prosthet Orthot Int*, vol. 29, no. 1, pp. 27–37, 2005, doi: 10.1080/17461550500069612.

[268] Z. E. H. Moore and J. Webster, “Dressings and topical agents for preventing pressure ulcers,” *Cochrane Database of Systematic Reviews*, vol. 2018, no. 12, 2018, doi: 10.1002/14651858.CD009362.pub3.

[269] M. Butcher and G. Thompson, “Dressings can prevent pressure ulcers: Fact or fallacy? The problem of pressure ulcer prevention,” *Wounds UK*, vol. 5, no. 4, pp. 80–93, 2009.

[270] B. G. Larsen, J. B. McLean, K. J. Allyn, J. T. Brzostowski, J. L. Garbini, and J. E. Sanders, “How do transtibial residual limbs adjust to intermittent incremental socket volume changes?,” *Prosthet Orthot Int*, vol. 43, no. 5, pp. 528–539, 2019, doi: 10.1177/0309364619864771.

[271] E. Nickel, K. Barrons, B. Hand, A. Cataldo, and A. Hansen, “Three-dimensional printing in prosthetics: Method for managing rapid limb volume change,” *Prosthet Orthot Int*, vol. 44, no. 5, pp. 355–358, 2020, doi: 10.1177/0309364620934340.

[272] S. Brunelli, A. S. Delussu, F. Paradisi, R. Pellegrini, and M. Traballesi, “A comparison between the suction suspension system and the hypobaric Iceross Seal-In® X5 in transtibial amputees,” *Prosthet Orthot Int*, vol. 37, no. 6, pp. 436–444, 2013, doi: 10.1177/0309364613476531.

[273] W. Do Kim, D. Kim, and K. S. Hong, “An evaluation of the effectiveness of the patellar tendon bar in the trans-tibial patellar-tendon-bearing prosthesis socket,” *Prosthet Orthot Int*, vol. 27, no. 1, pp. 23–35, 2003, doi: 10.3109/03093640309167974.

[274] J. E. Sanders, D. Lam, A. J. Dralle, and R. Okumura, “Interface pressures and shear stresses at thirteen socket sites on two persons with transtibial amputation.,” *J Rehabil Res Dev*, vol. 34, no. 1, pp. 19–43, Jan. 1997.

[275] H. Gholizadeh, E. D. Lemaire, and A. Eshraghi, “The evidence-base for elevated vacuum in lower limb prosthetics: Literature review and professional feedback,” *Clinical Biomechanics*, vol. 37, pp. 108–116, 2016, doi: 10.1016/j.clinbiomech.2016.06.005.

[276] J. E. Sanders, D. S. Harrison, T. R. Myers, and K. J. Allyn, “Effects of elevated vacuum on in-socket residual limb fluid volume: case study results using bioimpedance analysis.,” *J Rehabil Res Dev*, vol. 48, no. 10, pp. 1231–1248, 2011, doi: 10.1682/jrrd.2010.11.0219.

[277] A. Ogawa, G. Obinata, K. Hase, A. Dutta, and M. Nakagawa, “Design of lower limb prosthesis with contact pressure adjustment by MR fluid,” in *2008 30th Annual International Conference of the IEEE Engineering in Medicine and Biology Society*, 2008, pp. 330–333. doi: 10.1109/IEMBS.2008.4649157.

[278] J.-H. Seo *et al.*, “A Prosthetic Socket with Active Volume Compensation for Amputated Lower Limb,” *Sensors* , vol. 21, no. 2. 2021. doi: 10.3390/s21020407.

[279] R. W. Murdock, “Development of a Prosthetic Biofeedback Method and Device to Measure Quality of Fit for Trans-Tibial Amputees,” University of Waterloo, 2021.

[280] S. Portnoy *et al.*, “Internal mechanical conditions in the soft tissues of a residual limb of a trans-tibial amputee,” *J Biomech*, vol. 41, no. 9, pp. 1897–1909, 2008, doi: 10.1016/j.jbiomech.2008.03.035.

[281] J. Fergason and D. G. Smith, “Socket considerations for the patient with a transtibial amputation.,” *Clin Orthop Relat Res*, no. 361, pp. 76–84, Apr. 1999, doi: 10.1097/00003086-199904000-00011.

[282] T. A. Krouskop, “A synthesis of the factors that contribute to pressure sore formation,” *Med Hypotheses*, vol. 11, no. 2, pp. 255–267, 1983, doi: 10.1016/0306-9877(83)90067-1.

[283] M. P. Murray, A. B. Drought, and R. C. Kory, “Walking Patterns of Normal Men,” *J Bone Joint Surg Am*, vol. 46, pp. 335–360, Mar. 1964.

[284] E. J. Weathersby *et al.*, “Performance of an auto-adjusting prosthetic socket during walking with intermittent socket release,” *J Rehabil Assist Technol Eng*, vol. 9, Apr. 2022, doi: 10.1177/20556683221093271.

[285] A. J. M. Boulton, “The diabetic foot: grand overview, epidemiology and pathogenesis,” *Diabetes Metab Res Rev*, vol. 32, no. 30, pp. 13–23, 2008, doi: 10.1002/dmrr.

[286] M. Kazamel and P. J. Dyck, “Sensory manifestations of diabetic neuropathies: Anatomical and clinical correlations,” *Prosthet Orthot Int*, vol. 39, no. 1, pp. 7–16, Jan. 2015, doi: 10.1177/0309364614536764.

[287] P. Laszczak, L. Jiang, D. L. Bader, D. Moser, and S. Zahedi, "Development and validation of a 3D-printed interfacial stress sensor for prosthetic applications," *Med Eng Phys*, vol. 37, no. 1, pp. 132–137, 2015, doi: https://doi.org/10.1016/j.medengphy.2014.10.002.

[288] S. Ali, N. A. Abu Osman, A. Eshraghi, H. Gholizadeh, N. A. bin Abd razak, and W. A. B. Bin Wan Abas, "Interface pressure in transtibial socket during ascent and descent on stairs and its effect on patient satisfaction," *Clinical Biomechanics*, vol. 28, no. 9, pp. 994–999, 2013, doi: https://doi.org/10.1016/j.clinbiomech.2013.09.004.

[289] P. Dou, X. Jia, S. Suo, R. Wang, and M. Zhang, "Pressure distribution at the stump/socket interface in transtibial amputees during walking on stairs, slope and non-flat road.," *Clin Biomech (Bristol, Avon)*, vol. 21, no. 10, pp. 1067–1073, Dec. 2006, doi: 10.1016/j.clinbiomech.2006.06.004.

[290] J. E. Sanders, J. C. Cagle, K. J. Allyn, D. S. Harrison, and M. A. Ciol, "How do walking, standing, and resting influence transtibial amputee residual limb fluid volume?," *J Rehabil Res Dev*, vol. 51, no. 2, pp. 201–212, 2014, doi: 10.1682/JRRD.2013.04.0085.

[291] A. Eshraghi, N. A. A. Osman, H. Gholizadeh, M. Karimi, and S. Ali, "Pistoning assessment in lower limb prosthetic sockets," *Prosthet Orthot Int*, vol. 36, no. 1, pp. 15–24, Jan. 2012, doi: 10.1177/0309364611431625.

[292] R. Murdock, "Development of a Prosthetic Biofeedback Method and Device to Measure Quality of Fit for Trans-Tibial Amputees," University of Waterloo, 2021.

[293] P. Sewell, S. Noroozi, J. Vinney, and S. Andrews, "Developments in the trans-tibial prosthetic socket fitting process: A review of past and present research," *Prosthet Orthot Int*, vol. 24, no. 2, pp. 97–107, Aug. 2000, doi: 10.1080/03093640008726532.

[294] P. Saeedi *et al.*, "Global and regional diabetes prevalence estimates for 2019 and projections for 2030 and 2045: Results from the International Diabetes Federation Diabetes Atlas, 9(th) edition.," *Diabetes Res Clin Pract*, vol. 157, p. 107843, Nov. 2019, doi: 10.1016/j.diabres.2019.107843.

[295] Tekscan, "The Differences Between Force Sensitive Resistor Technologies: Assessing Linearity, Drift, and Other Performance Factors," 2016. https://www.tekscan.com/blog/flexiforce/differences-between-force-sensitive-resistor-technologies-assessing-linearity-drift (accessed Aug. 05, 2022).

[296] Adapttech, "Motio Stepwatch - Real-World Activity Monitor for Lower Limb Prosthetic Users," Apr. 20, 2023. https://www.adapttech.eu/motio-stepwatch (accessed Apr. 24, 2023).

[297] J. Tabor *et al.*, "Textile-Based Pressure Sensors for Monitoring Prosthetic-Socket Interfaces," *IEEE Sens J*, vol. 21, no. 7, pp. 9413–9422, 2021, doi: 10.1109/JSEN.2021.3053434.

[298] J. Wheeler, A. Mazumdar, L. Marron, K. Dullea, J. Sanders, and K. Allyn, "A pressure and shear sensing liner for prosthetic sockets.," *Annu Int Conf IEEE Eng Med Biol Soc*, vol. 2016, pp. 2026–2029, Aug. 2016, doi: 10.1109/EMBC.2016.7591124.

[299] J. W. Kwak *et al.*, "Wireless sensors for continuous, multimodal measurements at the skin interface with lower limb prostheses," *Sci Transl Med*, vol. 12, no. 574, p. eabc4327, Dec. 2020, doi: 10.1126/scitranslmed.abc4327.

[300] Z. Zhao *et al.*, "Machine-washable and breathable pressure sensors based on triboelectric nanogenerators enabled by textile technologies," *Nano Energy*, vol. 70, p. 104528, 2020, doi: https://doi.org/10.1016/j.nanoen.2020.104528.

[301] J. Lee *et al.*, "Conductive Fiber-Based Ultrasensitive Textile Pressure Sensor for Wearable Electronics," *Advanced Materials*, vol. 27, no. 15, pp. 2433–2439, Apr. 2015, doi: https://doi.org/10.1002/adma.201500009.

[302] O. Atalay, A. Atalay, J. Gafford, and C. Walsh, "A Highly Sensitive Capacitive-Based Soft Pressure Sensor Based on a Conductive Fabric and a Microporous Dielectric Layer," *Adv Mater Technol*, vol. 3, no. 1, p. 1700237, Jan. 2018, doi: https://doi.org/10.1002/admt.201700237.

[303] Y. Gao *et al.*, "Wearable Microfluidic Diaphragm Pressure Sensor for Health and Tactile Touch Monitoring," *Advanced Materials*, vol. 29, no. 39, p. 1701985, Oct. 2017, doi: https://doi.org/10.1002/adma.201701985.

[304] N. A. Abu Osman, W. D. Spence, S. E. Solomonidis, J. P. Paul, and A. M. Weir, "Transducers for the determination of the pressure and shear stress distribution at the stump—socket interface of trans-tibial amputees," *Proc Inst Mech Eng B J Eng Manuf*, vol. 224, no. 8, pp. 1239–1250, Feb. 2010, doi: 10.1243/09544054JEM1820.

[305] J. W. Wheeler *et al.*, "MEMS-based bubble pressure sensor for prosthetic socket interface pressure measurement," in *2011 Annual International Conference of the IEEE Engineering in Medicine and Biology Society*, 2011, pp. 2925–2928. doi: 10.1109/IEMBS.2011.6090805.

[306] C. Tawk and G. Alici, "A Review of 3D-Printable Soft Pneumatic Actuators and Sensors: Research Challenges and Opportunities," *Advanced Intelligent Systems*, vol. 3, no. 6, p. 2000223, Jun. 2021, doi: https://doi.org/10.1002/aisy.202000223.

[307] D. L. Bader, P. R. Worsley, and A. Gefen, "Bioengineering considerations in the prevention of medical device-related pressure ulcers.," *Clin Biomech (Bristol, Avon)*, vol. 67, pp. 70–77, Jul. 2019, doi: 10.1016/j.clinbiomech.2019.04.018.

[308] E. A. Al-Fakih, N. A. A. Osman, F. R. M. Adikan, A. Eshraghi, and P. Jahanshahi, "Development and Validation of Fiber Bragg Grating Sensing Pad for Interface Pressure Measurements Within Prosthetic Sockets," *IEEE Sens J*, vol. 16, no. 4, pp. 965–974, 2016, doi: 10.1109/JSEN.2015.2495323.

[309] Z. F. Zhang, X. M. Tao, H. P. Zhang, and B. Zhu, "Soft Fiber Optic Sensors for Precision Measurement of Shear Stress and Pressure," *IEEE Sens J*, vol. 13, no. 5, pp. 1478–1482, 2013, doi: 10.1109/JSEN.2012.2237393.

[310] E. A. Al-Fakih, N. A. Abu Osman, and F. R. Mahmad Adikan, "Techniques for Interface Stress Measurements within Prosthetic Sockets of Transtibial Amputees: A Review of the Past 50 Years of Research," *Sensors*, vol. 16, no. 7. 2016. doi: 10.3390/s16071119.

[311] J. E. Tanner and G. M. Berke, “Radiographic Comparison of Vertical Tibial Translation Using Two Types of Suspensions on a Transtibial Prosthesis: A Case Study,” *JPO: Journal of Prosthetics and Orthotics*, vol. 13, no. 1, 2001, [Online]. Available: https://journals.lww.com/jpojournal/Fulltext/2001/03000/Radiographic_Comparison_of_Vertical_Tibial.12.aspx

[312] S. Grevsten and U. Eriksson, “Stump-Socket Contact and Skeletal Displacement in a Suction Patellar-Tendon Bearing Prosthesis,” *JBJS*, vol. 56, no. 8, 1974, [Online]. Available: https://journals.lww.com/jbjsjournal/Fulltext/1974/56080/Stump_Socket_Contact_and_Skeletal_Displacement_in.20.aspx

[313] A. Eshraghi, N. A. A. Osman, H. Gholizadeh, M. Karimi, and S. Ali, “Pistoning assessment in lower limb prosthetic sockets,” *Prosthet Orthot Int*, vol. 36, no. 1, pp. 15–24, 2012, doi: 10.1177/0309364611431625.

[314] R. L. Newton, D. Morgan, and M. H. Schreiber, “Radiological evaluation of prosthetic fit in below-the-knee amputees,” *Skeletal Radiol*, vol. 17, no. 4, pp. 276–280, 1988, doi: 10.1007/BF00401811.

[315] H. Bateni and S. J. Olney, “Kinematic and Kinetic Variations of Below-Knee Amputee Gait,” *JPO: Journal of Prosthetics and Orthotics*, vol. 14, no. 1, 2002, [Online]. Available: https://journals.lww.com/jpojournal/Fulltext/2002/03000/Kinematic_and_Kinetic_Variations_of_Below_Knee.3.aspx

[316] Y. Hermodsson, C. Ekdahl, B. M. Persson, and G. Roxendal, “Gait in male trans-tibial amputees: a comparative study with healthy subjects in relation to walking speed.,” *Prosthet Orthot Int*, vol. 18, no. 2, pp. 68–77, Aug. 1994, doi: 10.3109/03093649409164387.

[317] H. Long *et al.*, “Prevalence Trends of Site-Specific Osteoarthritis From 1990 to 2019: Findings From the Global Burden of Disease Study 2019,” *Arthritis & Rheumatology*, vol. 74, no. 7, pp. 1172–1183, Jul. 2022, doi: https://doi.org/10.1002/art.42089.

[318] G. A. Hawker *et al.*, “Osteoarthritis-related difficulty walking and risk for diabetes complications,” *Osteoarthritis Cartilage*, vol. 25, no. 1, pp. 67–75, 2017, doi: https://doi.org/10.1016/j.joca.2016.08.003.

[319] L. K. King, T. Kendzerska, E. J. Waugh, and G. A. Hawker, “Impact of Osteoarthritis on Difficulty Walking: A Population-Based Study,” *Arthritis Care Res (Hoboken)*, vol. 70, no. 1, pp. 71–79, Jan. 2018, doi: https://doi.org/10.1002/acr.23250.

[320] V. L. Johnson and D. J. Hunter, “The epidemiology of osteoarthritis,” *Best Pract Res Clin Rheumatol*, vol. 28, no. 1, pp. 5–15, 2014, doi: https://doi.org/10.1016/j.berh.2014.01.004.

[321] G. M. Brouwer *et al.*, “Association between valgus and varus alignment and the development and progression of radiographic osteoarthritis of the knee,” *Arthritis Rheum*, vol. 56, no. 4, pp. 1204–1211, Apr. 2007, doi: https://doi.org/10.1002/art.22515.

[322] N. D’Souza *et al.*, “Are biomechanics during gait associated with the structural disease onset and progression of lower limb osteoarthritis? A systematic review and meta-

analysis.," *Osteoarthritis Cartilage*, vol. 30, no. 3, pp. 381–394, Mar. 2022, doi: 10.1016/j.joca.2021.10.010.

[323] B. E. Øiestad, C. B. Juhl, I. Eitzen, and J. B. Thorlund, "Knee extensor muscle weakness is a risk factor for development of knee osteoarthritis. A systematic review and meta-analysis.," *Osteoarthritis Cartilage*, vol. 23, no. 2, pp. 171–177, Feb. 2015, doi: 10.1016/j.joca.2014.10.008.

[324] V. Silverwood, M. Blagojevic-Bucknall, C. Jinks, J. L. Jordan, J. Protheroe, and K. P. Jordan, "Current evidence on risk factors for knee osteoarthritis in older adults: a systematic review and meta-analysis.," *Osteoarthritis Cartilage*, vol. 23, no. 4, pp. 507–515, Apr. 2015, doi: 10.1016/j.joca.2014.11.019.

[325] L. Sharma, J. Song, D. T. Felson, S. Cahue, E. Shamiyeh, and D. D. Dunlop, "The Role of Knee Alignment in Disease Progression and Functional Decline in Knee Osteoarthritis," *JAMA*, vol. 286, no. 2, pp. 188–195, Jul. 2001, doi: 10.1001/jama.286.2.188.

[326] T. P. Andriacchi, "Dynamics of knee malalignment.," *Orthop Clin North Am*, vol. 25, no. 3, pp. 395–403, Jul. 1994.

[327] T. Miyazaki, M. Wada, H. Kawahara, M. Sato, H. Baba, and S. Shimada, "Dynamic load at baseline can predict radiographic disease progression in medial compartment knee osteoarthritis," *Ann Rheum Dis*, vol. 61, no. 7, pp. 617 LP – 622, Jul. 2002, doi: 10.1136/ard.61.7.617.

[328] A. H. Chang *et al.*, "External knee adduction and flexion moments during gait and medial tibiofemoral disease progression in knee osteoarthritis.," *Osteoarthritis Cartilage*, vol. 23, no. 7, pp. 1099–1106, Jul. 2015, doi: 10.1016/j.joca.2015.02.005.

[329] K. L. Bennell, K.-A. Bowles, Y. Wang, F. Cicuttini, M. Davies-Tuck, and R. S. Hinman, "Higher dynamic medial knee load predicts greater cartilage loss over 12 months in medial knee osteoarthritis," *Ann Rheum Dis*, vol. 70, no. 10, pp. 1770 LP – 1774, Oct. 2011, doi: 10.1136/ard.2010.147082.

[330] N. Segal *et al.*, "Does the rate of knee OA progression increase with age? Articular cartilage changes over seven years in most," *Osteoarthritis Cartilage*, vol. 23, p. A178, 2015, doi: https://doi.org/10.1016/j.joca.2015.02.951.

[331] K. Magnusson, A. Turkiewicz, and M. Englund, "Nature vs nurture in knee osteoarthritis - the importance of age, sex and body mass index.," *Osteoarthritis Cartilage*, vol. 27, no. 4, pp. 586–592, Apr. 2019, doi: 10.1016/j.joca.2018.12.018.

[332] M. Blagojevic, C. Jinks, A. Jeffery, and K. P. Jordan, "Risk factors for onset of osteoarthritis of the knee in older adults: a systematic review and meta-analysis," *Osteoarthritis Cartilage*, vol. 18, no. 1, pp. 24–33, 2010, doi: https://doi.org/10.1016/j.joca.2009.08.010.

[333] S. L. Kolasinski *et al.*, "2019 American College of Rheumatology/Arthritis Foundation Guideline for the Management of Osteoarthritis of the Hand, Hip, and Knee," *Arthritis Care Res (Hoboken)*, vol. 72, no. 2, pp. 149–162, Feb. 2020, doi: https://doi.org/10.1002/acr.24131.

[334] N. J. Collins, H. F. Hart, and K. A. G. Mills, “Osteoarthritis year in review 2018: rehabilitation and outcomes.,” *Osteoarthritis Cartilage*, vol. 27, no. 3, pp. 378–391, Mar. 2019, doi: 10.1016/j.joca.2018.11.010.

[335] J. Martel-Pelletier *et al.*, “A new decision tree for diagnosis of osteoarthritis in primary care: international consensus of experts.,” *Aging Clin Exp Res*, vol. 31, no. 1, pp. 19–30, Jan. 2019, doi: 10.1007/s40520-018-1077-8.

[336] O. Aweid, Z. Haider, A. Saed, and Y. Kalairajah, “Treatment modalities for hip and knee osteoarthritis: A systematic review of safety.,” *J Orthop Surg (Hong Kong)*, vol. 26, no. 3, p. 2309499018808669, 2018, doi: 10.1177/2309499018808669.

[337] P. F. M. Choong and M. M. Dowsey, “Update in surgery for osteoarthritis of the knee,” *Int J Rheum Dis*, vol. 14, no. 2, pp. 167–174, May 2011, doi: https://doi.org/10.1111/j.1756-185X.2011.01617.x.

[338] P. Dieppe, K. Lim, and S. Lohmander, “Who should have knee joint replacement surgery for osteoarthritis?,” *Int J Rheum Dis*, vol. 14, no. 2, pp. 175–180, May 2011, doi: https://doi.org/10.1111/j.1756-185X.2011.01611.x.

[339] C. K. O’Neil, J. T. Hanlon, and Z. A. Marcum, “Adverse Effects of Analgesics Commonly Used by Older Adults With Osteoarthritis: Focus on Non-Opioid and Opioid Analgesics,” *Am J Geriatr Pharmacother*, vol. 10, no. 6, pp. 331–342, 2012, doi: https://doi.org/10.1016/j.amjopharm.2012.09.004.

[340] D. A. Marshall *et al.*, “Estimating the Burden of Osteoarthritis to Plan for the Future,” *Arthritis Care Res (Hoboken)*, vol. 67, no. 10, pp. 1379–1386, Oct. 2015, doi: https://doi.org/10.1002/acr.22612.

[341] K. Raja and N. Dewan, “Efficacy of Knee Braces and Foot Orthoses in Conservative Management of Knee Osteoarthritis: A Systematic Review,” *Am J Phys Med Rehabil*, vol. 90, no. 3, 2011.

[342] D. K. Ramsey and M. E. Russell, “Unloader braces for medial compartment knee osteoarthritis: implications on mediating progression.,” *Sports Health*, vol. 1, no. 5, pp. 416–426, Sep. 2009, doi: 10.1177/1941738109343157.

[343] M. Arazpour, S. W. Hutchins, M. A. Bani, S. Curran, and A. Aksenov, “The influence of a bespoke unloader knee brace on gait in medial compartment osteoarthritis: A pilot study,” *Prosthet Orthot Int*, vol. 38, no. 5, pp. 379–386, Feb. 2014, doi: 10.1177/0309364613504780.

[344] N. J. Giori, “Load-shifting brace treatment for osteoarthritis of the knee: a minimum 2 1/2-year follow-up study.,” *J Rehabil Res Dev*, vol. 41, no. 2, pp. 187–194, Mar. 2004, doi: 10.1682/jrrd.2004.02.0187.

[345] J. R. Basford and S. J. Johnson, “Form may be as important as function in orthotic acceptance: a case report.,” *Arch Phys Med Rehabil*, vol. 83, no. 3, pp. 433–435, Mar. 2002, doi: 10.1053/apmr.2002.29629.

[346] D. T. Felson, A. Naimark, J. Anderson, L. Kazis, W. Castelli, and R. F. Meenan, “The prevalence of knee osteoarthritis in the elderly. The Framingham Osteoarthritis Study.,” *Arthritis Rheum*, vol. 30, no. 8, pp. 914–918, Aug. 1987, doi: 10.1002/art.1780300811.

[347] R. D. A. Gaasbeek, B. E. Groen, B. Hampsink, R. J. van Heerwaarden, and J. Duysens, "Valgus bracing in patients with medial compartment osteoarthritis of the knee. A gait analysis study of a new brace.," *Gait Posture*, vol. 26, no. 1, pp. 3–10, Jun. 2007, doi: 10.1016/j.gaitpost.2006.07.007.

[348] A. J. Johnson, R. Starr, B. H. Kapadia, A. Bhave, and M. A. Mont, "Gait and clinical improvements with a novel knee brace for knee OA.," *J Knee Surg*, vol. 26, no. 3, pp. 173–178, Jun. 2013, doi: 10.1055/s-0032-1327452.

[349] D. Stamenović, M. Kojić, B. Stojanović, and D. Hunter, "Pneumatic osteoarthritis knee brace.," *J Biomech Eng*, vol. 131, no. 4, p. 45001, Apr. 2009, doi: 10.1115/1.3072890.

[350] J. J. Cherian, A. Bhave, B. H. Kapadia, R. Starr, M. J. McElroy, and M. A. Mont, "Strength and Functional Improvement Using Pneumatic Brace with Extension Assist for End-Stage Knee Osteoarthritis: A Prospective, Randomized trial," *Journal of Arthroplasty*, vol. 30, no. 5, pp. 747–753, 2015, doi: 10.1016/j.arth.2014.11.036.

[351] M. Khosravi, M. Arazpour, H. Saeedi, and M. Rezaei, "Design Evaluation in Novel Orthoses for Patients with Medial Knee Osteoarthritis.," *J Biomed Phys Eng*, vol. 9, no. 6, pp. 719–732, Dec. 2019, doi: 10.31661/jbpe.v0i0.965.

[352] K. Raja and N. Dewan, "Efficacy of knee braces and foot orthoses in conservative management of knee osteoarthritis: A systematic review," *Am J Phys Med Rehabil*, vol. 90, no. 3, pp. 247–262, 2011, doi: 10.1097/PHM.0b013e318206386b.

[353] J. Knoop *et al.*, "Proprioception in knee osteoarthritis : a narrative review," *Osteoarthritis Cartilage*, vol. 19, no. 4, pp. 381–388, 2011, doi: 10.1016/j.joca.2011.01.003.

[354] H. Hirai *et al.*, "Development of an ankle-foot orthosis with a pneumatic passive element," in *ROMAN 2006 - The 15th IEEE International Symposium on Robot and Human Interactive Communication*, 2006, pp. 220–225. doi: 10.1109/ROMAN.2006.314421.

[355] R. Chin *et al.*, "A pneumatic power harvesting ankle-foot orthosis to prevent foot-drop," *J Neuroeng Rehabil*, vol. 6, no. 1, pp. 1–11, 2009, doi: 10.1186/1743-0003-6-19.

[356] M. Takaiwa and T. Noritsugu, "DEVELOPMENT OF PNEUMATIC WALKING SUPPORT SHOES USING POTENTIAL ENERGY OF HUMAN," *Proceedings of the JFPS International Symposium on Fluid Power*, vol. 2008, no. 7–3, pp. 781–786, 2008, doi: 10.5739/isfp.2008.781.

[357] R. A. Shveda *et al.*, "A wearable textile-based pneumatic energy harvesting system for assistive robotics," *Sci Adv*, vol. 8, no. 34, p. eabo2418, Aug. 2022, doi: 10.1126/sciadv.abo2418.

[358] R. H. Gross, "Leg length discrepancy: how much is too much?," *Orthopedics*, vol. 1, no. 4, pp. 307–310, 1978, doi: 10.3928/0147-7447-19780701-08.

[359] H. G. P. V. da Silva, A. Cliquet Junior, A. R. Zorzi, and J. Batista de Miranda, "Biomechanical changes in gait of subjects with medial knee osteoarthritis.," *Acta Ortop Bras*, vol. 20, no. 3, pp. 150–156, 2012, doi: 10.1590/S1413-78522012000300004.

[360] W.-C. Hsu, Y.-C. Jhong, H.-L. Chen, Y.-J. Lin, L.-F. Chen, and L.-F. Hsieh, "Immediate and long-term efficacy of laterally-wedged insoles on persons with bilateral medial knee osteoarthritis during walking," *Biomed Eng Online*, vol. 14, no. 1, p. 43, 2015, doi: 10.1186/s12938-015-0040-6.

[361] P. Levinger, H. B. Menz, A. D. Morrow, J. R. Bartlett, J. A. Feller, and N. R. Bergman, "Relationship between foot function and medial knee joint loading in people with medial compartment knee osteoarthritis," *J Foot Ankle Res*, vol. 6, no. 1, p. 33, 2013, doi: 10.1186/1757-1146-6-33.

[362] K. Allen *et al.*, "Osteoarthritis physical activity care pathway (OA-PCP): results of a feasibility trial," *BMC Musculoskelet Disord*, vol. 21, no. 1, p. 308, 2020, doi: 10.1186/s12891-020-03339-6.

[363] K. L. Paterson, K. L. Bennell, T. V. Wrigley, B. R. Metcalf, J. Kasza, and R. S. Hinman, "Effects of footwear on the knee adduction moment in medial knee osteoarthritis: classification criteria for flat flexible vs stable supportive shoes," *Osteoarthritis Cartilage*, vol. 25, no. 2, pp. 234–241, Feb. 2017, doi: 10.1016/j.joca.2016.10.001.

[364] V. Racher, W. Wirth, G. Zimmermann, A. Bathke, and F. Eckstein, "Dependence of womac pain on radiographic knee oa status, age, sex, body mass index (BMI), race, and contralateral knee pain status," *Osteoarthritis Cartilage*, vol. 28, pp. S141–S142, 2020, doi: https://doi.org/10.1016/j.joca.2020.02.233.

[365] C. Ertürk, M. A. Altay, C. Sert, A. Levent, M. Yaptı, and K. Yüce, "The body composition of patients with knee osteoarthritis: relationship with clinical parameters and radiographic severity," *Aging Clin Exp Res*, vol. 27, no. 5, pp. 673–679, 2015, doi: 10.1007/s40520-015-0325-4.

[366] N. Foroughi, R. Smith, and B. Vanwanseele, "The association of external knee adduction moment with biomechanical variables in osteoarthritis: A systematic review," *Knee*, vol. 16, no. 5, pp. 303–309, Oct. 2009, doi: 10.1016/j.knee.2008.12.007.

[367] P. Thoumie *et al.*, "Effect of unloading brace treatment on pain and function in patients with symptomatic knee osteoarthritis: the ROTOR randomized clinical trial," *Sci Rep*, vol. 8, no. 1, p. 10519, 2018, doi: 10.1038/s41598-018-28782-3.

[368] C. S. Kothera, M. Jangid, J. Sirohi, and N. M. Wereley, "Experimental Characterization and Static Modeling of McKibben Actuators," *Journal of Mechanical Design*, vol. 131, no. 9, Aug. 2009, doi: 10.1115/1.3158982.

[369] M. G. Pandy and T. P. Andriacchi, "Muscle and Joint Function in Human Locomotion," *Annu Rev Biomed Eng*, vol. 12, no. 1, pp. 401–433, Jul. 2010, doi: 10.1146/annurev-bioeng-070909-105259.

[370] S. G. Kandlikar, "Chapter 3 - Single-phase liquid flow in minichannels and microchannels," in *Heat Transfer and Fluid Flow in Minichannels and Microchannels*, S. G. Kandlikar, S. Garimella, D. Li, S. Colin, and M. R. King, Eds., Oxford: Elsevier Science Ltd, 2006, pp. 87–136. doi: https://doi.org/10.1016/B978-008044527-4/50005-0.

[371] T.-S. Wong *et al.*, "Bioinspired self-repairing slippery surfaces with pressure-stable omniphobicity," *Nature*, vol. 477, no. 7365, pp. 443–447, 2011, doi: 10.1038/nature10447.

[372] R. K. Jones, G. J. Chapman, M. J. Parkes, Laura. Forsythe, and D. T. Felson, "The effect of different types of insoles or shoe modifications on medial loading of the knee in persons with medial knee osteoarthritis: a randomised trial," *Journal of Orthopaedic Research*, vol. 33, no. 11, pp. 1646–1654, Nov. 2015, doi: https://doi.org/10.1002/jor.22947.

[373] G. B. Sinclair and J. E. Helms, "A review of simple formulae for elastic hoop stresses in cylindrical and spherical pressure vessels: What can be used when," *International Journal of Pressure Vessels and Piping*, vol. 128, pp. 1–7, 2015, doi: https://doi.org/10.1016/j.ijpvp.2015.01.006.

[374] R. S. Hinman, K. A. Bowles, B. B. Metcalf, T. V Wrigley, and K. L. Bennell, "Lateral wedge insoles for medial knee osteoarthritis: Effects on lower limb frontal plane biomechanics," *Clinical Biomechanics*, vol. 27, no. 1, pp. 27–33, 2012, doi: https://doi.org/10.1016/j.clinbiomech.2011.07.010.

[375] A. Chang *et al.*, "The relationship between toe-out angle during gait and progression of medial tibiofemoral osteoarthritis," *Ann Rheum Dis*, vol. 66, no. 10, p. 1271, Oct. 2007, doi: 10.1136/ard.2006.062927.

[376] D. Knudson and B. Wallace, "Student perceptions of low-tech active learning and mastery of introductory biomechanics concepts," *Sports Biomech*, vol. 20, no. 4, pp. 458–468, May 2021, doi: 10.1080/14763141.2019.1570322.

[377] K. Lindvig and L. Ulriksen, "Different, Difficult, and Local: A Review of Interdisciplinary Teaching Activities," *Rev High Ed*, vol. 43, no. 2, pp. 697–725, 2019, doi: 10.1353/rhe.2019.0115.

[378] A. Jackson, N. Mentzer, and R. Kramer-Bottiglio, "Increasing gender diversity in engineering using soft robotics," *Journal of Engineering Education*, vol. 110, no. 1, pp. 143–160, Jan. 2021, doi: https://doi.org/10.1002/jee.20378.

[379] D. P. Holland, E. J. Park, P. Polygerinos, G. J. Bennett, and C. J. Walsh, "The Soft Robotics Toolkit: Shared Resources for Research and Design," *Soft Robot*, vol. 1, no. 3, pp. 224–230, Sep. 2014, doi: 10.1089/soro.2014.0010.

[380] D. P. Holland, S. Berndt, M. Herman, and C. J. Walsh, "Growing the Soft Robotics Community Through Knowledge-Sharing Initiatives," *Soft Robot*, vol. 5, no. 2, pp. 119–121, Apr. 2018, doi: 10.1089/soro.2018.29013.dph.

[381] A. Jackson, J. Zhang, R. Kramer, and N. Mentzer, "Board # 96 : Design-based Research and Soft Robotics to Broaden the STEM Pipeline (Work in Progress)," in *2017 ASEE Annual Conference & Exposition Proceedings*, ASEE Conferences. doi: 10.18260/1-2--27963.

[382] J. Zhang, A. Jackson, N. Mentzer, and R. Kramer, "A Modular, Reconfigurable Mold for a Soft Robotic Gripper Design Activity," *Front Robot AI*, vol. 4, Sep. 2017, doi: 10.3389/frobt.2017.00046.

[383] S. Shah, A. Beaudette, D. Bergandine, S. Devmal, C. Walsh, and H. Golecki, "Adapting Soft Robotics Outreach to Teacher-Delivered Curriculum in the Virtual Classroom (Work in Progress)," in *2021 ASEE Virtual Annual Conference Content Access Proceedings*, ASEE Conferences. doi: 10.18260/1-2--36651.

[384] T. Ashuri, A. Armani, R. Jalilzadeh Hamidi, T. Reasnor, S. Ahmadi, and K. Iqbal, "Biomedical soft robots: current status and perspective," *Biomed Eng Lett*, vol. 10, no. 3, pp. 369–385, 2020, doi: 10.1007/s13534-020-00157-6.

[385] U. Culha, J. Hughes, A. Rosendo, F. Giardina, and F. Iida, "Design Principles for Soft-Rigid Hybrid Manipulators," in *Soft Robotics: Trends, Applications and Challenges*, C. Laschi, J. Rossiter, F. Iida, M. Cianchetti, and L. Margheri, Eds., Cham: Springer International Publishing, 2017, pp. 87–94. doi: https://doi.org/10.1007/978-3-319-46460-2_11.

[386] T. S. Love, J. P. Cysyk, A. Attaluri, R. D. Tunks, K. Harter, and R. Sipos, "Examining Science and Technology/Engineering Educators' Views of Teaching Biomedical Concepts Through Physical Computing," *J Sci Educ Technol*, vol. 32, no. 1, pp. 96–110, 2023, doi: 10.1007/s10956-022-09996-7.

[387] J. A. White *et al.*, "Core Competencies for Undergraduates in Bioengineering and Biomedical Engineering: Findings, Consequences, and Recommendations," *Annals of Biomedical Engineering*, vol. 48, no. 3. Springer, pp. 905–912, Mar. 01, 2020. doi: 10.1007/s10439-020-02468-2.

[388] D. Knudson, "PHYSICS AND BIOMECHANICS EDUCATION RESEARCH: IMPROVING LEARNING OF BIOMECHANICAL CONCEPTS," in *31 International Conference on Biomechanics in Sports*, 2013. [Online]. Available: http://www.per-central.org/document/ServiceFile.cfm?ID=4517

[389] K. Ziegler-Graham, E. J. MacKenzie, P. L. Ephraim, T. G. Travison, and R. Brookmeyer, "Estimating the Prevalence of Limb Loss in the United States: 2005 to 2050," *Arch Phys Med Rehabil*, vol. 89, no. 3, pp. 422–429, 2008, doi: https://doi.org/10.1016/j.apmr.2007.11.005.

[390] E. M. Graham *et al.*, "Restoring Form and Function to the Partial Hand Amputee: Prosthetic Options from the Fingertip to the Palm," *Hand Clin*, vol. 37, no. 1, pp. 167–187, 2021, doi: https://doi.org/10.1016/j.hcl.2020.09.013.

[391] N. Guo *et al.*, "Simulation analysis for optimal design of pneumatic bellow actuators for soft-robotic glove," *Biocybern Biomed Eng*, vol. 40, no. 4, pp. 1359–1368, 2020, doi: https://doi.org/10.1016/j.bbe.2020.08.002.

[392] W. Jung, Y. Kang, S. Han, and Y. Hwang, "Biocompatible micro, soft bellow actuator rapidly manufactured using 3D-printed soluble mold," *Journal of Micromechanics and Microengineering*, vol. 29, no. 12, p. 125005, 2019, doi: 10.1088/1361-6439/ab477f.

[393] T. Ngah, "3916 Bemis Activated Sewfree Tape Datasheet," 2009.

[394] F. Schmitt, O. Piccin, L. Barbé, and B. Bayle, "Soft Robots Manufacturing: A Review," *Front Robot AI*, vol. 5, Jul. 2018, doi: 10.3389/frobt.2018.00084.

[395] A. Van den Beemt *et al.*, “Interdisciplinary engineering education: A review of vision, teaching, and support,” *Journal of Engineering Education*, vol. 109, no. 3, pp. 508–555, Jul. 2020, doi: https://doi.org/10.1002/jee.20347.

[396] L. D. Feisel and A. J. Rosa, “The Role of the Laboratory in Undergraduate Engineering Education,” *Journal of Engineering Education*, vol. 94, no. 1, pp. 121–130, Jan. 2005, doi: https://doi.org/10.1002/j.2168-9830.2005.tb00833.x.

[397] M. Prince, “Does Active Learning Work? A Review of the Research,” *Journal of Engineering Education*, vol. 93, no. 3, pp. 223–231, Jul. 2004, doi: https://doi.org/10.1002/j.2168-9830.2004.tb00809.x.

[398] W. Li, P. Shi, and H. Yu, “Gesture Recognition Using Surface Electromyography and Deep Learning for Prostheses Hand: State-of-the-Art, Challenges, and Future,” *Front Neurosci*, vol. 15, Apr. 2021, doi: 10.3389/fnins.2021.621885.

[399] P. Aggarwal and C. L. O’Brien, “Social Loafing on Group Projects,” *Journal of Marketing Education*, vol. 30, no. 3, pp. 255–264, Dec. 2008, doi: 10.1177/0273475308322283.

[400] A. Behrens *et al.*, “MATLAB Meets LEGO Mindstorms—A Freshman Introduction Course Into Practical Engineering,” *IEEE Transactions on Education*, vol. 53, no. 2, pp. 306–317, May 2010, doi: 10.1109/TE.2009.2017272.

[401] P. Weiner, J. Starke, F. Hundhausen, J. Beil, and T. Asfour, “The KIT Prosthetic Hand: Design and Control,” in *2018 IEEE/RSJ International Conference on Intelligent Robots and Systems (IROS)*, IEEE, Oct. 2018, pp. 3328–3334. doi: 10.1109/IROS.2018.8593851.

[402] J. L. Segil, S. A. Huddle, and R. F. ff. Weir, “Functional Assessment of a Myoelectric Postural Controller and Multi-Functional Prosthetic Hand by Persons With Trans-Radial Limb Loss,” *IEEE Transactions on Neural Systems and Rehabilitation Engineering*, vol. 25, no. 6, pp. 618–627, Jun. 2017, doi: 10.1109/TNSRE.2016.2586846.

[403] J. L. Segil, M. Controzzi, R. F. ff. Weir, and C. Cipriani, “Comparative study of state-of-the-art myoelectric controllers for multigrasp prosthetic hands,” *J Rehabil Res Dev*, vol. 51, no. 9, pp. 1439–1454, 2014, doi: 10.1682/JRRD.2014.01.0014.

Appendix A

Supporting Information for Chapter 5: Investigating Active Air Microfluidics with Overlapping Soft Fluidic Actuators for Smooth Sequential Gradient Compression

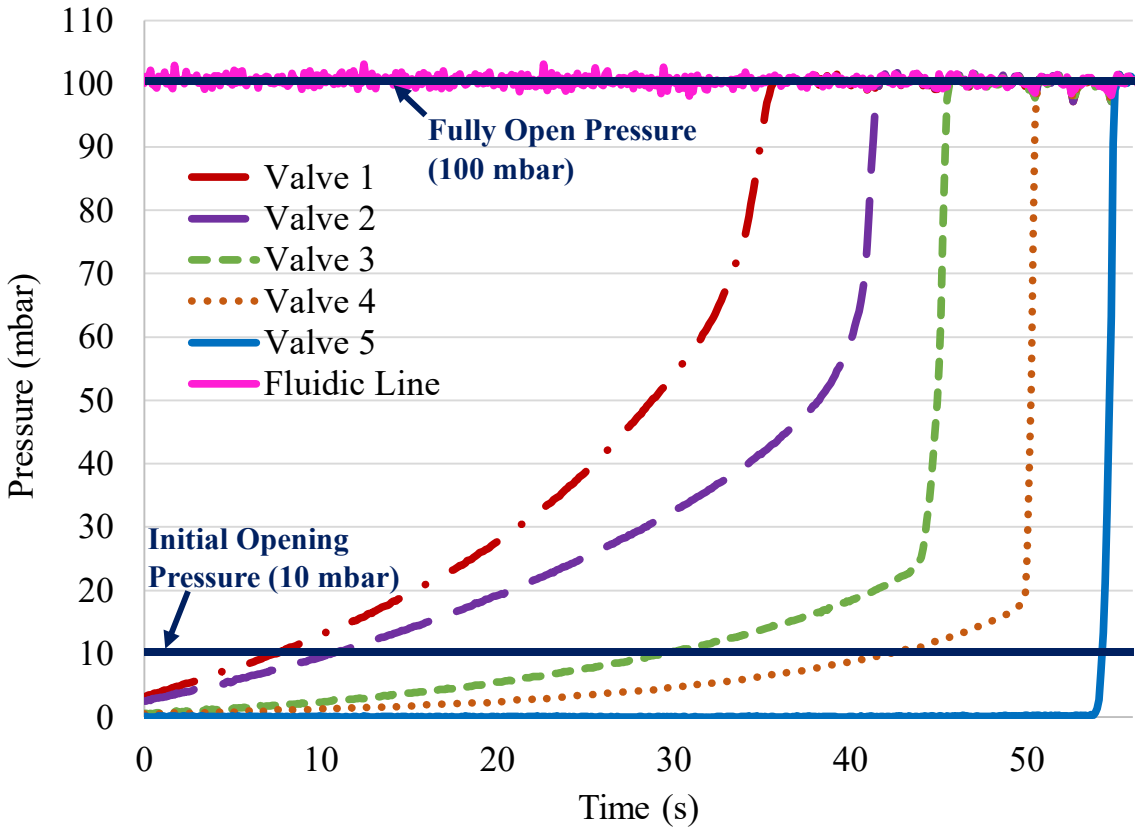


Figure A.1: Comparison of in-line valve with a good seal (Valve 5) and in-line valves with imperfect seals (Valve 1 to 4). Valve 5 shows almost the same initial opening and fully open pressures, indicated by the very straight vertical line. In contrast, Valve 1 had the worst seal, evident from the most curved line relative to others. The valve seals improve from Valve 1 to Valve 5 as their lines become straighter with less curvature.

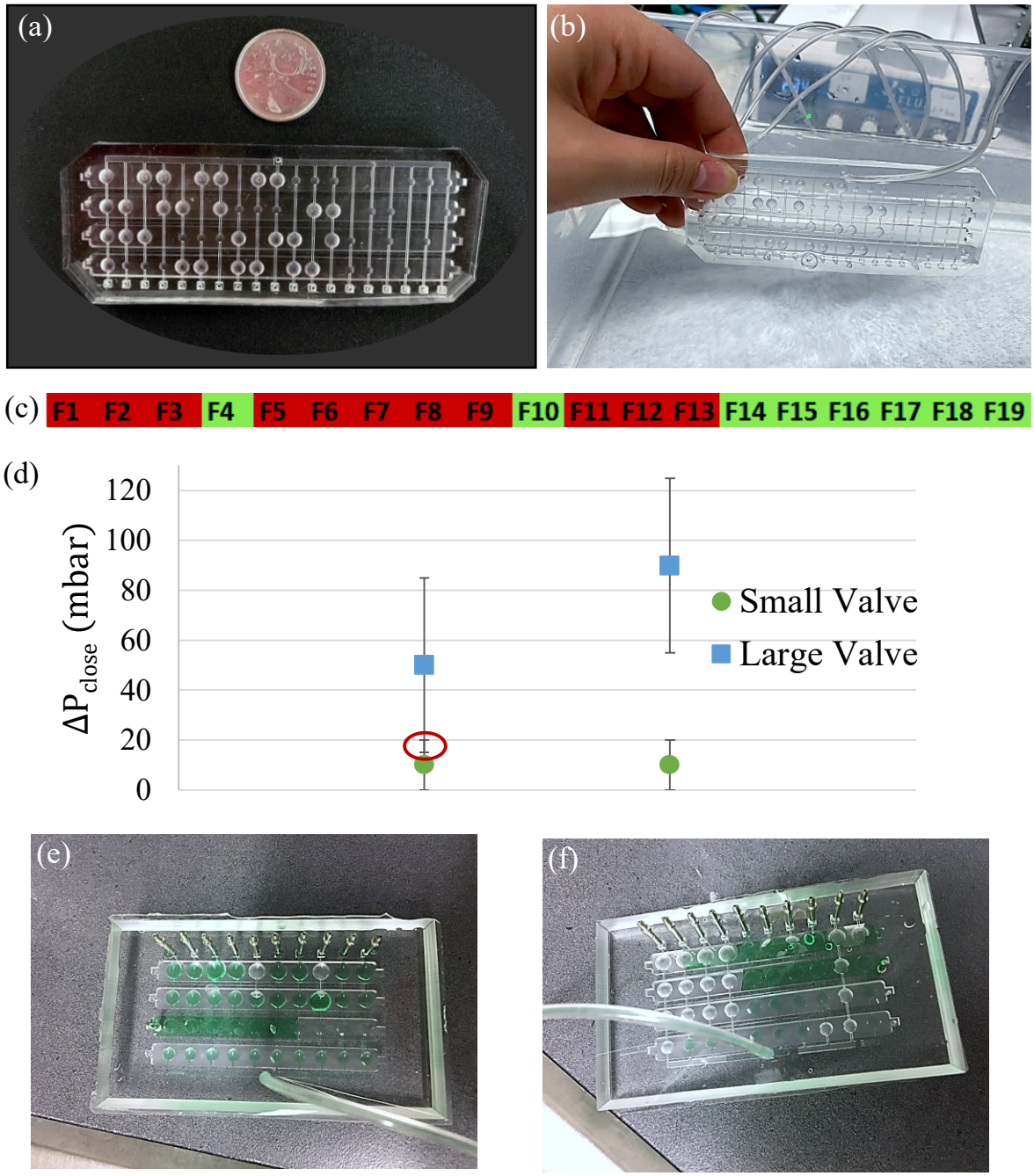


Figure A.2: (a) Image of a demultiplexing air microfluidic chip made out of PDMS with a Canadian quarter as a size reference. (b) Leak testing of the demultiplexing air microfluidic chip. Bubbles leaking from the chip into the water indicate imperfect valve sealing. (c) Fluid lines 1 to 19 with green color indicate proper operation without leakage, while red color indicates improper operation with leakage. (d) Some of the small and large valves of the demultiplexer have an overlap of ΔP_{close} (circled in red), which may lead to incorrect closure

of a fluid line. (e) and (f) show the results of the water (dyed green) pressurization test, indicating leakage from the fluid line through the ruptured membrane into the control line, rendering the demultiplexer inoperative. Large control line surface area and extensive free-floating membrane surface areas with weak points are potential locations that may experience rupture.

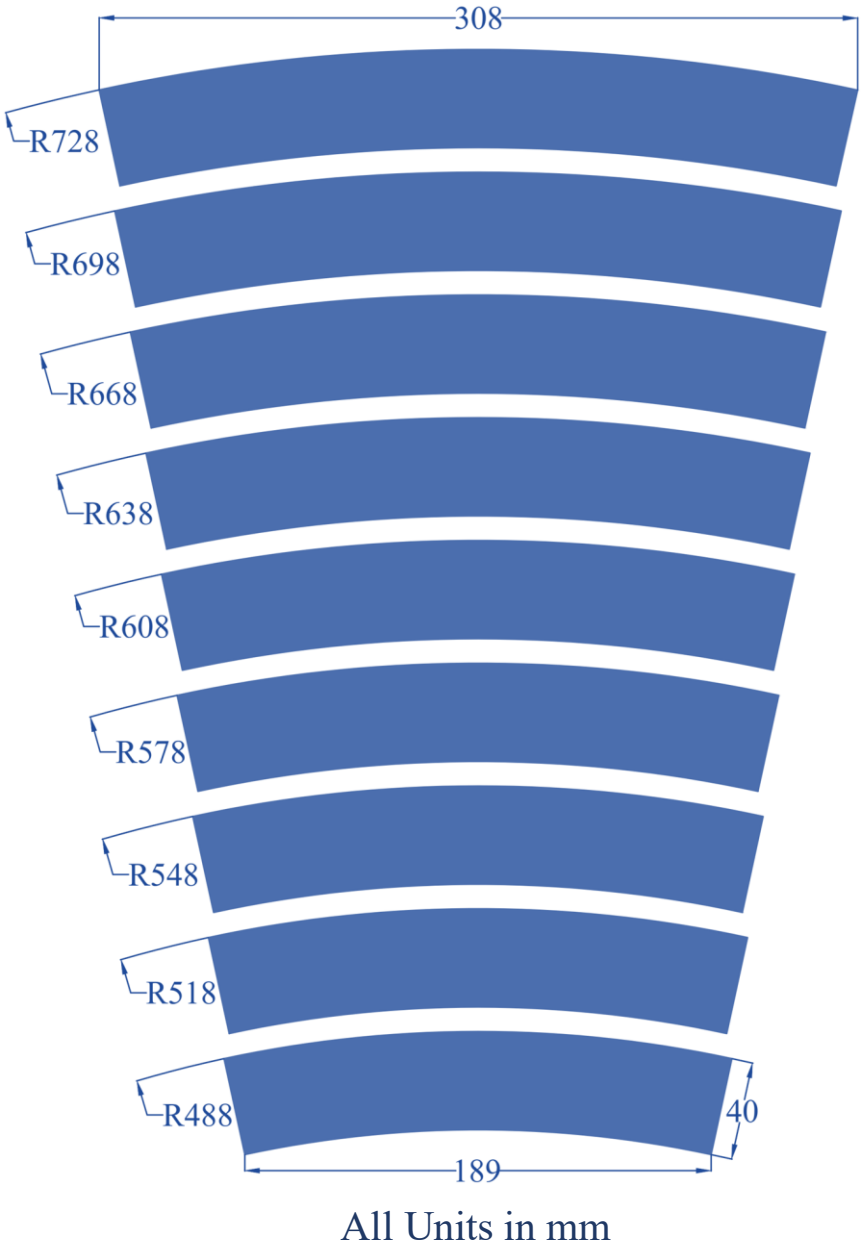


Figure A.3: Shape of the 9 SFAs used in the study, depicted without overlapping in the figure. The SFAs are arranged in ascending order, starting with the smallest SFA located at the bottom (wrist) and ending with the largest one at the top (elbow).

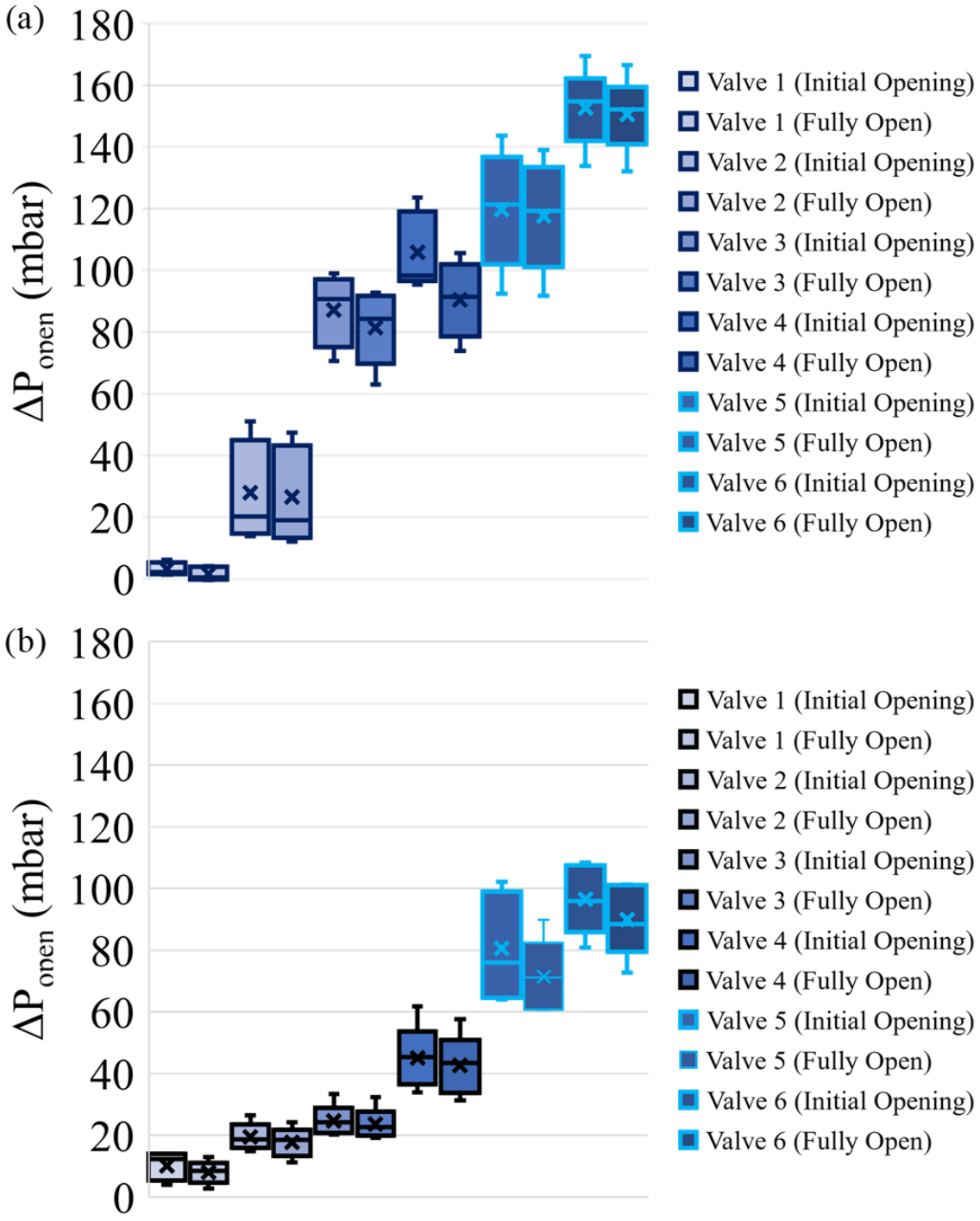


Figure A.4: Results presented as box-and-whisker plots for the systematic testing of in-line valves, showing both initial opening and fully open pressures. (a) $\Delta P_{(open)}$ for each valve size with 110 – 120 µm membrane thickness. (b) $\Delta P_{(open)}$ for each valve size with 80 – 90 µm membrane thickness.

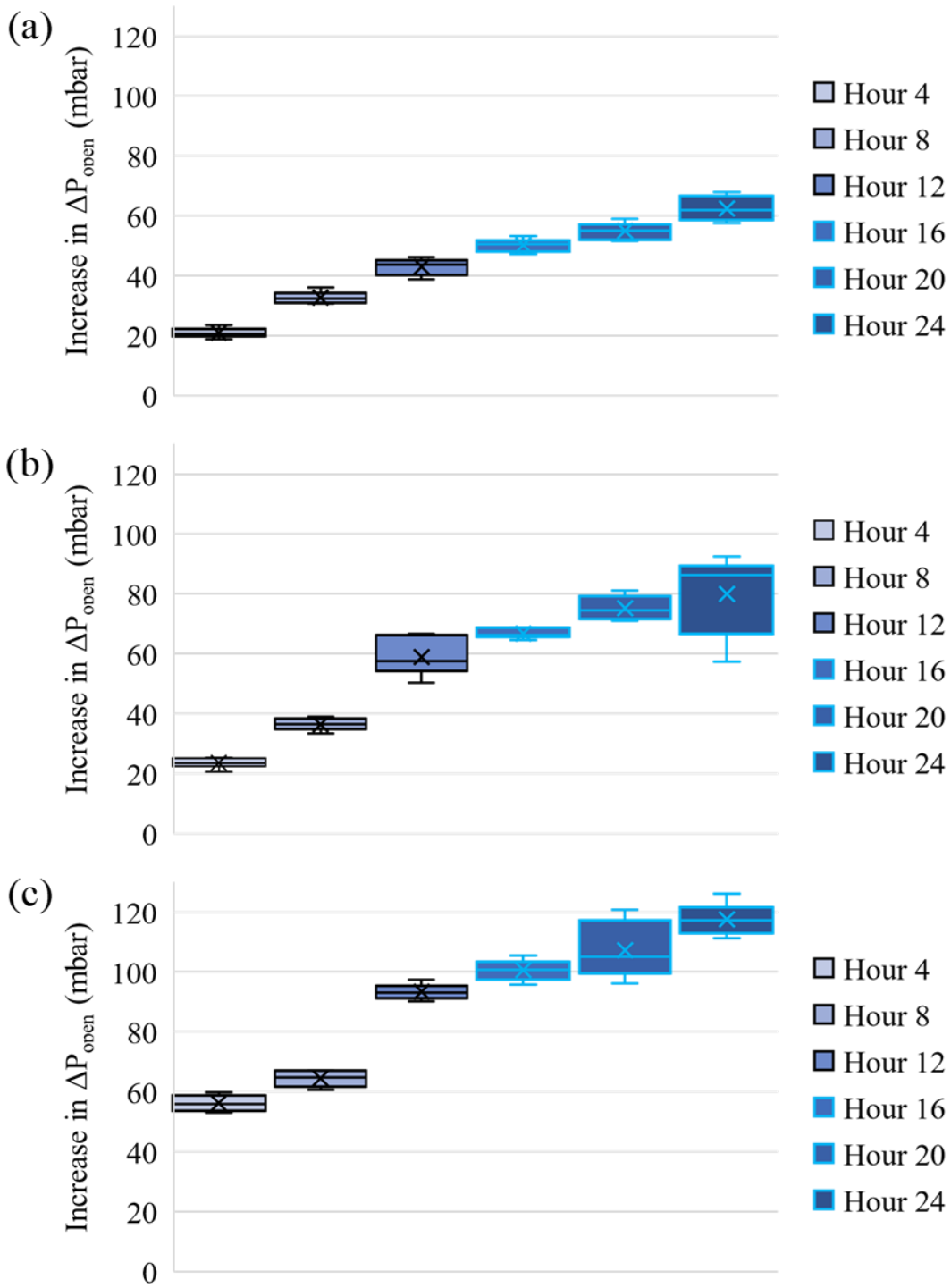
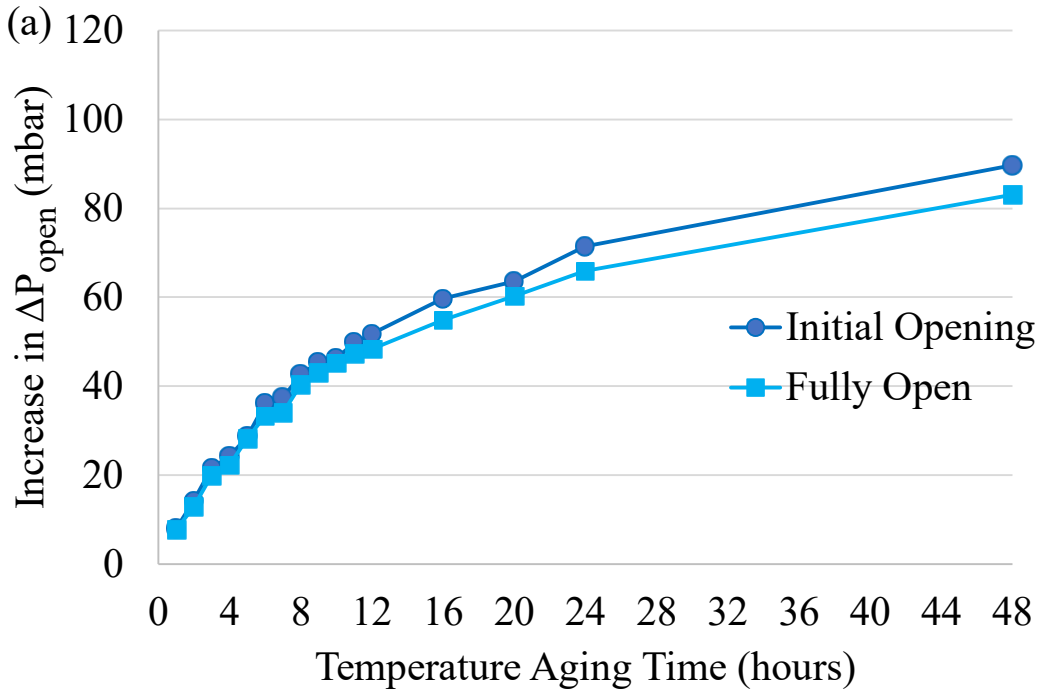
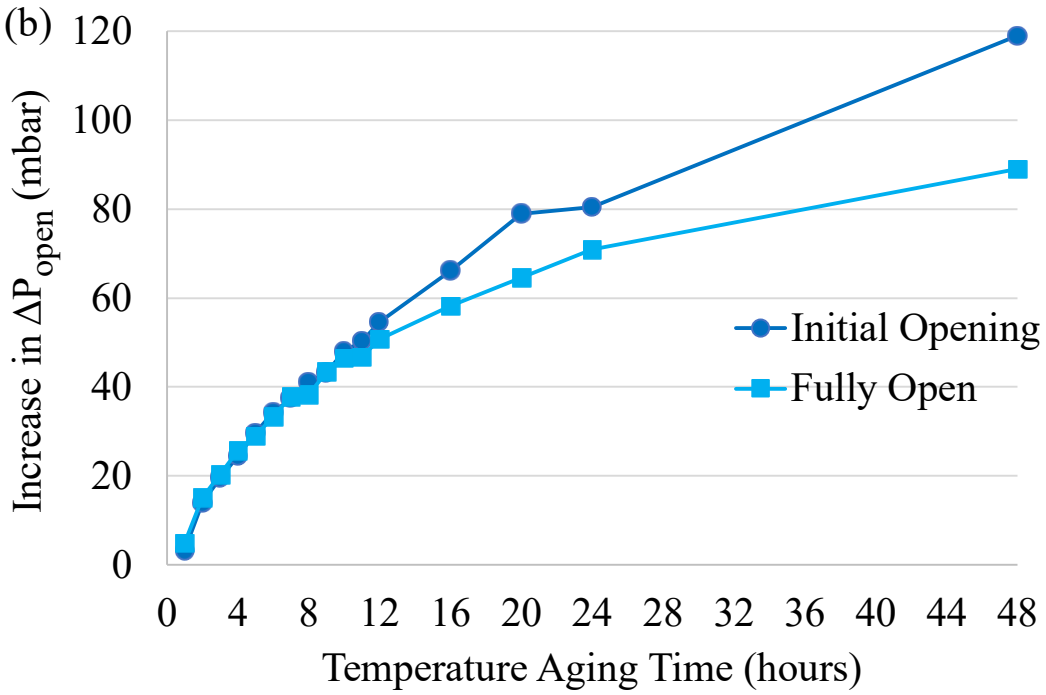
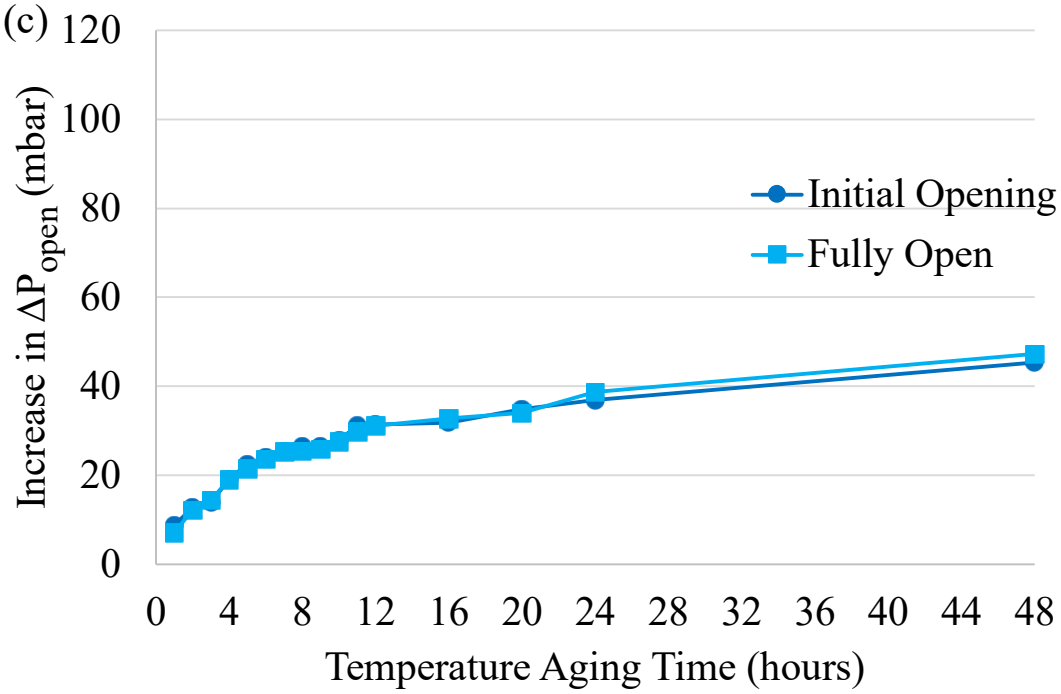


Figure A.5: Thermal aging results as box-and-whisker plots showing the increase in ΔP_{open} at 4, 8, 12, 16, 20, and 24-hour marks for (a) valve size II, (b) valve size III, (c) valve size IV. 3 samples were tested for each valve size; combining both initial opening and fully open pressures, resulting in 6 data points per hour mark. All valves had 110-120 µm thicken membrane.

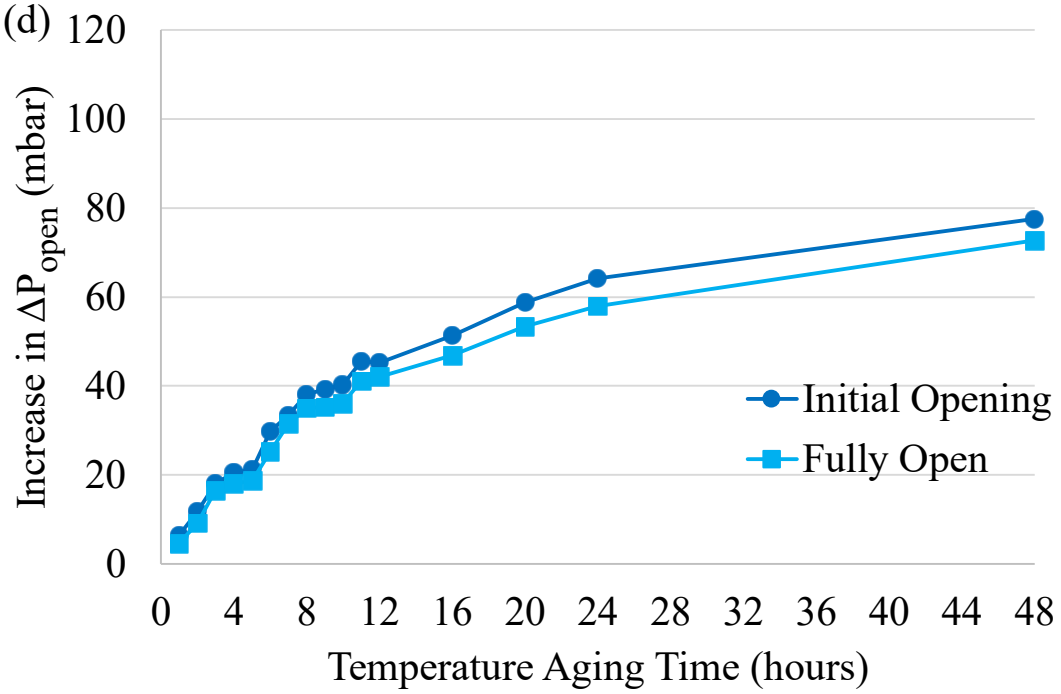

(a)
120
100
80
60
40
20
0
Increase in ΔP_{open} (mbar)
0 4 8 12 16 20 24 28 32 36 40 44 48
Temperature Aging Time (hours)
Initial Opening
Fully Open


(b)
120
100
80
60
40
20
0
Increase in ΔP_{open} (mbar)
0 4 8 12 16 20 24 28 32 36 40 44 48
Temperature Aging Time (hours)
Initial Opening
Fully Open

(c)


120
100
80
60
40
20
0
Increase in ΔP open (mbar)
Initial Opening
Fully Open
0 4 8 12 16 20 24 28 32 36 40 44 48
Temperature Aging Time (hours)

(d)


120
100
80
60
40
20
0
Increase in ΔP open (mbar)
Initial Opening
Fully Open
0 4 8 12 16 20 24 28 32 36 40 44 48
Temperature Aging Time (hours)

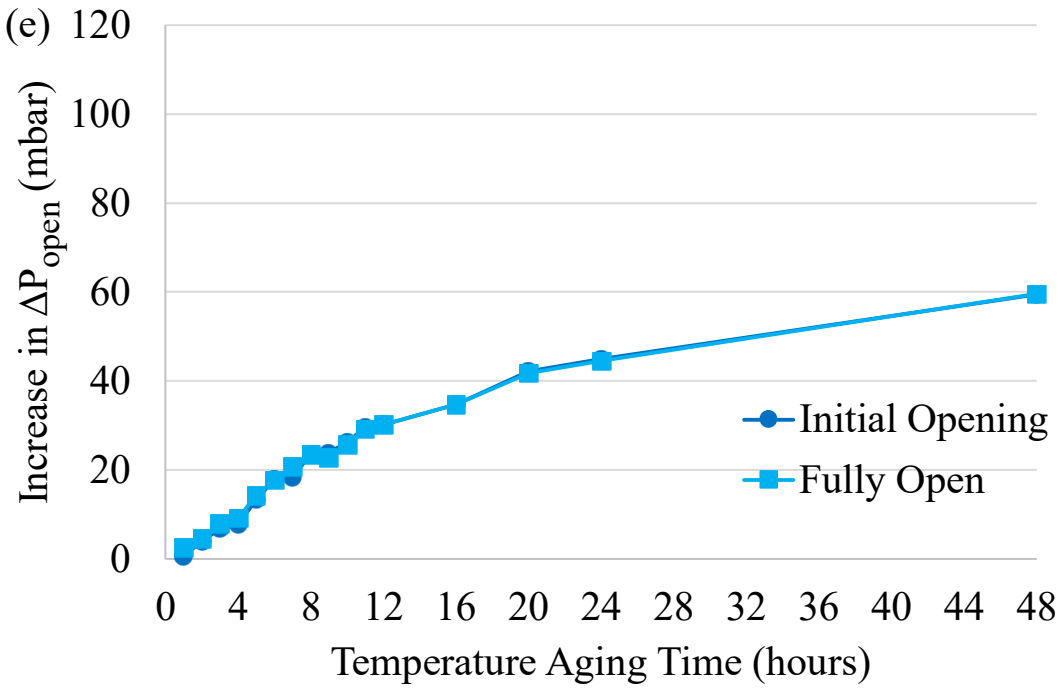


Figure A.6: Thermal aging data of individual samples for valve type VI with 110-120 µm membrane. (a) Sample 1. (b) Sample 2. (c) Sample 3. (d) Sample 4. (e) Sample 5.

Appendix B

Supporting Information for Chapter 6: Investigating Miniaturization of Soft Robotic Actuators for Prosthetic Socket Fitting

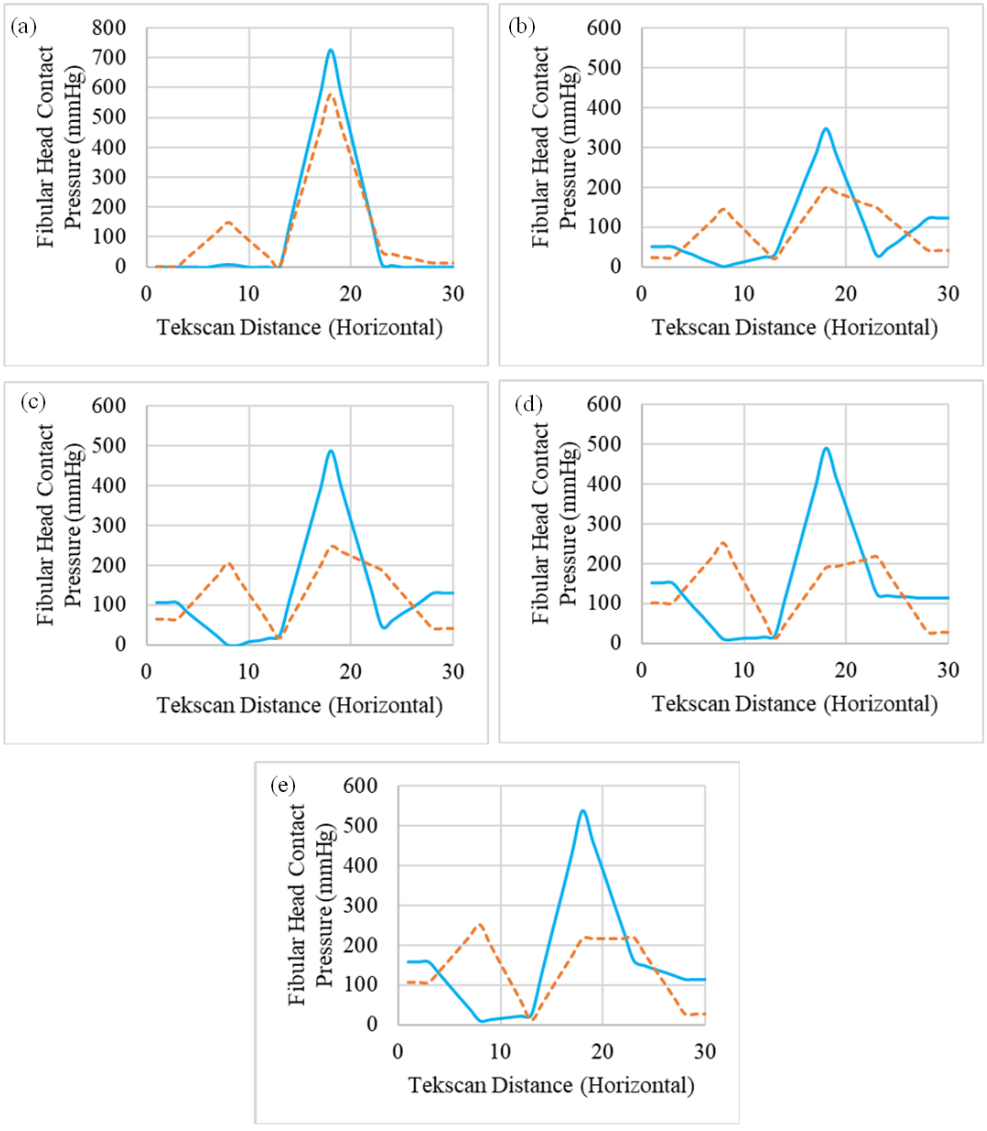


Figure B.7: Fibular head contact pressure under different weights with Tekscan sensor horizontal distance on the x-axis and contact pressure in mmHg on the y-axis. The blue line

displays the depressurized dynamic cushion and the orange dotted line displays the pressurized dynamic cushion. (a) No weight trial. (b) 20 kg trial. (c) 40 kg trial. (d) 60 kg trial. (e) 80 kg trial.

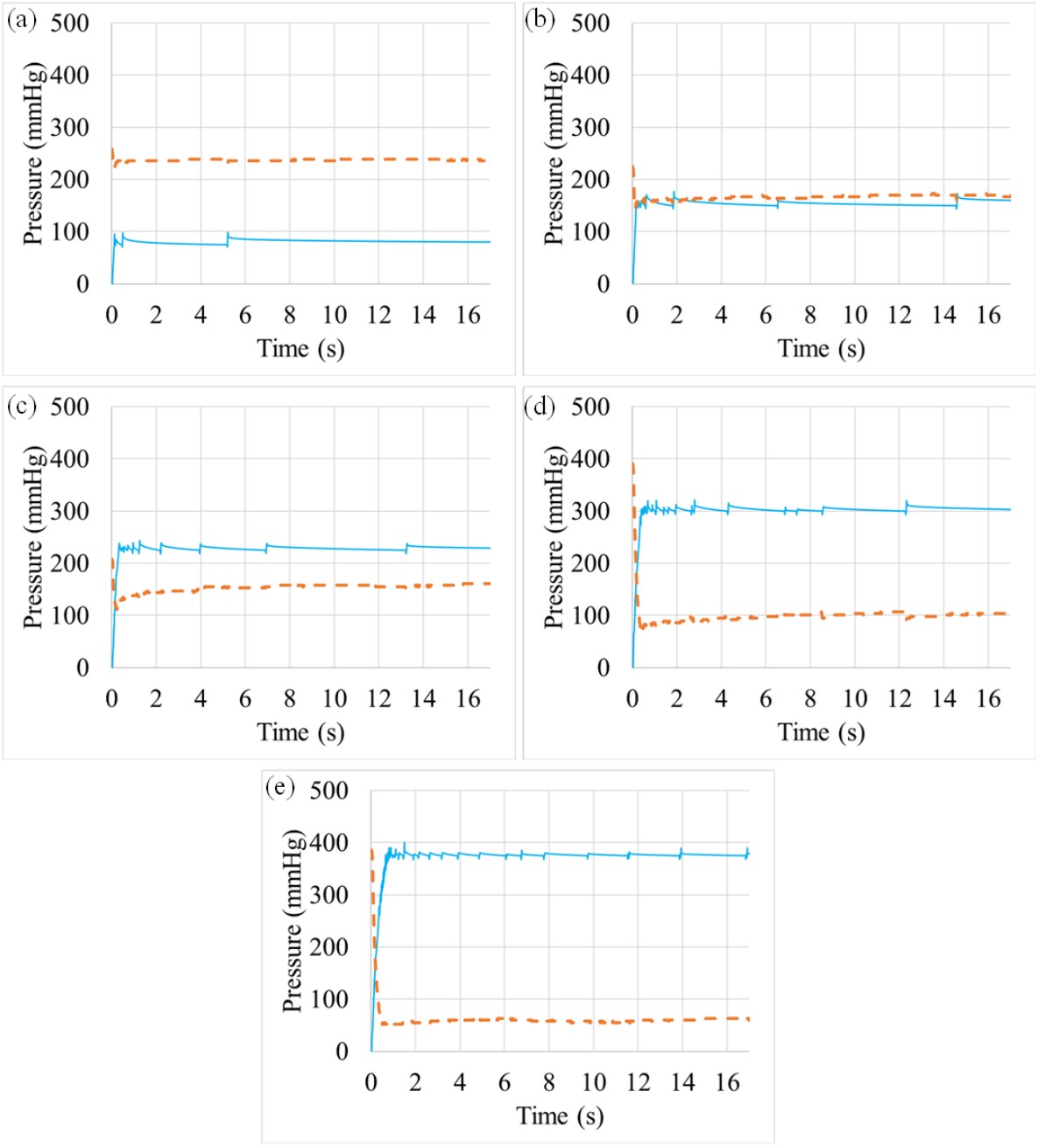


Figure B.8: Static pressure holding test with thin fibular head cover with preferred rectangular dynamic cushion at an internal pressure (solid cyan line) of (a) 75 mmHg, (b) 150 mmHg, (c) 225 mmHg, (d) 300 mmHg, (e) 375 mmHg. Fibular head peak contact pressure is shown by dotted orange line.

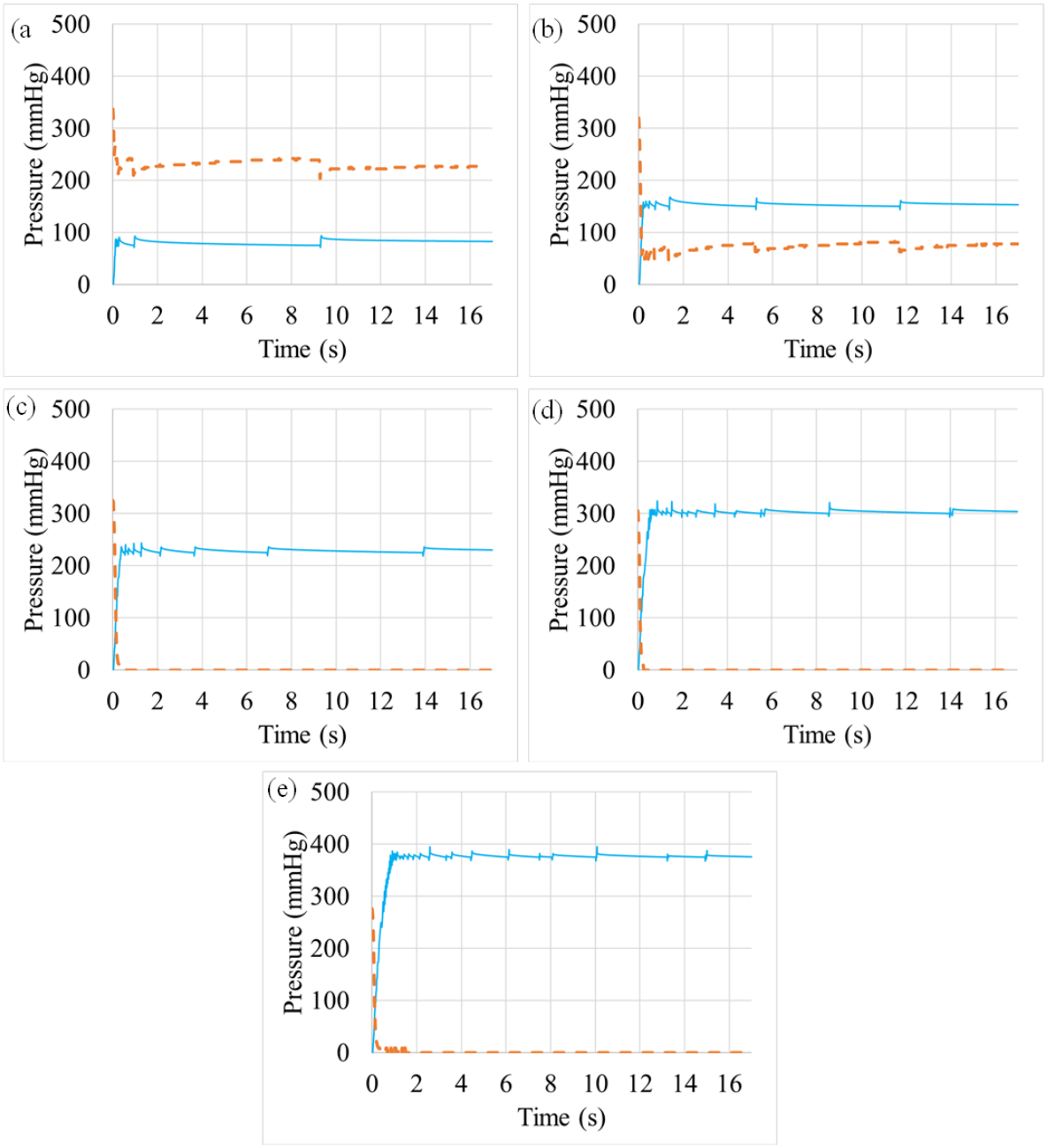


Figure B.9: Static pressure holding test with medium fibular head cover with preferred rectangular dynamic cushion at an internal pressure (solid cyan line) of (a) 75 mmHg, (b) 150 mmHg, (c) 225 mmHg, (d) 300 mmHg, (e) 375 mmHg. Fibular head peak contact pressure is shown by dotted orange line.

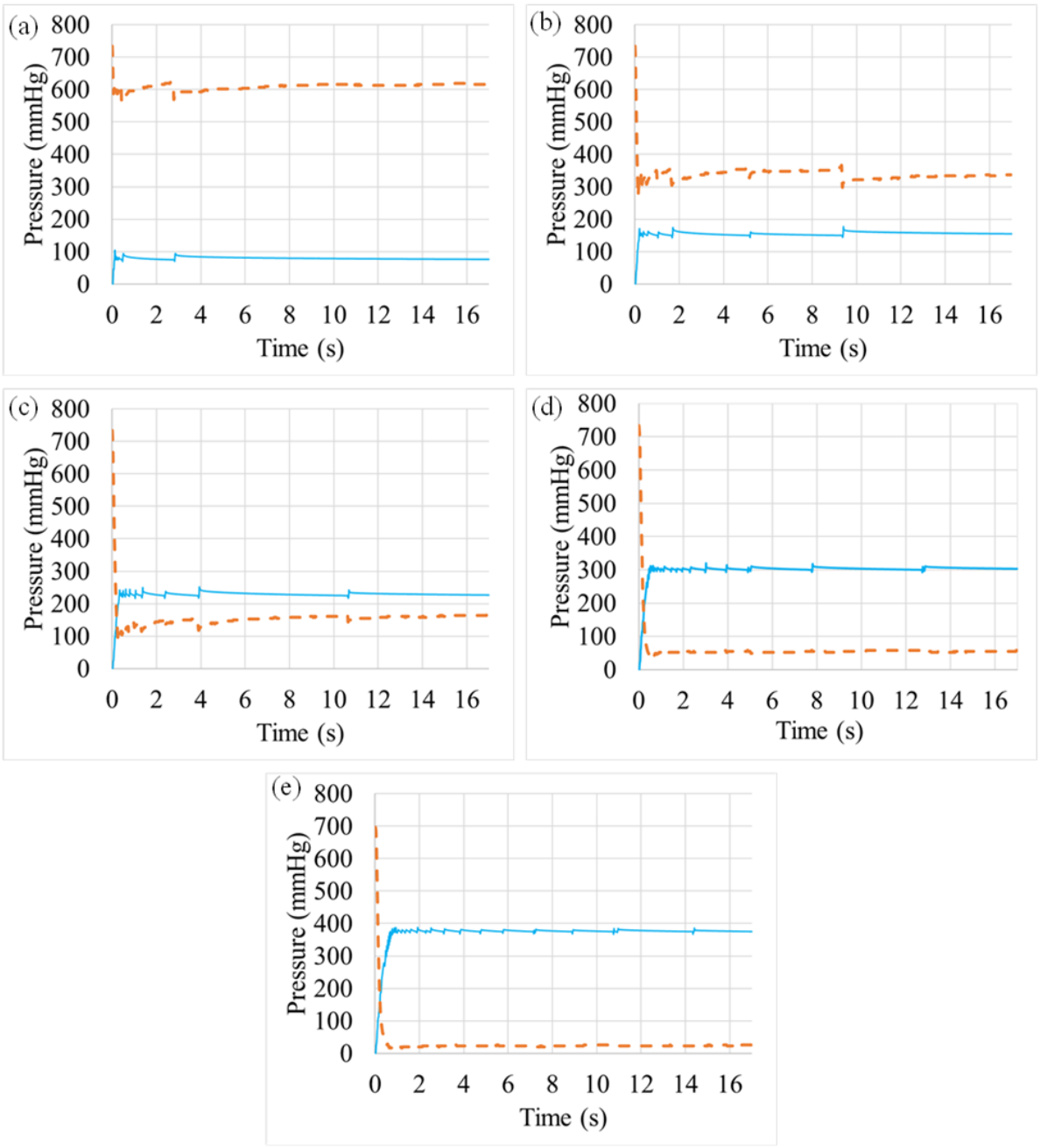
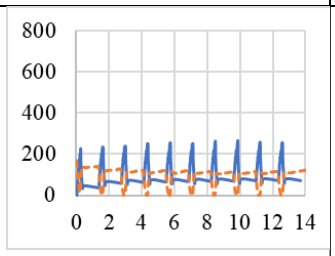
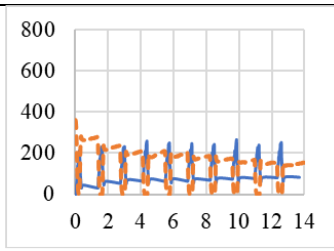
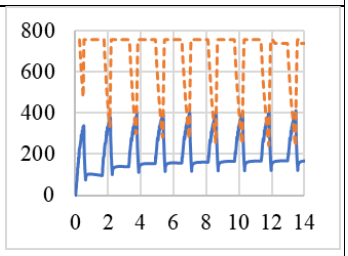
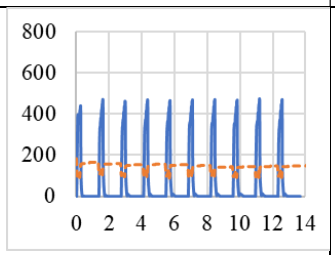
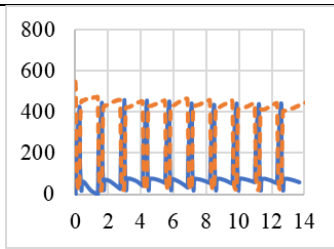
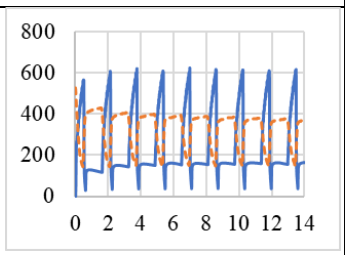
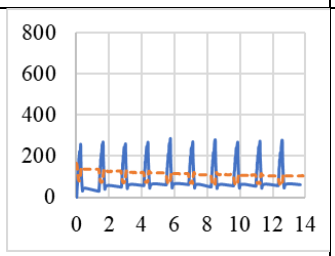
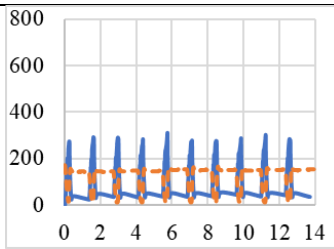
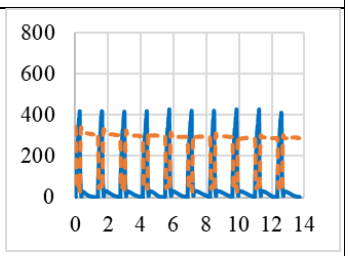
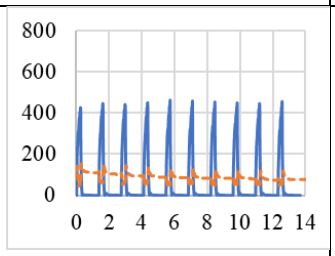
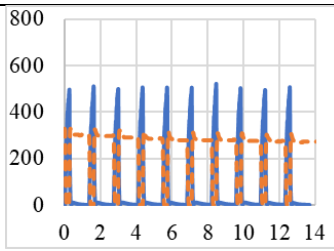
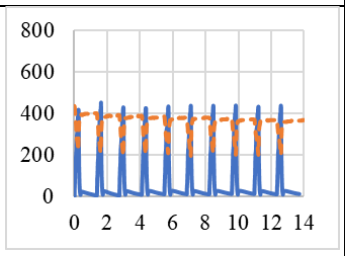


Figure B.10: Static pressure holding test with thick fibular head cover with preferred rectangular dynamic cushion at an internal pressure (solid cyan line) of (a) 75 mmHg, (b) 150 mmHg, (c) 225 mmHg, (d) 300 mmHg, (e) 375 mmHg. Fibular head peak contact pressure is shown by dotted orange line.

Table B.1: Dynamic gait test displaying internal pressure of dynamic cushion (solid blue line) and contact pressure at the fibular head (dotted orange line) over ten continuous pressurization/depressurization cycles. Pressure in mmHg is shown on the y-axis, and time in seconds is shown on the x-axis.

	Thin Fibular Head	Medium Fibular Head	Thick Fibular Head
4 Ellipse			
Horseshoe			
Rectangle			
Double Curved			

Appendix C

Supporting Information for Chapter 7 Investigating Miniaturization of Soft Robotic Sensor for Prosthetic Socket Fitting

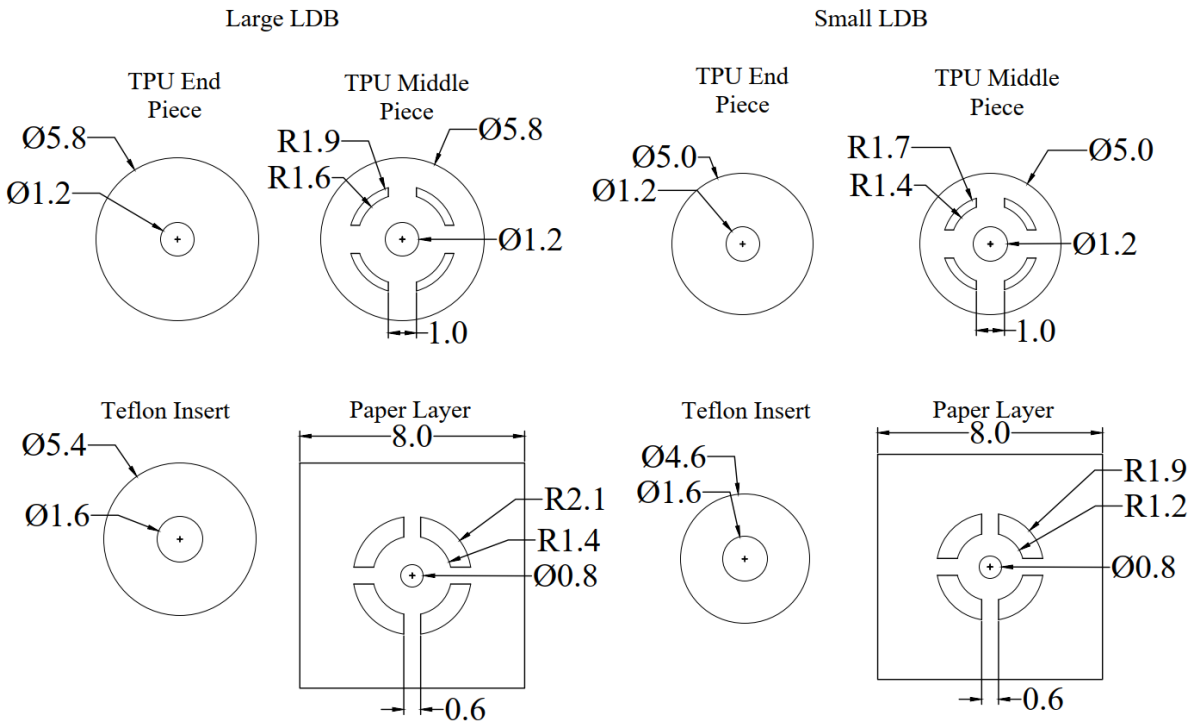


Figure C.1: LDB design illustrated with critical dimensions for both TPU and Telfon Insert. All dimensions are in cm. The paper layer is coated with Telfon and goes in between each LDB layer to prevent lamination. The four slots on the TPU middle piece allow air to pass through, and thus fluidly connect each LDB layer.

Initially, water was used as the medium of choice due to its incompressible nature. The first batch of LDBs manufactured was only one or two layers tall and had a thin wall thickness (150 microns). The LDBS were filled with water to the pressure at which water stopped leaving the bladder (i.e. the pressure from the water inside the LDB was equivalent to the atmospheric pressure). This was achieved by overfilling the LDB and letting them passively contract, squeezing out excess water, until an equilibrium was reached. Note that not all bladders were

tested as the largest bladder was deemed impractical for use within a socket due to their height. The long-term stability of the remaining LDBs can be seen in **Figure C.2**. Hysteresis testing for the water LDBs was performed following a slightly different procedure. A 5 stair-step pattern was still used, but the time between each step was only 60 seconds. Furthermore, the height of each step was 4% of the measured maximum height of each LDB. The authors later found it challenging to compare the results between hysteresis tests of different size LDBs, so the procedure was adjusted for future tests.

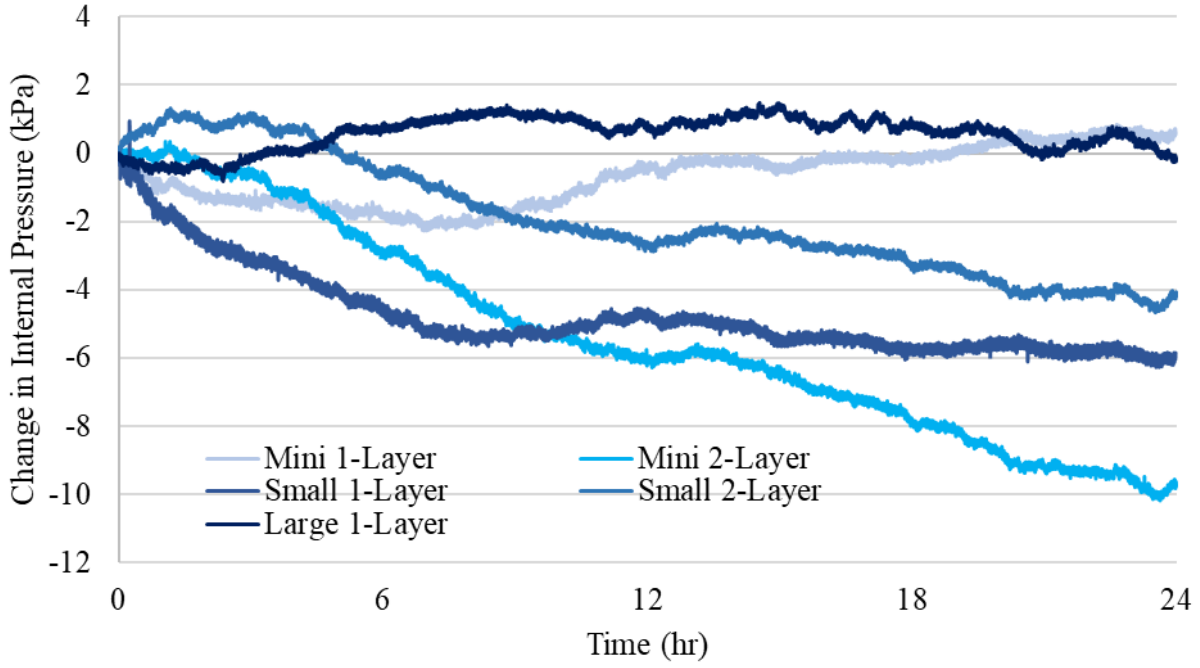


Figure C.2: Long-term stability of water LDBs.

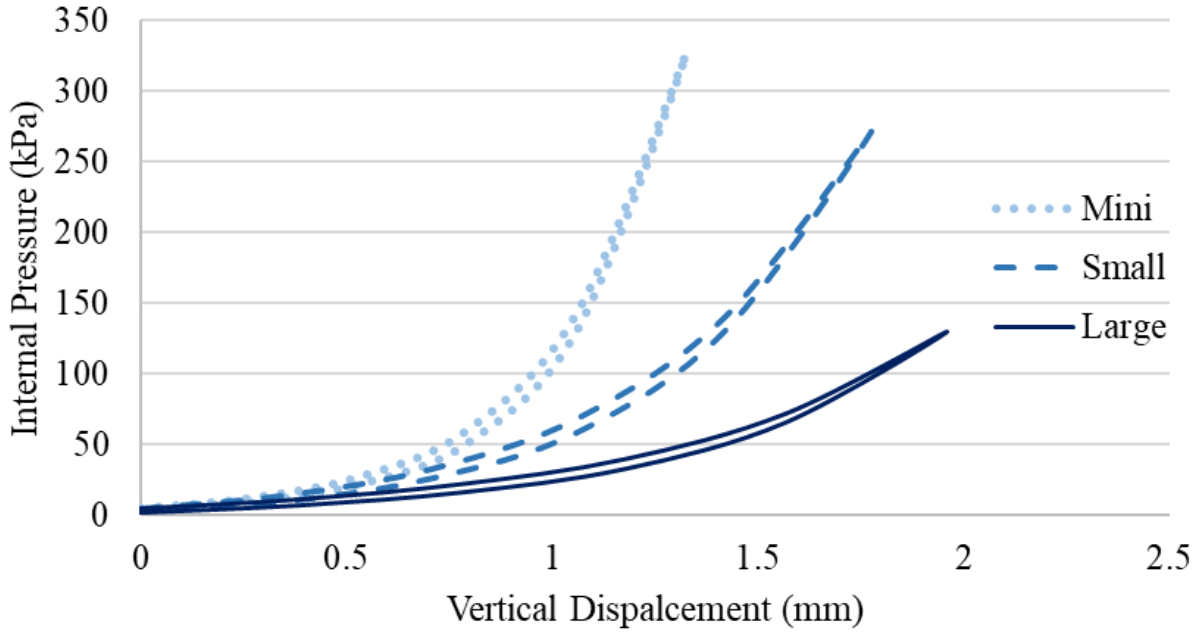
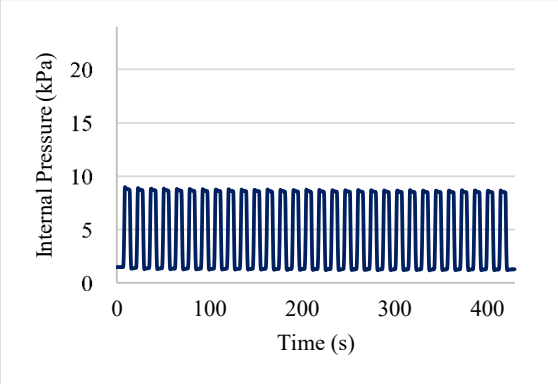
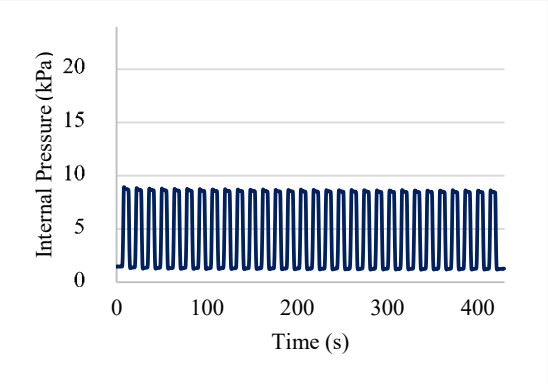


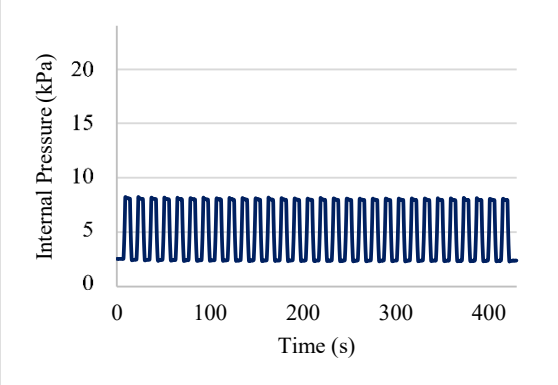
Figure C.3: Hysteresis of water LDBs. The mini LDB was discontinued in future tests as it reached high pressures before 1.5 mm of displacement and was challenging to manufacture due to its small size.


Internal Pressure (kPa)
20
15
10
5
0
0
100
200
300
400
Time (s)

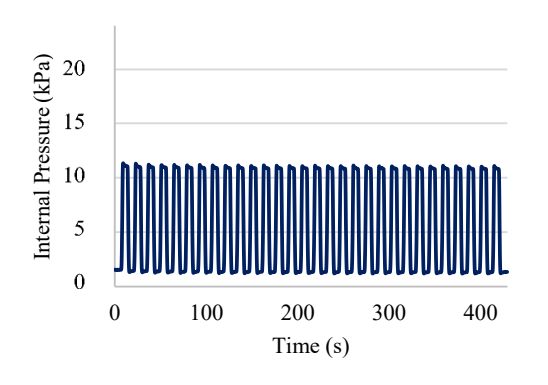
(a)


Internal Pressure (kPa)
20
15
10
5
0
0
100
200
300
400
Time (s)

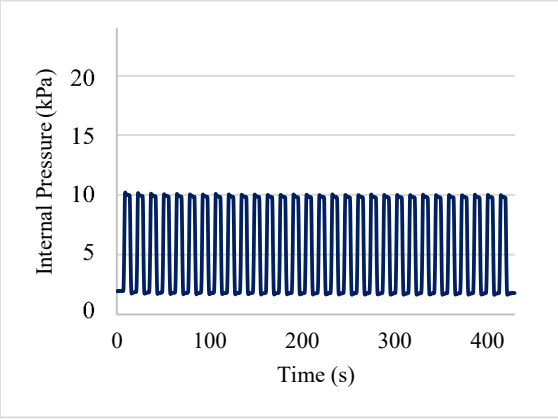
(b)


Internal Pressure (kPa)
20
15
10
5
0
0
100
200
300
400
Time (s)

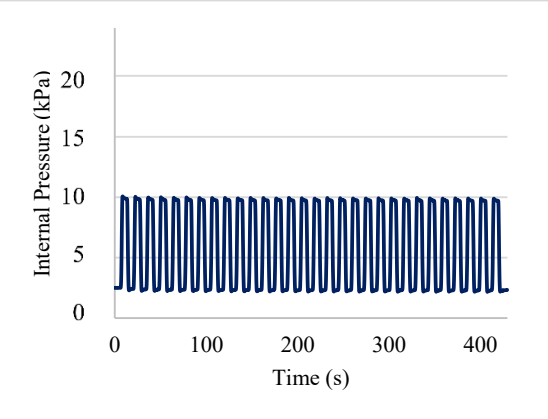
(c)


Internal Pressure (kPa)
20
15
10
5
0
0
100
200
300
400
Time (s)

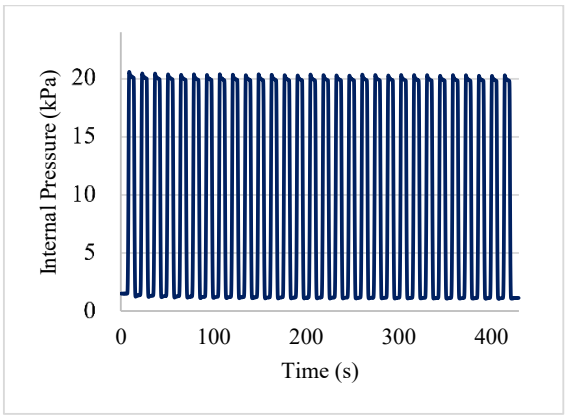
(d)


Internal Pressure (kPa)
20
15
10
5
0
0
100
200
300
400
Time (s)

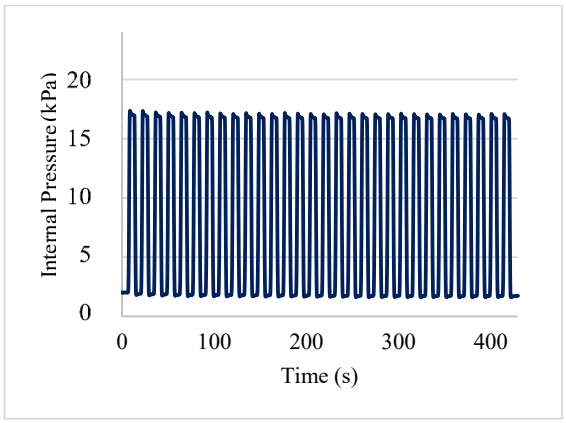
(e)


Internal Pressure (kPa)
20
15
10
5
0
0
100
200
300
400
Time (s)

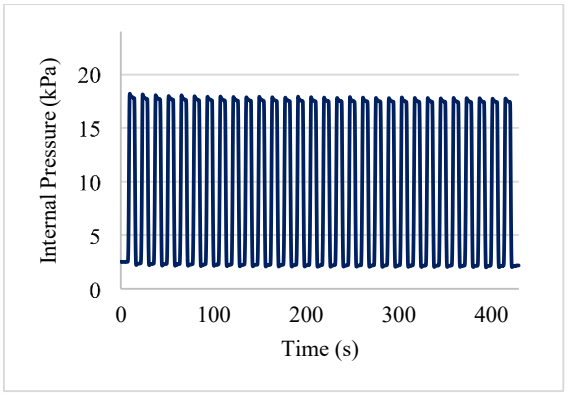
(f)


Internal Pressure (kPa)
20
15
10
5
0
0
100
200
300
400
Time (s)

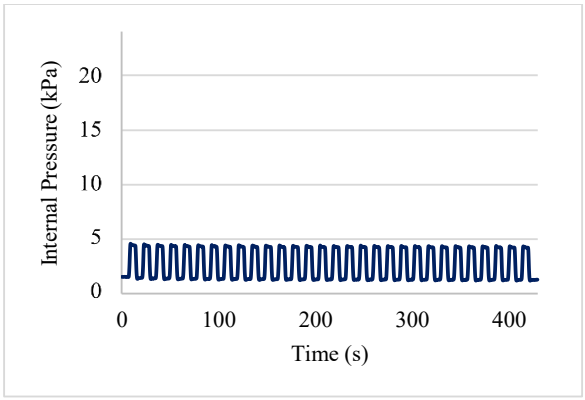
(g)


Internal Pressure (kPa)
20
15
10
5
0
0
100
200
300
400
Time (s)

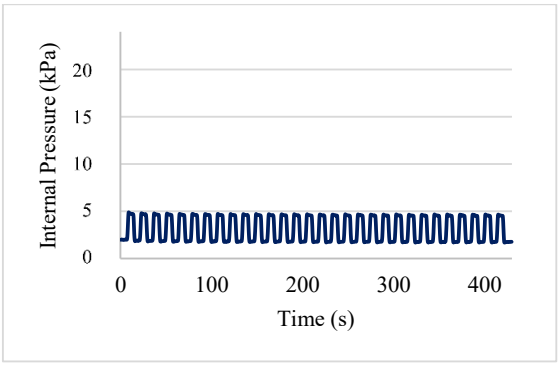
(h)


Internal Pressure (kPa)
20
15
10
5
0
0
100
200
300
400
Time (s)

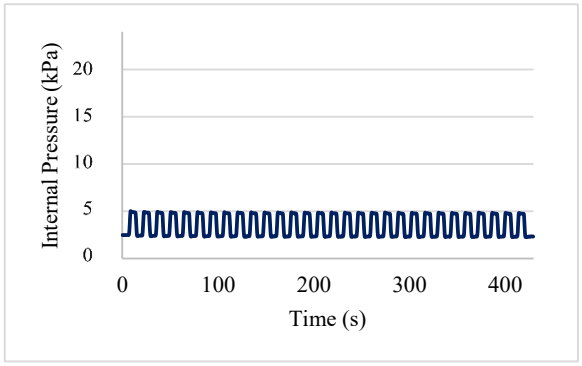
(i)


Internal Pressure (kPa)
20
15
10
5
0
0
100
200
300
400
Time (s)

(j)


Internal Pressure (kPa)
20
15
10
5
0
0
100
200
300
400
Time (s)

(k)


Internal Pressure (kPa)
20
15
10
5
0
0
100
200
300
400
Time (s)

(l)

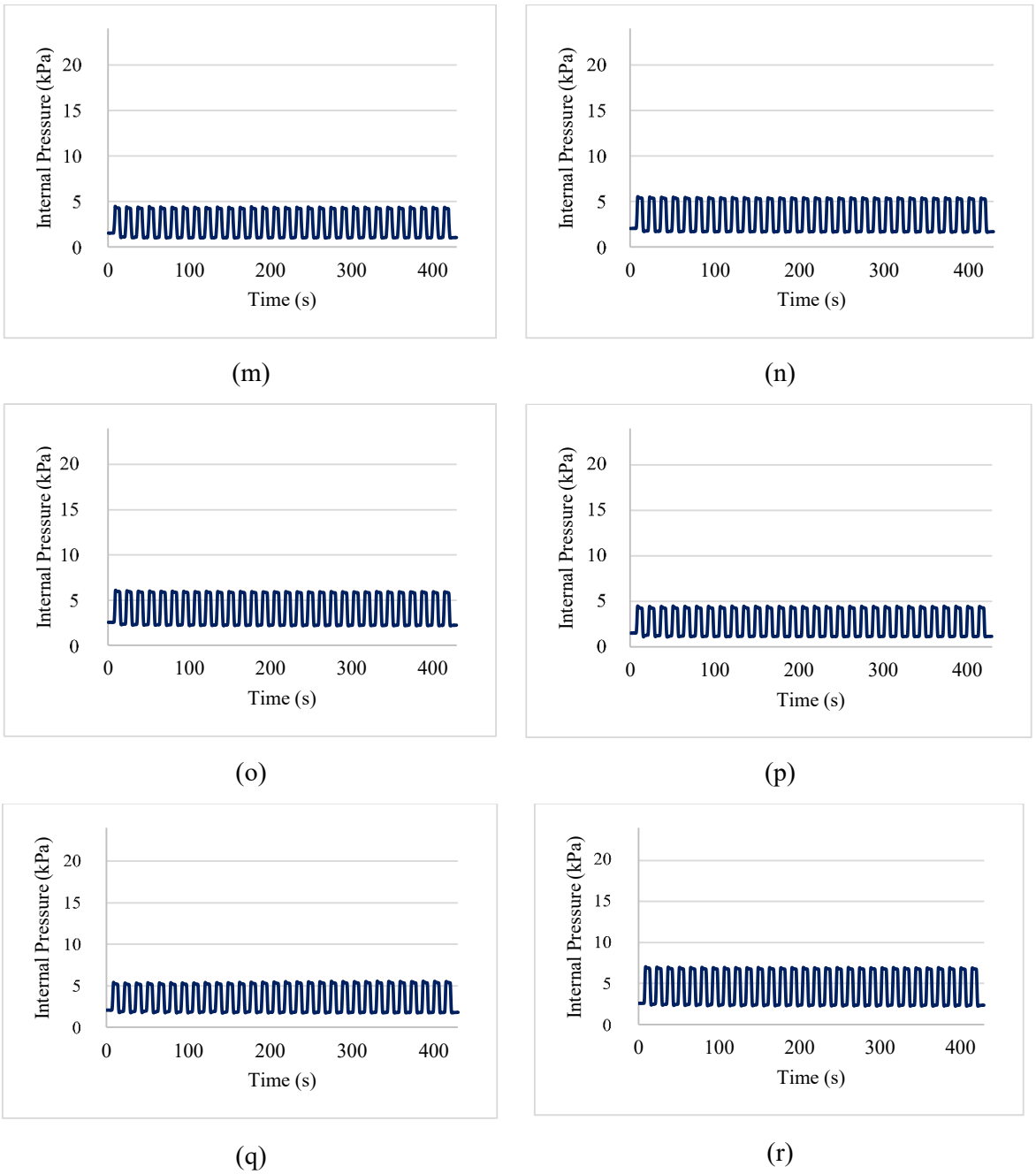
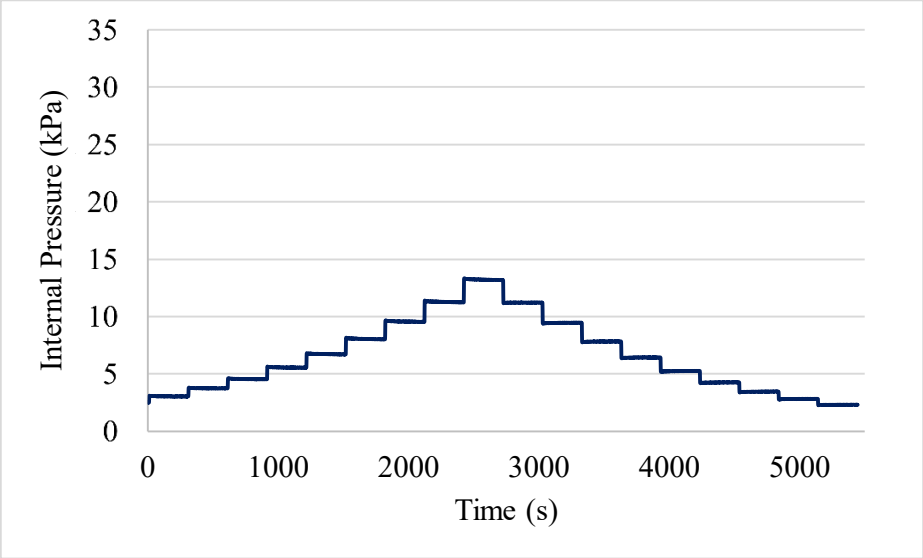
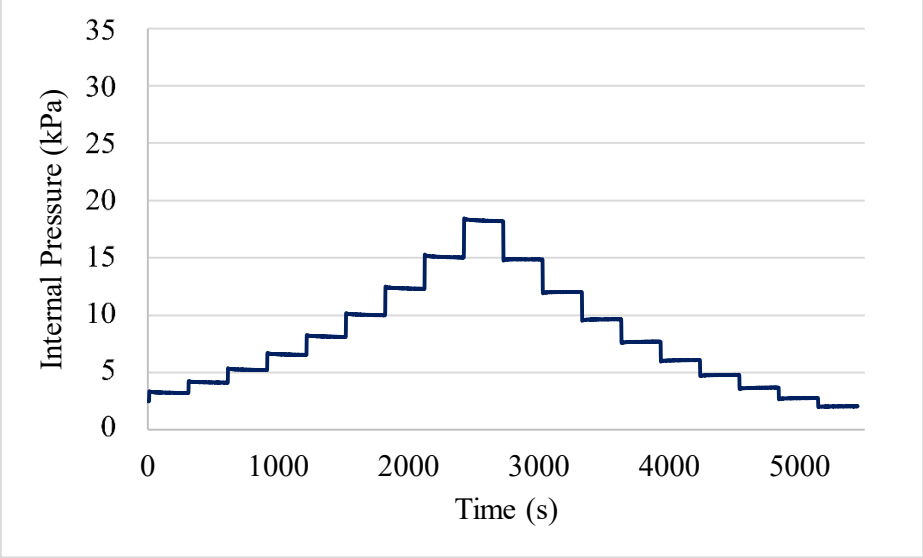


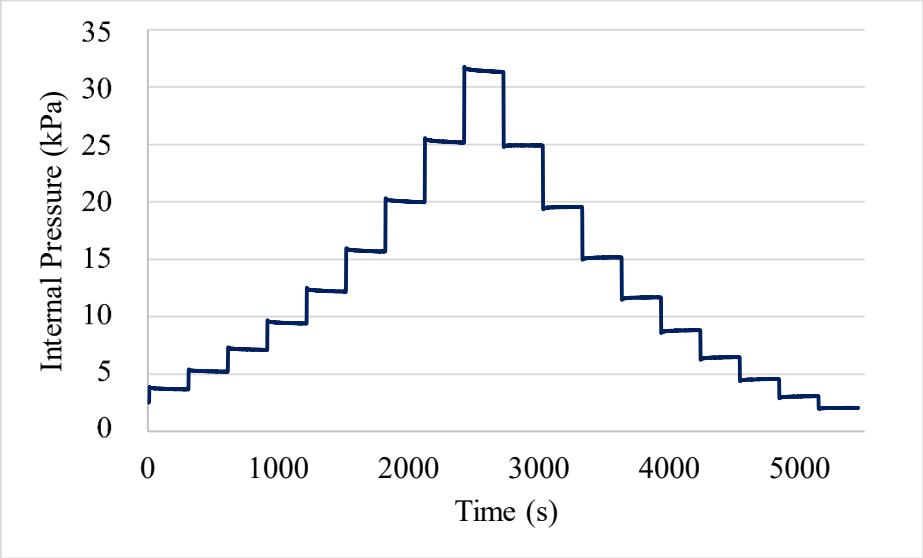
Figure C.4: Cyclic loading trial results for the following LDBs: (a) small-thin, 1.5 kPa (b) small-thin, 2 kPa (c) small-thin, 2.5 kPa (d) small-medium, 1.5 kPa (e) small-medium, 2 kPa (f) small-medium, 2.5 kPa (g) small-thick, 1.5 kPa (h) small-thick, 2 kPa (i) small-thick, 2.5 kPa (j) large-thin, 1.5 kPa (k) large-thin, 2 kPa (l) large-thin, 2.5 kPa (m) large-medium, 1.5 kPa (n) large-medium, 2 kPa (o) large-medium, 2.5 kPa (p) large-thick, 1.5 kPa (q) large-thick, 2 kPa (r) large-thick, 2.5 kPa.


Internal Pressure (kPa)
35
30
25
20
15
10
5
0
0
1000
2000
3000
4000
5000
Time (s)

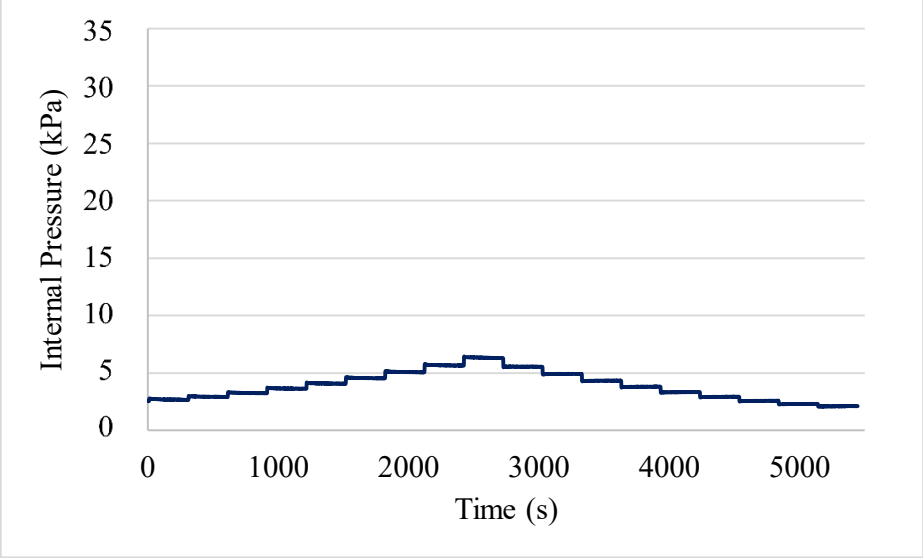
(a)


Internal Pressure (kPa)
35
30
25
20
15
10
5
0
0
1000
2000
3000
4000
5000
Time (s)

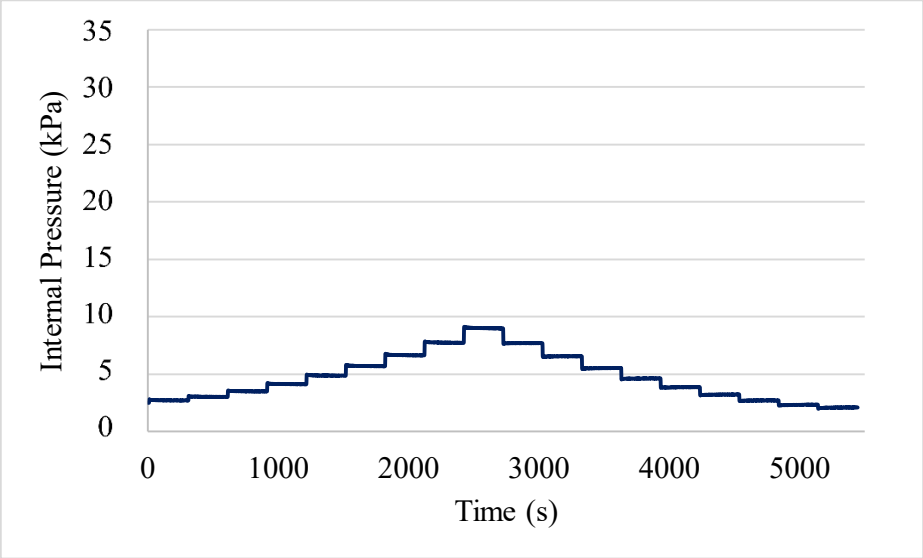
(b)


Internal Pressure (kPa)
35
30
25
20
15
10
5
0
0
1000
2000
3000
4000
5000
Time (s)

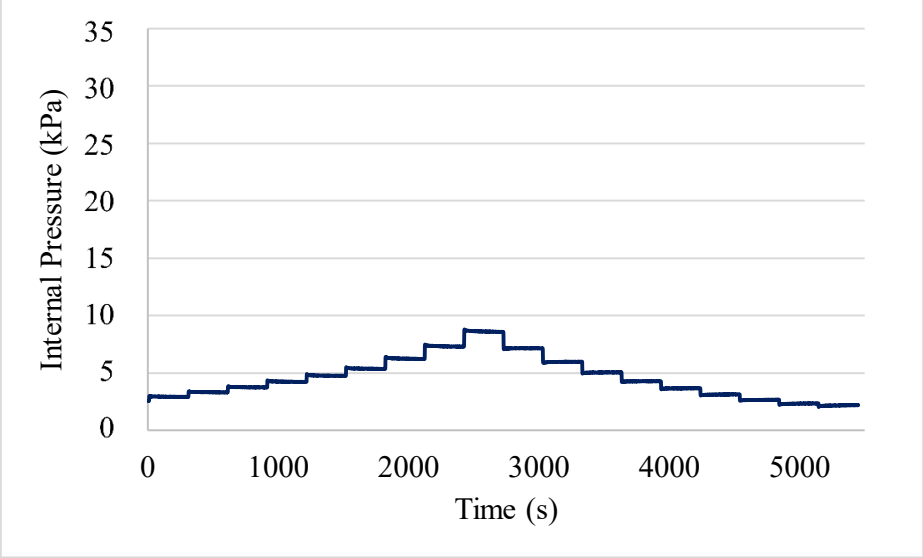
(c)


Internal Pressure (kPa)
35
30
25
20
15
10
5
0
0
1000
2000
3000
4000
5000
Time (s)

(d)



(e)



(f)

Figure C.5: Step-loading results for the following LDBs: (a) small-thin (b) small-medium (c) small-thick (d) large-thin (e) large-medium (f) large-thick.

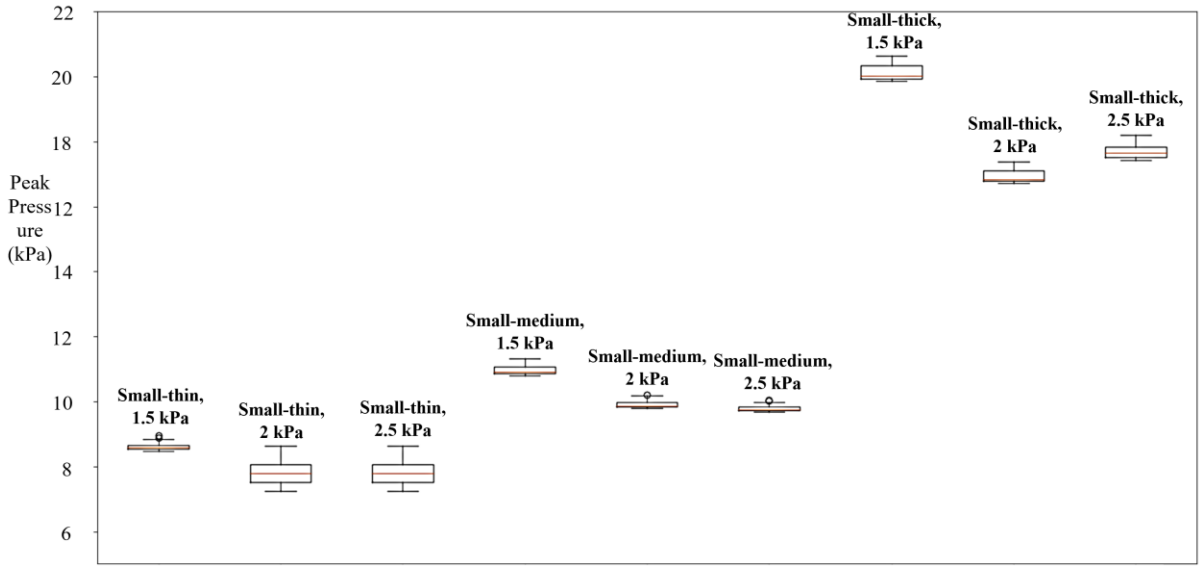
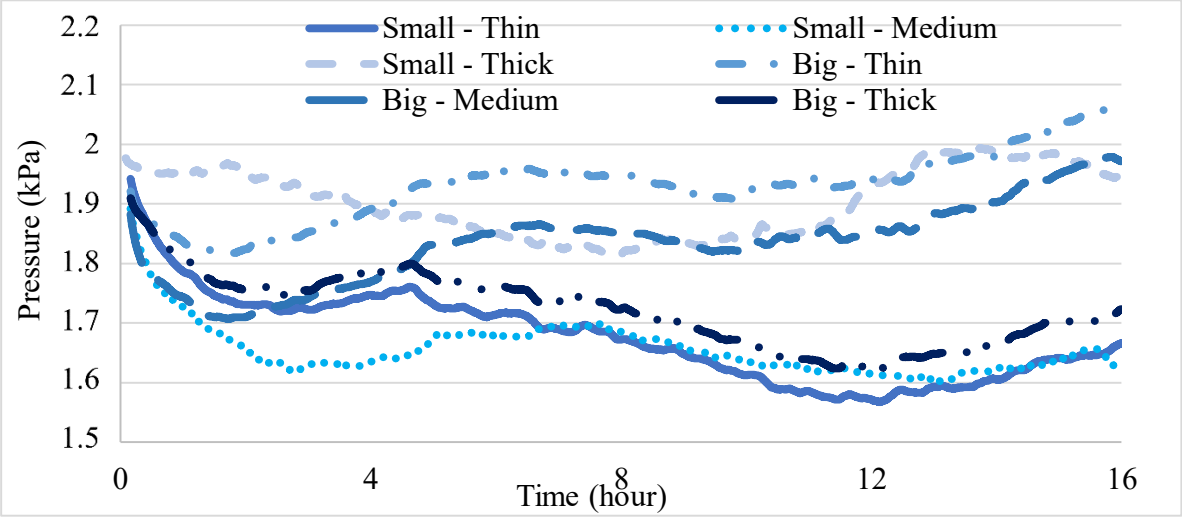
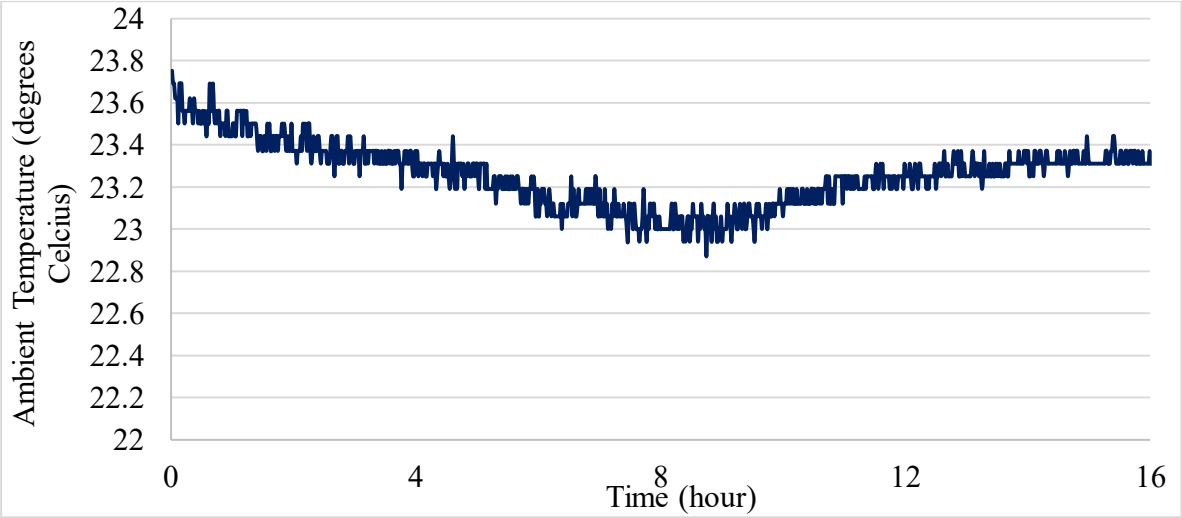


Figure C.6: Box-whisker plot for cyclic testing of small LDBs.



(a)



(b)

Figure C.7: Long-term stability testing: (a) Internal air pressure of all 3-layer LDBs over 16 hours at room temperature. (b) Room temperature was recorded by a thermocouple at the same time as the recording of the internal air pressure of the LDBs from (a).

Appendix D

Supporting Information for Chapter 7 Investigating Miniaturization of Soft Robotic Sensor for Prosthetic Socket Fitting

Distal-End Prosthetic Layered-Donut Balloon Sensor Fabrication Manual

Version 1.1

Introduction

The distal-end balloon was developed by researchers at the Neural and Rehabilitation Engineering Lab and Waterloo Microfluidics Laboratory. Its purpose is to act as a compression sensor that detects volume change downward movement and "pistonning" within pin-locking lower-limb prosthetic devices and can be modified for other types of suspension as well.

This sensor has been designed such that no specialized equipment or techniques would be required for fabrication. Hobbyist crafting machines like the Cricut Maker and a heat press are the main tools that will be used to create balloons. In addition, some simple electronic components will be used to detect the change in the balloon's internal pressure. In certain embodiments, a simple pressure gauge may be used instead of electronics, making it a purely mechanical system with no need of battery.

While these balloons have been successfully fabricated and tested in a controlled lab setting by engineers, they have yet to be used in patients or fabricated by prosthetists. By having others fabricate these balloons, we hope to evaluate the quality of balloons made outside of the lab, as well as the feasibility of the fabrication process.

Please refer to our publication, “Soft Robotics-Inspired Sensing System for Detecting Downward Movement and Pistoning in Prosthetic Sockets: Proof of Concept Study” (Yu et al.), for information about the proof of concept study. Please contact Adam Yu (adam.yu@uwaterloo.ca) or James Tung (james.tung@uwaterloo.ca) with any questions about the fabrication process or this manual.

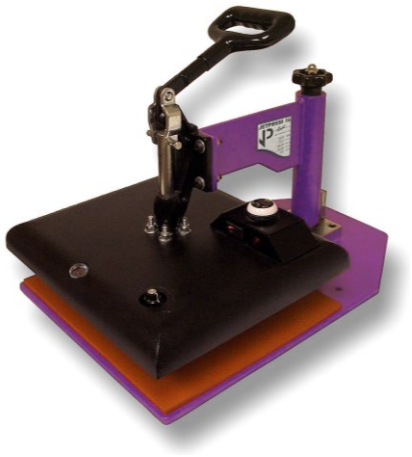
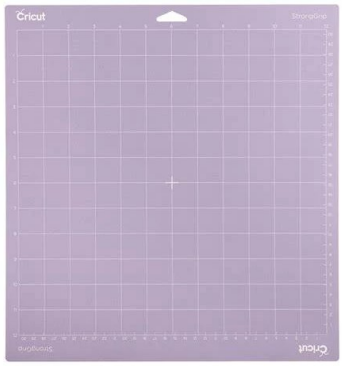
Important notes are highlighted in blue throughout the manual. An instruction video (**Appendix D-1**) accompanies this manual; please watch it before trying to fabricate balloons.

Materials

Tools

The following tools are used throughout the fabrication processes.

Cricut Maker 3 	The Cricut Maker is a hobbyist craft machine that performs precise programmed cuts. Material must be loaded in on a sticky cutting mat and a blade will automatically perform the cuts. This machine works in conjunction with the Cricut Design Workspace software. Cricut Maker Manual
Heat press	Used to anneal and bond layers of TPU. Always check the temperature of the press before use. Screw the black knob to adjust the height of the top plate of the press. Do not touch the top plate unless it is cool. Clean off dust and debris before turning the press on.

	
Mini iron 	The mini iron can be used to seal the tubing into the balloon and repair small patches.
Cutting mat 	A sticky mat that the Cricut will perform cuts of materials on. Try to avoid touching with fingers as oils may reduce the stickiness of the mat. If materials have a backing, be sure to place the backing side on the mat.
Rotary cutter 	Used to roughly cut materials to the right size to place on the cutting mat.
Ruler	Used to measure materials and act as a cutting guide for the rotary cutter.

Tweezers	Used to take materials off the mat.

Materials

TPU (Bemis 3916, 3914 or 3913 or similar) See **Figure C.1**	Thermoplastic polyurethane (TPU) is the material that will make the walls of the balloon. This material has one smooth side and one textured side and is stretchy and elastic. TPU is initially cloudy but when heated will become clear and shiny. To use, remove the membrane from the backing. The backing is the non-stick paper
Teflon sheet or PDMS membrane See **Figure. C.1**	Teflon sheet is a translucent material used to separate and prevent layers of TPU from sticking together. Or Polydimethylsiloxane (PDMS) membrane is a clear material used to separate and prevent layers of TPU from sticking together. When cutting, keep the membrane attached. When used in the final design, remove the membrane from the backing.
Glue (Loctite 495 or 4902 or similar adhesive for assembly of flexible devices) 	Glue is used to seal the tubing into the balloon and repair any small holes along the borders. A dispensing tip may need to be attached to the end of the glue bottle.
Tubing 	1/16” or any other size of inner-diameter Tygon tubing is fed into the balloon and connects the balloon to the electrical components or a pressure gauge.

Non-stick or parchment paper	The non-stick paper is used between the TPU layers to stop them from sticking to each other. This paper is the backing of the TPU.
Heat press or parchment paper	The heat press paper prevents the TPU from sticking to the heat press itself. Ensure that the non-stick side contacts the balloon or else the paper will stick to the balloon.
Y-splitter 	Y-splitters are used at junctions to divert the flow of air.
One-way valve 	One-way valves only allow air to flow in the direction of the arrow on the valve and are generally only used for testing purposes.

Electronics (optional)

Pressure Sensor 	The adafruit pressure sensor will sense pressure. Connect tygon tubing to the protruding port. The sensor will likely have headers pre-soldered so that the wires may be attached easily.
Microcontroller 	The Seeeduino Xiao is a microcontroller that is responsible for implementing pressure sensing. Wires can be attached to the headers. The pressure sensing code will be uploaded onto the Xiao.
Jumper wires	Jumpers are used to make electrical connections between the computer, microcontroller, and pressure sensor.

	
Laptop	Cricut Design Space will be used on the laptop. For benchtop testing, the laptop will also act as a power source instead of a battery.
USB cable	This cable connects the microcontroller to the laptop.

Software

The following software programs will need to be downloaded and set up before they can be used.

Cricut Design Space	Use this website to download Cricut Design Space. You will need to set up an account and sign into Design Space.
Arduino	Download they Arduino IDE app from this website.

Note: The electronic components and Arduino software are used for testing and actual sensing. Alternatively, a pressure gauge can be used, making the system purely mechanical.

Balloon Manufacturing

Shape Preparation

For the doughnut-shaped balloons, layers have already been prepared. These shapes are bitmat files (.bmp) and were generated using AutoCAD software. If needed, extra shapes can be made in AutoCAD (not covered).

1. Click on “New Project” to create a new project.

2. Click on “Upload” then “Upload Image” and select the shapes you need. If it is your first time using that shape in Cricut, you will have to upload and cut the shape. Refer to the video to see how to do this.
3. Next, add your desired shapes to the canvas. Add only shapes that will be cut of the same material on to the canvas.
4. Adjust the size in the top bar to match the actual size of the shape.
5. Press “Make It” in the top right corner. Set “Material Load Type” to “On Mat” and “Material Size” to the size of the sticky mat. The cut preview canvas will appear in the center of the screen.

Shape	**Size dimensions (cm)**
Small Teflon/PDMS insert	3.8 x 3.8
Small TPU middle/end	4.2 x 4.2
Small non-stick paper	6.0 x 6.0
Medium Teflon/PDMS insert	4.6 x 4.6
Medium TPU middle/end	5.0 x 5.0
Medium non-stick paper	8.0 x 8.0
Large Teflon/PDMS insert	5.4 x 5.4
Large TPU middle/end	5.8 x 5.8
Large non-stick paper	8.0 x 8.0

Material Preparation

1. Using the preview canvas as a reference, determine an appropriately sized rectangle of material.
2. Using the ruler to measure out the material, and then as a guide for the rotary cutter, cut out material with the backing attached.
3. Stick the material on the mat, ensuring that the material goes all the way to the corner of the sticky portion of the mat (and not past the border of the mat) and there are no bubbles or wrinkles underneath the material.

a. TPU - the backing can be kept on or removed. Remove the backing of larger pieces as the non-stick paper will be needed in the future. TPU without the backing can be challenging to stick on the mat. Spend the time to ensure the material is not wrinkled or else the Cricut may jam.
b. Insert:
    i. Teflon – avoid creasing the Teflon.
    or
    ii. PDMS - keep the backing on during the cutting phase. Place the backing side on the mat.

Cricut Cutting

1. Press "Continue" in the Design Space and connect the Cricut to your laptop via USB connection. Move around pieces on the canvas preview as desired.
2. Set the material and cutting pressure:
    a. Use "adhesive double sided" as the material and default or high pressure for TPU or Teflon
    b. Use "wax paper" as the material and default or less pressure for the non–stick paper
3. Using tweezers, peel the pieces off the mat. Peel off or scrape scraps using tweezers or a scraper. Try not to touch the mat with bare fingers as oils can reduce the durability of the mat.
4. Repeat 3.1-3.3 with other materials before moving on to 3.4.

*If the blade cuts deeply into the mat, reduce the pressure

Assembly With Heat Press

<u>1-Layered Balloons</u>

1. Layer the following materials in order, making them as centered as possible: TPU end piece, PDMS membrane/Teflon insert, non-stick paper insert (for tubing), TPU end piece.
    a. Use tweezers or clean fingers to center the layers.
    b. The non-stick paper insert can be made of scrap non-stick paper and should be a small rectangle, whose width is slightly larger than the outer diameter of the tubing.
2. Place the stack between heat press paper (can be an individual piece of paper folded or two separate pieces.
    a. Ensure that the non-stick side is contacting the TPU or else the balloons will stick to the paper.

b. Multiple balloons can be pressed at the same time.

3. Heat Press at 110 °C to 150 °C for 30 seconds, or until the TPU is clear (not cloudy) and glossy.
4. Let the TPU cool down; avoid accidentally touching new TPU to warm the balloon as the thermally active elastomer will bond.

Multi-Layered Balloons

1. For the end layers of the balloons, use a TPU end piece, then PDMS/Teflon insert, then a TPU middle piece. The tubing insert needs to be put in only one end layer.

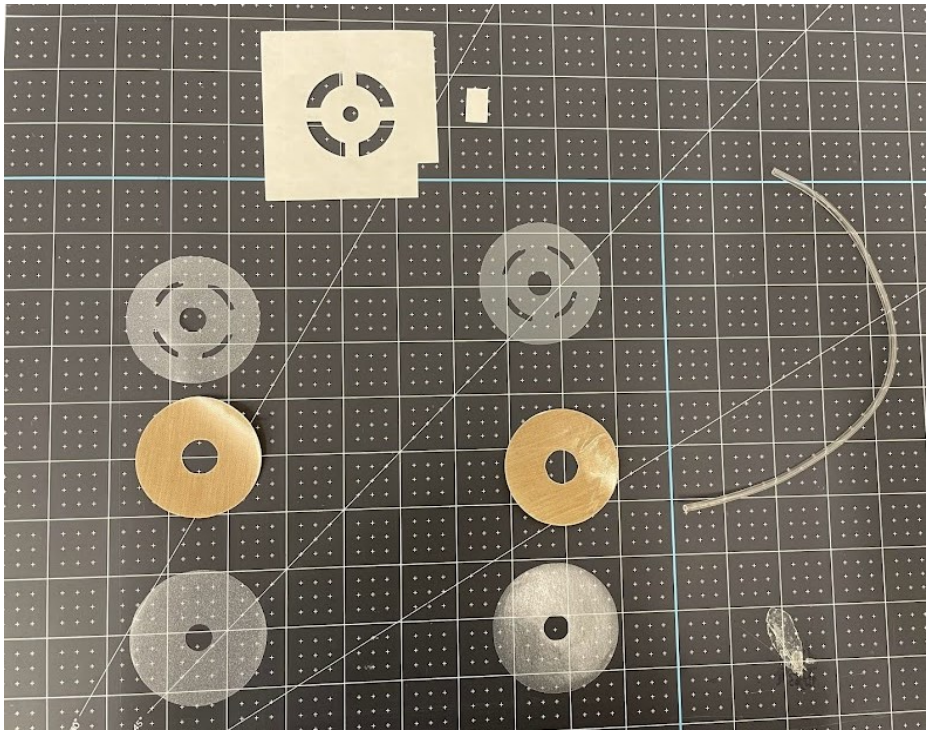


Figure D.1: Required materials for a 2-tiered balloon. From top to bottom: non-stick paper and tab, TPU middle piece, PDMS with brown backing/Teflon insert, TPU end piece.

2. For the middle layers, use two middle pieces sandwiching a PDMS/Teflon insert layer.

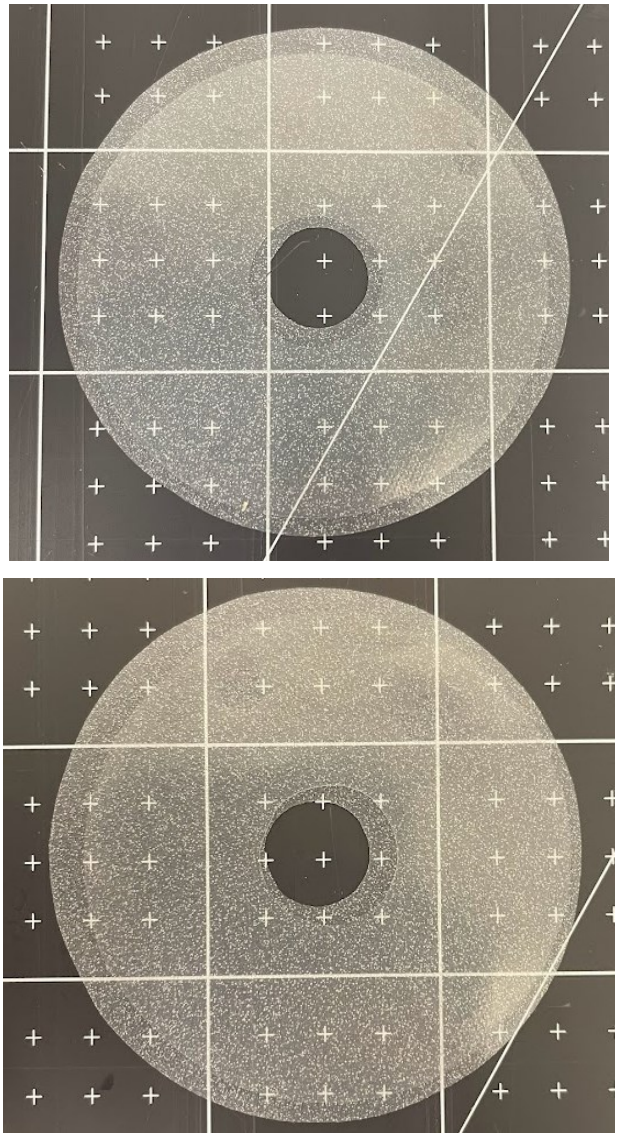


Figure D.2: Align the PDMS/Teflon insert centrally like the left. On the right, the PDMS/Teflon insert is too close to the center hole.

3. Press the individual layers together.

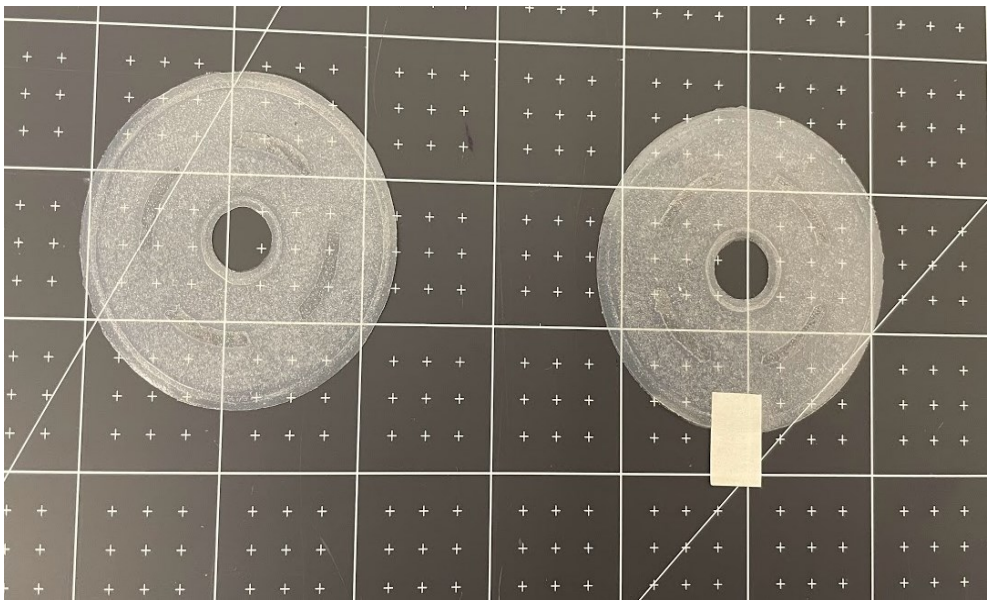


Figure D.3: Pressed layers. Do not forget to insert the tab in one of the layers.

4. Use the non-stick paper cutouts to separate layers, again keeping everything centered with respect to the central hole.

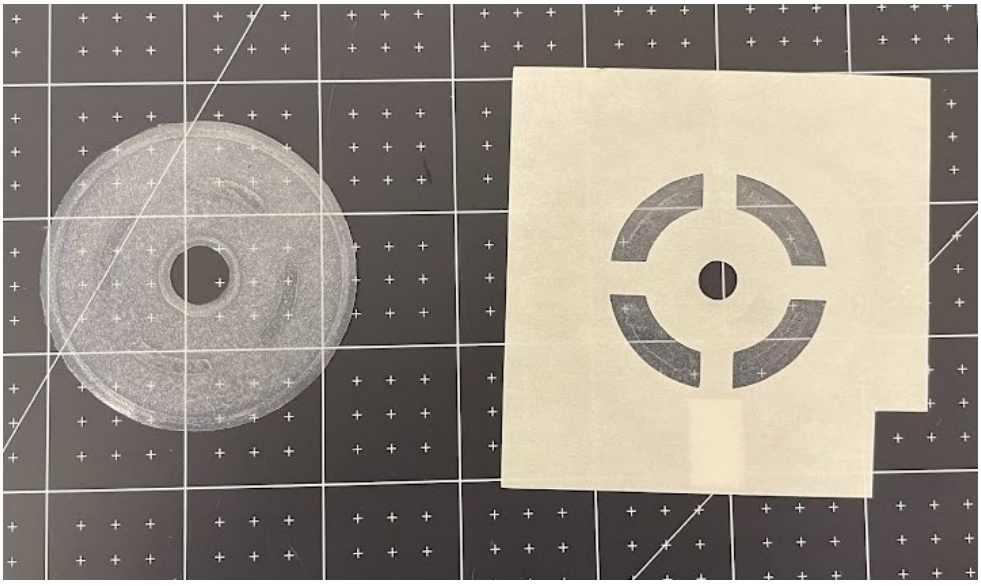


Figure D.4: Place the non-stick paper separator on one of the layers, then stack the second layer on top. Ensure that the middle pieces are touching. If done right after using the heat press, TPU pieces will instantly bond so ensure that parts are aligned.

5. For balloons greater than 2 layers tall, stack and heat press the layers one at a time, with the newest layer closest to the heated surface of the press. Note that you may not be able to “lock” the heat press.

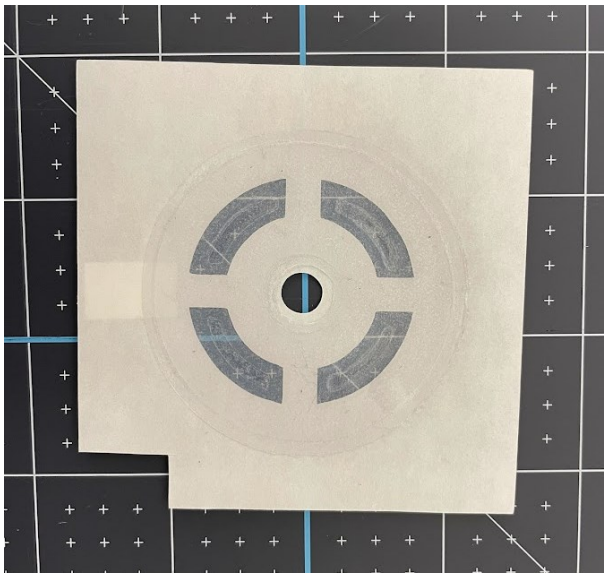


Figure D.5: Two-layer balloon after being pressed together.

*Note that the heat press paper can be reused multiple times

Final Assembly

1. Once cooled (at least 1-2 hours), insert the tubing with the tab in place.
2. Remove the tab using tweezers.
3. Thermally bond the elastomer adjacent to the tubing with the mini iron on the “low” heat setting. Place a layer of heat-press paper between the iron and TPU or else the TPU may melt.
4. Use glue to seal the tubing to the TPU. If needed, use a Teflon-lined pink needle dispense tip (Part #: 7005003, Nordson EFD) for a more precise flow.
5. Let dry for at least two hours and ideally overnight before inflating.
6. To test for leaks, submerge the inflated balloon in a clear tank of water and gently squeeze the balloon, while watching for bubbles. Let dry before use.

General Notes

1. Use clean hands when handing materials on the Cricut mat as oils and small pieces can reduce its tackiness.
2. Use tweezers to remove items from the Cricut mat to preserve its tackiness.
3. The Cricut may jam with material (generally TPU) if it is not stuck on hard enough. You may have to use a bit of tape along the border of the material to keep the machine from jamming.

    a. To clear jams, gently remove all of the material and discard any wrinkled material.
4. If the blade in the Cricut dulls it can be replaced easily with a new one.

Repairs

1. Small patches of TPU can be cut and heat pressed on the balloon to cover holes. Use the handheld iron for this application.
2. If leaks occur at the tubing junction, apply more glue; it will be hard to use TPU patches over glued parts.

Appendix D-1

This appendix is a video that shows the fabrications methods for Chapter 7

The file name is “Chapter 7 Video.mp4”.

If you accessed this thesis from a source other than the University of Waterloo, you may not have access to this. You may access it by searching for thesis at http://uwspace.uwaterloo.ca.

Appendix E

Supporting Information for Chapter 8 Investigating Miniaturization of Control System for Dynamic Knee Brace Using Gait

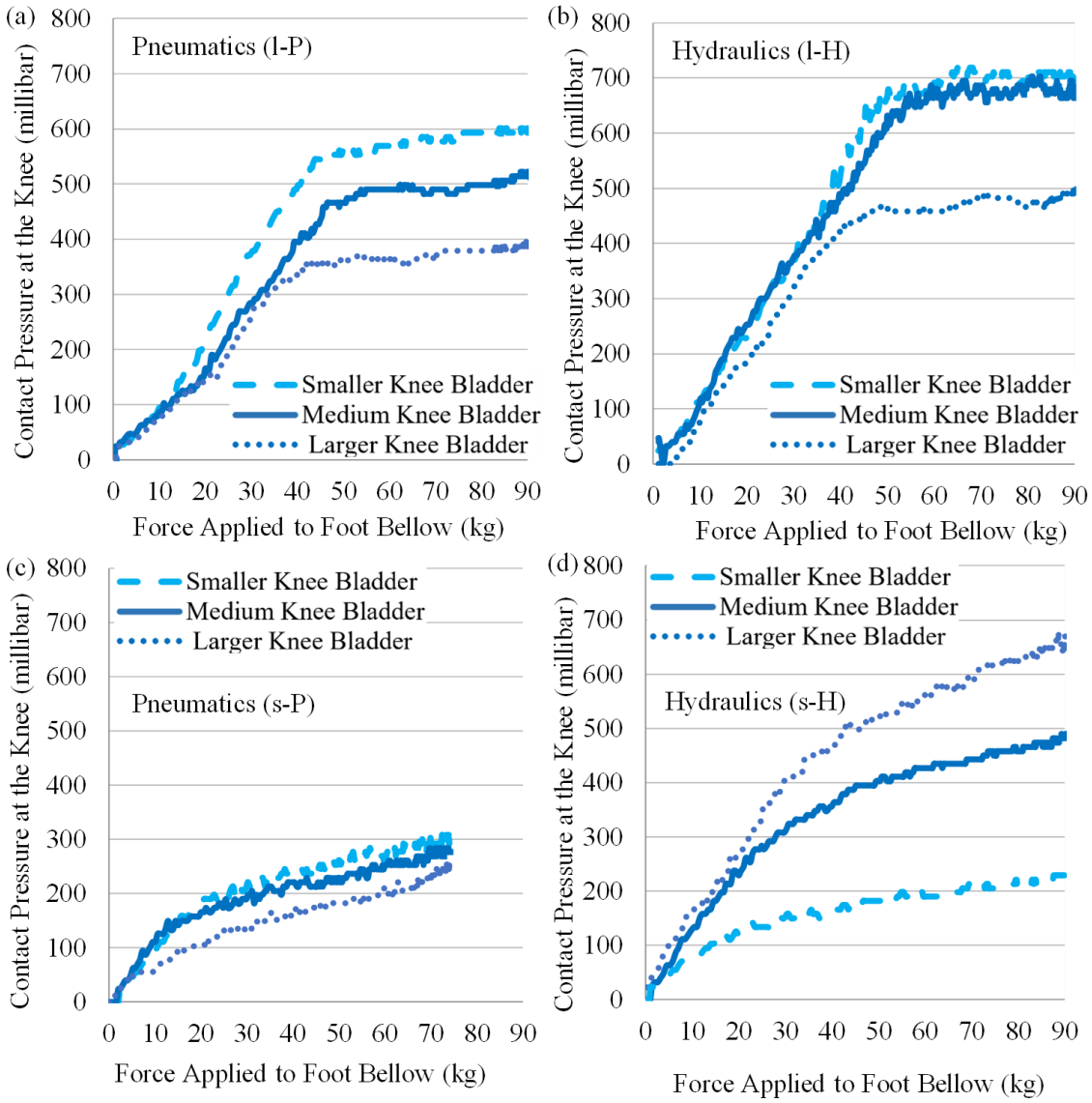


Figure E.1: Contact pressure testing results: (a) Contact pressure at the knee in response to progressive loading from 0 to 90 kg for system l-P with 38.1 mm (dashed red line), 40.6 mm

(solid blue line) and 45.4 mm (purple dotted line) diameter knee bladders. (b) Contact pressure at the knee in response to progressive loading from 0 to 90 kg for system l-H with diameter knee bladder 73.7 mm x 63.5 mm (oval) (solid blue line), 58.4 mm x 50.8 mm (oval) (dotted yellow line), and 50.8 mm (dashed red line) diameter knee bladders. (c) Contact pressure at the knee in response to progressive loading from 0 to 90 kg for system s-P with diameter knee bladder 30.5 mm (solid blue line), 31.8 mm (dashed yellow line), and 33 mm (dotted purple line) diameter knee bladders. (d) Contact pressure at the knee in response to progressive loading from 0 to 90 kg for system s-H with 40.6 mm (dashed red line), 50.8 mm (solid blue line) 58.4 mm x 50.8 mm (oval) (dotted purple line), diameter knee bladder.

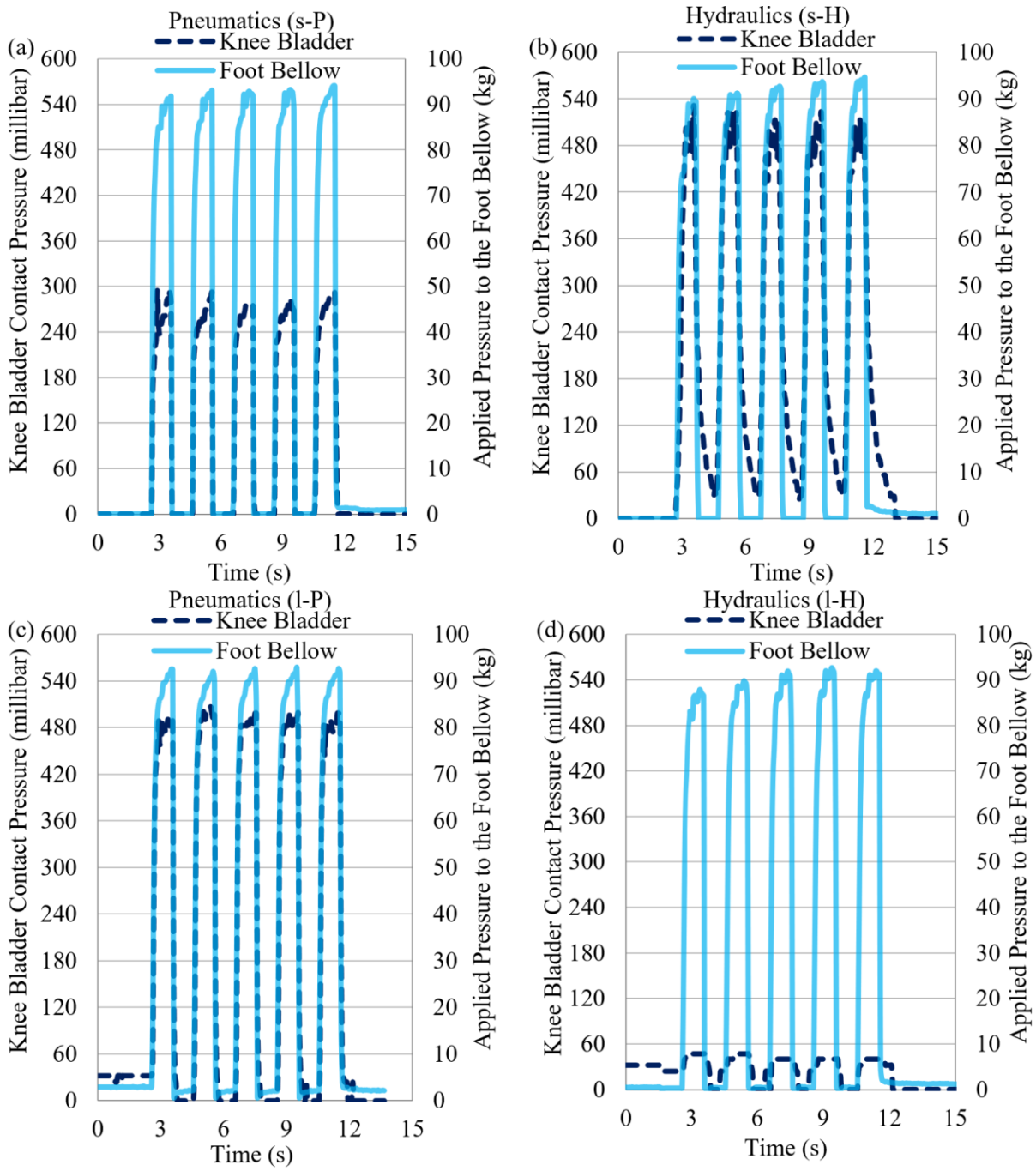


Figure E.2: Response time testing results: (a) Response time testing results showing contact pressure at the knee in blue (dotted) and applied pressure on the foot bellow in red (solid) for small pneumatic system (s-P) with 30.5 mm diameter knee bladder. (b) Response time testing results showing contact pressure at the knee in blue (dotted) and applied pressure on the foot bellow in red (solid) for small hydraulic system (s-H) with 50.8 mm diameter knee bladder. (c) Response time testing results showing contact pressure at the knee in blue (dotted) and applied pressure on the foot bellow in red (solid) for large pneumatic system (l-P) with 40.6 mm diameter knee bladder. (d) Response time testing results showing contact pressure at the knee

in blue (dotted) and applied pressure on the foot bellow in red (solid) for large hydraulic system (l-H) with 73.7 mm x 63.5 mm (oval) knee bladder.

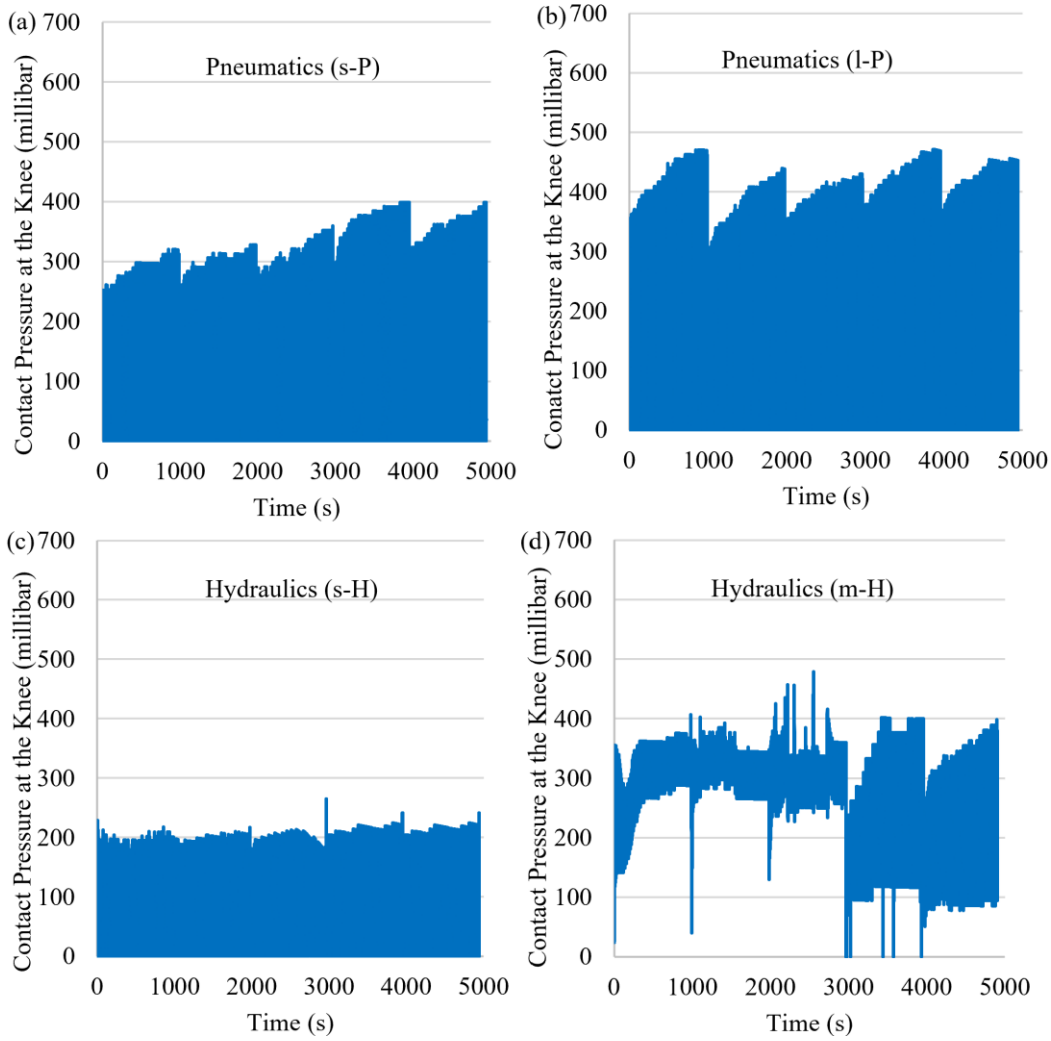


Figure E.3: Cyclic loading testing results: (a) Contact pressure at the knee for the complete 2500 steps during cyclic loading testing from the small pneumatic system (s-P) with 30.5 mm diameter knee bladder. (b) Contact pressure at the knee for the complete 2500 steps during cyclic loading testing from the large pneumatic system (l-P) with 40.6 mm diameter knee bladder. (c) Contact pressure at the knee for the complete 2500 steps during cyclic loading testing from the small pneumatic system (s-H) with 50.8 mm diameter knee bladder. (d) Contact pressure at the knee for the complete 2500 steps during cyclic loading testing from the medium hydraulic system (m-H) with 58.4 mm x 50.8 mm (oval) knee bladder.

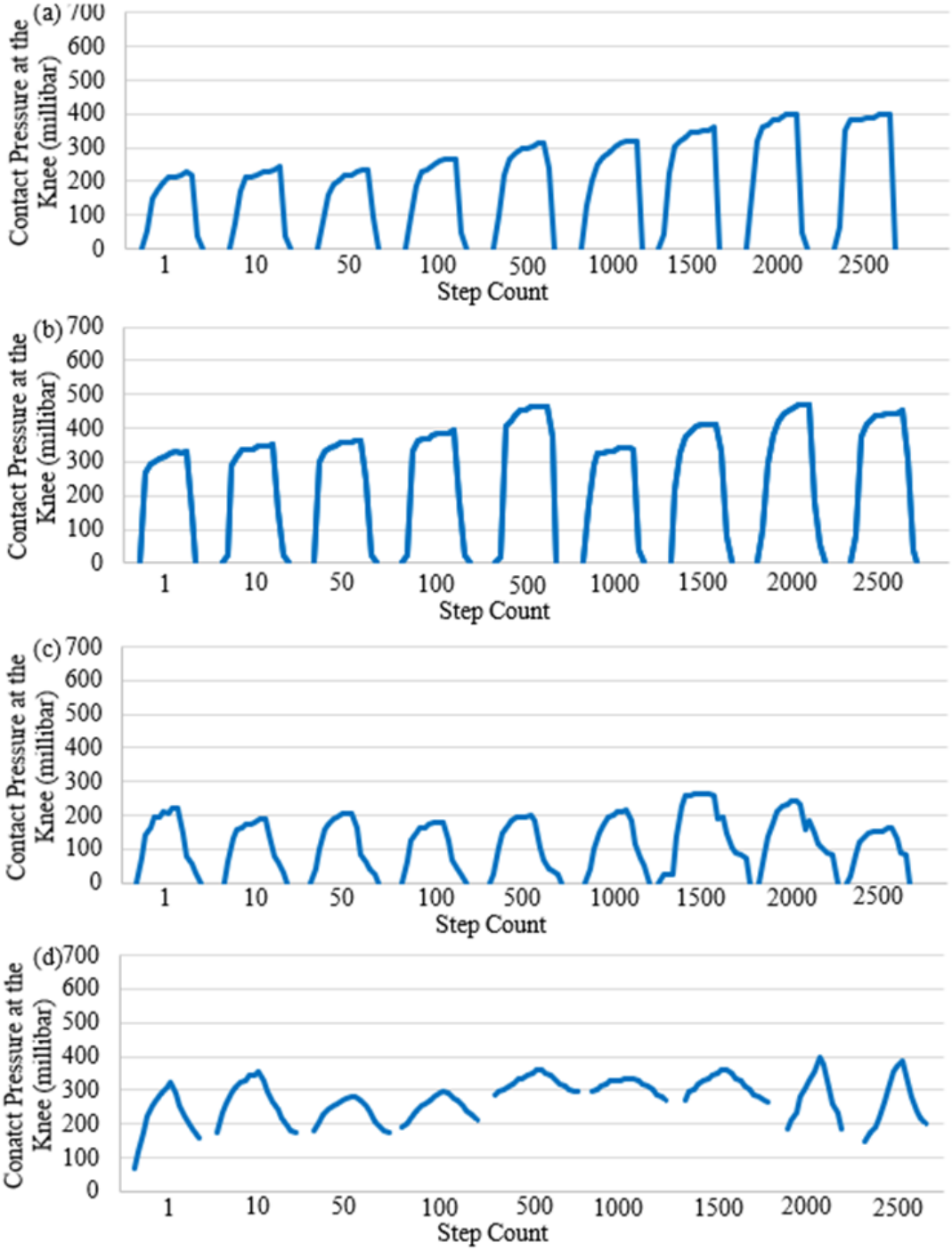


Figure E.4: Cyclic loading testing results: (a) Contact pressure at the knee for steps 1, 10, 50, 100, 500, 1000, 1500, 2000 and 2500, selected from cyclic loading testing for small pneumatic system (s-P) with 30.5 mm diameter knee bladder. (b) Contact pressure at the knee for steps 1, 10, 50, 100, 500, 1000, 1500, 2000 and 2500, selected from cyclic loading testing for large pneumatic system (l-P) with 40.6 mm diameter knee bladder. (c) Contact pressure at the knee for steps 1, 10, 50, 100, 500, 1000, 1500, 2000 and 2500, selected from cyclic loading testing for small hydraulic system (s-H) with 50.8 mm diameter knee bladder.

(d) Contact pressure at the knee for steps 1, 10, 50, 100, 500, 1000, 1500, 2000 and 2500, selected from cyclic loading testing for medium hydraulic system (m-H) with 58.4 mm x 50.8 mm (oval) diameter knee bladder.

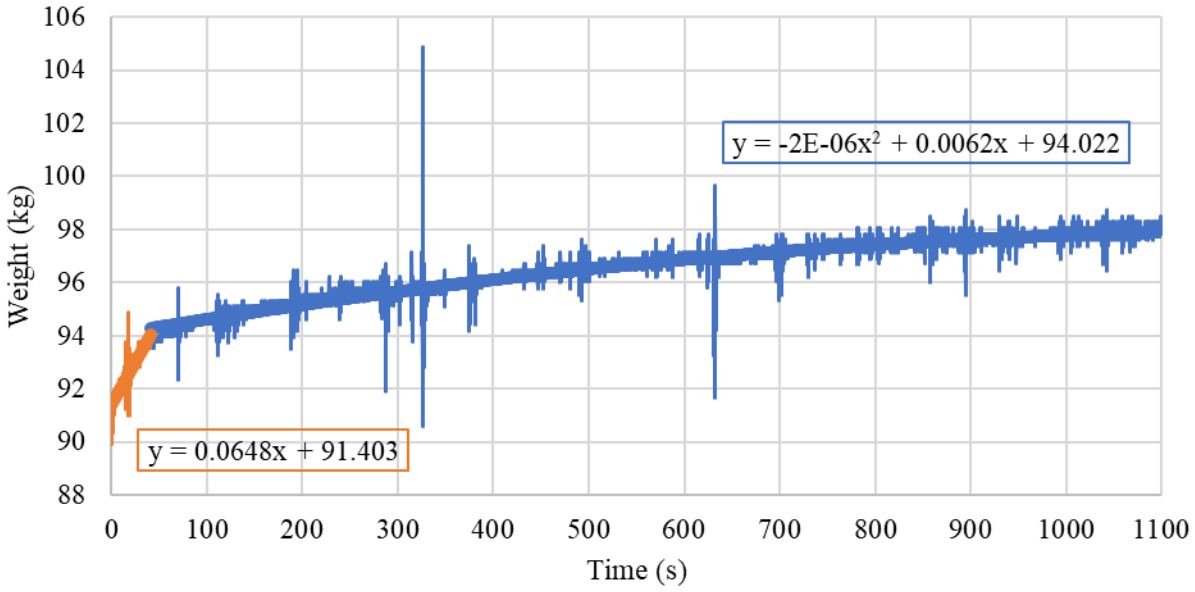


Figure E.5: Calibration curve used for Tekscan data based on a known weight of 90 kg. Two calibration equations were created, one for the segment from 0 to 100 seconds and one for the period from 100 seconds to 1000 seconds to match the nature of data in each interval. An error term was then calculated using the time as the dependent variable and the error was subtracted from the sensor read value. This new value was used for all following analysis.

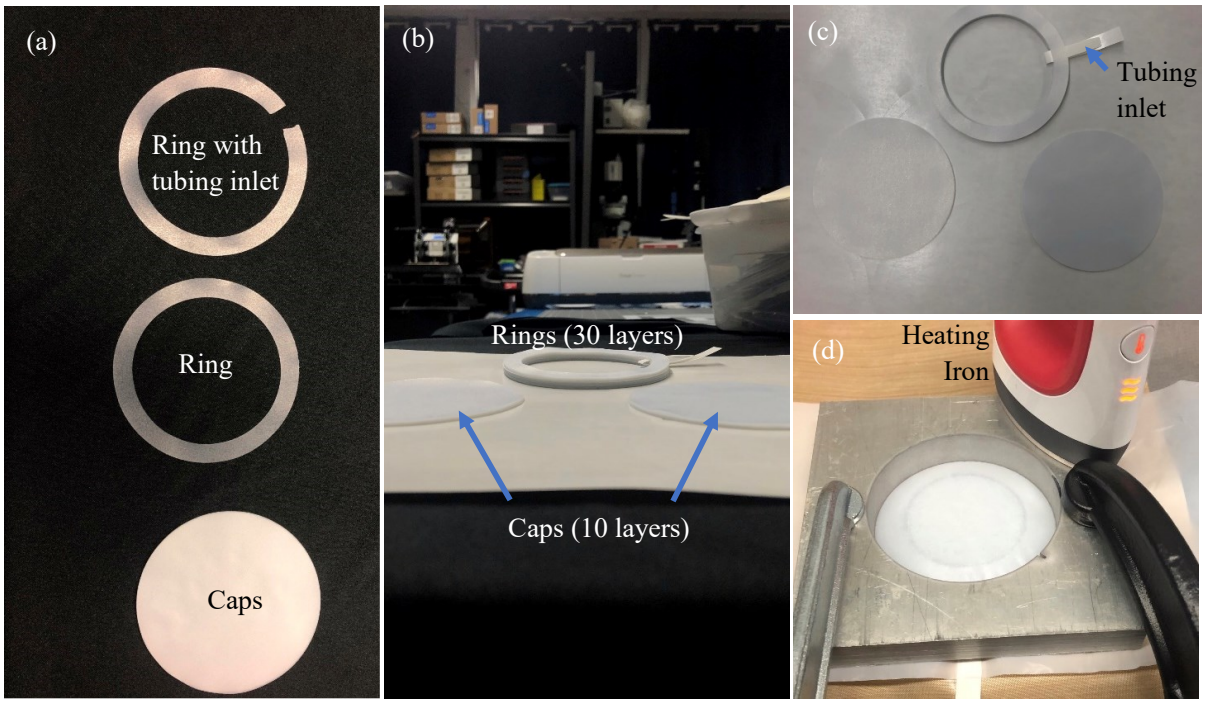


Figure E.6: Images for fabrication processes: (a) TPU shapes cut cuing computer controlled cutting machine, Cricut. (b) TPU shapes stacked into two 10-layer caps and one 30-layer ring. (c) Heat pressed caps and ring. (d) Assembled foot bellow during last round of heat press (Cricut EasyPress Mini) with the TPU ring and chosen spring sandwiched between the two TPU caps.

Appendix F

Supporting Information for Chapter 9 Miniaturization of

Appendix F-1

Lab 1: Soft Robotic Finger Prosthetics with Inertial Measurement Units (IMU)
Lab 2: EMG Control of Soft Robotic Finger Prosthetics

Purpose

Lab 1: The purpose of this lab is to learn how to fabricate soft-rigid hybrid robotic system, with a focus on finger prosthetics, set up control hardware, electronics, wiring, and the data acquisition system, actuate the prosthetic finger and collect the IMU data and analyze the data.

Lab 2: The purpose of this lab is to learn the control of soft-rigid hybrid robotic finger prosthetics using EMG sensor.

Learning Objectives

1. Understand the principles of robotic prosthetic systems
2. Learn to fabricate soft robotic actuators and finger prosthetics
3. Set up hardware and software for controlling finger prosthetics
4. Learn programming basics to control the finger prosthetics and analyze IMU data

Microcontroller and IMU Sensor:

- Microcontroller: Seeed Studio XIAO SAMD21 (smallest third-party Arduino)
- Connection to Computer: USB C
- IMU Sensor: MPU-6050 - Accelerometer, Gyroscope, 3 Axis Sensor
- Connection to accelerometer: Jumper Wire

Electrical Hardware to Actuate Soft Robotic Prosthetic Finger:

- Power: AC to DC 12V, 1A Adapter
- Connections: Breadboard and Jump Wires
- Air Pressure Source: Miniature Air Pump
- Air Pressure Exhaust: 3 port 2 way (3/2) – Solenoid Valve
- Air Pressure Sensor: MPRLS Ported Pressure Sensor
- Motor Driver: TB6612FNG
- EMG Sensor: SEN0240

Mechanical Components:

- Compliant Mechanism Hinge (SLA 3D Printed, Form 3 Flexible Resin)
- Prosthetic Finger (FDM 3D Printed, PLA)
- Low-Profile Multi-Layered Soft Fluidic Actuator (Thermal Laminated, Bemis 3916)

Tutorials (good to know before the lab):

- Arduino IDE Introduction
- Microcontroller Tutorial
- Air Pressure Sensor Tutorial
- IMU Tutorial
- Motor Driver Tutorial
- EMG Tutorial (lab 2)

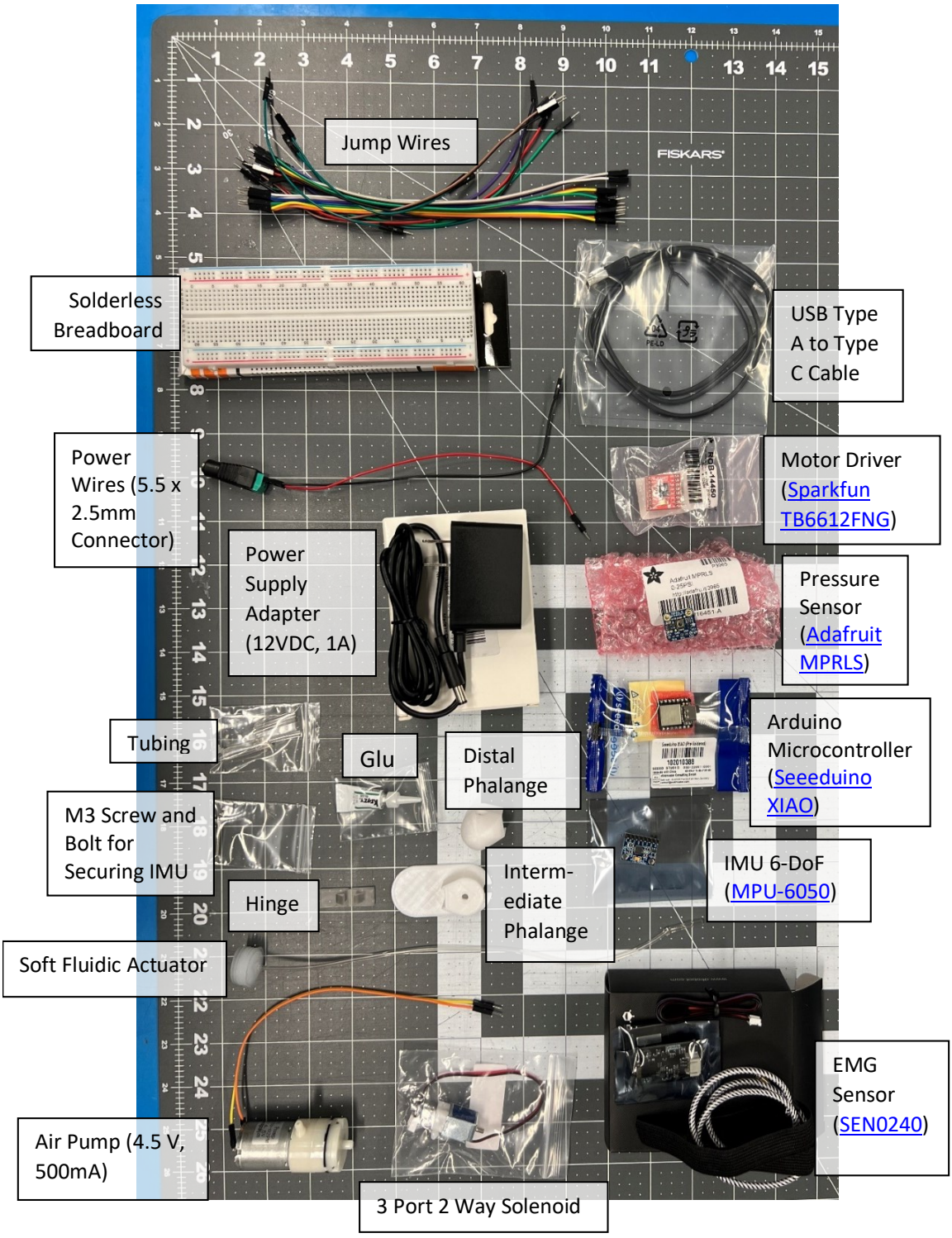
Required Software:

- Arduino IDE
- Any plotting software (e.g., Excel, MATLAB, etc.)

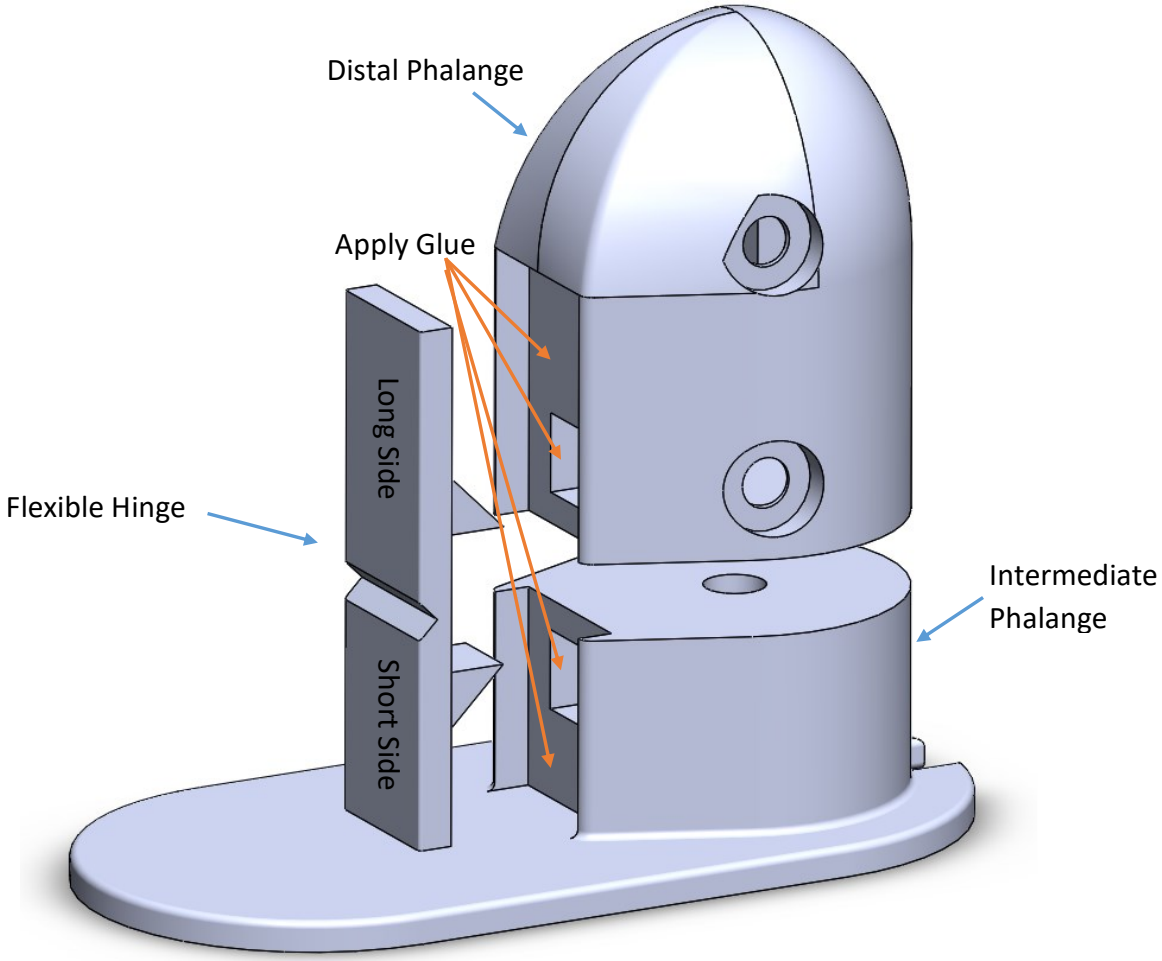
Provided Codes:

- Download from Learn Site

Step 1: *Components Overview*

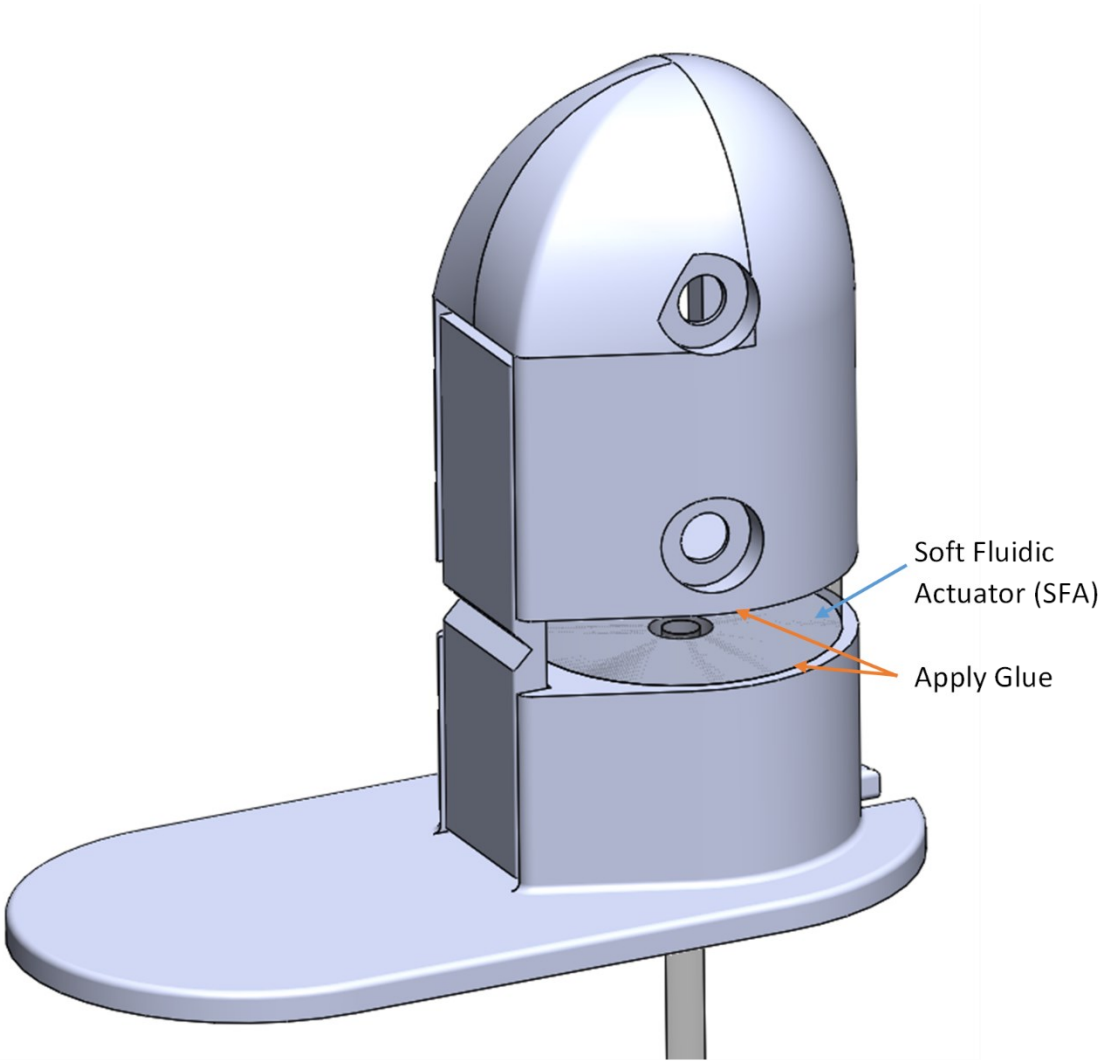


Step 2: *Assemble Soft Robotic Finger*



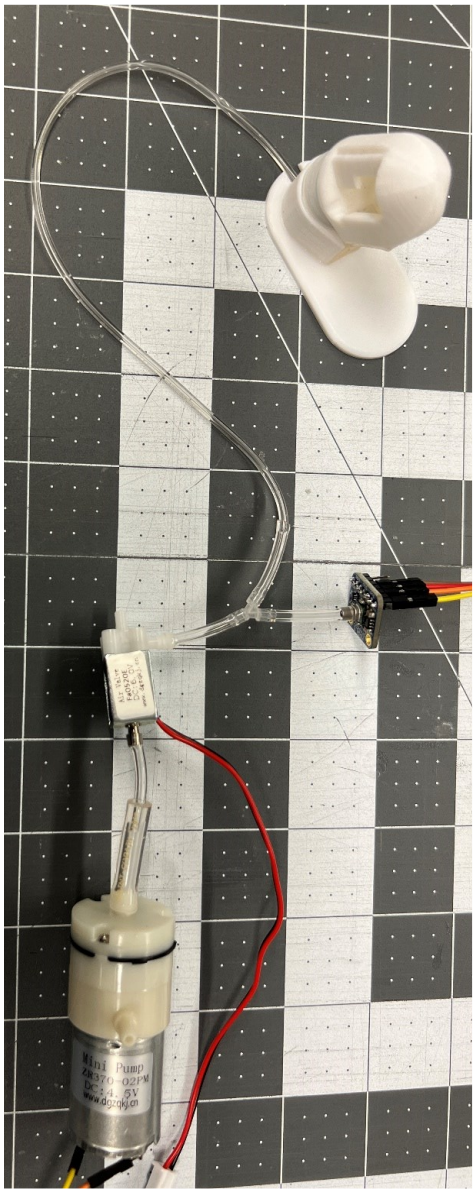
Please see **Appendix F-A** for step-by-step photos of the process for guidance.

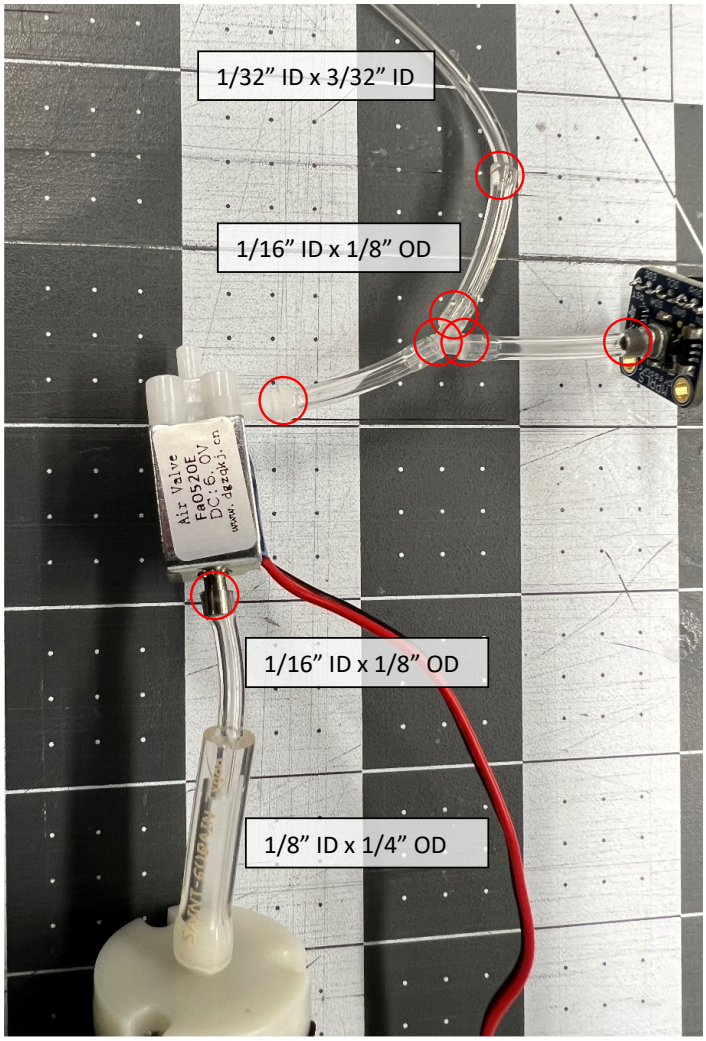
Important: Do not apply too much glue, and let the glue cure for at least **10 minutes** before proceeding to gluing soft fluidic actuator. Cyanoacrylate adhesives cure when exposed to moisture. Therefore, to improve curing speed, one can blow moist breath onto the glued surfaces.



Important: Apply a **single drop** of glue near/at the center of the soft fluidic actuator and ensure the glue does not seep into gaps in-between layers. (See **Appendix F-A**).

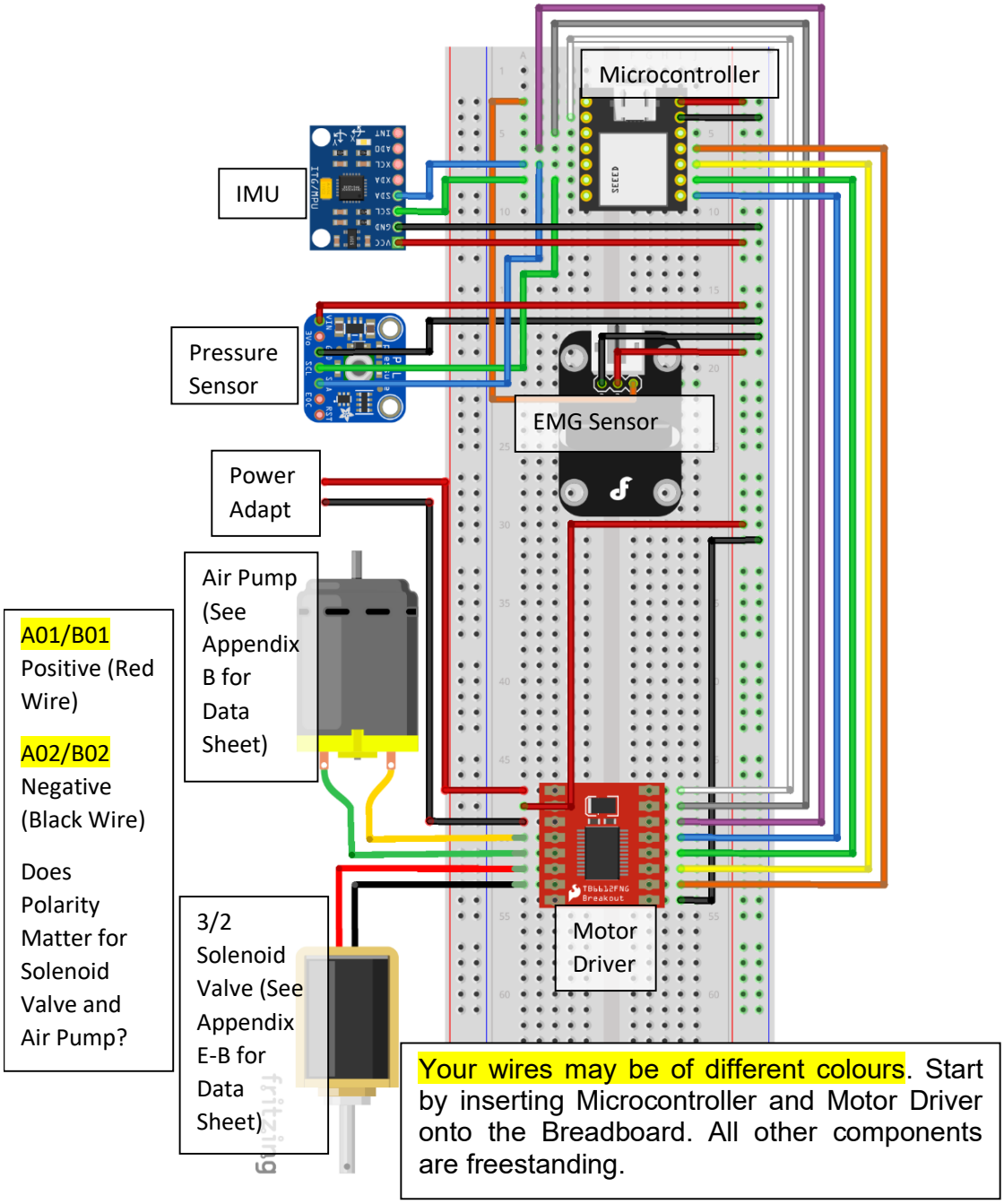
Step 3: *Connect Fluidic Tubing*





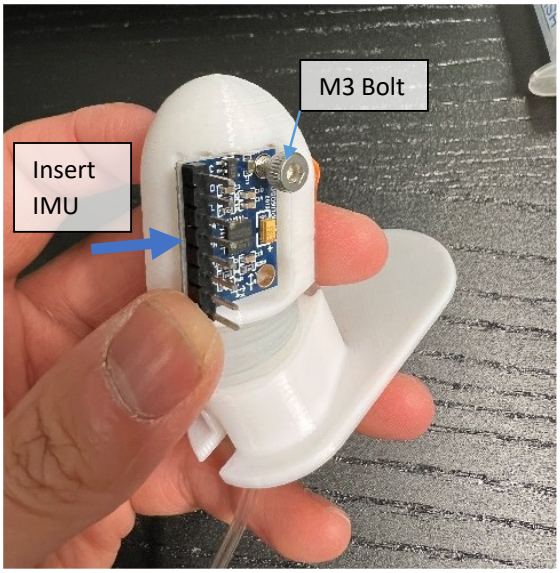
Tubing are squeeze fit. The connections are circled in red**.** Make sure the fittings are connected securely.

Step 4: *Connect Wires and Electronic Components*



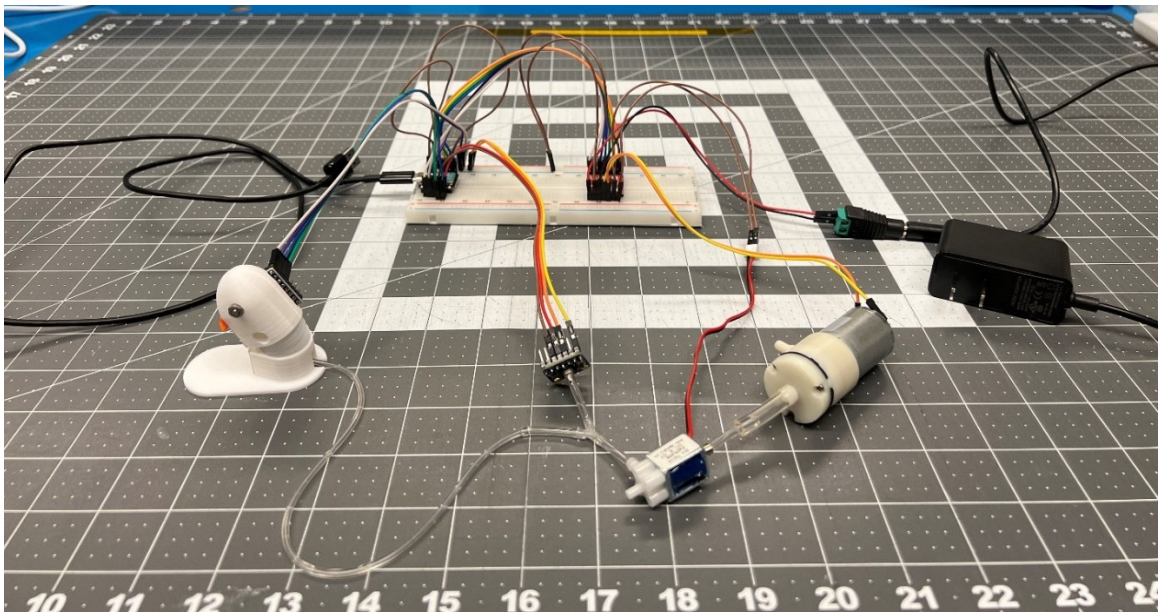
Step 5: *Final Assembly*

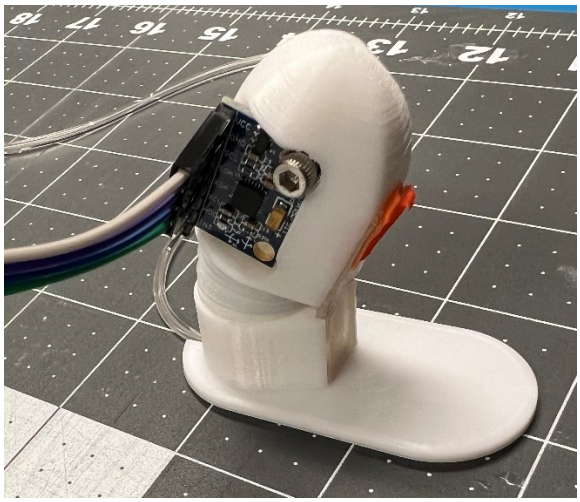
Insert IMU onto prosthetic finger distal phalange and secure using M3 nut and bolt. Hand tighten.

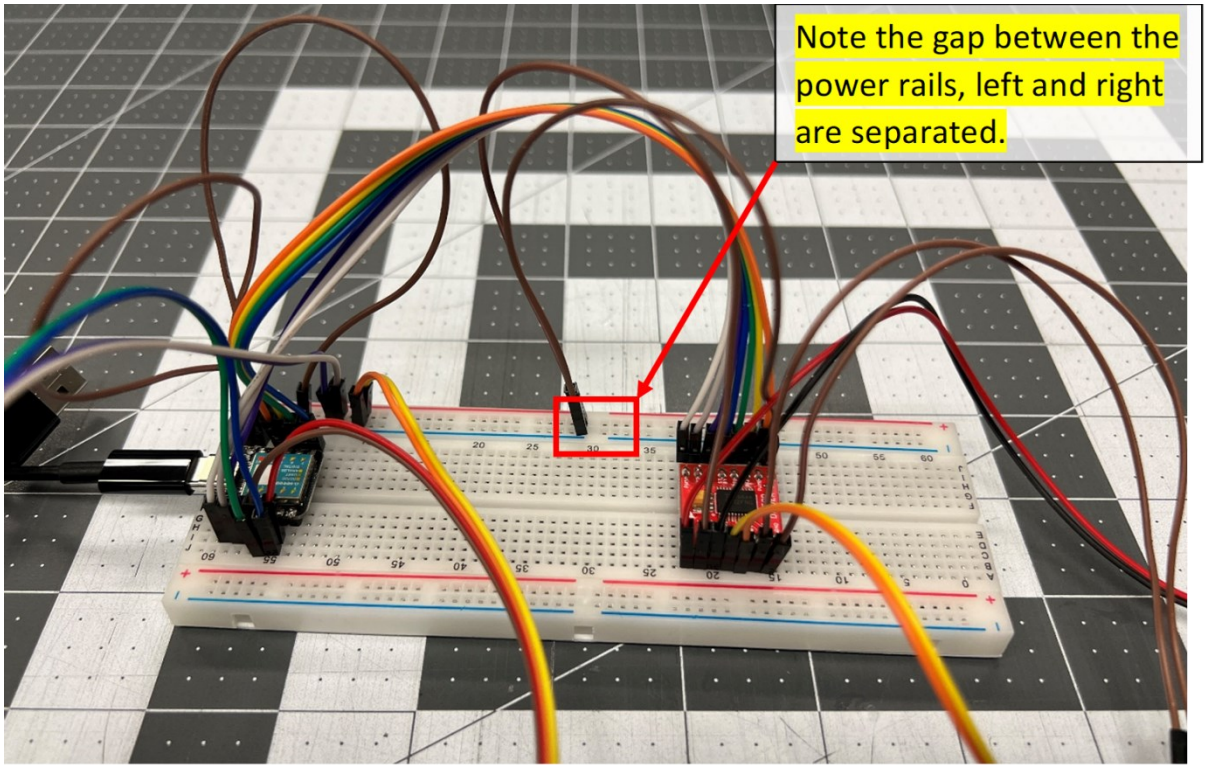




Connecting tubing to pump, solenoid valve, and pressure sensor, plug in power adapter






Note the gap between the power rails, left and right are separated.

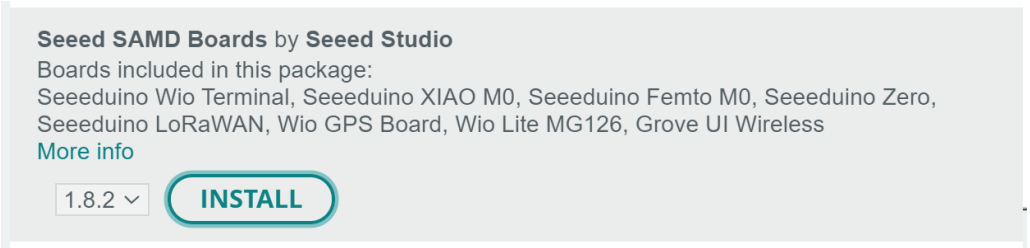
Step 6: *Software*

1. Install Arduino IDE. Arduino IDE is an open source software to program your microcontroller. An IDE in general is an integrated development environment and provides the tools for programmers to develop and test software. Depending on the version, your Arduino IDE may look different.

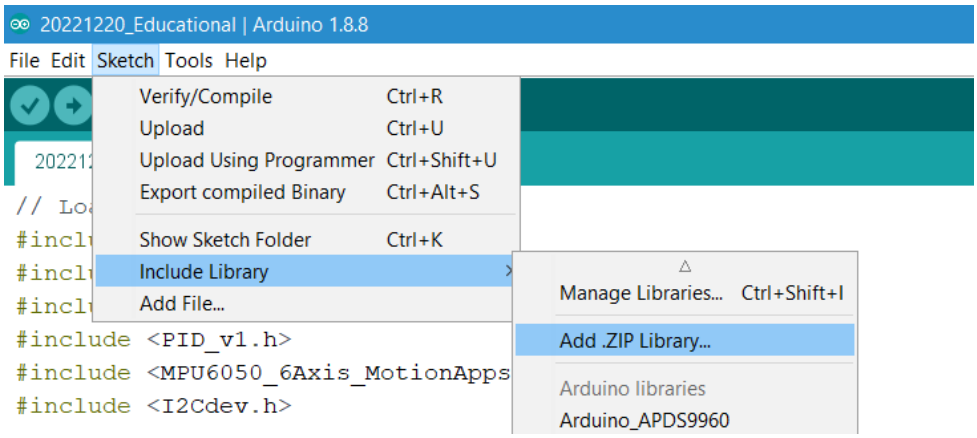
    a) Arduino IDE has a great forum to ask questions.
    b) You can also check out this Introduction to Arduino IDE to learn how Arduino codes work.

2. Install the Required Drivers: For some devices, drivers need to be installed to enable connection to other software or hardware. Install **Seeeduino XIAO** driver following the YouTube video from the link.

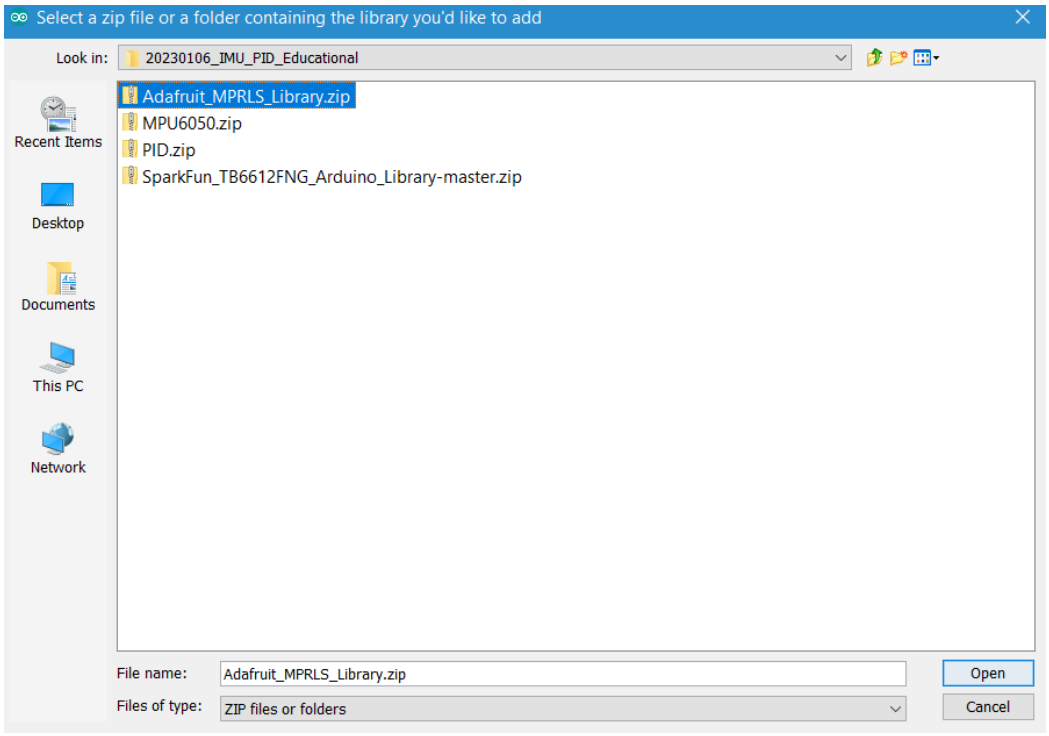
    https://files.seeedstudio.com/arduino/package_seeeduino_boards_index.json



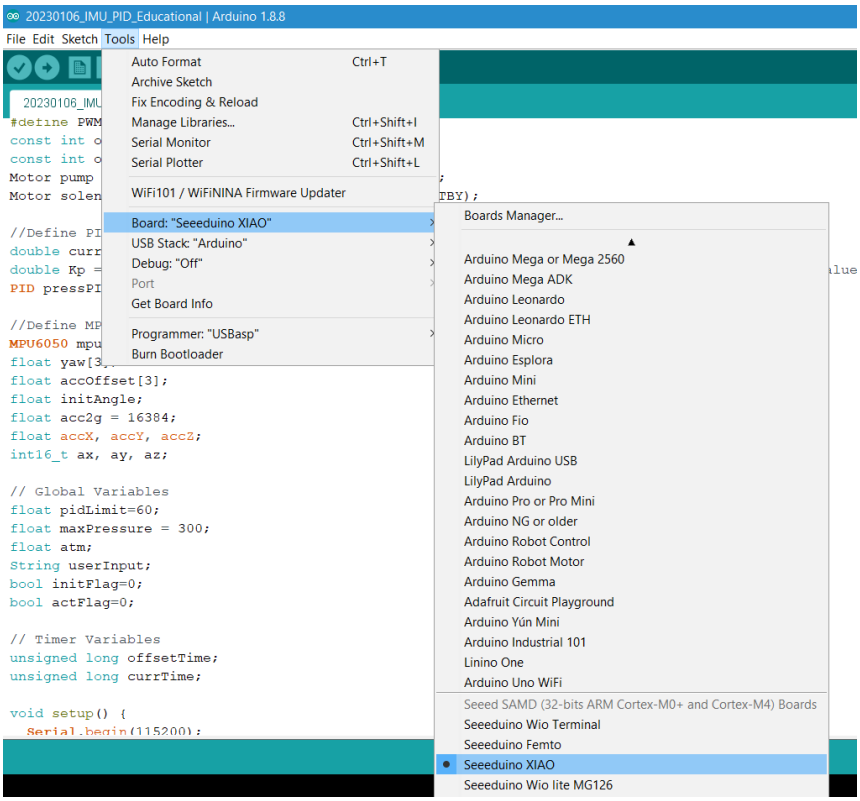
3. Install required Arduino Libraries by following steps below:
    a) Download the zip folders from LEARN and save them somewhere on your computer.
    b) In Arduino IDE -> Sketch -> Include Library -> Add .ZIP Library…



c) Add all four libraries one by one.

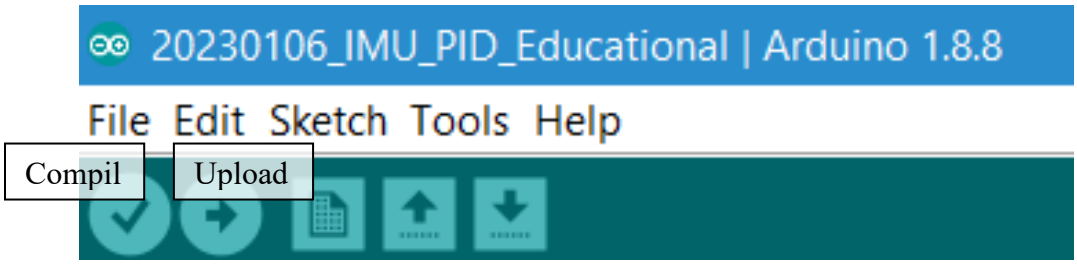


4. Compile and upload code to Seeeduino XIAO
    a) Download **20230106_IMU_PID_Educational.ino** from Learn and open it.
    b) Go through the code and review it.
    c) Select Seeeduino XIAO -> Tools -> Board -> Seeeduino XIAO

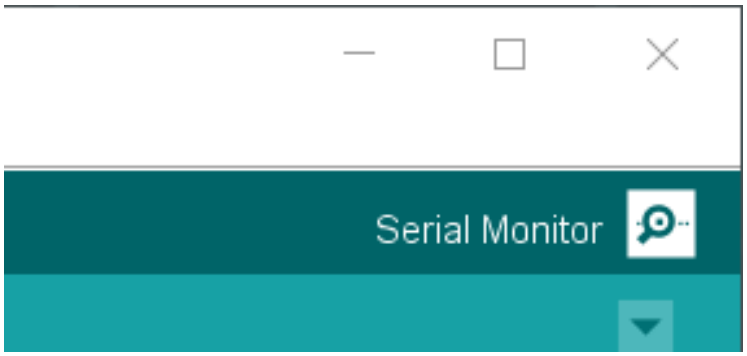


    d) Select the right COM Port -> Tools -> Port -> (Should just be the single port)

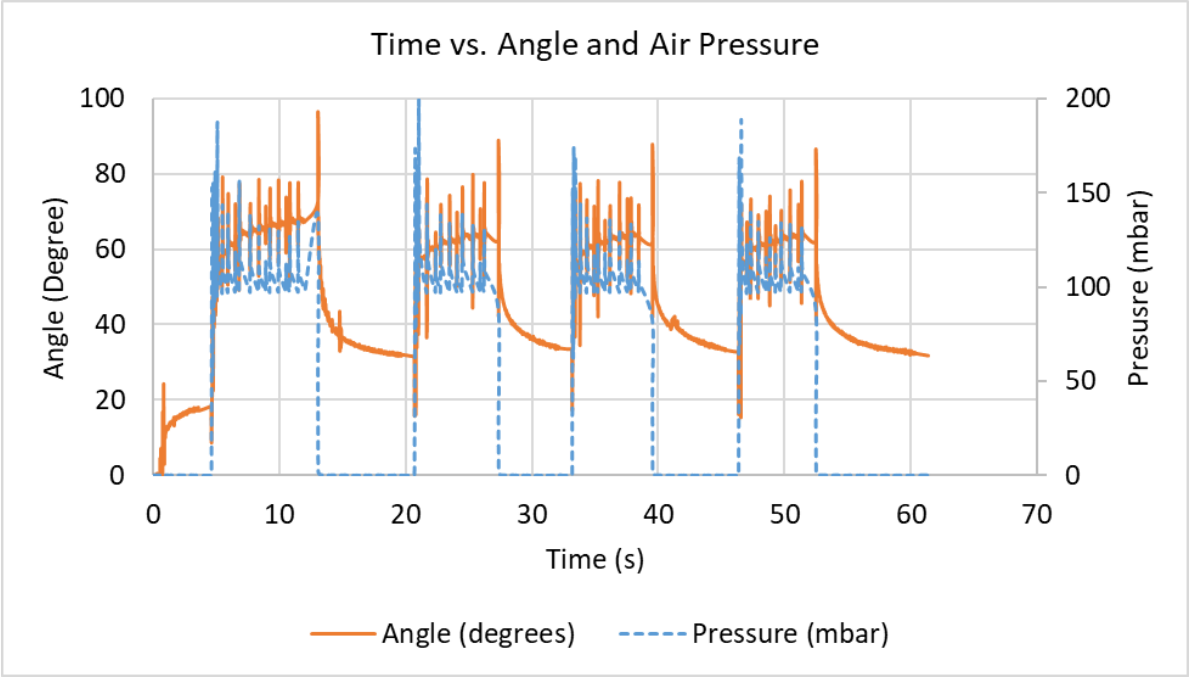
5. Compile the code first to see if everything's okay, then upload to Seeeduino XIAO.



6. Open Serial Monitor



7. Make sure the baud rate is selected as **115200**.
8. Follow the prompt on the screen. Type the letter and hit “Enter” key to input.
9. Try to get a plot like this (Uncheck Autoscroll and copy output and plot it using Excel, MATLAB, etc.):



10. Try changing the PID values (Kp, Ki, Kd) as well as the pressure setpoint.

```
//Define PID Controller
double currSetpoint, Input, Output;
double Kp = 10, Ki = 25, Kd = 0; //current PID setting, You may change this, max is 60 for each value.
PID pressPID(&Input, &Output, &currSetpoint, Kp, Ki, Kd, DIRECT);

//Define MPU-6050 IMU
MPU6050 mpu;
float yaw[3];
float accOffset[3];
float initAngle;
float acc2g = 16384;
float accX, accY, accZ;
int16_t ax, ay, az;

// Global Variables
float pidLimit=60;
float maxPressure = 300;
float atm;
String userInput;
bool initFlag=0;
bool actFlag=0;

// Timer Variables
unsigned long offsetTime;
unsigned long currTime;

void setup() {
  Serial.begin(115200);
  mpr.begin();

  pressPID.SetMode(AUTOMATIC);
  pressPID.SetSampleTime(10);
  pressPID.SetOutputLimits(0,pidLimit);

  currSetpoint = 100; //currently set to 100 mbar pressure. You may change this, max pressure is 300.
  Serial.println("Below is the order of the data columns:");
  Serial.println("Time [s],Pressure [mbar],Angle [deg]");
}
```

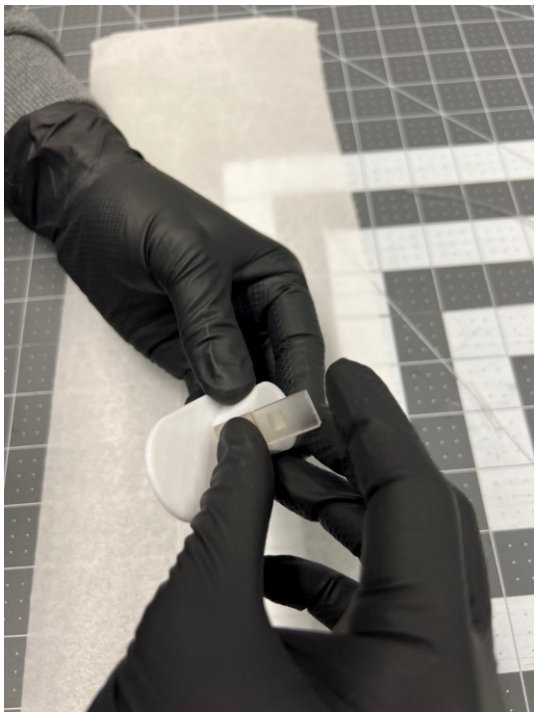
11. Shoot a video of your device working.
12. Think about what improvements can be made to the system.

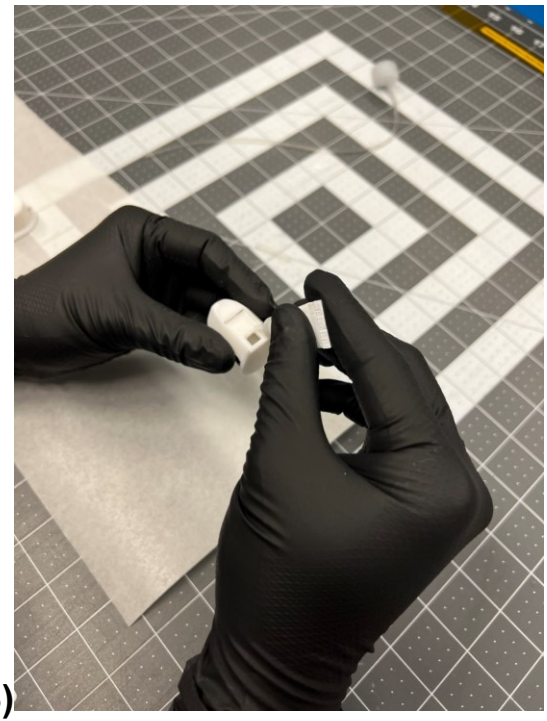
Upload the video, plot, and improvement suggestions to LEARN Dropbox.

Appendix F-A

Step by step images of assembling Soft Robotic Finger:

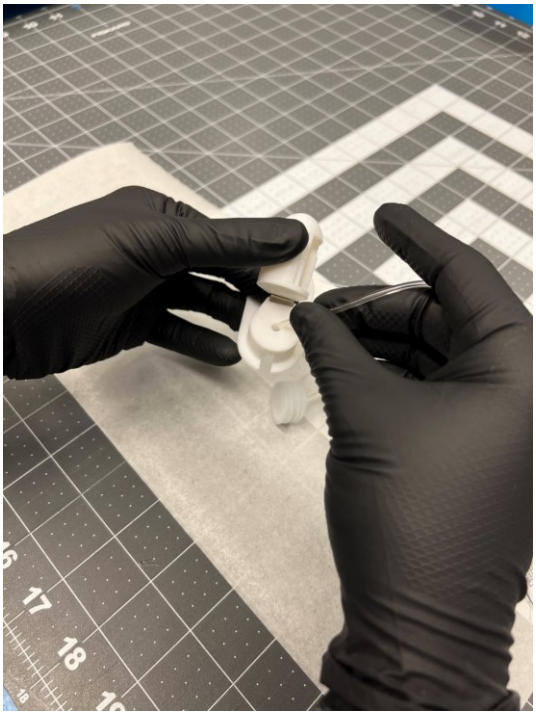
1) 

2) 

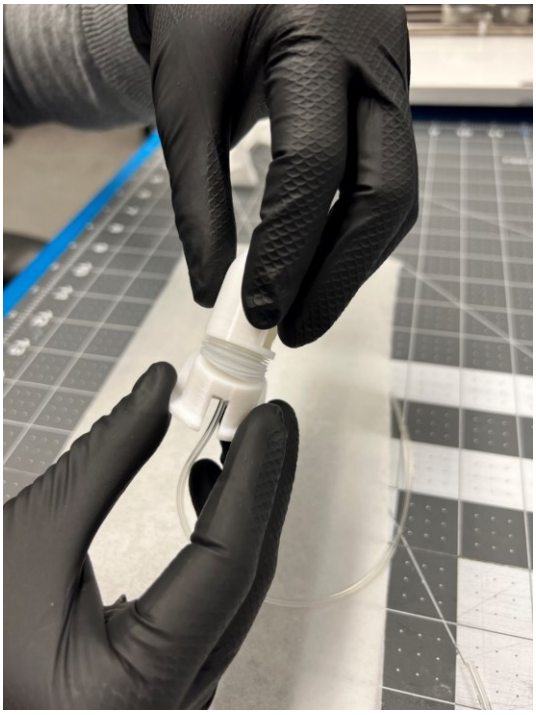
3) 

4) 

5) 

6) 

7) 

8) 

9) 

10) 

Appendix F-B

Pump and solenoid valve data sheets:

Micro Air Pump ZR370-02PM Specification

1. Scope of application

This specification is suitable for miniature air pump ZR370-2PM DC:4.5V DC:6V DC:12V DC:24V

2. Test conditions:

ambient temperature 20℃, relative humidity 65%RH is the standard

Test in the following environment: ambient temperature 5-45 ℃, relative humidity 30-80% RH

2-2 Test orientatior水平

2-3 load: air　　空氣 air

3. Performance:

3-1	Rated voltage	DC:4.5V	DC:6.0V	DC:12V	DC:24V
3-2	Use voltage	DC4.0V~5.0V	DC5.2V~6.5V	DC10.8V~13.2V	DC21.6V~26.4V
3-3	Load current	＜ 500mA	＜ 420mA	＜ 280mA	＜ 120mA

Note: The above load current refers to the current value when the rated voltage supply air pump is used to inflate to the highest pressure in a 100ml container.

3-4 Noise: Put a 5cm thick sponge under the pump body and place it 30cm away from noise meter

The suction pressure is measured from 0 to -40kpa under rated voltage.

Less than 65dB

3-5 Flow: ≥2.5 LPM

3-6 Maximum pressure: The maximum pressure value when the suction pressure is increased from 0 to stop when the rated voltage is used ≤ -55kpa

3-7 Operating temperature range:

The air pump works well between temperature 5℃ to 50℃ and humidity 30%RH to 80%RH.

3-8 Storage temperature range:

Keep the air pump in good condition between temperature -20℃ to 60℃

and humidity 30%RH to 85%RH.

4. Reliability test:

4-1 Low temperature characteristics:

After placing it at -20° C for 72 hours, take it out and place it at room temperature (20° C±5° C) for 2 hours. Re-test checks 3-3 3-4 3-5 3-6

The test results are normal.

4-2 High temperature characteristics:

After being placed at 60° C for 72 hours, take it out and place it at room temperature (20° C±5° C) for 2 hours. Re-test checks 3-3 3-4 3-5 3-6

The test results are normal.

4-3 High temperature and high humidity:

Leave out for 72 hours in an environment with a temperature of 60° C and a humidity of 80-85% and place it at room temperature (20° C±5° C) for 2 hours. Re-test checks 3-3 3-4 3-5 3-6

The test results are normal.

4-4 Low-temperature environment test:

After 5 hours at 5℃, there is no abnormality in the test at this temperature.

4-5 High temperature environment test:

There is no abnormality in the test at this temperature after 5 hours at 50℃.

4-6 Life test:

In a 500ml container, open for 10 seconds and stop for 5 seconds as a cycle test.

After 30,000, follow the test requirements of 3-3 3-4 3-5 3-6

Pressure within the attenuation range of 15%.

5. Other

5-1 Drop test: Use standard packaging methods and place them on the concrete floor from the front, side, and corners from a height of 50cm.

Its performance and structure are not abnormal in free fall.

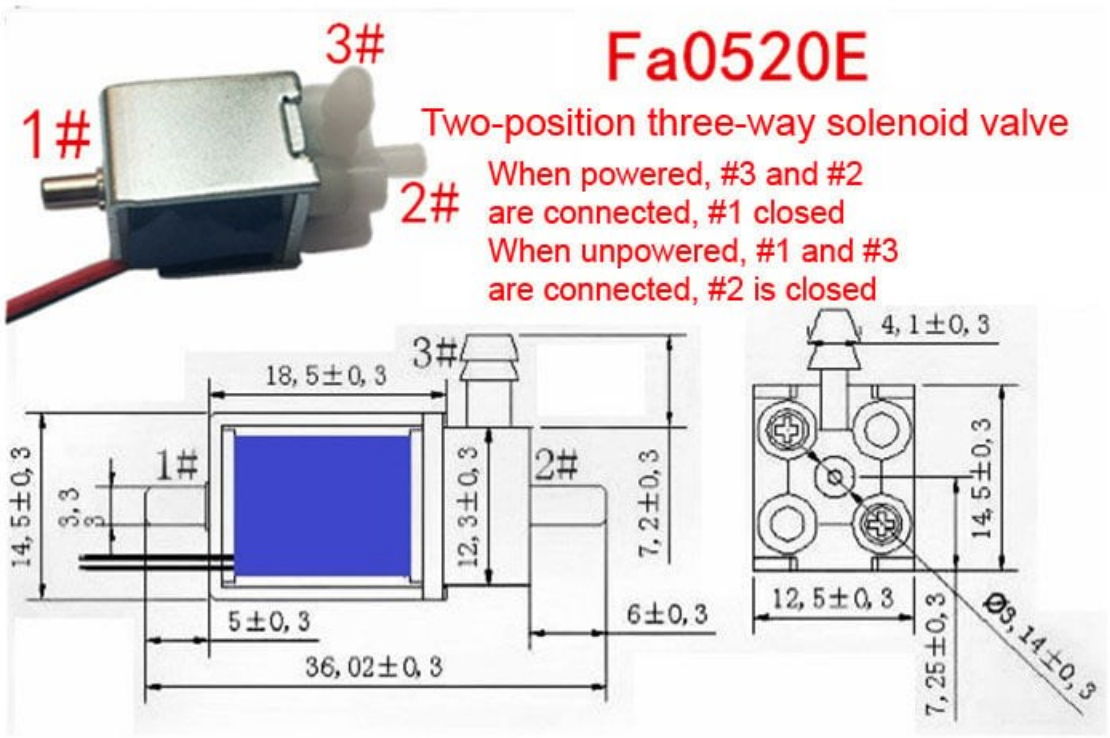
5-2 Abnormal test:

There is no burning or smoke after continuous power-on for 8 hours at the maximum voltage.

5-3 Motor terminal:

There is no abnormality with 0.3 kg weight and terminal load. The terminal must be soldered at a soldering iron temperature of 380℃, and the operation must be completed within 2S

5-4 Appearance: The product must not be damaged or dirty.



Appendix F-2

Lab 2: EMG Control of Soft Robotic Finger Prosthetics

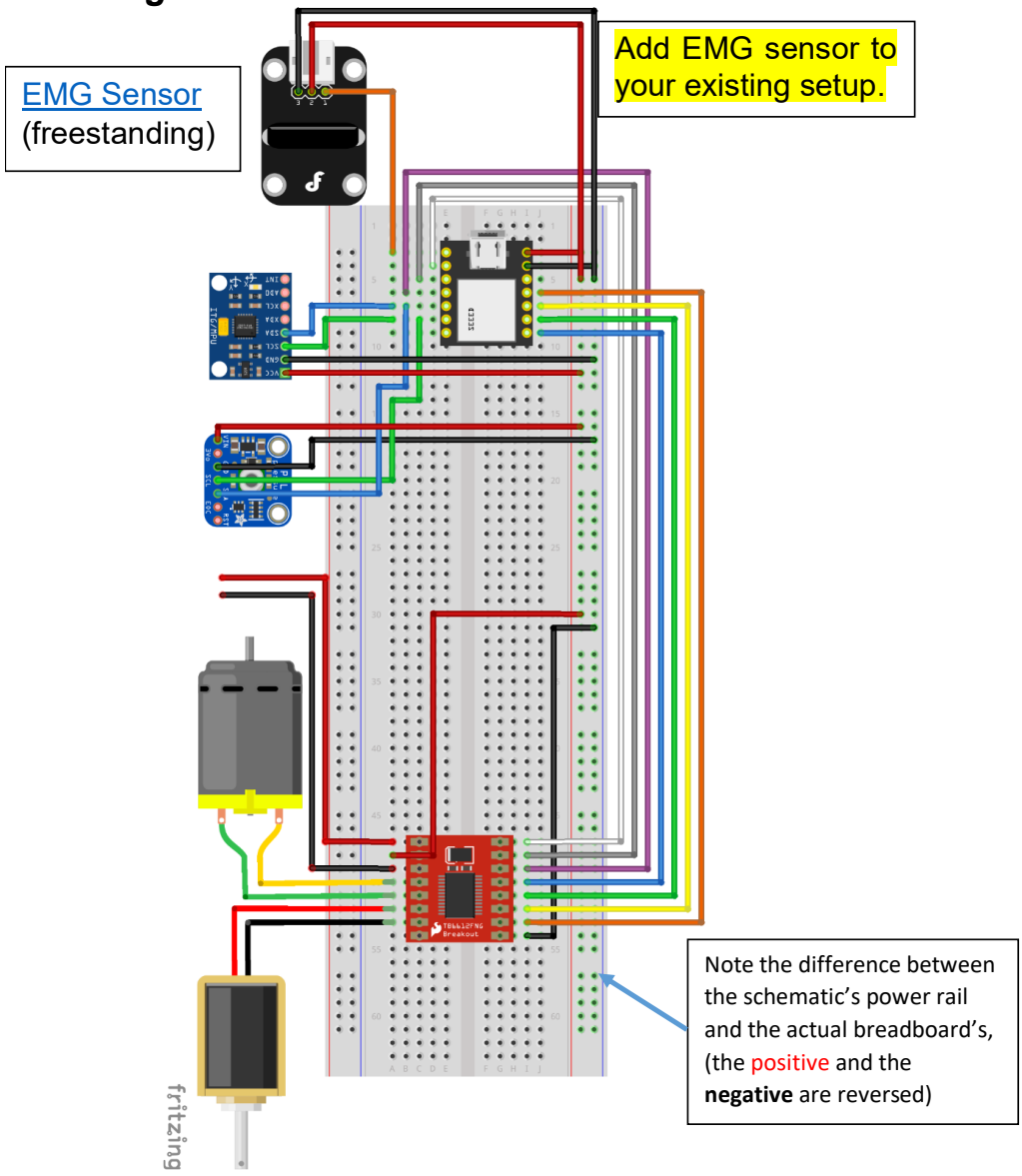
Purpose

Learn the control of soft-rigid hybrid robotic finger prosthetics using EMG sensor.

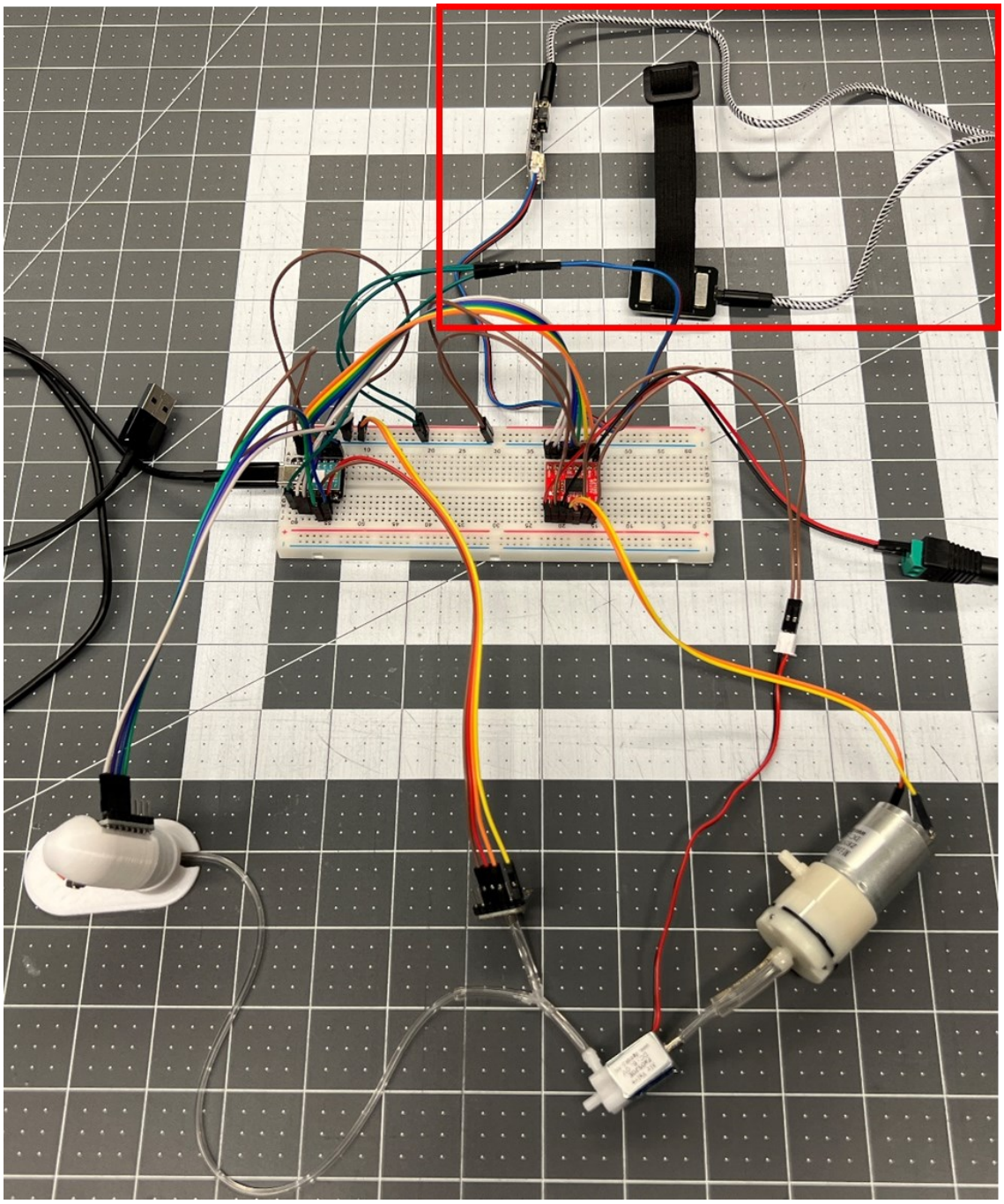
Step 1: *Components Overview*

Please refer to Lab 1 Manual.

Step 2: *Wiring*



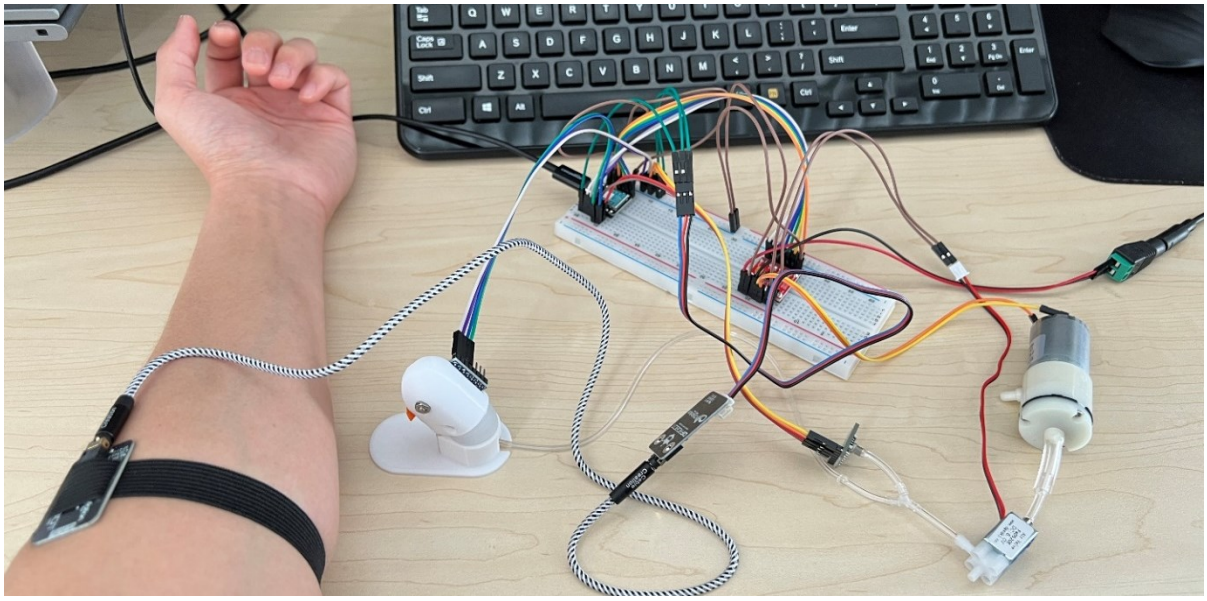
Step 3: ***Final Assembly***



Add EMG sensor (boxed in red) to your existing setup.

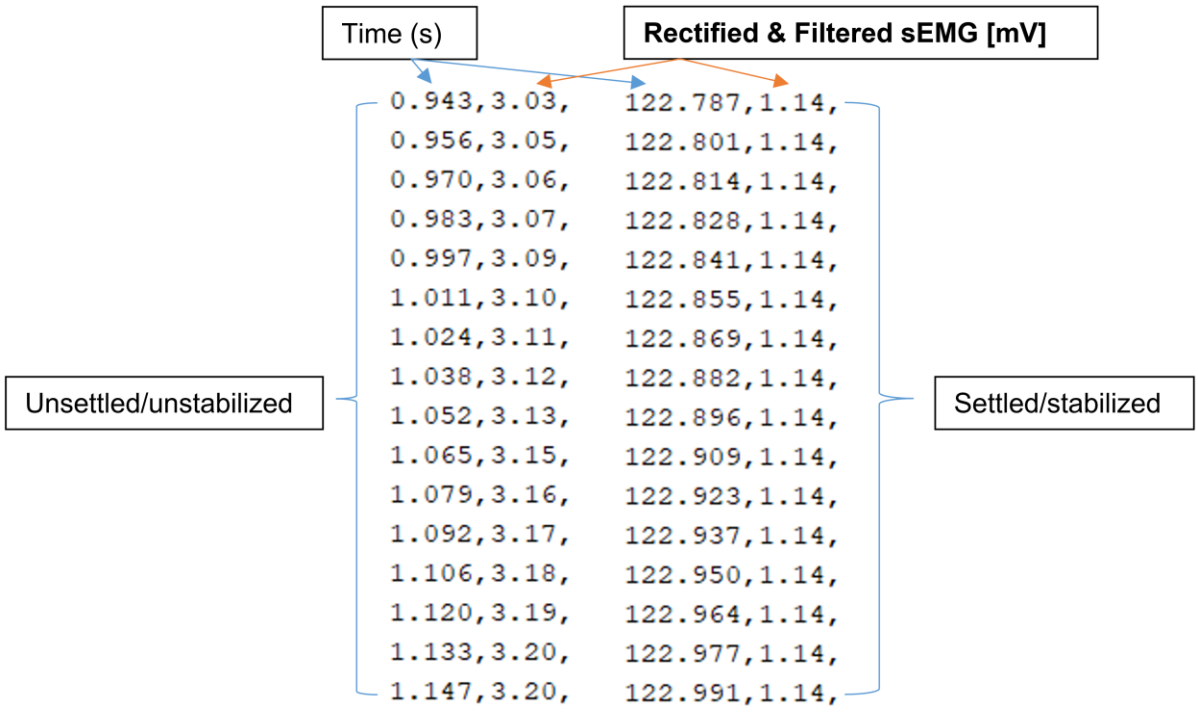
Step 4: ***EMG Electrodes Placement***

Strap EMG electrodes around the forearm or the upper-arm (i.e. belly of muscle and along the longitudinal midline of the muscle)



Step 5: *Software*

1. Compile and upload code to Seeeduino XIAO
    a) Download **20230123_IMU_PID_EMG_Educational.ino** from Learn and open it.
    b) Go through the code and review it.
    c) Select Seeeduino XIAO -> Tools -> Board -> Seeeduino XIAO
    d) Select the right COM Port -> Tools -> Port -> (Should just be the single port)
2. Compile the code first to see if everything's okay, then upload to Seeeduino XIAO.
3. Open Serial Monitor
4. Follow the prompt on the screen. Type the letter and hit "Enter" key to input.
5. Allow the EMG sensor to settle/stabilize (no longer dropping) by waiting a few minutes while arm is relaxed. (Look at the **Rectified & Filtered sEMG [mV]**, which is the last column. The first column is time in seconds).



6. Each person has a different **EMG threshold**. Look at your arm's relaxed and tensed (flex your muscle) **Rectified & Filtered sEMG [mV]** to determine the appropriate **threshold** (i.e., somewhere in-between relaxed and tense muscle EMG readings.)
   a) Above the threshold, the soft fluidic actuator will inflate. Under the threshold, the soft fluidic actuator will deflate.
   b) Go back to you code and change the **threshold**:

```
float threshold=100;
```

Default was 100 (which was way too high)

7. Now that the threshold is set, you want to see and record all the data including raw sEMG, Scaled sEMG, Rectified sEMG and angle.
8. Delete **ln** in Serial.println(",") and uncomment;

```
Serial.println(yk); //Serial.print(",");
```

Use ctrl+f to find these lines

9. Also, uncomment the following lines of code (**delete //**):

   Raw sEMG [mV]:

```
//Serial.print(sensorValue*(3.3/1023.0));Serial.print(",");
```

   Scaled sEMG [mV]:

```
//Serial.print(voltage);Serial.print(",");
```

Rectified sEMG [mV]

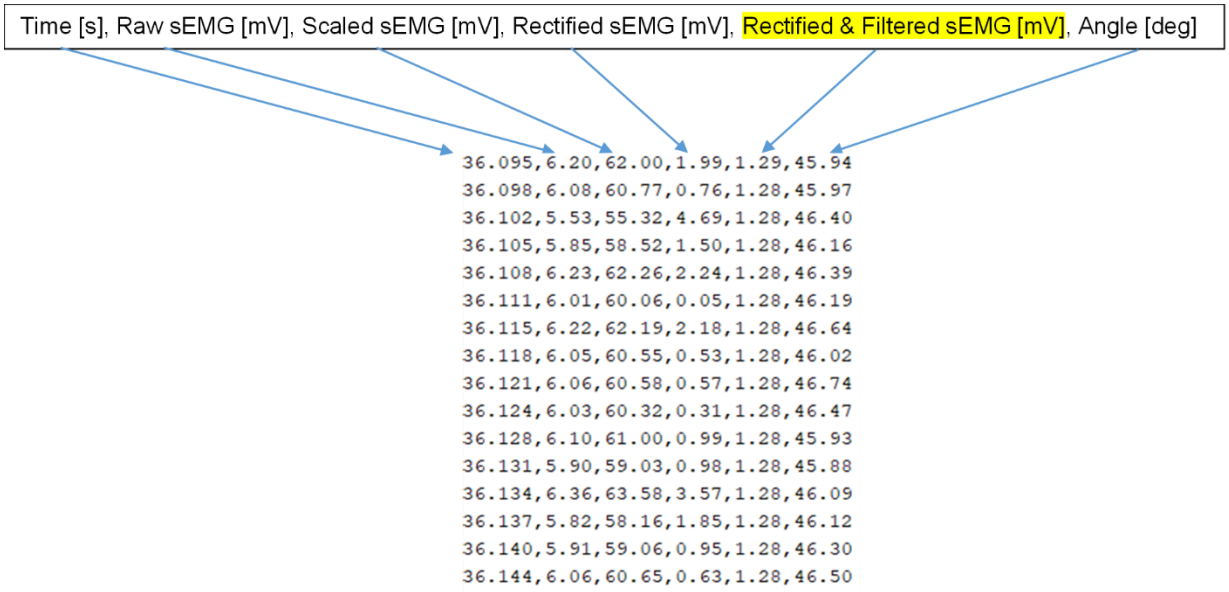
```
//Serial.print(rectified);Serial.print(",");
```

Angle [deg]:

```
//Serial.println(angleY);
```

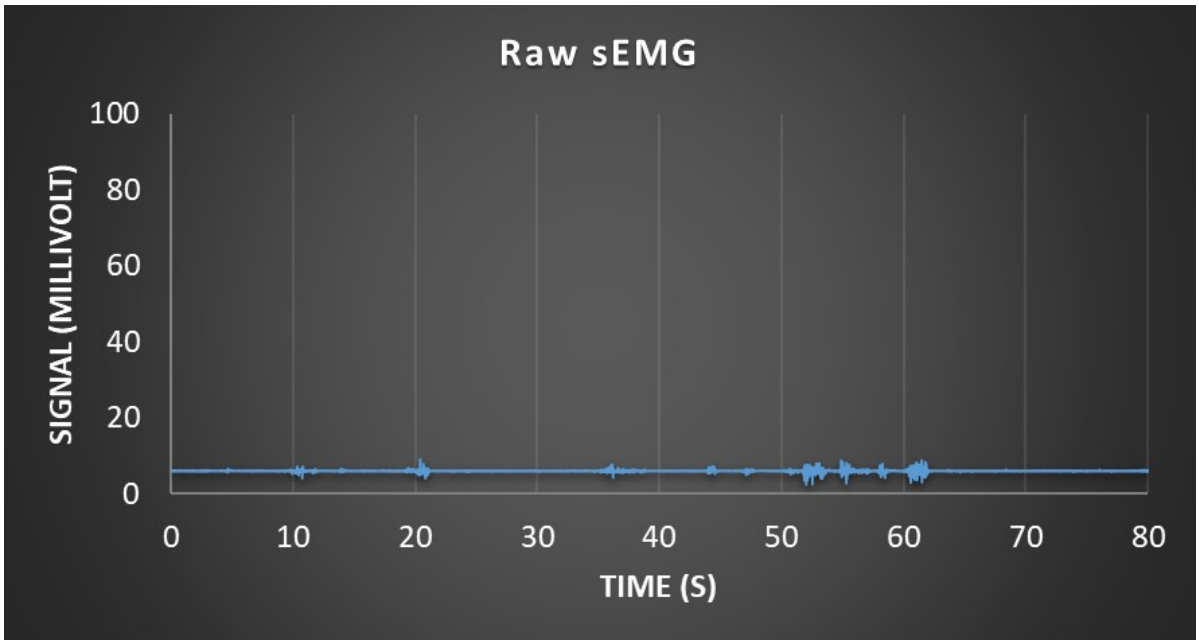
10. Re-upload the code (make sure the location of your EMG electrodes has not shifted)
11. Once again, wait until the EMG sensor has settled/stabilized (Rectified & Filtered sEMG [mV] no longer dropping).

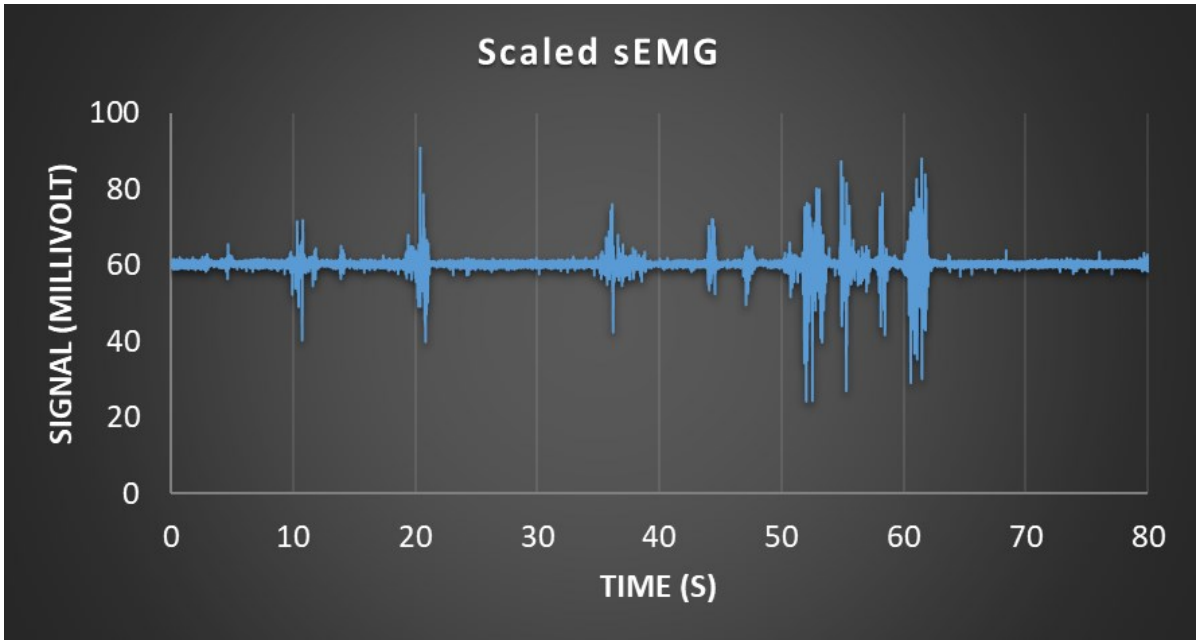
    NOTE each line in the serial monitor is now:

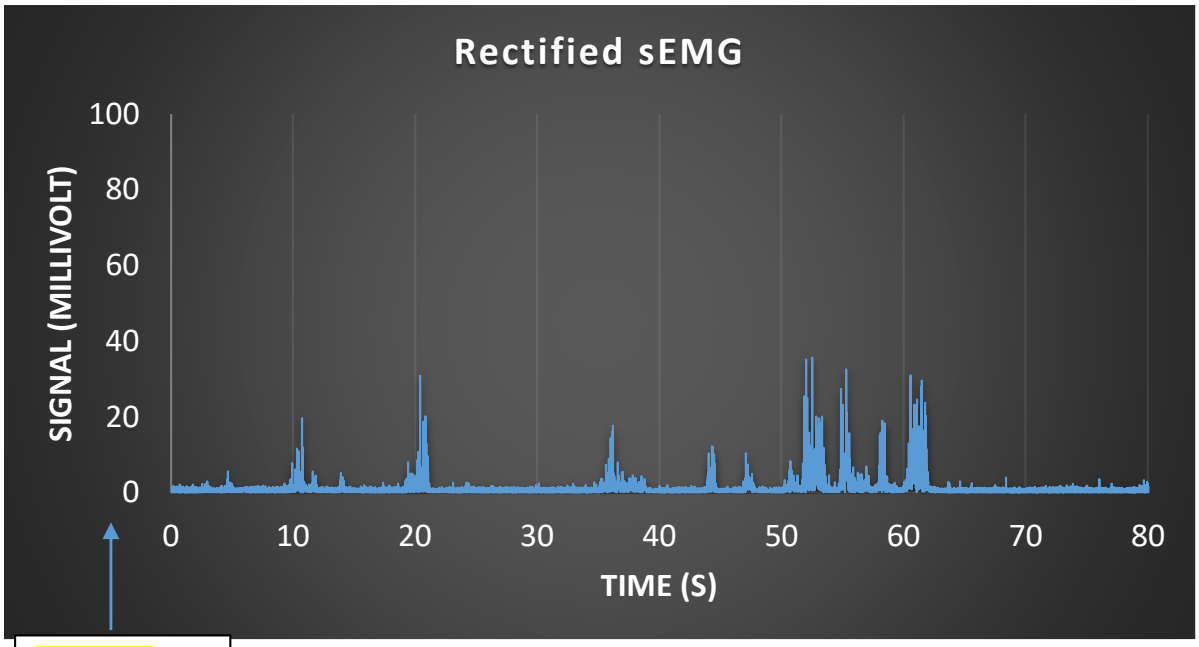


You may fine tune the threshold in the serial monitor by typing in 't' and hit "Enter" and type in the new threshold and hit "Enter". However, the threshold set this way will not be remembered after exiting the program.

12. Tense up your muscle which goes over the threshold and inflates the soft fluidic actuator, relax your muscle which falls below the threshold and deflates the soft fluidic actuator.
13. Take a video of your EMG controlling your device.
14. Try to get a plot like this (Uncheck Autoscroll and copy the output from serial monitor and plot it using Excel, MATLAB, etc.):

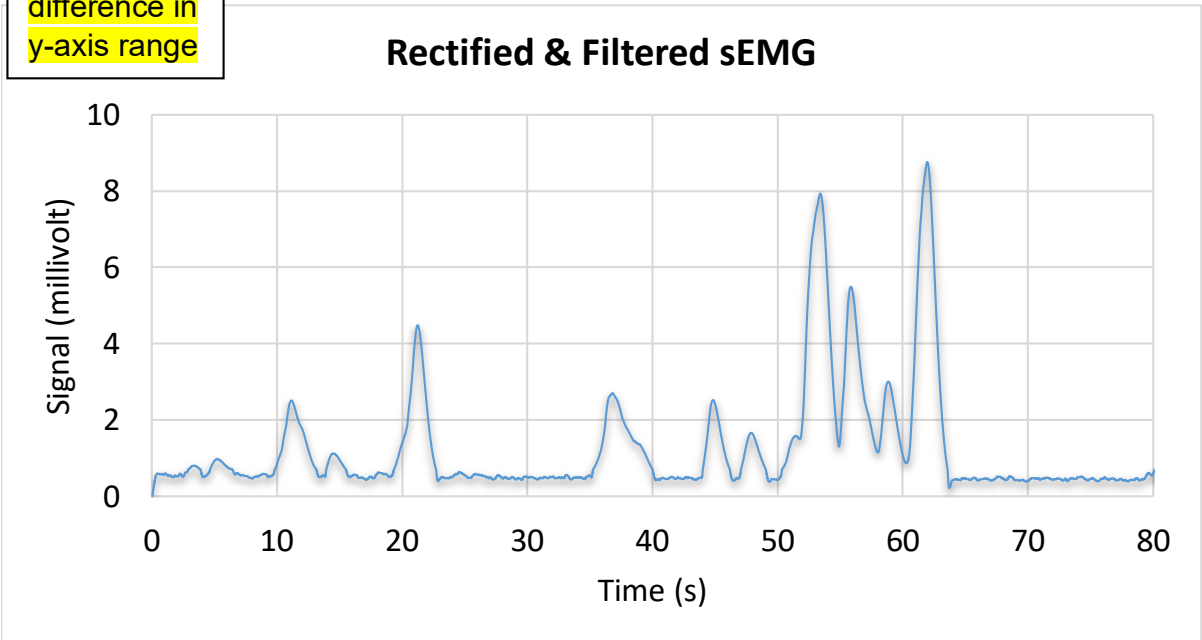

Raw sEMG
SIGNAL (MILLIVOLT)
100
80
60
40
20
0
0
10
20
30
40
50
60
70
80
TIME (S)

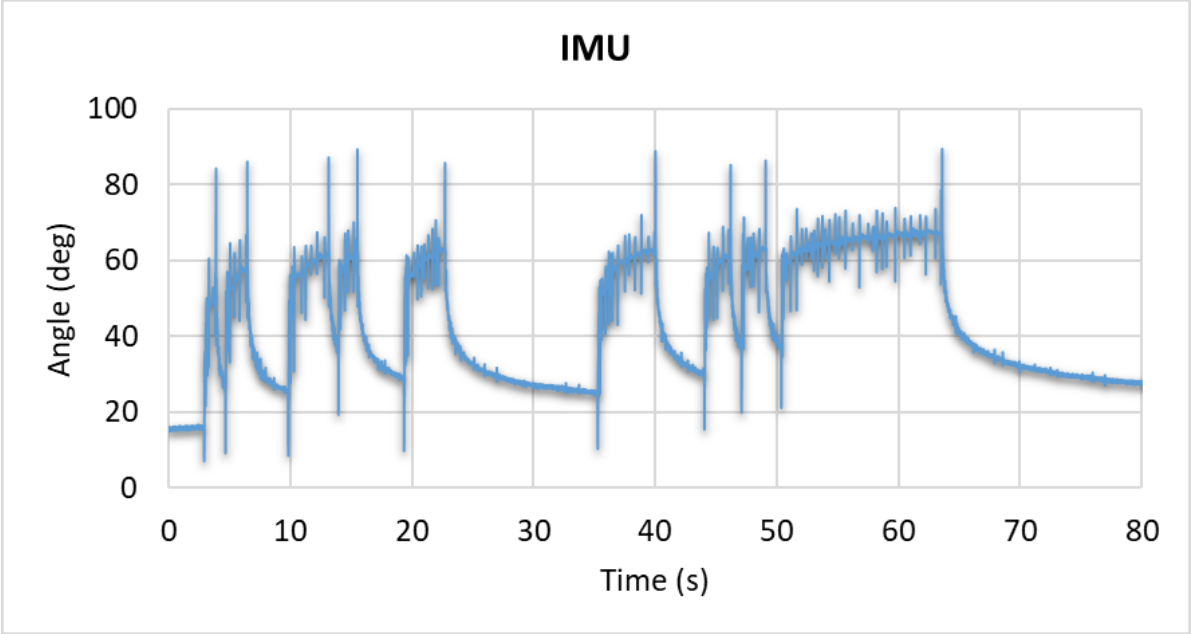

Scaled sEMG
SIGNAL (MILLIVOLT)
100
80
60
40
20
0
0
10
20
30
40
50
60
70
80
TIME (S)



Note the difference in y-axis range

Note the difference in y-axis range





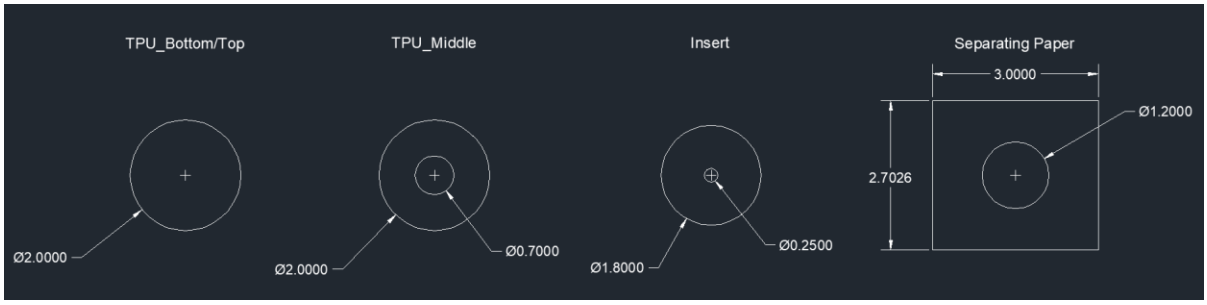
2. Why does the EMG take so long to settle/stabilize?
3. What is the benefit of this type of on/off control, and would a proportional control (i.e., different EMG signal amplitudes to different pressures and/or inflation/deflation rates) be better? Why?
4. What is the advantage/disadvantage of soft fluidic actuators versus motor-based systems?

Upload the video, plots, and your answers to the questions to LEARN Dropbox. These are for participation marks.

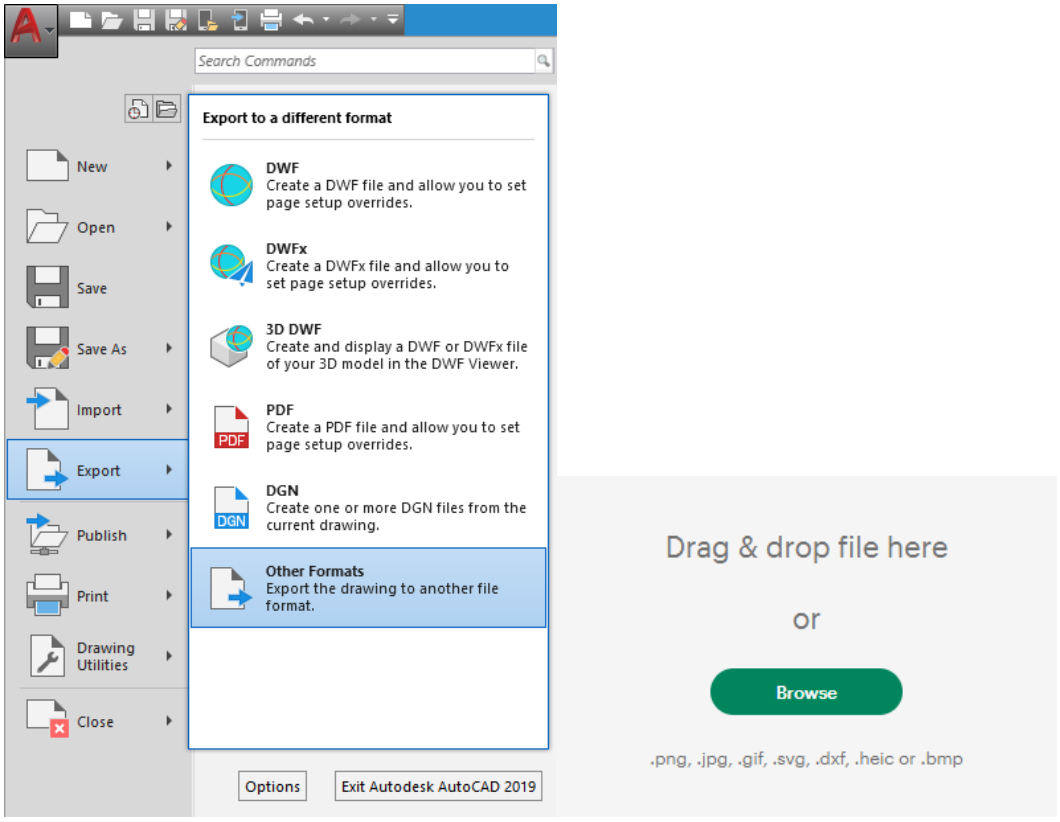
Appendix F-3

Step-by-Step Guide for Fabricating Low-Profile Bellows-Style Soft Fluidic Actuators

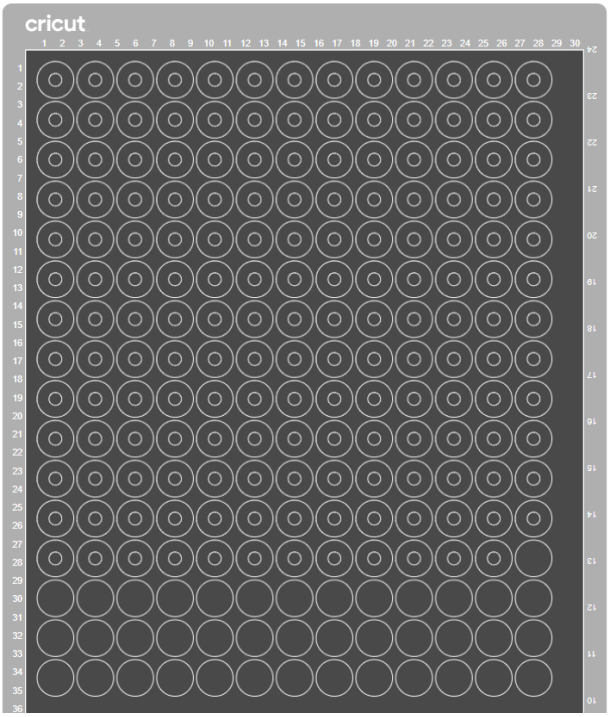
1. **Design the shapes of the inserts in AutoCAD.**



2. **Export design to Bitmap (.bmp) file format and import into Cricut Design Space.**

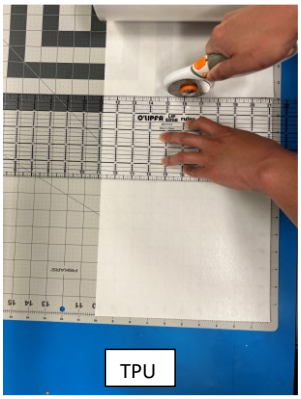


3. **In Cricut Design Space, check the dimensions and quantity.**

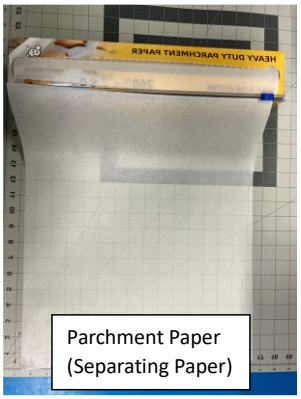


4. **Cricut Setup (same for all sheets, as blade gets dull, increase pressure or change blade accordingly).**
   - Blade type: Fine-Point Blade
   - Material: Adhesive Sheet, Double-sided
   - Pressure: Default\

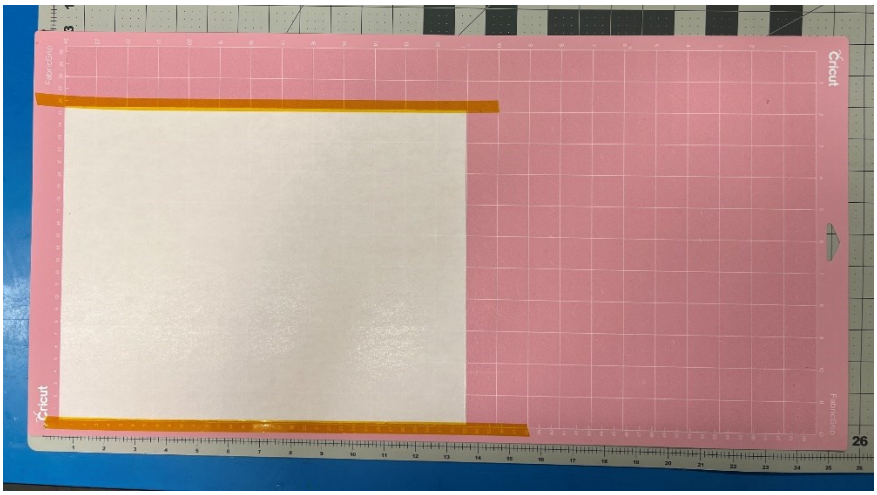
5. **Cut the TPU, Teflon, and separating paper roll into the required size.**
   User rotary cutter, cut on cutting board and use ruler for reference.







6. **Attach the material onto the cutting board (same for all sheets).**
   - Any type of board works.
   - Liner/backing side down.
   - Tape down edges as cutting board loses adhesive strength overtime.

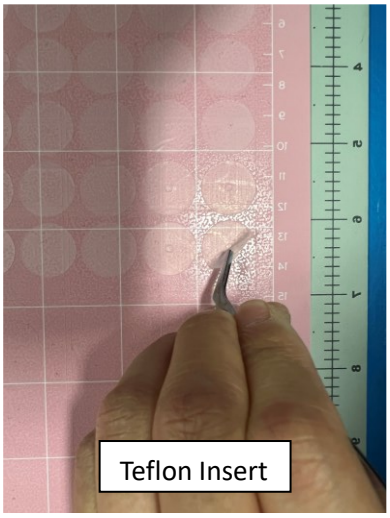


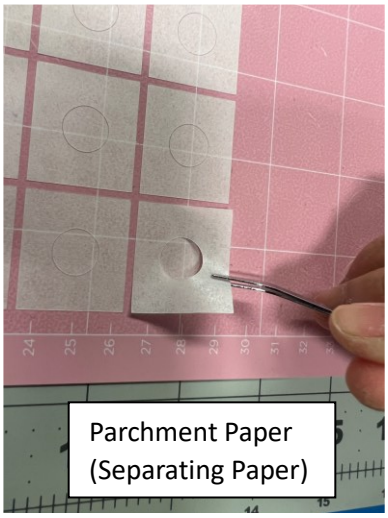
7. **Load the cutting board + material into the Cricut Maker and click physical GO button to start the job (same for all sheets).**
   - Make sure the job start correctly and click PAUSE button if needed.



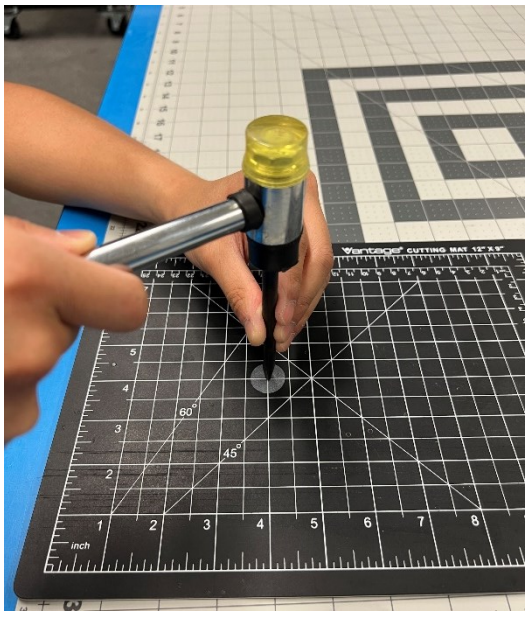
8. **Peel off individual sheets.**
    - Tweezers may help the peeling process.
    - Store sheets in a container or bag.

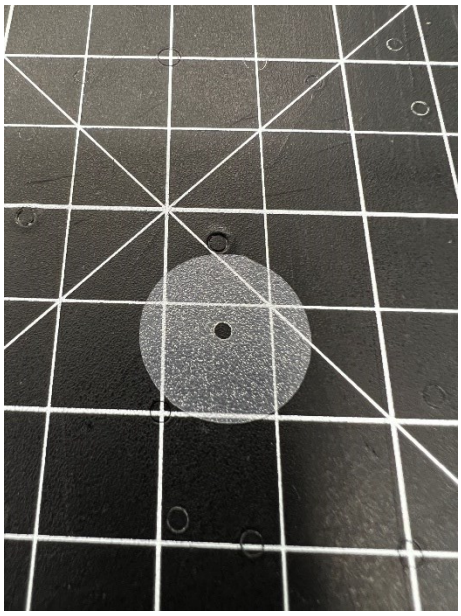




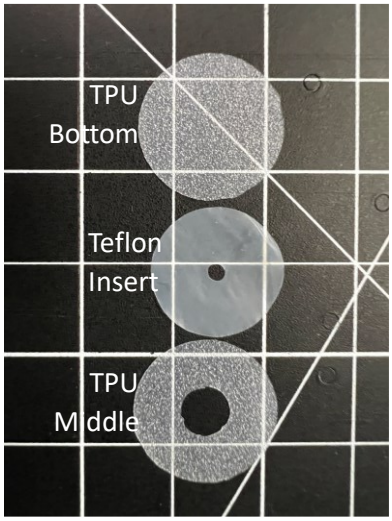


9. **Hole punch the TPU top sheet**
    - Use a cutting board and a mallet with a 2mm hole punch.
    - Hole punch in the center of the sheet. Can use the gridlines on the cutting board to center the hole punch.
    - Place the hole punch as vertically straight as possible.

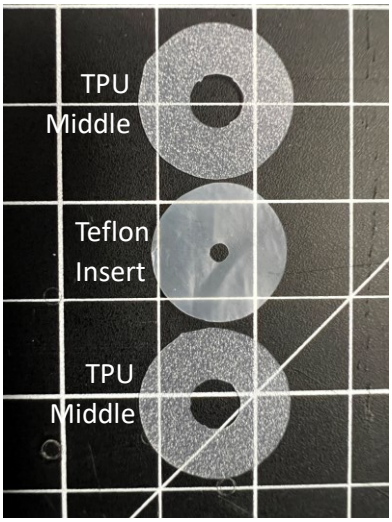




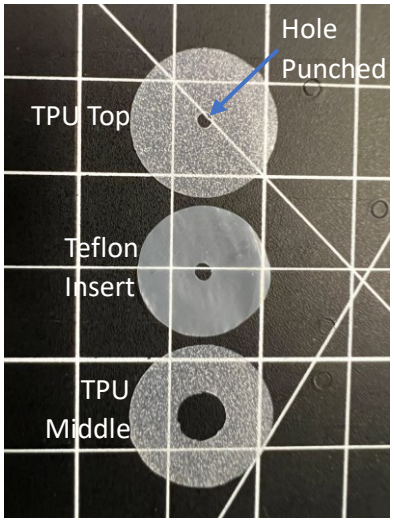
10. Heat press each layers individually.



Bottom Layer



Middle Layer

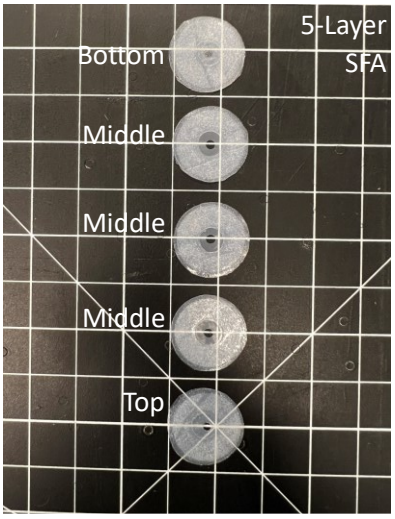


Top Layer

- Turn on Cricut Heat Press to lowest heat setting.
- Stack the sheet accordingly for each layer.
- Heat press each half of sheet separately, overlapping the pressed area slightly to ensure all of the sheet has been pressed. Each half press lasts at least 10 seconds. This is done is to allow easier delamination of the sheet from the heat press.
- Place Teflon sheet on the bottom of the heat press to prevent TPU sticking to the heat press. Similarly, place a Teflon sheet or parchment paper on the table to prevent TPU from sticking to the table.





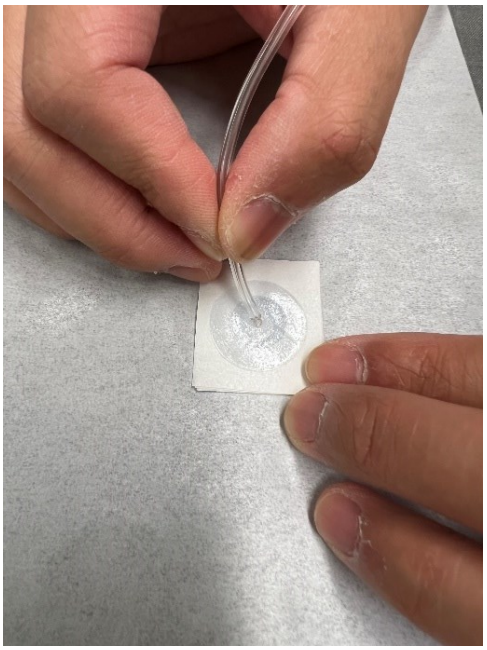


11. Stack the layers separated by the parchment/separating paper and heat press.

- Align the layers concentrically.
- Stack the layers right after heat pressing individual layers as the surface of the TPU remains a bit tacky allowing aligning the layers easier and prevent layers from shifting.
- Heat press each half of the stack for at least 20 seconds. Overlap the heat press area to ensure the entire surface has been heat pressed.
- After removing the heat press, press the stack with hand or fingers to ensure that all the layers are bonded. The reason this is done is because sometimes when lifting the heat press, certain layer may come apart a little bit.

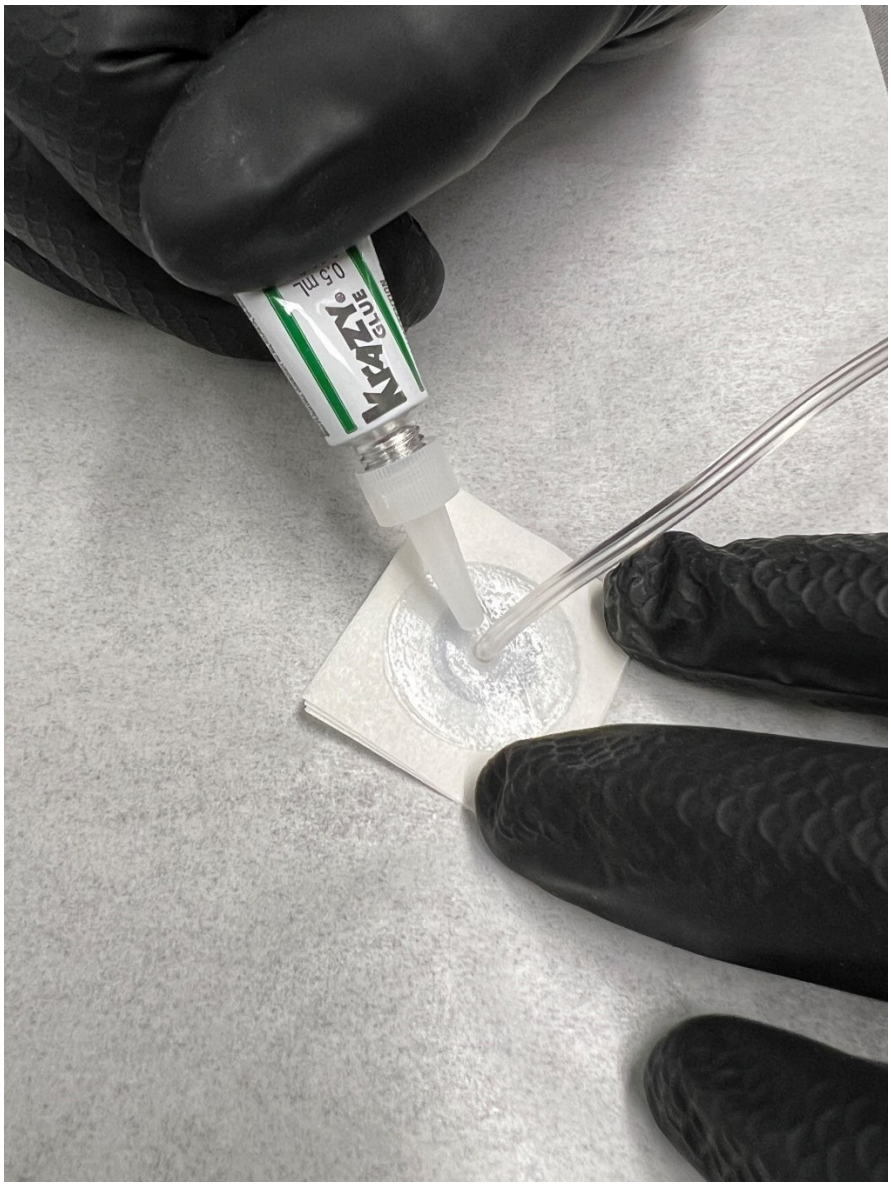


12. Insert the 1/32” ID by 3/32” OD tubing into the stack.



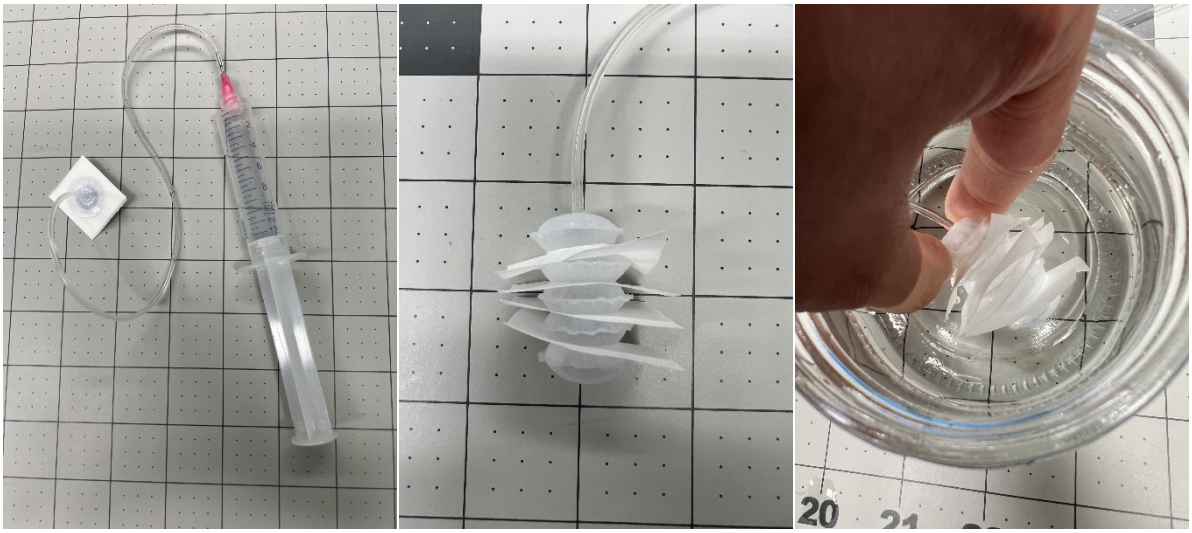
13. Apply glue to the bonding surfaces around the tubing.

- Do not apply too much, just enough to surround the tubing.
- Let the glue cure for at least 10 minutes. Cyanoacrylate adhesives cure when exposed to moisture. Therefore, to improve curing speed, one can blow moist breath onto the glued surfaces.



14. Inflate the SFA with a syringe (10 ml) with a pink stainless steel tip (gauge 20).

- Ensure the SFA does not leak by conducting a leakage test underwater. Do not tear off the parchment/separating paper yet.
- Fix any leakage by applying a bit more glue or heat press with a small TPU patch.



15. Tear off the parchment/separating paper. The SFA is ready for assembly with the rest of the components.



Appendix F-4

This appendix contains all the design and software files, which can be freely accessed under the Creative Commons license (CC BY 4.0) for Chapter 9.

The file name is “Chapter 9 files.zip”.

If you accessed this thesis from a source other than the University of Waterloo, you may not have access to this. You may access it by searching for thesis at http://uwspace.uwaterloo.ca.

Appendix F-5

This appendix is a video that shows a compilation of student teams’ submitted videos of their working prosthetic finger controlled by EMG for Chapter 9.

The file name is “Chapter 9 Video.mp4”.

If you accessed this thesis from a source other than the University of Waterloo, you may not have access to this. You may access it by searching for thesis at http://uwspace.uwaterloo.ca.